①

AGARD

ADVISORY GROUP FOR AEROSPACE RESEARCH & DEVELOPMENT

7 RUE ANCELLE 92200 NEUILLY SUR SEINE FRANCE

AGARD REPORT No.76

Special Course
on
Aerothermodynamics of
Hypersonic Vehicles

DTIC
ELECTE
OCT 11 1989
S B D

NORTH ATLANTIC TREATY ORGANIZATION

DISTRIBUTION AND AVAILABILITY
ON BACK COVER

89 10 11038

NORTH ATLANTIC TREATY ORGANIZATION

ADVISORY GROUP FOR AEROSPACE RESEARCH AND DEVELOPMENT

(ORGANISATION DU TRAITE DE L'ATLANTIQUE NORD)

AGARD Report No.761

SPECIAL COURSE

ON

AEROTHERMODYNAMICS OF HYPERSONIC VEHICLES

THE MISSION OF AGARD

According to its Charter, the mission of AGARD is to bring together the leading personalities of the NATO nations in the fields of science and technology relating to aerospace for the following purposes:

— Recommending effective ways for the member nations to use their research and development capabilities for the *common benefit of the* NATO community;

— Providing scientific and technical advice and assistance to the Military Committee in the field of aerospace research and development (with particular regard to its military application);

— Continuously stimulating advances in the aerospace sciences relevant to strengthening the common defence posture;

— Improving the co-operation among member nations in aerospace research and development;

— Exchange of scientific and technical information;

— Providing assistance to member nations for the purpose of increasing their scientific and technical potential;

— Rendering scientific and technical assistance, as requested, to other NATO bodies and to member nations in connection with research and development problems in the aerospace field.

The highest authority within AGARD is the National Delegates Board consisting of officially appointed senior representatives from each member nation. The mission of AGARD is carried out through the Panels which are composed of experts appointed by the National Delegates, the Consultant and Exchange Programme and the Aerospace Applications Studies Programme. The results of AGARD work are reported to the member nations and the NATO Authorities through the AGARD series of publications of which this is one.

Participation in AGARD activities is by invitation only and is normally limited to citizens of the NATO nations.

PREFACE

With new ventures in the hypersonic domain moving forward on both sides of the Atlantic — HERMES in Europe and the X-30 in the United States — it seemed timely to bring together researchers and engineers working in this field, as well as newcomers, for the purpose of presenting an up-to-date summary on continuum hypersonic flows with heat transfer.

Following a review of basic principles including real gas effects, a series of lectures were presented on experimental and computational methods specific to hypersonic flows. In other words, stress was placed on measurement techniques developed primarily for flows with heat transfer, chemical reactions, strong shocks, compressible boundary layers, etc. Both surface measurements and flow field measurements, including species concentration techniques, were discussed. The same spirit governed the lecture on computational methods: stress was placed on the new problems in CFD posed by high speeds and chemical reactions. The course finished with state-of-the-art reviews on three critical flow problems: transition flow problems: transition to turbulence, interactions between shocks and boundary layers, and shock/shock impingement.

The presentations and papers were characterized by an unusually high level in terms of both clarity and quality; this ensures that the present volume will serve as useful reference for some years to come. I use this occasion to express once again my sincere thanks to all the lecturers.

Thanks are extended also to the lecturers' organizations: the Wright Aeronautical Laboratories, USAF; the University of Maryland's College of Engineering; Complere Inc.; Calspan Corp.; the DFVLR-Göttingen; and both ONERA-Chalais Meudon and ONERA-CERT. Without the willingness of these organizations to allow the lecturers sufficient time to prepare their material, these courses could not be offered.

This Special Course was co-sponsored by the AGARD Fluid Dynamics Panel and the von Kármán Institute for Fluid Dynamics; it was implemented by the von Kármán Institute.

John F. WENDT,
Special Course Director

* * *

Vu le rythme d'avancement des nouveaux projets entrepris dans le domaine de l'hypersonique des deux côtés de l'Atlantique, c'est à dire le projet HERMES en France et le projet X-30 aux Etats-Unis, il a paru opportun de réunir les chercheurs et les ingénieurs travaillant dans ce domaine, ainsi que d'autres personnes qui découvrent ce sujet, dans le but de présenter une revue des connaissances dans le domaine des écoulements hypersoniques en régime continu avec transfert thermique.

Le Cours a commencé par un rappel des principes de base, et entre autres les effets du gaz réel, suivi d'une série de conférences sur les méthodes expérimentales et les méthodes de calcul spécifiques aux écoulements hypersoniques. En d'autres termes, l'accent à été mis sur les techniques de mesure développées principalement pour les écoulements avec transfert thermique, les réactions chimiques, les chocs forts, les couches limites compressibles etc... Les débats ont porté sur les mesures de surface ainsi que sur les mesures du champ d'écoulement, y compris les techniques de concentration des espèces. Le même esprit a présidé la conférence sur les méthodes de calcul: cette fois, l'accent a été mis sur les nouveaux problèmes posés dans le domaine du calcul en dynamique des fluides par les vitesses élevées et les réactions chimiques. Le cours s'est terminé par des revues de l'état de l'art concernant trois problèmes critiques de l'écoulement: la transition à la turbulence, les interactions entre les chocs et les couches limites et les contacts choc/choc.

Les présentations et les communications ont été caractérisées par un niveau exceptionnel de clarté et de qualité, et il s'ensuit que le présent volume servira d'ouvrage de référence dans ce domaine pour des années à venir. Je saisis l'occasion pour exprimer une nouvelle fois mes remerciements très sincères à tous les conférenciers.

Nos remerciements sont également dûs aux organisations dont dépendent les différents intervenants: les Wright Aeronautical Laboratories, USAF; l'University of Maryland College of Engineering, Complere Inc., Calspan Corp., DFVLR-Göttingen, l'ONERA Chalais Meudon et l'ONERA-CERT. Sans la coopération des ces organismes, qui ont bien voulu libérer les conférenciers le temps nécessaire pour la préparation des conférences, ces cours n'auraient pas pu avoir lieu.

Ce cours spécial a été présenté par l'Institut von Kármán, sous l'égide conjoint du Panel AGARD de la Dynamique des fluides et l'Institut von Kármán.

John F. WENDT
Directeur de Cours Spécial

iii

SPECIAL COURSE STAFF

Special Course Director: Professor J.F.Wendt
Head, Aeronautics/Aerospace Dept.
von Kármán Institute for Fluid Dynamics
72 Chaussée de Waterloo
1640-Rhode-Saint-Genèse
Belgium

Mr D.Arnal
ONERA—CERT
BP 4025
31055 Toulouse Cedex
France

Prof. J.D.Anderson, Jr.
University of Maryland
College of Engineering
Dept. of Aerospace Eng
Glenn L.Martin Inst. of Technology
College Park, MD 20742
U.S.A.

Dr B.Aupoix
ONERA-CERT-DERAT
2 Ave E.Belin
31400 Toulouse
France

Dr D.Boyer
Principal Aerodynamicist
Calspan Corporation
POB 400
Buffalo, N Y 14225
U.S.A.

Mr J.M.Delery
ONERA
8 Rue des Vertugadins
92190 Meudon
France

Dr F.K.Owen
Complere Inc.
POB 1697
Palo Alto, CA 94302
U.S.A.

Dr W.Kordulla
DFVLR SM-TS
Bunsenstrasse 10
3400 Göttingen
Federal Republic of Germany

Mr R. Neumann
AFWAL/FIMG
Wright-Patterson AFB
Ohio 45433
U.S.A.

LOCAL COORDINATOR

Professor J.Wendt
von Kármán Institute for Fluid Dynamics
Chaussée de Waterloo 72
B-1640 Rhode-St-Genèse
Belgium

AGARD REPRESENTATIVE

Mr M.C.Fischer
Fluid Dynamics Panel Executive
AGARD
7 rue Ancelle
92200 Neuilly sur Seine
France

CONTENTS

Missions and Requirements
by
Richard D. Neumann
Technical Manager for Aerothermodynamics
Air Force Wright Aeronautical Laboratories
Wright-Patterson Air Force Base, Ohio 45433 USA

Hypersonic Systems

The hypersonic domain is a large and poorly defined regime in which many potential systems can operate. These systems can vary widely from one another in both characteristics and required technologies for their implementation. In the United States there are at least five points of focus in hypersonics, each with a distinctive product and each pursuing that technology necessary to develop the product. These five study areas are (1) the study of lifting entry from low Earth orbits; (2) the study of efficient return from high energy orbits, the so called AOTV focus. (3) the study of ballistic entry. (4) the study of ballistic defense and (5) the study of entry into the atmospheres of other planetary bodies. Beyond these major catagories, there are many sub-catagories including the design of hypervelocity munitions and the study of hypervelocity anti-aircraft techniques. While this lecture will center on the evaluation of lifting, orbital entry from low Earth orbit, the point to be made is that this selected class of vehicles defines only one class of technologies; others are equally important to those who define hypersonic systems differently.

The hypersonic envelope is poorly defined. It starts at a Mach number like 5 and extends to a Mach number or velocity as high as need, the imagination and technology will allow. Likewise the envelope starts at the extent of the sensible atmosphere (a debatable dimension within the engineering connotation) and extends downward to the surface of a planet (normally but not exclusively Earth). Within that broadly defined environment the vehicle scale and angle of attack are important modifiers in the characteristics of hypersonic systems.

Operating angle of attack defines the fundamental relationships between the level of pressure drag and viscous drag forces; a significant parameter in understanding the complexity of the methodologies employed in the development process for such configurations. This relationship is modified by scale of the configuration. Angle of attack also impacts the relative importance of real gas effects on both the aerodynamics and materials aspects of the configuration. This lecture will concentrate on the requirements implicit in the design of lifting hypersonic systems as the operating angle of attack and the scale of these systems are systematically varied.

There are several fundamentally different hypersonic systems which operate as entry vehicles with increasing aerodynamic efficiency. They are (1) the ballistic systems employed by the Department of Defense (separated from the ballistic systems of years ago by their performance characteristics); (2) maneuvering re-entry vehicles; (3) low L/D lifting systems (separated from high L/D lifting systems by the relationship between pressure and viscous forces); (4) high L/D lifting systems which are viscous dominated systems and (5) Aerodynamic orbit transfer vehicles, AOTV's. Each of these has different developmental problems and a different technological base.

Ballistic systems, in general, are dominated by turbulent flow and a high degree of interaction between the imposed heating and materials response. They ablate! Although they are generally geometrically simple configurations, three dimensional effects are strong. Scale is small and the demand for autonomous accuracy is high requiring a substantial knowledge base be established in the development cycle.

Maneuvering reentry vehicles integrate the features of a ballistic system with the maneuverability of a lifting body. Maneuvering is employed for both terminal evasion and as a means of improving overall system accuracy. Terminal evasion may be required to enhance penetration against a potential adversary while system accuracy can be improved by performing navigation updates, either prior to or during reentry, and then maneuvering to correct for trajectory errors experienced during the earlier flight phase. See Harris, 1980.

Low L/D lifting systems have flown extensively and many of their technological problems have been evaluated and documented. Figure 1 demonstrates an Air Force low L/D vehicle, the SV5-D, which flew as a research project in the mid 1960's. Both the Gemini and the Apollo, seemingly ballistic shapes, as well as the Rockwell Space Shuttle are examples of such low L/D lifting entry systems. See Lukasiewicz, 1973. These systems are dominated by a small contribution of viscous effects on the aerodynamics and aerodynamic heating of the vehicle. A direct result of being pressure dominated is that developmental tests can, for the most part, be conducted in 'representative' hypersonic wind tunnels without the need for more exact duplication of flight characteristics.

Since the L/D of a system is directly related to the angle of attack of the configuration, low l/D shapes operate at higher angles of attack. The Rockwell Space Shuttle operates at 40 degrees angle of attack. At these high angles of attack and at the velocities of orbital entry, chemical activity within the local flow field is created by the large blunt nose of the configuration and sustained by the lower surface of that

class of configurations. Chemical effects can therefore be generally important on this class of configurations.

Hypersonic systems within the Air Force and NASA tend to be different because the design criteria stress different features. In broad terms, Air Force systems fly in regions of the atmosphere where it is difficult to operate and not necessarily where operating efficiencies are the highest nor of primary importance. This is also true for combat aircraft where the goal often is to maneuver decisively at transonic conditions, it is true for ballistic missile systems where the goal is to re-enter the atmosphere with an extremely low drag body which will decelerate at very low altitudes and it is true of hypersonic lifting entry systems which, for operational reasons, may stress aerodynamic efficiency during the entry process. The Air Force is driven by a different set of design criteria. In many cases this changes the design process somewhat. What may be a design goal for a conceptual NASA system (perhaps minimizing the aerodynamic heating) could become only a design constraint in an Air Force system (maximizing aerodynamic performance of a system design within the limits of available materials).

High L/D lifting systems operate at still lower angles of attack and are thus dominated by viscous contributions to the overall drag which is equal to or higher than the corresponding pressure contributions. As a result, developmental wind tunnel testing requires a higher degree of flight simulation. Parameters relating the Mach number and Reynolds number of flow, the so called 'V BAR parameters', must be simulated in testing rather than to merely generate 'representative' hypersonic data defined through Mach number independance. The importance of viscous effects in the observed aerodynamics and aerothermodynamics of the vehicle add a new complexity to the design process of such a configuration. This complexity is balanced by the ability to fly more efficiently within the atmosphere and/or achieve higher cross range during atmospheric entry. The importance of chemical activity within the local flow field for such configurations is far more problematical. High L/D configurations demand very small blunt nose shapes in order to reduce the drag and thus generate the required aerodynamic characteristics. The result is that the amount of high energy, chemically active flow processed is very small and the degree of chemical activity generated in the nose region cannot be sustained by the very low angle of attack compression surfaces of the configuration. Figures 2 and 3 indicate designs of hypersonic high L/D vehicles. The configuration in figure 3 is the Boost Glide vehicle, BGV, which was studied within the Flight Dynamics Laboratory.

Aerodynamic Orbit Transfer Vehicles, (AOTV's) operate in a confined velocity range bounded by the orbital velocities of the initial state (normally a high energy stationary orbit) and a low energy, low Earth orbit. For the most part, these AOTV configurations are low L/D configurations with substantial chemical activity and that chemical activity consists both of chemical dissociation (indicative of orbital entry conditions but with the added complexity of Nitrogen dissociation) and ionization which is indicative of higher temperature reactions at velocities in excess of those for low Earth orbit. Examples of such systems are shown in figures 4 and 5.

This cursory overview of hypersonic systems which present different developmental issues is intended to lead the reader to an appreciation of the complexity and diversity of hypersonics in the late 1980's. It has also introduced several terms and concepts which will be expanded upon later in this set of notes.

The only overriding aerothermodynamic requirement associated with the design of hypersonic systems is to contribute to a design that will sustain itself in the environment for a stated period of time and for stated cycles of that time and which will accomplish the flight objectives of the mission efficiently and at reasonable cost. Overall, the requirement is to support the goal with the means; the flight vehicle. From the standpoint of systems design this requirement implies participation in establishing mission goals for the proposed system's aerothermodynamic reliability and historical performance. From the standpoint of development,this requires an artful blending of classical engineering and numerical simulations; the old and the new hypersonics, to understand the heating imposed on the configuration and the dissipation of that heating through the thermal protection system and structure of the vehicle. From the standpoint of integration, this requires the management of error and uncertainty in the application of this less than perfect and less than complete developmental data to achieve the system's goals and lifetimes.

Above all, these aerothermal requirements require thoughtful application of a wide spectrum of engineering tools as TOOLS being careful that the whims of today's technology do not drive the development process and being mindful of the serious implications of cost as a driving force within the development process.

The features which are implicit in the design of a lifting entry vehicle with variable aerodynamic potential were summarized by Wake, 1987 in a figure entitled ... 'The Infernal Triangle'. Figure 6 is a reproduction of that figure from her paper. The basis of the figure is the inherent relationship between the angle of attack of the configuration and its performance which is stated as crossrange during the re-entry process. The figure further indicates the characteristics of the vehicle that flow from the choice of aerodynamic performance; the stated goals of the vehicle concept.

These characteristics include the amount of aerodynamic heating both in terms of the rate of surface heating and to total integrated heating load into the thermal protection system; the contribution of viscous phenomena which are directly related to the angle of attack of the vehicle and the amount of real gas phenomena which is related to the degree of bluntness of the vehicle and the angle of attack of the vehicle. There is an added dimension to this figure by Wake, the wing loading, which modifies all of these effects and which may challenge the type of thermal protection system selected and the amount of payload carryable on the vehicle.

The design problem is to balance all of these factors and produce a viable means to attain the goals set forth to guide the design of the configuration.

Once the Peak Heating Has Passed ...

Although there is a mathematically defined peak in the aerodynamic heating during re-entry, that peak is defined by a very restrictive 'model' of the entry process; an equilibrium glide trajectory. The problem is that the simplifying assumptions underlying and implied in that model have been, somehow, forgotten by those who use it. While it is true that aerodyamic heating is maximized at high velocities, the assumptions that underly that statement must also be respected. These assumptions are that ...

    1. That the configuration is on an equilibrium glide trajectory
    2. The state of the boundary layer does not change
    3. The trajectory parameter, W/CLA, remains constant which,
        in turn, implies that the angle of attack is constant.

The risk in focusing on one, single trajectory design point at which heating is maximized is that all other points are assumed relatively free of aerodynamic heating concerns. The thought process can extend that statement to include ... once the peak heating has passed I can drop the vehicle nose and maximize aerodynamic performance at lower velocities. The risk here is in exposing regions of the vehicle to flows that were aerodynamically shielded and thus of no design consequence at higher angles of attack and violating the model limitations since lift coefficient changes. The aerothermodynamic requirement requires an appreciation of all design points that may affect the sizing of the thermal protection system. There are three. The equilibrium glide design point, the design point defined by the initial altitude 'bucket' as the vehicle aerodynamics counter the effects of de-orbit retro-thrust which initiates re-entry and a potential point later in the re-entry process if the equilibrium glide parameter (W/CLA) is substantially changed.

Maximizing the lift during entry minimizes the initial entry 'bucket' in the transition from the initial de-orbit burn to the establishment of an equilibrium glide. The depth of this bucket, shown in figure 7, is directly a function of the glide parameter and more particularly the angle of attack of the vehicle. This is aerothermodynamic design point number 1. Once a stable, equilibrium glide is established in the atmosphere, the level of heating to most points on the vehicle is also minimized. Finally, entry at high angle of attack shields the sensitive or complex upper body regions of the vehicle against aerodynamic heating.

Experience with the Rockwell Space Shuttle demonstrated that focusing attention to the velocity of peak heating created an inordinate focus on conditions at 20,000 feet per second while minimizing concerns at far lower velocities where the angle of attack of the vehicle had been significantly changed to achieve glide ranges. Those effects effects at lower velocities were characterized by a complex flow interaction between the fuselage and wing which created a vortex along the fuselage. This vortex impinged on the orbital maneuvering system (OMS) pods as the vehicle angle of attack decreased as shown in figure 8. The increased heating caused by this angle of attack sensitive interaction overpowered the decrease in heating due to reduced velocity creating another and third aerothermodynamic design point.

It must be emphasized again that aerodynamic heating is always potentially dangerous. The danger is in relation to the materials system selected to contain it. There is not one single peak heating point but several, as described, and each of these points must be considered in the initial design of the configuration.

One of the major problems in defining developmental aerothermodynamic requirements for a new configuration is that of over-generalization. It is far too easy to generalize the success of a given configuration, such as the Rockwell Space Shuttle, to possible success with any arbitrary lifting entry configuration. Saying this somewhat differently, it is too easy and not correct to assume that the problems observed on the Rockwell Space Shuttle will generally be characteristic of all lifting entry configurations. Both of these forms of over-generalization need to be defended against by an understanding, in depth, of the cause and effect relationships implicit in specific phenomena on lifting entry configurations.

The Rockwell Space Shuttle was, for the most part, successfully tested on the ground with ground test data which was extrapolated to flight conditions. Is this problem generally solved?

Not only was the Rockwell developed Space Shuttle successfully tested on the ground but this testing was almost exclusively accomplished in lower Mach number test facilities with Mach numbers less than 10. If we look carefully at this configuration it becomes clear that the high angle of attack performance of this configuration was dominated by the nose bluntness of the vehicle. This bluntness generated a lower surface Mach number that was barely supersonic. There were few modifications apparent due to viscous phenomena as it affected the aerothermodynamics of the vehicle. The paper by Griffith and Maus, 1983, indicates some effects on the aerodynamic center of pressure location as shown in figure 9. This figure demonstrates the insensitivity of the configuration to typical hypersonic data at Mach 8 for high angle of attack flight as well as the presence of real gas phenomena in that could not be modelled with existing ground test facilities. The Shuttle was a pressure dominated vehicle that could be evaluated using typical hypersonic test facilities having a hypersonic Mach number; Mach 8 for instance.

This figure is particular to THAT SPACE SHUTTLE. Even so, the figure indicates a sensitivity to Mach number effects as the Shuttle angle of attack was reduced to improve its aerodynamic performance. The large increment present in aerodynamic center of pressure shift shown in this figure is an artifact of the extreme bluntness of that particular configuration and not a general feature of all hypersonic configurations. It is important that those using figures such as this understand the cause and effect relationships that produce such curves and do not attribute such phenomena to generalized hypersonic configurations.

Viscous flow effects in particular, if substantially present on the configuration, will modify the aerothermodynamic flow phenomena and must be evaluated over a spectrum of test conditions covering the anticipated viscous parameters. This requirement presents a new degree of freedom to the design engineer. It complicates the testing process over and above what was required on the Rockwell shape. More data or smarter testing will be required at a variety of test points and not just at representative hypersonic test points. Open to question are the need for new test facilities to support these generalized hypersonic configurations and more complex analysis techniques to transpose the test data to flight conditions.

Griffith and Maus, 1983, demonstrated that irrespective of the quality of experimental data taken in ground test facilities, there is an indespensible intermediate step required to apply that test data to a flight problem. That step is an extrapolation step which in the 1980's is accomplished through the use of computer simulations. The question posed is then ... if no data is fully satisfactory and in any case computer simulations are required, what is the extent and quality of experimental data required as the base with which to enter these simulations and what is the relationship between test complexity and cost and simulation complexity and cost?

It is at this point that there is a separation of those who are basically experimentalists and those who are basically numericists. The responses received to that question will range from ... very little data to ... a complete duplication of the numerical database. Of course the answer that will be given by any individual or group will be colored by corporate experience with numerics but let us try and develop some general strategy to approach the answer to that question which will generate sufficient developmental data to efficiently complete the design. Consider two premises as guidelines for discussing the relationship between numerics and experimentation in the aerothermodynamic design of arbitrary hypersonic lifting entry systems.

PREMISE 1. Experimental data must be sufficient to yield accurate trend data in each physical phenomena pertinent to the configuration under study.

The computer simulations based on the Navier Stokes codes have been presented to us as 'exact solutions' to that equation set. In fact, these equations are not exact but highly accurate models of nature. The Navier Stokes equations themselves are only models of physical phenomena although excellent models within their domain of applicability. Both the process of developing finite differencing techniques for these equations and the process of modeling the physical phenomena which are described in principle by the equation set introduce the concept of modeling into the equations and reduce the argument that the approach is exact. The obvious point always pointed to by the numericist is the infamous TURBULENCE MODEL that can always be counted on to explain the gap between computation and expectation but there are many more such models. The point is that even though the number may vary with a particular formulation, each model needs to be exercised against 'data'. This can only be accomplished in wind tunnel facilities.

PREMISE 2: Not all models can be exercised in wind tunnels. For the cases where this is true, the problem must be bounded with sensitivities defined and fundamental studies initiated where the sensitivities dictate.

Wind tunnels, for the most part, operate in perfect gas regimes but flight vehicles operate in a general reacting gas regime. Data taken on the ground may never exercise the thermodynamic, transport and reaction rate models implicit in the codes and yet these data and codes must be applied.

Techniques are required to challenge the codes wherever possible and, in addition, fundamental research activities are required to validate and improve those difficult models but at the base of it all, there is required engineering attention to the management of these possible error sources in the design process.

The Mutual Application of Experimental Test Facilities and Numerical Simulations

Griffith and Maus, 1983, described a new equilibrium between the competing tools of wind tunnel experimentation and numerical simulation in the development of new hypersonic configurations. There had always existed an understanding that ground test data required some extrapolation technique to be appropriate to flight conditions but the work of Griffith and Maus indicated that experimental data could be substantially modified through the use of numerical techniques ... even those data which were inadequate in the full understanding of the flight vehicle. More interesting yet, Griffith and Maus demonstrated that numerical techniques ... even those incompletely developed and only partially useful in the study could be used as TOOLS by engineers who were skilled. It was an exciting paper for what it said and what it implied.

In a sense the development of all hypersonic designs has followed the general path presented by Griffith and Maus. The Rockwell Space Shuttle followed this developmental philosophy as shown in figure 10. Being developed essentially in the pre-computational age, the Space Shuttle mixed the analytical closed form solutions available in the literature for flat plates, cones and spheres together with an extensive wind tunnel program which defined the differences between the elemental closed form solutions and the experimental data on the actual configuration as correction factors. It was the elementary solutions which were computed at flight conditions together with the correction factors which were assumed equal to their wind tunnel values in the flight application.

Adams, 1975, extended the fidelity of the numerical model by approximating the lower surface of the Shuttle as an axisymmetric hyperboloid and evaluating the flowfield about that computable shape. See figure 11. Again, this solution was compared with experimental data. This technique also allowed a first evaluation of equilibrium real gas and reacting gas effects by reducing the complexity of the Shuttle forebody to a more simple but representative axisymmetric shape.

Based on early developmental work by Cooke, 1961 in the United Kingdom, DeJarnette, 1971, developed an axisymmetric analogue technique that transforms the flow about a three dimensional shape into the corresponding flow about an axisymmetric, conic shape for purposes of computation simplicity. This process is schematically shown in figure 12. This technology has been exploited over many years for a variety of three dimensional configurations. While this technique better models the flow about complex shapes than did previous techniques, it still contains much empiricism which is open to questions and criticism.

The next series of improvements to the numerical modeling came during the later stages of the Shuttle project as Euler and Navier Stokes based computer codes were applied to the Shuttle and later to a series of other configurations. Griffith and Maus, 1983, worked with this current generation of numerical capabilities which even better modelled the exact configuration. Their paper compared wind tunnel data with both viscous (Navier Stokes based) and inviscid (Euler based) flowfield codes which were applied to pseudo configurations of the Space Shuttle thereby overcoming the limitations of the codes. In a real sense they were using this advanced technology as engineering tools wherein much of the skill and craftsmanship resides with the user.

Today we continue this process by which increasingly sophisticated numerical models are applied together with wind tunnel data and we continue to ask the basic question ... what is the proper equilibrium between the two in the developmental process?

There is today a strong school of thought that proposes the numerical approach as a `numerical wind tunnel` which will somehow replace the traditional function of experimental test facilities with numerical techniques. This school believes that the only limiting factor is the size of computers available to us. With sufficiently large computers, they argue, we could produce acceptable numerical simulations of new vehicles. To them, the wind tunnel component in this new equilibrium is very small consisting in an occasional `validation check` against the numerics.

It is my belief that both components are necessary. Both numerics and experimentation need each other and the engineering of hypersonic configurations requires a healthy tension between the two. While there is no doubt that experimentation will change in response to newer numerical techniques, that change appears to be in the direction of more sophisticated testing techniques and data capabilities rather than less testing. This point will be discussed in greater depth in a later section of these notes.

Numerical Surprises from Experimental Studies

In 1975 Chapman and others wrote an article `Computers vs Wind Tunnels for Aerodynamic Flow Simulations`. The premise of the article was that `...the remarkable advances in computer capability offer considerable promise for obtaining aerodynamic flow simulations

efficiently from methods quite independent of traditional wind tunnel testing'. Apart from the material presented in this article, the truth is that the only 'simulator' of aerodynamic flow is the computer. The wind tunnel doesn't need to simulate what is the 'real thing'.

There are two examples I'd like to present in which the experimentation was extremely valuable in illuminating flow features which were computed. Both examples are from the Soviet literature; the first is a computation of leading edge flows on a cranked w.ng configuration and the second is an experimental simulation of axisymmetric flow over an isentropic compression surface.

Figure 13 indicates both experimental and numerical data over a cranked wing shape. This study, conducted by Borovoy, 1983, was run at several Mach numbers including a very high Mach number run at Mach 15.5. The experimentation and numerical computations agreed at the lower Mach numbers but were in gross disagreement at Mach 15.5. The reason offered by Borovoy for the high Mach number disagreement was the inappropriate forebody computation which defined the flow field impinging on the main wing structure. The forebody flow was inappropriate in that an inviscid computation was generated which ignored the presence of the rather sizable boundary layer that grows in significance with Mach number. Ignoring the boundary layer caused the shock wave to lay closer to the strake portion of the wing and this, in turn, caused the strake/wing interaction to occur in the curved part of the configuration rather than further out on the wing. As a result, the numerical computations were grossly different than the corresponding experimental data.

Figure 14 indicates the heat transfer distributions about an axisymmetric, isentropic cone surface tested at Mach 5 in a conventional wind tunnel facility. The heating patterns shown are due to striation heating, which is a phenomena reported in technical literature over many years. The open symbols are data taken in a laminar boundary layer and the corresponding closed symbols are data taken with the flow tripped turbulent. The instrumentation used was 'thermal indicator coatings'. In this case there are no corresponding numerical data proven inadequate but it is clear that no similar numerical studies could be generated with existing computers to demonstrate this phenomenon. This is an excellent example of the limitations of the numerical techniques with regard to modeling. Limited because such phenomena as this striation heating is not modeled in the codes and limited because even if it were, the frequency of the oscilations is so high that present day computers would be inadequate to represent it with either Parabolized Navier Stokes or full Navier Stokes models.

There is information to gain from experimental facilities; information of value in judging the adequacy of numerical simulations. Conversely, numerical simulations using even 'exact formulations' can never obtain '...aerodynamic flow simulations ... from methods QUITE INDEPENDENT of traditional wind tunnels...'. Numerical simulations are, in all cases, limited by the modeling given to them by experimentation.

Relating the 'New' and the 'Old' Hypersonics

In 1984 Dr. Anderson presented an excellent, provocative review of 'then' and 'now' in hypersonics. It appears that his paper would somehow be diminished if it were not kept alive by stirring discussion and debate. It is in this spirit of lively discussion that I would like to discuss several aspects of Dr. Anderson's paper as it applies to this subject.

Condensing down the discussion to the basic point I wish to make, it appears that, in many respects, the 'new' hypersonics with its emphasis on computations should not be construed as a replacement for the 'old' hypersonics with its emphasis on classical analysis and wind tunnel experimentation. The new hypersonics is far more identifyable as a more controlled manner of conducting point experiments than an overall approach to engineering develop ant.

The weakness of the old hypersonics was a fundamental inability to model the geometrical and physical complexities of hypersonic flow situations and to obtain, from that modeling, a usable solution. The corresponding strength of the old hypersonics was that every trend relationship that we understand today in hypersonics was developed there. The concept of viscous interaction and the simplistic parameters that govern its variation through flight (equations 9 and 14 of Anderson's paper), the thickness of the laminar boundary layer (equation 3) and even the relationship between compressible and incompressible flow through reference temperature procedures (equation 15). The old hypersonics gave us the whole picture even though not in clear focus.

Enter the new hypersonics of the 1980's '... dominated by computational fluid dynamics...' with capabilities far improved '... the strength of the new hypersonics is the ability to tackle enormously complex hypersonic flows...' (ignoring for the moment questions regarding accuracy and appropriateness of such computations). Its corresponding weakness is the inability to create trend relationships. With the new hypersonics we get a potentially crisp focus on detailed features of the picture but we can't understand what it represents in overall features. Because of this, the two developments are not related in a seq·ential manner but both represent complementary elements of something even more fundamental.

We have gone through (and continue to go through) an infatuation with numerics. We have been saturated by the most amazing technical results - one after the other - and just when we had seen it all ... COLOR GRAPHICS'' Statics and movies and even 3-D. Dazzling stuff that has '... revolutionized the way we analyze aerodynamic flows...'. That's both good and bad. For all the beauty of color graphics and for all of the wealth of technical detail in all the presentations of CFD how many times have you used it as if it were data? How do you know it is right? How do you tell if it is right? How do you assemble composites of these incredibly detailed solutions to present a meaningful data trend?

We're starting to believe these results without question, to use them as an end in themselves and what's worse, we're training an age of engineers who cannot remember the old hypersonics which just happens to be the key toward validating the numerics and rationally applying that same numerics in a design environment.

This numerics of the new hypersonics has destroyed our appreciation of trends which are the cornerstone of the old hypersonics. This loss of appreciation of trends is a loss of perspective that not only threatens the design of vehicles but, on an even more basic plane, destroys our ability to critically evaluate the techniques of the new hypersonics.

The codes are NOT an end in themselves that should characterize the 'new hypersonics'. They represent engineering tools; tools that require engineering judgement to use and critical appraisal to understand. Hypersonics must be dominated by an increased understanding of fluid mechanic reality and an appreciation of the difference between that reality and the modeling of that reality. CFD represents the framework for that modeling study and experiments represent the technique for introducing physical reality into the modeling process. Finally, classical analytical theory and the trend information produced by theory gives us the direction with which to assemble the point data from these numerical solutions in an efficient and meaningful way to produce understanding.

I'd like to take several items from Dr. Anderson's paper and discuss them in somewhat greater detail and with a somewhat different point of view. The first item appears on pages 8 and 9 and states that ... 'If the shock layer over a hypersonic vehicle is computed from an accurate viscous flow technique, say by the numerical solution of the Navier-Stokes equations, then viscous interaction effects are automatically and properly accounted for -- they come out as a part of the solution'. Because the satisfaction of aerothermodynamic requirements for the development of hypersonic vehicles requires the design engineer to deal with advanced computer programs including those based on the Navier Stokes model of flow, understanding this statement is extremely important within the design context.

The use of an 'accurate viscous flow technique', such as the Navier Stokes MODEL of flow, does not in itself assure that the computed answers derived from that technique will be accurate. All that is assured is that the equation set which is the basis of the computation is a reasonably good model of fluid reality; a model that must be critically questioned in itself. There are regions where the Navier Stokes equations are not appropriate and, after all, this equation set is an approximation to the Boltzmann equations. Accurate solutions require not only an accurate basis of the computation but also accurate modeling of the physical phenomena which are introduced but not defined by that equation set as well as accurate numerical modeling of the equations which results in a correct computation. In our limited review of numerical modeling based on the Navier Stokes equation set, the rule is not that acurate solutions result from an accurate viscous flow technique but rather that inaccurate VISCOUS data results from unwarranted approximations to accurate equations.

Solution of viscous interaction phenomena brings into question the applicability of the basic equation set, the Navier Stokes equations in this example. There are certainly regions of viscous interaction for which the Navier-Stokes equations do not apply. Figure 7 from Anderson defines the limit of applicability of the Navier-Stokes equation set in terms of Knudsen Number and state that above that limit '... conservation equations do not form a closed set... .

The use of the Navier-Stokes equations certainly does AUTOMATICALLY account for viscous interaction effects; that is, the solution computes a boundary layer ... BUT ... there is no guarantee that the viscous interaction effects are PROPERLY accounted for in the solution. The computer solution of the Navier-Stokes equations deals with the numerical solution of differential equations on a computer and discretizes the equations introducing approximations with regard to that process. To be properly accounted for, the solution grid must be sufficiently dense and properly conform to the geometry under analysis. Neither of these practical elements are automatically accounted for in the solution of the equations. In fact, it is all too easy to prove that rather routine changes to the computational details will alter the computational answer. The mundane problems with the viscous computations by both Shang and Candler for the X-24C configuration are further proof of this fact as shown in figures 15 and 16.

The approximations introduced by the numerical gridding of the model and the discretation of the equation set are not the only approximations that can detract from the quality of the answer. Apart from the onerous 'turbulence model' that is all together too easy a target, thermodynamic and transport phenomena are modeled within the codes and these models are the sources of many errors. Questions to be answered by an analyst are ...

what is a perfect gas ?, ... what is a real gas ?, ... what equations are used to model the transport properties of viscosity, thermal conductivity and Prandtl number ? ... how do computations for wind tunnel data differ frum computations for flight conditions ?

Anderson goes on to say that ...'Such viscous shock layer calculations (using the Navier-Stokes equations) obviate the need to do anything 'special' to account for viscous interaction.' While it is true that the computation models the entire flow field about the configuration, both viscous and inviscid, the something special that is required is to verify that the answer derived is correct. Because of the modeling approximations introduced as just described, the answer cannot be assumed to be correct or even nearly correct. Verification requires one of two fundamentally different strategies to be employed. These are (1) to use the wealth of 'old hypersonics' information about flow fields to predict the answer that should be derived from the numerics and/or (2) to change the incidential features of the computation and observe the insensitivity of the resultant answer to these changes.

In truth, the use of numerical solutions based on the Navier Stokes equations to derive aerothermodynamic information is today more art than science. There is nothing in engineering that should be accepted without critical assessment. Numerical solutions are not an exception to that rule.

A second area of discussion that has an important impact on how the aerothermodynamic requirements in design are satisfied is to be found on page 7 of Anderson's paper. The quote is ... 'This work (Kutler, 1975) constituted the first detailed flowfield calculations on the shuttle design. It had, however, a major drawback (in Kutler's use of a PNS approach), namely, that the calculation would go unstable wherever a pocket of locally subsonic flow was encountered -- once again the problem of mixed elliptic and hyperbolic regions. (There is no practical way around this problem without going to a time dependant method, as described earlier (The full Navier Stokes equations)).'

This quote broadly deals with how limitations in engineering tools are circumvented. Further, this statement deals with the more basic question of how numerical fluid dynamic techniques are to be viewed in an engineering context. A discussion of this statement is vital to understand the different paths of effort that result from different views of how to circumvent a limitation ... in this case a fundamental limitation of the Parabolized Navier Stokes approximations to the Navier Stokes equations.

It is not strictly true that the solution goes unstable whenever a pocket of locally subsonic flow is encountered. The PNS approach computes through pockets of subsonic flow. Each delta wing leading edge is a pocket of locally subscnic flow. The expansion surface at angle of attack may be subsonic in the crossflow direc.ion. The PNS approach 'bombs' (goes unstable) when a subsonic region of flow is encountered in the direction of computation; not in another orientation. Thus, the leading edge region of the Rockwell Space Shuttle would create such a region to the computation. Figure 17 from Kutler indicates that region on the leading edge to be a region of 'embedded subsonic flow'. This flow is subsonic because the sweep of the wing , being 45 degrees, produces an Edney type V interaction. The wing sweep is not sufficient to produce a type VI interaction (after Edney).

There are two distinctly different techniques to circumvent this problem. The first was discussed by Anderson , to use a time dependent method (the full Navier Stokes equation set). The second was practiced by Griffith and Maus at AEDC and before them by Hamilton at NASA Langley; to modify the geometry such that no subsonic pocket is present on the leading edge of the wing. Figure 18 demonstrates the changes that were made. They include increasing the sweep angle from 45 to 55 degrees and filling in the upper surface of the configuration to allow a computation. This second solution strategy is, in my view, an engineering approach in that the PNS computation is used as a tool to gain insight into a problem. In this type of an application, the skill of the user is as important as the quality of the instrument. The alternative suggested by Anderson, the use of a time dependent method, is a science solution; a new approach in which compuations are not thought of as tools but as full simulations of the configuration under analysis. The choice to accept one or the other of these views of numerics in satisfaction of aerothermodynamic requirements for analysis opens fundamentally different paths of action to the person and organization making that choice.

The Reference Temperature Technique, a Blending of the old and new Hypersonics

White, 1974, devoted a section of his book to the reference temperature concept. This concept allows for an extension of the classical incompressible boundary layer theory to the compressible case. What seems to be a simple and reasrnable concept today was the subject of many papers in the early 1950's.

Having experimental data and defined relationships for skin friction available at incompressible conditions, the practical question was how these low speed concepts could be extended to flows at compressible conditions with heat transfer. The mechanism suggested was a reference temperature defined at some point in the vehicle boundary layer. The trick was to correctly define that reference location. von Karman suggested that the reference temperature should be equal to the wall temperature and Tucker suggested it should be some arithmetic mean of the wall and freestream temperature.

Several empirical estimates of the reference temperature were given by various authors, among them Eckert. Refinement of these estimates produced a form of the relation that was similar and roughly equivalent. Only years later did Dorrance demonstrate that these empirical expressions had a theoretical basis. What makes this process a blending of the old and new hypersonics is the fact that this development occurred in the 1950's which is considered to be in the classical period of the old hypersonics and yet the data used in the empirical development was not wind tunnel data but results from primitive CFD techniques of the new hypersonics.

Computational Fluid Dynamics in Design

The buzz word today is CFD and there are large efforts being taken to employ CFD in the design arena. The question is really, ... use CFD to do what? Two schools of though exist on the application of CFD technology. One is directed toward the use of CFD techniques as direct simulators to replace wind tunnels. Their view is that, given a large enough computer, CFD can correctly compute an entire configuration at arbitrary flight conditions generating, essentially a numerical wind tunnel result. The second school of thought is that CFD codes are engineering tools in which the skill of the user is important and the quality of the ultimate answer requires intervention and creativity of the user.

The development of CFD has progressed from an initial stage in which the "mechanical" problems of generating ANY numerical solutions have been solved and into the second stage where the quality of the computed results need to be critically evaluated. This is the "validation" phase and the general view is that experimental data are required to "validate" numerical solutions. Computations today are highly tied to experimental data ... a far cry from using wind tunnels to store numerical output. While validation is certainly required and while wind tunnels will certainly play an important part in that process, it is not sufficient to perform validation by matching experimental wind tunnel data with numerical computations. This point will be discussed shortly in greater detail.

In the computations which are made and reported in the literature today, pressure data can be generated with some accuracy while viscous parameters of heat transfer and skin friction can be generated only with difficulty and questionable accuracy. Accurate solutions are generated on relatively simple configurations where the flow field is implicitely understood by years of experience and closed form solutions. Surface geometry packages and the flow field gridding to efficiently attack complex problems are becoming available. In the continuum regime, CFD has two branches: the Parabolized Navier Stokes approach (PNS) and the full Navier Stokes computations (NS).

The PNS approach generates solutions in minutes on present day computers while the the full NS approach requires hours to accomplish the that task and employs a larger scale of computer in the process. This situation is changing but all the projected improvements will benefit both the PNS and NS approaches equally. The PNS techniques involve more modeling and thus more potential sources of error in the solutions. The full Navier Stokes approaches are somewhat freer of such modeling assumptions. The PNS solutions are more restrictive in application, being defeated by streamwise separation or embedded subsonic flow as in the case of the Shuttle leading edge, while the full Navier Stokes approach is more general in applicability.

A key issue in selecting either approach is engineering readiness for design applications. The PNS approach has a current and near term design capability. This is primarily due to the ability of the PNS solutions to return a solution in minutes allowing the engineer to empirically try different techniques and to arrive at a "correct" solution through a strategy of demonstrating the insensitivity of solutions to incidential computational parameters. This has allowed the PNS approach to produce engineering data whereas the corresponding full Navier Stokes approaches have still produced limited results. Figures 15 and 16 indicate several solutions compared with experimental data for the X-24C configuration. Only the PNS approach, at present, has been demonstrated to reproduce accurately the viscous effects observed on the X24-C through surface heat transfer measurements. The full Navier Stokes approach is still substantially in error in comparison with data.

There are two ways in which we can use CFD technology as exemplified by the level of PNS computations today. One way is to evaluate the entire flowfield over a somewhat idealized flight configuration; an approach described by Griffith and Maus. The second way is to build on our confidence with the solutions to simplified configurations in order to generate new insights into three dimensional flowfields.

There are understandings of flow that we can simulate with CFD techniques that we cannot generate experimentally. These understandings are important in our overall view of configuration development. Three examples of these understandings from our experience are (1) in depth understanding of shock interference phenomena wherein both cause and effect numerical results can be generated. The specific case to be discussed will be the aerodynamic heating to deflected control surfaces. (2) improvement of extrapolation processes by numerically understanding the variation of a parameter, the recovery factor, that cannot be experimentally measured and that is ASSUMED to be nearly a constant. (3) the enrichment of rapid design techniques through introduction of correlations from numerically generated "data" much as experimetally generated data was used years ago.

Years ago simplified techniques were developed directly from flat plate theory in which
the heat transfer rise within a shock intereference region was related to the pressure
rise in that region to some power. That development is shown in figure 19. From this
very simple theory, the heat transfer ratio (after to before the shock) was defined
through an exponent on the corresponding pressure ratio. From the simplified theory, this
exponent was 0.5 for laminar flow and 0.8 for turbulent flow. Many other exponents were
also empirically postulated but most of these were found to be the result of boundary
layer transition within the shock interaction region. Such boundary layer transition has
been the bain of the experimentalist due to the ease with which the process of shock
interaction causes boundary layer transition but these experimental difficulties are of
no consequence to the numeriscist who 'ordains' the state of the boundary layer under
analysis.

Experimentally, once the question of boundary layer state was resolved, it was found that
the turbulent data matched the theoretical model closely but that the laminar model was
far from the experimental data. The experiment was run several times with the same
result. An empirical exponent of 0.7 was observed from the data and used to replace the
theoretical constant of 0.5 but the experimental data scattered poorly about that
exponent as shown in figure 20.

With recent interest in numerically computing standard example cases, a substantial
numerical effort has been completed to assure that the computations on these example
cases are free of numerical errors. See Neumann and Patterson, 1988. As a result of this
numerical study, the exponent for shock interaction regions was numerically computed
together with the Reynolds analogy factor, RAF, for both laminar and turbulent
interactions in a perfect gas, Mach 20 flow. The results are shown in figure 21 and
indicate that in a laminar boundary layer interaction the Reynolds analogy factor differs
substantially from the undisturbed value ahead of the interaction process while for a
turbulent interaction the difference is far less. This numerical insight goes far to
explain the experimental observations of the pressure and heating rate. The fact is that
the flat plate theory applied made an incorrect simplifying assumption that was not
justified by the numerical result or reflected in the experimental data. The numerics
demonstrate additional insight into the interaction process. The challenge is and will
be to take advantage of that additional insight to formulate new design methods that more
closely model the interaction process.

The recovery factor; the temperature which will be achieved at an insulated wall at
conditions of zero heat transfer, cannot be easily measured in a flow. By convention, the
recovery factor is assumed to be related to the Prandtl number in a manner defined by the
state of the boundary layer. These relationships were defined years ago through pipe
flow experiments. The recovery factor is difficult to measure because of the presence of
re-radiation from the wall of the model as the surface temperature is increased toward
that for zero heat transfer. While some measurement techniques exist to circumvent the
question of re-radiation from the surface, they are expensive to use and rarely applied.
It will be shown later in my notes on aerothermal instrumentation that the assumption of
a constant recovery factor based on the state of the boundary layer is a questionable
premise for complex flows and it is conjectured that at least a part of the empirical
scatter in design methods is due to this effect. Numerically, the condition of an
adiabatic wall, that is a wall of zero heat transfer, with no re-radiation is nothing
more than a boundary condition in the computation. It is therefore possible that
numerical solutions of this parameter could be made that, together with experimental
data, could be used to improve the overall accuracy of design approaches both at the
conditions of the defining wind tunnel and, more importantly, at the flight conditions.

Even in the era of rapid and accurate numerical simulations based on the Navier Stokes
equations there is still a need for rapid design techniques. These techniques today are
the mainstay of preliminary design activities used to roughly screen potential
geometries. Numerical techniques could well be used to enrich these techniques through
the introduction of numerically derived data. Two specific areas that could profitably be
addressed are (1) improving the sensitivity of these design methods to geometric
variations and (2) demonstrate the validated capability of these design methods for data
significantly different than that produced in routinely operated wind tunnels.

In the first, there is reason to question whether the rapid methodology is indeed
sensitive enough to differentiate among small variations in geometry or whether the rapid
design methodology sees all geometries as the same and is only sensitive to variations in
the flight trajectory. Numerically derived data could improve this design sensitivity
and improve the quality of preliminary design screening of new configurations.

In the second, there is a concern that design codes may be too closely 'tuned' to the
features of workhorse hypersonic facility(ies) used initially to develop the techniques.
The validation of these techniques for new shapes in the same wind tunnels is scant
consolation. It may signify only a high fidelity of modeling for specific tunnel
conditions. The use of numerics and numerically derived data could present an alternative
data base or validating experiment at conditions far removed from the wind tunnel used to
formulate the initial technique.

All of these suggestions are alternative uses of numerics available with the current
state of development and potentially as important as the more routine use of numerics to
simulate in all detail the flowfield about a complex flight configuration.

Validation, Tougher than Matching Wind Tunnel Data:

If the last ten years have been spent working out the numerical details of generating a mechanically accurate numerical solution, this decade is the decade of validation. How does the numerical solution compare with experimental data?

The more this question is asked, the more difficult it becomes to answer. Chaussee, 1987, proposed that the answer lie in comparisons of the best experiment against numerical scatter and conversely the best numeric result against experimental scatter. See figure 22. While this is an approach, questions of what is scatter and what is bias come to mind. Numerical 'scatter' may, in fact be computations known to contain consistant numerical error and thus not scatter at all but bias. Similar comments can be made about the experimental data. In this particular example case it is known that part of the 'experimental scatter' shown is, in fact, inappropriate transitional data compared with fully turbulent numerical solutions. The fact is that neither experiment nor numerics are free of problems. Most of these problems are bias to the answer and not scatter. A good validation experiment will require an interactive dialogue between numeriscist and experimentalist; neither of which, at present, has an exceptional understanding of the technology of the other.

In a recent study by Neumann and Patterson, 1988, even more basic questions have been discussed. The primary question is ... is it sufficient to compare numerical heating rate to experimental heating rate and achieve validation? Working from a comparison of computed results submitted by U.S. indusrty and Government sources, Neumann and Patterson have found that both the modeling of transport phenomena (notably the thermal conductivity) and the modeling of fluid flow by a geometric finite grid introduces error that must be considered within the context of any validation experiment. The results of the study by Neumann and Patterson are shown in figure 23. These results suggest that differences of up to 20% can be expected in the numerical result alone based on implicit definitions of the transport phenomena, the normality of the grid to the body (noted also by Chaussee, 1987) and the rather arbitrary definition of the temperature slope at the wall. These numerical modeling questions will require the application of standardization to many routine computational sub-routines (as for instance the transport phenomena) and computational definitions (as for instance the definition of how the temperature slope at the wall is defined) before any meaningful validation of the computational process can be said to have been completed.

The Maturing of Computational Fluid Dynamics Products for Aerothermodynamics Applications

As a final remark with respect to computational techniques, let me spend a few minutes discussing the process of maturation that all computer codes must progress through. There are just two problems resulting from the current state of affairs in numerical fluid dynamics applied to aerothermal problems. These are:

1. Codes are not generally exported to a wide cross-section of design engineers who are competent to understand their results AS EXPERIMENTAL DATA. As Stollery, 1987, put it '...They are sophisticated, demanding and only available to a select minority'. That minority, in my view, is all too cohesive in their background and understanding.

2. We believe the results produced by these codes all out of proportion to the quality of analysis employeed in them. As Bradley, 1987, put it '...we do not understand the numerical physics that are in many codes that we use routinely'.

The effort to produce a design capable code from a research code requires is enormous. The easiest thing to do is for the developer to produce limited solutions from a new product. The tough step is to export that code to a third party user; one who knew nothing of the development process, who would apply the code to new design problems. Broadly, we have found that the development of a 'design capable' computer code requires at least three re-formulations or major re-writes of the code and a 6 to 10 year period of development and operational experience during which the obvious computing errors are eliminated from the code. This is not just the experience of those who would develop Navier Stokes based computer codes, it is historically the experience of those who have developed the Arbitrary Body class of codes attributed to Gentry and the Axisymmetric Analogue class of codes attributed to DeJarnette. Both of these far less exotic computer codes as well as others of similar capability are still in development years after their initial formulation.

There is only one way to mature these complex computer codes. That way is to export them to knowledgable, practical engineers who will critically challenge their advertised capabilities. A team approach is strongly recommended in code development. This team approach should bring into dialogue the developers and users of the code. We have used a loosely formed, nationally based users group approach as a technique to transition an extremely complex program from concept to engineering reality. Such a group magnifies the abilities of any single developmental group in order to find and correct errors in the code as well as judge the accuracy of the result.

As one selecting a new developmental code, the need is to understand the technology employed deep within the modeling of the code (just where the developer will swear that

no modeling exists) and to have an ability to review the source coding. Once in receipt of a developmental code, there is only one way to understand it, READ IT. The numerical physics is not known in codes routinely used because engineers tend to be intimidated by the coding and choose not to understand it. If we treat these codes as black boxes, we must be willing to accept whatever results come from them. Results that may bear little resemblence to physical reality.

Note: quotes from Stollery and Bradley used in this section of the notes were taken from the discussion section of AGARD CP 428.

Experimentation

Those who would experimentally evaluate the aerodynamic heating of new configurations have had a bad time in the past decade while the numeriscists have touted their capability. Experimental data is tough to generate. Some measurements supporting the acquisition of aerodynamic heating data, such as the evaluation of static temperature or pressure, are nearly impossible to experimentally generate. The numeriscists can point to the fact that large amounts of data are taken at ever increasing costs as shown in figure 24 and they are also quick to question the quality of the experimental data when comparisons with computations are less than anticipated. In spite of this, experimentation is not only a valuable adjunct to numerical computation but the necessary basis of the modeling efforts built into computer codes as well as a preceived requirement for the validation of completed codes.

This being said, the role of experimentation in the next decades will be fundamentally different than it has been is the classical past. A new equilibrium is being established between numerics and experimentation as competing and complementary design tools. This equilibrium point was earlier discussed in these notes as a by-product of the work by Griffith and Maus. Characteristics of this equilibrium point, from an experimental perspective, appear to be as follows:

1. Increased accuracy will be demanded in test point identification together with a reduction in the number of calibrated test points either required for product development or available in any given test facility. Gone will be the generation of parametric data. The goal will be the establishment of higher quality representative data which will be both highly accurate and relatively complete. These data will increasingly be used to validate numerical computations which, in turn, will perform the function of generating parametric data.

2. New instrumentation will be installed that, on the one hand, will more completely characterize the flowfield about the configuration through the use of non-obtrusive test techniques and; on the other hand, will radically reduce the cost of experimentation. These instruments will be used with artificial intelligence (AI) advances to control the progress of testing.

3. Experimental facilities will be called upon to produce the simulation required to stress many of the aspects of the numerical codes through experimental observations. This requirement will translate into a series of rather specialized 'phenomena' wind tunnels in which the various aspects of the numerics can be isolated and evaluated. Real gas test facilities, such as the European developments HEG (High Enthalpy Gottingen) and F4 in France, are examples of such facilities as well as quiet wind tunnels at NASA in the U.S.. The key to these facilities will be the emphasis on PHENOMENA rather than configuration evaluation.

Overall, the requirement in the 1990's with regard to experimentation will be to create and maintain a credible tension between those who would compute flowfields and those who would experimentally observe flowfields about configurations. Design efficiency would not be served by abandoning either critical experiments and their continued instrumentation improvement or by ignoring the newer numerical capabilities which are becoming available to us.

Instrumentation, An Integral Part of Experimentation

When numerical flow field solutions started to become credible, it became apparent that both the numerical solutions and the companion experimental data contained errors. Examples of these errors are to be found in recent papers by Boudreau, 1987, dealing with the expansion process in the AEDC Hotshot type facility, Tunnel 'F', and the paper by Thompson and Sutton, 1987, dealing with design errors in the Langley CF4 Tunnel. Ironically, in both cases, numerics were used to advantage to improve the experimental test capability of the respective facilities. At issue here is the need to accurately instrument both the freestream of the experimental facility as an accurate boundary condition for the experiment and the models themselves in order to generate higher quality test data.

Boudreau, 1987, concluded that '...Most hypersonic wind tunnels operating at or above Mach 8 appear to suffer a loss of freestream Mach number because of non-isentropic processes occuring in the expansion nozzles'. He further concluded that '...Conventional methods of determining freestream Mach number are insensitive to such non-isentropic processes'... such that freestream instrumentation which does not assume isentropic processes and which is sensitive to these phenomena are required. Techniques that moniter

the static temperature or density in the freestream appear to be required in order to
assure the calibration of high Mach number facilities where even small amounts of energy
may be initially tied up in chemistry and subsequently released to the flow. This same
instrumentation and more will be required for real gas test facilities; phenomena
tunnels, where the physical process of expanding the very high temperature test gas will
create constituents far removed from ambient flight air and where chemistry effects will
be poorly modeled in the nozzle expansion process leading to freestream non-uniformities
in both spatial and temporal dimensions.

Admittedly, the paper by Boudreau has met with some skepticism. Large scale re-
calibration of hypersonic test facilities has not been completed although instrumentation
to accomplish the task is available and could be installed in these facilities. In light
of Boudreau's paper, the lack of such action is a calculated risk that, at least, the
development engineer must consider as a potential source of error. Such phenomena is
potentially more serious for slender, hypersonic shapes where viscous effects dominate
the flow than for blunt bodies where Mach number effects are less obvious.

Model bourne instrumentation and test techniques will be discussed in greater detail
later in this short course. Instrumentation techniques which increase both the ability to
make complex measurements and to make measurements far more efficiently are becoming
available from a variety of sources. These will be discussed later. It does appear from
several sources that instrumentation to fully define the flow fields about these shapes
and instrumentation to evaluate both the very high frequency unsteady heat transfer as
well as steady state levels are available through either coax thermocouple designs or
newer instruments developed for compressor blade testing; dual film thin film gages.
Further, it appears that measurements can be made at a speed up to 100 times as fast as
just a decade ago leading to far more cost effective test facilities which are computer
controlled through AI techniques to optimize data return.

REFERENCES

Adams, J.C., "Real Gas Scale Effects on Hypersonic Laminar Boundary Layer Parameters
Including Effects of Entropy Layer Swallowing", AEDC TR 75-2, 1975

Anderson, J.D. , "A Survey of Modern research in Hypersonic Aerodynamics", AIAA 84-1578,
1984

Borovoy, V. Ya., Golubinskiy, A.A., Nersesov, G.G., Pokhvalinskiy, S.M., Struminskaya,
I.V. and Yumashev, V.L., "Hypersonic Flow Over a Planar, Variable-Sweep Wing with Rounded
off Edges", Uchenyye Zapinski TsAGI, Volume 16, Number 1, 1985

Boudreau, A.H., "Characterization of Hypersonic Wind Tunnel Flow Fields for Improved Data
Accuracy", AGARD CP xxx, 1987

Chaussee, D.S., "NASA Ames Research Center's Parabolized Navier-Stokes Code: A Critical
Evaluation of heat-Transfer Predictions", AIAA 87-1474, 1987

Cooke, J.C., "An Axially Symmetric Analogue for General Three-Dimensional Boundary
Layers", R and M Nr. 3200, British A.R.C., 1961

DeJarnette, F.R., "Calculation of Surface Streamlines and Heat Transfer to Shuttle Type
Configurations", Part 1., "Description of the Basic Method", NASA CR 111921, 1971

Dorrance, W.H., "Viscous Hypersonic Flow", McGraw Hill, 1962

Griffith, B.J., Maus, J.R., Majors, B.M. and Best, J.T., "Addressing the Hypersonic
Simulation Problem", AIAA 86-9775, 1986

Harris, T.B., Hall, D.W., and Martellucci, A., "Aerodynamic Prediction Methodology for
Maneuvering Reentry Vehicles", AIAA 80-1609, 1980

Kutler, P., "Progress in Fluid Dynamics", Springer-Verlag, Berlin, 1975

Lukasiewicz, J., Experimental Methods in Hypersonics, Marcel Dekker, Inc. 1973

Neumann, R.D. and Patterson, J.L., "Results of an Industry Representative Study of
Code to Code Validation of Axisymmetric Configurations at Hypervelocity Flight
Conditions", AIAA 88-2691, 1988

Stollery, J.L., "Hypersonic Flow Problems Associated with Future Space Shuttle Vehicles",
Cranfield College of Aeronautics report 8512, 1985

Thompson, R.A. and Sutton, K., "Computational Analysis and Preliminary Redesign of the
Nozzle Contour of the Langley Hypersonic CF4 Tunnel", NASA TM 89042, 1987

Wake, A.J., "Hypersonic Aerodynamics - Applications for Hotol", AGARD CP 428,
"Aerodynamics of Hypersonic Lifting Vehicles", 1987

White, F.M., "Viscous Fluid Flow", McGraw-Hill, ISBN 0-07-069710-8, 1974

Figure 1   The Martin SV-50 Prime Configuration

Figure 2   Example of a High L/D Entry System

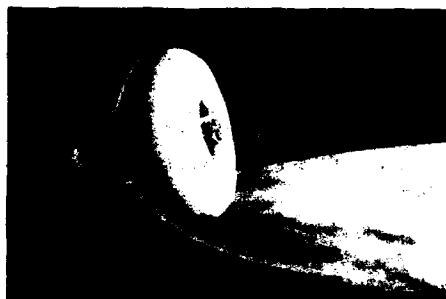Figure 3   Typical High L/D Boost Glide Vehicle Design
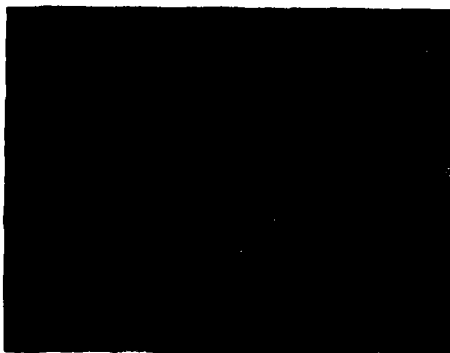

Figure 4   Low L/D AOTV Vehicle Design

Figure 5   Moderate L/D AOTV Vehicle Design

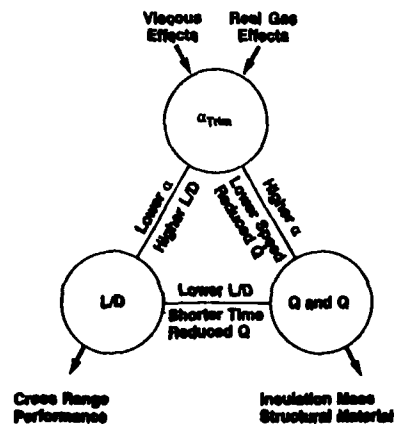## THE INFERNAL TRIANGLE

Figure 6   The Infernal Triangle After Wake
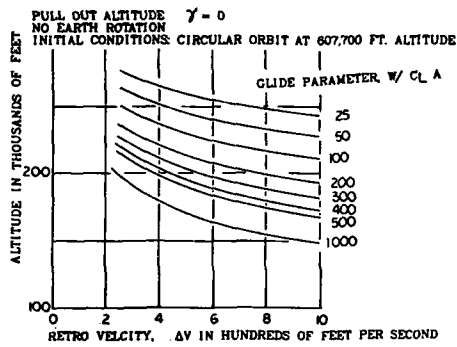
Figure 7 The Entry "Bucket" for an Orbital
Lifting Entry System

PULL OUT ALTITUDE $\gamma = 0$
NO EARTH ROTATION
INITIAL CONDITIONS: CIRCULAR ORBIT AT 607,700 FT. ALTITUDE

GLIDE PARAMETER, W/ C_L A

ALTITUDE IN THOUSANDS OF FEET

RETRO VELCITY, ΔV IN HUNDREDS OF FEET PER SECOND

Figure 10 Reduction of the Space Shuttle Geometry
into Classical Geometry Elements

EFFECTS OF ANGLE OF ATTACK ON OMS POD HEATING

H/H_e

FLIGHT DATA

WIND TUNNEL DATA

α-DEG

Figure 8 Effect of Angle of Attack on Space Shuttle
Orbital Maneuvering System (OMS) Pod Heating

ADAMS' HYPERBOLOID APPROXIMATION TO THE SPACE SHUTTLE FOREBODY
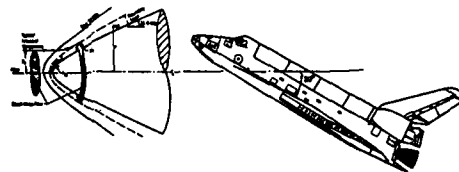
Figure 11 Reduction of the Space Shuttle Forebody
Geometry to Axisymmetric Geometry Element

THE AERHET AXISYMMETRIC ANALOG

$M_\infty = 23$

Equilibrium Air
Altitude = 73.2 km (240,000 ft)

Real Gas Effect

50 cm

25 cm

Perfect Gas
$\gamma = 1.4$

Mach Number Effect

Reference
$M_\infty = 8$, $\gamma = 1.4$, Perfect Gas

$\Delta x_{c.p.}$, in. (Forward)

α, deg

Figure 9 Mach and Real Gas Effects on the Center of
Pressure Location for the Space Shuttle

PRESSURE DISTRIBUTION

div $\vec{S}$

AXISYMMETRIC
BOUNDARY LAYER
EQUATION

HEATING RATE

BODY LENGTH
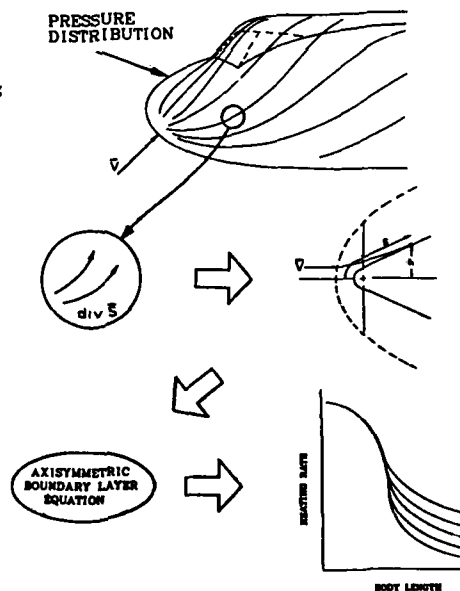
Figure 12 Simplification of Space Shuttle Fuselage
to Corresponding Axisymmetric Analog
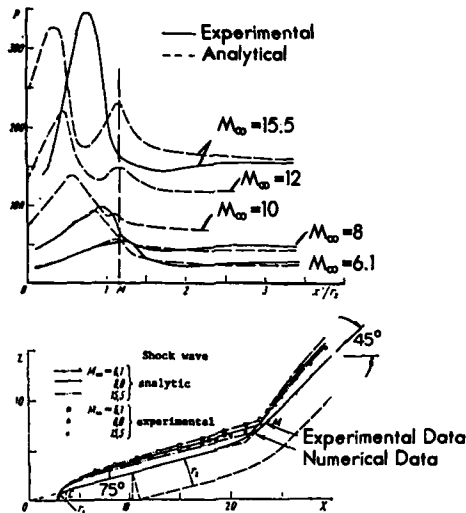
Figure 13 Experimental and Numerical Comparison of Flow Over Cranked Hypersonic Leading Edge
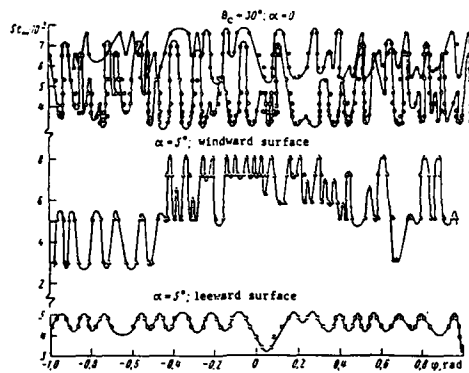
Figure 14 Experimental Heating Data Over an Isentropic Compression Surface at Mach 5
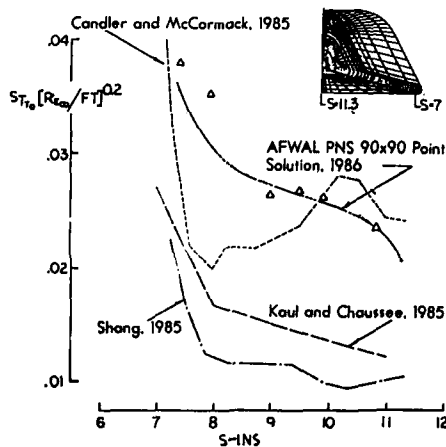
Figure 15 Comparison of Numerical and Experimental Data Over the Lower Surface of the X-24C
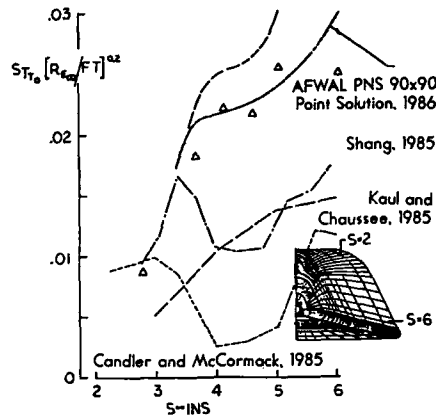
Figure 16 Comparison of Numerical and Experimental Data Over the Lee Surface of the X-24C
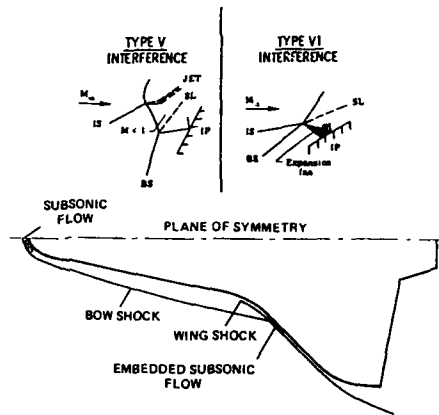

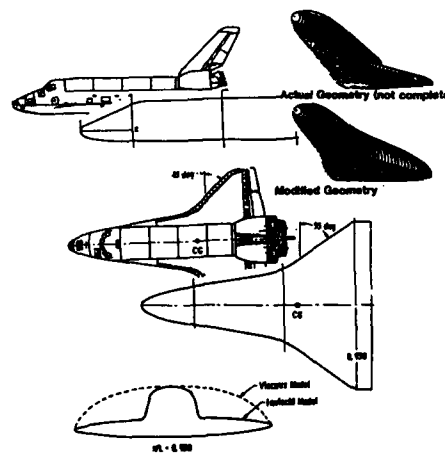Figure 17 Example of the Difficulty Encountered in the Computation of the Space Shuttle

Figure 18 Engineering Simplification of the Space Shuttle Configuration for Analysis

PRESSURE INTERACTION THEORY

The generalized expression for flat plate heating used previously is

$$St\,Re_{\infty_X}^{\;n} = A\,\Big[\frac{U_e\,P_e}{U_\infty\,P_\infty}\Big]^{1-n}\Big[\frac{T_\infty}{T^*}\Big]^{1-2n}\,C^{*n}$$

where

$A = 0.332$ and $n = 0.5$ for laminar flow

$A = 0.0296$ and $n = 0.2$ for turbulent flow

For the same free stream conditions at a given location on the plate and for an arbitrarily imposed pressure ratio

$$\frac{h_{P_{MAX}}}{h_{REF}} = \Bigg[\frac{\big(\frac{U_e}{U_\infty}\big)_{P_{MAX}}\big(\frac{P_e}{P_\infty}\big)_{P_{MAX}}}{\big(\frac{U_e}{U_\infty}\big)_{P_{REF}}\big(\frac{P_e}{P_\infty}\big)_{P_{REF}}}\Bigg]^{1-n}\Bigg[\frac{\big(\frac{T_\infty}{T^*}\big)_{P_{MAX}}}{\big(\frac{T_\infty}{T^*}\big)_{P_{REF}}}\Bigg]^{1-2n}\Bigg[\frac{C^*_{P_{MAX}}}{C^*_{P_{REF}}}\Bigg]^{n}$$

It is further assumed that

(1) the velocity, U_e, does not vary significantly from free stream values in the higher pressure interaction region so that

$$\Big(\frac{U_e}{U_\infty}\Big)_{P_{MAX}} \approx \Big(\frac{U_e}{U_\infty}\Big)_{P_{REF}}$$

(2) that a linear temperature viscosity relation exists so that

$$(C^*)_{P_{MAX}} \approx (C^*)_{P_{REF}}$$

(3) and that the reference temperature is not affected by the interaction so that

$$\Big(\frac{T_\infty}{T^*}\Big)_{P_{MAX}} \approx \Big(\frac{T_\infty}{T^*}\Big)_{P_{REF}}$$

The final approximation becomes

$$\frac{h_{P_{MAX}}}{h_{P_{REF}}} \approx \Big(\frac{P_{MAX}}{P_\infty}\Big)^{1-n}$$

Figure 19 Outline of the Pressure Interaction Theory
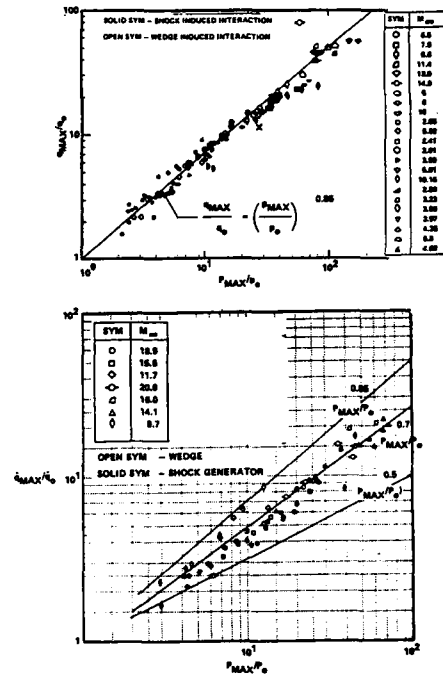
Figure 20 Turbulent and Laminar Interaction Correlations Based on Pressure Interaction Theory
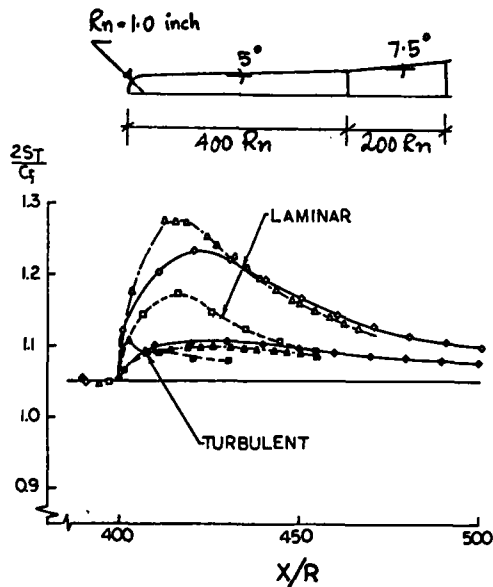

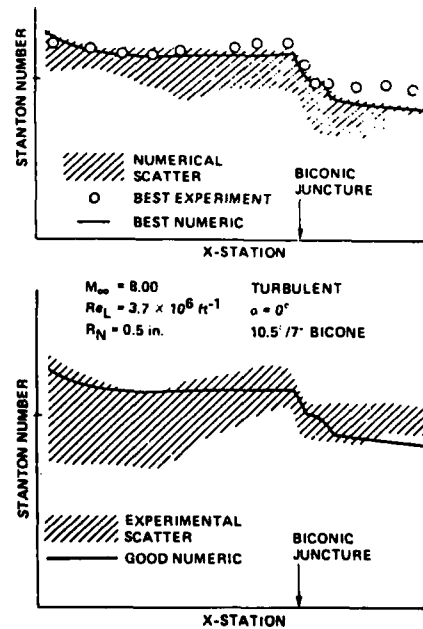Figure 21 Numerical Results for Reynolds Analogy Factor Across a Two Dimensional Interaction

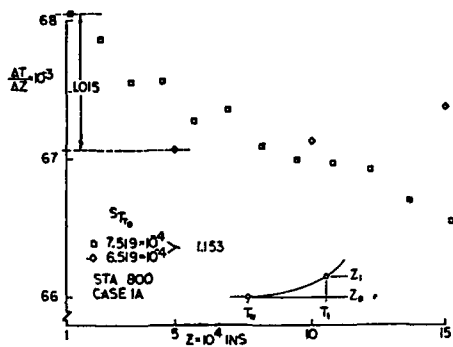Figure 22 Numerical and Experimental Results According to Chaussee

Figure 23 Difficulties in Determining Heat
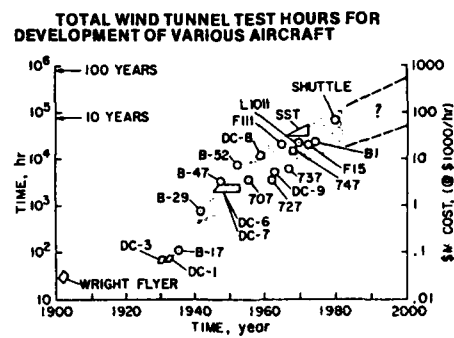Transfer from Numerical Computations

TOTAL WIND TUNNEL TEST HOURS FOR DEVELOPMENT OF VARIOUS AIRCRAFT

Figure 24 Demonstrated Trends in Experimentation
for Various Systems Applications

INVISCID AND VISCOUS HYPERSONIC
AERODYNAMICS -- A REVIEW OF THE OLD AND NEW

by

John D. Anderson, Jr.

Department of Aerospace Engineering
University of Maryland
College Park, Maryland 20742 USA

"Within recent years the development of aircraft and guided missiles has brought a number of new aerodynamic problems into prominence. Most of these problems arise because of extremely high flight velocities, and are characteristically different in some way from the problems which arise in supersonic flight. The term 'hypersonic' is used to distinguish flow fields, phenomena, and problems appearing at flight speeds far greater than the speed of sound from their counterparts appearing at flight speeds which are at most moderately supersonic. The appearance of new characteristic features in hypersonic flow fields justifies the use of a new term different from the well established term 'supersonic'."

Wallace D. Hayes and
Ronald F. Probstein, 1959

SUMMARY

This paper is a review of both inviscid and viscous hypersonic aerodynamics. It is tutorial in manner, and is addressed to students and workers who want to learn the subject, or need to review various aspects of the discipline. This paper also represents a survey of hypersonics, contrasting the "old with the "new". It covers both classical hypersonic considerations as well as the new hypersonics, which is heavily based on computational fluid dynamic methods. High temperature flows are also considered.

I.   INTRODUCTION

Interest and activity in hypersonic aerodynamics has exhibited an extreme cyclical behavior, going from a period of intensive development in the 1950's and early 1960's, to a period of extreme inactivity in the 1970's and early 1980's, and then emerging like the phoenix to a status of even greater glory in the late 1980's. The reasons for this behavior are described at length in Ref. 1, and hence are not repeated here. Suffice it to say that a number of new vehicle concepts have rejuvenated a great deal of modern interest in hypersonic aerodynamics, such as the aero-assisted orb tal transfer vehicle (AOTV), the transatmospheric vehicle (TAV) which is more recently called an aerospace plane, new generation space shuttles, and low hypersonic (M = 5-7) missiles at sea level as high kinetic energy penetrator weapons. Moreover, this interest in hypersonics has spread world wide, with substantial activity in England, France, Russia, Germany, and Japan, as well as the United States. In some respects, the present paper is a sequel, or maybe more appropriately, a "second edition" of Ref. 1.

Specifically, the present paper is primarily tutorial in nature, and is addressed to the non-expert as well as the specialist in the field. Here, we will devote great attention to the important physical aspects of hypersonic flow -- particularly those aspects which are different from the lower speed supersonic regime. Moreover, this paper will present a survey of both inviscid and viscous hypersonic aerodynamics, contrasting the "old" hypersonics of the 1950's and 60's with the "new" hypersonics of today. This survey is limited due to the length constraints of the present paper. However, the reader can find a much more extensive presentation of both classical and modern hypersonic aerothermodynamics in the author's new book (Ref. 2). For a background in the classical aspects of hypersonics, the reader is referred to five major textbooks published more than twenty-three years ago (Refs. 3-7). These five borks remained the only major texts in hypersonic flow until this year.

II.   HYPERSONIC AERODYNAMICS -- WHAT IS IT?

In most conventional aerodynamic textbooks, hypersonic flow is defined as flow at Mach 5 or greater. However, this is just a rule of thumb. There is no discontinuous change in behavior when Mach 5 is achieved, in contrast to the dramatic changes that occur when a flow expands from subsonic to supersonic flow at Mach one. Indeed, when a vehicle flying at Mach 4.99 is slightly accelerated to Mach 5.01, there is no clash cf thunder, and the flow does not change from green to red. Therefore, defining hypersonic flow as flow above Mach 5 is simply a convenience. This is reinforced by H.S. Tsien, who coined the word "hypersonic" in 1946 in an important paper which appeared in a rather obscure journal[a]. Tsien used the words "hypersonic flows" in the title, but did not specifically define the term nor point special attention to the fact that he was coining a new word. From his usage of the word, Tsien clearly inferred that a very high speed flow was being treated, at least high enough where a certain similarity principle held (to be discussed later). Therefore, the words, "hypersonic flow" appeared in our technical vocabulary in a somewhat casual fashion, without fanfare.

More realistically, hypersonic flow is defined as that regime of the high-speed flight spectrum where certain physical phenomena become important that were not significant at supersonic speeds. 'n the

remainder of this section, these phenomena will be described. Hence, the following discussion can be considered a lengthy definition of hypersonic flow.

Thin Shock Layers. Consider the flow over a hypersonic vehicle. At high Mach numbers, the density increase across shock waves supported by such a vehicle is large, and hence the mass flow behind the shock waves can easily squeeze through small areas. As a result, the distance between the body surface and a shock wave is small. The flow field between the shock and body is defined as the shock layer, and for hypersonic speeds, this shock layer can be quite thin. For example, consider the Mach 36 flow of a calorically perfect gas with ratio of specific heats, $\gamma = c_p/c_v = 1.4$ over a wedge of 15° half angle. From standard oblique shock theory (see for example Refs. 9 and 10), the shock wave angle will be only 18°, sketched in Fig. 1; if the high temperature effects of a dissociating and ionizing gas are taken into account, the shock wave will lie even closer to the body. Clearly, the shock layer over the wedge is thin. In turn, the assumptions of a thin shock layer allows the governing flow equations of continuity, momentum, and energy to be somewhat modified, leading to an analytical approach called thin shock layer theory (see for example Ref. 11, Chapter 5 of Ref. 12, and Chapter 4 of Ref. 2).

An even more striking simplification brought about by a thin shock layer can be seen in Fig. 2, which illustrates the streamline directions for the wedge flow in Figure 1. If you view this picture from across the room, it will appear as if the freestream streamlines are not deflected until the flow almost directly impinges on the surface, and thereafter the flow streamlines are very "bunched up" and move in a thin layer tangent to the surface. This picture is very similar to the flow model used by Issac Newton in his Principia of 1687, wherein he assumed that a fluid flow was a rectilinear stream of particles. Newton assumed that, upon striking a surface inclined at an angle θ to the flow, the particles would transfer all their normal momentum to the surface, but that their tangential momentum would be preserved. This flow model leads to an expression for pressure coefficient, c_p, along the surface as

$$c_p = 2 \sin^2\theta \tag{1}$$

-- Newton's famous sine-squared law. (For simple derivations of Eq. (1), see Refs. 2, 9 and 10). Equation (1) was used through the ensuing centuries for such applications as drag predictions on ship hulls, and lift/drag characteristics of heavier-than-air flying machines. All such applications were not very successful because the Newtonian flow model was totally inaccurate for low-speed flows. It was not until the mid-20th century that Newtonian flow finally found a reasonably plausible application -- to hypersonic flow. Looking at Fig. 2 from afar, we see a flow field that resembles a rectilinear stream of particles striking a surface, and then afterwards running parallel to the surface. Indeed, Eq. (1) does a reasonable job in predicting the pressure distribution over some surfaces in hypersonic flow. A modified formula due to Lester Lees at the California Institute of Technology in 1955 does even better. This "modified Newtonian" result is

$$c_p = c_{p_{max}} \sin^2\theta \tag{2}$$

where $c_{p_{max}}$ is the maximum pressure coefficient behind a normal shock at the freestream Mach number. With use of equations (1) and (2) for hypersonic flow, Newtonian theory had finally come into its own.

Entropy Layer. Consider the wedge shown in Figs. 1 and 2, however this time with a blunt nose, as sketched in Fig. 3. At hypersonic Mach numbers, the shock layer over the blunt nose is also very thin, with a small shock-detachment distance, d. In the nose region, the shock wave is highly curved, leading to extreme gradients of entropy in the blunt body shock layer. This "entropy layer" flows downstream, and essentially wets the body for large distances from the nose, as shown in Fig. 3. This entropy layer causes analytical problems when we wish to perform a standard boundary layer calculation on the surface, because there is a question as to what the proper edge conditions should be for the boundary layer. Somehow, the boundary layer must be allowed to "swallow" the entropy layer, as sketched in the insert shown in Fig. 3.

Viscous Interaction. Consider a boundary layer on a flat plate in a hypersonic flow, as sketched in Fig. 4. A high-velocity, hypersonic flow contains a large amount of kinetic energy which is partly dissipated within the boundary layer, causing large temperature increases as indicated in Fig. 4. In turn, the viscosity coefficient within the boundary layer is increased, and the density is greatly decreased. This causes the boundary layer thickness to grow more rapidly. Indeed, the flat plate compressible laminar boundary layer thickness grows essentially as

$$\delta \propto M_\infty^2 / \sqrt{Re_x} \tag{2a}$$

where M_∞ is the freestream Mach number, and Re_x is the local Reynolds number. Clearly, since from Eq. (2a) we see that δ varies as the square of M_∞, δ can become inordinately large at hypersonic speeds.

The thick boundary layers in hypersonic flow cause problems in a standard boundary layer analysis, where the edge conditions for the boundary layer are obtained from an inviscid flow analysis. Due to the extreme thickness of the boundary layer, a major interaction occurs between it and the outer inviscid flow -- giving rise to the viscous interaction phenomena. This viscous interaction can cause some first-order effects on the surface pressure distribution, hence lift, drag and stability on hypersonic vehicles. For example, Fig. 5 illustrates the viscous interaction on a sharp, right circular cone at zero degrees of angle of attack. Here, the pressure on the cone surface, p, is given as a function of distance from the tip. These are experimental results obtained from Ref. 13. If there were no viscous interaction, the surface pressure would be constant, equal to p_c. However, due to the viscous interaction, the pressure near the nose is considerably greater; the surface pressure distribution decays further downstream, ultimately approaching the inviscid value far downstream.

The boundary layer on a hypersonic vehicle can become so thick that it essentially merges with the shock wave -- a merged shock layer. When this happens, the shock layer must be treated as fully viscous,

and the conventional boundary layer analysis must be completely abandoned.

High Temperature Flows. The fact that hypersonic flow can involve high temperatures has already been discussed in conjunction with Fig. 4. However, this just scratches the surface of the subject. Clearly, the extreme viscous dissipation within hypersonic boundary layers can create high temperatures, leading to vibrational excitation, dissociation, and ionization of the gas. If the surface of the vehicle is protected by an ablative heat shield, then products of ablation are also present in the boundary layer, giving rise to some rather complex hydrocarbon chemical reactions. In both accounts, we see that the surface of a hypersonic vehicle can be wetted by a chemically reacting boundary layer.

The boundary layer is not the only region of high temperature flow over a hypersonic vehicle. Consider the nose region of a blunt body, as sketched in Fig. 6a. The bow shock wave is normal, or nearly normal, in the nose region, and the gas temperatures behind this strong shock can be enormous at hypersonic speeds. For example, Fig. 6b is a plot of temperature behind a normal shock wave as a function of freestream velocity, for a vehicle flying at a standard altitude of 52 km; this figure is taken from Ref. 10. Two curves are shown: (1) the upper curve which assumes a calorically perfect nonreacting gas with $\gamma = 1.4$, and which gives an unrealistically high value of temperature; and (2) the lower curve which assumes an equilibrium chemically reacting gas, and which is usually closer to the actual situation. This figure illustrates two important points: (1) by any account, the temperature in the nose region of a hypersonic vehicle can be extremely high, for example reaching approximately 11,000° K at a Mach number of 36 (Apollo re-entry), and (2) the proper inclusion of chemically reacting effects is vital to the calculation of an accurate shock layer temperature. So we see that, for a hypersonic flow, not only can the boundary layer be chemically reacting, but the entire shock layer can be dominated by chemically reacting flow.

High temperature chemically reacting flows can have an influence on lift, drag, and moments on a hypersonic vehicle. For example, such effects have been found to be very important for estimating the body flap deflection necessary to trim the space shuttle during high-speed re-entry. However, by far the most dominant aspect of high temperatures in hypersonics is the resultant high heat transfer rate to the surface. Aerodynamic heating dominates the design of all hypersonic machinery, whether it be a flight vehicle, a ramjet engine to power such a vehicle, or a wind tunnel to test the vehicle. This aerodynamic heating takes the form of heat transfer from the hot boundary layer to the cooler surface -- called convective heating, and denoted by q_C in Fig. 6a. Moreover, if the shock layer temperature is high enough, the thermal radiation emitted by the gas itself can become important, giving rise to a radiative flux to the surface -- called radiative heating, and denoted by q_R in Fig. 6a. For example, for Apollo re-entry, radiative heat transfer was more than 30% of the total heating. For the forthcoming Galileo probe for Jovian entry, radiative heating will be more than 95% of the total heating.

Low Density Flows. All of the above discussion assumes that the flow is a continuum. However, there are certain hypersonic applications which involve densities low enough such that the continuum assummption breaks down. For instance, as noted in Ref. 14 the flow in the nose region of the space shuttle cannot be properly treated by purely continuum assumptions for altitudes above 92 km (about 300,00 ft). As the altitude increases above this value, the normal viscous flow no-slip assumptions at the wall of (1) zero velocity, (2) gas temperature equals the wall temperature, begin to fail. They are replaced by slip effects, in which a velocity and temperature jump at the wall must be assumed. Finally, when the air density becomes rarefied enough, the mean distance a molecule moves between collisions, (the molecular mean free path, λ) can become as large as the scale of the body itself. This is the regime of free molecule flow, where the aerodynamic characteristics of the vehicle are determined by individual, scattered molecular impacts, and must be analyzed on the basis of kinetic theory. For the space shuttle, the free molecular regime begins above 150 km (500,000 ft). Therefore, we can visualize that a hypersonic vehicle moving from a very rarefied atmosphere to a denser atmosphere will shift from the free molecular regime, where individual molecular impacts are important, to the transition regime where slip effects are important, and then to the continuum regime. The similarity parameter that governs these different regimes is the Knudsen number, defined as $Kn = \lambda/L$, where L is a characteristic scale of the body. The values of Kn in the different regimes are illustrated in Figure 7, taken from Refs. 14 and 15. Note that the regions where the continuum Navier-Stokes equations hold are described by $Kn < 0.2$. However, Moss and Bird[14] state that slip effects must be included in the Navier-Stokes equations when $Kn > 0.03$. Free molecular flow begins around a value of $Kn = 1.0$. Hence, the transitional regime is essentially contained within $0.03 < Kn < 1.0$.

Low density effects on shock layer structure are illustrated in Fig. 8, taken from the work of Moss and Bird[14]. Here we see the temperature distribution along the stagnation streamline for the space shuttle nose at an altitude of 92.35 km (about 305,000 ft). (Note that $\lambda = 1$ ft at 342,000 ft, and the nose radius of the space shuttle is about 1 ft; hence, we would expect to see major low density effects for the conditions of the case shown in Fig. 8.) In Fig. 8, n is the distance measured upstream of the nose of the space shuttle; $n = 0$ is the body surface. The solid curve in Fig. 8 pertains to a calculation assuming continuum flow, namely using the viscous shock layer (VSL) technique (to be described later). The solid curve shows that T increases in the direction away from the nose, going from the relatively cool surface to the hot region behind the bow shock wave. The solid curve ends near n = 0.1, signifying the presence and location of a discontinuous, infinitely thin shock wave as appropriate to a continuum picture. In contrast, the open circles show the results of a calculation using the directed simulation Monte Carlo (DSMC) method, which takes into account the low density aspect of the gas. Note that the DSMC results show a continuous variation of T which reaches far upstream of the body. There is no discontinuous shock wave; rather, the "shock" is greatly smeared out over a large region in front of the body.

Low density flows are not an inherent part of the definition of hypersonic flow, and therefore this discussion is not legitimately part of the definition of hypersonic flow. However, hypersonic vehicles frequently fly at very high altitudes, and therefore will encounter low density conditions. Hence, the design and analysis of hypersonic vehicles will sometimes require the consideration of low density flow. We mention this phenomena here only to round out the physical aspects that can occur at hypersonic

2-4

flight conditions. From this point on in the present paper, we will deal with continuum flow only.

Summary

In this section, we have presented a rather lengthy definition of hypersonic flow. However, such a discussion is necessary, because once again we repeat that hypersonic flow is that portion of the high Mach number regime where certain physical phenomena become important, namely the phenomena discussed above, where these phenomena are not particularly important at lower supersonic speeds.

III. ORGANIZATION OF THIS PAPER

The purpose of this paper is to provide a survey of inviscid and viscous hypersonic flow. If this paper were being written 20 years ago, a certain bulk of material would be discussed which today is considered to be "classical" hypersonics. In the present paper, we will spend some time and effort to discuss this classical material, and we will label it simply the "old" hypersonics, as embodied in Refs. 3-7. To modern researchers in hypersonic flow, the "old" hypersonics is necessary knowledge, because it explains in fundamental terms some of the important results and consequences of hypersonic flight. However, since this paper is being written in 1988, we have a bulk of modern work in hypersonics to examine -- this modern work will be labeled the "new" hypersonics. To review the new hypersonics is also a major purpose of the present paper. Therefore, the organization of this paper is straightforward. We will first consider purely inviscid flow, discussing in sequence the old and the new hypersonics, and then we will consider viscous flow, again discussing the old and the new.

The reader will soon appreciate that the "new" hypersonics is dominated by two aspects: (1) the powerful impact of computational fluid dynamics, (2) the fact that manned hypersonic flight vehicles are now a reality, e.g., Apollo in 1969 and lasting into the early 1970's, and the space shuttle. These flight vehicles consumed a great deal of hypersonic aerodynamic resources during their design, and now they provide genuine flight test vehicles for the acquisition of baseline hypersonic aerodynamic data in the real world. In other words, modern hypersonic aerodynamics is dominated by APPLICATIONS, much more so than during the years represented by Refs. 3-7. As a result, this paper will examine some of these applications, both present and future.

Finally, this author makes an apology to all those investigators whose work is not mentioned in this survey. The material reviewed in this paper is limited by two aspects: (1) the author's own subjective views as to the status of modern hypersonics, and (2) practical constraints of time and space. The purpose of this paper is to paint a picture, and leave the reader with some thoughts and impressions. It does not claim to be an all-inclusive survey.

IV. INVISCID HYPERSONIC AERODYNAMICS -- THE OLD

It is well known[9],[10] that subsonic and supersonic flows dealing with small disturbances (e.g., thin bodies at small angles-of-attack) can be studied by means of linear theory. In contrast, at hypersonic speed, the assumption of small disturbances does not lead to linearized solutions -- hypersonic flow is essentially a non-linear phenomenum. Therefore, the classical linear theory developed by Ackeret and others[16] for supersonic flow cannot be simply carried over to the hypersonic regime.

In spite of this difficulty, by the early 1960's, approximate analysis of inviscid hypersonic flows produced some relatively practical results which could be used to estimate pressure distributions, hence lift and wave drag coefficients for some classes of hypersonic bodies. These approximate methods fall under one of two categories: (1) local surface inclination methods, where the pressure depends only on the local angle between a tangent to the surface and the freestream direction, and (2) approximate flow field solutions, where simplified equations of motion are used to calculate flow field properties as well as surface pressure distributions. Finally, the method of characteristics was well-known and understood in the 1950's and 60's. This provides an exact solution to inviscid flow fields which are locally supersonic or hypersonic everywhere. The method of characteristics is straightforward for a two-dimensional or axi-symmetric irrotational flow[10], but rapidly becomes computationally intensive for rotational flows, and especially for three-dimensional flows. Hence, the practical application of the method of characteristics for realistic body geometries had to wait for the advent of high speed digital computers. Therefore, in the present paper the method of characteristics will be considered under both the old and new hypersonics.

In the following paragraphs, we will briefly discuss the essence of several of the old techniques for the prediction of hypersonic flows. As you will see, there are some advantages to these classical methods which need to be appreciated even in the modern day. For a more detailed discussion of these matters, see Ref. 2.

Newtonian -- a local surface inclination method. The basis for the Newton model has already been discussed in Section II. The simple equations which result for pressure coefficient are given by straight Newtonian theory in Eq. (1), and in the modified form by Eq. (2). Newtonian theory was first applied to hypersonic flow by Epstein[17] in 1931 -- far ahead of the wave of interest in hypersonics that surfaces in the 1950's. Newtonian theory becomes more applicable as the Mach number increases. For example, the pressure coefficient on a 15-degree half-angle cone at zero degrees angle of attack is shown as a function of Mach number in Fig. 9. The curve is obtained from the classical Taylor-Maccoll solution (see, for example, Ref. 10), and is exact. Also shown is C_p for a 15-degree half-angle wedge, obtained from exact oblique shock wave theory. Both are compared with the Newtonian result (which of course is independent of M_∞). Note from Fig. 9 that: (1) the accuracy of Newtonian theory improves as M_∞ increases, and (2) Newtonian theory is more accurate for three-dimensional bodies (e.g., the cone) than for two-dimensional bodies (e.g., the wedge). These two trends are general conclusions that apply to Newtonian theory. Also note from Fig. 9 that, at Mach 20, the percentage error in using Newtonian theory is 19° and 5° for the wedge and cone respectively -- not as accurate as might be required for many applications. Therefore, we conclude that although Newtonian theory is very useful due to its

simplicity, in many applications its accuracy leaves something to be desired.

Fig. 9 illustrates another trend that is characteristic of hypersonic flow. Note that C_p for both the wedge and cone changes less and less as M_∞ increases, i.e., C_p becomes relatively insensitive to changes in M_∞ in high Mach numbers. This is an example of the Mach number independence principle, which holds also for hypersonic lift, drag, and moment coefficients. We will have more to say about Mach number independence shortly.

The results in Fig. 9 are obtained from Eq. (1), and apply to relatively slender bodies. In contrast, the modified result, Eq. (2), is more accurate for blunt-nosed bodies. For example, consider Fig. 10 (obtained from Ref. 10) which shows the pressure distribution over an axi-symmetric paraboloid at Mach 8. The solid line is from an exact time-dependent finite-difference solution of the blunt body flow field (to be discussed later); the squares are from modified newtonian given by Eq. (2). The circles are from a steady-state blunt body solution by Lomax and Inouye[18]. The important conclusion here is that Modified newtonian produces a reasonably accurate pressure distribution around the blunt nose.

From a purely theoretical mechanics derivation, Eqs. (1) and (2) should be corrected for centrifugal force effects experienced by the fluid elements in the flow field as they expand around the convex surface; such effects are not accounted for in Eqs. (1) and (2). However, the newtonian results with centrifugal force corrections do not agree well with experimental data in air with the ratio of specific heats $\gamma = c_p/c_v = 1.4$. The reasons for this anomaly are explained in Ref. 2. The answer lies in the fact that Newtonian flow results, which are approximate at finite Mach number for $\gamma = 1.4$, become theoretically exact in the combined limit of $M_\infty \to \infty$ and $\gamma \to 1.0$. See Ref. 2 for an extensive discussion of this matter.

Tangent wedge/Tangent cone -- local surface inclination methods. Consider a compression surface on a body at hypersonic speeds. Let θ be the local angle between the tangent line at a point on the body and the freestream direction. If the body is two-dimensional, calculate the pressure at this point as the pressure that exists behind an oblique shock wave at the freestream Mach number with a deflection angle θ. I.e., assume the pressure at that point is the pressure on a wedge of half-angle θ. If the body is axi-symmetric, calculate the pressure at the point as would exist on a cone with half-angle θ at the freestream Mach number. This is the simple essence of the tangent wedge/tangent cone methods. An example of the tangent cone method is shown in Fig. 11, taken from Ref. 19 (see also Refs. 2 and 7). Here, the surface pressure distribution is plotted versus distance along the ogive. Four sets of results are presented, each for a different value of $K = M_\infty$ (d/ℓ), where d/ℓ is the slenderness ratio of the ogive. The solid line is an exact results obtained from the rotational method of characteristics, and the dashed line is the tangent cone result. Very reasonable agreement is obtained. In Fig. 11, the parameter $K = M_\infty(d/\ell)$ is called the hypersonic similarity parameter; its appearance in Fig. 11 is simply a precurser to our discussion of hypersonic similarity in a subsequent paragraph.

Shock-expansion method -- a local surface inclination method. Consider a sharp-nosed two-dimensional or axi-symmetric body. Assume the nose is a wedge or cone with a semi-angle θ_n. Calculate the pressure at the nose by means of exact oblique shock theory or the exact conical theory[0]. Downstream of the nose, assume a local Prandtl-Meyer expansion along the surface. This is the essence of the shock-expansion method. Typical results are shown in Fig. 12, which shows the pressure coefficient over an ogive at zero degrees angle of attack. Fig. 12 is obtained from Ref. 20 (see also Refs. 2 and 7). The ogive has a slenderness ratio, $d/\ell = \tau = 1.3$. The circles are experimental data, the solid line represents an exact result from the method of characteristics, and the dashed line is from the shock-expansion method. Note that the shock-expansion method yields reasonable results.

Summary comments on the local surface inclination methods. It is not possible to state with any certainty which of the above methods is the best for a given application. All of these methods have their strengths and weaknesses, and some intuitive logic is required to choose one over the others for a given problem. One strength they all have is engineering simplicity. Hence, they are popular design tools for the investigations of large numbers of different hypersonic bodies. Indeed, all of the local surface inclination methods discussed above are embodied in an industry-standard computer program called the "Hypersonic Arbitrary Body Program" originally prepared by Gentry[21], and for this reason frequently referred to as the "Gentry program". This program has been in wide use throughout industry and government since the early 1970's. All of the methods discussed above are options within the Gentry program, and can be called at will for application to different portions of a hypersonic body. This program is mentioned here only to reinforce the engineering practicality of the methods discussed above.

Flow field considerations -- the governing equations. Consider an inviscid flow field. The governing equations for such a flow are the Euler equations, derived for example in Ref. 9 and 10. Written in cartesian coordinates they are:

$$\text{Continuity:} \quad \frac{\partial \rho}{\partial t} + \frac{\partial(\rho u)}{\partial x} + \frac{\partial(\rho v)}{\partial y} + \frac{\partial(\rho w)}{\partial z} = 0 \tag{3}$$

$$\text{x-Momentum:} \quad \rho\frac{\partial u}{\partial t} + \rho u\frac{\partial u}{\partial x} + \rho v\frac{\partial u}{\partial y} + \rho w\frac{\partial u}{\partial z} = -\frac{\partial p}{\partial x} \tag{4}$$

$$\text{y-Momentum:} \quad \rho\frac{\partial v}{\partial t} + \rho u\frac{\partial v}{\partial x} + \rho v\frac{\partial v}{\partial y} + \rho w\frac{\partial v}{\partial z} = -\frac{\partial p}{\partial y} \tag{5}$$

$$\text{z-Momentum:} \quad \rho\frac{\partial w}{\partial t} + \rho u\frac{\partial w}{\partial x} + \rho v\frac{\partial w}{\partial y} + \rho w\frac{\partial w}{\partial z} = -\frac{\partial p}{\partial z} \tag{6}$$

$$\text{energy} \quad : \quad \rho\frac{\partial e}{\partial t} + \rho u\frac{\partial e}{\partial x} + \rho v\frac{\partial e}{\partial y} + \rho w\frac{\partial e}{\partial z} = -p\left(\frac{\partial u}{\partial x} + \frac{\partial v}{\partial y} + \frac{\partial w}{\partial z}\right) \tag{7}$$

In Eqs.(3)-(7), the nomenclature is standard. These equations hold whether or not the flow is chemically reacting. For a nonequilibrium chemically reacting flow, another equation -- the species continuity equation -- must be added to the above system. This will be discussed later.

Mach number independence. If Eqs. (3)-(7) are properly nondimensionalized, and if the boundary conditions for the external flow over a body are taken in the limit of very high Mach number, then the system of equations and boundary conditions become independent of Mach number. Such results, derived in detail in Ref. 2, are mathematical proof for the trends observed and discussed in Fig. 9. As a consequence, pressure coefficient, as well as the lift and wave drag coefficients become independent of Mach number when M_∞ becomes high enough. Such trends are illustrated in Fig. 13, obtained from Ref. 7. In Fig. 13, the measured drag coefficients for spheres and for a large-angle cone-cylinder are plotted versus Mach number, cutting across the subsonic, supersonic, and hypersonic regimes. Note that, in the hypersonic regime, C_D for both the sphere and the cone-cylinder approach a plateau, and become relatively independent of Mach number as M_∞ becomes large.

The hypersonic small disturbance equations. The governing Euler equations (Eqs. (3)-(7)) can be reduced to a simpler system for the hypersonic flow over slender-bodies at small angles of attack. Define the perturbation velocities u', v' and w' as $u = V_\infty + u'$, $v = v'$, and $w = w'$, and form the nondimensional variables denoted by a bar as follows: $x = x/l$, $y = y/l\tau$, $z = z/l\tau$, $u' = u'/(V_\infty\tau^2)$, $v' = v'/(V_\infty\tau)$, $w' = w'/(V_\infty\tau)$, $p = p/(\gamma M_\infty^2 p_\infty)$, and $\rho = \rho/\rho_\infty$. With these quantities, and for an

adiabatic, inviscid (hence isentropic) steady flow, Eqs. (3)-(7) can be reduced by ignoring terms of order τ^2, where as before, τ is the slenderness ratio of the body. The resulting system is (see the detailed derivation in Ref. 2):

$$\frac{\partial \rho}{\partial x} + \frac{\partial (\rho v')}{\partial y} + \frac{\partial (\rho w')}{\partial z} = 0 \tag{8}$$

$$\rho \frac{\partial u'}{\partial x} + \rho 'v' \frac{\partial u'}{\partial y} + \rho w' \frac{\partial u'}{\partial z} = -\frac{\partial p}{\partial x} \tag{9}$$

$$\rho \frac{\partial v'}{\partial x} + \rho v' \frac{\partial v'}{\partial y} + \rho w \frac{\partial v'}{\partial z} = -\frac{\partial p}{\partial y} \tag{10}$$

$$\rho \frac{\partial w'}{\partial x} + \rho v' \frac{\partial w'}{\partial y} + \rho w' \frac{\partial w'}{\partial z} = -\frac{\partial p}{\partial z} \tag{11}$$

$$\frac{\partial}{\partial x}(\frac{p}{\rho^\gamma}) + v' \frac{\partial}{\partial y} (\frac{p}{\rho^\gamma}) + w' \frac{\partial}{\partial z}(\frac{p}{\rho^\gamma}) = 0 \tag{12}$$

Eqs. (8)-(12) are the hypersonic small disturbance equations. They closely approximate the hypersonic flow over slender bodies. They are limited to flow over slender bodies because terms of order τ^2 have been neglected. They are also limited to hypersonic flow because some of the nondimensional terms are of order-of-magnitude unity only for high Mach numbers (see extensive discussion in Ref. 2). Note that u' in the above system of equations appears only in Eq. (9). Hence, in the hypersonic small disturbance equations, u' is decoupled from the system. This is a mathematical ramification of the fact that the change in velocity in the flow direction over a hypersonic slender body is much smaller than the change in velocity perpendicular to the flow. This has implications in the blast wave theory, to be discussed later.

Hypersonic similarity -- an approximate flow field result. Eqs. (8)-(12), along with the appropriate boundary conditions, lead to the definition of a hypersonic similarity parameter $K = M_\infty\tau$, where as before τ is the slenderness ratio. The following hypersonic similarity principle holds:

Affinely related bodies with the same values of γ, K, and α/τ will have: (1) the same values of c_l/τ^2 and c_d/τ^3 for two dimensional flows, when referenced to the planform area; and (2) the same values of C_L/τ and C_D/τ^2 for three-dimensional flows when referenced to have area.

Here, c_l and C_L are lift coefficients, and c_d and C_D are drag coefficients. Also, C_p/τ^2 is a function of γ, K, and α/τ. Hypersonic similarity is nicely demonstrated in Fig. 14 (obtained from (Ref. 7), which gives the calculated pressure coefficient $C_p/Tan^2\theta_w$ versus the hypersonic similarity parameter $M_\infty Tan\theta_w$ for a series of wedges of different angles $\theta_w = \tau$. Note that the results for the different wedges tend to fall on the same curve, except for the very large values of θ_w and for low Mach numbers -- conditions for which Eqs. (8)-(12) do not hold and hence for which hypersonic similarity is not valid. The advantage of the hypersonic similarity principle is the same as any fluid dynamic similarity concept, namely, results for different flows over different bodies can be obtained by correlation from other known flows, thus reducing wind tunnel work and, today, the amount computer work necessary to study certain problems. Hypersonic similarity, which is derived from Eqs. (8)-(12), has been thoroughly verified by experiment (see Ref. 2).

Blast wave -- an approximate flow field method. All practical hypersonic vehicles have blunt noses and leading edges to reduce aerodynamic heating. Therefore, the calculation of the flow over a blunt body is of extreme interest. Prior to 1966, no truly practical solution to the direct blunt body problem existed, although many efforts were made during the "old" hypersonics to obtain it. However, for blunt-nosed slender bodies, a useful, approximate analysis called blast wave theory was developed during the 1950's and 60's. Blast wave theory assumes the following physical picture. Imagine a blunt-nosed slender hypersonic body moving through the air, as shown in Fig. 15. Imagine also a stationary plane in

front of the moving vehicle, perpendicular to the vehicle motion, as also shown in Fig. 15. As the vehicle crosses this plane, the flow field in the plane resembles the flow created by sudden energy addition at a point, and the creation of a unsteady "blast wave" that propagates outward from that point. The blunt nose "blasting" through the plane provides this energy source. In addition, the body surface crossing the plane as a function of time resembles an expanding "piston" in the plane, with the corresponding unsteady flow associated with the expanding piston. Clearly, examining Fig. 15, there is an equivalence between the unsteady flow in the plane shown at the right, and the spatial variation of the body coordinates and shock wave shown at the left. This figure illustrates a combination of both the blast wave analogy and what is frequently called the "hypersonic equivalence principle", relating a steady hypersonic flow to an equivalent unsteady flow in a plane perpendicular to the motion of the body.

This equivalence is easily seen mathematically by writing the Euler equations for an unsteady two-dimensional flow in the y-z plane

$$\frac{\partial \rho}{\partial t} + \frac{\partial (\rho v)}{\partial y} + \frac{\partial (\rho w)}{\partial z} = 0 \tag{13}$$

$$\rho \frac{\partial v}{\partial t} + \rho v \frac{\partial v}{\partial y} + \rho w \frac{\partial w}{\partial z} = - \frac{\partial p}{\partial y}$$

$$\rho \frac{\partial w}{\partial t} + \rho v \frac{\partial w}{\partial y} + \rho w \frac{\partial w}{\partial z} = - \frac{\partial p}{\partial z} \tag{15}$$

$$\frac{\partial}{\partial t}(\frac{p}{\rho^\gamma}) + v \frac{\partial}{\partial y}(\frac{p}{\rho^\gamma}) + w \frac{\partial}{\partial z}(\frac{p}{\rho^\gamma}) = 0 \tag{16}$$

Comparing Eqs. (13)-(16) with (8), (10)-(12) we that they are identical. I.e., the steady three-dimensional flow over a hypersonic slender body (Eqs. (8), (10)-(12)) is equivalent to the unsteady flow in one less space dimension (Eqs. (13)-(16)). Using this equivalence principle along with solutions of the flow behind a blast wave (such solutions for massive energy released at a point were first obtained by G.I. Taylor[22] in 1950), the shock wave shape, as well as the inviscid flow field between the shock and the body, can be calculated. Of particular importance, blast wave theory leads to the following equations for the pressure distributions over a blunt flat plate.

$$C_p = 0.17 \ C_D^{2/3} \ (x/d)^{-2/3} \tag{17}$$

and over a blunt cylinder

$$C_p = 0.094 \ C_D^{1/2} \ (x/d)^{-1} \tag{18}$$

where C_D is the drag coefficient of the blunt leading edge, x is the running length along the surface from the leading edge, and d is the plate thickness or cylinder diameter.

A detailed discussion of blast wave theory is given in Ref. 2, and a thorough experimental investigation of the accuracy of Eqs. (17) and (18) is given by Lukasiewicz[23].

Just for fun, let us use the "old" hypersonics to calculate the pressure distribution along the windward centerline of the space shuttle. Let L denote the length of the shuttle, and d the thickness of the fuselage near the canopy. From a good three-view of the shuttle (such as appears in Fig. 1 of Ref. 24), the finenes ratio, L/d = 7. Moreover, the drag coefficient of a hemisphere from the Newtonian theory[18] is $C_D = 1$. Substituting these values into Eq. (18) written as

$$C_p = 0.094 \ C_D^{1/2} \ (x/L)^{-1}(L/d)^{-1} \tag{19}$$

we obtain

$$C_p = 0.0134/(x/L) \tag{20}$$

Equation (20) holds for zero-degrees angle of attack. To take angle of attack, α, into effect, let us simply add the Newtonian contribution, $2 \sin^2 \alpha$, to Eq. (20) obtaining

$$C_p = 0.0134/(x/L) + 2 \sin^2 \alpha \tag{21}$$

Let us choose a point on the shuttle trajectory corresponding to α = 40° and $M_\infty = 21.6$. For α = 40°, Eq. (21) becomes

$$C_p = 0.0134/(x/L) + 0.826 \tag{22}$$

Results from Eq. (22) are plotted in Fig. (16) as the solid curve. These results are compared with actual flight data from the STS-3 (open circles) and STS-5 (solid circles) shuttle missions; these flight data are obtained from Ref. 25. The agreement between theory and flight data in Fig. 16 is quite remarkable, especially when considering that the theoretical curve can be calculated in a few minutes by hand. From this point of view, the "old" hypersonics can be very useful for some applications.

Thin shock layers -- an approximate flow field. We have discussed in Section II that shock layers over hypersonic bodies are thin (refer again to Figs. 1 and 2). This result can be used to some advantage in the development of approximate theories for the analysis of hypersonic shock layers, giving rise to a number of different approaches, all under the general heading of "thin shock layer theory". An interesting discussion of thin shock layer theory can be found in Ref. 26; additional discussion is given

in Ref. 12.

A good example of thin shock layer theory is the analysis of Maslen[27]. We do not have the space to outline this method here (see Ref. 2 for a lengthy discussion of Maslen's method). However, the method is simple, and leads to reasonable results as shown in Fig. 17. Here, the pressure distribution and shock shape are given for a hemisphere cylinder. Good agreement is obtained with the experimental results of Kubota[28]. Also shown are the numerical results of Inouye and Lomax[18].

V.   INVISCID HYPERSONIC AERODYNAMICS -- THE NEW

The "new" hypersonics is dominated by computational fluid dynamics (CFD), which has revolutionized the way we analyze aerodynamic flows for all speed regimes, not just hypersonics. A brief introduction to CFD is given in Ref. 10 as applied to high-speed flow. Ref. 29 is a survey of CFD, and Ref. 30 is a definitive textbook on the subject. Therefore, no further elaboration on the general aspects of CFD will be given here.

The techniques of computational fluid dynamics and the corresponding development of modern high-speed digital computers now makes it possible to accurately analyze the complete flow field around a three-dimensional vehicle for inviscid hypersonic flow. What a tremendous revolution in comparison to the few approximate methods from the "old" hypersonics! This revolution was started with the advent of time-dependent finite-difference solutions for flows over supersonic and hypersonic blunt bodies in the mid-1960's. The classic paper by Moretti and Abbett[31] represents the first practical solution of the supersonic blunt body problem -- a problem that, during the "old" hypersonics, treated the blunt body with the steady flow equations; it is well known that such steady flows are described by elliptic partial-differential equations in the subsonic region, and hyperbolic equations in the supersonic region. This mixed nature of the equations created great difficulty in calculating both the subsonic and supersonic regions consistently with the same technique. In contrast, the unsteady inviscid flow equations are hyperbolic with respect to time, no matter whether the flow is locally subsonic or supersonic. This leads to a well-posed initial value problem, wherein a time-dependent solution starts with arbitrary initial conditions throughout the flow field, calculates new values of the flow in steps of time, and approaches a steady-state at large times. This steady-state is the desired result; the time dependent calculations are just a means to that end. The typical performance of a time-dependent blunt body solution is shown in Figs. 18 and 19 obtained from Ref. 32. Fig. 18 illustrates the time-dependent motion of the bow shock wave on a parabolic cylinder at M_∞ = 4, starting with the assumed shock shape at time zero, and converging to the proper steady-state value at large times. These figures are shown just to illustrate the nature of the time-dependent technique. Perhaps the best indication of the revolution created by the time-dependent technique is that the blunt body problem that was once a serious, very challenging, and extremely difficult problem in the "old" hypersonics, requiring a large amount of intensive research, is now given as a homework problem in a computational fluid dynamic graduate course at the University of Maryland. (For an introductory discussion on the time-dependent technique, see Chpt. 12 of Ref. 10).

An excellent example of our current ability to calculate hypersonic inviscid flows is given by the work of Weilmuenster[25]. Here, a time-dependent method is used to calculate virtually the complete three-dimensional flow field about a shuttle-like vehicle. Embodied in a computer program called HALIS (High-Alpha Inviscid Solution) at the NASA Langley Research Center, this solution deals equally well with both the supersonic and hypersonic flows over most of the body, as well as the subsonic regions encountered in the nose region, and at the wing-body juncture. Moreover, it can readily treat high angle-of-attack cases, when large regions of subsonic flow can exist over the windward surface of the shuttle. However, such a code is not an "everyday" tool in everybody's inventory; HALIS is written for a vector processor, and a reasonable definition of the three-dimensional flow field requires close to 100,000 grid points. Nevertheless, it represents a benchmark in the "new" hypersonics. To emphasize this, you are reminded of a statement contained in the classic textbook of Liepmann and Roshko (Ref. 33) where, in their discussion of the flow over a simple supersonic blunt body at zero degrees angle of attack, they categorically state that "the shock shape and detachment distance cannot, at present, be theoretically predicted." Contrast this situation in 1957 with the "new" hypersonics illustrated in Fig. 20, obtained from Ref. 25. Here, we see the complete shock shape and location for a complex three-dimensional shuttle-like vehicle at high angle-of-attack -- calculated by means of the time-dependent technique. The solution also yields the complete inviscid flow field between the shock and the body, including the surface flow on the body.

If the flow field is completely supersonic or hypersonic, there is no need for a time-dependent technique; rather, the steady-state method of characteristics, or downstream-marching-finite-difference methods are sufficient. The method characteristics has been available since 1929, when Ludwig Prandtl and Adolf Busemann first used it in conjunction with supersonic nozzle flows. Therefore, it was part of the "old" hypersonics, and it represents an exact solution for the inviscid flow. However, for the three-dimensional rotational flows which are of primary interest in hypersonics, the method of characteristics becomes tedious, and requires a massive amount of computations. For this reason, the practical implementation of the method of characteristics had to wait for the digital computers of the 1960's, and therefore became part of the "new" hypersonics. The work by the late John Rakich and his colleagues is a good example of this technique[34,35]. In the past decade, forward marching, explicit finite-difference solutions have become more popular than the method of characteristics because they are inherently more straightforward to program. The pioneering work on this method was done by Paul Kutler and colleagues, who applied it to space shuttle flow fields[36-38]. This work constituted the first detailed flow field calculations on the shuttle design. It had, however, a major drawback, namely, that the calculation would go unstable whenever a pocket of locally subsonic flow was encountered -- once again the problem of the mixed elliptic and hyperbolic regions. (There is no practical way around this problem without going to a time-dependent method, as described earlier.) Such pockets of locally subsonic flow exist near the intersection of the shock waves from the body and wing; as soon as such a pocket is encountered, the calculations stop. This is why such calculations are carried out for only the forward portions of the shuttle. A more modern version of the forward marching finite-difference scheme

is the work of Marconi et al[39], which led to the development of the STEIN code. Maus et al[40] have used this code to study high temperature effects on the space shuttle flow field, as will be discussed later.

Note that both the method of characteristics and the forward marching schemes require starting conditions (initial data) along a surface downstream of the subsonic region at the nose. These initial data are usually supplied from an independent, time-dependent blunt body solution, as described earlier.

As an interim summary, clearly the "new" hypersonics has profited greatly from the advancements made in CFD for the calculation of inviscid flows. These are "exact" solutions in that the Euler equations (Eqs. (3)-(7)) are being solved exactly; no assumptions such as small perturbations or thin shock layers have to be made. A good example is the development of the HALIS code, used in Ref. 25 and described in more detail in Refs. 41 and 42. These Euler solutions are being made for three-dimensional flows over complete hypersonic vehicles -- something the "old" hypersonics only dreamed of.

It is appropriate to end this section with some results for hypersonic inviscid flows obtained in the era of the "new" hypersonics. For example Fig. 21, obtained from Ref. 40, shows the calculated windward pressure coefficient distributions over the space shuttle for two angles of attack, and at the widely different Mach numbers of 8 and 23. The detailed calculations are for inviscid flow, obtained in the nose region by a time-dependent technique, followed by an explicit forward-marching finite-difference solution in the supersonic/hypersonic regions. Note that the C_p distributions for the two different Mach numbers are virtually the same -- an excellent example of the Mach number independence principle. As an example of results obtained from the three-dimensional method of characteristics, Fig. 22 shows the surface pressure distribution over a blunt-nose cone (half-angle of 15 degrees) at an angle-of-attack of 10 degrees, obtained from the results of Rakich and Cleary[35]. The pressure coefficient distributions are given at three meridional angles; $\phi = 0°$ corresponds to the leeward meridional plane, $\phi = 180°$ to the windward plane, and $\phi = 90°$ half way around. Agreement between the calculations and experiment are excellent. Note on the windward side that the pressure goes through a local minimum. In expanding over the blunt nose, the pressure overexpands downstream of the shoulder, falling below the sharp cone result, and then recompreses to the sharp cone result far downstream. (We note here a weakness of the blast wave theory discussed in Section IV; blast wave theory is incapable of predicting the type of overexpansion and recompression seen in Fig. 22.) The overexpansion around the shoulder shown here is typical of hypersonic flow over blunt-nose axi-symmetric bodies. Note that a similar overexpansion is seen in the pressure distribution over the bottom surface of the space shuttle given in Fig. 21. Another recent example of hypersonic inviscid flow are the results of Pfitzner and Weiland[43] for a shuttle-like vehicle. The inviscid surface streamlines from their implicit, time-dependent, finite-difference calculations are shown in Fig. 23. Finally, a very recent space and time-marching solution of the Euler equations over an experimental hypersonic research vehicle configuration is reported by Newberry et al.[44] Using an advanced finite volume algorithm developed by Chakravarthy and Szema[45], the results shown in Fig. 24 were obtained. Shown here are the Mach number contours (a black and white copy of a color graphics display) at various longitudinal stations along the body. These results represent the present state-of-the-art in hypersonic inviscid flow field calculations.

IV. HIGH TEMPERATURE INVISCID FLOWS

Although high temperature flows are not a major aspect of the present paper (such matters are covered by B. Aupoix in a companion paper to this AGARD volume), they are indeed a major aspect of hypersonic flow. Hence, some coverage is appropriate here mainly to bring out the primary physical effects. For a self-contained introductory treatment of high temperature flows, see Chapters 13 and 14 of Ref. 10. For an in-depth presentation, see Ref. 2.

When a high speed flow is slowed, kinetic energy is converted to internal energy, thus increasing the gas temperature. At hypersonic speeds, these temperature increases can be severe, as discussed in Section II. The consequent effects -- dissociation, ionization, high convective and radiative heating rates, etc., all become a dominant aspect of hypersonics. This was recognized early in the evolution of hypersonic research, and massive efforts to properly account for these high temperature effects were mounted during the 1950's and 60's. Great progress was made during these years; the major aspects of a high temperature chemically reacting gas were generally understood, and numerical methods for including these aspects in flow calculations were developed. This state-of-the-art was represented quite well by the books written by Vincenti and Kruger[46], and by Clark and McChesney[47]. In addition, the important aspects of chemically reacting boundary layer theory was nicely described in the book by Dorrance[48].

The velocity-altitude regions where various high temperature effects are important for hypersonic flight are shown in Fig. 25, obtained from Ref. 49. Superimposed on this velocity-altitude map are several flight paths for hypersonic vehicles. Clearly, high temperature effects are important over a substantial portion of the flight paths.

In order to understand the nature of high temperature chemically reacting flow, consider the following. Let τ_f be the characteristic time for a fluid element to traverse a flow field of interest. Let τ_c be the characteristic time for chemical reactions and/or vibrational energy to approach equilibrium. Then, if $\tau_f \gg \tau_c$, the flow is considered to be in local thermal and chemical equilibrium. If $\tau_f \ll \tau_c$, the flow is assumed to be frozen. For all other cases, especially when $\tau_f \approx \tau_c$, the flow is nonequilibrium. For inviscid equilibrium flow, Eqs. (3)-(7) are sufficient, along with appropriate equations of state for the equilibrium reacting gas. For frozen flow, no chemical reactions occur and the vibrational energy does not change; this is our familiar calorically perfect gas with constant γ. However, for nonequilibrium flow, Eqs. (3)-(7) must be expanded to include the species continuity equation

$$\rho \left(\frac{\partial c_i}{\partial t} + u \frac{\partial c_i}{\partial x} + v \frac{\partial c_i}{\partial y} + w \frac{\partial c_i}{\partial z} \right) = \dot{W}_i \tag{23}$$

Here, c_i is the mass fraction of chemical species i, and W_i is the rate of change of species i due to chemical reactions. Eq. (23), coupled with the other Euler equations (3)-(7), determines the distribution of the various chemical species throughout the nonequilibrium flow field. Again, the reader is encouraged to study Refs. 2, 46, 47, and 48 for a detailed understanding of such flows.

A classic example of the high temperature nonequilibrium effects on a hypersonic blunt body flow field was shown in the pioneering study by Hall et al in 1962 (see Ref. 50). They presented calculated results along two streamlines in the blunt body flow field, streamlines A and B shown in Fig. 26. The temperature, pressure and density variations as a function of s, the distance along these two streamlines, are shown in Fig. 27. The temperature along streamline A, T_A, exhibits an initial rapid decrease behind the shock; this is due to the finite rate dissociation of both O_2 and N_2, and is very similar to the behavior observed in the nonequilibrium flow behind normal shock waves[2,16]. The more gradual decrease in T_A for $s/R_s > 0.2$ is due primarily to the gasdynamic expansion around the body. Similarly, the initially slight increase in p_A and the substantial increase in ρ_A are due to the chemical nonequilibrium effects, and their subsequent decreases beyond $s/R_s = 0.2$ are indicative of the gasdynamic expansion around the body. It is important to note that the flow field temperature is affected the most and the pressure the least by chemically reacting effects. In contrast to streamline A, streamline B crosses a much weaker portion of the bow shock, and the gasdynamic expansion effects are dominant over the purely chemically reacting effects. The corresponding variations of atomic oxygen and atom nitrogen concentrations are shown in Fig. 28. The increase in both these quantities along each streamline is due to the finite-rate progression of dissociation reactions in the high temperature flow.

Nonequilibrium processes introduce a scale effect into the flow field. For example, consider the supersonic or hypersonic flow of a calorically perfect gas over a wedge; we know from the standard oblique shock solutions that the shock wave is straight, and that a uniform flow exists between the shock and the wedge surface. The same is true for chemically equilibrium flow. However, in the nonequilibrium flow over the wedge, the shock wave becomes curved, and the flow is no longer uniform behind the shock. This scale effect is illustrated in Fig. 29, obtained from the work of Spurk et al[51]. Here, the pressure and temperature distributions along the surface of a wedge are given as functions of distance along the wedge. If the gas were perfect, T and p would be constant along the wedge surface: the variations shown in Fig. 29 are indicative of the substantial influence of nonequilibrium effects.

VII. VISCOUS HYPERSONIC AERODYNAMICS -- THE OLD

The early work on viscous flows in hypersonic aerodynamics centered around solutions of the boundary layer equations. In this section, to be consistent with our previous discussion on inviscid flow, we should display the complete Navier-Stokes equations, and then show the boundary layer equations as a simplified system obtained from an order-of-magnitude reduction of the Navier-Stokes equations. However, we can not afford the space to write these rather lengthy equations. Instead, you are encouraged to read the derivation of the Navier-Stokes equations in Ref. 9; these equations are the full equations of motion for a viscous, compressible flow, including the transport phenomena of viscosity, thermal conduction, and (for a chemically reacting gas) diffusion. The full Navier-Stokes equations for a chemically reacting gas are discussed at length in Ref. 2. Similarly, you are encouraged to read the derivation of the boundary layer equations, also given in Ref. 9. In our subsequent discussion, we will assume that the reader is familiar with both the Navier-Stokes and boundary layer equations.

Boundary layer results. The results obtained from various solutions of the boundary layer equations for hypersonic flow show that the skin friction and the heat transfer coefficients are both reduced as M_∞ increases. For example, Fig. 30 illustrates the variation of Stanton number with Reynolds number and Mach number for an insulated flat plate. Note that for both laminar and turbulent flow, the heat transfer coefficient (and skin friction coefficient, as well) decreases as M_∞ increases. The results of Fig. 30 are obtained directly from Ref. 52. Also obtained from Ref. 52 are equations for stagnation point heat transfer as follows

$$\text{(For a cylinder)} \quad q = 0.57 \, Pr^{-0.6} (\rho_e \mu_e)^{0.5} \sqrt{\frac{dU_e}{ds}} (h_{aw} - h_w) \tag{24}$$

$$\text{(For a sphere)} \quad q = 0.763 \, Pr^{-0.6} (\rho_e \mu_e)^{0.5} \sqrt{\frac{dU_e}{ds}} (h_{aw} - h_w) \tag{25}$$

where Pr is the Prandtl number, ρ_e and μ_e are the density and viscosity coefficient at the outer edge of the stagnation point boundary layer, dU_e/ds is the velocity gradient at the stagnation point, and h_{aw} and h_w are the adiabatic wall and actual wall enthalpy respectively. From Eqs. (24) and (25) note that, everything else being equal, q for a sphere is larger than for a cylinder. This is due the three-dimensional relieving effect, which leads to a thinner boundary layer on the sphere, hence higher temperature gradients within the thinner boundary layer. Also assuming modified Newtonian theory, Eq. (2), we can readily show (see Ref. 2) that at the stagnation point

$$\frac{dU_e}{ds} = \frac{1}{R} \sqrt{2(\frac{p_e - p_\infty}{\rho_e})} \tag{26}$$

Inserting Eq. (26) into Eqs. (24) and (25), we see that heat transfer at the stagnation point varies inversely with the square root of the nose radius -- leading to the conclusion that all hypersonic bodies should have blunt noses to reduce the heat transfer to the nose.

All of the above results are mentioned just to represent the status of the "old" hypersonics, as obtained from boundary layer solutions. Much was understood about hypersonic boundary layer

characteristics in the "old" hypersonics; this is nicely summarized in Ref. 6. Indeed, this era also saw some of the pioneering work on high temperature effects on hypersonic boundary layers. The classic paper by Fay and Riddell[53] on stagnation point heat transfer in dissociated air brought out the basic physical effects of a chemically reacting boundary layer assuming either frozen, equilibrium, or nonequilibrium flow. The effects of a catalytic wall were also first demonstrated here. For example, the boundary layer solutions in Ref. 53 were correlated by Fay and Riddell to obtain equations for heat transfer such as the following for an equilibrium boundary layer.

$$q = 0.76 \ Pr^{-0.6} (\rho_e \mu_e)^{0.4} (\rho_w \mu_w)^{0.1} \sqrt{\frac{dU_e}{ds}} \ (h_{o_e} - h_w) \ \{1 + (Le^{0.52} - 1)(\frac{h_D}{h_{o_e}})\}_i \tag{27}$$

Equations similar to Eq. (27) for frozen boundary layers with and without catalytic walls were also obtained. In Eq. (27), h_{o_e} is the total enthalpy at the outer edge of the boundary layer, and h_D is the average heat of formation for the gas mixture at the outer edge. Also, Le is the Lewis number, defined as $\rho D_{12} c_p/k$, where D_{12} is the binary diffusion coefficient. Mass diffusion plays a strong role in chemically reacting viscous flows (see the extensive discussions in Ref. 2), and the appearance of Le in Eq. (27) is a reflection of such diffusion effects. Finally, note the similarities between Eq. (27) for a chemically reacting gas, and Eq. (25) for a non-reacting gas. Typical results from the Fay and Riddell analysis are shown in Figs. 31 and 32. In Fig. 31 we see the stagnation point boundary layer profiles of temperature and atom mass fraction through the boundary layer, where η is a transformed coordinate normal to the wall. Two results are shown, one for an equilibrium boundary layer, and the other for a frozen boundary layer with a fully catalytic wall. (A fully catalytic wall is a surface that instantly enhances the recombination process, such that the chemical composition is in local equilibrium at the wall, no matter what the state of the boundary layer itself. In most cases, the wall is cool enough such that the equilibrium value of the atom mass fraction at the wall is zero, $C_{A,w} = 0$; i.e., in equilibrium at low enough temperature, the gas is all molecules and virtually no atoms.) Note in Fig. 31 that the equilibrium temperature is above the frozen temperature. This is because in equilibrium, the highly dissociated gas at the outer edge of the boundary layer, when encountering the cooler inner regions of the boundary layer, will recombine, releasing some of its chemical energy, and therefore keeping the temperature higher than in a frozen flow, where no chemical reactions occur. The equilibrium atom mass fraction is also shown in Fig. 31, showing a decrease from about 0.5 at the outer edge where the temperature is high, to zero at the wall, where the temperature is low. The frozen mass fraction also exhibits a similar variation, but for entirely different reasons. The fully catalytic wall insures $C_{Aw} = 0$ at the cold wall, and the frozen profile of C_A through the boundary layer is due entirely to diffusion -- it has nothing to do with any chemical reactions within the boundary layer, which of course do not occur by definition of a frozen flow. Stagnation point heat transfer results are shown in Fig. 32. Here, the heat transfer coefficient, $Nu/Re^{1/2}$ is given as a function of the chemical reaction rate; high rates at the right of Fig. 32 correspond to equilibrium flow, and the low rates at the left correspond to frozen flow. Note that, for a fully catalytic wall, the heat transfer rate is essentially the same, whether or not the flow is equilibrium, nonequilibrium, or frozen. Whether the chemical energy is released within the boundary layer (as in the case of equilibrium flow) or at the wall (as in the case of a frozen flow with a fully catalytic wall), about the same amount of energy is ultimately transferred to the wall. On the other hand, if the wall is non-catalytic, as the nonequilibrium boundary layer results progressively go from near equilibrium conditions to near frozen conditions, the heat transfer to the wall decreases, amounting to more than a 50 percent decrease at the left of Fig. 32. These results were the first to point out that the use of a non-catalytic wall can substantially reduce aerodynamic heating from a nonequilibrium boundary layer.

Non-similar chemically reacting boundary layer flows have been addressed by Blottner[54,55], among others. Blottner uses an implicit finite difference method for solving the boundary layer equations. Ref. 54 treats the case of a dissociating gas, and Ref. 55 extends this work to a partially ionized gas. Blottner's work soon became the standard method for calculating chemically reacting boundary layers around hypersonic bodies, and it remains so to the present day. A sample of Blottner's calculations for the nonequilibrium flow over a 10° cone at 100,000 foot altitude and V_∞ = 21000 ft/sec is given in Fig. 33. Here, the atom mass fraction is shown as a function of the normal coordinate across the boundary layer at several streamwise stations. Note that the atom mass fraction increases with distance downstream of the nose within the hot region of the boundary layer, approaching the equilibrium values far downstream.

Viscous interaction. The physical nature of the classic viscous interaction problem was discussed in Section II. It can be readily shown (see for example Ref. 2) that the governing viscous interaction parameter for pressure distribution is

$$\bar{\chi} = \frac{M_\infty^3}{\sqrt{Re}} \ \sqrt{C} \tag{28}$$

where $C = \rho_w \mu_w / \rho_e \mu_e$. The variation of pressure as a function of $\bar{\chi}$ depends on whether the viscous interaction is strong or weak. For the strong interaction region, the boundary layer grows very rapidly, the outer inviscid flow is greatly affected, and the effects on the inviscid flow feed back into the boundary layer itself. For the weak interaction regime, the feedback of the changes in the outer inviscid flow are small, and are not included. Typical viscous interaction results for both the strong and weak interaction regimes on an insulated flat plate are shown in Fig. 34, obtained from Hayes and Probstein[4]. Note that viscous interaction effects become stronger as M_∞ increases and Re decreases.

VIII. VISCOUS HYPERSONIC AERODYNAMICS -- THE NEW

Once again, the application of computational fluid dynamics distinguishes the "new" from the "old" hypersonic aerodynamics. In modern hypersonic aerodynamics, calculations are now made assuming the entire shock layer is viscous, all the way from the body to the shock wave. There is a hierarchy of solution techniques, generally classified under: (1) viscous shock layer (VSL) solutions, (2)

parabolized Navier-Stokes (PNS) solutions, and (3) full Navier-Stokes solutions. *There is no space in the present paper to do justice to these techniques -- see Ref. 2 for a detailed discussion. Only a brief mention is given in the following paragraphs.*

VSL technique. *In 1970, R.T. Davis presented a simplified fully viscous shock layer analysis for hypersonic flow[56]. This work was nicely extended to a detailed chemically reacting shock layer by Moss[57]. The work of Moss has been progressively extended to include shock layer radiation, ablating gases, turbulence and foreign planetary atmospheres.* Indeed, Moss's later work has led to a very exciting "first" in modern hypersonics -- the design of the Galileo heat shield by means of detailed flow field calculations. Previous reentry vehicles such as Apollo and the space shuttle were designed by means of a combination of wind tunnel data and approximate calculations. However, the final design of the heat shield for the Galileo Probe (planned for a future launch towards Jupiter), was performed on the basis of Moss's detailed viscous shock layer calculations. These calculations, and their progressive development, have been extensively published; for a recent summary, see Refs. 58 and 59, and the references contained therein. It should be noted that some results in Refs. 58 and 59 were also obtained by means of a time-dependent viscous shock layer analysis derived from the work of Kumar et al[60]. Typical results from Moss's work are shown in Figures 35 and 36, taken from Ref. 59. In Figure 36, the time-varying contours (due to surface ablation) are given for the Galileo probe for various times during its Jovian entry trajectory. Figure 35 gives the calculated radiative and convective heat transfer to the stagnation point; note in particular that the heating to the Galileo probe is predicted to be virtually all radiative, because the convective heating is negligible due to massive ablation. Again, it is this type of data that has gone into the detailed design of the Galileo heat shield -- truly a benchmark event in the development and use of detailed, modern hypersonic flow calculations.

PNS technique. Modern CFD applications for viscous shock layers have focused around a simplification of the Navier-Stokes equations, wherein the streamwise viscous terms are neglected. This leads to a system of parabolic partial differential equations called the parabolized Navier-Stokes (PNS) equations, which can be solved as a steady state problem, hence running in a fraction of the computer time that would be required for a time-dependent solution. Indeed, a rather standard PNS code has been developed which is now used by more than 50 laboratories and agencies throughout the country. This code has developed out of work originally carried out by Tannehill at Iowa State University (see for example Ref. 61), and refined by Schiff and Steger[62] and others[63-66]. A recent application of the PNS technique to the flow field over the space shuttle has been made by the late John Rakich and colleagues, as described in Ref. 67. More recent PNS calculations dealing with equilibrium and nonequilibrium viscous flows are given by Prabhu et al in Refs. 68 and 69.

Full Navier-Stokes solution. The complete Navier-Stokes equations are being solved by means of a time-marching finite difference approach. Perhaps the best example of this type of solution is the work of Shang and Scherr[70], where the hypersonic viscous flow over a complete airplane configuration, namely the X-24 research vehicle, was calculated. This is an historic calculation -- the first time that a Navier-Stokes calculation has been made for a complete airplane. A result of this work is shown in Fig. 37, which illustrates the surface streamline pattern (local directions of the shear stress).

Viscous interaction. In the "old" hypersonics, viscous interaction effects were treated as a coupled problem between the boundary layer displacement thickness and a generally approximate calculation of the outer inviscid flow. Today, such a philosophy can still be used combining modern inviscid three-dimensional flow solutions along with a three-dimensional boundary layer analysis. However, the coupling of these two analysis still leads to an approximate estimate of the viscous interaction effect. In contrast, a second philosophy, described in the previous paragraph, involves the solution of the complete viscous shock layer, wherein viscous interaction effects are naturally accounted for. A very interesting and definitive study of these two philosophies has been recently carried out by McWherter et al[71]. This work represents the best example to date of the modern hypersonic state-of-the-art for viscous interaction effects. In Ref. 71, both an inviscid/boundary layer technique and a PNS solution are used to calculate the hypersonic flow over slender, blunted cones at moderate angle of attack. Typical results are shown in Figs. 38 and 39, taken from Ref. 71. In Figure 38, the pressure distribution, p/p_∞ as a function of distance from the nose, is given for a blunt 4-degree cone in a Mach 10 flow at an angle-of-attack of essentially 3 degrees. Results are shown for both the windward ($\phi=0$) and leeward ($\phi=180°$) centerlines. The open symbols are experimental data from Ref. 72. Calculation for both the inviscid/boundary layer (3DV) and the fully viscous shock layer (PNS) are also shown. This figure illustrates three important trends:

(1) The difference between the 3DV and PNS calculated results clearly demonstrates the substantial magnitude of the viscous interaction effects.

(2) The fully viscous shock layer calculations (PNS) does a reasonable job of calculating the viscous interaction effect, as seen by its fairly good agreement with experiment.

(3) The viscous interaction effect is stronger on the leeward surface than on the windward surface; this is expected due to the locally higher Mach number and lower Reynolds number on the leeward surface.

The viscous interaction effect on axial force coefficient is shown in Fig. 39, where the two sets of calculations are compared with experimental data obtained from Ref. 73. Again, the PNS solution does a good job of predicting the data, and again the magnitude of the viscous interaction effect on C_A is substantial.

To conclude this section, something should be said about the effects of flow separation at hypersonic speeds, because this is truly a "viscous interaction" of the first magnitude. The prediction of flow separation has always been a challenging problem in fluid mechanics; hypersonics is no exception. In the "old" hypersonics, the analysis of three-dimensional flow separation was virtually nonexistent. However, for the new hypersonics, the power of CFD is opening greater possibilities for the solution of this

problem. An example is shown in Fig. 40, taken form the work of Gnoffo[74]. Here, a PNS code is used to calculate the flow over a bend biconic at Mach 6. Figure 40 is a velocity vector diagram in the cross-flow plane of the region near the leeward centerline when the body is at an angle-of-attack of 20 degrees. Note the region of flow separation. Figure 41, also taken from Ref. 74, shows the comparison between calculated and measured separation lines along the leeward surface for the same case. Excellent agreement is obtained, clearly illustrating the power of modern, detailed viscous flow calculations for the prediction of separated flows.

IX. CONCLUDING REMARKS

This survey of inviscid and viscous hypersonic aerodynamics is an attempt to wet the interest of the reader in learning about the important developments in the field since the early 1950's. We have only scratched the surface here. Again, the author begs forgiveness from his colleagues whose work is not listed here -- there simply was not room nor time to do so. The reader is strongly encouraged to read the hypersonic literature; the references listed here represent just a start. A much more thorough and reasonably complete discussion of hypersonic and high temperature gas dynamics can be found in Ref. 2, to which the reader is particularly directed for additional study.

REFERENCES

1. Anderson, John D., Jr., "A Survey of Modern Research in Hypersonic Aerodynamics," AIAA Paper 84-1578, invited paper presented at the AIAA 17th Fluid Dynamics, Plasma Dynamics, and Lasers Conference, Snowmass, Colorado, June 25-27, 1984.

2. Anderson, John D., Jr., Hypersonic and High Temperature Gas Dynamics, McGraw-Hill Book Co., to be published December 1988.

3. Truitt, R.W., Hypersonic Aerodynamics, Ronald Press, New York, 1959.

4. Hayes, W.D. and Probstein, R.F., Hypersonic Flow Theory, Academic Press, New York, 1959.

5. Chernyi, G.G., Introduction to Hypersonic Flow (translated from Russian by R.F. Probstein), Academic Press, New York, 1961.

6. Dorrance, W.H., Viscous Hypersonic Flow, McGraw-Hill Book Co., New York, 1962.

7. Cox, R.N. and Crabtree, L.F., Elements of Hypersonic Aerodynamics, Academic Press, New York, 1965.

8. Tsien, H.S., "Similarity Laws of Hypersonic Flows," Journal of Mathematics and Physics, Vol. 25, 1946, pp. 247-251.

9. Anderson, J.D., Jr., Fundamentals of Aerodynamics, McGraw-Hill Book Co., New York, 1984.

10. Anderson, J.D., Jr., Modern Compressible Flow: With Historical Perspective, McGraw-Hill Book Co., New York, 1982.

11. Roe, P.L., "Thin Shock-Layer Theory," in Aerodynamic Problems of Hypersonic Vehicles, edited by K. Enkenhus, J.F. Wendt and R.C. Pankhurst, AGARD Lecture Series No. 42, 1972, pp. 4-1 to 4-26.

12. Hayes, W.D. and Probstein, R.F., Hypersonic Flow Theory, Second Edition, Volume 1, Inviscid Flows, Academic Press, New York, 1966.

13. Anderson, J.D., Jr., "Hypersonic Viscous Flow Over Cones at Nominal Mach 11 in Air," ARL Report 62-387, Aeronautical Research Laboratories, Wright-Patterson Air Force Base, Ohio, July 1962.

14. Moss, J.N. and Bird, G.A., "Direct Simulation of Transitional Flow for Hypersonic Reentry Conditions," AIAA Paper No. 84-0223, Jan. 1984.

15. Bird, G.A., "Monte Carlo Simulation of Gas Flows," in Annual Reviews of Fluid Mechanics, Vol. 10, 1978, pp. 11-32.

16. Ferri, A., Elements of Aerodynamics of Supersonic Flows, MacMillan, New York, 1949.

17. Epstein, P.S., "On the Air Resistance of Projectiles," Proceedings of the National Academy of Sciences, Washington, D.C., Vol. 17, 1931, pp. 532-547.

18. Lomax, H. and Inouye, M., "Numerical Analysis of Flow Properties About Blunt Bodies Moving at Supersonic Speeds in an Equilibrium Gas," NASA TR-R-204, 1964.

19. Probstein, R.F. and Bray, K.N.C., "Hypersonic Similarity and the Tangent Cone Approximation for Unyawed Bodies of Revolution," Journal of the Aeronautical Sciences, Vol. 22, No. 1, Jan. 1955, pp. 66-68.

20. Eggers, A.J., Savin, R.C., and Syvertson, C.A., "The Generalized Shock-Expansion Method and its Application to Bodies Traveling at High Supersonic Airspeeds," Journal of Aeronautical Sciences, Vol. 22, pp. 231-238, 1955.

21. Gentry, A.E., "Hypersonic Arbitrary-Body Aerodynamic Computer Program (Mark III Version), Vol. 1 -- User's Manual." Rep. DAC 61552, McDonnell-Douglas Corp., April 1968.

22. Taylor, G.I., "The Formation of a Blast Wave by a Very Intense Explosion," _Proceedings of the Royal Society_, London, Series A, Vol. 201, 1950, pp. 159-186.

23. Lukasiewicz, J., "Blast-Hypersonic Flow Analogy -- Theory and Applications," American Rocket Society Journal, Vol. 32, No. 9, Sept. 1962, pp. 1341-1346.

24. Townend, L.H., "Research and Design for Lifting Reentry," _Progress In Aerospace Sciences_, Vol. 18, 1979, pp. 1-80.

25. Weilmuenster, K.J., "High Angle of Attack Inviscid Flow Calculations Over a Shuttle-Like Vehicle with Comparisons to Flight Data," AIAA Paper No. 83-1798, July 1983.

26. Roe, P.L., "Thin Shock-Layer Theory," in _Aerodynamic Problems of Hypersonic Vehicles_, AGARD Lecture Series No. 42, Vol. I, 1972, pp. 4-1 to 4-26.

27. Maslen, S.H., "Inviscid Hypersonic Flow Past Smooth Symmetric Bodies," _AIAA Journal_, Vol. 2, No. 6, June 1964, pp. 1055-1061.

28. Kubota, T., "Investigation of Flow Around Simple Bodies in Hypersonic Flow," Graduate Aeronautical Labs., California Institute of Technology Memo 40, 1957.

29. Kutler, P., "A Perspective of Theoretical and Applied Computational Fluid Dynamics,' AIAA Paper No. 83-0037, Jan. 1983.

30. Anderson, D.A., Tannehill, J.C., and Pletcher, R.H., _Computational Fluid Mechanics and Heat Transfer_, McGraw-Hill Book Co., New York, 1984.

31. Moretti, G. and Abbett, M., "A Time-Dependent Computational Method for Blunt Body Flows," _AIAA Journal_, Vol. 4, No. 12, 1966, pp. 2136-2141.

32. Ard-·son, J.D., Jr., Albacete, L.M. and Winkelmann, A.E., "On Hypersonic Blunt Body Flow Fields Obtained with a Time-Dependent Technique," Naval Ordnance Laboratory, White Oak, Md, NOLTR 68-129, 1968.

33. Liepmann, H.W., and Roshko, A., _Elements of Gasdynamics_, Wiley, New York, 1957.

34. Rakich, John V., "A Method of Characteristics for Steady Three-Dimensional Supersonic Flow with Application to Inclined Bodies of Revolution," NASA TN D-5341, 1969.

35. Rakich, John V., and Cleary, J.W., "Theoretical and Experimental Study of Supersonic Steady Flow Around Inclined Bodies of Revolution," _AIAA Journal_, Vol. 8, No. 3, 1970, pp. 511-518.

36. Kutler P. and Lomax, H., "Shock-Capturing Finite Difference Approach to Supersonic Flows," _Journal of Spacecraft and Rockets_, Vol. 8, No. 12, Dec. 1971, pp. 1175-1182.

37. Kutler, P., Warming, R.F., and Lomax, H., "Computation of Space Shuttle Flow Fields Using Noncentered Finite-Difference Schemes," _AIAA Journal_, Vol. 11, No. 2, Feb. 1973, pp. 196-204.

38. Kutler, P., "Computation of Three-Dimensional, Inviscid Supersonic Flows," in H.J. Wirz (ed.), _Progress in Numerical Fluid Dynamics_, Springer-Verlag, Berlin, 1975, pp. 293-374.

39. Marconi, F., Salas, M., and Yaeger, L.S., "Development of a Computer Code for Calculating the Steady Super/Hypersonic Inviscid Flow Around Real Configurations," NASA CR-2675, April 1976.

40. Maus, J.R., Griffth, B.J., Szema, K.Y. and Best, J.T., "Hypersonic Mach Number and Real Gas Effects on Space Shuttle Orbiter Aerodyanmics," _Journal of Spacecraft and Rockets_, Vol. 21, No. 2, March-April, 1984, pp. 136-141.

41. Weilmunster, K.J., and Hamilton, H.H., "Computation of Inviscid Flow Over Blunt Bodies Having Large Embedded Subsonic Regions," _Journal of Aircraft_, Vol. 19, No. 10, October 1982, pp. 839-844.

42. Weilmunster, K.J., and Hamilton, H.H., "Calculations of Inviscid Flow Over Shuttle-Like Vehicles at High Angles of Attack and Comparisons with Experimental Data," NASA TP 2103, May 1983.

43. Pfitzner, M. and Weiland, C., "3-D Euler Solution for Hypersonic Mach Numbers," in _Aerodynamics of Hypersonic Lifting Vehicles_, AGARD-CP-428, April 1987, pp. 22-1 to 22-13.

44. Newberry, C.F., Dresser, H.S., Byerly, J.W., and Riba, W.T., "The Evaluation of Forebody Compression at Hypersonic Mach Numbers," AIAA Paper No. 88-0479, 1988.

45. Chakravarthy, S.R., and Szema, K.Y., "An Euler Solver for Three-Dimensional Supersonic Flows with Subsonic Pockets," AIAA Paper No. 85-1703, 1985.

46. Vincenti, W.G., and Kruger, C.H., _Introduction to Physical Gas Dynamics_, John Wiley, New York, 1965.

47. Clarke, J.F. and McChesney, M., _The Dynamics of Real Gases_, Butterworths, Washington, 1964.

48. Dorrance, W.H., _Viscous Hypersonic Flow_, McGraw-Hill Book Co., New York, 1962.

49. Koppenwallner, G., "Fundamentals of Hypersonics: Aerodynamics and Heat Transfer," in von Karman Lecture Series _Hypersonic Aerothermodynamics_, Feb. 6-10, 1984.

50. Hall, J.G., Eschenroeder, A.A., and Marrone, P.V., "Blunt-Nose Inviscid Airflows with Coupled Nonequilbrium Processes," _Journal of the Aerospace Sciences_, Vol. 29, No. 9, Sept. 1962, pp. 1038-1051.

51. Spurk, J.H., Gerber, N., and Sedney, R., "Characteristic Calculation of Flowfields with Chemical Reactions," _AIAA Journal_, Vol. 4, No. 1, Jan. 1966, pp. 30-37.

52. van Driest, E.R., "The Problem of Aerodynamic Heating," _Aeronautical Engineering Review_, Oct. 1956, pp. 26-41.

53. Fay, J.A. and Riddell, F.R., "Theory of Stagnation Point Heat Transfer in Dissociated Air," _Journal of the Aeronautical Sciences_, Vol. 25, No. 2, Feb. 1958, pp. 73-85, 121.

54. Blotter, F.G., "Chemical Nonequilibrium Boundary Layer," _AIAA Journal_, Vol. 2, No. 2, Feb. 1964, pp. 232-240.

55. Blotter, F.G., "Nonequilibrium Laminar Boundary-Layer Flow of Ionized Air," _AIAA Journal_, Vol. 2, No. 11, Nov. 1964, pp. 1921-1927.

56. Davis, R.T., "Numerical Solution of the Hypersonic Viscous Shock-Layer Equations," _AIAA Journal_, Vol. 8, No. 5, May 1970, pp. 843-851.

57. Moss, J.N., "Reacting Viscous-Shock-Layer Solutions with Multicomponent Diffusion and Mass Injection," NASA TR-R-411, June 1974.

58. Moss, J.N., and Simmonds, A.L., "Galileo Probe Forebody Flowfield Predictions," in _Entry Vehicle Heating and Thermal Preuiction Systems: Space Shuttle, Solar Starprobe, Jupiter Galileo Probe_, ed. by P. E. Bauer and H. E. Colicott, Vol. 85 of the AIAA Progress in Astronautics and Aeronautics Series, 1983.

59. Moss, J.N. and Simmonds, A.L., Galileo Probe Forebody Flowfield Predictions During Jupiter Entry," AIAA Paper No. 82-0874, June 1982.

60. Kumar, A., Tiwari, S.N., Graves, R.A., and Weilmuenster, K.J., "Laminar and Turbulent Flow Solutions with Radiation and Ablation Injection for Jovian Entry," AIAA Paper 80-0288, Jan 1980.

61. Tannehill, J.C., Venkatapathy, E., and Rakich, J.V., "Numerical Solutions of Supersonic Viscous Flow over Blunt Delta Wings," _AIAA Journal_, Vol. 20, No. 2, Feb. 1982, pp. 203-210.

62. Schiff, L.B., and Steger, J.L., "Numerical Simulation of Steady Supersonic Viscous Flow," NASA TP 1749, 1981.

63. Chausee, D.S., Patterson, J.L., and Kutler, P., "A Numerical Simulation of Hypersonic Viscous Flows over Arbitrary Geometries at High Angle of Attack," AIAA Paper 81-0050, Jan. 1981.

64. Nicolet, W.E., Shanks, S., and Srinivasan, G., "Flowfield Predictions About Lifting Entry Vechicles," AIAA Paper 82-0026, Jan. 1982.

65. Rizk, Y.M., Chausee, D.S., and McRae, D.S., "Computation of Hypersonic Viscous Flow Around Three-Dimensional Bodies at High Angles of Attack," AIAA Paper No. 81-1261, June 1981.

66. Shanks, S.P., Srinivasan, G.R., and Nicolet, W.E., "AFWAL Parabolized Navier-Stokes Code: Formulation and User's Manual," AFWAL-TR-82-3034, June 1982.

67. Rakich, J.V., Venkatapathy, E., Tannehill, J.C., and Prabhu, D., "Numerical Solutions of Space Shuttle Orbiter Flowfield," _Journal of Spacecraft and Rockets_, Vol. 21, No. 1, Jan-Feb. 1984, pp. 9-15.

68. Prabhu, D.K., and Tannehill, J.C., "Numerical Solution of Space Shuttle Orbiter Flowfield Including Real-Gas Effects," _Journal of Spacecraft and Rockets_, Vol. 23, No. 3, May-June 1986, pp 264-272.

69. Prabhu, D.K., Tannehill, J.C., and Marvin, J.G., "A New PNS Code for Three-Dimensional Chemically Reacting Flows," AIAA Paper No. 87-1472, 1987.

70. Shang, J.S., and Scherr, S.J., "Navier-Stokes Solutions for a Complete Re-entry Configuration," _Journal of Aircraft_, Vol. 23, No. 12, December 1986, pp. 881-888.

71. McWherter, Mary, Noack, R.W., and Oberkampf, W.L., "Evaluation of Boundary-Layer and Parabolized Navier-Stokes Solutions for Re-Entry Vehicles," _Journal of Spacecraft and Rockets_, Vol. 23, No. 1, Jan-Feb. 1986, pp. 70-78.

72. Boylan, D.E., Strike, W.T., and Shape, F.L., "A Direct Comparison of Analytical and Experimental Surface and Flow-Field Data on a 4-degreed Cone at Incidence in a Hypersonic Stream with Laminar Boundary Layers," AEDC-TR-76-84, 1976.

73. Griffith, B.J., Strike, W.T., and Majors, B.M., "Ablation and Viscous Effects on the Force and Moment Characteristics of Slender Cone Models at Mach 10 Under Laminar Flow Conditions," AEDC-TR-75-109, 1975.

74. Gnoffo, P.A., "Hypersonic Flows Over Biconics Using a Variable-Effective-Gamma Parabolized-Navier-Stokes Code," AIAA Paper No. 83-1666, July 1983.
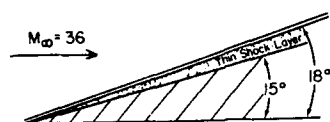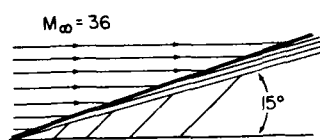
FIG. 1: Hypersonic thin shock layer.
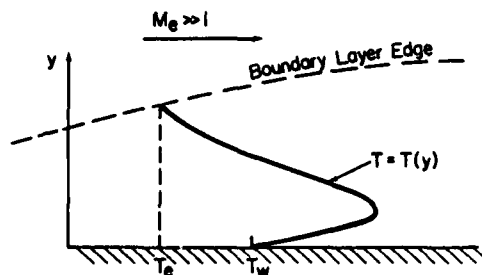

FIG. 2: Streamlines in thin shock layer.

FIG. 3: Entropy layer.

FIG. 4: Schematic of boundary layer
         temperature profile.
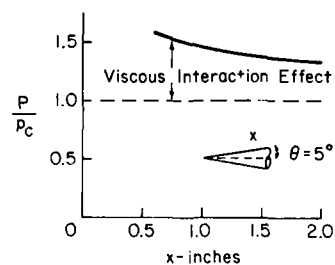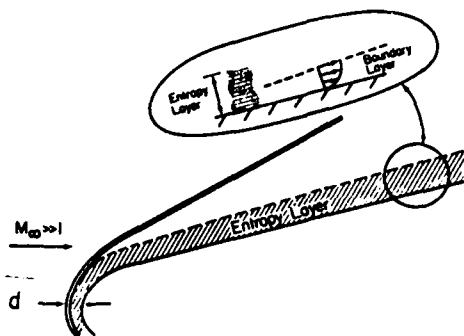

FIG. 5: Viscous interaction effect on cones.
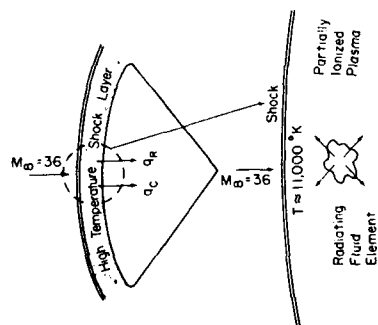 M_∞ = 11, Re = 1.88·10^5 per foot.
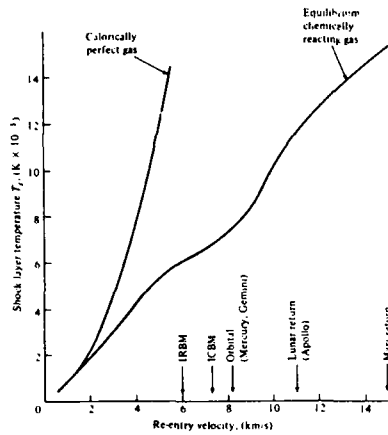

FIG. 6a: High temperature shock layer.

FIG. 6b: Temperature behind a normal shock wave as a function of freestream velocity at a standard altitude of 52 km (from Ref. 10).
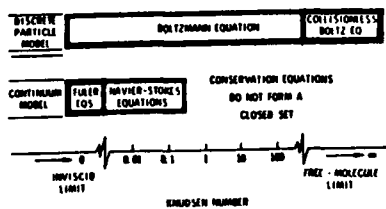

FIG. 9: Comparison of Newtonian theory with exact cone and wedge results.

FIG. 7: Regimes of applicability of various flow equations for low density flows (from Refs. 14 and 15).
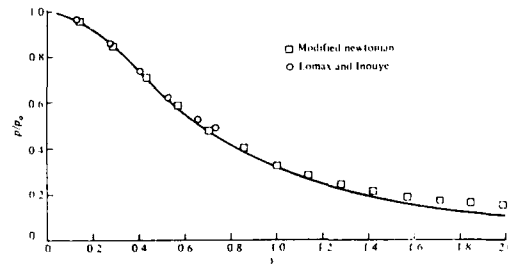
FIG. 10: Comparison of modified Newtonian theory with exact numerical results for flow over a blunt-nosed paraboloid (from Ref. 10).

FIG. 8: Calculated temperature distributions along the stagnation streamline for the space shuttle nose at an altitude of 92.35 km. Low density flow calculated by means of a Monte Carlo method (from Ref. 14).
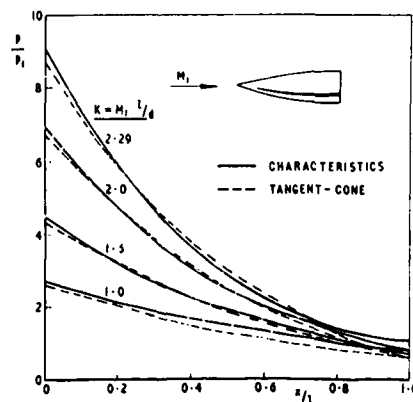
FIG. 11: Tangent cone results on an ogive (from Refs. 19 and 7).
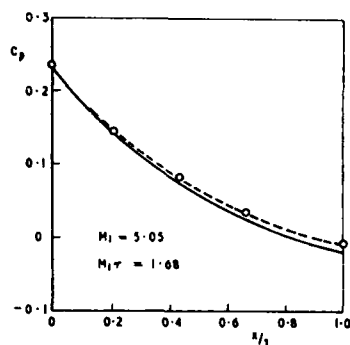
FIG. 12: Shock-expansion results for an ogive
(from Refs. 20 and 7).
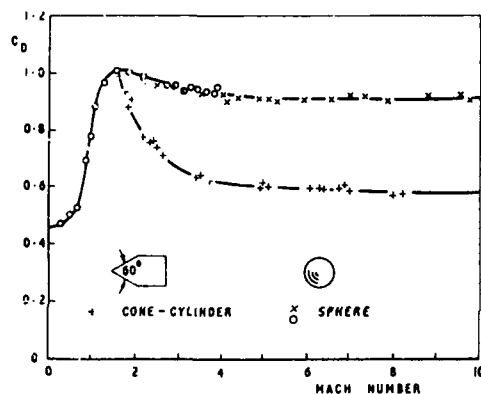
FIG. 13: Data showing mach number independence
for blunt bodies (from Ref. 7)
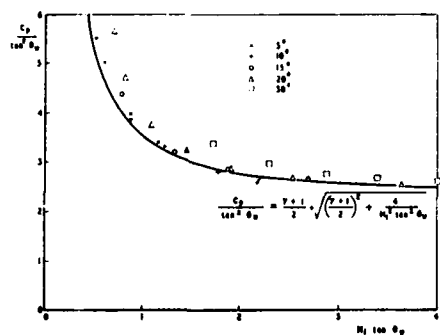
FIG. 14: Results demonstrating hypersonic
similarity (from Ref. 7).
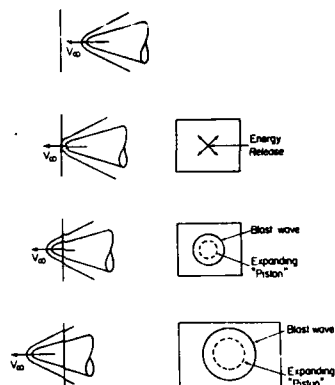
FIG. 15: Illustration of the combined blast
wave analogy and the hypersonic
equivalence principle.
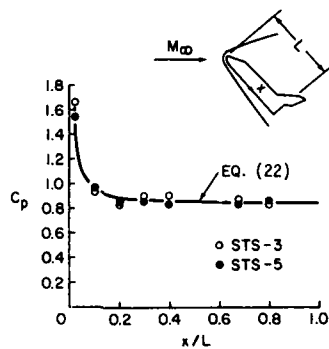
FIG. 16: Comparison of pressure coefficients
obtained with combined blast wave/
Newtonian theory with flight data for
the space shuttle. Windward centerline.
M_∞ = 21.6, α = 40°.
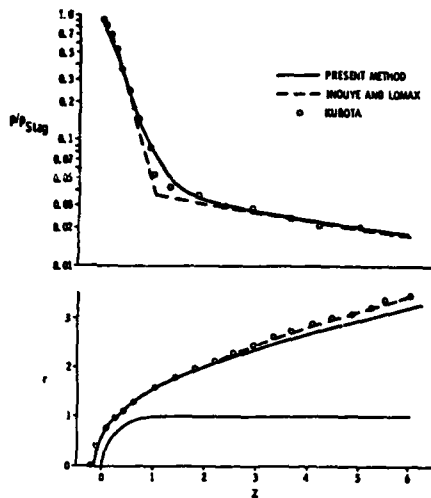
FIG. 17: Pressure distribution and shock shape for a hemisphere cylinder. $M_\infty = 7.7$, $\gamma = 1.4$ (from Ref. 27).
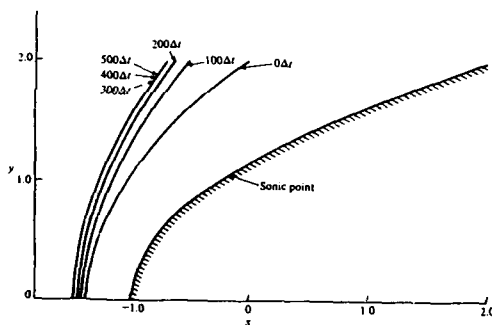
FIG. 18: Time-dependent shock wave motion, parabolic cylinder, $M_\infty = 4$ (from Ref. 10).
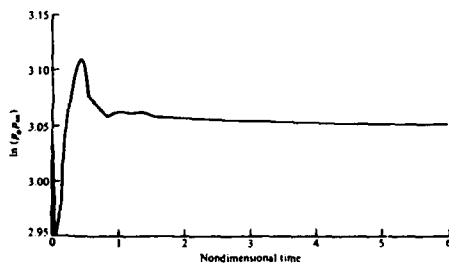
FIG. 19: Time-variation of stagnation point pressure, parabolic cylinder, $M_\infty = 4$ (from Ref. 10).

FIG. 20: Calculated shock wave shape around a shuttle-like vehicle. $M_\infty = 6$, $\alpha = 26.6°$, $\gamma = 1.4$ (from Ref. 25).
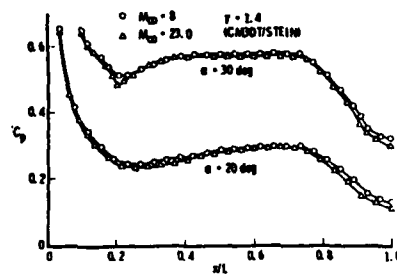
FIG. 21: Calculated pressure coefficient distributions along the windward centerline of the space shuttle (from Ref. 40).
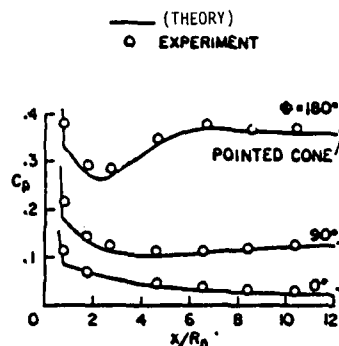
FIG. 22: Surface pressure distribution over a blunt-nosed cone at angle of attack of 10°; method of characteristics (from Ref. 35).
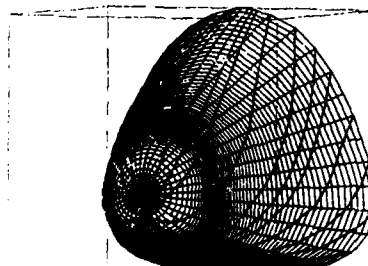
FIG. 23: Hypersonic inviscid flow streamlines over the blunt nose of a shuttle-like vehicle. $M_\infty = 8.0$, $\alpha = 30°$ (from Ref. 43).
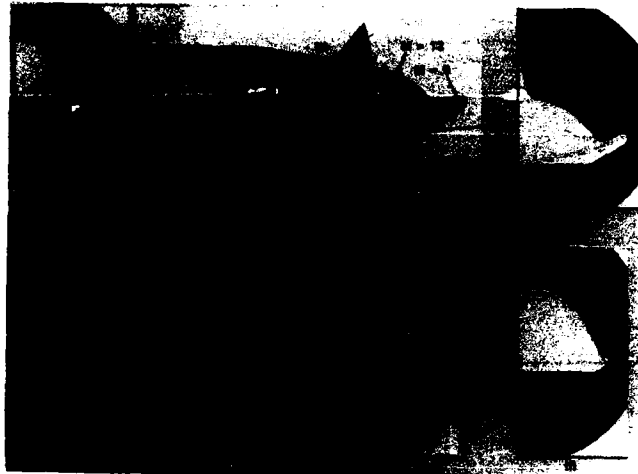
FIG. 24: Mach number contours for a hypersonic vehicle. Inviscid finite
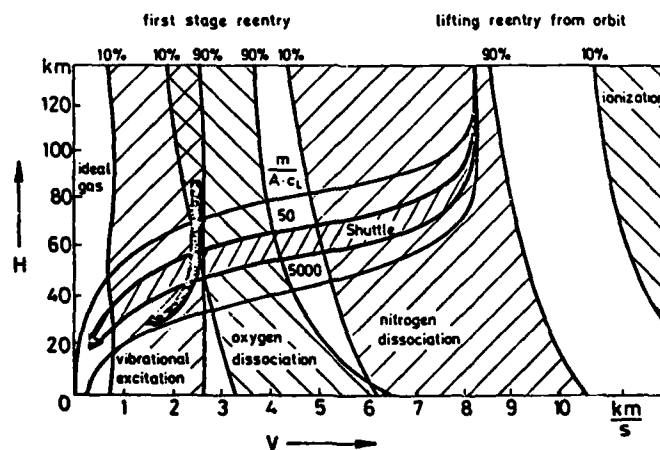volume calculations from Ref. 45.

FIG. 25: Velocity-altitude map showing regions where various high
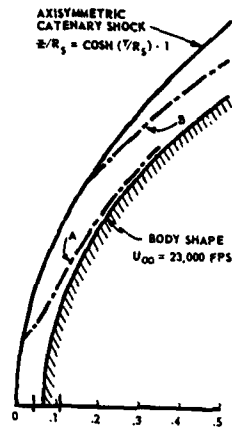temperature effects are important (from Ref. 49).

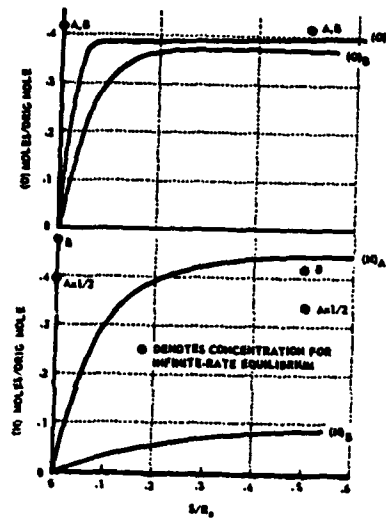FIG. 26: Blunt body and streamline shapes from Ref. 50.

FIG. 28: Atomic oxygen and nitrogen concentration variations along the streamlines shown in Fig. 26 (from Ref. 50).
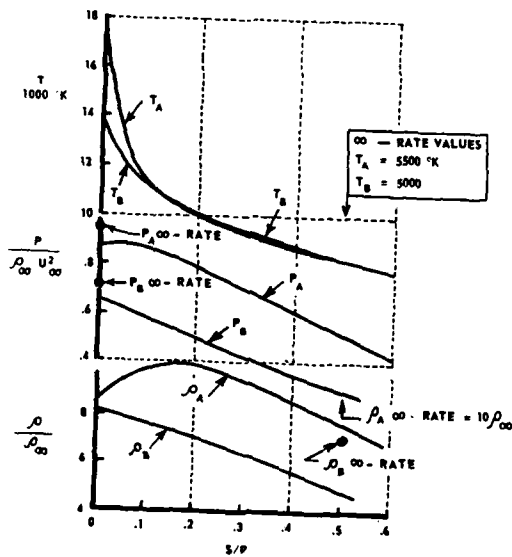

FIG. 27: Temperature, pressure and density streamlines for the nonequilibrium flow along the streamlines shown in Fig. 26 (from Ref. 50).
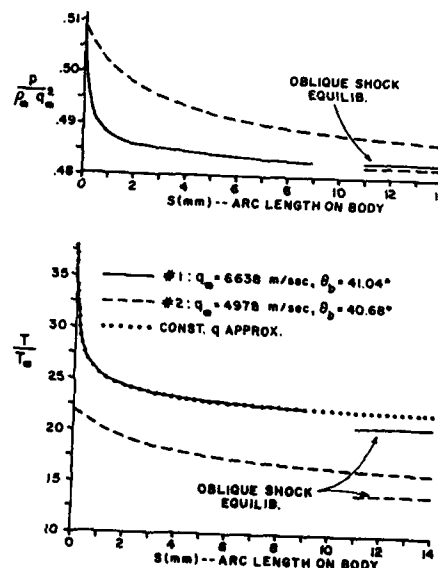

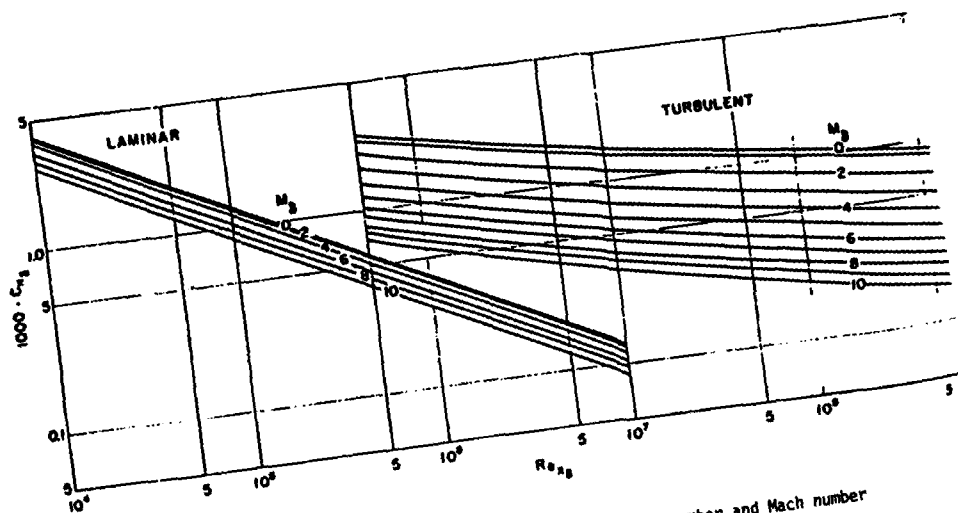FIG. 29: Nonequilibrium flow over a wedge (from Ref. 51).

FIG. 30: Variation of Stanton number with Reynolds number and Mach number on an insulated flat plate (from Ref. 52).
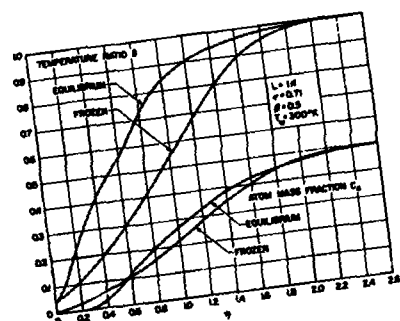
FIG. 31: Temperature and atom mass fraction profiles through a stagnation point boundary layer (from Ref. 53).
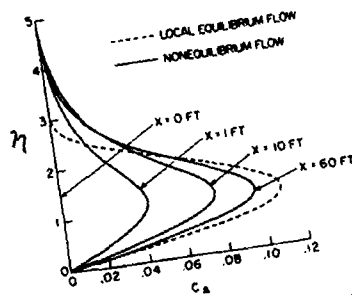
FIG. 33: Atom mass fraction profiles through a boundary layer on a cone (from Ref. 54).
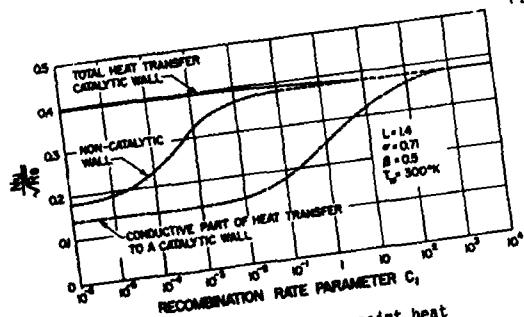
FIG. 32: Variation of stagnation point heat transfer as a function of the gas rate constant, including the effects of catalytic wall (from Ref. 53).
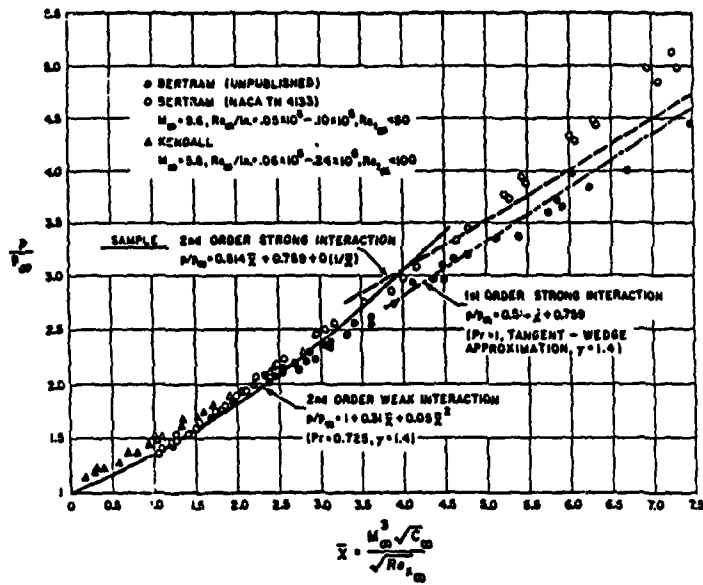
FIG. 34: Induced pressures on a flat plate (from Ref. 4).
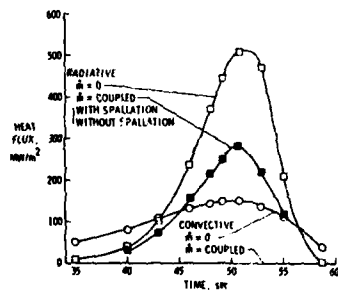

FIG. 35: Calculated radiative and convective heat transfer to the Galileo probe during Jovian entry (from Ref. 59).
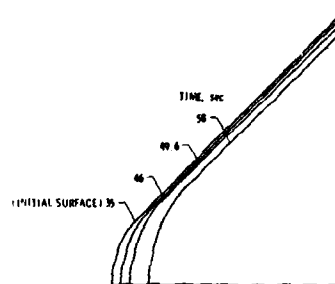

FIG. 36: Predicted time-varying contours for the Galileo probe during Jovian entry (from Ref. 59).

$M_\infty = 5.95$
$Rey = 1.64 \times 10^7/m$
$\alpha = 6$ degrees
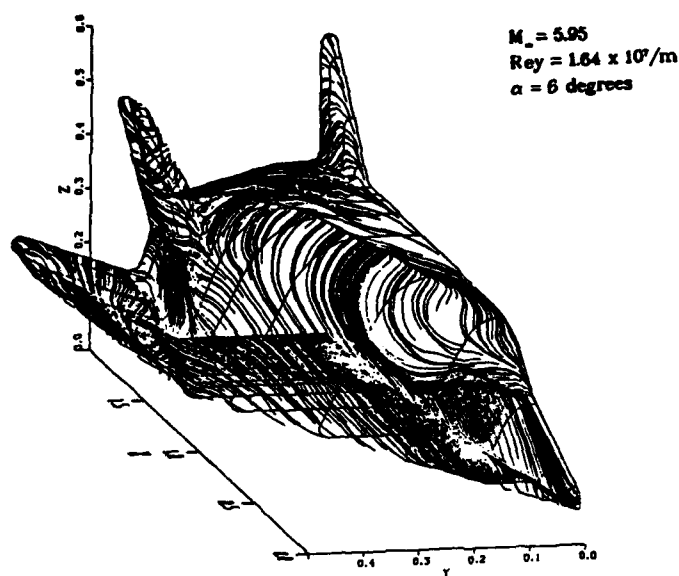
FIG. 37: Surface shear directions from a full Navier-Stokes calculation (from Ref. 70).

$M_\infty = 9.82$ $\theta_c = 4°$
$R_{\infty L} = 0.459 \times 10^6$ $D_n/D_b = 0.22$
$T_w/T_o = 0.42$
$\alpha = 2.97°$

Data, $\phi°$
• 0
• 180
— 3DV
···· PNS
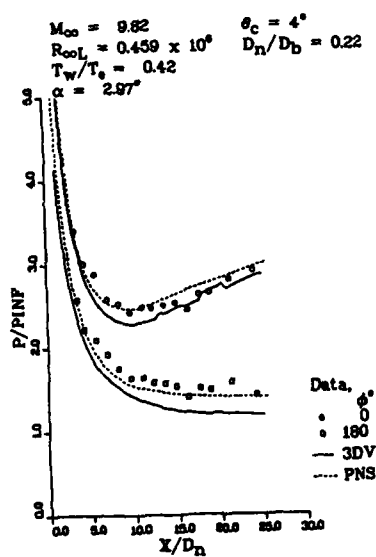
FIG. 38: Surface pressure distribution along a blunt cone at angle of attack, comparing inviscid/boundary layer calculations (3DV) with a parabolized Navier-Stokes calculation (PNS) (from Ref. 71).

$M_\infty = 9.81$ $R_{\infty L} = 0.43 \times 10^6$
$T_w/T_o = 0.41$
$\theta_c = 4°$ $D_n/D_b = 0.05$
○ Data,
— 3DV
···· PNS
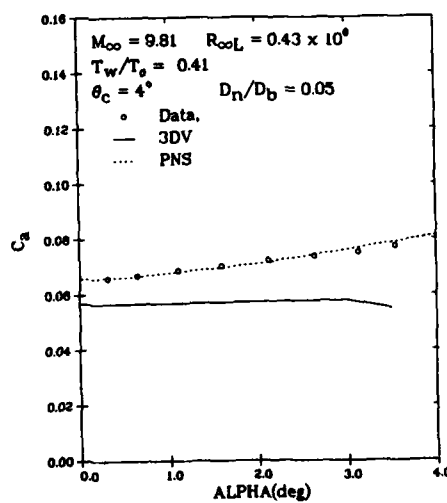
FIG. 39: Axial force coefficient for a blunt cone versus angle of attack (from Ref. 71).

FIG. 40: Velocity vector diagram in the cross-
flow plane of the region near the
leeward centerline of a bent biconic
at Mach 6, illustrating a region of
calculated separated flow (from Ref. 74).

FIG. 41: Comparison of calculated and measured
separation lines for a bent biconic.
$M_\infty = 6$, $\alpha = 20°$, Re = 8.2×10^6 (from
Ref. 74).

AN INTRODUCTION TO REAL GAS EFFECTS

B. Aupoix
ONERA-CERT
Department of Aerothermodynamics
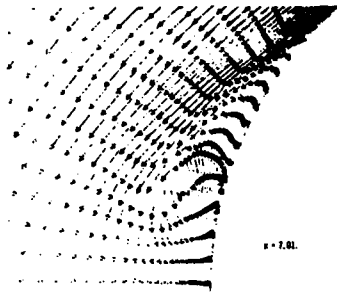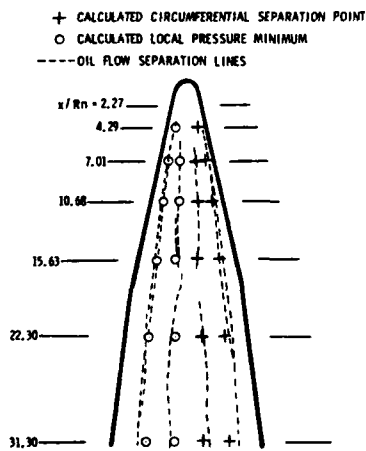31055   TOULOUSE CEDEX

Summary

Real gas effects are due to the transformation of an hypervelocity flow into an hyperenthalpy flow. The flow is thus the room of various phenomena, chemical reactions leading to dissociation and ionisation, energy exchanges between degrees of freedom of particles ...

The physical background is introduced in the first section. The thermodynamic properties of molecules and atoms are first described. The flow equations are derived from description of the microscopic behaviour of particles. The chemistry, either in the gas or at gas/surface interfaces is discussed. Results for air at chemical equilibrium are presented as an illustration. A simple model is also given.

Examples of flow with real gas effects, relevant to space shuttle reentry, are given in the second part. The relaxation behind the shock wave is first studied. Shock layer and boundary layer flows around the body are then investigated. At last, the ionisation problem is mentionned.

Introduction

At room temperature, air can be modelled as an *ideal* gas, i.e a gas the thermodynamic properties of which do not depend upon the temperature ($C_p, C_v, \gamma \ldots$ = constants). This is not so when the temperature, or the energy of the gas, increases. For example, for a shuttle reentry, at 70 km altitude, the Mach number is about 25, so that, behind a front shock wave,

according to Rankine–Hugoniot formulae, the Mach number should decrease to 0.38 and the static temperature be multiplied by 122.5, leading to temperatures in the shock layer of about 25000K. The transformation of kinetic energy into thermal energy, or of an hypervelocity flow into an hyperenthalpy flow is such that air can no longer be considered as an ideal gas. Energy is then stored in the internal degrees of freedom so the above mentionned coefficients vary with temperature. Moreover, chemical reactions occur at these temperatures, leading to dissociation of air molecules and ionization of the flow.

The study of high temperature flows has been called *aerothermochemistry* by the late Professor Th. Von Kármán. This lecture is aimed to give the reader a first flavour of aerothermochemistry.

The first part deals with the basic physics needed to study high energy flows, i.e the description of thermodynamical properties of molecules and atoms, the derivation of the governing equations from the description of the microscopic behaviour of particles, and the chemistry. The radiation phenomena, which is important at very high temperatures, will not be addressed here.

The second part is devoted to some examples to bring into evidence the rôle of various phenomena in hypersonic flows. For the sake of simplicity, we shall restrict us to reentry problems for space shuttles or missiles.

PART ONE :   PHYSICAL BACKGROUND

It is not our purpose to make the reader an expert in physical gas dynamics in such a short course, but just to provide him the basic ideas of the physics of aerothermochemistry. The reader is asked to refer to standard textbooks [26] [31] [42] [63] [105] for a more complete information.

1   Thermodynamic background

1.1   Energy levels in a molecule

Energy can be stored in various ways in a molecule as depicted on figure 1. The first mode is the kinetic energy due to the Brownian motion of the molecule. This Brownian motion corresponds to three degrees of freedom. When the molecules are excited, energy can be supplied to the electrons, so that they can move to higher energy levels. Climbing energy levels requires energy, while falling down leads to an energy release, e.g a photon emission. At high excitation levels, the electron leaves the molecule, it is the ionization process. Molecules can also rotate around their center of mass. As the bound between the atoms is very rigid, diatomic molecules can be viewed as dumb-bells, the axis of which is a very rigid spring. When molecules collide, energy can be supplied to the rotation motion. For a diatomic molecule, rotation has two degrees of freedom, as the inertia with respect to the molecule axis is negligible. At last, excited molecules can vibrate, i.e the
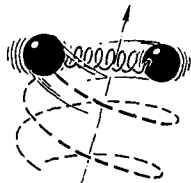
Figure 1: Diatomic molecule energetic modes (from[57])

"spring" between two atoms allows them to move along the axis with respect to each other. The vibrational energy is due both to the kinetic energy of the vibrational motion and to the potential energy of the bound. When the vibration energy is large, the atoms may part, it is the dissociation process. The internal energy of the nucleus is neglected as no nuclear reactions are accounted for.

Atoms also have translation and electronic excitation energy but they cannot vibrate and the rotation motion can hardly be excited by collisions and is negligible.

All energy levels are quantified. Changes in rotational or vibrational levels may also correspond to a photon emission. Translational energy states are determined by the set of quantum numbers l, electronic energy states by s, rotational energy states by j and vibrational ones by v.

Collisions between particles tend to homogenize the probability of the energetic state of particles so that they tend towards thermodynamic equilibrium in which energy is "equally" distributed among particles and energetic modes.

1.2 Partition function

The important Boltzmann H theorem will not be demonstrated here, readers are referred to standard textbooks [42] [63] [105]. An application of this theorem is however given in section 2.3.1. This theorem shows that, for a given energy, a given number of particles in an insulated volume tend towards the most probable energy distribution, i.e the Boltzmann distribution. This is not true at very low temperatures which are out of concern here.

As pointed out previously, the energy is quantified, i.e it does not vary continuously but on a set of discrete energy levels. A given energy level ε_i can however be obtained in various ways, the *degeneracy* g_i of the energy levels is the number of ways they can be obtained.

If n_i is the number of particles at the energy level i, N the total number of particles and E the energy of the system, it is obvious that

$$N = \sum_i n_i$$
$$E = \sum_i n_i \varepsilon_i$$

The Boltzmann distribution (see section 2.3.1) gives the number of particles in each energy level as

$$n_i = A g_i \exp\left(\beta \varepsilon_i\right)$$

where A and β are constants. The number of particles in each energy level can be expressed as

$$n_i = N \frac{g_i \exp\left(\beta \varepsilon_i\right)}{Q} \qquad \text{where} \qquad Q = \sum_i g_i \exp\left(\beta \varepsilon_i\right)$$

Q is the *energy partition function* of the system, it represents how the energy levels are populated.

The coefficient β can be calculated in various ways, either from the system entropy to fit statistical thermodynamics [105] or by considering an atom gas without electronic excitation [42]. It is then shown that

$$\beta = -\frac{1}{kT}$$

where k is the Boltzmann constant. So the population reads

$$n_i = N \frac{g_i \exp -\frac{\varepsilon_i}{kT}}{Q} \qquad Q = \sum_i g_i \exp -\frac{\varepsilon_i}{kT}$$

i.e at a given temperature, the population decreases exponentially with the energy of the level while the population increases with the temperature for the most energetic levels.

The energy of a given state is the sum of the energy of the differents modes $\varepsilon_i = \varepsilon_l + \varepsilon_s + \varepsilon_j + \varepsilon_v$ while the degeneracy is the product $g_i = g_l g_s g_j g_v$ so that the partition function reads

$$Q = \sum_l \sum_s \sum_j \sum_v g_l g_s g_j g_v \exp -\frac{\varepsilon_l + \varepsilon_s + \varepsilon_j + \varepsilon_v}{kT}$$

(obviously, for atoms $\epsilon_j = \epsilon_v = 0$, $g_j = g_v = 1$). If the energy states are independent, the partition function can be expanded as

$$Q = Q_{\text{trans}} Q_{\text{elec}} Q_{\text{rot}} Q_{\text{vib}}$$

$$Q_{\text{trans}} = \sum_l g_l \exp -\frac{\epsilon_l}{kT}$$

$$Q_{\text{elec}} = \sum_s g_s \exp -\frac{\epsilon_s}{kT}$$

$$Q_{\text{rot}} = \sum_j g_j \exp -\frac{\epsilon_j}{kT}$$

$$Q_{\text{vib}} = \sum_v g_v \exp -\frac{\epsilon_v}{kT}$$

The expressions of these different partition functions will now be detailled.

1.2.1 Translation

For N particles of mass m inside a box of size (a_1, a_2, a_3), the energy levels are obtained from quantum mechanics as

$$\epsilon_i = \epsilon_{n_1 n_2 n_3} = \frac{h^2}{8m}\left[\frac{n_1^2}{a_1^2} + \frac{n_2^2}{a_2^2} + \frac{n_3^2}{a_3^2}\right]$$

where h is the Planck constant. As each energy level can be obtained only in one way, the partition function reads

$$Q_{\text{trans}} = \sum_{n_1=1}^{n_1=\infty} \sum_{n_2=1}^{n_2=\infty} \sum_{n_3=1}^{n_3=\infty} \exp\left(-\frac{h^2}{8mkT}\left[\frac{n_1^2}{a_1^2} + \frac{n_2^2}{a_2^2} + \frac{n_3^2}{a_3^2}\right]\right)$$

When the box sizes tend towards infinity, the quantified levels become very close so that the above sum can be approximated by an integral. As

$$\int_0^\infty \exp\left(-\frac{n_1^2}{a_1^2}\frac{h^2}{8mkT}\right) dn_1 = a_1\sqrt{\frac{2\pi mkT}{h^2}}$$

the translation partition function of the system reads

$$Q_{\text{trans}} = V \left(\frac{2\pi mkT}{h^2}\right)^{\frac{3}{2}}$$

On the other hand, either from gas kinetic theory (see e.g equation 10) or from thermodynamics (see section 1.3 below), the volume can be linked to the pressure and temperature as

$$pV = NkT$$

so that the partition function for a particle can be expressed as

$$\frac{Q_{\text{trans}}}{N} = k\left(\frac{2\pi mk}{h^2}\right)^{\frac{3}{2}}\frac{T^{\frac{5}{2}}}{p}$$

1.2.2 Electronic excitation

The electronic excitation partition function reads

$$Q_{\text{elec}} = \sum_s g_s \exp -\frac{\epsilon_s}{kT}$$

ϵ_s/kT is usually large so that only a few levels are populated and the sum can be restricted to the first terms. It must be mentionned that the ground energy corresponds to zero energy ($\epsilon_0 = 0$).

1.2.3 Rotation energy

For the sake of simplicity, only diatomic molecules will be considered since CO_2 and H_2O are negligible in air. If m_1 and m_2 are the masses of the two atoms and r_0 the distance between their centers, the inertia moment of the molecule for a rotation axis normal to the molecule axis is $I = m_1 m_2/(m_1 + m_2)r_0^2$ or $I = \frac{1}{2}mr_0^2$ for a symmetrical molecule.

Quantum mechanics give the energy for the state j as

$$\epsilon_j = j(j+1)\frac{h^2}{8\pi^2 I}$$

while the degeneracy is $g_j = 2j + 1$. The partition function reads

$$Q_{\text{rot}} = \sum_j (2j+1)\exp\left(-\frac{j(j+1)h^2}{8\pi^2 IkT}\right) = \sum_j (2j+1)\exp\left(-\frac{j(j+1)\theta_{\text{rot}}}{T}\right)$$

where the rotation temperature is defined as $\theta_{\text{rot}} = h^2/(8\pi^2 Ik)$. As the rotation temperature is small (5.8K for N_2, 2.5K for NO), the above sum can be approximated by an integral so that

$$Q_{\text{rot}} = \frac{T}{\theta_{\text{rot}}}$$

The above presented formulae are for heteronuclear molecules. For homonuclear molecules, a rotation of 180 degrees do not modify the molecule, so a correction must be introduced. The partition function reads

$$Q_{rot} = \frac{1}{\sigma} \frac{T}{\theta_{rot}}$$

where σ is the *symmetry number* that is 1 for heteronuclear molecules and 2 for homonuclear molecules.

1.2.4 Vibrational energy

From the previously introduced analogy between atom bound and a spring, the molecule can be modelled as an harmonic oscillator. Quantum mechanics state that the energy levels are

$$\epsilon_v = (2v + 1)\epsilon_0 \qquad \epsilon_0 = \frac{1}{2}h\nu$$

and no degeneracy is allowed. As the ground state $v = 0$ corresponds to no vibrational energy, this energy is substracted so that $\epsilon_v = vh\nu$ and the partition function reads

$$Q_{vib} = \sum_v \exp - \frac{vh\nu}{kT}$$

and since $1 + z + z^2 + z^3 \ldots = \frac{1}{1-z}$ the vibration partition function can be approximated as

$$Q_{vib} = \frac{1}{1 - \exp - \frac{\theta_{vib}}{T}} \qquad \text{where} \qquad \theta_{vib} = \frac{h\nu}{k}$$

1.2.5 Anharmonicity

The harmonic oscillator hypothesis is however too crude and anharmonic effects must be introduced. On Figure 2, the potential energy and vibrational levels of a diatomic molecule are represented as function of the distance r between the centers of the two atoms. The real curve is the solid line. As interatomic forces are attractive at large distance and repulsive at small distance, an equilibrium situation exists for r_0. When the interatomic distance increases, the potential energy increases up to the dissociation energy D. The harmonic oscillator is a fair approximation for interatomic distances close to the equilibrium situation but fails for large departures from the equilibrium situation as it is easier to move the atoms apart than closer. The harmonic oscillator and the equally spaced vibrational levels are indicated by dashed lines. The real vibrational levels are indicated by solid lines, their spacing decreases when the energy increases.
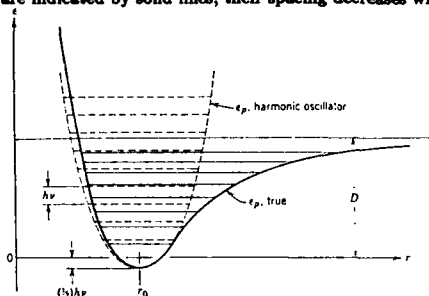

Figure 2: Potential energy and vibrational levels for a diatomic molecule (from [105])

The harmonic oscillator model gives however fair predictions, except for high energies which correspond to an important population of the upper vibrational levels. Approximate corrections methods have been proposed to take into account the anharmonicity.

1.2.6 Coupling of the rotation and the vibration

Vibration changes the distance between the two atoms and the inertia moment of the molecule, so that the vibration and rotation are coupled. The effect of this coupling is of the same order of magnitude as the anharmonicity so that both are sometimes modelled together [105].

This coupling can be accounted for by defining rotational states for each vibrational level [2]. The partition function now reads

$$Q = Q_{trans} Q_{elec} Q_{vib,rot}$$

and the vibration–rotation partition function reads

$$Q_{vib,rot} = \frac{1}{\sigma} \sum_v \sum_j g(v,j) \exp - \frac{\epsilon_{(v,j)}}{kT}$$

where σ is the symmetry number introduced in section 1.2.3 and still $g(v,j) = 2j+1$. The energy level can be approximated,

by neglecting the higher powers of j and v as [2]

$$\varepsilon_{v,j} = hc\left[\left(\omega_e - \omega_e x_e\right)v + \left(B_e - \frac{1}{2}\alpha_e\right)j\left(j+1\right) - \omega_e x_e v^2 - \alpha_e v j\left(j+1\right) - D_e j^2\left(j+1\right)^2\right]$$

1.2.7 Use of spectroscopic data

As mentionned previously, changes in electronic excitation, rotational or vibrational levels may correspond to the emission or the absorption of a photon. The quantum theory selection rules allow changes of only $\pm$ one level, and the frequency ν' of the emitted or absorbed light is given by the Bohr equation

$$h\nu' = \varepsilon_{i+1} - \varepsilon_i$$

where i is the quantum number of the lower energy state (electronic excitation, rotation or vibration).

The energy levels can thus be determined from absorption and emission spectra of molecules. For example, rotational spectra of molecules shows up in the far infrared v. iile vibrational spectra in the near infrared. Both emission and absorption techniques are used. The above spectroscopic constants ω_e, $\omega_e x_e$, B_e, α_e, D_e are so determined. A review of spectroscopic data can be found in [23] to calculate the energy partition function.

1.3 Determination of thermodynamic functions

The thermodynamic functions which are used to represent the state of the system can be calculated from the partition function. The partition function for a system of N particles reads

$$Q = \sum_i g_i \exp -\frac{\varepsilon_i}{kT}$$

while the energy is given by

$$E = \sum_i n_i \varepsilon_i = \sum_i \frac{N g_i \exp -\frac{\varepsilon_i}{kT}}{Q}\varepsilon_i$$

From these two relations, the energy can easily be computed as

$$E = NkT^2 \frac{\partial \ln Q}{\partial T}$$

From the Boltzmann H theorem, the entropy of the system is

$$S = Nk\left[\ln \frac{\sum_i g_i \exp -\frac{\varepsilon_i}{kT}}{N} + 1\right] + \frac{E}{T}$$

so that it can be expressed as

$$S = Nk\left[\ln \frac{Q}{N} + 1 + T\frac{\partial \ln Q}{\partial T}\right]$$

The Helmholtz free energy is defined as

$$F = E - TS \tag{1}$$

and is so

$$F = -NkT\left[\ln \frac{Q}{N} + 1\right]$$

Differenciation of equation (1) together with the Gibbs equation

$$dS = \frac{1}{T}dE + \frac{p}{T}dV - \frac{1}{T}\sum_I n_I \mu_I dN_I \tag{2}$$

where S is the entropy, μ_I is the chemical potential per particle and capital subscript I indicates chemical species, leads, for a pure gas, to

$$p = NkT\frac{\partial \ln Q}{\partial V}$$

which reduces to the standard form $pV = NkT$ since Q_{trans} is proportional to the volume while the contribution of internal modes are independent of the volume. This equation can be written in various forms, by introducing the density $\rho = Nm/V$ and the molar mass $M = \mathcal{N}m$ where $\mathcal{N}$ is the Avogadro number

$$pV = NkT$$
$$p = \frac{\rho}{m}kT = \frac{\rho}{M}\mathcal{N}kT$$
$$= \rho\frac{\mathcal{R}}{M}T = \rho RT$$

where $\mathcal{R} = \mathcal{N}k$ is the universal gas constant while $R = \mathcal{R}/M$ is the gas constant for the studied gas. The expression for the chemical potential can also be derived from equations (1) and (2) as

$$\mu_I = -kT \ln \frac{Q}{N}$$

The enthalpy is defined as $H = E + pV$ i.e

$$H = NkT^2 \frac{\partial \ln Q}{\partial T} + NkT$$

and the Gibbs free energy can be expressed either as

$$G = E + pV - TS = H - TS$$

or as

$$G = N\mu_I$$

All the above values (except the chemical potential) where obtained for N particles. The molar values are obtained by letting $N = \mathcal{N}$. Moreover, the formation enthalpy of the species must be accounted for. By convention, this enthalpy is null for species existing at standard conditions (O_2, N_2, Ar) and also for the electron. If H_I^0 is the molar formation-enthalpy of species I, the above relations read, for molar values

$$\begin{aligned}
G_I = \mu_I &= H_I^0 - RT \ln Q_I \\
H_I &= H_I^0 + RT^2 \frac{\partial \ln Q_I}{\partial T} \\
E_I &= H_I - RT
\end{aligned}$$

It is also interesting to introduce the *specific heat coefficient* at constant pressure

$$C_{PI} = \frac{\partial H_I}{\partial T} = -T^2 \frac{\partial^2 \mu_I}{\partial T^2}$$

1.4 Contribution of the degrees of freedom to the energy

As, in a first approximation, the partition function can be expressed as

$$Q = \prod_{\text{modes}} Q_{\text{modes}}$$

and the mean energy per particle reads

$$e = kT^2 \frac{\partial \ln Q}{\partial T}$$

the mean energy per particle can be expressed as

$$e = kT^2 \frac{\partial \sum \ln Q_{\text{modes}}}{\partial T} = \sum_{\text{modes}} kT^2 \frac{\partial Q_{\text{modes}}}{\partial T} = \sum_{\text{modes}} e_{\text{modes}}$$

i.e if the energy modes are assumed to be uncoupled, the energy is the sum of the energy of each mode.

The energy of each mode will be expressed to compare their relative order of magnitude:

- The translation energy partition function for a particle reads

$$Q_{\text{trans}} = V \left(\frac{2\pi mkT}{h^2} \right)^{\frac{3}{2}}$$

so that the translation energy is

$$e_{\text{trans}} = kT^2 \frac{\partial \ln Q}{\partial T} = kT^2 \frac{3}{2} \frac{\partial \ln T}{\partial T} = \frac{3}{2} kT$$

i.e the translation energy is proportional to the temperature, or, more precisely, the temperature is defined from the translation energy.

- The electronic excitation can be represented by only considering the first two states as

$$Q_{\text{elec}} = g_0 + g_1 \exp\left(-\frac{\varepsilon_1}{kT}\right) = g_0 + g_1 \exp\left(-\frac{\theta_1}{T}\right)$$

so that the energy reads

$$e_{\text{elec}} = k\theta_1 \frac{\frac{g_1}{g_0} \exp\left(-\frac{\theta_1}{T}\right)}{1 + \frac{g_1}{g_0} \exp\left(-\frac{\theta_1}{T}\right)}$$

i.e the electronic excitation energy is an always increasing function from zero at 0K to an asymptotic value of $k\theta_1 g_1/(g_0 + g_1)$. As an illustration, $\theta_1 g_1/(g_0 + g_1)$ is equal to 4560K for O_2, 87K for NO and 19800K for N. This asymptotic limit has little meaning as higher levels are substantially populated at high temperatures. It however shows that NO will be more easily excited and ionised than O_2 or N.

- The rotation partition function can be approximated as

$$Q_{\text{rot}} = \frac{T}{\theta_{\text{rot}}}$$

so that the rotation energy reads

$$e_{\text{rot}} = kT$$

i.e the rotation energy is two third of the translation energy.

• The vibrational partition function can be approximated as

$$Q_{\text{vib}} = \frac{1}{1 - \exp\left(-\frac{\theta_{\text{vib}}}{T}\right)}$$

and the vibrational energy is

$$e_{\text{vib}} = \frac{k\theta_{\text{vib}}}{\exp\left(\frac{\theta_{\text{vib}}}{T}\right) - 1}$$

i.e this contribution increases with temperature from zero at 0K to kT at high temperature, i.e while at low temperature the rotational energy is already equal to kT and the vibrational energy is negligible, the vibrational energy is equal to the rotational energy when the temperature is large compared with the characteristic vibrational temperature which is about 3000K for nitrogen, oxygen or nitrogen monoxide. As temperatures around bodies in reentry flows are usually about 5000K, the vibration energy is smaller than the rotation energy but however of the same order of magnitude.

1.5 Gas mixtures

1.5.1 State equation

The Dalton law can be demonstrated either from the above thermodynamic approach or with the help of gas kinetic theory (see e.g equation (11) in section 2.5). The pressure is the sum of the partial pressures of the various species. Each species behaves like a perfect gas, so

$$pV = \sum_I p_I V = \sum_I N_I kT = NkT$$

where N_I is the number of particles of species I in the volume V. This equation can also be rearranged by introducing the density of the species ρ_I and their molar masses M_I as

$$p = \sum_I \frac{\rho_I}{m_I} kT = \sum_I \frac{\rho_I}{M_I} \mathcal{R}T$$

A *mean molar mass* $\overline{M}$ can be defined as

$$\rho = n\overline{M} = \sum_I \rho_I$$
$$n = \frac{\rho}{\overline{M}} = \sum_I n_I = \sum_I \frac{\rho_I}{M_I}$$
$$\frac{1}{\overline{M}} = \sum_I \frac{\frac{\rho_I}{\rho}}{M_I} = \sum_I \frac{Y_I}{M_I}$$

where $Y_I = \rho_I/\rho$ are the *mass fractions*, and n the number of moles per unit volume. The pressure can thus be expressed as

$$p = \rho \frac{\mathcal{R}}{\overline{M}} T$$

The *compressibility factor* is defined as the ratio between the mean molar mass of the mixture and its value M_0 for non–dissociated gas as

$$Z = \frac{M_0}{\overline{M}}$$

so that the state equation reads

$$p = Z R_0 \rho T \qquad R_0 = \frac{\mathcal{R}}{M_0}$$

where R_0 is the gas constant for non–dissociated gas. Conversely, the partial pressure of a species can be expressed in terms of the mixture pressure as

$$p_I = \frac{n_I}{n} p = \frac{\rho_I/M_I}{\rho/\overline{M}} p$$

1.5.2 Thermodynamic properties of a mixture

The enthalpy of a gas mixture is the sum of the enthalpy of all particles. It is convenient to define the enthalpy per mass unit for each species

$$h_I = \frac{H_I}{M_I} \qquad H_I : \text{molar enthalpy}$$

so that the mixture enthalpy reads

$$\rho h = \sum_I \rho_I h_I \qquad h = \sum_I Y_I h_I$$

Similarly, the energy of a gas mixture is the sum of the energies of all particles.

The Gibbs free energy of a gas in a mixture depends upon its partial pressure as

$$G_I = H_I^0 - \mathcal{R}T \ln Q_I + \mathcal{R}T \ln \frac{p_I}{p^+}$$

where p^+ is a reference pressure (1 atm). The mixture Gibbs free energy is thus obtained similarly as

$$g = \sum_I Y_I g_I \qquad g_I = \frac{G_I}{M_I}$$

The specific heat of the mixture is still defined as

$$C_P = \frac{\partial h}{\partial T}\bigg)_P$$

so that, from the definition of the mixture enthalpy, it reads

$$C_P = \sum_I Y_I \frac{\partial h_I}{\partial T} + \sum_I h_I \frac{\partial Y_I}{\partial T} = \sum_I Y_I C_{PI} + \sum_I \frac{\partial Y_I}{\partial T} h_I$$

where the C_{PI} are here the specific heat per mass unit (i.e the above defined molar specific heat divided by M_I). The problem is to evaluate the partial derivative of mass fractions with respect to temperature. This has generally no meaning, except for two cases

- When the species mass fraction are constant. The "frozen" specific heat is then defined as

$$C_{Pf} = \sum_I Y_I C_{PI}$$

- When the flow is at chemical equilibrium. In this case, the mass fraction and all thermodynamic properties depend upon only two thermodynamic variables, e.g the pressure and the temperature. The derivative $(\partial Y_I/\partial T)$ at constant pressure can be defined (see section 4).

1.6 Practical evaluation of thermodynamic properties

The thermodynamic properties of each species and of the mixture can be calculated from the knowledge of the partition function. But this function is, as already seen, quite complex to evaluate. Spectroscopic data can be found in [23].

Slighlty simplified models have been proposed by Allison [2] and by Schäfer [94] in which the anharmonicity and the vibrational-rotational coupling are treated simply. These models are however still costly as the partition function calculation requires the evaluation of several exponential functions.

Polynomial fits for the entropy, the enthalpy and the specific heat as function of temperature are given in [52] [69]. These fits are quite accurate and computational time saving.

At last, thermodynamic properties are tabulated as function of the temperature in JANAF Thermodynamic tables [101]. Some results on thermodynamic properties of air at chemical equilibrium will be presented in section 4.

It must be mentionned that all this thermodynamic study has been done assuming that particles have undergone enough collisions for their energy to be "equally" distributed over all energetic modes. This is not always so as will be shown in section 2.6.3. The reader is referred to standard textbooks (e.g [105]) for further information.

2 Gaz kinetic theory

The Navier equations can be derived from tensorial analysis, the transport coefficients are then to be fitted with experimental values. Gas kinetic theory provides a tool to derive, from a description of particles behaviour at the microscopic level, both the flow governing equations at a macroscopic level and formal expressions for the transport coefficients.

Three length scales are to be considered, i.e

- A characteristic length scale of the flow at the macroscopic level, e.g the length of the body or the thickness of the boundary layer or the shock layer

- The mean free path, i.e the mean distance a particle travels between two collisions with other particles

- The interaction distance, i.e the distance at which interparticle forces act, or the maximum distance between two particles for their trajectories to be modified by the presence of the other particle

Herein, we shall restrict ourselves to the case of a *dilute* gas, i.e the interaction distance is small compared with the mean free path. The collisions between particles are unaffected by the presence of other particles. This is not always so for plasmas in which coulombic forces can have a long action range. Consequently, only two-particles collisions are to be accounted for.

Moreover, we shall assume the flow to be a *continuous* medium at the macroscopic scale, the mean free path being small compared with the flow characteristic length scale. Rarefied gas, in which this hypothesis is not fulfilled, will not be addressed here.

The following presentation of gas kinetic theory is widely influenced by Brun [26] and Hirschfelder [63] textbooks.

2.1 Description of the collision

The basis of gas kinetic theory is the description of the behaviour of particles at the microscopic level. With the above hypotheses, particles have a random walk, made up with straight lines and deviations due to collisions. These collisions reflect the fact that, when two particles are close enough, their electronic clouds are distorted. At "moderate" distances, particles attract each other but repeal at "shorter" distances. As a first approximation, particles will be described as points having mass and momentum but no internal energy. No exchange of internal energy occurs during collisions, the collisions are *elastic*. The anisotropy of the particles will also be neglected.

2.1.1 Interaction potential

For elastic collisions, the interaction force between non-polar particles depends only upon the distance r between the particles. This force F can then be related to a potential φ, the *interaction potential* as

$$F(r) = -\frac{d\varphi}{dr}$$

Various forms have been proposed to describe this interaction potential. The simplest one is the rigid sphere potential in which particles are described as billard balls which cannot interpenetrate and reflect speculary. The potential (Figure 3)

$$r \leq d \quad \varphi \to \infty$$
$$r > d \quad \varphi = 0$$

leads to very simple calculations. A more realistic, and very popular, potential is the Lennard–Jones potential which describes both the attractive and the repulsive zones as

$$\varphi = 4\epsilon \left[\left(\frac{d}{r}\right)^{12} - \left(\frac{d}{r}\right)^{6} \right]$$

where the two coefficients ϵ and d represent respectively the strength of the attraction and the distance at which repulsion occurs (Figure 4). These coefficients have to be obtained from experiment, e.g by fitting values of the gas viscosity. Other
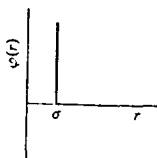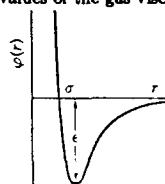

Figure 3: Rigid sphere potential

Figure 4: Lennard–Jones potential

simple models are available such as the Sutherland or the Buckingham potentials. For interactions between atoms, the potential can be linked to spectroscopic data of the molecule they can form [66] [104].
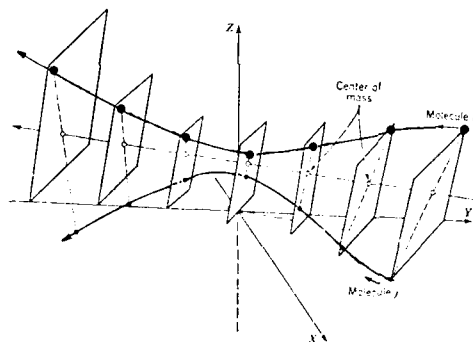

Figure 5: Three dimensional representation of the collision (from [63])

2.1.2 Reduction of the collision

The collision between two particles is a priori a three dimensional problem as depicted on figure 5. However, as the two particles form an isolated system, the study of invariants will enable us to simplify the analysis.

- The conservation of momentum implies that the trajectory of the center of mass of the two colliding particles is not modified, as shown on figure 5.

- As the interparticle force is an axial force, the angular momentum of the system formed with the two particles is also conserved. The separation vector between the two particles thus remains normal to a constant direction. At each time, the two particles lie in a plane normal to this direction (Figure 5). All these planes can be collapsed into a single one in such a way that the center of mass is a single point (Figure 6).

This representation brings into evidence the parameters which describe the collision, i.e

- The impact parameter b, i.e the distance of closest approach in absence of interparticle forces
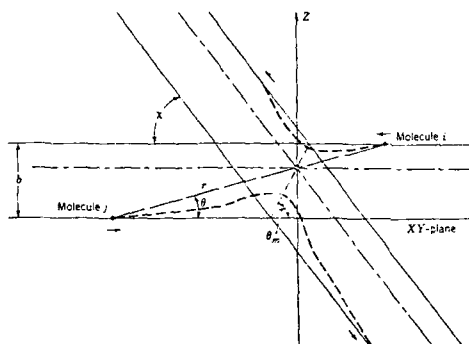
- The deflection angle χ

Figure 6: Two dimensional representation of the collision (from [63])

The trajectories of the two particles during the collision are described by the interparticle distance r and the angle θ. From the conservation of the angular momentum and of the total (potential + kinetic) energy of the two particles, the problem can again be reduced to the evolution of an hypothetical particle of mass $\mu = m_i m_j/(m_i + m_j)$ where m_i and m_j are the masses of the two colliding particles, moving with the relative velocity $g = v_i - v_j$ as depicted on figures 7 and 8. Figure 8 illustrates the influence of the interaction potential. We shall see later that the angle of deflection χ is the only practical parameter in transport properties calculations. It depends upon the impact parameter b, the relative velocity g of the particles and the interaction potential φ as

$$\chi(b,g) = \pi - 2b \int_{r_m}^{\infty} \frac{dr/r^2}{\sqrt{1 - \left(\varphi(r)/\frac{1}{2}\mu g^2\right) - (b^2/r^2)}} \tag{3}$$

where r_m is the distance of closest approach given by

$$1 - \frac{\varphi(r_m)}{\frac{1}{2}\mu g^2} - \frac{b^2}{r_m^2} = 0 \tag{4}$$

MOLECULE-MOLECULE POTENTIAL,U
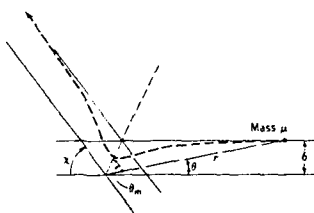
ATOM-ATOM POTENTIAL,U

Mass μ

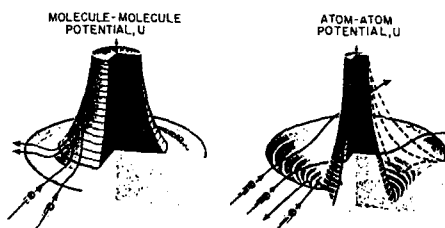Figure 7: One body description of the collision (from [63])

Figure 8: Artist view of the collision showing the rôle of the interparticle force (from [57])

2.2 Boltzmann equation

2.2.1 Density probability function and macroscopic properties of the flow

For free molecular flows, i.e when the mean free-path is of the order of magnitude of the flow length scale, the description of the collision is sufficient to follow the trajectories of individual particles. As we are concerned with the continuous regime, the number of particles is so large that this task is out of reach. Statistical tools will be used. Let us denote f the probability density to have particles in an elementary volume of space around point r with a velocity v. The number of particles per unit volume n is thus

$$n(r,t) = \int f(r,v,t)\, d^3v$$

The macroscopic value (noted $< Q >$) of any quantity Q linked to the particles can be defined as

$$n < Q >= \int Q(r,v,t) f(r,v,t)\, d^3v \tag{5}$$

and the average gas velocity is so defined as

$$n u = \int v f\, d^3v \qquad u = < v >$$

It is also interesting to introduce the *peculiar velocity* of the particles

$$c = v - u$$

as the fluid energy can be splitted into two parts

$$\int \frac{1}{2}mv^2 f d^3\underline{v} = \int \frac{1}{2}m(u+c)^2 f d^3\underline{v} = \int \frac{1}{2}mu^2 f d^3\underline{v} + \int \frac{1}{2}mc^2 f d^3\underline{v}$$

the first part being the macroscopic kinetic energy of the flow while the second represents the translation energy of the particles.

The flux of a quantity Q through a surface moving with the macroscopic flow can also be defined with the help of the probability density function. The number of particles passing through and elementary surface ds having a normal vector $\underline{N}$ during time dt is

$$\int (\underline{N} \cdot \underline{c}) f d^3\underline{c}\, ds\, dt$$

so that the flux of the quantity Q reads

$$\int Q\,(\underline{N} \cdot \underline{c})\, f\, d^3\underline{c}\, ds = \underline{N} \cdot \left[\int Q f \underline{c}\, d^3\underline{c} \right]\, ds$$

where $\int Q f \underline{c} d^3\underline{c}$ is the flux of Q. Let us consider some examples.

- The mass flux ($Q = m$ mass of the particles)

$$\int m f \underline{c}\, d^3\underline{c} = nm < \underline{c} >= 0$$

It must however be pointed out that the mass flux is zero because we are dealing with identical particles. For a gas mixture, each species has its own peculiar velocity which represents its diffusion. The mass flux is thus linked to the species diffusion (see section 2.5).

- The momentum flux ($Q = m\underline{c}$ momentum of the particles)

$$\int m\underline{c} f \underline{c}\, d^3\underline{c} = nm < \underline{cc} >= \rho < \underline{cc} >$$

This second order tensor represents momentum exchanges inside the gas, it is the *stress tensor*.

- The energy flux ($Q = \frac{1}{2}mc^2$ Translation energy of the particles, as no internal energy is accouted for)

$$\int \frac{1}{2}mc^2 f \underline{c}\, d^3\underline{c} = \frac{1}{2}nm < c^2\underline{c} >= \frac{1}{2}\rho < c^2\underline{c} >$$

This vector represents translation energy exchanges, it is the *heat flux*.

Once the density probability function f is known, this approach gives the expressions of the mass diffusion, the stress tensor and the heat flux.

2.2.2 The Boltzmann equation

The flow governing equations can also be derived with the use of the probability density function f. Its time variation is first studied. For an infinitesimal time dt, it reads

$$f(\underline{r}',\underline{v}',t') - f(\underline{r},\underline{v},t)$$

where

$$\begin{aligned} \underline{r}' &= \underline{r} + \underline{v} dt \\ \underline{v}' &= \underline{v} + \underline{F} dt \\ t' &= t + dt \end{aligned}$$

where $\underline{F}$ is an external force field (e.g gravity). For the sake of simplicity, it will be neglected herein. Derivation of the equations with an external force field is given in [63]. The total derivative of the probability density function can be expressed as

$$\frac{df}{dt} = \frac{\partial f}{\partial t} + \underline{v} \cdot \text{grad} f \qquad \text{where grad} = \frac{\partial}{\partial \underline{r}}$$

This term represents the evolution of the probability density function along particle trajectories. The variation is only due to collisions, and can be evaluated by considering collisions with a particle α. The particles β colliding with α are described by their impact parameter b, their relative velocity g and their probability density function f_β. During an infinitesimal time dt, the number of such particles β colliding with α is thus proportional to the impact section $2\pi b\, db$, to the particle displacement $g\, dt$ and to the density of particles $f_\beta d^3\underline{v}_\beta$. If we note ' the values after the collision, and noticing that both the impact parameter b and the relative velocity g are not changed by the collision, the balance between gained and lost particles reads

$$\frac{df_\alpha}{dt} = \int \left(f'_\alpha f'_\beta - f_\alpha f_\beta \right) g 2\pi\, db\, d^3\underline{v}_\beta \qquad (6)$$

This is the Boltzmann equation, the integral holds over all impact parameters b and all the velocity space $\underline{v}_\beta$. The interparticle force appears through the relations between the probability density function before and after the collision.

2.2.3 Derivation of the master equations

The Boltzmann equation could be used to compute the probability density function f and so obtain the macroscopic quantities. It is however simpler to only use it to derive an evolution equation for macroscopic quantities. The Boltzmann equation can be expressed as

$$\frac{df_\alpha}{dt} = J_\alpha = \int J_{\alpha\beta} d^3\underline{v}_\beta$$

where J is the collisional term. The evolution equation of the macroscopic value $< Q >$ can be derived by multiplying the Boltzmann equation by Q and integrating over velocity space

$$\int \left[\frac{\partial f_\alpha}{\partial t} + \underline{v}_\alpha \frac{\partial f_\alpha}{\partial \underline{r}} \right] Q_\alpha d^3\underline{v}_\alpha = \frac{\partial}{\partial t} \int f_\alpha Q_\alpha d^3\underline{v}_\alpha - \int f_\alpha \frac{\partial Q_\alpha}{\partial t} d^3\underline{v}_\alpha + \frac{\partial}{\partial r} \int f_\alpha \underline{v}_\alpha Q_\alpha d^3\underline{v}_\alpha - \int f_\alpha \frac{\partial Q_\alpha \underline{v}_\alpha}{d\underline{r}} d^3\underline{v}_\alpha$$

$$= \int Q_\alpha J_{\alpha\beta} d^3\underline{v}_\alpha d^3\underline{v}_\beta$$

As $\underline{v}$ and $\underline{r}$ are independent variables, and from the definition of the macroscopic value (Equation 5), the above equation reads

$$\frac{\partial}{\partial t} n < Q > -n \left\langle \frac{\partial Q}{\partial t} \right\rangle + \frac{\partial}{\partial \underline{r}} n < \underline{v}Q > -n \left\langle \underline{v} \frac{\partial Q}{\partial \underline{r}} \right\rangle = \int Q_\alpha J_{\alpha\beta} d^3\underline{v}_\alpha d^3\underline{v}_\beta \tag{7}$$

The integral is cumbersome to evaluate for arbitrary Q, however, it can be easily shown that it is zero for collision invariants. We shall therefore develop the above equation for the three collision invariants

- Conservation of the mass m

$$\frac{\partial \rho}{\partial t} + \frac{\partial}{\partial \underline{r}} \rho \underline{u} = 0 \qquad (\underline{u} = < \underline{v} >) \quad \rho = nm)$$

or, introducing the total derivative along streamlines

$$\frac{D}{Dt} = \frac{\partial}{\partial t} + \underline{u} \cdot \frac{\partial}{\partial \underline{r}}$$

the *continuity equation* reads

$$\frac{D\rho}{Dt} + \rho \operatorname{div} \underline{u} = 0$$

- Conservation of the momentum $m\underline{v}$

$$\frac{\partial}{\partial t} (\rho \underline{u}) + \frac{\partial}{\partial \underline{r}} (\rho < \underline{v}\underline{v} >) = 0.$$

The velocity product can be decomposed with the help of the peculiar velocity as

$$< \underline{v}\underline{v} > = \underline{u}\underline{u} + < \underline{c}\underline{c} >$$

The second term is, once multiplied by ρ, the stress tensor previously introduced. After some algebra, and with the help of the continuity equation, the *momentum equation* reads

$$\rho \frac{D\underline{u}}{Dt} + \operatorname{div} \underline{\tau} = 0 \qquad \underline{\tau} = \rho \langle \underline{c}\underline{c} \rangle$$

- Conservation of the energy $\frac{1}{2}mv^2$

$$\frac{\partial}{\partial t} \left(\frac{1}{2} \rho < v^2 > \right) + \frac{\partial}{\partial \underline{r}} \frac{1}{2} \rho < v^2 \underline{v} > = 0$$

which can be developed, by introducing the peculiar velocity, as

$$\frac{\partial}{\partial t} \left(\frac{1}{2} \rho u^2 \right) + \frac{\partial}{\partial t} \left(\frac{1}{2} \rho < c^2 > \right) + \operatorname{div} \left(\frac{1}{2} \rho u^2 \underline{u} \right) + \operatorname{div} \left(\frac{1}{2} \rho < c^2 \underline{c} > \right) + \operatorname{div} \left(\rho \underline{u} < \underline{c}\underline{c} > \right) + \operatorname{div} \left(\frac{1}{2} \rho \underline{u} < c^2 > \right) = 0$$

which expresses the conservation of the kinetic energy of the macroscopic motion $\underline{u}$ plus the translation energy. Let us notice that the fourth term is the heat flux previously introduced. Defining the translation energy per mass unit $U_t = \frac{1}{2} < c^2 >$, and with the help of the momentum and the continuity equation, the *energy equation* can be expressed as

$$\rho \frac{DU_t}{Dt} = -\operatorname{div} \underline{q}_t - \underline{\tau} \cdot \operatorname{grad} \underline{u}$$

where q_t is the heat flux.

It must be noticed that the translation temperature can be defined from the above translation energy as

$$\frac{1}{2} m < c^2 > = \frac{3}{2} kT$$
$$\text{or} \qquad U_t = \frac{3}{2} \frac{k}{m} T$$
$$= \frac{3}{2} \frac{\mathcal{R}}{M} T$$

Other equations could be derived in this way but the collision term should be evaluated. The above set of equation is sufficient to describe the macroscopic fluid motion. Practical expressions for the stress tensor and the heat flux are needed to be able to use these equations. This requires the knowledge of the probability density function f.

2.3 Equilibrium distribution function

2.3.1 H theorem – Maxwellian distribution

The important Boltzmann H–theorem states that the entropy is an always increasing function. A simple application can be used for the evolution of the probability density.

Let us consider a quantified system, in which N_α particles have the velocity $\underline{v}_\alpha$, N_β the velocity $\underline{v}_\beta \cdots$ The total number of particles is

$$N = \sum_\alpha N_\alpha$$

and the probability W to have a given classification is

$$W = \frac{N!}{N_\alpha! N_\beta! \cdots} = \frac{N!}{\prod_\alpha N_\alpha!} \tag{8}$$

According to Stirling's formula $\ln(N!) \sim N \ln N - N$ when N large

$$\ln W = N \ln N - \sum_\alpha N_\alpha \ln N_\alpha$$

Similarly, when the system is not quantified, the above expression can be extended with the use of the probability density function f (and neglecting a constant linked to the total number of particles) as

$$H(t) = \ln W = -\int f_\alpha \ln f_\alpha \, d^3\underline{v}_\alpha \, d^3\underline{r}$$

The time evolution of the H function can be obtained by multiplying the Boltzmann equation by $(1 + \ln f)$ and integrating over velocity and space. After some algebra it leads to

$$\frac{dH}{dt} = -\frac{1}{4} \int \ln\{\frac{f'_\alpha f'_\beta}{f_\alpha f_\beta}\} \left(f'_\alpha f'_\beta - f_\alpha f_\beta\right) 2\pi b g \, db \, d^3\underline{v}_\alpha \, d^3\underline{v}_\beta \, d^3\underline{r}$$

and as the term under the integral is like $(y - x) \ln \frac{y}{x} = x \left(\frac{y}{x} - 1\right) \ln \frac{y}{x}$ the integral is always positive. Consequently, the H function can only decrease. Since it is obvious from the quantified definition of W (Equation 8) that $W > 1$ and hence H has a lower bound, an equilibrium state must be obtained which corresponds to $dH/dt = 0$ i.e $f'_\alpha f'_\beta = f_\alpha f_\beta$. The equilibrium solution corresponds to a state in which the probability density function is not modified by the collisions. Turning back to the Boltzmann equation (6), this means that the collision term is larger than the total derivative of the probability density function. The probability density function is thus imposed by collisions. It is the *collision dominated regime*.

It can be noticed that the equilibrium equation also reads

$$\ln f'_\alpha + \ln f'_\beta = \ln f_\alpha + \ln f_\beta$$

so that $\ln f$ is another *collision invariant*. It therefore can be expressed as the sum of the three collision invariants, $m, m\underline{v}, \frac{1}{2}mv^2$ or in terms of moments of f from the three relations

$$
\begin{aligned}
n &= \int f \, d^3\underline{v} \\
n\underline{v} &= \int \underline{v} f \, d^3\underline{v} \\
\frac{3}{2} nkT &= \int \frac{1}{2} mc^2 f \, d^3\underline{v}
\end{aligned}
\tag{9}
$$

From the properties of Eulerian integrals, the probability density function is obtained as

$$f = n \left(\frac{m}{2\pi kT}\right)^{\frac{3}{2}} \exp\left(-\frac{mc^2}{2kT}\right)$$

This equilibrium solution is called the *maxwellian distribution*. It is a gaussian distribution, centered upon the macroscopic velocity. It must be noticed that, while it corresponds to an equilibrium regime for the collisions, it does not depend upon the interparticle potential.

2.3.2 Derivation of the Euler equations

As the probability density function has been determined, the stress tensor and the heat flux can be computed. It can be verified that

$$
\begin{aligned}
\tau_{xx} = \rho < c_x c_x > &= \rho \left(\frac{m}{2\pi kT}\right)^{\frac{3}{2}} \int_{-\infty}^\infty c_x^2 \exp\left(-\frac{mc_x^2}{2kT}\right) dc_x \int_{-\infty}^\infty \exp\left(-\frac{mc_y^2}{2kT}\right) dc_y \int_{-\infty}^\infty \exp\left(-\frac{mc_z^2}{2kT}\right) dc_z \\
&= nkT
\end{aligned}
$$

and similarly $\tau_{yy} = \tau_{zz} = nkT$ while $\tau_{xy} = \tau_{xz} = \tau_{yz} = 0$ as they are integrals of odd functions. For the same reason, the heat flux is also null. The only stress is thus the hydrostatic pressure due to the particle motion.

$$\underline{\underline{\tau}} = p\underline{\underline{\delta}} \qquad \text{where } \underline{\underline{\delta}} \text{ is the unit tensor}$$

$$\text{with} \qquad p = nkT \tag{10}$$

The set of continuity, momentum and energy equation thus reduces to the *Euler* equations.

2.4 Non–equilibrium state

The maxwellian distribution corresponds to an equilibrium state in which the behaviour of the probability density function is ruled by the collision; it is the solution of $J = 0$. Dimensional analysis is used to study the balance between the total derivative df/dt and the collision term J. The Boltzmann equation can be rewritten as

$$\frac{df^*}{dt^*} = \frac{\tau_{\text{macroscopic flow}}}{\tau_{\text{collisions}}} J^*$$

where $*$ denotes a dimensionless variable. The ratio between the collision time scale and the macroscopic flow time scale is known as the *Knudsen* number Kn. For free molecular flows $Kn \to \infty$ while for the continuous regime $Kn \to 0$. Asymptotic expansion with respect to $\varepsilon = Kn$ can be used to study the continuous regime. The probability distribution function is expanded as

$$f^* = f^{*0} + \varepsilon f^{*1} + \dots$$

while the Boltzmann equation reads

$$\frac{df^*}{dt^*} = \frac{1}{\varepsilon} J^*$$

so that, to the zeroth order (i.e terms of order $\frac{1}{\varepsilon}$)

$$J^0 = 0 \quad \text{where} \quad J^0 = \int \left(f'^0_\alpha f'^0_\beta - f^0_\alpha f^0_\beta \right) 2\pi g b \, db \, d^3 \underline{v}_\beta$$

The zeroth order solution is the limit when $Kn \to 0$, i.e when the flow is dominated by collisions. The maxwellian distribution is thus the solution.

The first order expansion leads to

$$\frac{df^0}{dt} = J^1 \quad \text{where} \quad J^1 = \int \left(f'^0_\alpha f'^1_\beta + f'^1_\alpha f'^0_\beta - f^0_\alpha f^1_\beta - f^1_\alpha f^0_\beta \right) 2\pi g b \, db \, d^3 \underline{v}_\beta$$

The computation of the term f^1 is lengthy and will only be summarised herein. The procedure is due to Chapman and Enskog [31] [63] [105]. The solution is looked for as

$$f^1 = f^0 \varphi \quad \text{with } \varphi \ll 1$$

i.e the second order term is supposed to be only a small perturbation. The macroscopic variables (density, velocity, temperature) are still linked to the zeroth order term. f^0 is solution of the equations (9). The global probability density function $f^0 + f^1 = f^0 (1 + \varphi)$ must also satisfy these equations; this imposes constraints upon φ.

The probability distribution function correction φ is looked for as the sum of a solution of the equation $J^1 = 0$ and of a particular solution of the equation $df^0/dt = J^1$. The solution of the first equation $J^1 = 0$ can obviously be expanded on a basis formed with the collision invariants while the expression of df^0/dt lead to express the peculiar solution in terms of grad T and grad $\underline{u}$. The various coefficients are expanded in terms of Sonine polynomials (These polynomials are used as they are eigenfunctions of the collision operator). One polynomial is enough to give a fair description but the results are improved when two are accounted for.

The probability distribution function correction φ so determined can be used to compute the stress tensor and the heat flux as

$$\underline{\underline{\tau}} = \int f^0 (1 + \varphi) \underline{cc} \, d^3\underline{c} = p\underline{\underline{\delta}} + \int f^0 \varphi \underline{cc} \, d^3\underline{c} = p\underline{\underline{\delta}} - \mu \left(\text{grad } \underline{u} + \text{grad}^t \underline{u} - \frac{1}{3} \underline{\underline{\delta}} \text{div } \underline{u} \right)$$

$$\underline{q} = \int f^0 \varphi \frac{1}{2} m c^2 \underline{c} \, d^3\underline{c} = -\lambda \text{grad } T$$

where grad^t $\underline{u}$ denotes the transpose of grad $\underline{u}$.

With the above expressions for the stress tensor and the heat flux, the *Navier* equations are obtained.

It must be pointed out that the transport properties of the fluid are due to the non–equilibrium probability density function. They are properties of the fluid and not of the motion, i.e a fluid at rest already has viscosity and thermal conductivity which are only due to particle Brownian motion.

2.4.1 Collision integrals

The solution now depends upon the collision process. The expression of the correction φ is intricate and practical ways to compute the viscosity μ and the thermal conductivity λ have been proposed [31] [63]. It is based upon the fact that the various coefficient which appear in the calculations can be reduced to a set of integrals, called *collision integrals* and defined as

$$\Omega^{(l,s)}(T) = \sqrt{\frac{kT}{\pi m}} \int_0^\infty e^{-\gamma^2} \gamma^{2s+3} \left[2\pi \int_0^\infty \left(1 - \cos^l \chi \right) b \, db \right] d\gamma$$

where $\gamma^2 = mg^2/kT$ and the deflection angle χ is given by the equations (3) and (4). It is customary to compare these integrals obtained for a given interparticle potential to those obtained for rigid spheres of diameter σ (Figure 3) as

$$\Omega^{(l,s)*} = \frac{\Omega^{(l,s)}}{\Omega^{(l,s)}_{\text{rigid sphere}}} = \frac{\Omega^{(l,s)}}{\frac{1}{2} (s+1)! \left(1 - \frac{1}{2} \frac{1+(-1)^l}{1+l} \right) \pi \sigma^2 \sqrt{\frac{kT}{\pi m}}}$$

The expression for the viscosity and the thermal conductivity are thus

$$\mu = \frac{5}{16} \frac{\sqrt{\pi m k T}}{\pi \sigma^2 \Omega^{(2,2)*}}$$

$$\lambda = \frac{25}{32} \frac{\sqrt{\pi m k T}}{\pi \sigma^2 \Omega^{(2,2)*}} \frac{C_v}{m}$$

where C_v is the specific heat coefficient *at constant volume*. The others collision integrals, corresponding to other sets (l,s), will be used later when considering gas mixtures.

2.5 Extension to gas mixtures

2.5.1 Non reacting gas

The gas is now a mixture of species I (capital letter subscripts designate the species). A probability density function is defined for each species as

$$n_I = \int f_I(\underline{r}, \underline{v}_I, t) d^3\underline{v}_I$$

where n_I is the number of particles of the species I per unit volume and $\underline{v}_I$ the velocity of a particle of species I.

The macroscopic values are now linked to the species

$$n_I < Q_I > = \int Q f_I d^3\underline{v}_I$$

so that a macroscopic velocity is defined for each species

$$n_I \underline{u}_I = \int \underline{v}_I f_I d^3\underline{v}_I$$

The velocity of the gas mixture is defined as a mass–averaged velocity as momentum is a collision invariant while velocity is not. It reads

$$\rho \underline{u} = \sum_I \rho_I \underline{u}_I \qquad \text{where } \rho = \sum_I \rho_I = \sum_I n_I m_I$$

The peculiar velocity of a particle is

$$\underline{c}_I = \underline{v}_I - \underline{u}$$

while the *diffusion velocity*

$$\underline{u}_I - \underline{u} = < \underline{c}_I >$$

is now introduced. It must be noticed that $\sum_I \rho_I < \underline{c}_I > = 0$.

As previously, the master equations can be derived. New equations are obtained which express the individual conservation of species

$$\frac{\partial n_I}{\partial t} + \text{div } n_I \underline{u}_I = 0$$

or, once multiplied by m_I,

$$\frac{\partial \rho_I}{\partial t} + \text{div } (\rho_I \underline{u}) = -\text{div } (\rho_I < \underline{c}_I >)$$

where the RHS represents the diffusion of species I. The sum of these equations for all the species leads to the continuity equation. The momentum equation has the same form as for a pure gas, while an extra term due to species diffusion appears in the energy equation as

$$E_t = \frac{3}{2} k T = \frac{1}{n} \sum_I \frac{1}{2} m_I c_I^2 f_I d^3\underline{v}_I$$

$$n \frac{D E_t}{D t} = -\text{div } q_t - \underline{\underline{\tau}} \cdot \text{grad } \underline{u} + E_t \text{div } \left(\sum_I n_I < \underline{c}_i > \right)$$

The stress tensor and the heat flux also account for the various species as

$$\underline{\underline{\tau}} = \sum_I \underline{\underline{\tau}}_I = \sum_I m_I \int \underline{c}_I \underline{c}_I f_I d^3\underline{v}_I$$

$$\underline{q}_t = \sum_I \underline{q}_{tI} = \sum_I \int \frac{1}{2} m_I c_I^2 \underline{c}_I f_I d^3\underline{v}_I$$

The Boltzmann equation must now account for elastic collisions between all species and can be written as

$$\frac{d f_I}{d t} = \sum_K J_{IK}$$

The zeroth order solution, which corresponds to collision equilibrium, still reads

$$f_I^0 = n_I \left(\frac{m_I}{2\pi k T} \right)^{\frac{3}{2}} \exp \left(-\frac{m_I c_I^2}{2kT} \right)$$

and still leads to the Euler equations plus an advection equation for each species without diffusion. The pressure is now given as

$$p = \sum_I p_I = \sum_I n_I k T = n k T \qquad (11)$$

which is known as the Dalton law.

The first order solution is still obtained following the Chapman–Enskog procedure. The diffusion velocity reads

$$< \underline{c}_I > \; = \; \frac{n^2}{\rho n_I} \sum_{K \neq I} m_K D_{IK} \underline{d}_K - \frac{1}{n_I m_I} D_T^I \frac{1}{T} \mathrm{grad}\; T$$

$$\text{where} \qquad \underline{d}_K \; = \; \mathrm{grad}\; \frac{n_K}{n} + \left[\frac{n_K}{n} - \frac{\rho_K}{\rho} \right] \frac{1}{p} \mathrm{grad}\; p$$

The species diffusion is due to multicomponent diffusion via the coefficient D_{IK} with respect to the mole fraction gradient and the pressure gradient, and to thermal diffusion via the coefficient D_T^K with respect to the temperature gradient. Multicomponent diffusion tends mainly to homogeneize the mixture while thermodiffusion effect (the Soret effect) moves light species towards hot regions and heavy species towards cold regions. The Soret effect was first predicted and afterwards observed experimentally. It is a weak effect, sometimes called second order effect, as it requires a two Sonine polynomial expansion to be obtained.

The stress tensor expression is unchanged while the expression of the viscosity is much more intricate. At last, the heat flux now account for species diffusion as

$$\underline{q}_i = -\lambda \mathrm{grad}\; T + \sum_I \lambda_I \underline{d}_I$$

Another equivalent expression for the heat flux will be given later (equation 17) as the λ_I must be expressed.

For a mixture made up with ν species, $\frac{\nu(\nu+1)}{2}$ different collisions have to be accounted for and ν probability density functions must be determined. Therefore, the various transport coefficients can be obtained only as solution of νth order linear system (or $(2\nu)^{th}$ order for the thermal diffusivity). The reader is refered to standard textbooks [31] [63] for the details of the calculus of transport coefficients and the final expressions.

A new problem appears for plasma as the mass of the electron is very small compared with the masses of the atoms or the molecules. The translational energy exchange during electron/particle collision is weak. Sonine polynomial expansion must be extended to higher order to achieve a good convergence. The present theory has been modified for plasma by Devoto [39] [40] [41] and Bonnefoi [21] by neglecting the electron/particle collisions and modifying the flux expressions.

2.5.2 Reacting gas

For a reacting mixture, two kinds of collision must be accounted for, i.e the elastic collisions previously introduced and "reacting collisions" leading to change in the mixture composition. The Boltzman equation can be rewritten as

$$\frac{df_I}{dt} = \sum_K J_{IK}^{\text{elastic}} + \sum_K \sum_L J_{KL}^{\text{I - reacting}}$$

provided a collision between species K and L may lead to formation or destruction (when K or L equals I) of the species I. The order of magnitude analysis of the Boltzmann equation leads obviously to the following equation

$$\begin{aligned} \frac{df_I^*}{dt^*} \; &= \; \frac{\tau_{\text{macroscopic flow}}}{\tau_{\text{elastic collisions}}} \sum_K J_{IK}^{*\text{elastic}} \\ &+ \; \frac{\tau_{\text{macroscopic flow}}}{\tau_{\text{reacting collisions}}} \sum_K \sum_L J_{KL}^{*\text{I - reacting}} \\ &= \; \frac{1}{\varepsilon_{\text{elastic}}} \sum_K J_{IK}^{*\text{elastic}} + \frac{1}{\varepsilon_{\text{reacting}}} \sum_K \sum_L J_{KL}^{*\text{I - reacting}} \end{aligned}$$

so that two expansion parameters now appear. It can be assumed that only a few collisions leads to reactions so that $\varepsilon_{\text{elastic}} \ll \varepsilon_{\text{reacting}}$. The study of two parameter expansion is detailed in section 2.6.2 or in [26] [27] [112]. When $\varepsilon_{\text{reacting}} < 1$, the chemistry should affect the probability density function and thus the expression of the transport coefficients. This effect is weak and is neglected [63].

However, the master equations are modified. The collision invariant are now the total mass of the two colliding species (and not the individual masses of each species as previously), the momentum, and the sum of the translation energy and the internal energy of species as the species formation energy must be accounted for (and later, the internal degrees of freedom). Turning back to the master equation (7), the species equation now include a new term $d < Q > /dt$ due to the creation or the destruction of species by chemical reactions

$$\frac{\partial \rho_I}{\partial t} + \mathrm{div}\; (\rho_I \underline{u}) = \omega_I - \mathrm{div}\; (\rho_I < \underline{c}_I >)$$

and, as chemical reactions do not create or destroy mass,

$$\sum_I \omega_I = 0$$

so that the continuity equation is still obtained as the sum of the species evolution equations. The momentum equation is unchanged, and the energy equation has the same form, provided that E_i now represents the sum of the translation and of the internal energy of species.

2.5.3 Schmidt, Prandtl and Lewis numbers

The species conservation equation have be written using either the number of particles per volume unit n_I or the species density ρ_I. It is also useful to introduce the mass fraction $Y_I = \rho_I/\rho$. The species conservation equation thus reads

$$\rho\frac{\partial Y_I}{\partial t} + \rho\underline{u} \cdot \text{grad} Y_I = \omega_I + \text{div}\left(-\underline{q}_I\right)$$

$$\underline{q}_I = \rho_I < \underline{c}_I >$$

$$(12)$$

The equation can be simplified when only two species are present and when the thermal diffusion effect, which is a second order effect, and the pressure induced diffusion are neglected. The diffusion flux then reads, for a mixture of species A and B

$$\underline{q}_A = \frac{\rho_A n^2}{\rho n_A} m_B D_{AB} \text{grad} \frac{n_B}{n} = -\rho D_{AB} \text{grad} Y_A = -\rho D \text{grad} Y_A$$

$$(13)$$

This is known as the second Fick's law which directly links the diffusion flux in a two-species mixture to the gradient of the mass fraction. It must be pointed out that the Fick's law can be derived *only* for binary mixtures. It is however a fair approximation in other cases.

The relative order of magnitude of the species and the momentum diffusion can be evaluated with the help of the *Schmidt number*

$$S = \frac{\mu}{\rho D}$$

It is classical to evaluate also the ratio between momentum and energy diffusion with the help of the *Prandtl number*, in which, for gas mixtures, the frozen specific heat has to be used

$$P = \frac{\mu C_{Pf}}{\lambda}$$

and the *Lewis number* is also introduced as the ratio of species and heat diffusion as

$$\mathcal{L} = \frac{\rho D C_{Pf}}{\lambda}$$

Evolution of these characteristic numbers will be presented in section 4. It must be pointed out that, for dissociated air, they are of order unity.

2.5.4 Equilibrium flow, frozen flow

The evolution of the species mass fraction (Equation 12) results from a balance between advection, diffusion and chemical production. A characteristic time scale can be associated with each process. Outside of the boundary layer (or more generally, the viscous or more properly diffusive regions) the diffusion time scale is large when compared with the advection time scale while they have the same order of magnitude in the viscous regions. Consequently, the chemical reaction time scale has to be compared only with the advection time scale.

Three cases must be considered

- $\tau_{Chemistry} \gg \tau_{Advection}$

  The chemical reaction are so weak that they do not modify the composition of the gas mixture. The flow is thus said to be *frozen*. The mass fraction evolution equation reduces to

  $$\rho\frac{\partial Y_I}{\partial t} + \rho\underline{u} \cdot \text{grad} Y_I = \text{div}\left(-\underline{q}_I\right)$$

  where the diffusion flux has been included for viscous regions. In inviscid regions of the flow, the mass fractions of the species remain constant along streamlines.

  In viscous regions, they can be modified by the diffusion process. If the pressure gradient is null (e.g in a boundary layer where the normal pressure gradient is zero and the longitudinal diffusion effects are neglected) and if the thermal diffusion effect is neglected, an asymptotic solution to the above equation is $Y_I = $ constant provided it agrees with boundary conditions (e.g the wall must be non catalytic. see section 3.3).

- $\tau_{Chemistry} \ll \tau_{Advection}$

  In this case, the flow is governed by the chemical reactions. The mass fraction equation can be reduced to its dominant term as

  $$\omega_I = 0$$

  The flow is thus at *chemical equilibrium* as chemical reactions do not destroy or produce any species. Its composition can be computed from two thermodynamic variables (e.g temperature and pressure). Properties of air at chemical equilibrium will be presented in section 4.

- $\tau_{Chemistry} \sim \tau_{Advection}$

  In this case, no term can be neglected. The chemistry processes with a time scale similar to the advection, the flow is said to be in *chemical non-equilibrium*.

2.6 Effect of the internal degrees of freedom of the molecules

Up to now, only particles without internal degrees of freedom have been considered. When internal degrees of freedom are accounted for, *inelastic collisions* in which internal degrees of freedom of the colliding molecules are modified, must be introduced. The internal energy of the molecule ε_i is quantified and the total energy of a molecule in a given energy state can be expressed as $\frac{1}{2}mv_i^2 + \varepsilon_i$ where the subscript i indicates the energy level. A probability density function for each energy state can be introduced so that, as previously

$$n = \sum_i \int f_i d^3\underline{v}_i$$

$$n\underline{u} = \sum_i \int f_i\underline{v}_i d^3\underline{v}_i$$

$$\underline{c}_i = \underline{v}_i - \underline{u}$$

$$nE_t = \sum_i \int f_i \frac{1}{2}mc_i^2 d^3\underline{v}_i$$

$$nE_{int} = \sum_i \int f_i\varepsilon_i d^3\underline{v}_i$$

$$E_{tot} = E_t + E_{int}$$

The collision invariants are still the mass and the momentum but the total energy of the two particles (translation + internal energy). The master equation reflects this fact as the energy equation is now obtained for the total energy. The stress tensor expression is unchanged but the heat flux now includes an internal energy flux

$$\underline{q} = \underbrace{\sum_i \int \frac{1}{2}mc_i^2 f_i\underline{c}_i\, d^3\underline{c}_i}_{\underline{q}_t} + \underbrace{\sum_i \varepsilon_i \int f_i\underline{c}_i\, d^3\underline{c}_i}_{\underline{q}_{int}}$$

The Boltzmann equation must account for the elastic and inelastic collisions

$$\frac{df_i}{dt} = J_i^{\text{elastic}} + J_i^{\text{inelastic}}$$

or under the dimensionless form

$$\frac{df_i^*}{dt^*} = \frac{1}{\varepsilon_{\text{elastic}}}J_i^{\text{elastic*}} + \frac{1}{\varepsilon_{\text{inelastic}}}J_i^{\text{inelastic*}}$$

$$\varepsilon_{\text{elastic}} = \frac{\tau_{\text{elastic collisions}}}{\tau_{\text{macroscopic flow}}} \qquad \varepsilon_{\text{inelastic}} = \frac{\tau_{\text{inelastic collisions}}}{\tau_{\text{macroscopic flow}}}$$

Various situations occur according to the relative magnitude of the two time scale ratios ε [26] [27] [112]. However, the elastic collision time scale will always remains smaller than the inelastic collision one and, as only the continuous regime is considered $\varepsilon_{\text{elastic}} \ll 1$.

2.6.1 Thermal equilibrium

The first case corresponds to $\varepsilon_{\text{elastic}} \ll \varepsilon_{\text{inelastic}} \ll 1$. Both collision time scales are small compared with the macroscopic flow time scale so that, the zeroth order expansion reads

$$J_i^{0\,\text{elastic}} + J_i^{0\,\text{inelastic}} = 0$$

the solution of which is

$$f_i^0 = n\left(\frac{m}{2\pi kT}\right)^{\frac{3}{2}}\exp\left(-\frac{mc_i^2}{2kT}\right)\frac{\exp\left(-\frac{\varepsilon_i}{kT}\right)}{\sum_i \exp\left(-\frac{\varepsilon_i}{kT}\right)}$$

i.e as previously a maxwellian distribution for the velocity and a Boltzmann distribution for the internal degrees of freedom. As the two collision time scales are small when compared with the macroscopic flow time scale, the internal energy is in equilibrium with the translation energy. The flow is in thermodynamic equilibrium.

The first order solution is still obtained with the help of the Chapman–Enskog expansion

$$\frac{df_i^0}{dt} = J_i^{1\,\text{elastic}} + J_i^{1\,\text{inelastic}} \qquad \text{and} \qquad f_i^1 = f_i^0(1 + \varphi_i)$$

but the set of polynomials is different. The stress tensor and the heat flux are thus

$$\underline{\underline{\tau}} = p\underline{\underline{\delta}} - \mu\left(\text{grad}\underline{u} + \text{grad}^t\underline{u} - \frac{1}{3}\underline{\underline{\delta}}\text{div}\underline{u}\right) - \eta\,\text{div}\underline{u}$$

$$\underline{q} = -\lambda_t\text{grad}T - \lambda_{int}\text{grad}T$$

The coefficient η is the *bulk viscosity*, and corresponds to a "relaxation time" i.e the characteristic time for the energy to be transferred from the translational to the internal degrees of freedom when the fluid is compressed or expanded. (This term does not intervene in "incompressible" flows for which $\text{div}\underline{u} = 0$)

The internal energy conductivity λ_{int} could be computed as the other transport coefficients. However, if the Lewis number is close to unity, which is true for air, it can be approximated as

$$\lambda_{int} = \frac{4}{15}\left(\frac{C_{pl}}{R} - \frac{5}{2}\right)\lambda_t$$

which is the Eucken correction.

2.6.2 Frozen internal degrees of freedom

The second case corresponds to $\varepsilon_{\text{elastic}} \ll 1 \ll \varepsilon_{\text{inelastic}}$. The expansion leads to

$$J_i^{0\,\text{elastic}} = 0$$

$$\frac{df_i^0}{dt} = J_i^{1\,\text{elastic}}$$

i.e the probability density function is independent of the inelastic collisions as the inelastic collision time scale is larger than the macroscopic flow time scale. It can then be easily shown that the population of each energy level n_i is preserved as its evolution equation, derived in a similar way than the other master equations, reads

$$\frac{\partial n_i}{\partial t} + \text{div}\,n_i\underline{u} = \int J_i^{\text{inelastic}} d^3\underline{c_i} = 0 \qquad \text{as } J_i^{\text{inelastic}} = 0$$

and also that, at the zeroth order (the Euler equations), the internal energy is constant along streamlines.

While in the first case the internal degrees of freedom were in equilibrium with the translation, here they are frozen, i.e the macroscopic flow evolution is too fast for internal degrees of freedom to adjust and they remain unchanged, when considered at macroscopic flow time scale.

2.6.3 Thermal non-equilibrium

The last case is $\varepsilon_{\text{elastic}} \ll 1 \sim \varepsilon_{\text{inelastic}}$. It corresponds to situations in which the inelastic collisions have a time scale similar to the macroscopic flow one. The dimensionless Boltzmann equation now reads

$$\frac{df_i^*}{dt^*} = \frac{1}{\varepsilon_{\text{elastic}}} J_i^{\text{elastic*}} + J_i^{\text{inelastic*}}$$

so that the expansion leads to

$$J_i^{0\,\text{elastic}} = 0$$

$$\frac{df_i^0}{dt} = J_i^{1\,\text{elastic}} + J_i^{0\,\text{inelastic}}$$

So that the zeroth order does not depend upon inelastic collisions. The probability distribution function f_i^0 is thus the same as in the frozen case. But the evolution equation for the populations n_i now reads

$$\frac{\partial n_i}{\partial t} + \text{div}\,n_i\underline{u} = \int J_i^{0\,\text{inelastic}} d^3\underline{c_i}$$

where the right hand side is no longer null.

The study of population relaxation requires now much information about the physics. Usually, very few collisions are needed to equilibrate the rotation with the translation so that they can always be assumed to be at equilibrium (except for H_2 for which the relaxation process is longer). Electronic states can also be assumed to be at equilibrium, excitation of electrons leading rapidly to ionization. The vibration energy however is more difficult to equilibrate as it may require about one thousand collisions. The above analysis can be revised to only consider vibrational relaxation, the previously called "inelastic collisions" are thus only collisions in which vibrational energy is modified. This can be done in two ways, either by transformation of the translation energy of a molecule into vibrational energy of the other (T–V collision) or by modification of the two molecules vibrational energy (V–V collision). For translation temperature less than about 5000K, the vibrational relaxation of a molecule can be modelled by the Landau–Teller law

$$\frac{DE_{\text{vib}}}{Dt} = \frac{E_{\text{vib}}^* - E_{\text{vib}}}{\tau}$$

$$\text{with e.g} \quad \tau = C\frac{\exp\left(\frac{K_2}{T}\right)^{\frac{1}{3}}}{p}$$

where E_{vib}^* is the equilibrium vibrational energy i.e the vibrational energy of molecules at thermodynamic equilibrium having the same translation energy. The coefficients C and K_2 can be found in [105]. Other expressions for the relaxation time have been proposed (see e.g [81] [87]).

Readers interested in relaxation processes can find more informations in standard textbooks [26] [72] [105] and in some publications such as [26] [28] [73] [74] [78] [85] [89] [103] ...

A last comment on thermal nonequilibrium concern another phenomenon. In plasma, interactions between electrons and other particles are weak, due to the small mass of the electron. Consequently, the translation temperature of the electron can be different from the translation temperature of the other particles. Readers interested in plasma may refer to [4] [21] [39] [40] [41] [71] [73] [74].

2.7 Conclusions

2.7.1 Flow governing equations

For a reacting gas mixture, with vibrational non–equilibrium, the flow is governed by the species evolution equations

$$
\begin{aligned}
\frac{\partial \rho_I}{\partial t} + \underline{u}\,\mathrm{grad}\rho_I &= \rho\omega_I - \mathrm{div}\underline{q}_I \\
\underline{q}_I &= \sum_{J\neq I} \frac{M_I M_J}{\overline{M}^2} D_{IJ}\underline{d}_J - D_I^T \frac{1}{T}\mathrm{grad}T \\
\underline{d}_I &= \mathrm{grad}\frac{n_I}{n} + \left(\frac{n_I}{n} - \frac{\rho_I}{\rho}\right)\frac{1}{p}\mathrm{grad}\,p
\end{aligned}
\tag{14}
$$

the sum of which gives the continuity equation

$$
\frac{\partial \rho}{\partial t} + \mathrm{div}\rho\underline{u} = 0
\tag{15}
$$

together with the momentum equation

$$
\begin{aligned}
\rho\frac{\partial \underline{u}}{\partial t} + \rho\underline{u}\,\mathrm{grad}\underline{u} &= -\mathrm{div}\underline{\underline{\tau}} \\
\underline{\underline{\tau}} &= p\underline{\underline{\delta}} - \mu\left(\mathrm{grad}\underline{u} + \mathrm{grad}^t\underline{u} - \frac{1}{3}\underline{\underline{\delta}}\mathrm{div}\underline{u}\right) - \eta\mathrm{div}\underline{u}
\end{aligned}
\tag{16}
$$

the energy equation for the total energy E

$$
\begin{aligned}
\rho\frac{\partial E}{\partial t} + \rho\underline{u}\,\mathrm{grad}E &= -\mathrm{div}\underline{q}_t + \underline{\underline{\tau}}\cdot\mathrm{grad}\underline{u} \\
\underline{q}_t &= -\lambda\mathrm{grad}T + \sum_I h_I q_I + \mathcal{R}T\sum_I\sum_J \frac{n_J}{n}\frac{1}{M_I}\frac{D_I^T}{D_{IJ}}\left(\frac{\underline{q}_I}{\rho_I} - \frac{\underline{q}_J}{\rho_J}\right)
\end{aligned}
\tag{17}
$$

(D_{IJ} is the binary diffusion coefficient i.e the diffusion coefficient of species I in J for a mixture made only with these two species). At last, relaxation equations for the vibrational energy of each kind of molecules can be included

$$
\frac{DE_{\mathrm{vib}}}{Dt} = \frac{E_{\mathrm{vib}}^* - E_{\mathrm{vib}}}{\tau_{\mathrm{vib}}}
\tag{18}
$$

For the sake of simplicity, this set of flow governing equations will later be referred to as *Navier* equations. This in incorrect as Navier only derived the equations for a one species gas at thermal equilibrium.

2.7.2 Transport coefficients

The calculation of all the transport coefficients (μ, η, λ, D_{IJ}, D_T^I, D_{IJ}) requires first the knowledge of all the interaction potential between the species, i.e for a ν species mixture $\frac{\nu(\nu+1)}{2}$ different interactions. This is still a running question, e.g for air plasma [7] [14] [15] [37] [93]. Once these potentials are known, the collisions integrals must be calculated. The computation of all transport properties usually requires the knowledge of $\Omega^{(1,1)}, \Omega^{(1,2)}, \Omega^{(1,3)}, \Omega^{(2,2)}$ and finally, transport coefficients are obtained by solving linear systems of ν or 2ν equations.

This task may however be simplified as

- For classical interaction potentials, collision integrals are tabulated [63]. Yos [109] [110] computed the various collision integrals for air. Collision integrals for air species were also tabulated by Yun [111]. The accuracy of all these values is however questionnable [29]. Moreover, analytical forms for some integrals have been proposed and integral ratios can be assumed constant to simplify the computation [5] [60] [100].

- Approximate formulae are available to evaluate transport coefficients without solving large linear systems.

  The viscosity can be computed with the Wilke's formula [108] or, for plasma, the Armaly one [5].

  When the thermal diffusion effects are neglected, the thermal conductivity, already simplified with the help of the Eucken correction for internal energy, can be evaluated either using a sort of Wilke formula due to Mason [79] or the one proposed by Peng et al [90].

  At last, the multicomponent diffusion can be obtained with Obermeier model [83]. Another procedure is to use the binary diffusion coefficients instead of the multicomponent diffusion coefficient. This alternative is discussed at length in [29]. The Fick's law can also be used to evaluate the species diffusion, a constant Lewis number is then usually assumed, but a variable one can be used [44].

  In the case of dissociated air (without ionization) a simple model, based upon an atom/molecule approach, as been developed by Straub [100], from previous extensive studies of air properties by Mason's group [79] [82] [111].

  Studies of approximate equations for transport coefficients of mixtures have also been proposed by Kee et al [68] or Picone [91].

  Cohen [33], Hansen [57] [58] and Yos [109] [110] have computed the transport properties of air at chemical equilibrium. Blottner [19] has tabulated Yos data. Other more recent curve fits are available [13] [29] [92].

Some results concerning air transport properties will be presented in section 4. .

3 Chemistry

As already mentionned, chemical reactions may occur in high energy flows. The modification of the flow equations to account for chemistry has been presented in the previous section. This section will focus on the description of chemical reactions not only in gas phase but also at gas/solid interface.

3.1 Chemical reactions in gas phase

3.1.1 Basic description of a reaction

The mechanism for chemical reaction is here again collisions between particles. If colliding particles have a sufficient relative translational energy, the two particle may get close enough during the collision process to form an activated complex which gives new chemical species. This can be illustrated by some simple examples.

- In a dissociation reaction due to the collision of two molecules, as depicted on figure 9 the two molecules get close
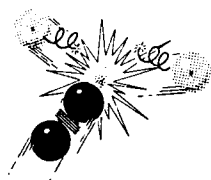
Figure 9: Artist view of a molecule collision leading to dissociation (from [57])

  enough to form a four atom complex. A part of the internal energy of the "black" molecule or a part of the relative translational energy is then used to break the bound between the two atoms of the "grey" molecule. This reaction is called *endothermic* as it requires energy to break the molecule bound.

- The reciprocal situation is the collision of two atoms to form a molecule. When two atoms can get close enough to form a molecule, the molecule is in an excited state and is unstable as it has an internal energy larger than the one required to bind the two atoms. A collision with a *third body* is thus mandatory to transfer the energy excess to the third body and form a stable molecule. The excess energy is then distributed in the flow via collisions. Such a reaction leading to an energy release is called *exothermic*.

- A third example is a shuffle reaction such as

$$N_2 + O \rightarrow NO + N$$
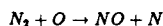
  in which a molecule and an atom collide. They first form a three atom complex which may break as a new molecule and an atom. This reaction may be either exothermic or endothermic, the needed (resp. released) energy being taken from (resp. released as) internal or translational energy of the incident (resp. parting) particles.

These examples bring into evidence some main features of chemical reactions.

- What appears as a reaction at the macroscopic level is in fact a set of elementary steps at the microscopic level, with first a collision, formation of activated complex, parting of new species and perhaps third body collision. This description may itself be a simplification of the complete process, as a reaction may in fact be a chain reaction formed of elementary reactions (e.g in combustion processes).

- All collisions cannot lead to a reaction as there exists an *energy barrier* to overcome. If the relative translation energy of the two particles is too weak, they cannot form an activated complex. This is illustrated on figures 10 and 11 where the evolution of the sum of the internal energy of the two particles is plotted versus time for an endothermic and an exothermic reaction. As the total energy is conserved during the collision, a part of the relative translational energy is required to overcome the energy barrier, i.e to work against repulsive forces at small separation and form a complex.

- Species can be required for the reaction to occur but are not modified at the end of the reaction process, as the third body in the atom recombinaison process or the impiging molecule in the dissociation. These species can however control the effectiveness of the reaction process and act as *catalyst*.

3.1.2 Kinetic theory of reactions

The gas kinetic theory can be applied to study chemical reactions. A very simple reaction, denoted as

$$A + B \rightarrow AB$$
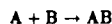
will be considered herein. The collision can be described with the help of the relative velocity g and the impact parameter b as shown in section 2.1.2. For an infinitesimal time dt, the flux of particles with such impact parameter is $2\pi b db \, g dt$ so that the total number of collision for a unit volume and unit time reads

$$\frac{1}{s} \int f_A(\underline{\varsigma}_A) f_B(\underline{\varsigma}_A + \underline{g}) \, 2\pi b g \, db \, d^3\underline{\varsigma}_A \, d^3\underline{g}$$
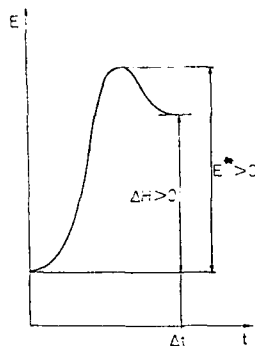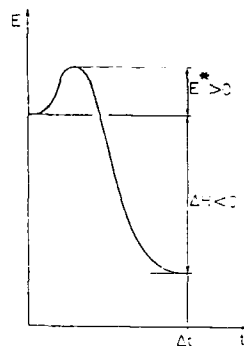
Figure 10: Endothermic reaction

Figure 11: Exothermic reaction

where s is the symmetry number introduced to avoid counting twice collisions ($s=1$ when A and B are different, $s=2$ when A=B). Maxwellian probability density functions are assumed to be valid for the two species. After some algebra (see e.g [59]) the above integral reads

$$\frac{n_A n_B}{s} \left(\frac{\mu}{2\pi kT}\right)^{\frac{3}{2}} \int 4\pi g^2 \exp\left(-\frac{\mu g^2}{2kT}\right) 2\pi b \, db \, g dg$$

where $\mu = m_A m_A/(m_A + m_B)$ is the reduced mass introduced in section 2.1.2. The integral $\int 2\pi b db$ represents the collecting section for colliding particles and is called the collision cross section $\sigma(g)$. Introducing the relative translational energy $E = \frac{1}{2}\mu g^2$, the above integral reads

$$\frac{n_A n_B}{s} \left(\frac{8kT}{\pi\mu}\right)^{\frac{1}{2}} \frac{1}{(kT)^2} \int E\sigma(E) \exp\left(-\frac{E}{kT}\right) dE$$

which gives the total number of collisions per unit time and unit volume.

Among these collisions, only the collisions the energy of which is larger than the *activation energy* E^* may lead to a reaction. Moreover, all the collisions of sufficient energy do not lead to a chemical reaction, either because the activation

energy barrier is not stepped over or because the formed complex leads to the same products. A probability correction $P(E)$ has to be introduced to give the number of collisions which lead to a reaction. The variation of the number of particle per unit volume due to the chemical reaction thus reads

$$
\begin{aligned}
\frac{dn_{AB}}{dt} = -\frac{dn_A}{dt} = -\frac{dn_B}{dt} &= \frac{n_A n_B}{s} \sqrt{\frac{8kT}{\pi\mu}} \frac{1}{(kT)^2} \int_{E^*}^{\infty} E\sigma(E)P(E)\exp\left(-\frac{E}{kT}\right) dE \\
&= k_D n_A n_B \\
\text{with} \quad k_D &= \frac{1}{s}\sqrt{\frac{8kT}{\pi\mu}} \frac{1}{(kT)^2} \int_{E^*}^{\infty} E\sigma(E)P(E)\exp\left(-\frac{E}{kT}\right) dE
\end{aligned}
\tag{19}
$$

(In this section k_D and k_R indicate direct and reverse reaction rate constants and must not be confused with the Boltzmann constant k)

The evaluation of the reaction rate constant requires the knowledge of the product of the collision cross section and the probability function, often called the excitation section or the reaction cross section. Assuming it is constant and equal to S_0 leads to

$$k_D = \frac{S_0}{s}\sqrt{\frac{8kT}{\pi\mu}} \left(\frac{E^*}{kT} + 1\right) \exp\left(-\frac{E^*}{kT}\right)$$

Other forms for the excitation function have been proposed, leading to various laws for the reaction rate constant [49] [59]. The excitation function can be evaluated from quantum mechanics but this approach requires very large computations [59].

Figure 12 illustrates the influence of the temperature upon the evolution of the reaction rate. The excitation function depends only upon the relative translational energy of the particles while the energy distribution function varies with the temperature. The higher the temperature, the larger the number of particles having enough energy to react.

3.1.3 Arrhenius law

In 1889, Arrhenius [6] proposed, from studies of inversion of sucrose, to express the temperature dependence of the reaction rate constant by his celebrated law

$$k_D = A \exp\left(-\frac{E_A}{kT}\right)$$

This form has later been extended, to cover a wider range of reactions, as

$$k_D = BT^s \exp\left(-\frac{E_A}{kT}\right)$$

which is sometimes referred to as non–Arrhenius behaviour.

Figure 12: Variation of the reaction rate constant with temperature
(a) Energy distribution function $E \exp\left(-\frac{E}{kT}\right)$
(b) Excitation function
(c) Product (a)*(b) the integral of which is proportional to k_D

(from [49])

The *activation energy* E_A in Arrhenius law is different from the previously introduced activation energy E^*. In the Arrhenius law, the activation energy E_A can be obtained as

$$E_A = -k \frac{\partial \ln k_D}{\partial \frac{1}{T}}$$

From the general expression of the reaction rate constant (Equation 19), it can be easily shown that

$$E_A = \frac{\int_{E^*}^{\infty} E^2 \sigma(E) P(E) \exp\left(-\frac{E}{kT}\right) dE}{\int_{E^*}^{\infty} E \sigma(E) P(E) \exp\left(-\frac{E}{kT}\right) dE} - 1.5kT$$

so that $E_A \rightarrow E^*$ as $T \rightarrow 0$.

However, Arrhenius or non–Arrhenius laws gives fair representations of the reaction rate constants as function of temperature. Reaction rate constants are therefore commonly given under Arrhenius or non–Arrhenius forms.

3.1.4 Determination of reaction rates

The above kinetic theory, and more elaborate theories (see e.g [35] [49] [59]) are able to give reaction rate constants with an accuracy of about one order of magnitude. The reaction rate constants are therefore mainly determined by experimental

techniques. It must be pointed out that such experiments are very difficult to design and analyze as it is impossible to isolate a single reaction, the formation of new species leading to new and unwanted chemical reactions in the experiment.

The reliability of experimental data is also questionnable. Various experimental determinations of the reaction rate constant for the shuffle reaction

$$NO + O \rightleftharpoons N_2 + O$$

are compared on figure 13. They are divided by the recommended value according to NBS [11] [107]. The two horizontal dotted lines indicate the range of confidence according to NBS [107]. The [ ] indicate the range of temperature upon which the proposed Arrhenius expressions are supposed to be valid, when known. Even more recent determinations such as the one from Gardiner [49] lie out of the confidence range. A ratio of about three is a good estimate of the experimental discrepancy for such a reaction.

For some reactions of oxygen dissociation $O_2 + M \rightleftharpoons O + O + M$ where $M = N_2$, NO, N, Oertel [84] gives reaction rates two to four order of magnitude larger than other models as shown on figure 14. The discrepancy of the other data is large as the ratio of extreme data is about eight (Oertel's data excluded).

This brings into evidence the lack of accurate and reliable data for the reaction rate constants. In the case of reentry flows, experimental data are available while for very high temperature such as the one encountered around the AOTV, experimental laws have to be extrapolated out of their experimental determination range or theoritical data, deduced from quantum mechanics, have to be used.

At last, it must be mentionned that, for the sake of consistency with the presentation of the gas kinetic theory, the n denotes the number of particles per volume unit. Therefore, the reaction rate constant in equation (19) has dimensions of (particle per volume unit)$^{-1}s^{-1}$. The common practice in chemistry is to deal with number of moles per volume unit. Translation from one system to the other only requires ad-hoc multiplication or division by powers of the Avogadro number.

3.1.5 Influence of the internal degrees of freedom

The energy stored in the internal degrees of freedom of molecules can also participate to the reaction process. Figure 9 gives an artist view of the enhancement of dissociation rate with the impiging molecule vibrational energy. Generally, vibrational excitation enhance the reaction rate constant by several orders of magnitude [49]. This problem is discussed at length in [28] [59] [78] [103].

A semi–empirical procedure to extend the available data at thermodynamic equilibrium to vibrational excited air plasma has been proposed by Park [87] and extended to other reactions by Danton [37].
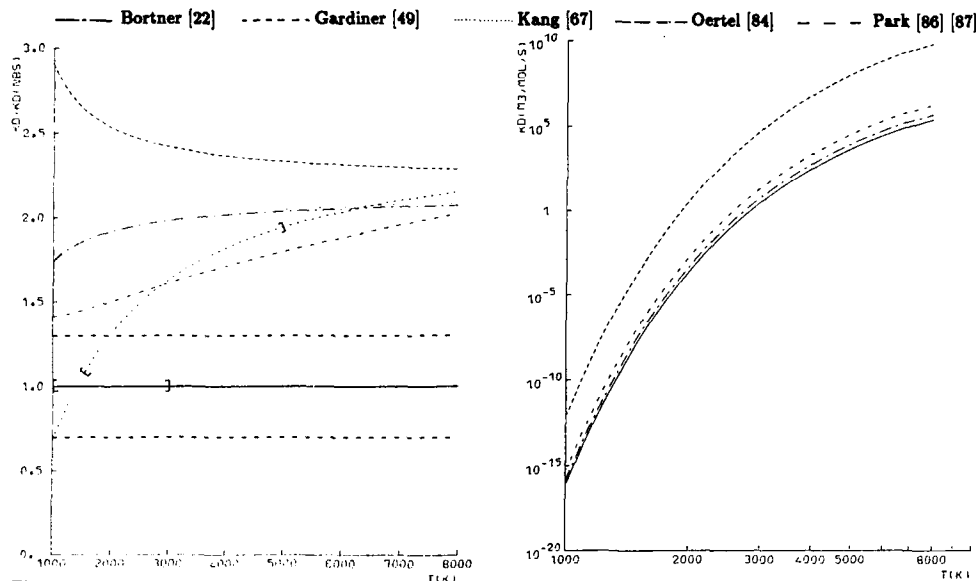
Figure 13: Comparison of reaction rate constant determinations for the $NO + O \rightleftharpoons O_2 + N$ shuffle reaction (from [44])
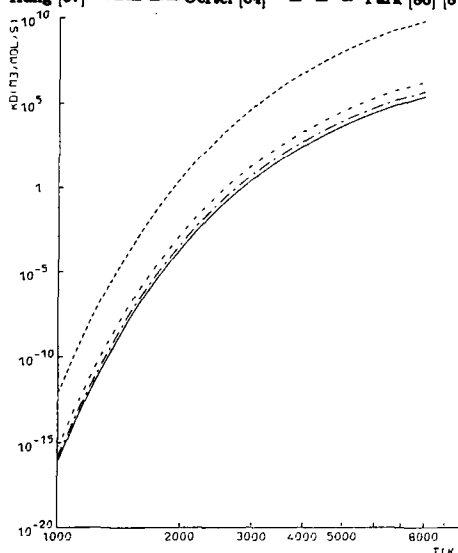
Figure 14: Comparison of reaction rate constant determinations for the $O_2 + N_2 \rightleftharpoons O + O + N_2$ dissociation reaction (from [44])

3.1.6 Direct and reverse reaction constants

Up to now, only one way chemical reactions have been considered. However, chemical reactions may proceed in both ways, and, while some combustion reactions are quite irreversible, the chemical reactions encountered in reentry flows are likely to occur in both directions.

Using the *Penner notation*, a chemical reaction can be written as

$$\sum_I \nu_I' A_I \underset{R}{\overset{D}{\rightleftharpoons}} \sum_I \nu_I'' A_I$$
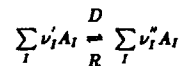
where D and R indicate the direct and reverse reactions, the A are the chemical species and the ν the stoechiometric coefficients. The difference $\nu_I = \nu_I'' - \nu_I'$ must be introduced as it indicates whether the species A_I is destroyed or produced by the direct reaction. The evolution of the reactants is given by the following expressions which are generalisations of the equation (19)

- For the direct reaction

$$\frac{dn_I}{dt} = k_D \nu_I \prod_J (n_J)^{\nu_J'}$$

- For the reverse reaction

$$\frac{dn_I}{dt} = k_R \nu_I \prod_J (n_J)^{\nu_J''}$$

where $\prod_J$ indicates a product over all values of J, and k_D and k_R are respectively the direct and reverse reaction constants. The production rate of species I is the balance between the two terms

$$\frac{dn_I}{dt} = \nu_I \left[k_D \prod_J (n_J)^{\nu_J'} - k_R \prod_J (n_J)^{\nu_J''} \right]$$

Further information about the direct and reverse reaction rate constants can be obtained by considering *chemical equilibrium*. Chemical equilibrium is obtained for a reaction when the direct and reverse reactions exactly balance. As the production is zero, the reaction rate constants can be linked to the n_I

$$\prod_I (n_I \text{ eq})^{\nu_I} = \frac{k_D}{k_R}$$

or, using the state equation $p_I = n_I kT$,

$$\prod_I \left(p_I \text{ eq}\right)^{\nu_I} = \frac{k_D}{k_R} (kT)^{\sum_I \nu_I} = K_P (T)$$

which is known as the *mass action law*. This law can also be deduced from thermodynamics arguments, as the equilibrium state corresponds to the minimum of the Gibbs free energy of the system formed by the species involved in the chemical reaction. The equilibrium constant K_P and the mixture composition can be determined from thermodynamical data. The ratio of the direct and reverse reaction rate constants can be obtained so. This has two important consequences

- While the reaction rate contants are known with a large uncertainty, their ratio can be easily and accurately obtained from thermodynamical data.

- The ratio of the direct and reverse reaction rate computed from the energy partition function does not have a non–Arrhenius form. This shows again that Arrhenius and non–Arrhenius forms are only good fits for reaction rate constants over a wide range of temperature.

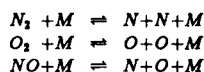## 3.2 Chemistry models for reentry flows

For a mixture made up with ν species, $\frac{\nu(\nu+1)}{2}$ different binary collisions can occur. Moreover, a given collision may lead to different products. At last, third bodies are sometimes required for a reaction to proceed.

The choice of the chemical species to be accounted for and of the chemical reaction among them is thus a difficult task, too few species may lead to important errors if a neglected species acts as a catalyst and enhance an important reaction, too many species and therefore too many reactions lead to too large computing time.

For dissociation problems, it is common practice to only take into account molecular and atomic nitrogen and oxygen and nitrogen monoxide (N_2, O_2, NO, N, O) and to neglect argon, carbon dioxide and water vapour. For ionization studies, the nitrogen monoxide gives the major part of the electrons for reentry flows up to $6000 ms^{-1}$. Simple models only consider ionized nitrogen monoxide and the electron (NO^+, e^-). For velocities larger than $9000 ms^{-1}$, the ionization is mainly due to atomic nitrogen and oxygen. Moreover, the ionized molecular nitrogen, although at very low concentrations, intervene in a very fast reaction (see e.g [37]) and should be accounted for. A good model is thus to include all the single charged ions corresponding to the dissociation model to have an eleven species model ($N_2, O_2, NO, N, O, N_2^+, O_2^+, NO^+, N^+, O^+, e^-$). Other species may be accounted for, according to the range of pressure and temperature considered. (see section 4 for informations about the species that appears e.g at important pressure and section 9 for an example).

Among these species, the most likely to occur reactions are to be selected. The probability of multiple collisions is weak, so that mainly two–body reactions must be considered. However, as pointed out previously, third bodies can play

an important rôle as catalyst in atom recombination processes. The reactions usually selected for studies of flows around bodies during reentry are [67] [87] [88]

- Dissociation reactions

$$\begin{aligned} N_2 + M &\rightleftharpoons N + N + M \\ O_2 + M &\rightleftharpoons O + O + M \\ NO + M &\rightleftharpoons N + O + M \end{aligned}$$

where M stands for any of the eleven species, except the electron. The dissociation of ionized species is generally not accounted for. The dissociation reactions in which ionized species acts as third bodies are also often neglected.
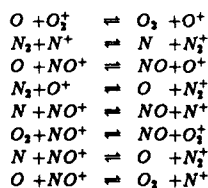
- Shuffle reactions

$$\begin{aligned} NO + O &\rightleftharpoons N + O_2 \\ O + N_2 &\rightleftharpoons N + NO \end{aligned}$$
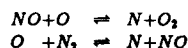
It must be noticed that the direct formation reaction for the nitrogen monoxide

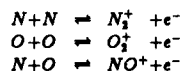$$N_2 + O_2 \rightleftharpoons NO + NO$$

introduced in early models (see e.g [84]) is now usually discarded as it can be obtained as a combinaison of dissociation and shuffle reactions.
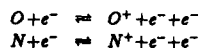
- Charge exchange reactions

$$\begin{aligned} O + O_2^+ &\rightleftharpoons O_2 + O^+ \\ N_2 + N^+ &\rightleftharpoons N + N_2^+ \\ O + NO^+ &\rightleftharpoons NO + O^+ \\ N_2 + O^+ &\rightleftharpoons O + N_2^+ \\ N + NO^+ &\rightleftharpoons NO + N^+ \\ O_2 + NO^+ &\rightleftharpoons NO + O_2^+ \\ N + NO^+ &\rightleftharpoons O + N_2^+ \\ O + NO^+ &\rightleftharpoons O_2 + N^+ \end{aligned}$$

- Associative ionization

$$\begin{aligned} N + N &\rightleftharpoons N_2^+ + e^- \\ O + O &\rightleftharpoons O_2^+ + e^- \\ N + O &\rightleftharpoons NO^+ + e^- \end{aligned}$$

- Electron impact ionization

$$O + e^- \rightleftharpoons O^+ + e^- + e^-$$
$$N + e^- \rightleftharpoons N^+ + e^- + e^-$$

Some other reactions, as radiative recombinaison, can play an important rôle in some cases [37]. The above list includes 46 reactions. It is usually simplified for practical use.

Non–Arrhenius expressions for the reaction rate constants can be found in various publications, either from reviews of data for combustion [11] [49] [107] or from papers dealing with reentry problems [22] [30] [61] [67] [84] [87] [88] [106] ...

3.3 Heterogeneous catalysis

The rôle of metallic surfaces in reaction rate enhancement is well known and widely used in chemical industry [20]. Catalysts do not change the equilibrium state of the system but modify the reaction rates. A convenient choice of catalysts can select between competing process and enhance the formation of the wanted species or delay the formation of unwanted ones in a chemical reactor.

While catalytic effect is looked for in chemical industry, it represents a disadvantage in aeroheating problems. Wall temperatures are always "moderate" (let say about 1000K) so that equilibrium condition at the wall (see section 4) corresponds to no dissociation of the gas. The catalytic action of the wall forces atoms to recombine while the latent heat of dissociation of molecules is transferred to the wall, leading to an undesired increase in the wall heating.

3.3.1 The heterogeneous catalysis process

The heterogeneous catalysis phenomenon occurs in three basic steps.

- Particles that diffuse to the surface either reflect specularly or are adsorbed at the surface. Only chemisorption, i.e creation of chemical bounds between the surface atoms and the adsorbed particle may lead to catalysis. This first step depends upon both the impiging particle and the surface. This surface selectivity is widely used in chemical engineering. For example, metal surfaces can easily adsorb oxygen atoms (excepted gold, but who plan to build a gold–plated shuttle?) while metal oxide surfaces are more reluctant to adsorb oxygen. Heterogeneous catalysis is usually favoured by the fact that the energy barrier for the adsorption process is lower than the energy barrier for gas phase reactions.

- Once the particle is inserted inside a site of the surface, it may react with either another particle adsorbed in another site (the Langmuir–Hinshelwood process) or by collision with a particle in the gas (the Eley–Rideal process). The wall atoms the adsorbed particle is bound with act as third bodies as they provide or dissipate the necessary or excess energy for the reaction. Sites are very efficient third bodies as surface atoms are bound to other atoms, i.e have a large number of degrees of freedom. Here again, the energy barrier for reaction of adsorbed species is lowered as the site may contribute to the process.
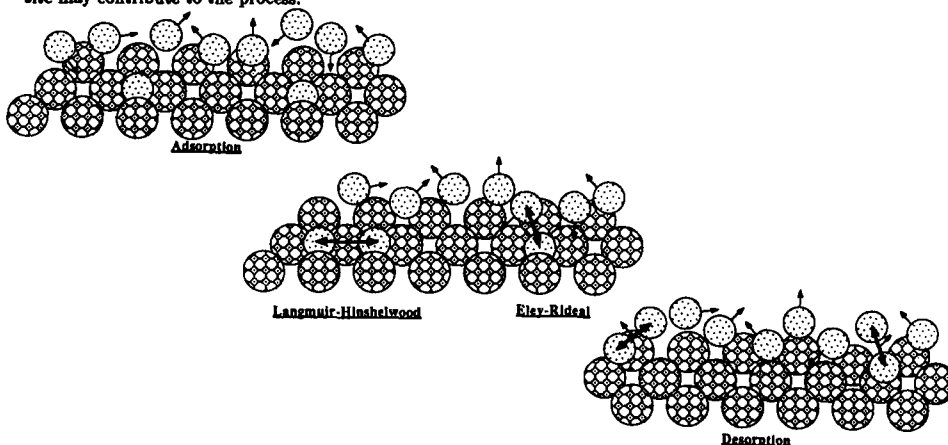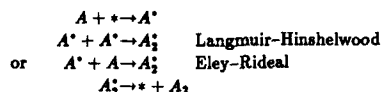

Figure 15: Representation of the three steps of heterogeneous catalysis

- The third step is the desorption of the new species from the wall, the surface site is now free and the process can occur again (figure 15).

3.3.2 Modelling of heterogeneous catalysis

If the site is viewed as a chemical species, the process can be treated as a series of elementary reactions, which are, for an atom recombination process

$$A + * \to A^*$$
$$A^* + A^* \to A_2^* \qquad \text{Langmuir-Hinshelwood}$$
$$\text{or} \qquad A^* + A \to A_2^* \qquad \text{Eley-Rideal}$$
$$A_2^* \to * + A_2$$

where the * denotes a site or an adsorbed species. Each elementary step can be described by an evolution equation similar to equation (19). The point is now to determine which is the slower step which controls the whole process. This is discussed at length in [10] [29].

The problem is however much more intricate as different species can adsorb simultaneously to lead to different surface catalysed reactions. Goulard [53] has proposed to model wall catalysis effect with the help of an Arrhenius law. The flux of species at the wall due to catalysis is expressed as

$$q_{I\text{cat}} = k_{Iw} \left(\rho_w Y_{Iw} \right)^m \tag{20}$$

where the subscript w indicates values at the wall and the reaction order m should be between one and two. Scott [96] proposes to use an order m equal to one and to express the reaction constant as

$$k_{Iw} = \frac{\gamma_I}{2 - \gamma_I} \sqrt{\frac{kT}{2\pi m_I}} \tag{21}$$

where γ_I is the fraction of impiging atoms at the surface which recombine. It must be noticed that, if the order m is equal to one, the reaction rate constant k_{Iw} has the dimension of a velocity.

The above introduced catalysed reaction rate constants are not independent. The sum of all the fluxes at the wall should be zero. Moreover, wall catalysis cannot turn to alchemy, the chemical elements must be conserved. So, for a mixture of ν species made from μ chemical elements, only $\nu - \mu$ coefficients are independent. On the other hand, the adsorption process is easier for atoms than for molecules, so that, for dissociating air, the catalysed reaction rate constants are given only for atomic oxygen and nitrogen and, assuming that nitrogen monoxide is not adsorbed or formed at the wall, the fluxes of diatomic oxygen and nitrogen can be derived.

At last, measurements [56] [80] have brought into evidence that the recombination energy is not fully transferred to the wall but that molecules can leave the wall in an excited state. As, on the one hand very little is known about this phenomenon and, on the other hand, this energy excess of desorbing molecules may be transferred back to the wall, this phenomenon is usually neglected [96].

3.3.3 Catalytic and non catalytic walls

As pointed out previously, the heterogeneous catalysis first depends upon the ability of the surface to adsorb gas species. These various behaviours are reflected by the values of the reaction rates coefficients k_{Iw}. When the coefficients tend towards zero, the species are not modified at the wall. The wall is thus said *non catalytic*. On the contrary, when the coefficients tend towards infinity, the species arriving at the wall react very quickly. The flow tends towards chemical equilibrium at the wall. The wall is said *catalytic*. Let us notice that the wall temperature is "low" (i.e up to 1500K) otherwise the wall material is damaged. Therefore, for a catalytic wall, chemical equilibrium means almost complete recombination of atoms at the wall as air hardly dissociates even at low pressure for these temperatures (see section 4). These above two cases are extreme cases which are not encountered practically. Real materials have a *finite catalycity*.

Silicate and ceramics are fair approximations to non catalytic surfaces while metals and metal oxides are highly catalytic. Measurements on the space shuttle surface insulation [95] lead to values of the catalysed reaction rate constants for atomic oxygen and nitrogen of about 1 ms^{-1}. Further estimates from flight data [113] give a larger variation of the atomic oxygen constant k_O with wall temperature but the same order of magnitude.

The evaluation of the catalycity of a material in presence of given species is difficult to determine experimentally and flight conditions are difficult to reproduce [24] [46] [50] [51] [95] [96].

Moreover, plasma reactor measurements have shown that the catalytic efficiency varies with time, a material designed to be weakly catalytic becomes more and more catalytic. This seems to be due to two phenomena; the adsorption–desorption process on the one hand leads to surface modification and an increase in surface porosity so an increase in the number of available sites, on the other hand the adsorption–desorption process induces migration of atoms inside the material which may come to pollute the surface and increase its catalycity (Gicquel, private communication). These surface modifications may also lead to a change in the surface emissivity. This is consistent with the observation of an increase in wall heat fluxes on the space shuttle from flight STS–2 to STS–5 [96].

4 Air at chemical equilibrium

In the absence of any constraint, a system generally tends towards an equilibrium solution. Gas mixtures thus tend towards thermodynamic and chemical equilibrium. It is then important to know the equilibrium state as it is the asymptotic solution. Moreover, the study of chemical equilibrium gives informations about the final composition of the gas mixture and the species to be accounted for. The study of equilibrium air will also provide us an illustration of the evolution of transport properties.

4.1 Computation of chemical equilibrium

As pointed out previously, the equilibrium situation can be obtained from a thermodynamic point of view. From the laws of thermodynamics, it is shown that the chemical equilibrium corresponds, at thermodynamic equilibrium, to the minimum of the Gibbs free energy (see e.g [105]). However, the minimization of the Gibbs free energy is not sufficient to determine the mixture composition, otherwise the solution would be that the mixture is made only with the species of lowest Gibbs free energy. The conservation of each chemical element must also be satisfied.

As the equilibrium constants for chemical reactions are also determined from minimization of the Gibbs free energy for the species involved in the reaction, the equilibrium state can be determined by imposing the production rates of a suitable set of chemical reactions to be zero.

The Gibbs free energy of a species in a mixture depends upon the temperature and the pressure. Therefore, equilibrium depends upon pressure and temperature or any pair of thermodynamical variables.

While a bathed system evolves at constant temperature, the natural evolution of a gas mixture without forcing occurs at constant enthalpy as chemical reactions require or release energy, leading to temperature variations. However, for the sake of simplicity, most of the following results will be given as function of the temperature. The mixture composition is first computed from the Gibbs free energy minimization and thus, all thermodynamics and transport properties of the mixture can be derived.

4.2 Composition of air at chemical equilibrium

Figures 16 and 17 give the evolution of mole fractions of air component at two temperatures which are relevant to reentry flows, as function of the density (ρ_0 is a reference density of air at standard conditions 1 atm 273.15K). At 2000K, only oxygen can dissociate significantly at low density (i.e low pressure). Argon, nitrogen monoxide and dioxide, neon and carbon oxides are only traces. This is not so at 6000K where a significant dissociation of both oxygen and nitrogen can be observed. Ionisation also occurs at low pressure and is first due to nitrogen monoxide and, at lower pressures to atomic oxygen and nitrogen.

The influence of pressure and temperature is better illustrated on figures 18 to 24 on which the variations of mass fractions are plotted versus temperature for different pressures. Oxygen dissociates first at about 2500K while nitrogen dissociates at only 5000K. The dissociation of nitrogen occurs when the dissociation of oxygen is nearly complete. This will be used later in section 5 to derive a simplified model.

It must be noticed that the dissociation is easier at low pressures. The evolution of nitrogen monoxide also reflects this fact as its mass fraction increases with the pressure. While its mass fraction remains very low, nitrogen monoxide plays an important rôle as it is a link between the nitrogen and oxygen chemistries. The formation of nitrogen monoxide at moderate temperatures (about 3000K) leads to a first decrease in molecular nitrogen mass fraction (Figure 18). The air chemistry
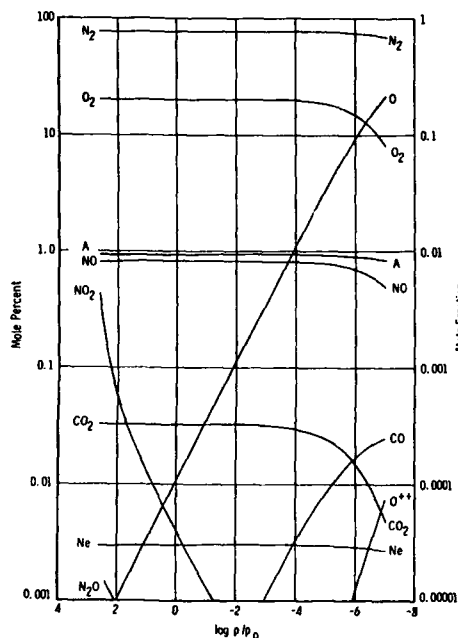

Figure 16: Mole fractions for air at chemical equilibrium at 2000K (from [62])
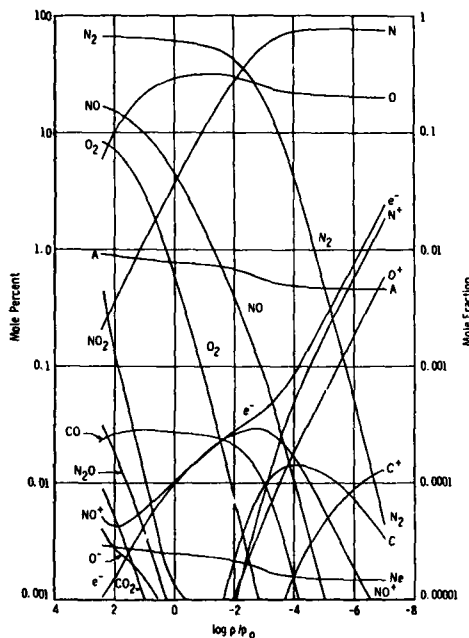

Figure 17: Mole fractions for air at chemical equilibrium at 6000K (from [62])
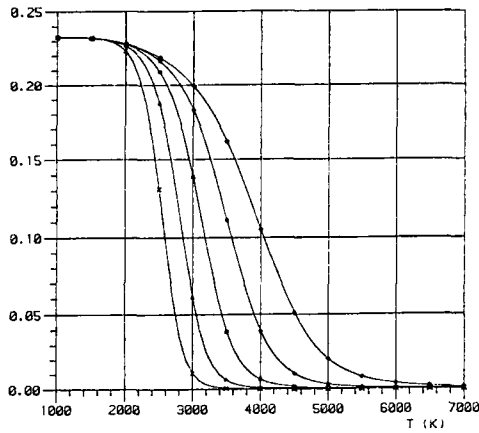
Figure 18: Evolution of molecular nitrogen mass
fraction as function of temperature and pressure
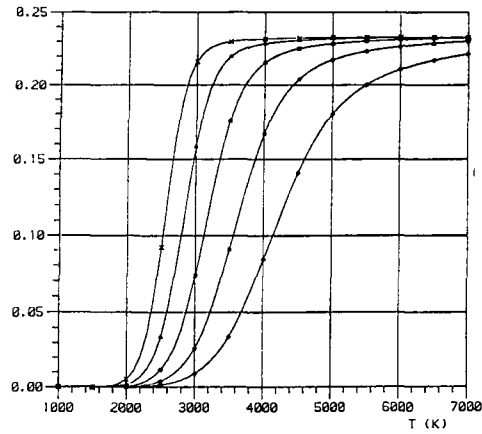(from [36] [44])

Figure 19: Evolution of atomic nitrogen mass
fraction as function of temperature and pressure
(from [36] [44])

Pressure (Atm)
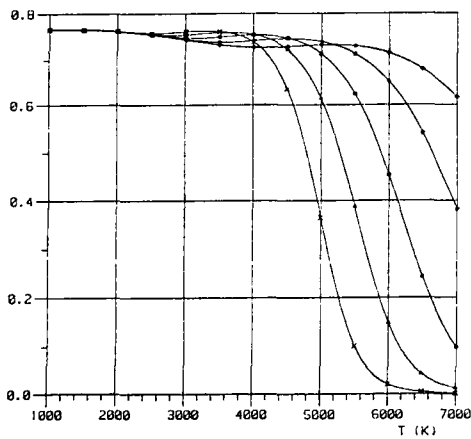
× 0.001

△ 0.01

□ 0.1

★ 1.0

◇ 10.

Figure 20: Evolution of molecular oxygen mass
fraction as function of temperature and pressure
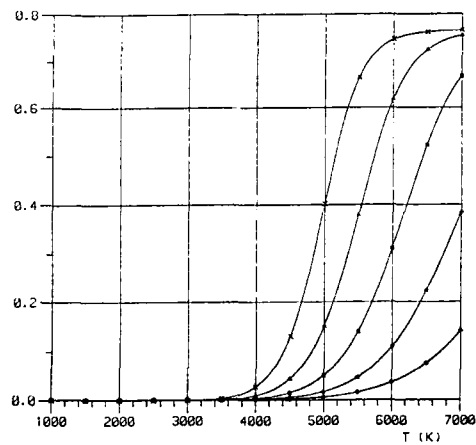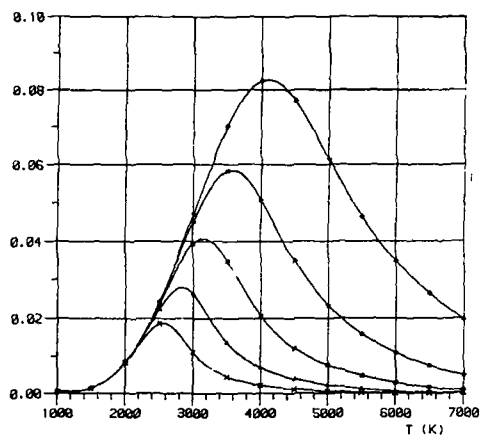(from [36] [44])

Figure 21: Evolution of atomic oxygen mass
fraction as function of temperature and pressure
(from [36] [44])

Figure 22: Evolution of nitrogen monoxide mass fraction as function of temperature and pressure (from [36] [44])
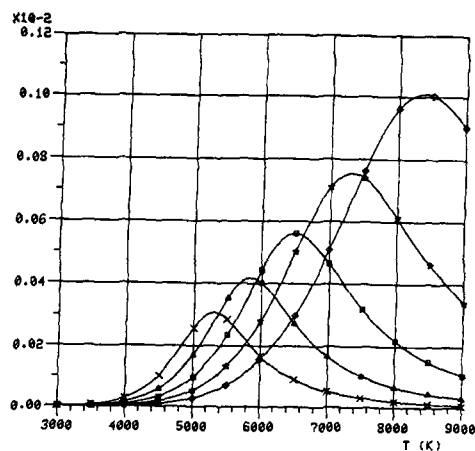

Figure 23: Evolution of ionized nitrogen monoxide mass fraction as function of temperature and pressure

Pressure (Atm)
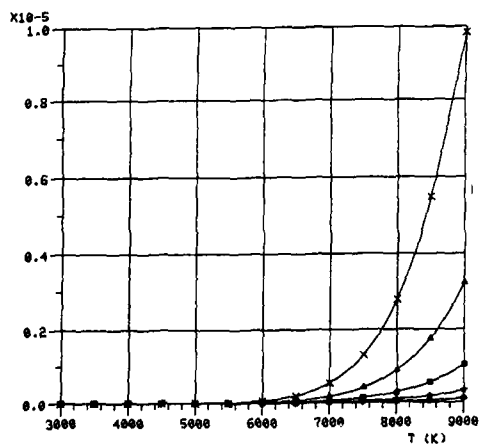
× 0.001

△ 0.01

□ 0.1

★ 1.0

◇ 10.

Figure 24: Evolution of electron mass fraction as function of temperature and pressure
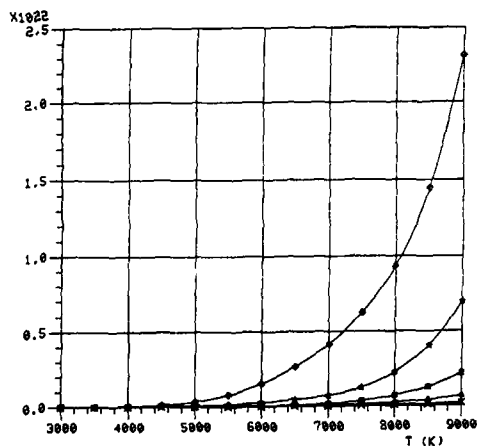

Figure 25: Evolution of electron density as function of temperature and pressure

up to about 5000K can be modelled with only three chemical reactions known as the Zeld'ovich process
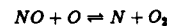
- The oxygen dissociates by collision with nitrogen which is the most probable species

$$O_2 + N_2 \rightleftharpoons O + O + N_2$$

- The so formed atomic oxygen reacts with the nitrogen and gives nitrogen monoxide

$$N_2 + O \rightleftharpoons NO + N$$

- The nitrogen monoxide is consumed by reaction with the atomic oxygen

$$NO + O \rightleftharpoons N + O_2$$

so that a little amount of nitrogen monoxide is the result of two important competing processes.

The electrons are mainly due, for shuttle reentry flows, to the ionization of nitrogen monoxide. Ionized nitrogen monoxide mass fractions are given on figure 23 and electron mass fractions and densities on figures 24 and 25. It can be observed that ionization is very weak as only about one percent of nitrogen monoxide ionizes. Electron mass fractions are very small due to the mass of the electron so that it is more convenient to consider electron density, i.e the number of electrons per volume unit (here per cubic meter). Electron density is an important parameter as it governs the radio transmission properties of the plasma (see section 9).

4.3 Thermodynamical properties of equilibrium air

The state equation can be written as

$$p = \sum_I p_I = nkT = ZR_0\rho T$$

where Z is the compressibility factor and R_0 the gas constant under standard conditions. The evolution of the compressibility factor is given on figure 26. At low temperatures, it is equal to one and increases with temperature as the dissociation and ionization phenomena occur. A first plateau about 1.2 is observed which corresponds to complete oxygen dissociation. Nitrogen dissociation leads to a plateau at a value of 2 as each molecule has now given two atoms. Complete ionization of the flow leads to a final plateau at a value of 4, each initial molecule has given four particles, i.e two ionized atoms and two electrons.
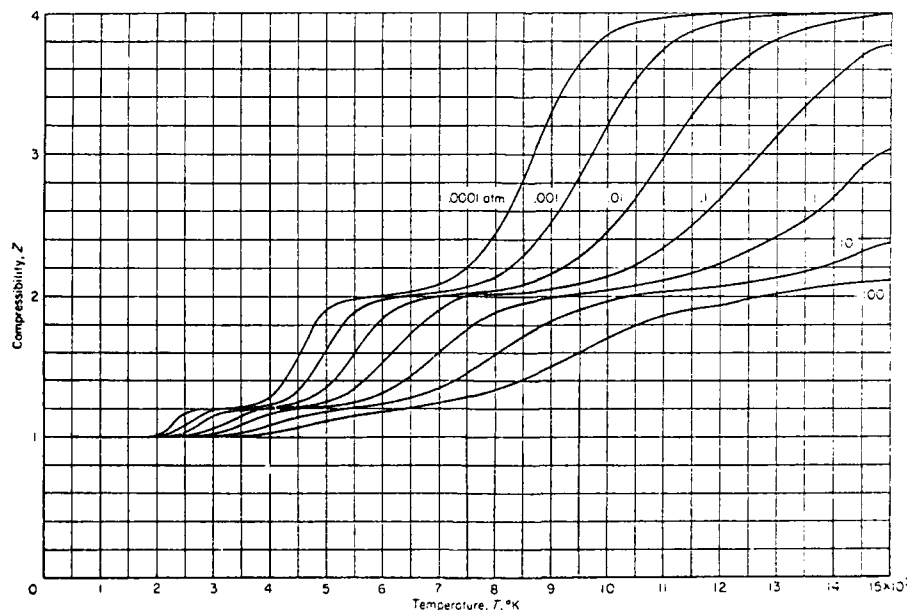

Figure 26: Evolution of the compressibility factor as function of temperature and pressure (from [58])
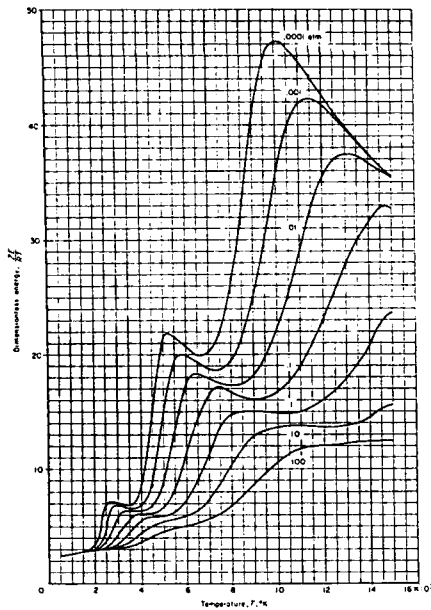
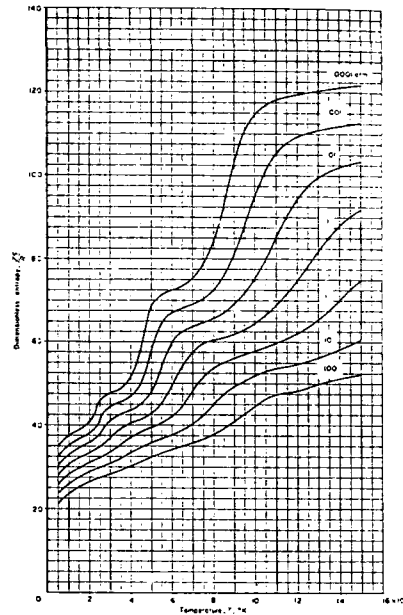Figure 27: Evolution of dimensionless energy ZE/RT as function of temperature and pressure (from [58])

Figure 28: Evolution of dimensionless entropy ZS/RT as function of temperature and pressure (from [58])

The influence of the two separate dissociation and of the ionization processes is also observed on the evolution of the dimensionless energy ZE/RT and entropy ZS/RT (figures 27 and 28) where the energy and the entropy are given per air mole.

From the definition of the enthalpy $H = E + pV$ and the state equation, it can be easily shown that

$$\frac{H}{RT} = \frac{E}{RT} + Z$$

so that the evolution of the enthalpy is similar to the energy. The evolution of dimensionless enthalpy H/RT and specific
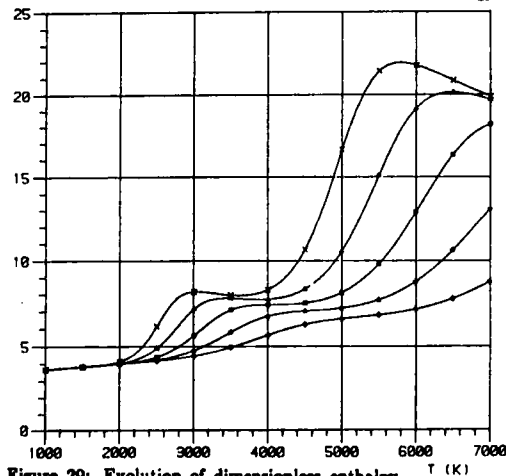

Figure 29: Evolution of dimensionless enthalpy H/RT as function of temperature and pressure (from [36] [44])
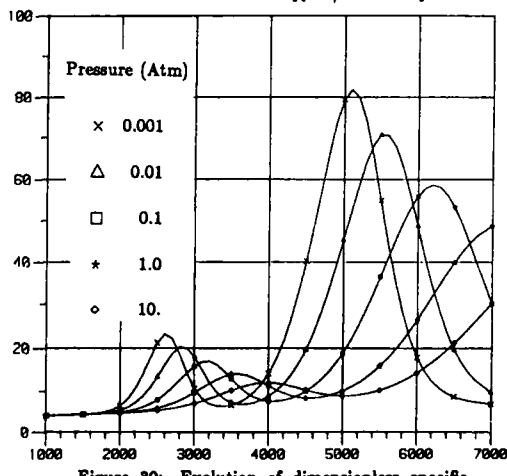

Figure 30: Evolution of dimensionless specific heat C_P/R as function of temperature and pressure (from [36] [44])

heat C_P/R are given on figures 29 and 30. The specific heat remains constant up to about 2000K, air can be considered

as an ideal gas up to that temperature. The two maxima in the specific heat correspond to the dissociation of oxygen and nitrogen.

Let us mention another thermodynamic variable, the speed of sound

$$a^2 = \left(\frac{\partial p}{\partial \rho}\right)_S$$

since the above derivative can be computed at chemical equilibrium. It is found that $a^2 \sim p/\rho$, the coefficient varying from 1.4 for non–dissociated air to values about 1.1–1.2 [58]. For flows out of chemical equilibrium, the speed of sound depends upon the wavelength. If the wavelength is long when compared with the chemical relaxation length, an "equilibrium" speed of sound can be used while for short wavelength with respect to the chemical relaxation length a "frozen" speed of sound is introduced. All frequencies do not propagate at the same speed in non–equilibrium flows [32] [112].

Curve fits of the thermodynamic properties of equilibrium air can be found in [54] [98].

4.4 Transport properties of equilibrium air

All the transport properties and the numerous multicomponent and thermal diffusion coefficients will not be presented for the sake of simplicity. The influence of real gas effects can be seen on the evolution of the viscosity and the thermal conductibility which now depend upon both the temperature and the pressure (Figures 31 and 32). As the temperature increases, the viscosity deviates from the Sutherland law. As the pressure decreases, the dissociation is more important and both the viscosity and the thermal conductivity increase.

Transport properties can also be illustrated by dimensionless coefficients. The Prandtl number, i.e the ratio between momentum and heat transport, is weakly affected by oxygen dissociation but varies with nitrogen dissociation (Figure 33). However, for most reentry flows, it can be assumed constant. The ratio between mass diffusion and heat transfer is characterized by the Lewis number. If air is assumed to be made up with atoms and molecules, only one diffusion coefficient has to be introduced and can be expressed as a Lewis number as shown on figure 34. It must be pointed out that the Lewis number decreases with enthalpy or temperature, i.e the commonly assumed value 1.4 is valid at low temperatures but not for reentry flows (see e.g [36] [44]).

More recent estimates of equilibrium air transport properties are available (see e.g [93]) and lead to similar conclusions. Curve fits are also available.
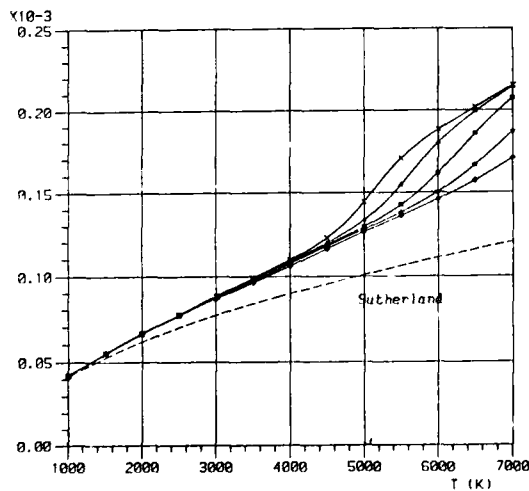
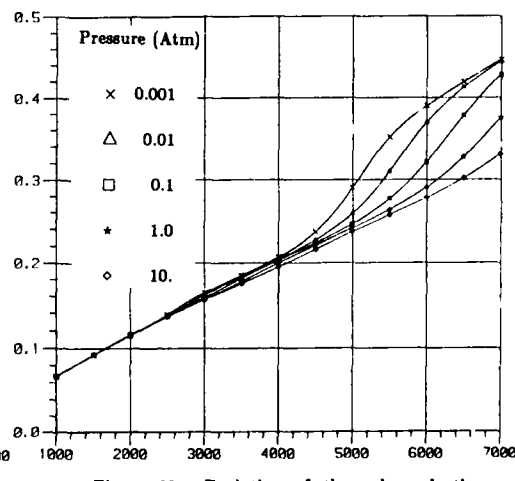Figure 31: Evolution of viscosity as function of temperature and pressure (from [36] [44])

Figure 32: Evolution of thermal conductivity as function of temperature and pressure (from [36] [44])
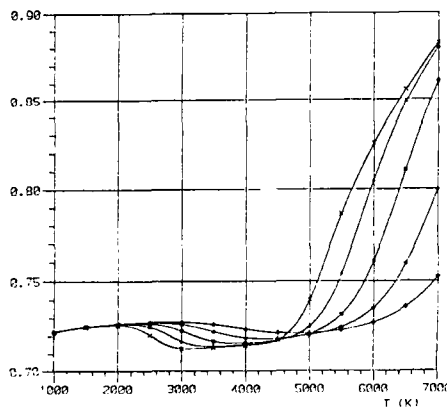
Figure 33: Evolution of Prandtl number as function of temperature and pressure (from [36] [44])
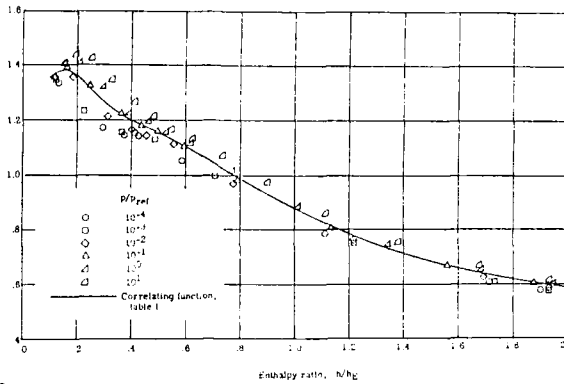
Figure 34: Evolution of Lewis number ($p_{\text{ref}} = 1\text{atm}, h_E = 19.7 \, 10^6 JKg^{-1}$) as function of temperature and pressure (from [33])

5 The diatomic dissociating gas assumption

For reentry flows, ionisation is weak and can be neglected (see sections 4 and 9). Moreover, thermodynamic non-equilibrium rapidly relaxes downstream of the shock wave so that it can be neglected in various applications.

In section 4, it has been shown that the dissociation of nitrogen proceeds when the dissociation of oxygen is complete. So at "moderate" temperatures, the gas is roughly a mixture of molecular nitrogen and both molecular and atomic oxygen and, at "higher" temperatures a mixture of atomic oxygen and both molecular and atomic nitrogen. Moreover oxygen and nitrogen have similar masses, transport properties and, in the range of temperatures relevant to reentry flows, similar thermodynamical properties.

The problem can then be simplified by considering a gas made with only two species, i.e molecules A_2 and atoms A. This model, and the simplifications from complete gas kinetic theory has been first investigated by Lighthill [76] [77] and widely adapted and used for hypersonic flows (see e.g [47]).

5.1 Basic relations

The following relationships can easily be verified

- Masses of the species $m_{A_2} = 2m_A$ $M_{A_2} = 2M_A$

- Mass fractions $Y_{A_2} = 1 - Y_A$ so that most of the following variables will be expressed in terms of Y_A

- The partial pressures are expressed as

$$P_A = \rho_A \frac{\mathcal{R}}{M_A} T = Y_A \rho \frac{\mathcal{R}}{M_A} T = 2Y_A \rho \frac{\mathcal{R}}{M_{A_2}} T$$

$$P_{A_2} = \rho_{A_2} \frac{\mathcal{R}}{M_{A_2}} T = Y_{A_2} \rho \frac{\mathcal{R}}{M_{A_2}} T = (1 - Y_A) \rho \frac{\mathcal{R}}{M_{A_2}} T$$

so that the total pressure reads

$$P = P_a + P_{A_2} = (1 + Y_A) \rho \frac{\mathcal{R}}{M_{A_2}} T = Z \rho R_0 T \qquad \text{where } Z = 1 + Y_A \qquad R_0 = \frac{\mathcal{R}}{M_{A_2}}$$

- The enthalpy per mass unit of each species reads

$$h_A = h_A^0 + \int_0^T C_{PA} dT$$

$$h_{A_2} = \int_0^T C_{PA_2} dT$$

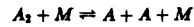and since $C_{PA} \sim C_{PA_2}$, the mixture enthalpy reads

$$h = Y_A h_A + Y_{A_2} h_{A_2} = h_{A_2} + Y_A (h_A - h_{A_2}) = h_{A_2} + Y_A h_A^0 + Y_A \int_O^T (C_{PA} - C_{PA_2}) dT \sim h_{A_2} + Y_A h_A^0$$

and the frozen specific heat is

$$C_{Pf} = C_{PA_2} + Y_A (C_{PA} - C_{PA_2}) \sim C_{PA_2}$$

5.1.1 Chemistry

The chemistry of the atom/molecule mixture can be represented with a single chemical reaction

$$A_2 + M \rightleftharpoons A + A + M$$

where the third body M stands for both the molecule A_2 and the atom A. The chemical reaction rate can be obtained as

$$\frac{dn_A}{dt} = 2k_D n_M n_{A_2} - 2k_R n_M n_A^2$$

so that, introducing the chemical equilibrium values (subscript E), and with the auxiliary relations $n_M = n_A + n_{A_2}$, $n_A = \rho Y_A / m_A$ the above equation reads

$$\frac{dn_A}{dt} = -k_R \frac{\rho^3}{m_A^3} (1 + Y_A) \frac{Y_A^2 - Y_{AE}^2}{1 - Y_{AE}^2}$$

One of the advantage of this relatively simple expression for the chemical reaction rate is to bring into evidence that, as most reentry flows are governed by dissociation process, the chemical time scale varies roughly like ρ^{-3}, i.e the lower the altitude, the higher the density and the smaller the chemical time scale, or, in other words, the flow get closer to chemical equilibrium as the altitude decreases.

5.1.2 Transport

A derivation of transport coefficients from gas kinetic theory can be found in [77]. It must be reminded that, for a binary mixture, the mass diffusion can be represented with the help of a Fick law (Equation 13) provided thermal diffusion effects are negligible and pressure gradients are small. The transport properties of the mixture are thus usually represented by assuming constant Prandtl and Lewis numbers. The Sutherland law is sometimes used to compute the viscosity, as it leads to about 10% error for air at chemical equilibrium (see e.g [47]).

The various fluxes thus read

$$\underline{d}_A = -\rho D \text{grad} Y_A \qquad \rho D = \frac{\mathcal{L}}{P} \mu$$

$$\underline{\tau} = p \underline{\delta} - \mu \left(\text{grad}\underline{u} + \text{grad}^t \underline{u} - \frac{1}{3} \underline{\delta} \text{div } \underline{u} \right) - \eta \text{div}\underline{u}$$

$$\underline{q}_t = -\frac{\mu}{P} \left(\text{grad}h + (\mathcal{L} - 1) (h_A - h_{A_2}) \text{grad} Y_A \right) \qquad \text{with } h_A - h_{A_2} \sim h_A^0$$

It must be pointed out that this model is however a very crude one which needs some tuning to give good results according to the range of temperature considered. If $C_{P N_2} \sim C_{P O_2}$, the formation enthalpy are different as $h_{N_2}^0 \sim 2h_{O_2}^0$, and the reaction rate coefficients for oxygen and nitrogen dissociation are different.

Applications of this diatomic gas model will be presented in section 8.

PART TWO :   ILLUSTRATIONS OF REAL GAS EFFECTS IN REENTRY FLOWS

The aim of this part is not to give the reader an expensive review of all the published works on flows with real gas effects. Such an information can be partly obtained from references [3] [38] [55] [75] [96] as concerns computations and references [38] [55] [64] [65] [99] as concerns experiments.

Our aim is to present some examples of flow from which the various real gas effects can be brought into evidence in order to give the reader an overall picture of what kind of phenomenon is to be expected in what part of the flow. Mainly shuttle reentry conditions, i.e velocities of about $7000ms^{-1}$ will be considered.

Reentry flow conditions are very difficult to simulate in a wind tunnel (see section 6). Moreover, only a few variables are usually measured and data about mass fractions or vibrational energy are rare for reentry flows. Numerical examples have been selected as they have the advantages of providing all the required data for analysis, and also enabling one to switch off a parameter to measure its importance. They also have the disadvantage that the real physics is remplaced by models which have to be trusted.

6   Nozzle flow

In order to simulate the flow around a reentry vehicle, a flow with low temperature (about 200K) and high velocity (about $7000ms^{-1}$) must be achieved in the wind tunnel test section upstream of the model. This means that the fluid must have

a very large total enthalpy (enthalpy + kinetic energy). For that the fluid is usually first heated either with an arc heater (see e.g [34]) or by compression in a shock tube (see e.g [65] [99]) in a region where its velocity is small and accelerated downstream by expansion in a nozzle.

To achieve pressure levels similar to flight or only to avoid air liquefaction during the expansion, an important pressure level is required in the heater.

Neglecting viscous and real gas effects, the form of the nozzle can easily be calculated from linear supersonic theory, to obtain a uniform flow with the desired velocity in the test section. Of course, the final shape can be designed by taking into account viscous and real gas effects (see e.g [34]). Several solutions can be found but, to avoid both too long wind tunnels and a too important heating of the nozzle, short and rapidly expanding nozzles are usually designed.

In the expansion, the flow is strongly accelerated and its temperature falls rapidly. The pressure and the density also decrease very rapidly. As the temperature and the density decrease, the collision time scale increases while the mean flow time scale is very short. This is a typical situation of a frozen flow as presented in sections 2.5.4 and 2.6.2.

Both the species composition of the flow and the energy partition among the energy modes cannot adapt themselves to the flow evolution and the flow is frozen from both a thermodynamical and a chemical point of view. This can be illustrated by figures 35 and 36 on which the pressure and temperature evolutions are plotted versus distance for the nozzle of a planned hypersonic facility [34]. When non–equilibrium effects are accounted for in the computations, the freezing of vibrational energy is brought into evidence. The vibrational energy is here presented as a vibrational temperature, i.e the temperature of the same gas at thermodynamic equilibrium having the same vibrational energy. The total enthalpy must be conserved in the inviscid core of the flow; this means that to achieve the same enthalpy level, the translational energy must be smaller when the flow is in thermal non–equilibrium as shown on figure 36. Thermal non–equilibrium also affects the evolution of the other variables, either the pressure or the density or the mass fractions. Similarly, the flow freezes from a chemical point of view, the mass fractions do not change after a certain distance from the nozzle throat, so that the flow is dissociated in the test section.

If the freezing phenomenon is unwanted in hypersonic facilities, as it leads to a vibrationally excited and dissociated flow upstream of the shock wave, it can be looked for in other applications such as gas lasers in which important vibrational populations are so obtained to induce laser emission (see e.g [26]).

This example, to illustrate how a flow can freeze from both a thermodynamical and a chemical point of view, has brought into evidence one of the difficulties to properly simulate hypersonic flight conditions as the thermodynamic and chemical state of the gas upstream of the shock wave cannot easily be duplicated in the test section. Let us take the opportunity to mention another problem related to simulation of real gas effects in wind tunnels.

For supersonic flow, similarity between flight and experiment requires the conservation of, at least, both the Mach and the Reynolds numbers. When similarity conditions are expressed for flows with real gas effects, another parameter is brought into evidence, which is the ratio between real gas effects (usually chemistry) and mean flow time scales, known as the Damkhöler number. As the models are much smaller than the real reentry vehicles, Mach number, Reynolds number and Damkhöler number cannot easily be reproduced at the same time. The reader is referred to [65] [99] for a further discussion.

7 Relaxation behind a shock wave

The gas kinetic theory presented in section 2 is not valid inside a shock wave as the mean free path is no longer small compared with the mean flow characteristic length scale, i.e the shock wave thickness. Description of the shock can be done with the *Burnett equations* which are obtained from higher order expansions (see e.g [105]).

However, shock waves can be treated as discontinuity surfaces in the Navier equations. When conservation rules are applied to the flow equations (14) to (18), mass fractions and internal energy are conserved through the shock wave while velocity and total energy are modified. Only translational energy is thus modified through the shock wave, the flow is in strong thermal and chemical non–equilibrium. The flow evolution downstream of the shock wave is due to thermal and chemical relaxations and the coupling between both.

A first illustration of flow behind a shock wave is the calculation of Allen et al experiment [1] by Park [87]. Park's model is an extension of Lee's model [73] in which the thermal non–equilibrium is accounted for by assuming that the electron temperature and the various molecule vibrational temperatures are equal. Influence of vibrational non–equilibrium is taken into account in the chemistry model.

Upstream of the shock wave, the static pressure is equal to 0.1 Torr, the translation temperature to 300K, the vibrational temperature to 5000K and the velocity to $10,000ms^{-1}$. The calculation brings into evidence an important increase of translation temperature through the shock wave (Figure 37). Two processes compete to deplete the translation energy: on the one hand the gas dissociates and ionizes as shown on figure 38 and on the other hand the vibrational energy relaxes. The limits indicated on the right side of both figures correspond to ˙ ermal and chemical equilibrium. It can be noticed from this that thermal non–equilibrium relaxes faster than chemical non–equilibrium. The evolution of chemical species (Figure 38) also reflects the variation of the temperature evolution as ionized species are first formed just behind the shock wave and decrease later downstream with translation temperature.

Another example of flow relaxation behind a shock wave, in a situation similar to shuttle reentry, has been studied by Brun et al [28]. The model used takes into account vibrational non–equilibrium for nitrogen and oxygen and a different translation energy for the electrons. The vibrational temperature of charged molecules is assumed equal to that of the corresponding neutral species and nitrogen monoxide thermal non–equilibrium is neglected as it relaxes very rapidly. Four temperatures are thus defined for the flow. The chemical model is modified to account for thermal non–equilibrium. Thermal non–equilibrium relaxation takes into account the T–V and V–V energy exchanges (see section 2.6.3).
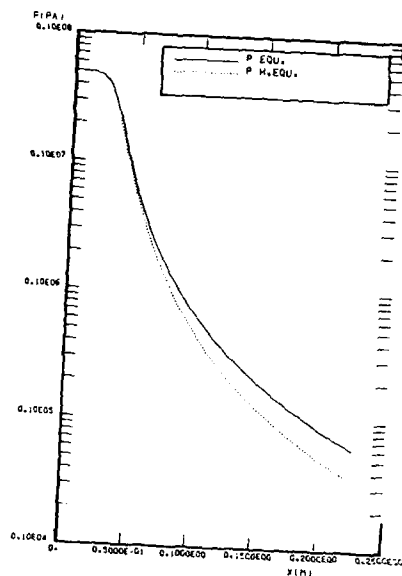
Figure 35: Evolution of the static pressure in the nozzle (from [34])

P EQU. Pressure assuming the flow in thermal equilibrium

P H.EQU. Pressure assuming the flow out of thermal equilibrium
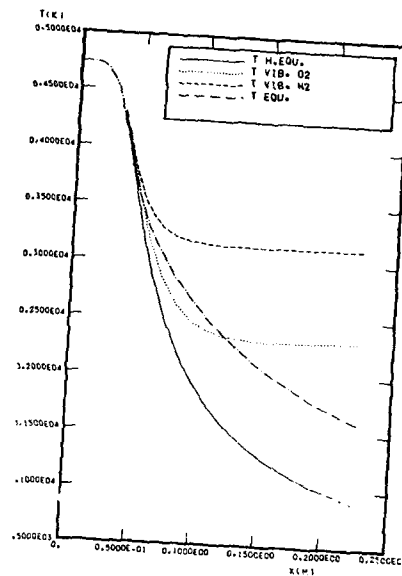
Figure 36: Evolution of the temperature in the nozzle (from [34])

T EQU. Temperature of the flow assuming thermal equilibrium

T H.EQU. Translation temperature for flow in thermal non–equilibrium

T VIB. O2 Vibrational temperature of oxygen

T VIB. N2 Vibrational temperature of nitrogen

Figure 37: Evolution of translational and vibrational temperatures downstream of the shock wave (from [87])

Figure 38: Evolution of species mole fractions downstream of the shock wave (from [87])

Evolution of temperatures and species mass fractions are presented on figures 39 to 41. The upstream Mach number is

Figure 39: Evolution of temperatures downstream of the shock wave (from [28])

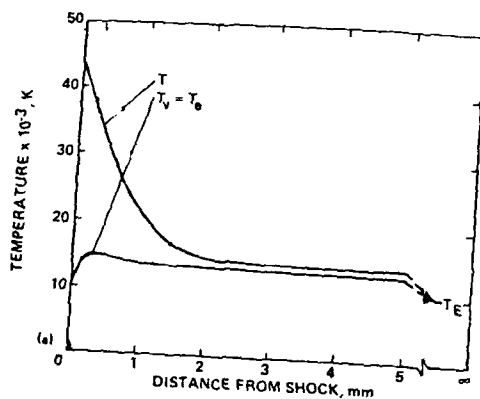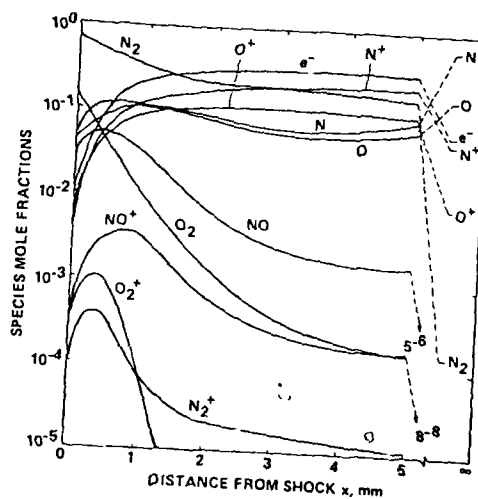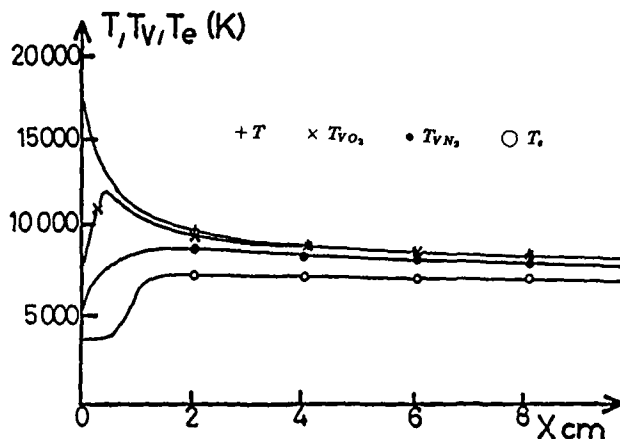25, the pressure 8.5 Pa and the temperature 205K. Thermal and chemical equilibrium are assumed upstream of the shock wave. Figure 39 shows the relaxation of the various temperatures. Oxygen is more easily excitated by T–V exchanges and later accelerate nitrogen relaxation via V–V coupling. Thermal relaxation is very long in this case. It must be reminded that, for a shuttle, the shock stand–off distance is about 10cm so that the electron are out of thermal equilibrium in the boundary layer.

Species evolutions are given on figures 40 and 41. The coupling between thermal and chemical relaxation is studied in great detail in [28] as each process can easily be switched off in the calculations. As expected, vibrational relaxation delays the species relaxation while, conversely, chemical relaxation delays thermal relaxation.

The evolution of ionized species bring into evidence their small percentage in a shuttle reentry flow (figure 41) when compared to AOTV related problems in which the velocities are more important (figure 38).

The comparison between these two examples brings into evidence the problem of model definition. On the one hand, the model must be tractable: Park's model is very convenient for practical use as it only requires two temperature calculations while Brun's model is much more sophisticated and can give more information about thermal non–equilibrium. On the other hand, the model must fit the physics: Park's model is well suited for AOTV flows where oxygen rapidly dissociates while the electron translation temperature tends to ajust to the nitogen vibrational temperature [74] but is not relevant to space shuttle reentry flows.

At last, the model must be validated. Allen experiment [1] only gives data upon the radiation so that another code is needed to compute the radiation and compare the prediction and the experiment. Park [87] has shown that the radiation emission computed from the above presented results is valid with an uncertainty factor of ±2, discrepancies are due to uncertainties in chemical reaction rates or collision integrals.

8 Hypersonic boundary layers and shock layers

One of the key problems of reentry is the heating of the vehicle. Wall heat fluxes can be computed using boundary layer theory. At the present time, viscous shock layer solutions or Navier solutions are also used to compute the complete flow field around the vehicle (see e.g [13] [38] [92] [96] [97]). However, as the viscous shock layer or Navier solutions are cumbersome, the effort in such cases is upon the numerics more than upon the real gas model.

Many studies have been devoted to the real gas modelling, mainly for boundary layer flows, and some of them, either very famous or well–known to the author, will be presented in order to bring into evidence the rôle of the various phenomena or the importance of model uncertainties.

During a shuttle reentry, such as the STS–2 reentry the main characteristics of which are given on figure 42, the maximum heating occurs at altitudes of about 70 km as shown on figure 43. The second peak in the temperature histories is due to laminar/turbulent transition. The maximum heating thus occurs in the laminar regime, as at high altitudes the density is low so that the Reynolds number is low. Only laminar flows will be investigated here.

Two simplifying hypothesis are usually done in studies of hypersonic flows for shuttle reentry flows.

- The flow is considered as a continuous medium, i.e even near the wall the mean free path is small compared with the distance to the wall. This is not true at high altitudes where rarefied gas effects are to be accounted for in the wall region, leading to a slip velocity and a temperature jump at the wall.

- Ionisation is neglected as it is very weak for shuttle reentry conditions and do not alter the flow predictions (see section 9).
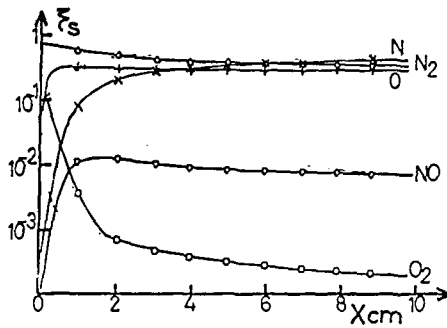
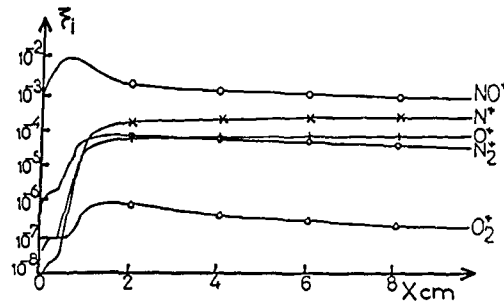Figure 40: Evolution of neutral species mass fractions downstream of the shock wave (from [28])

Figure 41: Evolution of charged species mass fractions downstream of the shock wave (from [28])

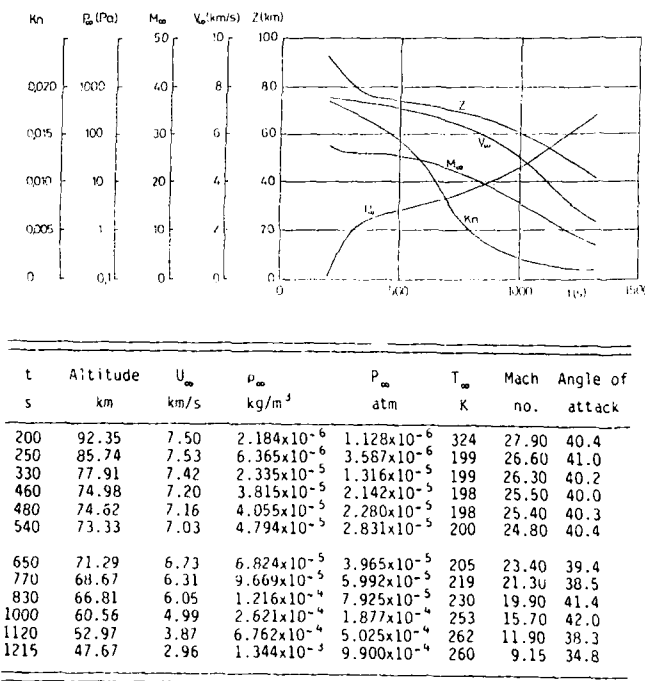| t	Altitude	U_∞	ρ_∞	P_∞	T_∞	Mach	Angle of
s	km	km/s	kg/m^3	atm	K	no.	attack
200	92.35	7.50	2.184×10^{-6}	1.128×10^{-6}	324	27.90	40.4
250	85.74	7.53	6.365×10^{-6}	3.587×10^{-6}	199	26.60	41.0
330	77.91	7.42	2.335×10^{-5}	1.316×10^{-5}	199	26.30	40.2
460	74.98	7.20	3.815×10^{-5}	2.142×10^{-5}	198	25.50	40.0
480	74.62	7.16	4.055×10^{-5}	2.280×10^{-5}	198	25.40	40.3
540	73.33	7.03	4.794×10^{-5}	2.831×10^{-5}	200	24.80	40.4
650	71.29	6.73	6.824×10^{-5}	3.965×10^{-5}	205	23.40	39.4
770	68.67	6.31	9.669×10^{-5}	5.992×10^{-5}	219	21.30	38.5
830	66.81	6.05	1.216×10^{-4}	7.925×10^{-5}	230	19.90	41.4
1000	60.56	4.99	2.621×10^{-4}	1.877×10^{-4}	253	15.70	42.0
1120	52.97	3.87	6.762×10^{-4}	5.025×10^{-4}	262	11.90	38.3
1215	47.67	2.96	1.344×10^{-3}	9.900×10^{-4}	260	9.15	34.8

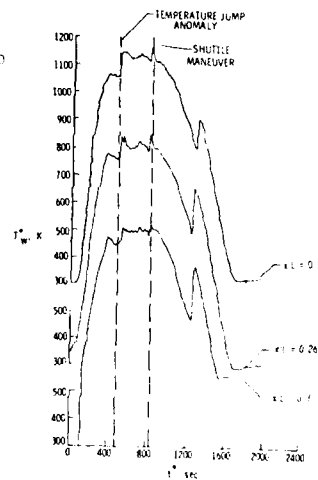Figure 42: Trajectory reentry for space shuttle flight STS-2 (from [97])

Figure 43: Time evolution of temperatures on shuttle during STS-2 reentry (from [97])

- The flow in the boundary layer is assumed to be in thermal equilibrium. This hypothesis is not always satisfied as the thermal relaxation length behind the shock wave can be comparable with the shock stand–off distance as shown on figure 39. Moreover, wall catalysis may lead to the formation of vibrationally excited molecules at the wall (see section 3.3). Thermal equilibrium is also sometimes assumed in the whole shock layer, which is certainly wrong just behind the shock wave [97].

As concerns boundary layer flows, it must be pointed out that generally, a single boundary layer cannot be defined as there exist velocity, temperature and species boundary layers. However, as for air, in the relevant range of pressure and temperature, the Prandtl and the Lewis number are close to unity, the diffusions of momemtum, heat and mass are likely, so that the various boundary layers have similar thicknesses and a single boundary layer can be defined.

In what follows, mainly boundary layer flows will be investigated. Viscous shock layer solutions will be explicitly mentionned ⁼ ₁ referred. As the wall is heated by the flow, the wall heat flux is negative. In the formulae, the correct sign will alw₋ⱼ be used. However, only the magnitude of the wall heat flux will be plotted on some figures and comparison of wall heat flux magnitudes in the text will also deal with their modulus.

8.1 Influence of wall catalysis

A particular and important feature is the presence of the wall, the catalytic efficiency of which can deeply affect the species profiles inside the boundary layer.

8.1.1 Fay and Riddell stagnation point solutions

This was first investigated by Fay and Riddell [47] who studied axisymmetric stagnation point heat transfer. The stagnation point solutions are obtained with the help of the Levy-Lees space coordinate transformation [42]

$$\xi = \int_0^x \rho_w \mu_w U_e R^2 dx \qquad \eta = \frac{RU_e}{\sqrt{2\xi}} \int_0^y \rho dy$$

where the subscript w indicates wall values, U_e is the velocity outside the boundary layer, R the distance to the symmetry axis ($R \sim x$ near the stagnation point), x and y the boundary layer coordinates respectively along the body and normal to the wall. With this set of space variables, the boundary layer equations are written for the reduced velocity, enthalpy and energy profiles

$$f' = \frac{U}{U_e} \qquad g = \frac{h_i}{h_{i_e}} \qquad Z_I = \frac{Y_I}{Y_{I_e}}$$

where h_i is the total enthalpy and the subscript e denotes values outside of the boundary layer. Self similar solutions can be obtained at the stagnation point, the boundary layer equations reduce to a set of coupled ordinary differential equations.

Extra simplifications were introduced by Fay and Riddell to study the axisymmetric stagnation point.

- An atom/molecule approach (see section 5) was used.

- Reacting flows were investigated with a simple model for the reaction rate constant $k_R \sim T^{-1.5}$. Chemically frozen flows and chemical equilibrium flows were also studied. Let us mention that wall catalysis plays no rôle for chemical equilibrium flows as the species mass fractions at the wall are then imposed by the equilibrium condition.

- Transport properties of the fluid were represented by a simple model for the viscosity, using either Sutherland law or equilibrium data, and constant Prandtl and Lewis numbers.

- To solve the set of ordinary differential equations, boundary conditions are needed, both at the wall and at the outer edge of the boundary layer. Fay and Riddell and following authors assumed the flow have enough time to relax between the shock wave and the boundary layer edge and is at chemical equilibrium there. This chemical relaxation may not be complete in real cases as shown on figures 40 and 41.

All the results presented herein are for the same conditions, i.e a Lewis number equal to 1.4, a Prandtl number of 0.71, a wall temperature of 300K and a wall enthalpy/external enthalpy ratio of 0.0123.
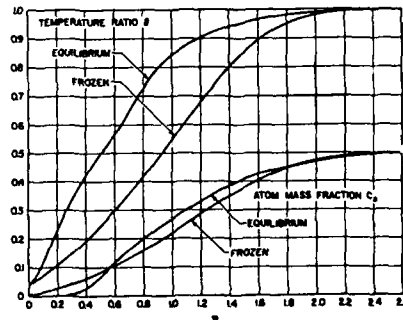

Figure 44: Temperature and atom mass fraction profiles for frozen and equilibrium flows (from [47])

At the stagnation point, only the velocity component normal to the wall is not null, the species mass fraction profiles thus result from a balance between advection towards the wall, chemistry and diffusion. The atom mass fraction profiles for a frozen flow on a catalytic wall are given on figure 44. For a frozen flow on a non-catalytic wall, the atom mass fraction is constant throughout the boundary layer and equal to the external value (see section 2.5.4). The wall catalycity modifies the boundary condition at the wall and strongly affects the whole atom mass fraction profile.

The wall heat flux is also affected by the wall catalysis. From a study over a wide range of altitudes from 7.5 km to 36 km and velocities from 1.8 to 7 kms^{-1}, and for different values of the Prandtl and Lewis numbers, Fay and Riddell proposed fits for the wall heat flux as

$$\frac{\Phi_w}{h_w - h_{i_e}} = A\left(1 + \left[\mathcal{L}^{0.52} - 1\right]\frac{h_{D_e}}{h_{i_e}}\right) \qquad \text{Chemical equilibrium flow} \qquad (22)$$

$$\frac{\Phi_w}{h_w - h_{i_e}} = A\left(1 + \left[\mathcal{L}^{0.63} - 1\right]\frac{h_{D_e}}{h_{i_e}}\right) \qquad \text{Frozen flow – Catalytic wall} \qquad (23)$$

$$\frac{\Phi_w}{h_w - h_{i_e}} = A\left(1 - \frac{h_{D_e}}{h_{i_e}}\right) \qquad \text{Frozen flow – Non-catalytic wall} \qquad (24)$$

$$\text{with} \qquad A = 0.76\left(P\frac{\rho_e\mu_e}{\rho_w\mu_w}\right)^{0.4}\frac{1}{P}\sqrt{\rho_w\mu_w\left(\frac{dU_e}{dx}\right)_0} \qquad (25)$$

where the subscript 0 indicates values at the stagnation point and h_D is the dissociation enthalpy per mass unit, i.e the atom formation enthalpy times their mass fraction.

These formulae bring into evidence the influence of wall catalysis upon heat flux. Atoms diffuse towards the wall and, for a catalytic wall, recombine and release their dissociation energy. This leads to an higher wall heat flux for the catalytic wall. As the wall heat flux can be expressed as

$$\Phi_w = -\lambda\frac{\partial T}{\partial y} - \rho D\left(h_A - h_{A_2}\right)\frac{\partial Y_A}{\partial y} \qquad (26)$$

the flux on a non-catalytic wall is only due to the temperature gradient while both terms intervene for a catalytic wall. The contribution of both terms is given on figure 45 on which the frozen flow corresponds to a zero recombination rate parameter. The contribution of mass fraction gradients, i.e the energy release due to atom recombination at the wall, is the main part of the wall heat flux under these conditions.
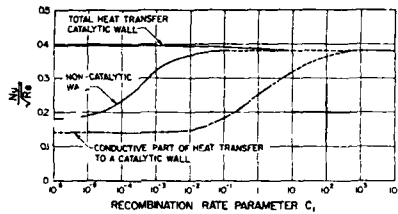

Figure 45: Heat transfer parameter as function of the recombination rate parameter

$$\frac{Nu}{\sqrt{Re}} = \frac{-\Phi_w}{(h_w - h_{i_e})\sqrt{\rho_w\mu_w\left(\frac{dU_e}{dx}\right)_0}}$$

(from [47])

Figure 46: Atom mass fraction profile at the stagnation point on a non-catalytic wall as function of the recombination rate parameter (from [47])

8.1.2 Goulard extension to finite catalysis

The study of frozen flow axisymmetric stagnation point was extended by Goulard [53] to account for finite catalytic recombination rate at the wall (equation 20). Figure 47 shows the influence of finite wall catalycity and flight velocity upon the wall heat flux. In order to compare the different cases, the wall heat flux is presented in reduced form, i.e divided by its value for a catalytic wall. The faster the wall recombination, i.e the more catalytic the wall, the higher the heat flux as more atoms can recombine at the wall and release their formation enthalpy. As the velocity increases, the gas is more and more dissociated outside of the boundary layer so that the energy release due to atom recombination on a catalytic wall is more and more important. The heat flux reduction due to a non-catalytic wall so increases with velocity.

For a shuttle reentry at 7 kms^{-1}, a non catalytic wall leads to a heat reduction of 70% and the reaction–cured glass used for the space shuttle thermal protection system, with a recombination rate constant of about $1ms^{-1}$, to a reduction of about 50%.

An interesting point mentionned by Goulard is the evolution of wall heat flux with temperature on a finite catalytic wall. The catalytic rate coefficient increases with temperature (see equation 21), i.e as the wall temperature increases the wall becomes more and more catalytic so that the wall heat flux may *increase* with wall temperature.
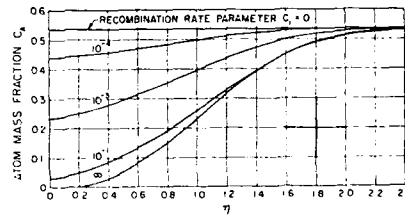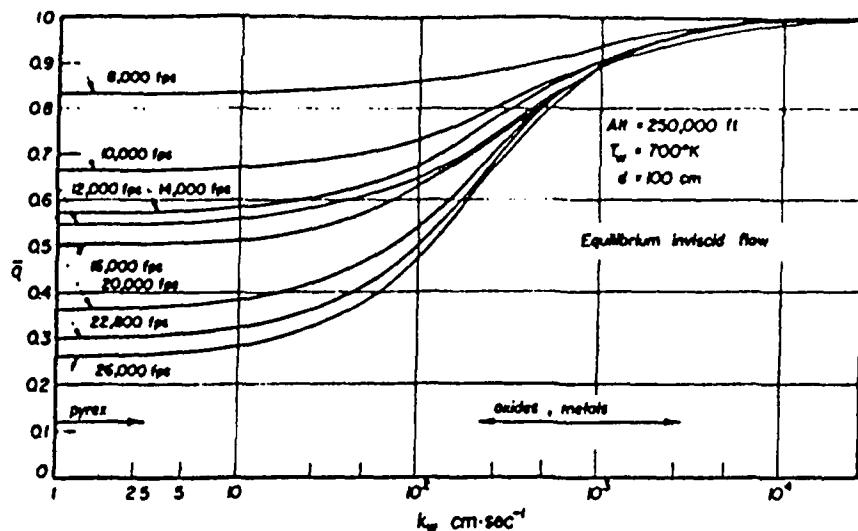
Figure 47: Reduced heat transfer as function of catalytic recombination rate and flight velocity at 250,000ft (from [53])

8.1.3 Study of the STS-2 reentry

Later studies were devoted to boundary layers flows along bodies (see e.g [16] to [19]). A sensitivity study of boundary layer to the real gas model has recently been performed by Eldem [8] [9] [36] [44] for the STS-2 flight reentry.

Thanks to computer power increase, a more detailled model has been used: the five main neutral species are accounted for (N_2, O_2, NO, N, O), the chemistry is described with the fifteen dissociation reactions and the two shuffle reactions, thermodynamical properties are computed with Schäfer model [94] and transport properties with Straub model [100].
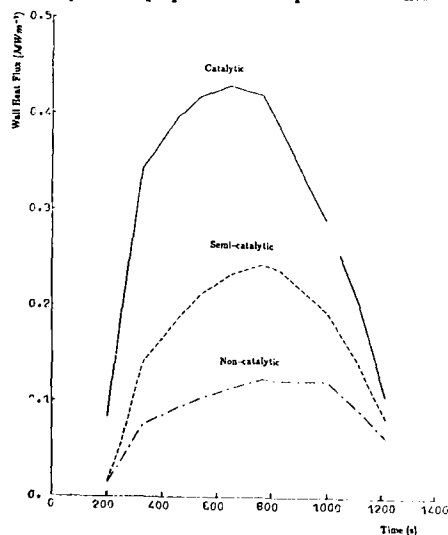

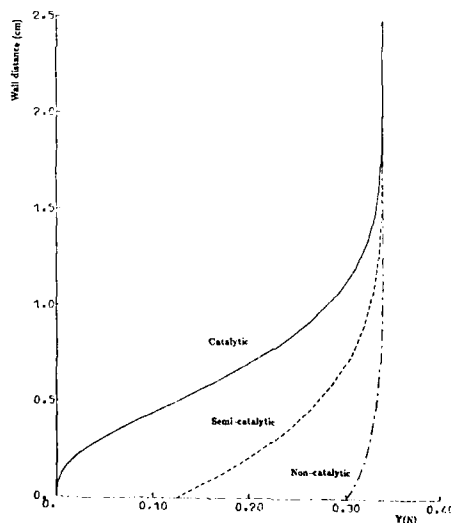Figure 48: Stagnation point wall heat flux during STS-2 flight reentry (from [44])

Figure 49: Atomic nitrogen stagnation point profiles at 71.29 km (from [44])

Computations have been performed over axisymmetric hyperboloids at zero degree incidence which are supposed to represent the space shuttle windward symmetry line [97].

The stagnation point wall heat flux evolution during the reentry is plotted on figure 48 for a catalytic wall, a non-catalytic wall and a wall with finite catalycity according to Scott data [95], assuming a constant wall temperature of 1500K. The agreement with Goulard results is fair as the maximum wall heat flux is reduced by about 70% for a non-catalytic wall and 40% for a wall with finite catalycity. These reductions remain important during all the reentry, not only at the
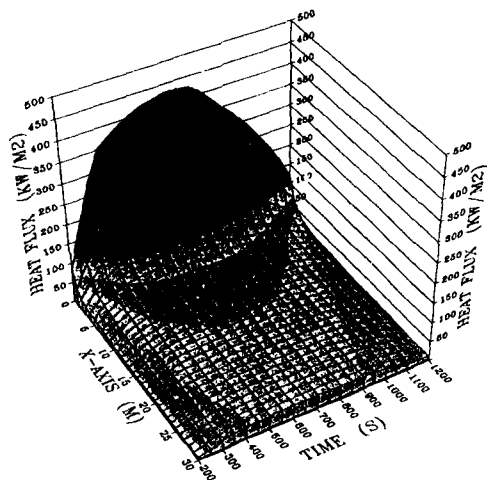

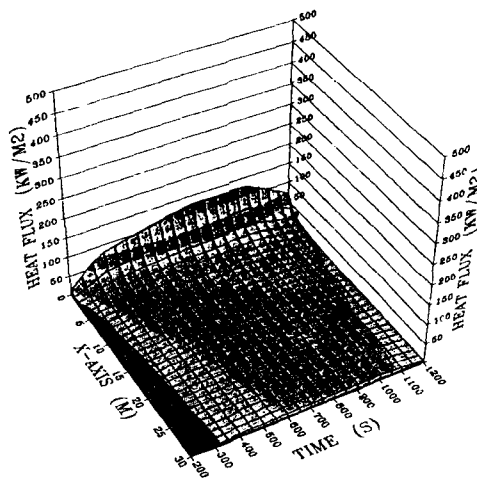Figure 50: Wall heat flux for a catalytic wall (from [9])

Figure 51: Wall heat flux for a non-catalytic wall (from [9])

stagnation point but also all along the body as shown on figures 50 and 51 on which the wall heat flux evolution along

the windward centerline during the reentry has been plotted. The wall heat flux reduction due to a non-catalytic wall is roughly constant all along the body.

The atomic nitrogen mass fraction profiles are plotted on figure 49. As thermal diffusivity is accounted for, the slope of the profile at the wall is no longer null for a non-catalytic wall. Moreover, chemistry leads to nitrogen recombination in the boundary layer, but the nitrogen mass fraction does not vary significantly when the wall is non-catalytic. Nevertheless, the reduction of atomic nitrogen with increasing wall catalycity is clearly brought into evidence.

The practical importance of wall catalycity is shown on figures 52 and 53 on which the wall temperatures are plotted for non catalytic and catalytic walls, at the stagnation point during all the reentry (figure 52) and along the body at 71.29 km altitude (figure 53). These wall temperatures are computed by assuming the wall to be at radiative equilibrium, i.e the heat flux convected to the wall is reemitted as radiation. If heat conduction in the thermal protection system is neglected, the wall temperature remains constant as observed during flight (see figure 43). The radiative equilibrium condition reads

$$\Phi_w + \epsilon\sigma T_w^4 = 0$$

where σ is the Stefan-Boltzmann constant and ϵ the wall emissivity coefficient (0.89 for the space shuttle thermal protection system). A non-catalytic wall leads to a reduction of the maximum temperature of 450K at the stagnation point and about 250K all along the body. In the following presentation of Eldem's results, the wall temperature is always 1500K which is an overestimation of flight temperature (see figure 43) as the aim of his study is not to compute real fluxes but to analyze the model sensitivity.

Eldem [44] compared his results with the Fay and Riddell formulae. While these formulae were obtained for frozen flows, Eldem's results account for chemical non-equilibrium. For a catalytic wall, the agreement is within 5% as it will be shown in the next section that the wall heat flux is then not sensitive to chemical reaction rates. For a non-catalytic wall, the agreement is poor, Fay and Riddell formulae underestimate the heat flux by about 50%. Corrections are proposed [44] but have not been validated for other situations than the STS-2 reentry.

Other interesting parameters can be obtained from boundary layer computations such as the skin friction coefficient to know the viscous contribution to the drag or the displacement thickness to estimate viscous/inviscid coupling effects. These parameters are related to the velocity and density profiles as

$$C_f = \frac{\tau_w}{\frac{1}{2}\rho_e U_e^2} = \frac{\mu_w \left(\frac{\partial U}{\partial y}\right)_w}{\frac{1}{2}\rho_e U_e^3} \qquad \delta_1 = \int_0^\infty \left(1 - \frac{\rho U}{\rho_e U_e}\right) dy$$

The velocity profile is hardly modified by the wall catalycity, as shown on figure 54. For a catalytic wall, the fluid is less dissociated in the wall region as shown on figure 49 so that the temperature is higher as less energy is stored as species
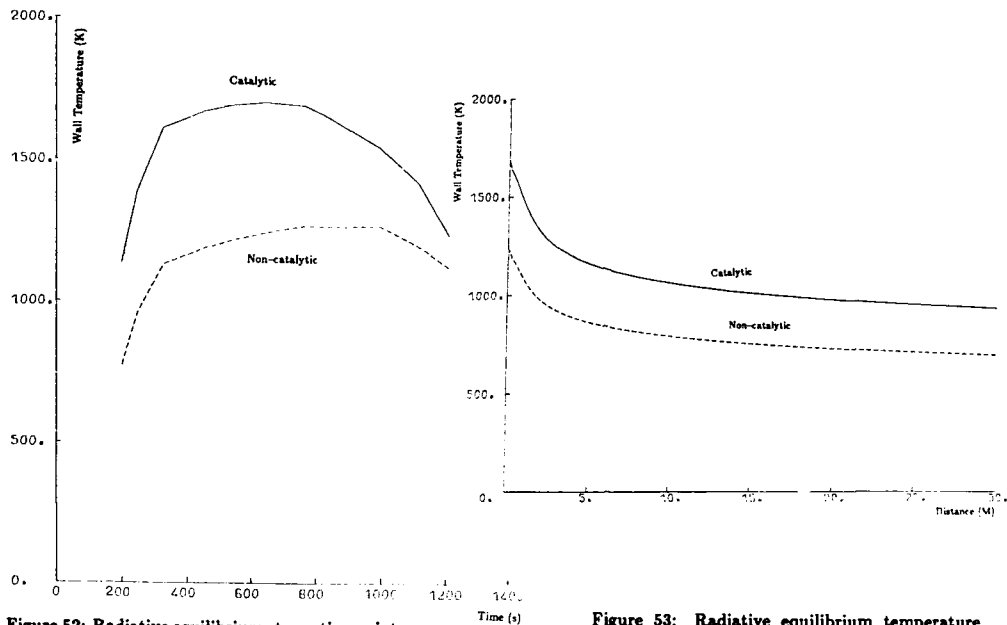
Figure 52: Radiative equilibrium stagnation point temperature (from [44])

Figure 53: Radiative equilibrium temperature along the shuttle centerline at 71.29 km altitude (from [44])
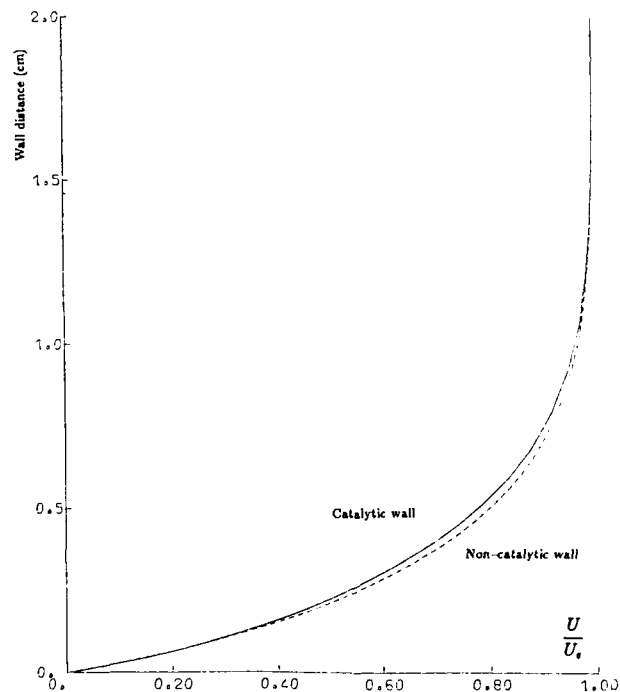
Figure 54: Influence of the wall catalycity on the stagnation point velocity profile at 71.29 km (from [36])
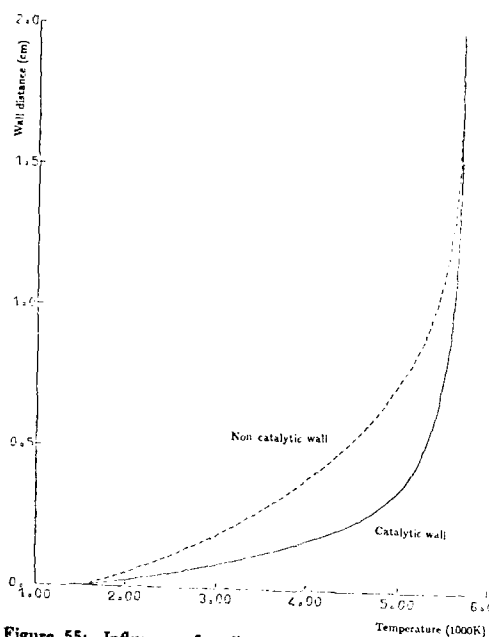
Figure 55: Influence of wall catalycity on the stagnation point temperature profile at 71.29 km (from [36])

Figure 56: Influence of wall catalycity on the stagnation point density profile at 71.29 km (from [36])

Figure 57: Influence of the wall catalycity upon the skin friction coefficient at 71.29 km (from [44])

Figure 58: Influence of the wall catalycity upon the displacement thickness at 71.29 km (from [44])

formation enthalpy (figure 55). According to the state equation (11),the density depends upon both the temperature and the dissociation level. Catalytic walls increase the temperature but decrease the dissociation level so that 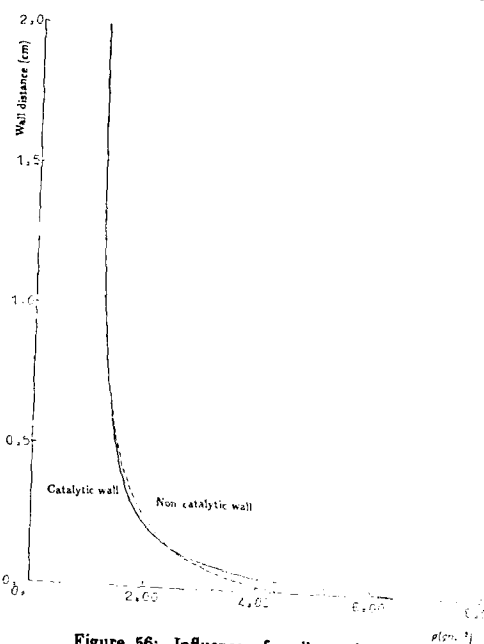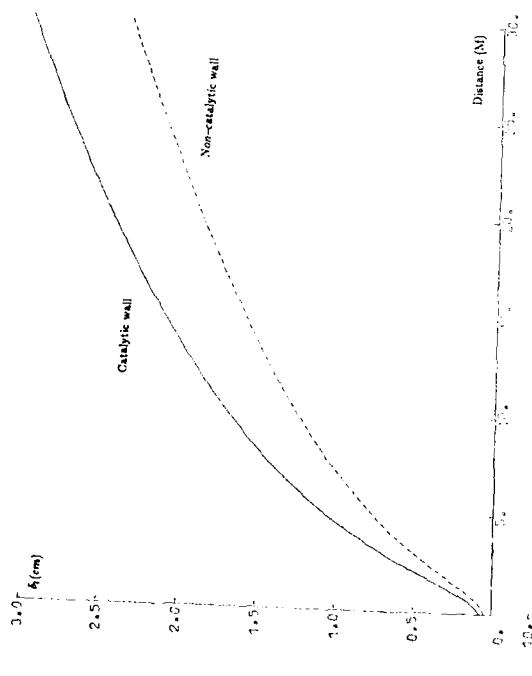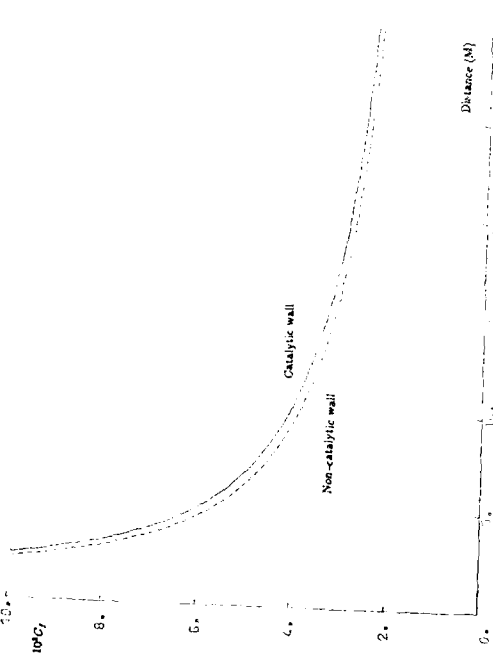the influence on density profile cannot be estimated a-priori from the state equation (11). The variation of density with surface catalysis is not always the same in the boundary layer as shown on figure 56.

Consequently, the skin friction is hardly affected by the wall catalycity (figure 57). The skin friction coefficient is very large for a laminar boundary layer. This is due both to the low Reynolds number and to the cold wall temperature. The influence of wall catalycity upon the displacement thickness is clear on figure 58 but cannot be a-priori estimated. It must be pointed out that the displacement effect is very weak as the wall temperature is low. The rapid increase of density in the wall region (figure 56) reduces the mass flow loss in the boundary layer. Negative displacement thicknesses can be observed at high altitudes or for lower and more realistic wall temperatures. Viscous/inviscid interaction should be very weak.

Similar results have been previously obtained by Shinn [97] with a simpler real gas model but using a viscous shock layer approach.

8.2 Influence of the chemical rates

8.2.1 Fay and Riddell results

The influence of chemical reaction rates was brought into evidence by Fay and Riddell [47] for the stagnation point and confirmed by Blottner [16] for boundary layers along bodies.

In the Fay and Riddell axisymmetric stagnation point solutions, the chemistry is modelled by a single reaction. Boundary layer equations under similarity form bring into evidence the coefficient

$$C_1 = \frac{2k_R p^2}{R^2 T^2 \left(\frac{dU_s}{dx}\right)_0}$$

nammed recombination rate parameter which represents the ratio between mean flow and chemical reaction time scales.

The influence of the recombination rate parameter upon stagnation point solutions is shown on figures 45 and 46. Figure 46 shows the atom mass fraction profiles for a non-catalytic wall. As atom recombination is not imposed at the wall, the more important the recombination rate, the more the atoms recombine in the cold region near the wall. This recombination leads to an heat release which is mainly convected to the wall so that the wall heat flux for a non-catalytic wall increases with the recombination rate parameter (figure 45).

For a catalytic wall, the wall heat flux is due to two terms (Equation 26)

- The temperature gradient at the wall which depends upon the energy release due to atom recombination inside the boundary layer

- The mass fraction gradient at the wall as each species diffuses with its own enthalpy. This term represents the energy release due to atom recombination at the wall

The sum of these two terms is hardly affected by the recombination rate which modify the region where atoms recombine as the energy release is eventually convected to the wall. Figure 45 shows that the wall heat flux on a catalytic wall is weakly dependent upon the recombination rate parameter. When the recombination rate parameter increases, more atoms recombine in the boundary layer so that the term linked to the wall temperature gradient increases. The decrease of the wall heat flux for large recombination rate parameter is due to the fact that an important part of the recombination then occurs in the outer part of the boundary layer and the heat released there is not fully transmitted to the wall but partly advected downstream.

Chemical equilibrium is the limiting case of infinite recombination rate parameter. Formulae 22 and 23 shows, in agreement with figure 45, that the heat flux for a chemical equilibrium flow and a frozen flow on a catalytic wall are very close since $\mathcal{L} \sim 1$ and that the heat flux is slightly higher for the frozen flow on a catalytic wall as $\mathcal{L} > 1$.

8.2.2 STS-2 prediction sensitivity to the chemistry model

It has been shown previously that the reaction rate constants are known with some uncertainty (see figures 13 and 14). Eldem [8] [9] [36] [44] investigated the influence of existing chemical models on space shuttle wall heat flux predictions. The STS-2 reentry trajectory is still used and, for the sake of simplicity, the wall temperature is assumed constant and equal to 1500K.

Four chemical models are compared, i.e the chemical equilibrium which corresponds to infinite reaction rate constants and the sets of reaction rate constants published by Bortner [22], Gardiner [49] and Oertel [84]. It must be mentionned that Gardiner data are the same as Baulch ones [11] which are the NBS recommanded rate constants [107], except for the two shuffle reactions.

The variation of the stagnation point wall heat flux prediction with the chemical reaction rate constants is shown on figure 59. For a catalytic wall, the wall heat flux does not depend upon the reaction rate as shown previously. A slightly larger wall heat flux is obtained for flow at chemical equilibrium. This seems at variance with Fay and Riddell results and is due to the fact that they considered very low wall temperatures so that, at chemical equilibrium, the recombination occurs far from the wall as shown on figure 44 and a part of the released heat is not transmitted to the wall. In Eldem's computation, as the wall temperature is higher, the recombination occurs close to the wall and is more complete for equilibrium flows, so that both the heat release and the wall heat flux are slightly increased.
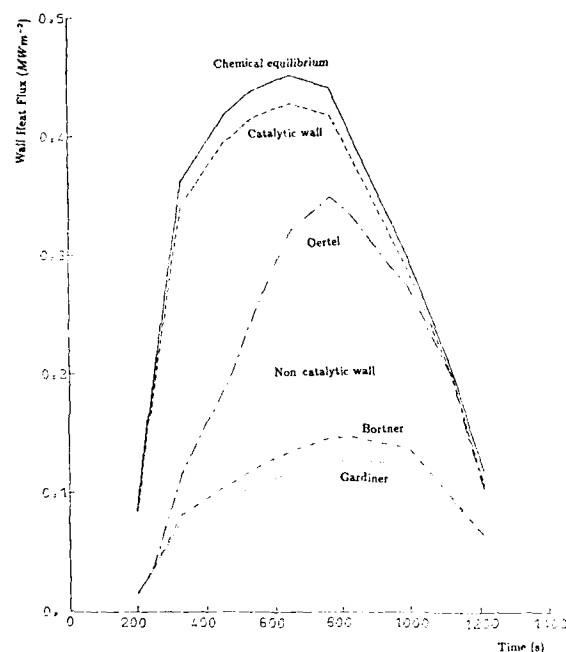
Figure 59: Influence of the chemical reaction rate on the stagnation point wall heat flux (from [44])

For a non-catalytic wall, a large discrepancy is observed as the wall heat flux depends only upon the wall temperature gradient, i.e upon the energy release due to chemical reactions inside the boundary layer. Oertel chemical model gives a faster dissociation rate of oxygen (see figure 14) and hence a faster recombination rate in the cold region close to the wall. A higher wall heat flux is so predicted. Gardiner and Bortner models, which are within the present uncertainty range, lead to a 12% difference in wall heat flux, i.e roughly a 3% difference for the wall temperature or about 40K.

The influence of the chemical rate constant on the wall heat flux predictions along the shuttle centerline is shown on figures 60 to 63 for various points along the reentry trajectory. All along the body, during all the reentry, the wall heat flux on the shuttle centerline does not depend upon the chemical model if the wall is catalytic. The wall heat flux predicted for flow at chemical equilibrium is again slightly larger than the one for a catalytic wall. The arguments presented for the stagnation point still hold. For a non-catalytic wall, the sensitivity of the wall heat flux prediction to the chemical model reflects the variations of flow conditions during reentry.

- At higher altitudes (figures 59 and 60), the density is very low, even behind the shock wave. The chemical time scale is very long and the flow is almost frozen. The results are then hardly sensitive to the chemical model.

- When the altitude decreases, the density increases very rapidly as shown on figure 42. The chemical time scale decreases rapidly so that the flow is in chemical non-equilibrium (figures 59 and 61). Oertel's model gives larger oxygen recombination and higher wall heat flux. Some discrepancies are observed between Bortner and Gardiner models.

- At lower altitudes (figures 59 and 62) the density still increases and the flow is still in chemical non-equilibrium. The discrepancies are amplified. Oertel's model get close to catalytic wall results as it tend to recombine all the oxygen. Bortner's model predicts a wall heat flux roughly 40% larger than Gardiner's model, i.e about 70K discrepancy in radiative equilibrium wall temperature on the rear part of the shuttle.

- At lower altitudes (figures 59 and 63), the velocity has decreased while the density still increases so that the flow get closer to chemical equilibrium. As the velocity is lower, only oxygen dissociates now. Oertel's model gives predictions similar to equilibrium flow. Bortner and Gardiner models agree and still show a wall catalycity effect, i.e chemical equilibrium is not yet reached.

It must be mentionned that the circles on figures 60 to 63 are flight data. They must not be compared with the computations as in the computations the wall temperature was overestimated and the heat fluxes so underestimated. Moreover, entropy swallowing effects were not accounted for and the geometry was only an approximate one.

The study of the influence of chemical reaction rate on the other boundary layer parameters shows that the velocity profile is not modified while the mass fraction and temperature profile depend upon the reaction rate, so that the evolution

Figure 60: Influence of the chemical reaction rate on the wall heat flux at 85.74 km (from [44])

Figure 61: Influence of the chemical reaction rate on the wall heat flux at 77.91 km (from [47])
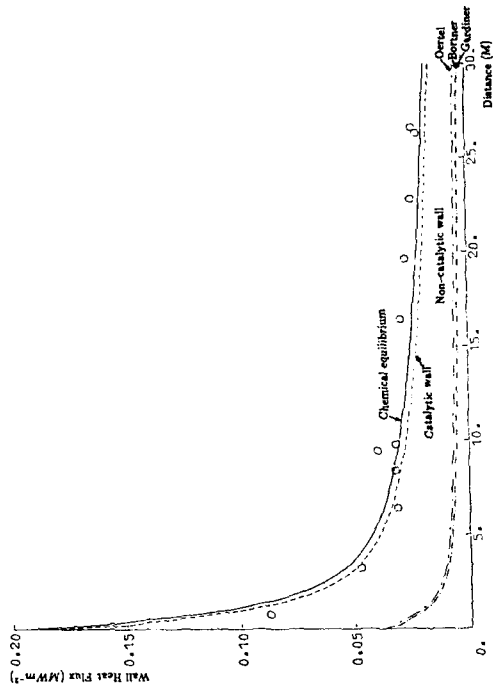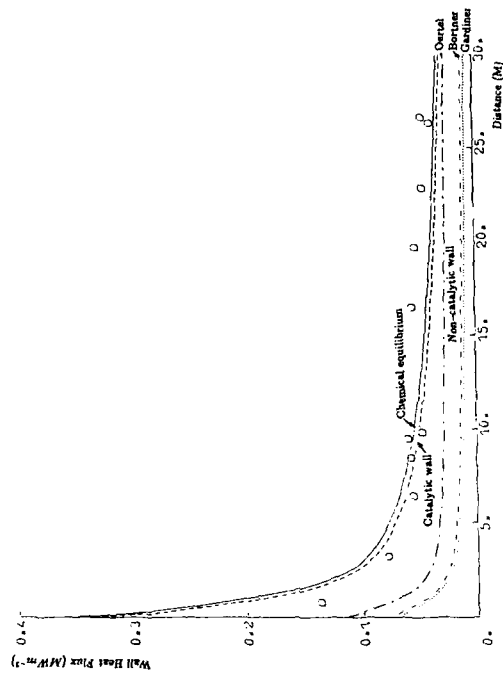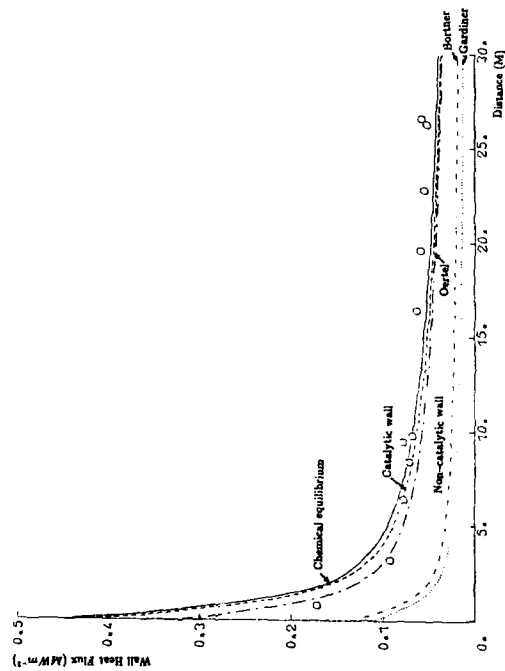

Figure 62: Influence of the chemical reaction rate on the wall heat flux at 71.29 km (from [44])
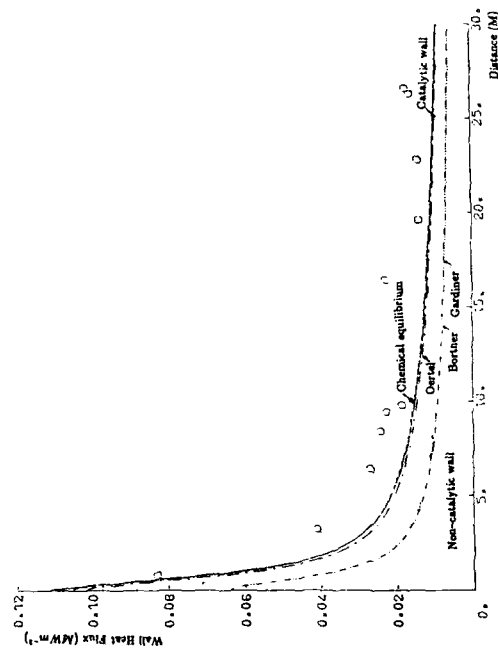
Figure 63: Influence of the chemical reaction rate on the wall heat flux at 47.67 km (from [44])

of the density profile cannot be a-priori predicted. Consequently the skin friction coefficient is not significantly modified by the chemical model while large variations of the displacement thickness, of about a factor of two are observed.

The influence of reaction rate was also studied by Shinn [97] who only compared finite reaction rates chemical equilibrium in viscous shock layer computations. If the flow is assumed to be at chemical equilibrium, it is already dissociated downstream of the shock wave while for finite reaction rates, the species mass fractions are conserved through the shock wave and the flow relaxes downstream. The temperature profiles are thus different as in equilibrium flow a part of the energy has been
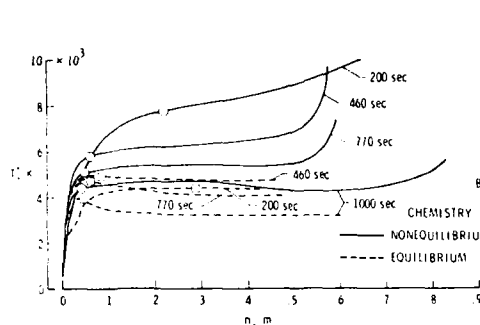
Figure 64: Shock layer temperature profiles on STS-2 centerline at 30% chord (from [97])
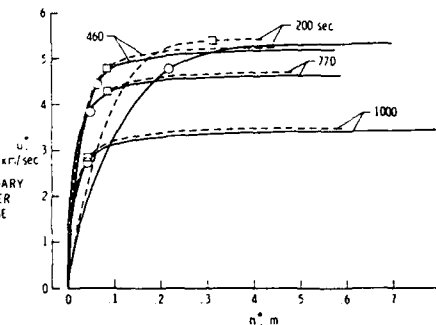
Figure 65: Shock layer velocity profiles on STS-2 centerline at 30% chord (from [97])

removed as species formation enthalpy, so that the temperature is lower for equilibrium flows (figure 64). The mass fraction profiles are also affected not only just behind the shock wave but down to the wall (figures 66 and 67). However, the velocity profiles are very close (figure 65) although the shock layer thicknesses are different.

8.3 Model reduction for boundary layer flows

In order to reduce the computation time, model simplifications are usually introduced. A systematic study of model simplifications from the analysis of "complete" model calculations has been performed by Eldem [8][9] [36] [44] for boundary
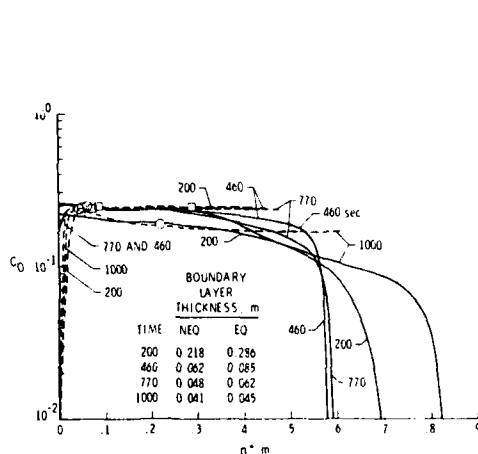
Figure 66: Shock layer atomic oxygen mass fraction profiles on STS-2 centerline at 30% chord (from [97])
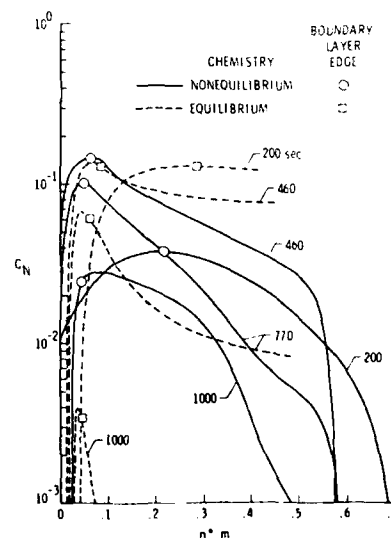
Figure 67: Shock layer atomic nitrogen mass fraction profiles on STS-2 centerline at 30% chord (from [97])

layer flows on the STS-2 reentry.

As concerns chemistry, a good approximation to represent all the process with a reduced set of chemical reactions is the Zeld'ovich model, i.e

$$O_2 + N_2 \rightleftharpoons O + O + N_2$$
$$N_2 + O \rightleftharpoons NO + N$$
$$NO + O \rightleftharpoons N + O_2$$
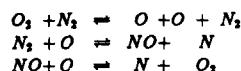
At low altitudes, the prediction can be improved by taking into account two more oxygen dissociation reactions

$$O_2 + O_2 \rightleftharpoons O + O + O_2$$
$$O_2 + O \rightleftharpoons O + O + O$$

as only oxygen dissociates at the end of the reentry due to the decrease of the velocity. These results are in agreement with previous results obtained by Blottner [17] who brought into evidence the major rôle of the oxygen dissociation and the shuffle reactions. To get a perfect agreement with the complete calculations all over the reentry trajectory, five more reactions of nitrogen and nitrogen monoxide dissociation are needed.

$$N_2 + N_2 \rightleftharpoons N + N + N_2$$
$$N_2 + N \rightleftharpoons N + N + N$$
$$NO + N_2 \rightleftharpoons N + O + N_2$$
$$NO + N \rightleftharpoons N + N + O$$
$$NO + O \rightleftharpoons N + O + O$$

The seven other reactions play no rôle and can be neglected.

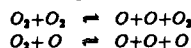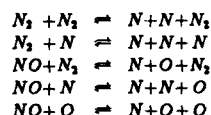As concerns the transport, the thermal diffusion is a second order effect and can be neglected. Moreover, the Prandtl number remains quite constant in all the flow during the whole reentry so that a constant Prandtl number can be assumed without modifying model predictions. At last, analysis of the species diffusion shows that it can be roughly modelled by a Fick law but that the Lewis number is not the standard 1.4 value but closer to 1, in agreement with Cohen results [33] (figure 34). A value of 1.2 gives fair predictions all over the STS-2 reentry trajectory.

At last, polynomials fits to thermodynamic functions [52] give the same results than calculations from the partition function.

Readers can refer to [8] [9] [36] [44] for more details.

9   Flows with ionization

Ionisation is an important parameter as it alters radio transmissions and is responsible for black-out phenomenon during reentry or radar detection as concerns missiles. Plasma is a high-pass filter the cut-off frequency of which can be expressed as

$$f_c = 8.97\sqrt{N_e}$$

where f_c is in Herts and N_e is the electron density, i.e the number of electrons per volume unit (here per cubic meter). This electron density can be expressed from the electron mass fraction as

$$N_e = \frac{\rho Y_e}{m_e}$$

This explains why the black-out phenomenon does not occur at the beginning of the reentry when the vehicle has the maximum velocity (and hence the maximum electron mass fraction is achieved) as the air density is too weak. Black-out is observed at lower altitudes when the vehicle velocity is still large enough while the pressure and thus the density have increased.

9.1   Flow around bodies

In section 8, it has been stated that the ionisation can be neglected for boundary layer calculations at shuttle reentry conditions. This can be stated from figures 16, 17 24, 25 and 41 which shows that, in such conditions, ionisation is very weak. Electrons are mainly due to ionisation of nitrogen monoxide but only about one–percent of nitrogen monoxide ionises. The ionisation process consequently does not affect the thermodynamic budget of the flow as the energy required for flow dissociation is much more larger than for flow ionisation. The energy, mass fraction and velocity profiles are thus unchainged by the ionisation process (see e.g [25]).

For higher velocities, the ionisation is no longer due to nitrogen monoxide ionisation but to atomic nitrogen and oxygen ionisation. This can be seen from figures 23 and 24 on which the ionised nitrogen monoxide mass fraction decreases at high temperatures while the electron density increases. This can also been observed on figure 17 assuming that a density decrease at constant temperature has the same effect as a temperature increase at constant pressure.

Evans [45] proposed a maximum velocity of $6000 ms^{-1}$ below which only nitrogen monoxide ionisation is to be accounted for and a minimum velocity of $9000 ms^{-1}$ above which the ionisation is due to atomic oxygen and nitrogen.

Dunn [43] showed that for reentry plasma around the RAM–CII body, at velocities of about $7500 ms^{-1}$, the above presented eleven species model must be used (see section 3.2).

All the above mentionned studies were done with a thermodynamic equilibrium assumption. Only recent calculations account for electron temperature non–equilibrium as the one performed by Park [87] and presented in section 7.

9.2 Wakes

Because or their length and level of observability, blunt body wakes are of practical importance in missile detection. The state-of-the-art twenty years ago is published in [48]. A particular feature of wake flow is the large range of pressure and temperature conditions encountered as the flow relaxes from the hot shock layer around the body to a cool expanding far wake. Therefore, negative ions and nitric oxides which are stable only at low temperatures must be accounted for in the far wake model while they are negligible around the body. This can be shown from figure 68. Succesive regimes are observed
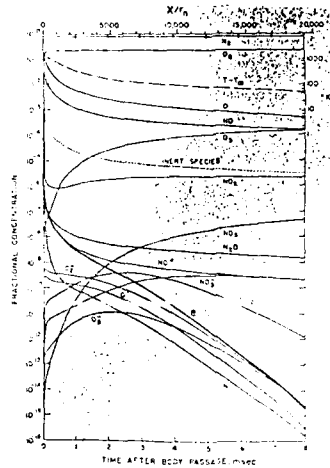

Figure 68: Species mole fractions in the wake of a 4.76mm diameter sphere at $5730ms^{-1}$ in a 520 Pa atmosphere (from [102])

- Very close to the body, the electrons are mainly due to nitrogen monoxide ionization as stated before but, at larger distances, other processes become important.

- At about 1000 radii behind the body, the gas is less hot ($T{\sim}1000K$) and electron density is depleted by the neutralization process

$$NO^+ + e^- \rightleftharpoons N + O$$
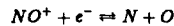
and by the O_2^- formation

$$e^- + O_2 + M \rightleftharpoons O_2^- + M$$

while sustained by O^- and O_2^- neutralization reactions

$$
\begin{array}{rcl}
O_2^- + M & \rightleftharpoons & O_2 + e^- + M \\
O_2^- + O & \rightleftharpoons & O_3 + e^- \\
O^- + O & \rightleftharpoons & O_2 + e^- \\
O^- + NO & \rightleftharpoons & NO_2 + e^-
\end{array}
$$
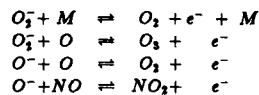
- In the far wake, at about 10000 body radii, the temperature has felt to ambient level. Electrons are now lost either by

$$NO^+ + e^- \rightleftharpoons N + O$$
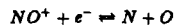
or by formation of NO_2^- and NO_3^- while a complex exchange cycle takes place between O^-, O_2^- and O_3^-.

Sutton study deals with a pure air experiment. Much more complex chemistry model may be needed when carbon-dioxide is present and leads to other ionized species or when other species, either ablated species or ad-hoc species such as sodium, are injected in the flow to modify the electron density [30].

This last example shows how the chemical model may vary with the temperature and pressure conditions. It must be reminded that Arrhenius forms are just fair fits to measured reaction rate coefficients and may not be valid over the whole range of temperature. Zonal models are thus required in such conditions [102].

Conclusions

Real gas effects are due to the transformation of an hypervelocity flow in an hyperenthalpy flow. The high temperature flow is thus the room of various phenomena, either thermodynamic or chemical non-equilibria and relaxations.

The classic aerodynamics used for sub- and supersonic flows of ideal gases is no longer valid and new physics must be introduced. Description of the basic phenomena leads to the knowledge of the flow behaviour. The knowledge of the way energy is stored in particles provides all the thermodynamic description while the knowledge of the way particle interact at the microscopic level leads to the flow governing equations and to the chemical model.

Two main problems are then to be faced. The first is due to the model uncertainties. The interparticle potentials from which the transport properties are computed are not well known. The uncertainties upon reaction rate constants lead to large discrepancies in the flow computation, e.g 40% uncertainties in wall heat fluxes.The determination of surface properties (catalycity, emissivity) and their time evolution is also an important problem for vehicle optimisation. Basic experiments are required to improve the current state-of-art.

The second one is the choice of the adequate model. Simplified models are always looked for to save computational time. The validity of a simplified model can only be proved by comparison with a more complete model. But leading phenomena depend upon the pressure, the temperature and the boundary conditions. They also depend upon what is looked for. For example, very sophisticated models are not required to compute the heat flux on a space shuttle with a catalytic wall while thermal relaxation is the main parameter in laser flows to determine the vibrational level populations and the radiation. Similarly, the choice of the important chemical species may strongly depend upon the considered part of the flow as shown in the last example.

Finally, as the vehicle design relies upon both numerical methods and wind-tunnel testings, it must be stressed that hypersonic facilities are very useful to simulate one phenomenon but are unable to duplicate all the flight conditions. As extrapolation from wind-tunnel data to flight are sometimes hazardous (see e.g [70]) flight experiments in realistic situations are required to validate numerical models.

References

[1] R.A. Allen P.H. Rose J.C. Camm *Nonequilibrium and Equilibrium Radiation at Super-Satellite Reentry Velocities* Research Report 156 AVCO-Everett Research Laboratory 1962

[2] D.O. Allison *Calculation of Thermodynamic Properties of Arbitrary Gas Mixtures with Modified Vibrational-Rotational Corrections* NASA-TN-D-3538 1966

[3] J.D. Anderson *A Survey of Modern Research in Hypersonic Aerodynamics* AIAA Paper 84-1578

[4] J.P. Appleton K.N.C. Bray *The Conservation Equations for a Nonequilibrium Plasma* Journal of Fluid Mechanics Vol 20 Part 4 pp 659-672 1964

[5] B.F. Armaly K. Sutton *Viscosity of Multicomponent Partially Ionized Gas Mixtures* AIAA Paper 80-1495

[6] S. Arrhenius *Über die Reaktiongeschwindigkeit bei der Inversion von Rohrzucker durch Säuren* Z. Physik Chem Vol 4 No 226 1889

[7] J. Aubreton *Etude des propriétés thermodynamiques et de transport dans les plasmas thermiques à l'équilibre et hors d'équilibre thermodynamiques: Applications aux plasmas de mélange Ar-H2 et Ar-O2* Thèse d'état Université de Limoges. 1985

[8] B. Aupoix C. Eldem J. Cousteix *Couche limite hypersonique. Etude paramétrique de la représentation des effets de gaz réel* Aerodynamics of Hypersonic Lifting Vehicles AGARD-CP-428 1987

[9] B. Aupoix D. Arnal C. Eldem *Problèmes de couches limites liés au projet Hermès* AAAF 24-ième Colloque d'Aérodynamique Appliquée. Poitiers 1987

[10] M. Barrère R. Prud'homme *Equations fondamentales de l'aérothermochimie* Masson 1973

[11] D.L. Baulch D.D. Drysdale D.G. Horne *Evaluated Kinetic Data For High Temperature Reactions. Volume 2: Homogeneous Gas Phase Reactions of the H2 - N2 - O2 System* London Butterworths 1973

[12] P. Benedek F. Olti *Computer Aided Chemical Thermodynamics of Gases and Liquids* Wiley-Interscience Publication John Wiley & Sons 1985

[13] B.A. Bhutta C.H. Lewis F.A. Kautz *A Fast Fully Iterative Parabolized Navier-Stokes Scheme For Chemically-Reacting Reentry Flows* AIAA Paper 85-0926

[14] L. Biolsi P.M. Holland *Transport Properties for some Atom-Ion Interactions in Air* AIAA Paper 85-0915

[15] L. Biolsi D. Biolsi *Transport Properties of Ions* AIAA Paper 87-0409

[16] F.G. Blottner *Chemical Nonequilibrium Boundary Layer* AIAA Journal Vol 2 No 2 pp 232-240 1964

[17] F.G. Blottner *Nonequilibrium Laminar Boundary Layer Flow of Ionized Air* AIAA Journal Vol 2 No 11 pp 1921-1927 1964

[18] F.G. Blottner *Electron Number Density Distribution in the Laminar Boundary Layer on Sharp Cones* AIAA Journal Vol 7 No 6 pp 1064-1069 1969

[19] F.G. Blottner *Finite Difference Methods of Solution of the Boundary Layer Equations* AIAA Journal Vol 8 No 2 pp 193-205 1970

[20] G.C. Bond *Heterogeneous Catalysis. Principles and Applications* Oxford Science Publications 1987

[21] C. Bonnefoi *Contribution à l'étude des méthodes de résolution de l'équation de Boltzmann dans un plasma à deux températures: exemple le mélange Argon-Hydrogène* Thèse d'état. Université de Limoges 1983

[22] M.H. Bortner *A Review of Rate Constants of Selected Reactions of Interest in Re-entry Flow Fields in the Atmosphere* NBS Technical Note 484 1969

[23] S. Bourcier *Diatomic Molecules. A Critical Bibliography of Spectroscopic Data* Tables Internationales de Constantes. Centre National de la Recherche Scientifique 1973 – 1975

[24] D. Boyer *Species Composition Measurements in Non Equilibrium High Speed Flows* Aerodynamics of Hypersonic Vehicles AGARD-FDP-VKI Lecture 1988

[25] J.P. Brazier B. Aupoix *Découplage de l'ionisation dans les couches limites hypersoniques* Rapport technique DERAT 21/5005 1988

[26] R. Brun *Transport et relaxation dans les écoulements gazeux* Masson 1986

[27] R. Brun *Non-Equilibrium Effects in High Speed Flows: Modeling and Experimentation* First Joint Europe-US Short Course on Hypersonics Paris. 1987 (To Le published by Birkauser Boston)

[28] R. Brun P. Colas P. Gubernatis D. Zeitoun *Etude théorique du non-équilibre physico-chimique à l'aval d'un choc fort* Contrat d'étude et de Recherche AMD-BA No 5-RDMF 86 Université de Provence Laboratoire S.E.T.T.

[29] C. Bruno *Real Gas Effects* First Joint Europe-US Short Course on Hypersonics Paris. 1987 (To be published by Birkauser Boston)

[30] M.L. Carnicom *Reaction Rates for High-Temperature Air with Carbon and Sodium Impurities* Sandia Laboratories SC-R-68-1799 1968

[31] S. Chapman T.G. Cowling *Mathematical Theory of Non Uniform Gases* Cambridge University Press 1939

[32] J.F. Clarke *Physico-Chemical Gas Dynamics* First Joint Europe-US Short Course on Hypersonics Paris. 1987 (To be published by Birkauser Boston)

[33] N.S. Cohen *Correlation Formulas and Tables of Density and Some Transport Properties of Equilibrium Dissociating Air for Use in Solutions of the Boundary Layer Equations* NASA-TN-D-194 1960

[34] H. Consigny C. Pacou O. Papirnyk P. Sagnier J.P. Chevallier *Préparation d'essais probatoires d'un générateur de plasma pour l'alimentation d'une soufflerie hypersonique* Aerodynamics of Hypersonic Lifting Vehicles AGARD-CP-428 1987

[35] D.M. Cooper R.L. Jaffe J.O. Arnold *Computational Chemistry and Aeroassisted Orbital Transfer Vehicles* Journal of Spacecraft Vol 22 No 1 pp 60 67 1985

[36] J. Cousteix B. Aupoix *Calculations of Hypersonic Laminar Boundary Layers* First Joint Europe-US Short Course on Hypersonics Paris. 1987 (To be published by Birkauser Boston)

[37] C. Danton *Modélisation de l'évolution des concentrations dans un jet raréfié de plasma d'azote en déséquilibre thermique* Thèse Université de Paris-Sud Orsay 1988

[38] G.S. Deiwert *Aerothermodynamics Research at NASA Ames* Aerothermodynamics of Hypersonic Lifting Vehicles AGARD-CP-428 1987

[39] R.S. Devoto *Transport Properties of Ionized Monoatomic Gases* The Physics of Fluids Vol 9 No 6 pp 1230-1240 1966

[40] R.S. Devoto *Transport Coefficients of Partially Ionized Argon* The Physics of Fluids Vol 10 No 2 pp 354-364 1967

[41] R.S. Devoto *Simplified Expressions for the Transport Properties of Ionized Monoatomic Gases* The Physics of Fluids Vol 10 No 10 pp 2105-2112 1967

[42] W.H. Dorrance *Viscous Hypersonic Flow* Mc Graw-Hill Book Company 1962

[43] M.G. Dunn S.W. Kang *Theoritical and Experimental Studies of Reentry Plasma* NASA CR-2232 1973

[44] C. Eldem *Couches limites hypersoniques avec effets de dissociation* Thèse ENSAE No 9-1987

[45] J.S. Evans C.J. Schexnayder P.W. Huber *Computation of Ionization in Re-entry Flowfields* AIAA Journal Vol 8 No 6 pp 1082-1089 1970

[46] P. Fauchais *Measurement Techniques in High Temperature Gases: Temperatures, Equilibrium Conditions, Species Densities, Flow Velocity* First Joint Europe-US Short Course on Hypersonics Paris. 1987 (To be published by Birkauser Boston)

[47] J.A. Fay F.R. Riddell *Theory of Stagnation Point Heat Transfer in Dissociated Air* Journal of the Aeronautical Sciences vol 25 No 2 pp 73-85 1958

[48] *Fluid Physics of Hypersonic Wakes* AGARD CP No 19 1967

[49] W.C. Gardiner Jr *Combustion Chemistry* Springer Verlag 1984

[50] A. Gicquel S. Cavadias J. Amouroux *Heterogeneous Catalysis in Low-Pressure Plasma* Journal of Physics D Applied Physics Vol 19 pp 2013-2042 1986

[51] A. Gicquel *Etude des processus catalytiques hétérogènes dans les milieux plasmas basse pression hors-équilibre* Thèse d'état Université Paris 6 1987

[52] S. Gordon B.J. Mc Bride *Computer Program for the Calculation of Complex Chemical Equilibrium Compositions, Rocket Performance, Incident and Reflected Shocks and Chapman-Jouguet Detonations* NASA SP 273 1971

[53] R. Goulard *On Catalytic Recombination Rates in Hypersonic Stagnation Heat Transfer* Jet Propulsion pp 737-745 1958

[54] M. Grabau *A Method of Forming Continuous Empirical Equations for the Thermodynamic Properties of Air from Ambient Temperature to 15000K with Applications* AEDC TN-59-102 1959

[55] R.A. Graves Jr J.L. Hunt *NASA's Hypersonic Fluid and Thermal Physics Programm (Aerothermodynamics)* AIAA Paper 85-0922

[56] B. Halpern D.E. Rosner *Chemical Energy Accomodation at Catalyst Surfaces* Chemical Society of London Faraday Transactions I Physical Chemistry Vol 74 Part 8 pp 1883-1912 1978

[57] C.F. Hansen S.P. Heims *A Review of the Thermodynamic, Transport, and Chemical Reaction Rate Properties of High-Temperature Air* NACA TN 4359 1958

[58] C.F. Hansen *Approximations for the Thermodynamic and Transport Properties of High Temperature Air* NASA TR R-50 1959

[59] C.F. Hansen *Rate Processes in Gas Phase* NASA Reference Publication 1090 1983

[60] U.R. Hattikudur G. Thodos *Equations for the Collision Integrals $\Omega^{(1,1)*}$ and $\Omega^{(2,2)*}$* Journal of Chemical Physics Vol 52 p 4313 1970

[61] J. Heicklen *Gas-Phase Chemistry of Reentry* AIAA Journal Vol 5 No 1 pp 4-15 1967

[62] J. Hilsenrath M. Klein *Tables of Thermodynamics Properties of Air in Chemical Equilibrium Including Second Virial Corrections from 1500K to 15000K* AEDC-TR-65-58 1965

[63] J.O. Hirschfelder C.F. Curtiss R.B. Bird *Molecular Theory of Gases and Liquids* John Wiley and Sons 1954

[64] M.S. Holden *A Review of Aerothermal Problems Associated with Hypersonic Flight* AIAA Paper 86-0267

[65] H. Hornung *Laboratory Simulation of the Real Gas Effects of Reentry* Fluid Dynamics & Space ESA-SP-265 1986

[66] H.M. Hulburt J.O. Hirschfelder Journal of Chemical Physics vol 35 p 1901 1961

[67] S.W. Kang M.G. Dunn *Theoritical and Measured Electron Density Distributions for the RAM Vehicle at High Altitudes* AIAA Paper 72-689

[68] R.J. Kee J. Warnatz J.A. Miller *A FORTRAN Computer Code Package for the Evaluation of Gas-Phase Viscosities, Conductivities, and Diffusion Coefficients* Sandia Report SAND83-8290 1983

[69] R.J. Kee F.M. Rupley J.A. Miller *The CHEMKIN Thermodynamic Data Base* Sandia Report SAND87-8215 1987

[70] G. Koppenwallner *Low Reynolds Number Influence on Aerodynamic Performance of Hypersonic Vehicles* Aerodynamics of Hypersonic Lifting Vehicles AGARD-CP-428 1987

[71] K. Koura *Electron and Vibrational Energy Conservation Equations for Aeroassisted Orbital Transfer Vehicles* AIAA Journal Vol 25 No 1 pp 178-179 1987

[72] J.D. Lambert *Vibrational and Rotational Relaxation in Gases* Clarendon Press Oxford 1977

[73] J.H. Lee *Basic Governing Equations for the Flight Regimes of Aeroassisted Orbital Transfer Vehicles* AIAA Paper 84-1729

[74] J.H. Lee *Electron-Impact Vibrational Excitation Rates in the Flow Field of Aeroassisted Orbital Transfer Vehicles* AIAA Paper 85-1035

[75] C.H. Lewis *Current Status of Computational Aerothermodynamics* AIAA Paper 86-0229

[76] M.J. Lighthill *Dynamics of a Dissociating Gas Part 1. Equilibrium Flow* Journal of Fluid Mechanics Vol 2 pp 1-32 1957

[77] M.J. Lighthill *Dynamics of a Dissociating Gas Part 2. Quasi-equilibrium Transfer Theory* Journal of Fluid Mechanics Vol 8 pp 161-182 1960

[78] P.V. Marrone C.E. Treanor *Chemical Relaxation with Preferential Dissociation from Excited Vibrational Levels* The Physics of Fluids Vol 6 No 9 1963

[79] E.A. Mason C.S. Saxena *Approximate Formula for the Thermal Conductivity of Gas Mixtures* The Physics of Fluids Vol 1 p 361 1958

[80] G.A. Mellin R.J. Maddix *Energy Accomodation During Oxygen Atom Recombination on Metal Surfaces* Faraday Society Transactions Vol 67 pp 198-211 1971

[81] R.C. Millikan D.R. White *Systematics of Vibrational Relaxation* Journal of Chemical Physics Vol 39 No 12 pp 3209-3213 1963

[82] L. Monchick K.S. Yun E.A. Mason *Formal Kinetic Theory of Transport Phenomena in Polyatomic Gas Mixtures* The Journal of Chemical Physics Vol 39 No 3 pp 654-669 1963

[83] E. Obermeier A. Schaber *A Simple Formula for Multicomponent Gaseous Diffusion Coefficients Derived from Mean Free Path Theory* International Journal of Heat and Mass Transfer Vol 20 pp 1301-1306

[84] H. Oertel *Stoßrohre* Springer-Verlag 1966

[85] F. Offenhäuser A. Frohn *Deviations from the Boltzmann Distribution in Vibrationally Excited Gas Flows* 10th ICDERS Berkeley 1985

[86] C. Park G.P. Menees *Odd Nitrogen Production by Meteroids* Journal of Geophysical Research Series C Vol 83 No 8 pp 4029-4035 1978

[87] C. Park *Problems of Rate Chemistry in the Flight Regimes of Aeroassisted Orbital Transfer Vehicles* AIAA Paper 84-1730

[88] C. Park *On Convergence of Computation of Chemically Reacting Flows* AIAA Paper 85-0247

[89] C. Park *Assessment of Two-Temperature Kinetic Model for Dissociating and Weakly-Ionizing Nitrogen* AIAA Paper 86-1347

[90] T.C. Peng A.L. Pindroh *An Improved Calculation of Gas Properties at High Temperatures: Air* American Rocket Society Fourth Biennal Gas Dynamics Symposium 1961

[91] J.M. Picone E.S. Oran *Approximate Equations for Transport Coefficients of Multicomponent Mixtures of Neutral Gases* NRL Memorandum Report 4384 1980

[92] D.K. Prabhu J.C. Tannehill J.G. Marvin *A new PNS Code for Chemical Nonequilibrium Flows* AIAA Paper 87-0284

[93] S. Raffanel *Propriétés thermodynamiques et de transport de mélanges gazeux: Azote / Oxygène / Argon dans les domaines 1 <p< 200 atm, 1000 < T< 30000K* Thèse Université Paul Sabatier Toulouse No 170 1987

[94] K. Schäfer *Statistiche Theorie der Materie. Bd. I* Göttingen Vandenhoek 1960

[95] C.D. Scott *Catalytic Recombination of Nitrogen and Oxygen on High-Temperature Reusable Surface Insulation* AIAA Paper 80-1477

[96] C.D. Scott *The Effects of Thermochemistry, Nonequilibrium, and Surface Catalysis in the Design of Hypersonic Vehicles* First Joint Europe-US Short Course on Hypersonics Paris. 1987 (To be published by Birkauser Boston)

[97] J.L. Shinn J.N. Moss A.L. Simmonds *Viscous Shock-Layer Heating Analysis for the Shuttle Windward Symmetry Plane with Surface Finite Catalytic Recombination Rates* AIAA Paper 82-0842

[98] S. Srinivasan J.C. Tannehill K.J. Weilmuenster *Simplified Curve Fits for the Thermodynamic Properties of Equilibrium Air* Engineering Research Institute Iowa State University 1986

[99] R.J. Stalker *Shock Tunnels for Real Gas Hypersonics* Aerodynamics of Hypersonic Lifting Vehicles AGARD–CP–428 1987

[100] D. Straub *Exakte Gleichungen für die Transportkoeffizienten eine Fünfkomponentengemisches als Modellgas dissoziieter Luft* DLR-FB 72–34 1972

[101] D.R. Stull H. Prophet *JANAF Thermochemical Tables* National Standard Reference Data System NSRDS–NBS 37 1970

[102] E.A. Sutton *Chemistry of Electrons in Pure-Air Hypersonic Wakes* AIAA Journal Vol 6 No 10 pp 1873–1882 1968

[103] C.E. Treanor P.V. Marrone *Effects of Dissociation on the Rate of Vibrational Relaxation* The Physics of Fluids Vol 5 No 9 1962

[104] J.T. Vanderslice E.A. Mason E.R. Lippincott W.G. Malsch Journal of Chemical Physics vol 32 p 515, vol 33 p 615 1960

[105] W.G. Vincenti C.H. Kruger Jr *Introduction to Physical Gas Dynamics* Robert E. Krieger Publishing Company 1965

[106] F. Wecken *Données concernant la cinétique des réactions dans l'air entre 500 K et 10000 K* Note de Documentation Institut Saint Louis D 4/68 1968

[107] F. Westley *Table of Recommended Rate Constants for Chemical Reactions Occuring in Combustion* NSDRS–NBS 67 1980

[108] C.R. Wilke *A Viscosity Equation for Gas Mixtures* The Journal of Chemical Physics. Vol 18, No 4 pp 517–519 1950

[109] J.M. Yos *Transport Properties of Nitrogen, Hydrogen, Oxygen and Air to 30000K* Research and Advanced Development Division AVCO Corporation RAD–TM–63–7 1963

[110] J. Yos *Revised Transport Properties for High Temperature Air and Its Components* AVCO 1967

[111] K.S. Yun E.A. Mason *Collision Integrals for the Transport Properties of Dissociating Air at High Temperatures* The Physics of Fluids. Vol 5 No 4 pp 380–386 1962

[112] B. Zappoli *Asymptotic Solution of the Diatomic Boltzmann Equation* The Physics of Fluids Vol 26 No 1 pp 50–51 1983

[113] E.V. Zoby R.N. Gupta A.L. Simmonds *Temperature Dependent Reaction Rate Expression for Oxygen Recombination at Shuttle Entry Conditions* AIAA Paper 84–0224

AEROTHERMODYNAMIC INSTRUMENTATION

by

Richard D. Neumann
Technical Manager for Aerothermodynamics
Air Force Wright Aeronautical Laboratories
Wright-Patterson Air Force Base, Ohio 45433 USA

Section I
INTRODUCTION

Engineering involves understanding the response of a physical system to changes in imposed criteria or ground rules. Engineering solutions are, therefore, not static nor absolute but vary with the nature of the problem posed. Serious difficulties can be introduced by a routine engineering response to a newly posed question; the 'force-fitting' of yesterday's technology to tomorrow's problems.

Instrumentation being a sub-set of engineering problems follows this trend. Instrumentation solutions are NEVER static nor absolute, they change with the nature of the problem that is posed. There are several reasons for investigating instrumentation. They are:

    1. To be able to measure what has not been measured before; a reason driven by the very healthy contemporary tension between computational fluid dynamics (CFD) and experimentation.

    2. To upgrade routine measurements with newer, state of the art instrumentation devices. An example of this is the replacement of older mechanical scani-valve pressure measuring systems with newer electronic scanning pressure measurement systems.

    3. To employ test facilities more effectively. This reason refers both to technical and economic responses to the changing costs of experimental facilities, their instrumentation and test models.

The first reason is a response to a new technology, Computational Fluid Dynamics (CFD), that burst on the engineering scene as a supposed threat to experimentation but which, in retrospect, depends to a large extent upon experimentation and in turn challenges experimentation and instrumentation. In truth, CFD is not a threat but a spur to experimentation which, in turn, challenges our ability to instrument those experiments. CFD must start with experimental results to formulate the many models which are internal to the program and rely on a variant of that same experimentation to 'validate' the final composite product. Experimentation produces that data but in so doing must admit the difficulty in producing needed measurements as well as the inherent errors in measurement technology; errors made more obvious by highly sophisticated numerical modeling of the flow field. An excellent paper demonstrating this process of interaction between numerics and experimentation is that of Griffith et al, 1983, which discusses the application of aerodynamic coefficient data taken at Mach 8 to flight conditions shown in figure 1.

The second reason for investigating instrumentation is both a response to newer technology and a response to economics. Newer instrumentation technology continually requires a re-assessment of the cost of measurements and the efficiency with which they can be accomplished. Newer gages may well be faster and less prone to malfunction and thus must be considered.

The third reason for investigating instrumentation is a response primarily to economics. Chapman, 1975, highlighted a frustrating trend in experimentation; an ever increasing use of wind tunnels to develop new aircraft. The Rockwell Space Shuttle is a stellar datapoint in this respect; an enormous application of experimentation. Experimentalists were required to respond to that trend as well as to new economic realities caused by the cost of energy. A fascinating feature about such a response is that it is rarely linear. Each level of challenge brings about new options in addition to the obvious option of improving past activities. The response to the challenge of higher energy costs has been to accomplish more with numerics as well as to compress testing times by orders of magnitude through the introduction of new test technologies. This area, which I call 'dynamic testing' will be discussed in greater detail later in these notes.

In the previous paragraph, the terms 'instrumentation' and 'experimentation' have been used somewhat interchangeably. Experimentation, within the context of these notes, is the use of wind tunnel type test facilities to produce a flow field that can be observed and understood. Instrumentation involves the techniques used to achieve and quantify those observations. Viewed in this manner instrumentation encompasses more than physical devices; it encompasses both the physical hardware and the mathematical software with which to understand flowfields. In recent years, an increasing percentage of time and effort is associated with this software and this relationship will be discussed in these notes.

The ability to measure a quantity of interest must be developed in relationship to the characteristics of the experiment undertaken. For a wind tunnel experiment, these characteristics are connected with the experimental facility and its limits; the model

used in '' : wind tunnel facility and the required response characteristics of the signal being measured. Further, that which is being measured may well be an intermediate step between the experiment and the desired knowledge. Not every quantity is directly measurable but every physical quantity is observable, either directly or indirectly, through experimental measurements.

This presentation on thermal instrumentation will progress from a discussion of the features of thermal instrumentation to a discussion of the thermal model simplifications implicit in thermal instruments to a definition and discussion of thermal gages, the products of these simplifications.

WHAT CONSTITUTES USEFUL HEAT TRANSFER DATA?

All of the problems and associated sources of error to be discussed in these notes can be made apparent by careful consideration of the answer to this question. The final objective of any heat transfer test is the determination of whether or not a particular structure will survive or fail at the thermal conditions to which it will be subjected. The goal then is the ability to compute real structural temperatures at real environmental conditions to be found in flight. In order to compute what these temperatures are going to be we must be able to predict the amount of heat transmitted to the structure from the environment in which it is to operate. This environment probably will not be reproduced in the test facility employed. If it is not, then the experimenter must be able to extrapolate the data obtained to the actual flight conditions. If this cannot be accomplished, the data will have no engineering value. A case in point is transitional data which is all too easy to generate but difficult to impossible to extrapolate to flight conditions.

The question then is 'how to measure the heat transfer rate in the test facility in such a way that it can be used to compute real structural temperatures in real operating environments?' Do we want to measure the heat transfer rate at the model wall or do we want to measure the heat transfer coefficient of the flow field at a specific location? There is a significant difference. The HEAT TRANSFER RATE at the model wall is a function not only of the flowfield but also of the model thermal properties and the structural configuration. These data cannot be used to predict the heating rate that would occur under either different flow conditions or on another model having a different internal structure and/or thermal properties. That is, the data so generated cannot be extrapolated to real flight hardware conditions. It is 'tainted' by the incidental features of the experiment and thus valid only for the particular test hardware and at the conditions of the test. The HEAT TRANSFER COEFFICIENT on the other hand is primarily a property of the flowfield. Defining the heat transfer coefficient through testing produces the correct boundary condition from which the surface heat transfer rate can be computed for any wall temperature. A finite element conduction code, which will be discussed later in these notes and which models the response of any particular wall structure, can then use this general boundary condition to predict both surface and in-depth temperatures as a function of time.

Obviously, the intent is to measure the heat transfer coefficient of the flow field. A measurement of only the heat transfer rate is of limited value. The heat transfer coefficient is, however, only a definition of the local relationship between the surface heat transfer rate, the flowfield recovery temperature and the wall temperature of the model.

$$h = q \; / \; (Tr - Tw)$$

A sensor which produces useful heat transfer data must provide both surface heating rate and wall temperature and be supported by either measurements or prior knowledge of recovery temperature. The sensor must also isolate the convective heating from the sum of all modes of heat transfer. Finally, it must not affect the flowfield of the test article in which it is placed. We must understand that the test article and the flow field are an inter-related physical system; one affects the other. The flowfield produces aerodynamic heating at the model surface by converting the kinetic energy of the flow into thermal energy through boundary layer deceleration. The thermal energy is dissipated through conduction and radiation according to the thermal model and structural properties. This dissipation of energy determines the surface temperature history. The surface temperature, in turn, affects the boundary layer thickness which, in turn, can affect the inviscid flow field. A change in the flow field in turn changes the level of aerodynamic heating.

It would seem at first observation that no useful data can ever be obtained in a test facility which can be reliably extrapolated to other conditions. As in all engineering problems, there are compromises and tradeoffs. In this case, the key is to minimize the effects of the model surface temperature on the flowfield by judicious design of the test model and its instrumentation. In particular, the test article must be designed so that its surface temperature will remain as isothermal as possible. The definition of the heat transfer coefficient will then be valid and useful for moderate variations in the global surface temperature.

This simple rule is difficult to implement and is the most often violated rule in the field of aerothermal instrumentation. If a gage is not thermally matched to the model wall then it not only disturbs the flowfield but also induces lateral conduction of heat between the gage and the surrounding model structure. In this case, the gage is now

measuring the sum of the aerodynamic heating caused by the flowfield deceleration and that of conduction. Unless the thermal model used in the data reduction program can account for all modes of heat conduction (which is very difficult), the resultant data is in error.

The answer to the original question then is that we must determine the heat transfer coefficient through the inference of the surface heating rate on an isothermal surface. No matter what type of gage is used to obtain the surface heating rate, it must be thermally matched to the model surface and provide an accurate surface temperature measurement as well. If not perfectly matched then the reduction technique must at least accurately model all modes of heat transfer to and from the sensing element.

WHAT IS A HEAT TRANSFER GAGE?

A heat transfer gage is the physical embodiment of a concept that reduces the general flow of heat into a structure to a more simplified and, hopefully, a uni-directional flow of heat and infers from that flow of heat the rate of surface heat transfer through strategic measurement(s) of temperature within the gage.

These gages must be both LOCALLY WELL DESIGNED and GLOBALLY WELL INTEGRATED. Locally well designed to simplify internal heat paths and heat modes while minimizing losses; classically the isolated heat transfer gage design problem. Globally well integrated into the model since convective heat transfer is a function of the flow history over the model as it affects the streamline washing the gage as well as the converging or diverging character of streamlines in the vicinity of the gage. It will be demonstrated that many of the 'classical' errors in measuring heat flux violate one of these basic assumptions.

WHY DOES THE METHOD OF HEAT TRANSFER MEASUREMENT CHANGE WITH TIME?

Why are we discussing the measurement of heat transfer at all? Clearly, there are many handbooks and sales brochures which cover commercial hardware for the measurement of heat transfer. What can we learn about the measurement of heat transfer that is not in these handbooks and above all, why not just continue to measure heat transfer as it has been measured in my particular laboratory for the past decades?

Heat transfer, as with many engineering subjects is part art and part science. The science part; the laws of heat flow and the modes of heat transfer, is well documented in textbooks and develops slowly. The art; the engineering application of this science to a particular situation, is not well documented. In fact, it may be totally overlooked in technical literature.

There are two reasons for continually upgrading and improving the quality of measurements being taken. Those reasons are:

1. To improve the informational content of the measurement. Here we can consider improving the sensitivity of a steady state measurement to accurately evaluate lower strength signals or the development of more rapidly responding instruments to understand the higher frequency aspects of a measurement. Consider two examples. Recently Professor Bogdenoff and others have started to investigate the high frequency aspects of pressure measurement - particularly for measurements in or near a separated flow region. Since most pressure transducers will not discriminate such a signal, newer instruments are required together with their associated data acquisition, conditioning, storage and analysis capabilities. As a second example, the shock tunnel experimenters have known for some time that very high frequency data from thin film transducers display the inherent characteristics of the boundary layer in which they are placed. In fact, much of the 'noise' associated with such gages is, rather, the measurement of the transitional behavior of the boundary layer over the gages. Conversely, there is growing understanding, to be demonstrated later, that an understanding of the boundary layer state is required. Such a merging of need and capability would require upgraded instrumentation.

2. To improve the economics of measurement. There are measurements that require substantial time to achieve. Reducing that time can reduce the cost of the measurement. Costs are reduced by either reducing 'air on' test times in the acquisition of measurements or by reducing the amount of labor intensive work to reduce measurements to useful data. An example here is the use of temperature sensitive paint to 'map' the heating to the surface. Such paints produce photographic data which is labor intensive to reduce and interpret. Similar data might be achieved using, instead, computer based data acquisition and processing equipment. These data, with the aid of VERY cost effective computers, can be handled much more effectively than reading photographs. As a second example, thin skin heat transfer 'gages' were used for decades to achieve point measurements of heating. These devices allowed the generation of a single condition during a tunnel run. Newer gages of a different design allow the generation of an entire pitch cycle of data during the same tunnel run. Tunnel operating costs are thus reduced and data quality is increased through the use of newer gages and their associated computer data manipulation techniques.

WHAT'S THE DIFFERENCE BETWEEN...

To further introduce the topic of aerothermal instrumentation, the following paragraphs will describe several similar physical situations which will be used to introduce concepts which will be discussed later in the notes.

Figure 2 indicates two gages similar in that both wrap metallic strips about the top of a cylinder. On the left, the strip is a wire (or film) of Platinum, a single metallic material. On the right, the strip is a wire of Platinum and Rhodium joined at the center of the cylinder. What's the difference ...? The two sketches in figure 2 demonstrate two completely different ways of 'measuring' temperature. On the left is a resistance thermometer which measures resistance in the Platinum film and relates that resistance to temperature through prior calibrations. The instrument employes a bridge circuit to measure the out of balance resistance of the film. The bridge requires an active current flow to measure the resistance and thus the resistance thermometer is termed a powered gage.

On the right is a thermocouple in which, at the junction of the dissimilar materials, an electromotive force (EMF) is generated and measured by a sensitive voltmeter. This EMF is related to temperature through prior calibrations. As an EMF is generated, no active current flow is required through the gage and it is termed unpowered. Both instruments are the basis of instrumentation used in test facilities and each will be discussed later.

Figure 3 demonstrates two thermocouples each on the surface of the cylinder of insulating material. In both cases the thermocouple junction is located at the same position. On the left, the wires eminating from the junction are immediately drawn away from the surface of the cylinder. On the right, the wires eminating from the junction remain on the surface of the cylinder for a short distance. What's the difference ? Metallic wires have a very different thermal response than insulators. As both cylinders in the figure heat up, the wires that more readily conduct heat will remain cooler than the cylinder which is an insulator. Heat will conduct from the insulator into the wires. The longer the length of wire on the surface of the cylinder about the junction, the less the temperature gradient at that junction. With a sufficient surface wire length, an thermal equilibrium is established between the wire and the insulator. Conversely, the shorter the surface wire length, the higher the thermal gradient in the wire. The gage on the right is an isothermal staple gage in which the heat removal by conduction at the junction of the thermocouple is minimized. The gage at the left would not be useful because of conduction losses down the wires and from the insulative cylinder into the wires.

Figure 4 shows a coaxial thermocouple arrangement set into cylinders. Coaxial thermocouples are constructed by placing a wire of one thermocouple material into a hollow cylinder of the dissimilar material. The two materials are then separated by an electrical insulation except where a junction is desired. The coax thermocouple on the left is placed in an insulator. The gage on the right is placed into a conductor whose properties match those of the thermocouple material. What's the difference ?

The difference is in the materials match between the coax thermocouple and the surrounding cylinder. Installing a coax thermocouple into an insulator creates a thermal heat sink and disturbs the thermal environment of the insulator. The coax thermocouple, as in the previous case, draws heat from the surrounding materials that, by virtue of their thermal properties, are hotter for the same uniform heat input. This gage further creates a cold spot on the surface of the cylinder. When the thermocouple and surrounding cylinder are convectively heated, the cold spot disturbs the thermal boundary layer changing the heat transfer to the surface.

These features of thermal instrumentation; how temperature is 'measured' and how temperature sensors are integrated into the structure of the model will be discussed further in these notes.

THE RELATION OF THIS REFERENCE TO THE WORK OF OTHERS

Schultz and Jones, 1973, produced an AGARDograph entitled 'Heat Transfer Measurements in Short Duration Hypersonic Facilities'. While this document was independently produced, a review of their work indicates how closely they are allied. Schultz and Jones have produced an excellent review of instrumentation processes for short duration facilities that, in many respects, can only be referenced reverently in these notes.

There are, however, several areas where these notes diverge from the previous work. First, the present notes are not focused on short duration facilities. These notes cover conventional test facilities as well. Second, there is a general updating and broadening of the database to include international instrumentation references. These references, indicate the creativity of researchers worldwide. Finally, these notes contain more personal commentary than the notes of Schultz and Jones. It is the intent of these notes to provide educational notes on instrumentation that indicate some opportunities in the field of instrumentation as well as current experiments to validate those opportunities. Our ability to improve our measurement capabilities is fundamental to more general developments in hypersonics.

In addition to the excellent review document by Schultz and Jones, two other reference documents are recommended. These are (1) Chapter 4 of Dr. Richards book, 1977, dealing with unsteady fluid dynamic phenomena; a book produced by the von Karman Institute. This chapter was prepared by T.V. Jones and is in some respects an update of the earlier work by Schultz and Jones and (2) a section of a more recent book entitled 'Methods of Experimental Physics', 1981, which was prepared by Thompson. All three of these references present excellent material on the general subject of aerothermal instrumentation.

CONCEPTUAL METHODS OF MEASURING HEAT FLUX

Thompson, 1981 prepared an excellent and concise review of heat transfer gages. In that review, he listed three conceptual methods for 'measuring' heat flux. They are:

(1) heat flux may be related to the temperature gradient set up in a thin material layer. These were termed 'sandwich' gages.

(2) heat may be captured within a thermal mass which acts as a calorimeter and whose transient temperature change can be related to heat flux.

(3) a heat balance in steady state may be established between in incoming aerodynamic heating and a calibrated heat removal process.

These conceptual methods of inferring heat flux should be kept in mind as we look at the many ways in which heat flux is measured.

The reader is cautioned however that although these categories represent fundamentally different methods for generating aerodynamic heating, there is not a unique relationship between the methods stated and their physical embodiment in a gage. The same physical gage, as for instance a wafer of material with a thermocouple attached to both the heated and backface surfaces, can be used to generate heat flux by any of the three stated methods. The differences among the methods have to do with the incidental interaction between the thermal diffusion time and test time.

Clearly, the gage shown in figure 5 is a 'sandwich gage'; Thompson's category 1. However, if the material properties are such that the heat does not diffuse to the backface surface within the test duration, the backface thermal sensor is not responsive and the gage becomes one in which the thermal pulse is 'captured' within the material mass. This is a Thompson category 2 gage and an example of it is a thin film gage. If the wafer of material is very thin and has high conductivity, the heated and backface temperatures will be the same (after a very short transition period due to thermal diffusion). The use of either thermocouple (the backface thermocouple is easier to use) will give rise to a calorimeter known as a thin skin gage. This is also a Thompson class 2 gage. Finally, if the backface of the wafer is heated or cooled with an active energy source (water or a Nichrome heater for instance), then this same device becomes a Thompson class 3 gage.

The gages to be discussed are designed through BOTH an understanding of various thermal models AND an appreciation of the limits of those models with thermal diffusion time.

THE INFLUENCE OF WIND TUNNEL TEST FACILITIES ON INSTRUMENTATION

The selection of aerothermal instrumentation is strongly influenced by the nature of the wind tunnel model, the type and quality of data required and the characteristics of the test facility employed.

THE NATURE OF THE WIND TUNNEL MODEL:

Historically, wind tunnel models were constructed of materials adequate to the test environment to be encountered and simple enough not to be the focus of the experiment itself. The materials of aerothermal wind tunnel models were classically either metallics, generally steels, or insulators. The principle characteristic of the models being that the materials and construction techniques were established as reliable.

Very recently, the concept of 'aero-structural' models has been introduced. Models in this form of testing are actual structural elements constructed of actual flight structural materials. The use of these materials complicates both the instrumentation and test issues. This type of testing will be discussed later in the notes.

TYPE AND QUALITY OF DATA REQUIRED:

There are several reasons for conducting aerothermal experiments and each requires a level of instrumentation somewhat different from the others. The reasons for testing are:
1. The development and validation of 'models'.
2. The understanding of the deviation of actual flow from established and normally closed form analytical models of flow.
3. The 'validation' of numerical computations.

In the past, most testing has been conducted to understand the deviation of the actual flow over a complex, three dimensional body from simplified flow models which were amenable to closed form analytic solution. This technique reached its ultimate application in the design of the Rockwell Space Shuttle where an extensive wind tunnel data base was established. The primary intent of this data base was to 'correct' the closed form analysis techniques about cones, cylinders and plates to account for three-dimensional effects that were not defined through the simplified solutions. This 'effect' testing required substantial heat transfer measurements supported by far less flow field data. It is termed 'effect testing' because the intent is to observe the effect rather than to define the cause of that effect.

In the same general time interval (although extending back to the late 1930's) there has also been a smaller and far more detailed effort to define and validate models of the flow. These models, such as turbulence models, reference temperature models, real gas flow models, definitions of Reynolds analogy factors and adiabatic wall temperatures to name a few were developed from empirical data of extremely high quality using far more detailed 'cause and effect' instrumentation. Such instrumentation is necessarily of higher quality and self supporting.

The 'validation' of numerical codes is a newer but still largely ill-defined use of experimentation. While such testing is discussed with increasing urgency of recent date, the design of such experiments, the necessary instrumentation and the underlying test philosophy are still undefined features of such testing. In general, there will be a need for far more detailed data, higher volumes of high quality data and the acquisition of far more complex measurements which stress cause and effect relationships in any flowfield.

THE CHARACTERISTICS OF AEROTHERMODYNAMIC TEST FACILITIES

There is a strong and emotional interrelationship between instrumentation and the basic characteristics of aerothermodynamic test facilities. From an instrumentation standpoint, the differentiating characteristics of these facilities are (1) the duration of the test and (2) the level of heating rate achieved during the test.

TEST DURATION:

Current and anticipated wind tunnel facilities operate or will operate from hundreds of microseconds to many minutes per run. Aerothermal instrumentation problems with regard to this time spectrum range from making ANY measurement in the very short run time test facilities to making accurate measurements during very long duration tests of actual flight hardware. Both ends of the time spectrum represent challenging technological problems in instrumentation. Both require an openness to new instrumentation hardware, acquisition techniques and analysis techniques.

Increased test Duration Is Not Always Good

There are several reasons why increased test duration is not of value in a new hypersonic test facility. Several of these reasons deal with the interaction between instrumentation and the test facility characteristics. Consider the following:

1. Model temperatures increase as the test duration increases. They create un-anticipated and un-measured thermal paths in the instrumentation due to conduction along or normal to the measurement surface and may even thermally deform or melt the model.

2. Model temperatures increase non-uniformly producing surfaces which are no longer isothermal

3. There are several instrumentation techniques which are invalidated by temperature increases in the model. These are based, for instance, on the piezoelectric effect. Extended duration tests require instrumentation that is not sensitive to temperature changes within the model. Local skin friction, for instance, can be routinely measured in a shock tunnel using piezoelectric gages but it is extremely difficult to measure in a continuous flow test facility.

4. Measurements that are not concurrently made may not be consistent. Heat transfer measurements are made within 2 seconds of injection. Pressure measurements require somewhat longer time and traditionally force and moment measurements are made with the model held in the tunnel for extended periods of time with surface temperatures approaching recovery conditions. For a heated test facility, the surface temperature of the model can vary by hundreds of degrees between these measurements. The ratio of wall to total temperature, which is varied, is a sensitive indicator of phenomena like separation. It is possible that under this test scenario one set of measurements would be conducted under conditions of control separation (the pressures and force and moment data) while another set of data would be conducted with no separation because of the gross differences in the ratio of the wall to total temperature between the two sets of data.

TEST ECONOMICS

Perhaps a decade ago the entire subject of test economics would never have been considered. Certainly the question presupposes an ability to make measurements at all. The newer test facilities exemplified by the development of Tunnel 9 at the Naval Surface Weapons Center are very expensive; typically $20,000 per one second run, and require attention to test efficiency. How much can be accomplished in a one second run?

The large aerodynamic test facilities at the Arnold Engineering Development Center, AEDC, represent another "opportunity" for creative instrumentation based upon the existing test economics. These facilities operate continuously for an entire test shift. Much of the airflow time is wasted during the aerothermodynamic tests because there is no model in the test section. At $10,000 per hour, these testing inefficiencies must be addressed in the instrumentation. A substantial contributor to wasted airflow time in these facilities is the physical manipulation of the model during the test process. Gaining access to the model can use 10 minutes of airflow time each time. During one typical test entry under the Space Shuttle program $40,000 was consumed manually changing the model control deflections. Newer instrumentation and model design concepts can dramatically reduce that cost. There are direct implications here for automated model changes; the use of motor driven control surfaces and alternative test techniques; the use of reversible temperature indicating coatings rather than irreversible coatings. These newer techniques are driven by economic rather than technical considerations. They are replacement techniques which reduce the overall cost of test operations and increase test efficiency.

NON-ISOTHERMAL WALL EFFECTS

The successful measurement of aerodynamic heating in either a ground test facility or in flight requires that the experimenter (1) properly locate thermal sensors in the structure of the model such that heat flux may be deduced through the application of simplified thermal models and (2) that these measurements be made so that the material does not know there is a thermal sensor installed. The second criterion implies, in part, that the model under consideration have no local disruption of the thermal boundary layer due to the presence of a gage; the model must be isothermal. Figure 6 from Schultz, 1965, indicates graphically the effects of placing poorly integrated gages into wind tunnel models.

This subject has been stressed throughout the years and yet again and again this criterion is violated and poor data are the result. Non-isothermal surfaces can be caused either by poorly integrated instrumentation (normally the use of off the shelf gages that are thermally far different from the model in which they are placed) or by models fabricated of dissimilar materials or having dissimilar physical characteristics in the same material. Consider for example the fabrication of a model from insulative materials except in the nose where, for thermal reasons, the model has a steel nosecap. Similarly, a model fabricated entirely of stainless steel where the nose is solid but aft of the nose thin skin construction is used for heat transfer measurements will cause analysis difficulties.

Non-isothermal gages generate incorrect heat flux for two reasons. First, the installed gage creates either a heat sink or hot spot on the surface of the model which distorts the boundary layer and generates a different heating rate over the gage. Second, the installed gage exchanges heat with the surrounding model, either drawing in heat or giving it up in a manner not considered by the thermal model forming the basis of the instrument.

The classic example of this is the installation of heat sink instrumentation in the insulative structure of the Space Shuttle external tank. The resultant error in the measured heating rate caused by this mismatch in surface temperatures was a factor of 2! Similarly, poorly matched gages have been routinely installed in insulative wind tunnel models to aid in the calibration of some survey technique for measuring heat flux. These data were grossly in error as the temperature difference between the insulator and the gage increased.

There are techniques available for the evaluation of heat flux under non-isothermal conditions. All of these techniques require knowledge of the streamline history of the flow which, for a general body, may be difficult to accurately determine. Correspondingly, these effects increase in severity with test time and locally imposed heating rates. Rapid data acquisition can reduce non-isothermal effects. The reader is encouraged to carefully design the model and integrate the instrumentation so that problems of this type do not occur in the first place.

The problem occurs because off the shelf instrumentation is applied without an understanding of integration problems. Instrument manufacturers are not concerned with the installed performance of their device; their concern is with the design of a self contained and properly sensed thermal model that can be screwed or potted into whatever model is being tested. It is the experimenter who must beware of the integration problem. A wide variety of validated instrumentation exists which integrates well into the structure of the wind tunnel model contemplated. Proper selection of that instrumentation will reduce the difficulties of non-isothermal wall effects.
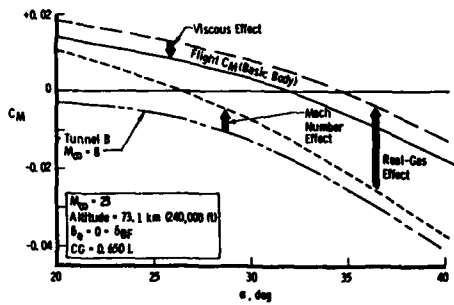
Figure 1   The Interaction of Numerics
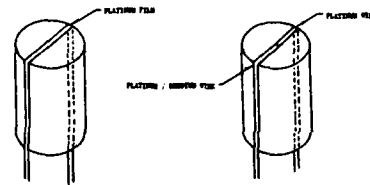and Experimentation in Data Development

Figure 2   The Difference Between
Thermocouples and Thin Film Resistance
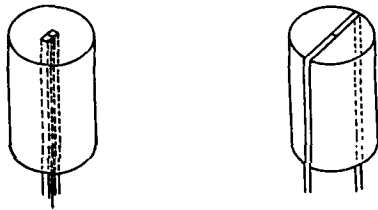Thermometers

Figure 3   Thermocouple Configurations
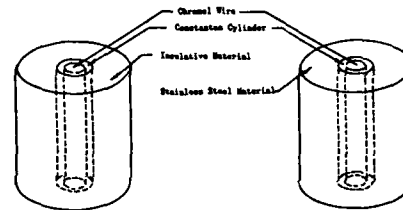which Affect Thermal Losses

Figure 4   Thermocouple Installations
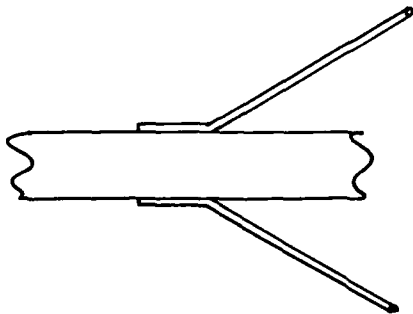which Affect Thermal Losses
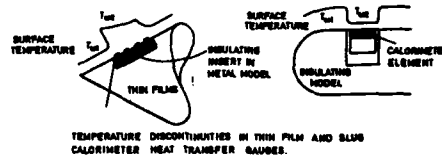

Figure 5   Generic Heat Flux Gage

Figure 6   Surface Temperature Pertubations
Caused by Thin Film and Slug Calorimeter
Heat Transfer Gages

Section II
Thermal Models

Thermal models are mathematical representations of the flow of heat within media. In the present context, thermal models define the response of the physical wind tunnel model and its instrumentation to an imposed heat transfer. Figure 7 shows schematically that heat transferred to the surface by forced convection is dissipated in all directions by a combination of conduction, radiation and internal convection. While these heat transfer mechanisms can include the effects of thermal radiation from the surface of the model either inward or outward toward the walls of the facility, radiation may be ignored for the majority of wind tunnel applications. What remains is a balance between the imposed convective heating caused by the test stream and the conductive dissipation of that heat throughout the structure.

Thermal models may either be formulated as closed form solutions for restrictive cases or numerical in nature. Numerical applications divide the modeled structure into small elements of geometry that are free to communicate with one another in accordance with the laws of heat flow. Thermal models may also be direct in that the thermal dissipation of a known heat input is desired or inverse in that, given a description of the temperature profile within a structure with time, the heating rate that caused that dissipation is described. Those interested in the thermal analysis of structures apply the direct method to problems while those interested in the design of aerodynamic heating instrumentation apply the inverse techniques.

The goal of aerothermal instrumentation is to reduce the general problem of three modes of aerodynamic heating operative in three dimensions to a far simpler system in which one dimensional flow of a single mode of heating is allowed and that mode of heating is conduction within the model and instrument structure. Every successful heat gage is based on a design that accomplishes that single task. These notes will discuss simple thermal models and the gages that try to mimic them.

For long time period tests, including flight testing, it is not always possible to create and install a gage that fully mimics a simple thermal model. In these cases, the heating inference from imbedded thermal sensors will require the application of a more complete thermal model in which the complexities of multi-dimensional flow of all modes of heat will be modeled. Structural aerothermal testing is an example which requires this approach.

It was shown in figure 7 that several modes of heat transfer occur simultaneously on any surface exposed to aerodynamic heating. These general problems of heat dissipation can be solved by finite element numerical techniques. The method of solution begins by dividing the structure into a set of small elements among which heat can be exchanged. It is assumed that the mass of each element is concentrated at a node in the center of that element. This node is connected to each of its neighboring nodes by a conductor. The thermal properties of the conductor depend on the properties of the adjoining elements and its cross-sectional area is equal to the surface area between the elements.

The thermodynamics of each element can be written as:

$$q \text{ net} = q \text{ in} + q \text{ ext} - q \text{ out}$$

where:

    q net is the heat absorbed by a node
    q in   is the heat conducted into a node from
         surrounding nodes
    q ext is the net heat transferred into a node
         from external sources
    q out is the heat conducted into the surrounding nodes

In a typical case, q ext is the net difference between the heat convected into and radiating away from a surface node. This value is usually zero for sub-surface elements.

Since q net is absorbed by the node, the rate of heat transfer can be written:

$$q \text{ net} = m \text{ Cp } (dT/dt)$$

If a forward difference method is applied to this equation and it is assumed that the heat transfer at the beginning of a time interval is constant during that interval of time, then the temperature change can be written as:

$$T = (q \text{ net } /m \text{ Cp}) \quad t$$

In calculating the terms in q net the various paths joining the nodes are treated as thermal conductors. The quantity 'thermal conductance' has been used to define the term which makes the following relation valid:

$$q = K \quad T$$

where   T is the temperature difference between adjacent nodes and q is the heat transfer between them. The thermal conductance for conduction problems is defined as:

$$K = (k \; A/x)$$

where:

    k is the effective thermal conductivity of the conductor
    A is the cross-sectional area of the conductor
    x is the length of the conductor

In most cases, the effective conductivity is that of the nodal material. However, in special cases of a conductor connecting nodes of different materials, the effective properties must be determined. The thermal conductance is the reciprocal of the thermal resistance which can be linearly summed across a series of resistors.

As an example, the effective thermal conductance for two dissimilar nodes shown below is found to be:

$$k_{eff} = \frac{k_1 k_2 (X_1 + X_2)}{X_1 k_2 + X_2 k_1}$$

With these relations defined, the heat transmitted between each element and its neighbors is computed for small time increments. The resulting change in temperature of each node is then computed and the process is repeated. In this way the internal temperature history of a structure can be determined from a known and externally applied heat transfer distribution. The same method can be applied in reverse. If the temperature history of a set of internal nodes is known through measurements then the external heating rate causing these internal temperatures can be computed.

A contemporary example of thermal model analysis is found in figure 8 where the influence of edge effects on a recessed thin skin surface is evaluated.
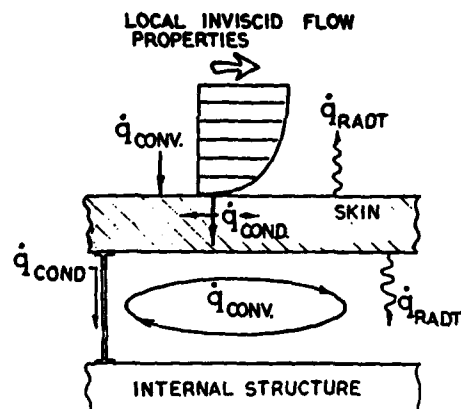

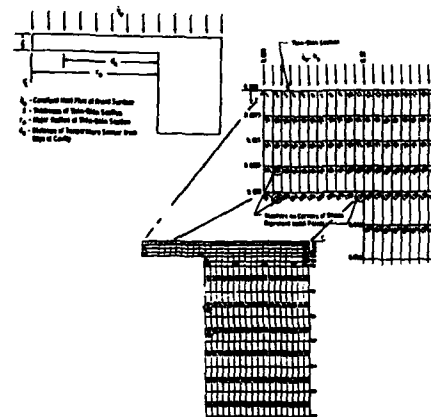Figure 7 Possible Modes of Heat Transfer Into a Model Structure

Figure 8 Example of a Numerical Thermal Model Used to Define Instrumentation Accuracy

Section III
SEMI-INFINITE SLAB THERMAL MODEL

INTRODUCTION:

The semi-infinite slab thermal model referred to by Thompson, 1981, as a gage which "captures" heat within the thermal mass is the most widely used thermal model for the inference of aerodynamic heating. Notwithstanding the pervasive use of the thin skin model in continuous and blowdown wind tunnels, the semi-infinite slab thermal model is the basis of many flight measurements, all of the survey techniques involving paint, reversible coatings and IR radiation as well as the thin film gages used in impulse tunnels. This same thermal model is adaptable to instrumentation requirements in millisecond shock tunnels, in continuous facilities operating for seconds and in flight with vehicles operating for a 1000 seconds such as in the flight of the Rockwell Space Shuttle.

The basis of this thermal model is a set of assumptions that define the heat flow within the model material. These assumptions and the boundary conditions for both the heated and isothermal backface are shown in figure 9. The heat pulse is captured for test durations less than the thermal diffusion time, tD. Test times for various materials are shown in figure 10.

This section will discuss both the application of the semi-infinite slab thermal model analysis to survey techniques as well as point measurements in both impulse and continuous flow test facilities. Survey techniques are defined as those in which an overall view of the model is generated in a continuous manner using a "massless" temperature indicator attached to the surface. Point measurements are made with distinct instruments attached at point locations on a surface of a model.

There are three forms of temperature indicators employed in survey techniques; (1) irreversible temperature sensitive coatings such as Detecto-Temp(R) and Tempilaq(R) which can be sprayed on and cleaned off after a single test injection, (2) reversible thermo-phosphers or liquid crystal coatings which remain active on the model for extended cycles of test time and (3) stabilized emittance surfaces used with remotely located Infrared detectors to define a surface temperature field. In all of these various techniques as well as the point measurement techniques to follow, the overriding feature is that the surface indicator be a material whose presence does not affect the basic thermal performance of the thick substrate, backing materials. In addition, the materials upon which the indicator is applied must not violate the semi-infinite slab model (that is, the thermal pulse must not reach and affect the backface of the material during the period of data acquisition). This feature may be relaxed through corrections to the thermal model which will be discussed later.

There are several forms of temperature indicators used for point measurements with the semi-infinite slab thermal model. Those using the basic model material as a semi-infinite slab (1) thin wire "iso-thermal staple gages" either applied on the surface or imbedded in the surface and either used singly or in groups. (2) thin film resistance thermometers commonly constructed of Platinum material. Apart from these sensors which rely on the model material itself to form the gage, there are several self contained gages which create point measurements. These are (1) Coax gages, and (2) Schmidt-Boelter gages. These gages will be discussed later in section VI.

A Review of Survey Test Techniques

There are essentially four types of survey test techniques in use today. These are: (1) temperature sensitive coating techniques, (2) thermographic phosphor techniques, (3) liquid crystal techniques and (4) IR radiation techniques. Each of these will be discussed in turn.

Temperature Sensitive Paint Techniques

Two types of temperature sensitive paints have been used in the United States over the past quarter of a century. These are a paint known by the trade name of Detecto-Temp (R) and a coating known as Temilaq (R). Although both techniques have been used, earlier studies were conducted with a Detecto-Temp paint. This technology was eliminated by a landmark paper by Jones and Hunt, 1965, which cast doubt on the Detecto-Temp (R) technique, supported the alternate Tempilaq material and quantified the entire procedure of data acquisition and analysis. The Tempilaq material is a fusible temperature coating which undergoes a phase change from a opaque solid to a clear liquid at a known and repeatable temperature. There is a single line of transformation and the technique is not reversible. The coating is applied to low conductivity models constructed of insulative materials which satisfy the semi-infinite slab thermal model. The test sequence starts with a model injection and ends with either a complete phase change or with the imposed heat pulse soaking through the model materials. This time depends upon the material selected and its thicknesses. Test durations vary from 10 to 30 seconds. Figure 11 shows the results of a French Detecto-Temp paint test.

Data reduction employs the standard, one dimensional heat flow equation with surface and isothermal backface boundary conditions as well as an imposed heating rate at the surface of the model. This equation and its solution is shown in figure 9.

Thermographic Phosphor Technique

Thermographic phosphors were first applied to wind tunnel models by Czysz and Dixon, 1969. The phosphor coating is sensitive to the energy of the activating ultraviolet radiation and is quenched by increasing surface temperature as shown in figure 12. The phosphor coating is reversible, unlike the surface temperature coatings previously discussed. The basic data reduction equation is the same as previously described. In all applications to date the phosphor coating has been applied to an insulative material. The phosphor coating response must be calibrated as a change in light intensity vs the surface temperature. Primary data are photographic or videographic data of the model which appears as shades of grey as in figure 13. These grey shades correspond to the levels of aerodynamic heating imposed on the configuration. Tare runs are also made in the facility without air in order to subtract grey shadings due to lighting shadows. Unlike the temperature paint technique, the phosphor data reduction can readily be automated through video imaging techniques with tare pictures subtracted from the actual data automatically. The resultant shades of grey can then be assigned artificial colors as in figure 14 to identify various heating regions. This technique was initially developed for the McDonnell Hotshot wind tunnel and later it was adapted to the continuous flow test facilities at AEDC. It has also been applied in shock tunnel test facilities at Calspan Corporation with some difficulty.

Calibration of the phosphors during tunnel operation is accomplished by placing thermal gages within the field of view of each picture. These gages must not affect the flow in which the data is being taken. Past instruments did not meet this goal. Figure 15 indicates gages used in the past which yielded poor technical results. Figure 16 indicates the newer isothermal staple gage which has been quite successful in this capacity.

Liquid Crystals:

There are a class of materials available that selectively reflect light as they are heated and their temperature changes. Many commercial applications are available for such materials including that of a throw away thermometer. These materials have been used on models to yield a temperature indicating surface which is reversible like the thermographic phosphors. The crystals are suitable for wind tunnel tests at lower temperatures (as, for instance, for supersonic flows or flows in Helium tunnels or in impulse type test facilities). They have not been extensively used in supersonic test facilities in the U.S. although they have been used to advantage in Ludwig tube testing in Germany. Figure 17 indicates their use by Scholer in a shock interaction experiment. View angles are critical with these materials and it is reported that they can be pressure as well as temperature sensitive.

Infrared Scanning

Temperatures can be measured on a model by remotely scanning the surface of the model with a commercial IR scanning camera. The surface is normally coated to stabilize the surface emittance. Very fast scanning cameras are commercially available although equipment of this type is expensive to purchase and develop. Several of the Space Shuttle tests were run in hypersonic test facilities with IR measurements over insulated surfaces. Figure 18 indicates the quality of the produced IR data. Figure 19 indicates problems in accurately defining small regions of differing heat transfer on large scale models. The data were generally as good as the standard thin skin thermocouple data with two exceptions: (1), the scanning camera has a finite spot diameter that may observe both the aerodynamically heated surface of the model and the cool tunnel in background simultaneously (near leading edges for instance). The signal produced integrates both environments and the resultant data cannot be used. (2) the gage has a large minimum spot size, 3/8 inch in diameter, associated with large scale tunnel applications which limits its use in regions of high heating gradients and shock interaction regions. With these exceptions, the pictures produced are extremely visual and the data acquisition and analysis process can be automated through standard videographic techniques.

Common to all of these survey techniques is a series of possible error sources shown graphically in figure 20. Overall, this figure indicates that error sources can be substantial and, as well, an optimum test time is defined where the uncertainty bucket is a minimum.

<div align="center">

CRITICISM OF
TEMPERATURE SENSITIVE PAINT TECHNIQUES

</div>

There are several criticisms of the use of temperature sensitive paint techniques that should be carefully considered by the experimentalist before their selection and use.

Economics:

Temperature sensitive paint applications are labor intensive, slow and mechanical operations. For continuous flow test facilities, the amount of hand labor required to 'turn the model around' is nearly prohibitive. Considering the test cycle times achieved at the AEDC, only one run every 15 minutes can be made. The limiting factor is the physical effort required to reach the model through the model injection system. This criticism is specific to continuous flow facilities and does not apply to transient test

facilities where large energy costs connected with an 'on-line' test facility operation are not involved.

Temperature Peaks:

Temperature sensitive paint applications are relatively poor in defining either the absolute level of heating in regions of high thermal gradient or, conversely, the level of heating in regions of very low thermal gradient. The heating rate is calculated from the observed melt time referenced to the beginning of the heat pulse. This definition of zero time can be somewhat vague for models being injected through the tunnel boundary layer. For regions of high heating, the melt time can also be quite short leading to potentially severe errors in defining this incremental time from the start of heating to a clearly defined peak heating line. Regions of low thermal gradient are also difficult to observe as paint contour lines are not distinct and are affected by inaccuracies in the technique. Such data is of lesser value and will appear in the output as wavy lines. There is a relatively small window of opportunity defined previously through the error bucket, shown in figure 20, in which to generate high quality temperature paint data. To operate within this window of opportunity, an approximation of the answer sought experimentally must be known already, namely some estimate of the actual heating rate in the interaction region. Paint techniques are excellent for defining the 'region' where high and localized heating will occur. They are far less accurate in defining the actual peak within the region. If a clear estimate of the level of heating in the peak interaction region is required, paints with several activation temperatures are required to 'shift the event' into the window of opportunity. This can be done but it is quite expensive.

Person-power Intensive:

The generation and reduction of temperature paint data is labor intensive and bad on the eyes. Many hours are required to trace off the contour lines from the film record.

Physical Model Limitations:

There are real limits to what can be observed with the paint.
The paint model design must minimize the placement of load-distributing steel structure in regions near where measurements are to be made. That alone is frustratingly difficult given that the model materials most useful with this technique are not structurally sound. Thick sections of insulative material are required to assure the semi-infinite slab thermal model is respected. In many cases that is not possible. Thin sections of the model will limit the application of the semi-infinite slab thermal model even further reducing the window of opportunity for testing. In some physically simple cases, corrections may be applied to the data reduction to account for the finite slab effects but these corrections are only valid for limited special cases.

A usual argument for the use of temperature sensitive paint techniques is that such techniques define the location of high heating regions that can then be properly instrumented to define the magnitude of the effect. This is clearly a legitimate need and the paint is satisfactory as a technique to meet this need. In fact, the Space Shuttle development program used this technique effectively.

While this CAN be done, it is far from the best technique to achieve the goal. It simply is not cost effective. In time alone, this technique requires an entry into the test facility, the generation of film data, its reduction and interpretation, the integration of that data into the DESIGN of a point measurement model (since model structure cannot be defined until measurement regions are understood) and then the secondary test of the properly instrumented model. From the standpoint of cost, unique models must be constructed, engineering time invested and wind tunnel time expended. It appears, all in all, that this technique is a support to define the distribution of complex flow phenomena. Given that exists, wouldn't it be cheaper and faster to instrument the point measurement model to cover any contingency; activating the sensors as required to react to the heating patterns observed? Paint model costs can easily top $100,000.00. That pays for a lot of instrumentation!! But there is even a better method than heavily instrumenting a point sensor model. The use of dynamic test techniques, which will be discussed later, gives us the option to use a FEW integrating sensors in such regions and observe the level of heating as the model orientation sweeps the region of high heating over the gage(s). This type of testing is an order of magnitude faster than thin skin testing and 100 times faster than paint techniques.

In the following sections of the notes alternative survey testing techniques will be discussed. These alternative techniques tend to increase the productivity of survey testing and may be more useful than paint techniques if that form of testing is required.

Introduction to Point Gage Designs
Based on the Semi-Infinite Slab Thermal Model

There are several possible gage configurations for the point measurement of heat transfer using the semi-infinite slab thermal model. These various gages are distinguished by the type of surface sensor employed and the type of backing material to which the surface sensor is applied. Figure 21 indicates the matrix of such gages as well as combinations

4-14

of parameters for which no gages are known to exist. Each of these gages will be discussed in the notes that follow.

Of the gage types shown in figure 21, the 'thin film' and 'coax' designs are actively used at present. The 'MIT gage' is an earlier design of Covert and Gollnick, 1968. The 'McDonnell Gage' was also an earlier design based on the interesting properties of semi-conductors as temperature sensors, see Dixon, 1968. The semi-conductor temperature sensor was later used by Jenke, 1978 and termed the 'Temp Sensor Gage' in his AIAA paper. The instrument is a commercial product.

Even this matrix is not strictly confining for the spectrum of gages which could be produced. The blank squares do not all represent gage impossibilities but rather a lack of gage applications. In some cases, the gages which would be represented in these blocks offer no unique advantage to the experimenter. In other cases, as for example the thin film resistance thermometer attached to a conductor, the combination is technically difficult. The thin film gage is electrically powered requiring that the film be electrically insulated from the substrate.

Thin film gages are 'powered' gages in which a voltage is applied to the resistance gage. Figure 22 indicates the bridge circuit and equations used to obtain heating rates. The heat flow through the film which is attached to a substrate material is analogous to the current flow through an R-C circuit. Figure 23 indicates that analogy. Through this analogy current flow through the thin film gage may be converted directly into heating rate information through a series of R-C circuits.

CALIBRATIONS REQUIRED OF THIN FILM GAGES PRIOR TO USE

There are two basic calibrations required for thin film gages prior to their use. These are:

1. the calibration of the temperature coefficient of resistance, alpha, which defines the characteristics of the resistance thermometer composed of, nominally, platinum film.

2. the substrate characteristics, beta, defined as the square root of the product of thermal conductivity, density and specific heat.

Calibration of the Temperature Coefficient of Resistance,

The resistance of the installed platinum film, from which temperature is deduced during the test as an out-of-balance resistance in a bridge circuit, requires developing the required temperature/resistance relationship through pre and post test calibrations. A thermally controlled oil bath can conveniently be used to produce this calibration. Miller quotes a maximum uncertainty in this parameter to be less than 3%.

Calibration of Thin Film Substrate Materials

The thermal properties of any substrate are not known to sufficient detail for calibration purposes. Further, there is some indication that the physical properties of the substrate immediately behind the thin film are affected by the film which is fused to the substrate surface (see for instance Reddy, 1980). There are several techniques available to experimentally determine the parameter beta as shown below.

Measurement of Stagnation Point Heating
Use of a Pulsed External Heat Source
Dissipation of Pulsed Current Through the Gage
Application of the 'Relative Calibration Technique'

One straightforward technique is to use the fabricated gage at the stagnation region of a sphere in a calibration shock tube. Knowing the stagnation point heating from the Fay and Riddell theory (model), the substrate characteristics of the material can be deduced from the experiment.

The thin film gage itself may be used in the calibration process by pulsing a current through the film and observing the dissipation of that current through the substrate material. This technique requires an accurate measurement of the surface area covered by the film; a difficult measurement for a gage of irregular shape with inexactly defined surface boundaries.

The relative calibration technique has been used in several forms in order to eliminate the need to precisely define the surface area covered by the film. In this technique either an external energy source (see Epstein, 1986) or an internal energy source such as a current pulse is used. The heat is dissipated through the resistance gage substrate material with the gage placed in air and through both the resistance gage substrate material AND a fluid of known thermal properties when the gage is placed in that fluid. The assumption is made that the heated gage in the designated fluid will loose heat evenly to both gage substrate and fluid. Knowledge of the surface area covered by the film is not required because the air calibration is related to the fluid calibration. Figure 24 outlines the technique from a paper by Epstein, 1986.

Several fluids have been used in the relative calibration technique. Distilled water was suggested as its lumped thermal properties approximate those for Pyrex(R). For uncoated gages, distilled water has been replaced by a Dow Corning Silicon fluid. More recently, Epstein, 1986, used Dibutyl Phthalate as a calibration fluid.

The calibration techniques reviewed have in common the observation that uncommon substrate materials (other than Pyrex(R)) present calibration data quite different than handbook published values. Further, these calibration data contain the largest potential source of error - both in the substrate being calibrated and in the reference calibration fluid.

Thin Film Gages - Sources of Error

There are several sources of error in measurements made with thin film gages. These have been listed by Miller, 1981, as follows:

1. The value of the substrate thermal properties; density, specific heat and thermal conductivity which, taken collectively, are termed 'Beta'.

2. The value of the temperature coefficient of resistance which is termed 'Alpha'

3. The measurement of the voltage output of the circuit Eo

4. Accounting for the variation of substrate thermal properties with temperature.

5. Correction for current variation during the test

6. Possible loss of semi-infinite slab behavior for the substrate. This will be discussed shortly in these notes.

7. Possible measurement of an integrated heating rate in regions of highly variable surface heating rates.

8. Resistance of the leads as a non-negligible percentage of the resistance of the sensing element.

Not all of these POTENTIAL problems will be important in any given application. They are listed here because they CAN be significant. They should be considered because routine use of this instrumentation will tend to numb the experimenter to the possibility of errors of this type.

Thin Film Gages - Overall Accuracy:

Overall accuracy for the thin film technique has been quoted at +/- 5% when all factors are considered. However, since these gages have such a low mass (the film being extremely thin), they respond to many imposed phenomena including transition. In fact, the gage output has a distinctive 'fingerprint' , demonstrated by Schultz et al. and shown in figure 25, that a trained analyst can use to determine the state of the boundary layer. When the gages respond to transition, they will sense turbulent 'bursts' convecting across the gage. If these data are reduced by integrating the signal over time, 'apparent' scatter of the data results. This is strictly NOT error but it may be observed as error following the comments of Stein in the use of the data.

The Application of Thin Film Gages to Extended Duration Testing

Thin film gages have been successfully used in shock tunnels and shock tubes for the past quarter century. Their response characteristics uniquely suited them to these facilities and they were relatively simple to construct and operate. Their application to extended duration test facilities has been far less universal but none the less accepted for many years.

Edney, 1968, produced the first record of this application. H is use of thin film gages in conjunction with shock interaction investigations was accepted without concern for gage suitability. The gage concept was selected because thin film gages could be applied in the detail he required.

The author was first exposed to the use of thin film gages in blowdown tunnels at the von Karman Institute in 1971. Such instrumentation was routinely used by students in the H-3 test facility.

Miller, 1981, applied thin film instrumentation technology and test models used in impulse type Facilities to measure heat transfer in the Langley 31 inch hypersonic facility. His work is also carefully documented together with several facility induced phenomena which were considered as error sources in data analysis.

Based on the author's experience with thin film gages at VKI and faced with the need to conduct leading edge tests on the Space Shuttle at AEDC, thin film instrumentation was developed and applied to these facilities. The results were documented by Matthews, 1985. This application was somewhat different than others in that the fundamental modeling assumptions implicit in the semi-infinite slab analysis were violated by the leading edge

dimensions and the tunnel operating times. The corrections that were applied involved the use of a finite element conduction code and will be discussed shortly.

In the early 1980's Hayashi, Sakurai and Aso, 1984, developed a variant of the thin film technology which they termed the 'multi-layered thin film heat transfer gage'. This gage uses two thin film resistance thermometers to measure temperatures across a slab of insulator. The data reduction employs the finite slab thermal model, not a semi-infinite slab.

Finally, Hayes, 1982, developed a thin film gage for use in a Mach 3 facility operating at ambient temperature. Again, this is a variant of classical thin film technology closely allied to the gage of Hayashi et al.

CORRECTION OF THIN FILM INSTRUMENTATION FOR SMALL LEADING EDGE MEASUREMENTS

It is possible to generate heat transfer data on small leading edges in long running flow facilities but the process may be distasteful to purists and certainly demonstrates a new equilibrium between those who conduct experiments and those who compute phenomena.

In shock tunnels the test times are sufficiently short that the resulting heat penetration into the substrate materials can essentially be ignored. That same leading edge geometry tested in a wind tunnel with longer model exposure time will cause greater heat penetration into the substrate and violate the semi-infinite slab thermal model causing the need for either far more complex data reduction procedures or some data corrections.

These corrections were provided through the use of a finite element, transient heat conduction code as a thermal model. Figure 26 schematically demonstrates this correction process. The overall intent of the correction process is to relate the actual thermal model which is more complex than the semi-infinite slab model to that more simple model. This is accomplished numerically by defining a heat input, H INPUT to the thermally modeled leading edge. The output of this thermal model computation is a matrix of temperatures on the surfaces of each node in the model. The temperature vs time trace shown in the figure is that at the stagnation point of the model on the outer surface; essentially, the temperature that would be measured by a thin film gage. This numerically derived temperature response was then used to evaluate a corresponding heating rate through a semi-infinite slab analysis program previously discussed. Comparing the input and output heating rates; that is, the heating rate selected to initiate the computation and the heating rate reduced from the measured surface node BY ASSUMING A SEMI-INFINITE SLAB THERMAL MODEL, a numerically derived correction factor was defined. For the nose radii of interest, this correction was 10 to 20% of the actual heating.

It is clear from both intuition and these numerical results that the magnitude of the correction factor increase with decreasing radius, increasing test duration and increasing thermal diffusivity, alpha. While the correction levels are not trivial, they are manageable. The issue with which the reader must contend is whether such NUMERICALLY based correction factors are acceptable in an experimental application. In making that judgement, the reader must understand that even this computer code is a model in some sense of the physical heat flow within the material and, as such, is an approximation to reality.

Advanced Multi-Layered Thin Film Gages

There exists an entirely new type of gage based on the thin film sensor technology previously discussed. These gages were an outgrowth of international studies on the heat transfer to turbojet engines and references from Doorly, 1987 of the Oxford University group and Epstein, 1986 of the Massachusetts Institute of Technology group. In addition, Hayashi, 1984 of Kyushu University has produced such a gage for aerodynamic heating studies. This section will begin with a discussion of the Japanese gage and then progress to these newer and more extensive applications of the advanced technology.

In the last several years the Hayashi and coworkers, 1984 have developed a hybrid gage and published details on its construction and application. Figure 27 indicates the structure of the gage which Hayashi et al have termed a 'multi-layered thin film gage'. The intent of the gage was to combine the rapid response characteristics of thin film instruments with the long term application of a sandwich type gage. In its intended application, the gage measures the temperature difference between the heated face and the backface. The heat resistant layer creates a thermal choke and the gage is placed on a heat conductor so that the thermal reservoir of constant temperature is, for all practical purposes, infinite. In this respect, the operation of the Hayashi gage acts as a Thompson type 3 gage where the heat conductor plays the part of the active source.

The gage has been employed by Hayashi to generate dynamic test data. The model including the single gage was placed in the flow and the shock generator drawn across the gage as shown in figure 28. Continuous data are then taken through the interaction as shown in this figure. Comparison pressure data are also taken as shown in that figure.

The only criticism of this application may be in the possible development of a non-isothermal boundary layer pertubation caused by the 'heat resistant layer' in a conducting steel model although the assumption made by the authors was that this is not

the case. This non-isothermal surface may present particular difficulties in regions where shock interaction regions are present since (1) it may be impossible to separate one affect from the other and (2) temperature pertubations may cause different phenomena in a flow situation near separation.

In spite of these difficulties, the gage is an interesting application of instrumentation technology in the development of a dynamic test capability. Such a capability is an important productivity aid in the economical development of large amounts of understandable data through the use of continuous data traces.

More recently, Epstein of M.I.T., 1986, and Doorly of Oxford University, 1987, have documented very interesting gages based upon dual thin films deposited on a thin, insulative sheet. This technology , in both cases, is motivated by gas turbine research.

Characteristics of this type of gage are shown in figure 29. Epstein states that this gage is useful to 400 degrees C with high frequency response to 100 kHz. The gage operates either as a sandwich gage for low frequency operations or as a semi-infinite slab gage for very high frequency operations. Intermediate frequency data are obtained through numerical signal processing reconstruction.

The Epstein and Doorly papers present an outstanding and comprehensive review of this type of gage and its application.

The McDonnell Semiconductor Gage

Heat transfer gages have been fashioned of semiconductor materials. One example of this is the McDonnell gage shown in figure 30. Although non-linear, the gage is highly sensitive. While the gage concept remains viable and is being commercially produced, the gage is not widely used to measure aerodynamic heating.

The MIT Heat Transfer Gage

In the late 1960's, engineers at the Massachusetts Institute of Technology designed a unique heat transfer gage for use in their hyper-core tunnel at Mach 3.7. The gage, shown in figure 31, had a wire sensor; a 0.005 diameter iron/constantan thermocouple wrapped around a lava plug. Essentially, this is a semi-infinite slab thermal model with a 'massless' thermal sensor, the iron/constantan thermocouple attached to the front surface of the semi-infinite slab. The gage was used at MIT for several test programs by Covert and Gollnick, 1968, but the design was not exported to other test installations. No further references can be found to the gage.

In-Depth Thermocouple Gage

Figure 32 presents a schematic view of an in-depth thermocouple gage; a gage using the natural insulative capabilities of the wind tunnel model together with one or a series of thin wire thermocouples placed at different depths in the material.

In depth thermocouple gages are used extensively in flight test applications. They are also known as 'Isothermal Thermocouple Gages' because there is a substantial length of wire on either side of the thermocouple bead at the same temperature as the bead. This wire length acts to reduce the conduction losses away from the thermocouple as the result of temperature gradients caused by the routing of the thermocouple wires into insulative materials.

These gages have also been used to advantage in wind tunnel testing. Years ago, they were used in continuous high speed tunnels which had no injection capability. By using the indepth feature of the gage; long term, steady state heating rates could be measured without the need for rapid injection.

The Isothermal Staple Gage

A variant of the in-depth thermocouple gage is the isothermal staple gage shown in figure 16. This gage has a single wire thermocouple laid on the surface of the insulator. Like the in-depth gage, the staple gage uses the natural insulation material as the backing material of the gage but, the staple gage is a true analogue to the thin film gage wherein the in-depth gage is a 'sandwich' type gage.

Recently, this gage was used to 'calibrate' heat transfer survey technique results at AEDC. The gage was applied to an insulative survey model in order to 'calibrate' selective points along the model surface. In the past, disruptive heat gages, such as Gardon gages, were installed in the insulative model as shown in figure 15. The staple gages were cast onto the Stycast model and an evaluation of the results indicated that both the survey technique and the staple gage gave the same result.

SEMI−INFINITE SLAB ANALYSIS

$$T(y,0) = T_i$$
$$T(\infty,t) = T_i$$
$$\partial T/\partial y(0,t) = \frac{h}{k}\left[T_{\infty}-T(0,t)\right]$$
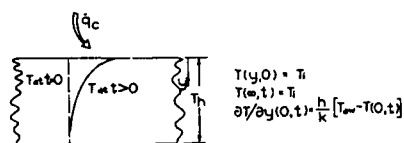
ASSUMPTIONS:

INITIALLY ISOTHERMAL MODEL
HEAT PENETRATION SMALL COMPARED WITH WALL THICKNESS
COATING (THERMAL SENSOR) IS MASSLESS
HEATING STEP OF CONSTANT MAGNITUDE APPLIED
MATERIAL PROPERTIES ARE KNOWN AND DO NOT VARY WITH TIME

Figure 9 The Boundary Conditions and Assumptions forming the Semi-Infinite Slab Thermal Model

$$t_D \simeq \frac{0.2(TH^2)}{\alpha}$$
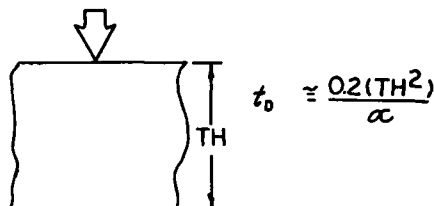
THERMAL DIFFUSION TIME FOR 6 MM OF ...

COPPER .... ~0.1 SECONDS
17.4 PH STAINLESS STEEL .... ~2 SECONDS
MACOR MACHINABLE GLASS .... ~9 SECONDS
PYREX GLASS .... ~10 SECONDS
STYCAST INSULATOR .... ~16 SECONDS
TEFLON INSULATOR .... ~70 SECONDS

Figure 10 The Thermal Diffusion Time of Various Materials

Figure 11 Temperature Profiles Defined through Detecto-Temp(R) Paint from the work of Ponteziere, 1967
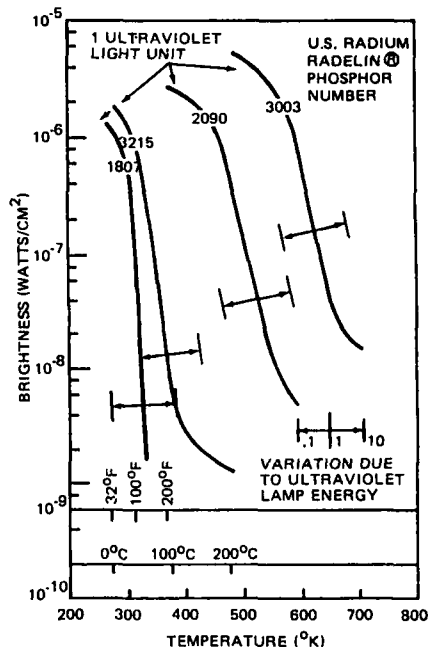

Figure 12 Quenching Characteristics of Commercially Available Thermographic Phosphors with Temperature

THERMOGRAPHIC PHOSPHOR COATED MODEL ACTIVATED BY ULTRAVIOLET RADIATION

Figure 13 Thermographic Phosphor Coated Model Activated by Ultraviolet Radiation

PHOTOGRAPH OF PHOSPHOR "DATA" WITH ACTUAL GRAY SHADES REPLACED BY ARTIFICIAL COLORS THROUGH COMPUTER PROCESSING

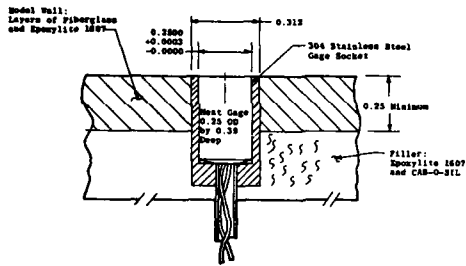Figure 14 Phosphor 'Data' with Actual Gray Shades Replaced by Artificial Colors through Computer Processing

Figure 15 Massive Steel Heat Gage used
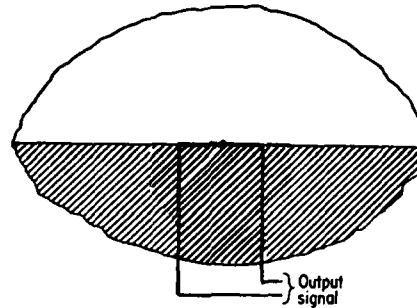with Insulative Models Yielded Non-
Isothermal Wall Effects

Figure 16 Non-obtrusive "Staple" Heat
Gage used with Insulative Models
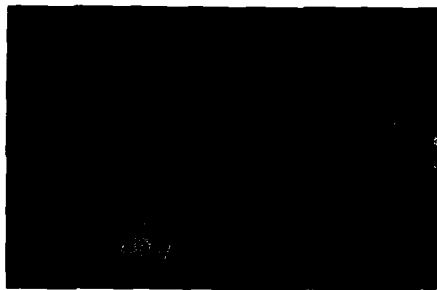did not Affect the Wall Temperature

Figure 17 Example of Temperature
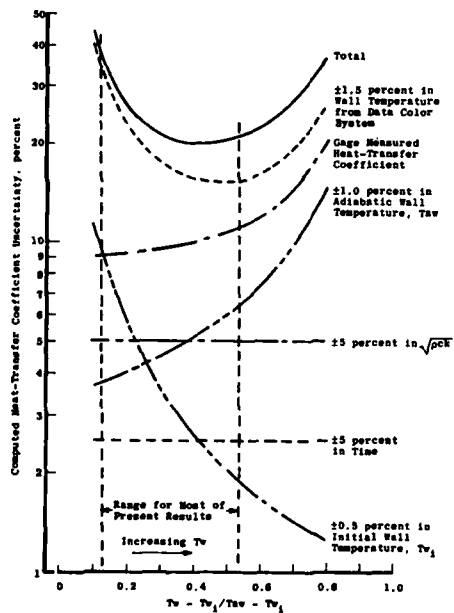Profile using Liquid Crystals from
Scholer

Figure 18 IR Derived Data Compared with
Laminar and Turbulent Theories

Figure 20 Error Buildup for
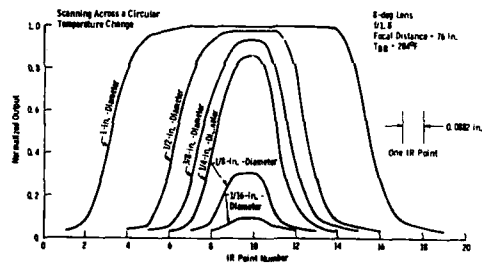Temperature Paint Technique

Figure 19 Effect of Thermally Distinct
Spot Size on IR Derived Temperature
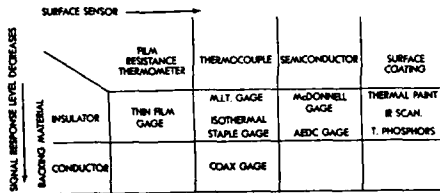Output from AEDC Test

4-20

Figure 21 Matrix of Gage Designs Based on the Semi-Infinite Slab Thermal Model
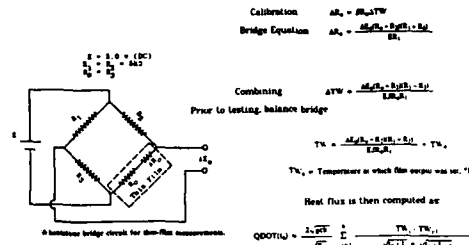
Figure 22 Bridge Circuit Used to Measure Thin Film Resistance and Reduction Equations

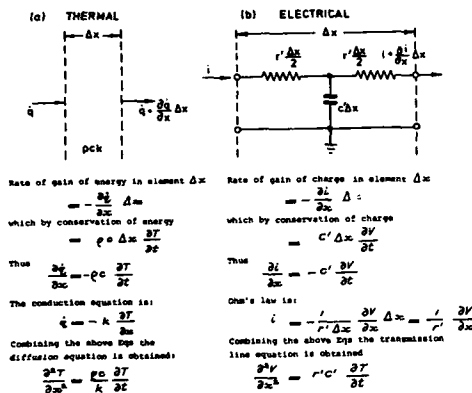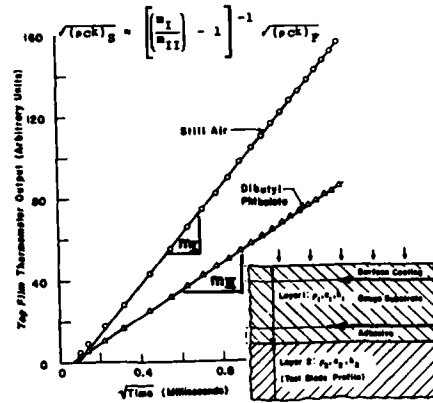Figure 23 Outline of Electrical Analogy to Heat Flux in a Semi-Infinite Thermal Model

Figure 24 Outline of the Relative Calibration Technique Using Still Air and Dibutyl Phthalate (after Epstein)
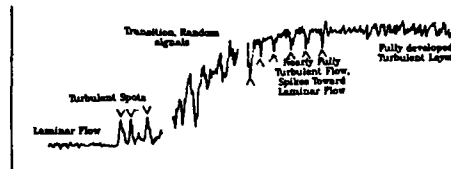
Figure 25 Thin Film Gage 'Fingerprints' of the Boundary Layer State from Schultz
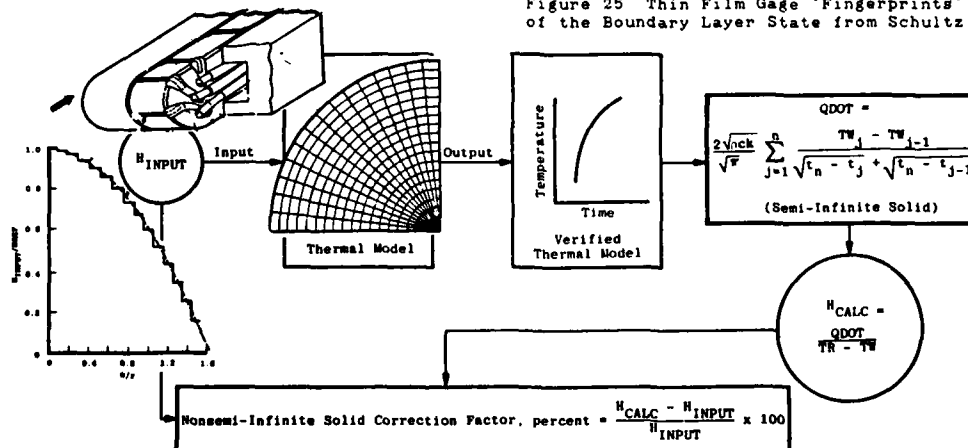
Figure 26 Numerical Methodology to Correct Thin Film Data for Configurations Violating the Semi-Infinite Slab Thermal Model
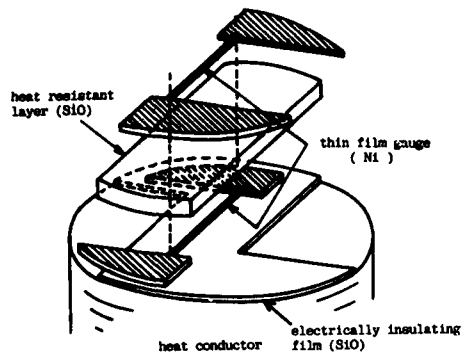
Figure 27 Structure of the Japanese Multi-Layered Thin Film Gage after Hayashi, 1984

Figure 28 Application of Japanese Thin Film Gage Shown in Figure 27 to Dynamic Testing Application after Hayashi, 1984

Figure 29 Detail of Epstein High Frequency, Dual Film Thin Film Gage
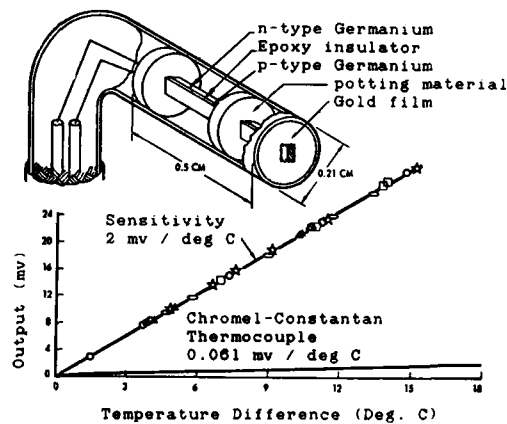
Figure 30 Semiconductor Based Temperature Gage after Czysz, 1969

Figure 31 MIT Wire Heat Transfer Gage after Covert, 1968

Figure 32 In-Depth Thermocouple Plug Placed in a Thick Wall Model

Section IV
THIN SKIN THERMAL MODEL

THE THIN SKIN TECHNIQUE IN HISTORICAL PERSPECTIVE

The thin skin technique has been successfully used for the past 30 years and it is still considered to be the standard technique by which heat transfer is inferred through wind tunnel measurements. While it is hard to argue the merits of this technique (while understanding its limits in any given application), there have been technology changes over th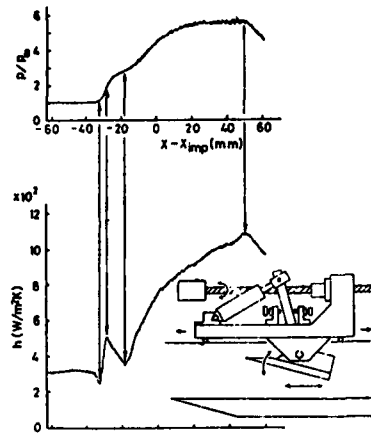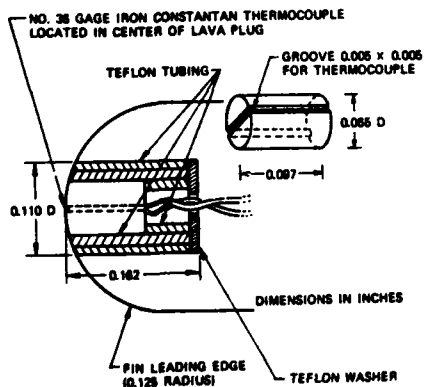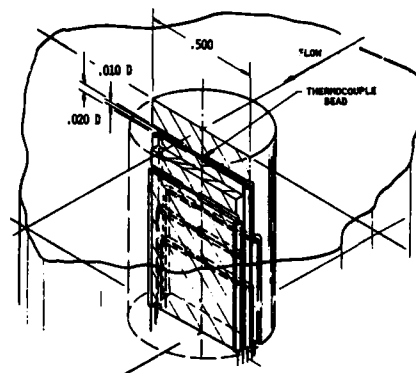is past 30 years that argue for a re-evaluation of the thin skin technique. This re-evaluation, is, in the view of the author, painfully slow because tunnel operators are comfortable with the technique and wind tunnel users, by and large, tend to accept those techniques with which the wind tunnel operators are comfortable.

There are several reasons to argue for the replacement of the thin skin technique. These are:

1. The technique is slow and costly. Each run generates one point of data and must be followed by a relatively long cool down period in which the heat energy transferred to the model is rejected. Five seconds in the flow followed by 50 to 120 seconds of cooling, outside the flow.

2. The models are special purpose and expensive. Whereas force and moment or pressure models are built of thick stock, this type of heat transfer model requires the build-up of thin sheets and the design of transfer mechanisms wherein the loads are carried by a hardback structure. Surface buckling or wrinkling is common in regions of non-uniform heating and these same non-uniform regions are difficult to construct for this technique by any means.

3. The scheme was devised years ago because the data acquisition and reduction techniques (the computer) were the weak link in the data analysis. Thin skin data could be reduced by rudimentary computation - even by hand or using a hand calculator as shown in figure 33. This reason is no longer appropriate; acquisition and analysis computers are far more effective and much cheaper than air-on wind tunnel time.

4. The economics have changed. Test costs are a factor of 100 times higher today than 30 years ago arguing for a shift from wind tunnel costs (minimize the air-on test time) to analysis costs (maximize the exercise of computers) in the overall acquisition of data.

5. The thin skin technique simply cannot generate the amounts or quality of data required today for a reasonable cost. The dynamics of the boundary layer are lost in the sluggish response of a thin skin gage but those same dynamics are clearly defined in more responsive, lower inertia instrumentation.

HISTORICAL NOTE:

Durand and Rhudy, 1959, documented the techniques of the day for the generation of heat transfer data from thin skin models. Discussing the generation of data on the X-15 aircraft in the AEDC Tunnel 'B', the model was exposed to the flow for about five minutes and then cooled for about five minutes. The technique was to generate high speed temperature-time data using recorders for 30 seconds and then to continue to heat the model in the tunnel for an additional four minutes to generate 'equilibrium temperature data'. This excessively long test duration was followed by a cooling period of five minutes in which the temperature of the model was reduced to 100 degrees F prior to the second injection in the series.

Thin skin heat transfer testing has changed little from these early experiments of 30 years ago. Overall, the intent is to expose the model to the flow as a step function; generate a stream of temperature vs time data on recorders and then cool the model back to a reference temperature. The difference is that the cycle took 10 minutes in 1959 and today it takes one minute. No longer is equilibrium temperature data generated because such data, being corrupted by the thin skin model design, was found not to be equal to the recovery temperature and thus of no value in the overall data analysis. Presently, the intent is to generate temperature-time data as fast as possible (about 5 seconds) and then retract and cool the model to ambient temperature conditions, about 540 degrees Rankine (80 degrees F).

The thin skin technique has been successfully applied to the generation of heat transfer data for the past 30 years. The technique, is straightforward in application and accurate in results. It is limited in applicability by the appearance of non-uniform surface temperatures introduced by extremes in curvature or regions of highly localized interference heating.

BASIS OF THE TECHNIQUE

With a thin skin model, heat transfer is inferred from a heat balance equation written as follows:

$$\dot{q}_{conv} = \rho \ C_p b \ \frac{\partial T}{\partial t}$$

Because of the operating temperatures of current day hypersonic test facilities, radiation heat transfer can be ASSUMED to be negligible. Radiative heat transfer is a function of the fourth power of the temperatures difference as follows:

$$\dot{q}_{rad} = \epsilon \ \sigma \ (T_2^4 - T_1^4)$$

Conduction losses, while conveniently ASSUMED to be negligible may have an important effect on the measurement and must be considered in detail. Conduction losses (or gains) may occur in three areas: (1) conduction through the skin to backing material behind the thin skin, (2) conduction along the skin caused by surface temperature distributions along the surface of the model and (3) conduction losses associated with the temperature sensor itself; temperature gradients down the thermocouple wires.

CONDUCTION EFFECTS IN THIN SKIN MODELS

NORMAL CONDUCTION TO BACKING MATERIAL:

The thin skin material can be either structurally sound and thus open to the internal surface of the model between strengthening stringers or it can be less structurally sound and thus backed by some insulative material. Heat transfer can occur between the thin skin and the backing material. The rate of loss is far greater if the backing material is conductive. Even the use of air as a backing material can cause some heat loss. Certainly, stagnant air at ambient tunnel conditions causes small losses which can be neglected. However, improper model design can cause internal airflow which will produce forced convection on the backface of the heated surface and losses which are measurable. While no one would knowingly vent the internal airflow in a model, lack of attention to detail can produce this effect. As an example, a Space Shuttle model in Tunnel `9` (test duration of less than 2 seconds) had its instrumentation wires `scoured` by an inadvertent sub-mold-line flow. This scouring destroyed the wire insulation.

CONDUCTION ALONG THE SURFACE OF THE MODEL:

Dramatic errors in measured heating can be observed as a result of conduction of heat along the skin. These errors are induced by non-uniform heating of the surface creating, with time, non-isothermal wall temperatures. Shock interaction regions create losses which easily obscure the measurement to be made. Corrections can be made to these measurements ... but with great difficulty. At a given time, the magnitude of conduction losses along the skin are proportional to the second derivative of the surface temperature with distance along the surface. Classically simple to produce through curve fitting techniques, this correction requires substantial numbers of surface measurements not always present and high measurement accuracy in order to generate numerically meaningful second derivatives. Because of measurement inaccuracies, this technique is rarely used in practice.

With time, each measurement location is subjected to increased conduction losses as the surface temperature levels increase. It is also possible to extrapolate data from a given gage back to low time where conduction effects are less important. Such a strategy requires a clear understanding that the measured heat flux at a given station is affected only be conduction as the test time is reduced. Other effects can occur. Transient starting shocks must be considered.

Kidd, 1983, presented a significant review of lateral conduction effects which are present on thin skin models. Kidd presented several recommendations with regard to the design of thin skin models having nominal skin thicknesses of 0.030 inches. These recommendations, reproduced from his paper, are as follows:

    1. If the model is to be designed with locally thin skin cavities which are machined into a relatively thick material, these should be at least 1.1 inches in diameter.

    2. If two dimensional slots are machined into the model, the width of these slots should be at least 1.0 inch.

    3. If the airloads are distributed within thin skin models through the use of a hardback system consisting of bulkheads, thermocouples should be located at least 0.45 inches from these structural members.

    4. The local radius of curvature at the point of measurement for bodies of revolution should be at least 1.5 inches.

The reader should note that these recommendations are for stainless steel models with a skin thickness of 0.030 inches to be used in facilities like those at AEDC.

The recommendation to have a radius of curvature greater than 1.5 inches is different than AFWAL experience in testing slender delta wings. Data of acceptable quality was generated on such models using leading edges of 0.50 inches radius. Irrespective of such differences in detail, the basic fact is that there are limitations in the use of thin skin models that must be understood. There are also analysis techniques available to accomplish that job.

The conduction of heat into and away from the thermocouple will cause errors in the measurement of heat transfer into the model surface. Figures 34 and 35 demonstrate traces that indicate surface heating with conduction. In figure 34 a natural log function is formed from the temperature data and plotted as a function of test time. This function will generate a straight line in the absence of conduction. If conduction is present, the curves will not be linear. Data should only be used within the linear portion of the curve. Figure 35 demonstrates another approach toward reducing conduction effects. In this technique, the reduced heat transfer data is plotted as a function of time for a single gage and the curve fitted to the reduced data is driven back to zero time. This figure demonstrates two forms of conduction; that caused by temperature gradients along the skin caused by aerodynamic heating and that caused by any initial degree of model non-isothermality prior to test.

CONDUCTION OF HEAT DOWN THE THERMAL SENSOR WIRES:

Kidd, 1985, discussed the loss of heat down thermocouple wires attached to a thin skin surface. Using the `TRAX` thermal model, Kidd developed a series of ground rules relative to this phenomena. The experimenter is caught between two effects in the selection of thermocouple wire diameter. On the one hand, small diameter wire may fail more easily during test and is certainly harder and more tedious to install. On the other hand, large diameter wire drains away heat due to conduction effects.

A conclusion figure from Kidd's paper is shown as figure 36 of these notes. Based upon his analysis, wire diameters of 0.005 inch or less are recommended with the thermocouple material as low in thermal conductivity as possible. Chromel/Constantan thermocouples are noted as the best from this standpoint. Highly conductive Copper is not recommended.

ATTACHMENT OF THIN SKIN THERMOCOUPLE WIRES:

Several studies have been conducted concerning the best technique for attaching thermocouple wire to wind tunnel models. In general, thermocouple wire can be attached either normally to or tangentially to the surface of the model. The application of wire normal to the surface maximizes the loss of heat down the wires. tangential attachment creates less conduction loss by having more of the thermocouple length at the same temperature as the model surface. Figure 37 from Kidd's paper indicates the preferred attachment technique. Apart from conduction losses down the wire, there are several other criteria implicit in the location and attachment of thermocouple wires. First, the thermocouple junction formed by the wires must occur at the surface of the model. Care must therefore be taken not to create a junction below the surface of the model. Twisting the wires together... and it has been done ... is unacceptable. Second, the location of the surface thermocouple junction must be known exactly. The tangential location of thermocouples introduces some difficulties in this respect.

ERRORS IMPLICIT IN THE THIN SKIN MEASUREMENT TECHNIQUE

The several errors implied in the evaluation of heat through the thin skin technique are (1) an error in the measurement of skin thickness at the instrument locations , (2) an error in the material properties of the instrumented surface and (3) conduction errors previously discussed.

SKIN THICKNESS MEASUREMENT:

Careful measurement of the skin thickness at each gage location is required. The heating rate is directly related to the accuracy of these measurements. An accuracy of measurement of +/- 3% is required to match the overall accuracy of the instrumentation system. Measurements are particularly important when electroformed models are employed since these models have, traditionally, poor fabrication quality control in regions of high surface curvature where they are employed

MATERIAL PROPERTIES:

Over the years it has become clear that the material properties quoted for a particular class of stainless steel are approximate and must be verified through a batch analysis of the material to be used for the model in question. The evaluation of material properties, particularly the property of specific heat is required.

SPECIFYING THE ADIABATIC WALL CONDITION:

Figure 38 indicates the sensitivity of the deduced heat transfer coefficient to errors in specifying the adiabatic wall temperature. This effect will be discussed in Section VII. It is sufficient to note here that errors in specifying the adiabatic wall temperature can translate into substantial errors in the resulting heat transfer coefficient as the total temperature of the test facility approaches the wall temperature of the model. This

normally occurs in heat transfer tests conducted at low Mach numbers in test facilities designed to produce only enough heat to avoid liquefaction effects.

APPLICATION OF THE THIN SKIN TECHNIQUE TO A
HOTSHOT TUNNEL

In 1965 Harvey discussed the application of thin skin techniques to models tested in impulse facilities operating nominally for 100 msec duration. In Harvey's application, the measurement surface was "clad" to the stress carrying model by double backed tape. The cladding was very thin, 0.002 inch stainless steel stock to which Chromel/Alumel thermocouples 0.001 inch in diameter were spot welded. The stress carrying model was locally cut away at the measurement stations by a hole 0.25 inch in diameter about the thermocouple.

$$q = rho \times Cp \times b \times dT/dt$$
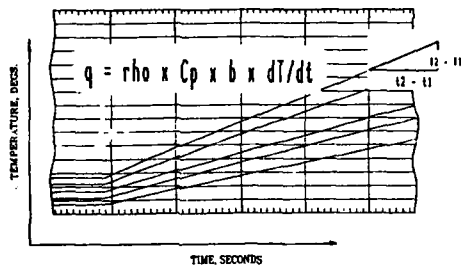
Figure 33 Temperature / Time Output from Thin Skin Data
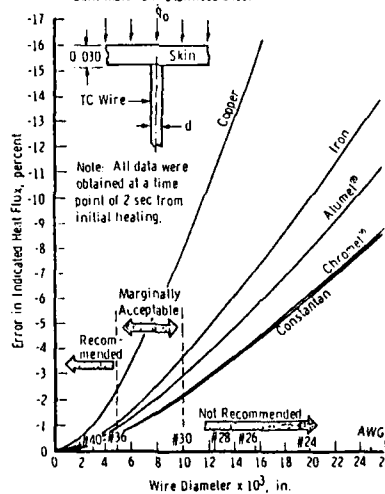
Figure 34 Errors in Thin Skin Measurements Due to Conduction Down Gage Wires

Aerodynamic Heating (h) Assumed to be Applied to Bottom Surface of Thin-Skin Section Shown Above

Figure 37 Typical Thin Skin Thermocouple Installation

Figure 35 Log Difference Temperature / Time Response From Thin Skin Data
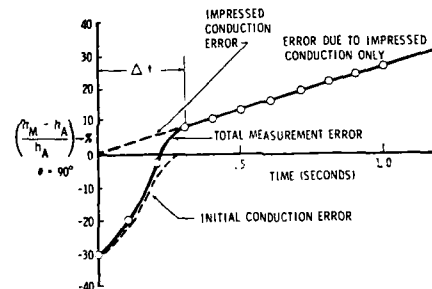
Figure 36 Time Wise Heat Conduction Correction for Thin Skin Thermocouples
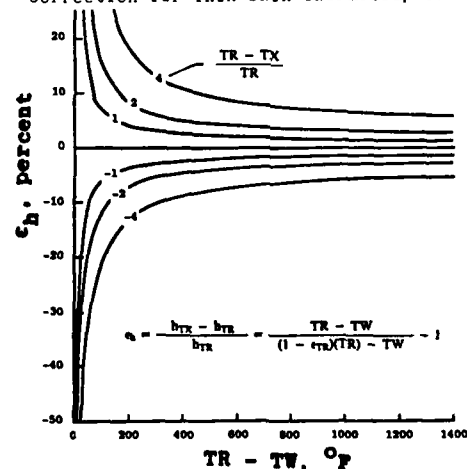
Figure 38 Errors in Thin Skin Heating Data due to Errors in Estimating T_{aw}

Section V
GARDON GAGES

Figure 39 from an excellant basic reference by Hornbaker and Rall, 1968, indicates the general arrangement of the heat transfer gage known as a Gardon gage. The Gardon gage was developed by Robert Gardon, 1956 as a radiation gage. The gage concept and the design was transferred into the measurement of convective heat transfer and was used until recently in both wind tunnels and flight research.

The gage has an interesting characteristic in that heat flux is proportional to the output signal of the sensor. It has one other interesting characteristic for the engineer; it is dangerous to use because it tends to create a non-isothermal spot on the model which may well produce data in substantial error. The use of this gage is not recommended.
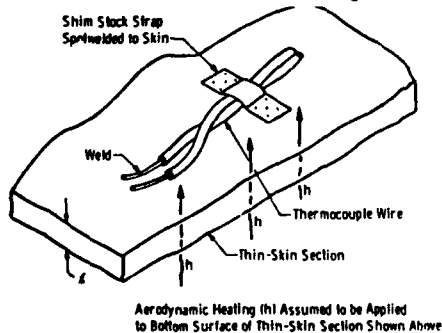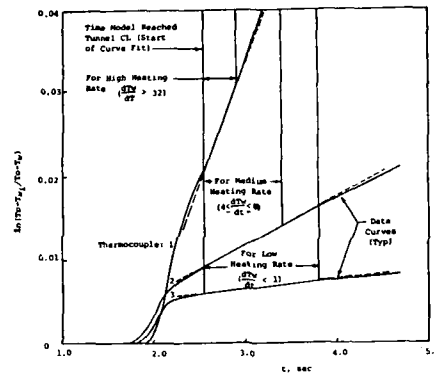
In Thompson's view, this would be considered as either a type 1 or type 3 gage depending upon the time scale of the application. The gage design sets up a radial temperature gradient between the thin foil and the heat sink surrounding it. One dimensional heat flow in a radial direction is postulated. The heating rate is proportional to the temperature difference between the hot center region of the thin foil and the cold edge junction of the heat sink. Increased gage sensativity can be introduced by replacing the single temperature measurement on the thin foil by a thermopile design.

The problem with this gage is that it can never be well integrated into a model since it presents two fundamentally different structures to the flow; a thin foil that heats quickly and a heat sink that, ideally, does not change in temperature during the run. These different structural elements heat at different rates and cause a non-isothermal surface temperature which perturbs the boundary layer flow and causes errors in surface heating rate measurements. This class of gages has repeatedly been used in flight applications - each time with bad results.
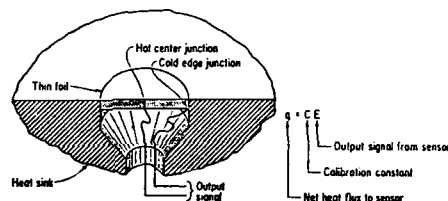

Figure 39 Gardon Heat Gage

Section VI
STATIC VS DYNAMIC MEASUREMENTS

Historically, some 30 years ago when heat transfer measurements were first made at the Arnold Engineering Development center; back when the X-15 was being tested, a single test point of heat transfer data required 60 seconds of testing during which the model was in the tunnel. 20 years later during the Space Shuttle development program, that same test point required 5 seconds in the tunnel. Of course, in addition to the actual test time, there was a substantial time required to cool the model and return it to a cooled, test ready state. This time is proportional to the amount of heat that the model receives, (time in the tunnel) and the quality of the cooling system. During the Space Shuttle development, the time between test points was of the order of 5 minutes but more recently, the time interval between successive injections has reduced to 1 minute. At this point, the thin skin technique appeared to have reached a plateau of capability in which it could not be improved further. Newer instrumentation techniques that allows for 'dynamic testing' have reduced the test intervals even further. Today, a series of 10 data points that at one time required 600 seconds can now be accomplished in less than 200 seconds - including cooling time. That's equivalent to three runs per minute.

Dynamic testing as a heat transfer test technique refers to the ability to generate multiple points of test data during a single injection as the model configuration is maneuvered through the test section or modified as a function of time. Several examples of dynamic testing have been demonstrated to date. This technique requires the use of an integrating heat gage which measures the variation of temperature in depth as a function of time and which, through data reduction, can be interrogated to yield the level of heating at the instrument point as a function of time and hence configuration orientation.

The several examples of 'dynamic testing' explored to date are as follows:

1. Space Shuttle with Rapid Pitch Sweep
2. Dynamic Shock Impingement Studies
3. Space Shuttle Remotely Driven Flap
4. Fully Integrated X-24C Model
5. Slender Cone Rotating and Oscillating in Pitch

The particular characteristics of these model applications will be discussed in somewhat greater detail later in this section of the notes. For now, it is important to understand why dynamic testing would be required in a wind tunnel model and under what circumstances it would be used.

There are two basic reasons for the development of dynamic measurement techniques. They are (1) the generation of higher quality data and (2) the generation of higher quality data at lesser cost and in shorter periods of time. Two examples are worth discussing here.

First, shock interaction phenomena create highly localized regions of aerodynamic heating with large thermal gradients about the peak. Since the location of the peak is not clearly known, some initial and exploratory measurements are required to locate the peak. Once located, instrumentation is strategically placed to measure peak values. The process is costly in both development time and wind tunnel time. Dynamic testing allows the placement of gages in the approximate location of the heating peak. The peak is then defined by observing the relative output of this gage array as a function of the local motion of the configuration (such as the angle of attack of the model).

Second, a slender vehicle with a deflected control surface causing local separation was tested in a continuous flow wind tunnel facility. Both pressure and heat transfer were taken by conventional techniques. The experimentally defined separation characteristics of that deflected flap were entirely different between the two measurements. The differences were due to a difference in surface temperature at which the measurements were taken. A difference that is directly attributable to the test instrumentation; a difference that disappears with dynamic test techniques.

In present day engineering, cost is an integral factor in all engineering decisions. Dynamic test techniques minimize the cost of test facilities by maximizing the productive work from each hour of testing. In most cases, this process requires an entire systems evaluation of cost factors in which the model cost and the data reduction and manipulation costs are an important part.

Dynamic test techniques require developments both in the area of advanced sensors, which I have termed 'integrating sensors' as well as in test techniques which optimize the dynamic movement of the model within the test section environment.

Integrating sensors are those which respond rapidly to changes in the test environment, which absorb and retain the entire heat pulse obtained in the tunnel and which can be decoded to yield data from continuously changing test maneuvers. Four such gage designs are (1) coax gages, (2) Schmidt-Boelter gages, (3) isothermal staple gages and (4) thin film gages. Only the first two have been used in a dynamic mode. All such gages are based upon the semi-infinite slab analysis and modifications which account for a finite backface temperature rise.

Dynamic testing involves a continuous movement of the model within the test section. Such movement can be classed as either slow or fast with respect to the response characteristics of the gage. In the former case the data reduction may be considered as quasi-steady state. In the latter case the data reduction requires a more complex reconstruction of the imposed signal through fast Fourier transforms.

TECHNIQUES FOR QUASI-STEADY STATE DATA ACQUISITION

This application of instrumentation began in the early 1980's when AFWAL tested a Space Shuttle model in the NSWC Tunnel 9. The facility is a fast blowdown tunnel operating for less than 2 seconds at substantial cost. Our goal was to make maximum use of the test environment by driving the test model through a complete pitch cycle in one second. The model shown in figure 40 was pitched at rates from 40 to 85 degrees per second during which time valid heating data were acquired. Figure 40 shows the quality and completeness of the data as a function of the vehicle angle of attack for a single run.

Building on this success, experiments were formulated for continuous wind tunnel facilities at AFWAL and at AEDC. Two experiments were run at AFWAL, both stressing complex shock interactions in a Mach 6 facility. In the first experiment, the interaction region ahead of a cylinder attached to a flat plate was instrumented with a single gage. The model was pitched during a single rate and interaction data were generated. The interaction data were unique in that through pitching the model, the interaction process 'swept' across the limited instrumentation defining the true peak heating. The second experiment, also run at Mach 6, evaluated heating to deflected control surfaces in the same manner using miniature coax gages. That model is shown in figure 41 with the flap and instrumentation detail shown in figure 42.

A larger Space Shuttle model was tested hypersonically at AEDC. This model, shown in figure 43, was modified to power the body flap during test. Data during a single run were taken as the flap moved. Phenomena, such as flap induced separation, was observed continuously rather than at discreet flap angles. The onboard motor eliminated the manual flap adjustments required during previous tests. This saving was estimated at $30,000.00. More data were taken during a single shift of dynamic testing than during the entire Space Shuttle development program !

DYNAMIC TESTING; THE APPLICATION OF FAST FOURIER TRANSFORMS IN THE LIMIT OF RAPID MODEL MOVEMENT RELATIVE TO GAGE RESPONSE

There are two options with regard to data acquisition systems; a traditional measurement system in which the response is related to the measurement by a simple constant, k, or an alternative scheme in which the instrument produces a distorted response which can be corrected off line through software. In dynamic testing where the measurement signal is distorted by the rapid model motion and instrument response limits, signal reconstruction with Fourier transforms has been successful.

Fourier transforms have been discussed by several authors including Harting, 1972. Essentially, Fourier established a unique transform between the time and frequency domains. Because of their assumed LINEARITY, systems could change their distributions only in amplitude and phase between the input and output data. The basis of the technique is the Fourier integral (Fourier transform). Harting describes in detail the use of the Fourier transform to compensate for transient data distortion.

The technique involves generating a calibration response to a defined input signal which, by design, contains sufficient information over the bandwidth of interest. See figure 44. Both calibration input and response are digitalized. These signals are transformed from the physical to the frequency domain and then ratioed, output/input, to produce the transfer function for the gage, H. The transfer function is a complex number having both a magnitude and phase angle. Favour, 1966, details the mathematical method and its limitations.

Distorted data from a test program are then corrected through the application of the previously defined transfer function in the frequency domain. Distorted data transformed into the frequency domain can be divided by the transfer function to provide correction and then transformed back into the physical domain. This corrected signal provides an excellent simulation of the true signal that would be observed by an infinitely responsive gage.

In practice, an application of this technique has been reported by Jenke and Strike, 1978 and Strike, 1979. In their application to an oscillating sharp cone which is graphically described in figures 45 through 47, The Gardon gage used in the Jenke experiment was calibrated with a square pulse signal which , because of the frequency limitations of the Gardon gage, creates a distorted response in time as shown in figure 45. Both the input and output signals are transformed into the frequency domain as shown on the right side of the figure. 60 Hz carrier noise is clearly visible in the transformed gage output. The components of the transfer function, the magnitude and phase angle, are shown in figure 46 produced by ratioing the input to output of the transformed signal. Figure 47 then indicates both the distorted test signal and its transform as well as the corrected test signal transformed back from the frequency to the time domain.

Limitations of this techniques were outlined by Favour, 1966, as follows:

1. The transformation only works with systems where the input and output are simply related by a linear relationship in the time domain.

2. The limits of integration of the transformation function with respect to time MUST contain the complete transient to which the instrument is subjected.

3. The limits of integration for the re-transformation process must contain the complete frequency spectrum of the transient

4. Since all time functions are defined by discrete samples, the sampling rate must satisfy the inequality

$$\Delta t < \frac{\pi}{2\omega_m}$$

to assure an accurate representation of the Fourier transform in the range of frequencies which define the complete frequency spectrum of the transient. In this inequality omega m is the highest frequency component in radians per second of the time function.

5. Since each Fourier transform is defined at discrete frequencies over the range of interest in the transient, the resolution of the Fourier transform must satisfy the inequality

$$\Delta\omega < (\pi/T)$$

where T is the length of the transient in time. In other words, the minimum frequency of interest must be greater than the delta omega described by the inequality.

$$\omega_{min} \geq \Delta\omega$$

6. In the calibration process, the input calibration transient selected must represent significantly all frequencies of interest in the test transient.

There are also requirements with respect to the character of the calibration pulse generator which must be considered. *These are given in the reference by Favour, 1966.*

THE SCHMIDT-BOELTER GAGE

HISTORICAL NOTE:

Heat flux can be deduced under steady state conditions by measuring the temperature drop across a surface of known material properties and known thickness. This is a Thompson type 1 gage. E. Schmidt appears to have designed the first instrument making use of this observation. His instrument consisted of a rubber strip around which was wound a `pile` of 100 thermocouples wound is such a way that the junctions are alternately in the middle of one surface and then the other surface of the rubber strip as shown in figure 48.

Boelter (L.M.K. Boelter) introduced an ingenious modification to this gage by wrapping the rubber strip (plastic in the case of Boelter) with Constantan wire and then silver plating half of the wires to form a silver-constantan thermopile.

Hence, the Schmidt-Boelter gage is intrinsically a thermopile gage using the temperature drop across a material of known thermal and physical properties. The thermopile being cleverly formed by wrapping the material with a single thermocouple material and then plating the second material over half of the wires to form the series of junctions needed to form the thermopile.

Because of the thermopile design, the output signal from the gage is substantial and that feature may well be important in its practical application in wind tunnel testing.

The drawing on the right side of figure 48 indicates the current gage design based on the Schmidt-Boelter principle. This gage is `semi-contourable` in that normal to the strip of anodized Aluminum, the gage can be contoured.

CURRENT USE:

The Arnold Engineering Development Center is a large and enthusiastic user of the Schmidt-Boelter gage. Matthews, 1987, lists several advantages of the gage including durability, sensitivity (by virtue of the thermopile feature), semicontourability and a self-generating output signal proportional to the incident heat flux imposed upon it. One disadvantage noted is `...some concern about hot-spot effect...`; in effect, non-isothermal wall effects. This may limit its long duration applicability in tests. The commercial `Micro-Foil` heat gage, shown in figure 49, is an outgrowth of the Schmidt-Boelter gage.

THE COAX GAGE

The coax gage created an instrument based on a one dimensional thermal model with heat flow INTO the structure. The coax gage is a THICK wall gage based upon the capture of heat within the thermal mass of the instrument. In its most simple form, the coax gage is a semi-infinite slab gage as is the thin film gage. It is a Thompson class 2 gage. Modified versions of this gage eliminate the requirement that the gage have an isothermal back face temperature and, in so doing, change the character of the gage making it closer to a Thompson class 1 gage; a sandwich gage.

The gage, which we call today a coax gage, has been used to measure heat transfer for nearly a half century. Early use of the gage was the instrumentation of gun barrels. Ferri used such a gage in the 1950's as shown in figure 50. Fabrication technology has improved over the past 30 years but the concept has remained the same.

Semi-infinite slab gages respond to imposed heating as their substrate responds. If the substrate is an insulator (as in the case of a thin film gage described earlier), the response is strong and the temperature increases rapidly. If the substrate is a conductor (as in the case of the coax gage), the response is moderated by conductive heat dissipation through the substrate and the temperature rise is lower. If the temperature rise of the gage is low, the measurement of temperature is difficult and can produce error. The amount of this error depends upon the level of imposed heating rate. Statements to the effect that the gage has a ...` limited use in continuous tunnels...` are incomplete. They presuppose a level of heating which varies widely among continuous tunnels. It is the imposed heating rate that determines usefulness of the gage together with the interest of the experimenter in post test data smoothing.

THE EXTENDED DURATION COAX GAGE

Coax gages are limited in test duration not by the diffusion time of materials as suggested in the literature but by the limitations of the thermal model and its bounding conditions. Certainly, within a short time, the heat pulse from the heated face of the gage will diffuse to the rear surface of the gage. This thermal diffusion time can be modified somewhat by changing the thickness of the gage.

When the diffusion time is exceeded, the backface temperature of the gage will increase
and the semi-infinite slab thermal model is no longer useful. This does not limit the
usefulness of gage. Use of the gage for times exceeding the diffusion time however
requires more sophistication in formulating the thermal model, additional measurements
and, perhaps, another example of the integration of numerics and experimentation.

There are available so called 'three wire Coax gages' shown schematically in figure 51.
These gages measure both the heated surface and backface temperature and thus eliminate,
for a time, the limitations imposed by the semi-infinite slab thermal model. Three wire
gages are commercially available and have been used in wind tunnel tests to generate
valid test data for up to 30 seconds. This upper time limit is caused not by the fact
that there no longer exists a temperature difference between the front and backface of
the gage but because the minor differences in the thermal properties between the gage and
the model cause extraneous heating through the sides of the gage leading to inaccuracies
in the measurement. Of course, three-wire Coax gages require additional data acquisition
capacity and fewer gages can be sensed during any one entry into the tunnel.

Another solution to this problem is the use of the two-wire gages together with a finite
slab numerical thermal model. The numerical computation of the backface temperature
would replace its measurement in the three wire gage by a liner extrapolation of inner
node temperatures. Since the backface temperature is not extremely sensitive to test
motions in the wind tunnel, the computational estimate of the backface temperature will
generate data of acceptable quality. _his technique again opens some questions about
'pure experiments' that, in the last analysis, must be answered by the experimenter.

Data Reduction of Coax Gages

Figure 52 outlines two techniques for the reduction of coax gage data. Each begins from
an exact formulation of the semi-infinite slab thermal model. Both techniques, termed the
direct method and the indirect method, have been reduced to a finite difference
representation in this figure.

The DIRECT METHOD computes the rate of heat transfer directly from temperature data on
the surface, $T(t)$. The INDIRECT METHOD first computes the integral of the heating rate
with time, $Q(t)$, and then differentiates this quantity to generate the rate of heat
transfer. Neither technique has an obvious advantage over the other. The indirect method
results in smoother data because of the implicit smoothing in the intermediate step of
computing the integral of heating rate. Both techniques are slow as they integrate from
an initial time to generate results at each computational step.

Figure 53 indicates both surface and backface temperatures generated during an example
case which simulates model heating of 10 Btu/ft2 sec in a wind tunnel. Note the
parabolic nature of the surface temperature; a characteristic of this type of gage. The
surface temperature demonstrates two tunnel induced features. Early in the test there is
a 'blip' in the surface temperature caused by the model traversing the tunnel shear layer
upon injection. At times greater than 8 seconds the model is withdrawn and the surface
temperature decreases. The backface temperature is isothermal until the model has been
in the tunnel for 2 seconds.

Figure 54 indicates the reduction of this example data using a semi-infinite slab thermal
model. Deviation of the reduced data from the input heating level of 10 Btu/ft2 sec is
observed for times greater than 5 seconds. Reduction of these same sample data with a
finite slab thermal model is shown in figure 55. Accounting for the backface temperature
rise results in properly reduced data. Figure 56 demonstrates a reduction of the same
example data by the same techniques. In this figure, the resultant heat transfer is not
10 Btu/ft2 sec but 11. The reason for this is that the recorded temperature data, the
basis of the data reduction, was numerically affected by random timing errors. The result
of such errors which can be common in data acquisition is the generation of incorrect
heat flux data. The reader is cautioned that successful application of this integrating
technique requires numerically smooth input temperature data.
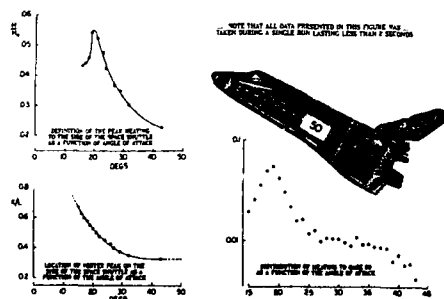
Figure 40   Example of Coax Gage Data
Taken on a Space Shuttle Model
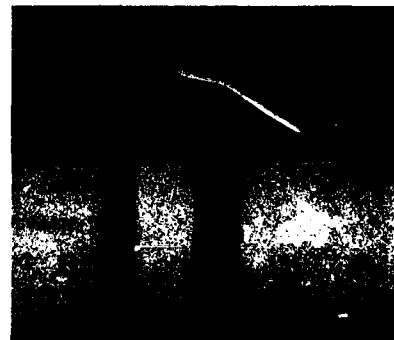
Figure 41   Very Small Scale Space Shuttle
Model Used to Acquire Coax Heat Flux Data

Figure 42   Flap Detail for Model Shown in Figure 41. Coax gage circled.

Figure 45   Calibration and Transformation of Gardon Gage Signal by the Fourier Transform Technique

Figure 43   Space Shuttle Heating Model with a Powered Flap to Acquire Coax Data.

Figure 46   Ratio of Transforms to Produce the Transfer Function in Magnitude and Phase Angle.

Figure 44   Outline of Fast Transform Technique for Data Reconstruction

Figure 47   Correction of Dynamic Test Data Taken at 5 Hz. by the Fourier Transform Technique

Figure 48 Development of the Modern
Schmidt-Boelter Heat Gage

Figure 49 Micro Foil (R) Heat Gage

Figure 50 Development of the Coax Gage
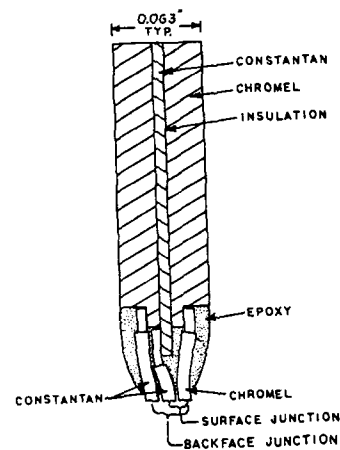
Figure 51 The Modern 'Three-Wire' Coax
Gage

DIRECT METHOD

$$\dot{q}(t) = \left(\frac{\rho c k}{\pi}\right)^{0.5} \int_0^t \frac{dT(\tau)}{d\tau} \frac{d\tau}{\sqrt{t-\tau}}$$

where t = time, from start of heating
T(t) = surface temperature rise
ρ = gage material density
c = gage material specific heat
k = gage material thermal conductivity

The finite-difference representation of this equation is
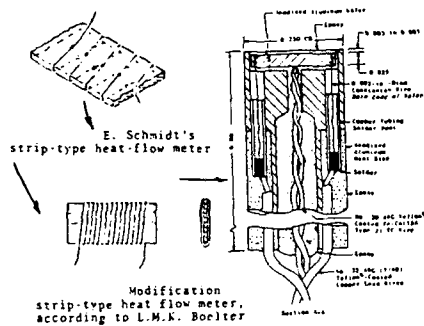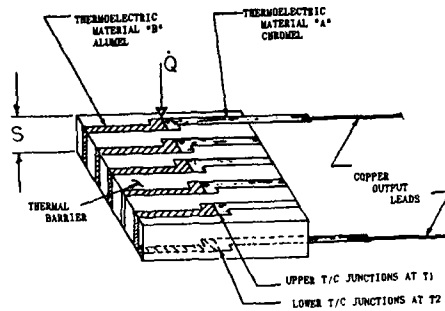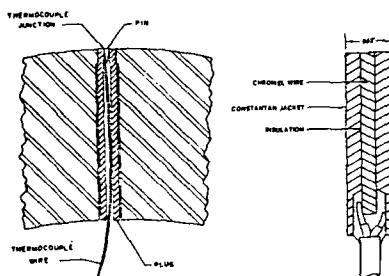
$$\dot{q}_n = 2\left(\frac{\rho c k}{\pi}\right)^{0.5} \sum_{j=1}^n \frac{T_j - T_{j-1}}{\sqrt{t_n - t_j} + \sqrt{t_n - t_{j-1}}}$$

INDIRECT METHOD

$$Q(t) = \left(\frac{\rho c k}{\pi}\right)^{0.5} \int_0^t \frac{T(\tau)}{\sqrt{t-\tau}} d\tau$$

and the finite-difference representation is

$$Q_n = \left(\frac{\rho c k}{\pi}\right)^{0.5} \sum_{j=1}^n \frac{T_j + T_{j-1}}{\sqrt{t_n - t_j} + \sqrt{t_n - t_{j-1}}} (t_n - t_{n-1})$$

An expression for differentiating the discrete function Q(t) is

$$\dot{q}_n = \frac{dQ}{dt} = \frac{1}{40(t_n - t_{n-1})} \left[-2Q_{n-8} - Q_{n-4} + Q_{n+4} + 2Q_{n+8}\right]$$

Figure 52 Data Reduction Techniques for
Coax Gages
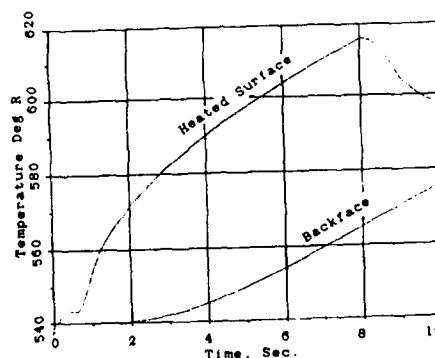
Figure 53 Surface and Backface
Temperature Data for Example Case

SEMI-INFINITE SLAB REDUCTION

FINITE SLAB REDUCTION

Figure 54 Reduced Surface Heat Flux
Data from Example Case According to
the Semi-Infinite Slab Thermal Model

Figure 55 Reduced Surface Heat Flux
Data from Example Case According to
the Finite Slab Thermal Model

$$Q_n = \left(\frac{\rho c k}{\pi}\right)^{0.5} \sum_{j=1}^{n} \frac{T_j + T_{j-1}}{\sqrt{t_n - t_j} + \sqrt{t_n - t_{j-1}}} (t_n - t_{n-1})$$

An expression for differentiating the descrete function $Q(t)$ is

$$\dot{q}_n = \frac{dQ_n}{dt} = \frac{1}{40(t_n - t_{n-1})} \left[-2Q_{n-8} - Q_{n-4} + Q_{n+4} + 2Q_{n+8}\right]$$
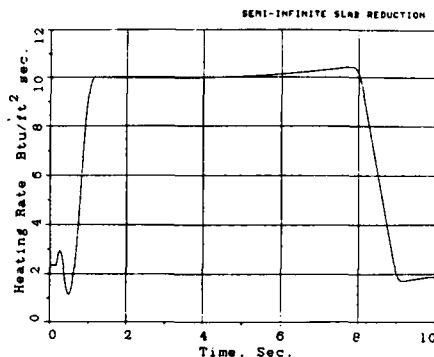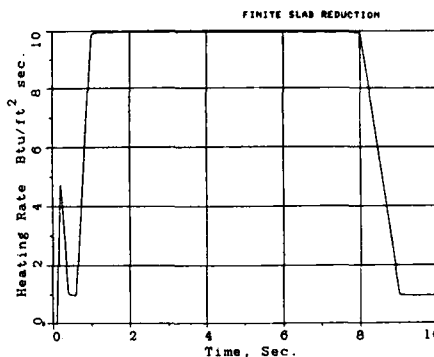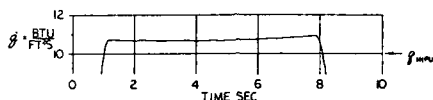
Figure 56 Reduced Surface Heat Flux
Data using the Finite Slab Thermal
Model with Random Timing Errors Imposed

Section VII
ADIABATIC WALL TEMPERATURES

Understanding aerodynamic heating requires a knowledge of the heating rates to the surface as well as the adiabatic temperature available to the surface. Supersonically, both terms are important with the relative sensitivity of the adiabatic wall temperature diminishing as the Mach number increases. Hypersonically, although an accurate definition of the adiabatic wall temperature is significant, it is difficult to measure and therefore normally neglected in experimentation. Numerical approximations or an accepted convention are generally used in its place.

Classically, from the definition of an adiabatic surface, the adiabatic wall temperature can be found by holding a model in the tunnel until the rate of heat transfer to the surface goes to zero. The resultant surface temperatures are ideally the adiabatic wall temperatures (plural because they are a function of surface orientation among other factors). Early tests employed this technique both at supersonic and later hypersonic speeds. The major problem with this 'classical' technique was that a special model was required which was perfectly insulated so that conduction effects were negligible. Another problem was that radiation to the tunnel walls becomes significant at hypersonic test conditions when the surface temperature approaches the adiabatic wall temperature. This factor cannot be adequately accounted for in practical data reduction and is not considered in the definition of the recovery temperature(s). Finally, in the absence of radiation, inferred heating rates approaching zero at the adiabatic wall condition imply that the temperatures within the model material approach a constant value (dT/dx = 0) and that temperature gradients with time, dT/dt, within the model material at strategic points (those required to define a thermal model) also approach zero. Since most heat flux inference techniques rely on one of these gradient of temperature, the accuracy of the measurement becomes very poor.

Supersonically, techniques exist to measure directly the adiabatic wall condition and these techniques appear accurate. Hypersonically, several techniques have been attempted with varying degrees of success. Two hypersonic techniques attempted in the recent past are:

1. model exposure for extended test periods monitoring the output of heat gages as the surface temperature APPROACHES the adiabatic condition. The adiabatic temperature (at the gage) being defined as an extrapolation of the heating rate level with increasing surface temperature.

2. successive tests made at discreet and increasing surface temperatures approaching the adiabatic wall condition. In this case, testing and instrumentation is conventional and the pre-test model conditioning system is used to produce an isothermal model at the desired surface temperature.

The first technique produces questionable results because of non-isothermal wall effects. Success (in terms of accurate determination of adiabatic temperatures) requires exceptional integration of the instrumentation into the model. Few thermal instruments can achieve that level of integration. The second technique is straightforward and has been used by AFWAL in a demonstration project to generate detailed information. It is expensive data to generate because the model temperature must be stabilized and uniform at several elevated temperatures outside of the tunnel. Instrument integration, while still a problem, is less demanding because testing begins from a uniform model temperature with heating data taken rapidly before non-isothermal wall effects are present.

The presence of non-isothermal model surface temperatures creates a severe problem in the conduct of these and all heat transfer measurements. A classic paper on the subject was written by Gates and Allen, 1974. Figure 57 from that paper indicates that the level of the recovery factor is directly proportional to the difference between the supply temperature, To, and the throat temperature. Further, Gates and Allen have demonstrated that the effects of a non-isothermal wall at the leading edge of the model are both substantial and enduring far downstream of the non-isothermal wall juncture. The paper is an excellent reference and should serve as a warning that these measurements of recovery factor are difficult to generate and prone to measurement errors.

Similar results were obtained by AFWAL. Using a successive test injection technique, adiabatic temperatures were inferred on a shock interference model as shown in figure 58. These data as well as the more conventional forcing temperature based on total temperature were used to compute the heat transfer coefficients as shown in figure 59. Use of the measured adiabatic wall temperatures increases the heat transfer coefficient substantially in the interaction region.

For these data it appears that the level of adiabatic wall temperature is sensitive to the features of the shock interaction process and by inference to many other local flow phenomena including, perhaps, vortical phenomena. To the extent that these details of the adiabatic wall are not measured, uncertainties will persist in the data. It is possible that vortical flow on the fuselage of the Space Shuttle extrapolated poorly to flight for this reason.
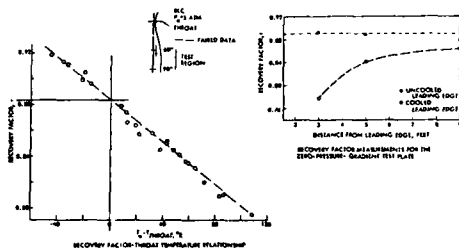

Figure 57 Effects of Non-Isothermal Wall Effects on Recovery Factor Data
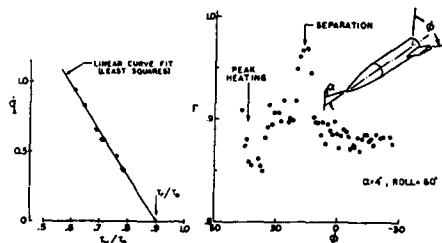

Figure 58 Recovery Factor Determination for Complex Model Using Transient Technique
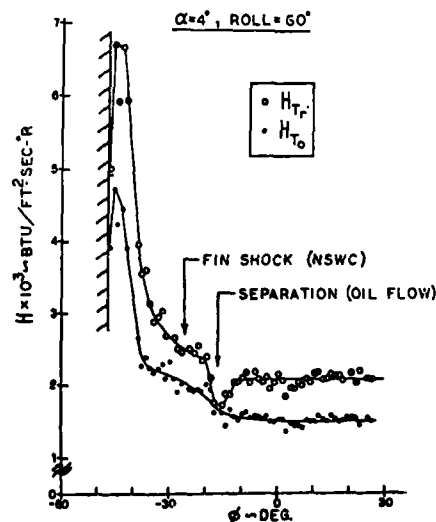
Figure 59 Effect of Recovery Factor on Reduced Heat Transfer Data

Section VIII
THE FABRICATION OF WIND TUNNEL MODELS

INTRODUCTION

Wind tunnel models used to generate aeromechanic test data are fabricated either by (1) building up the model of metallic sub-elements, (2) electroforming the model of metallic materials or (3) casting or forming the model of insulative materials. Each of these techniques will be discussed.

More recently, there has been interest in the ground test evaluation of structural elements of the configuration. These tests are uniquely different from the classical generation of aeromechanic data and present significant challenges to those who would design and fabricate the model and to those who would install instrumentation in the test model designed for these applications.

The practical evaluation of heat transfer data to three dimensional hypersonic configurations has been conducted for the past 25 years using the 'thin-skin' technique. Models to support this technique are built up of metallic sub-elements; normally, formed stainless steel sheet. In the build up process, the instrumented thin skin surface of the model is supported by a structural hard back which accommodate the loads imposed on the configuration by the test environment. The instrumented portion of the model is relatively thin, 0.030 inches (7 to 8 mm).

Extremely complex configurations involving compound curvature are difficult to fabricate with the thin skin technique using material sheet construction. Although recently CAM (computer aided manufacturing) techniques have improved our capabilities, many of these extremely complex shapes are fabricated by electroforming a thin skin section and attaching that section to the structural hardback. Electroforming limits the selection of materials available to the designer; materials which, generally, have higher thermal conductivity and are thus more susceptible to measurement losses caused by heat flow along the surface.

Insulative models have been used for the past quarter century to generate survey data as discussed in section III. Several materials and corresponding fabrication techniques have been used. In general, these insulative materials are not structurally sound and require a structural hardback of metallic materials. Insulative materials selected and used in the past include, typically, castable Stycast (R) and machinable Teflon (R).

ELECTROLESS PLATING

The use of electroless plating techniques allow for the fabrication of extremely complex aerodynamic shapes and/or the highly detailed instrumentation of aerodynamic shapes of interest. A recent paper by Avery, 1984, presented an extremely detailed and informative picture of the capabilities and difficulties of this technique. Figure 60 is a composite from that reference.

Avery's model, while not complex aerodynamically was instrumented with 256 thermocouples in an extremely dense array. Two features from this experiment deserve consideration. First, the plating techniques and the ability to plate the model to a thickness of 0.025 inches are somewhat unique and second, instrumentation of this model using a single Constantan wire with the junction formed between the Constantan and the electroformed nickel, Niculoy 22 is unique. This technique has been conducted in much the same manner as the Soviet microthermocouples. Several problems were uncovered and discussed in the report. They included the tolerance on plating thickness, cleaning of and activating the plating surface, pitting and surface roughness and delaminations in the plating process and during testing. Similar but earlier results were reported by Stalmach,1975
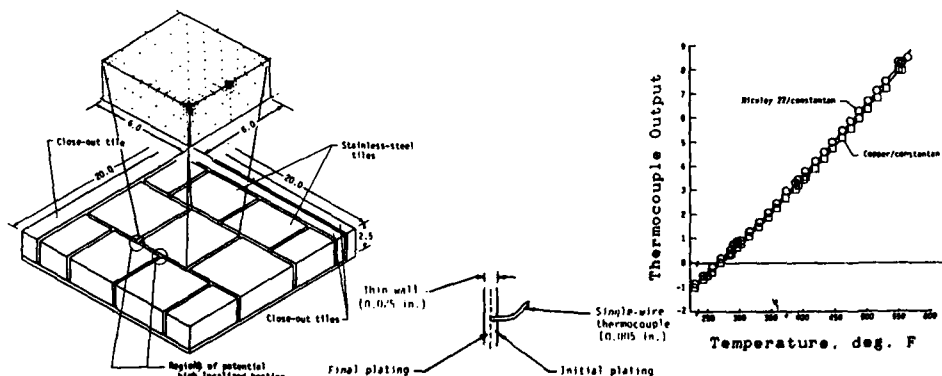

Figure 60 Electroless-Plating Technique for Fabricating Thin Wall Convective Heat-Transfer Models after Avery, 1984

Section IX
INSTRUMENTATION IN SHOCK INTERACTION REGIONS

Regions of shock interaction present a particularly complex problem for thermal instrumentation. These regions have high localized aerodynamic heating with large surface temperature gradients about the peak heating. Further, the location and extent of these critical peak heating locations are not precisely known (or vary with time) so that instrumentation is placed with some uncertainty. Finally, conventional model designs employ metallic surface materials which create conduction losses along the surface of the skin and away from the peak heating locations. Scale is also an important consideration. Small scale shock interaction models may not be instrumentable because of the small size of shock interaction features and/or losses due to heat conduction. Those who manage the development of flight vehicles seem fixated on the evaluation of all such phenomena using scaled model configurations. With shock interaction phenomena, this strategy is rarely acceptable. The results of its use, which are all too often seen, produce biased, low heating rates. As an example, the leading edge region of the Rockwell Space Shuttle was instrumented to obtain shock interaction data. The instrumentation, thermocouples attached to a thin skin model, was improper for shock interactions on a model of this small scale in a continuous flow wind tunnel. The result was that the measured heating values were 1/3 the actual value of the heating rate impressed on the model by the test facility.

The Rockwell Space Shuttle, as well as several other development programs, have used survey test techniques (discussed in section 3) to determine the location of such peak regions. Unfortunately, as has been discussed, these highly localized regions are not clearly observed with such survey instrumentation. The result is that highly approximate locations of the interference peak are observed with the resultant level of the peak heating poorly defined.

Point measurements of interference heating peaks require either the use of metallic models or the use of insulative models with either thin film gages or isothermal thermocouple staple gages. The metallic models generate substantial conduction losses along the surface and the corresponding insulated material models can crack due to thermal shock caused by the severe thermal gradients in the small interaction regions (as in the case of Macor (R) models). Both the thin film and staple gages may span the entire shock interaction region (depending on its dimensions and the orientation of the gage in the flow along the gage sensing element). These effects require corrections for non-constant surface heating in the data reduction and analysis phase.

With this brief introduction to the problem, let us consider several gages with which to evaluate shock interaction phenomena.

THE COAX GAGE WITH UNIFORM HEATING

A thermal model was used to evaluate the response of a coax gage installed in a block of 17-4 PH stainless steel which was subjected to uniform external heating. The gage and the surrounding stainless steel were the same thickness to minimize the thermal differences between the two materials. Figure 61 indicates the response of the gage for (a) the gage in intimate thermal contact with the surrounding material as used in the classical mode wherein only the heated surface is measured and the backface is assumed to be isothermal; (b) the gage in intimate thermal contact with the surrounding material but with both the heated and backface temperature measured or inferred through computations and (c) the gage insulated from the surrounding stainless steel with a Teflon (R) insulating ring.

The classic operation of the coax gage assumes that the backface is isothermal limiting the application of the gage to times less than that required for the thermal pulse from the test to reach the backface of the gage. This is clearly seen in the response of the gage as shown in the figure. Good data is generated for a few seconds and then the gage drifts off and is not useful. This shortcoming of the coax gage can be overcome by either measuring the backface temperature or computing that temperature through the thermal model employed. With these improvements, the gage is useful for extended periods of test time. Here, the output to 30 seconds is shown. Installing a Teflon(R) cylinder about the gage was attempted to enforce the one dimensionality of the assumed thermal model. We were surprised at the response of the gage in this configuration. The increase in heating observed in this figure is due to the fact that the insulation material, for the same constant heating rate, creates a differential temperature history with respect to the coax gage and feeds heat into the sides of the gage. The result, as shown in the figure, invalidated the gage and is a dramatic example of how difficult measurements are in even a uniform heating environment.

THE COAX GAGE WITH NON-UNIFORM HEATING

Figure 62 indicates a further complication to the idealized case of a uniform heating pulse. In this figure a heating pulse of magnitude equal to the uniform case was imposed over only a 1/4 inch interval as shown in figure 63. Five lines are shown on this figure representing the spectrum of responses caused by the coax gage being progressively wrapped in a Teflon(R) insulation material. In this non-uniform heating case, the gage installed directly into the 17-4 PH stainless steel creates a non uniform response even though both the heated surface and backface surface is measured. The reason for this is

that the thermal gradient produced across the heated plate draws heat from the gage. At the other extreme, the Teflon(R) insulated gage, as before, has the reverse effect. With the non uniform heating across the plate, the Teflon(R) is thermally drained both into the coax gage and into the cold surrounding 17-4 PH stainless steel structure. The lines between these two extremes represent different configurations of the Teflon(R) insulator. The line closest to the actual 5 Btu/ft2 sec input is an optimized (and perhaps idealized) design.

There are several consequences of the data presented in this figure. First, the trends presented in this figure are somewhat idealized although illustrative of the problem. The design of an experiment will require a more detailed analyses using the thermal model as well as validation of such a model. Secondly, the consequences of this figure are the following:

1. It is necessary to use not only intuition but also numerical modeling techniques to correctly integrate instrumentation into a model for difficult situations such as shock interaction. The competing consequences of complex heat flows cannot be adequately deduced by ad-hoc rules of thumb. A correlary to that remark is that the details of this or any other installation will change with regard to the heating imposed and the incidental features of the model in which the gage is placed.

2. The figure demonstrates characteristic curves which are related to specific phenomena. These characteristic curves can be used to understand the results of the experiment with regard to the instrumentation and the corrections that must be applied after the experiment to correct the data of the incidental features of the model. Certainly is is best to design the experiment correctly but, in spite of best efforts, these features may still be present and require correction.

3. The characteristic shape of the curve can, itself, be used to understand more about the experiment and extract more data from the experiment. This is an area called "Parameter Estimation" and it is possible that an experiment, properly strategized, could generate not only the required data but secondary information on the quality of the instrumentation as well.

In the final analysis, this type of 'thick wall' STATIC instrumentation is not all that useful in the evaluation of interference heat pulses.

Studies were also conducted on the DYNAMIC case of a heating pulse sweeping past a coax instrument. Figure 64 indicates the results of that numerical experiment. Clearly, sweeping the heat pulse eliminates many of the conduction loss problems observed with the static instrumentation by distributing the temperature rise across the surface of the model. The results again support the need to consider not only advanced instrumentation but also advanced instrumentation strategies in the acquisition of complex data.
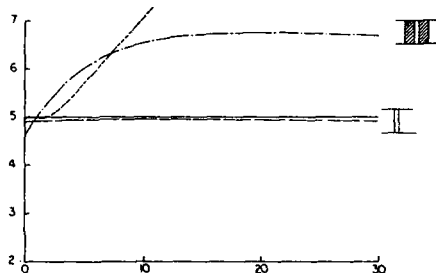

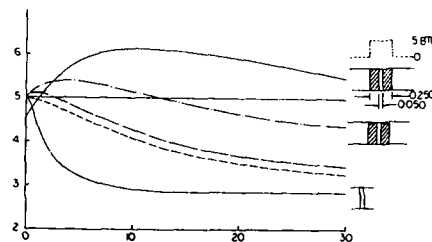Figure 61 Effect of Installation Details on the response of a Coax Gage to a Uniform Heating Pulse

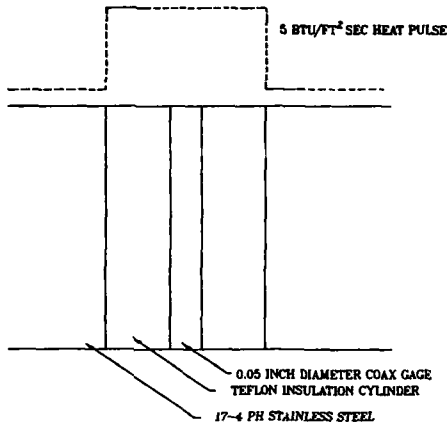Figure 62 Effect of Installation Details on the respose of a Coax Gage to a Non-uniform Heating Pulse

5 BTU/FT² SEC HEAT PULSE

0.05 INCH DIAMETER COAX GAGE
TEFLON INSULATION CYLINDER

17-4 PH STAINLESS STEEL

Figure 63   Character of the Non-Uniform
Heating Pulse

0.25 inch wide pulse moving at
1 inch/second past a 0.05 inch
diameter coax gage

Heating Rate in Btu/ft2 sec

Time in seconds
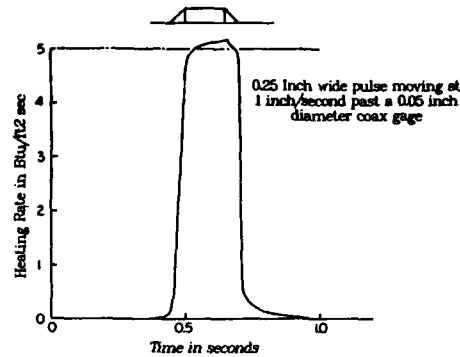
Figure 64   Coax Gage Response to a Swept
Pulse of Heating

REFERENCES

Aliotta. J., "Effects of Impurities on the Thermoelectric Properties of Platinum" Instruments and Control Systems. March 1972, pp 106-107

Avery. D.E., Ballard, G.K. and Wilson, M.L., "Electroless-Plating Technique For Fabricating Thin-Wall Convective Heat-Transfer Models", NASA TP 2349, 1984

Bendersky. "A Special Thermocouple for Measuring Transient Temperatures", Mech. Engr., Feb. 1953, pp 117-121

Bickle, L. W. and Dove, R.C., "Numerical Correction of Transient Measurements", ISA Transactions, Volume 12, Nr. 3, 1973, pp 286-295

Borell, G.J. and Diller, T.E., "A Convection Calibration Method for Local Heat Flux Gages", Jour. of Heat Transfer, February 1987, Volume 109, pp 83-89

Borovoy, V. Ya, Osipov, V.V. et al, "Effect of Mach and Reynolds Numbers on the Heat Exchange on a Blunted Leading Wing Edge of Varible Sweepback in the Region of Incidence of the Bow Wave", TsAGI Uchenye Zapiski. (ISSN 0321-3429) volume 14, Nr. 2, 1983, pp 58-66

Borovoy, V. Ya, "Flow of Gas and Heat Exchange in Zones of Reaction of Shock Waves with Boundary Layers", Techeniye Gaza i Teploobmen v Zonakh Vzaimodeystviya Udarnykh Voin s Pogranichnym Sloyem", 1983

Boylan, D.E., Carver, D.B., Stallings, D.W. and Trimmer, L.L., "Measurement and Mapping of Aerodynamic Heating Using a Remote Infrared Scanning Camera in Continuous Flow Wind Tunnels", AIAA 78-799, 1978

Covert, G. and Gollnick, A.F., Jr. "Calibration of a Small Heat Transfer Gage and Its Applications", ISA Paper 68-535

Creel, T.R., Jr., "A Device For Rapid Determination of Thermophysical Properties of Phase Change Wind Tunnel Models", NASA TN D-3421, 1976

Cresci, R.J. and Libby, P.A., "Some Heat Conduction Solutions Involved in Transient Heat Transfer Measurements", WADC TN 57-236, 1957

Cutting, J.C. and Fay, J.A., "High Heat Flux Effects in Wire Heat Gages", Jour. of Aerospace Sci., April 1961, pp 342-343

Czysz, P. and Dixon, W.P., "Quantitative Heat Transfer Measurement Using Thermographic Phosphors", S.P.I.E. Journal, March 1969, pp 77-79

Dean, W.G. and Connor, L.E., "A Study For Development of Aerothermodynamic Test Model Materials and Fabrication Techniques", NASA CR 2065, 1972

Dixon, W.P., "Precise Heat Transfer Measurements with Surface Thermocouples", Eighth Annual Conference on Thermal Conductivity. Purdue University, October 1968

Durand, J.A., and Rhudy, J.P., "Procedure Used For X-15 Heat Transfer and Pressure Distribution Tests at Hypersonic Speeds", AEDC TN 59-04, 1959

Doorly, J.E. and Oldfield, M.L.G., "The Theory of Advanced Multi-Layer Thin Film Heat Transfer Gauges", Intl. Jour. of Heat and Mass Transfer, Volume 30, Nr 6, pp 1159-1168, 1987

Edney, "Anamalous Heat Transfer and Pressure Distributions on Blunt Bodies at Hypersonic Speeds in the Presence of an Impinging Shock", FFA 115, 1968

Ehrich, F.F., "Differentiation of Experimental Data Using Least Squares Fitting", Jour. of Aeronaut. Sci., April 1961, pp 133-134

Epstein, A.H., Guenette, C.R., Norton, R.J.G. and Yuzhang, C., "High Frequency Response Heat-Flux Gage", Review of Scientific Instrumentation, Volume 57, (4), pp 639-648, 1986

Favour, J.D., "Transient Data Distortion Compensation", Shock and Vibration Bulletin, Nr. 35. Part 4, Feb. 1966, pp 231-237

Feldstein, N., "Selective Electroless Plating Techniques: A Survey", August 1978

Foster, T.F. and Wallace, G.A., "Photoetching Roughness Application and Transient Backwall Thermocouple Technique For Hypersonic Blowdown Wind Tunnel Models", ISA, 1980, ISBN 87664-473-6

Gates, D.F. and Allen, R.W., "Experimental Measurements of Upstream History Effects in Turbulent Supersonic Flow", 1974 Heat Transfer and Fluid Mechanics Institute, paper 21.

Giedt, W.H., "The Determination of Transient Temperatures and Heat Transfer to a Gas-Metal Interface Applied to a 40 mm Gun Barrel", Jet Propulsion, April 1955, Volume 25, Number 4, pp 158-162

Griffith, B.J. Maus, J.R. and Best, T., "Explanation of the Hypersonic Longitudinal Stability Problem - Lessons Learned", NASA CP 2283, 1983

Grossman, D.G., "Machining a Machinable Glass-Ceramic", Vacuum, Volume 28, Number 2. pp 55-61

Harting, D.R., "Digital Transient-test Techniques", Experimental Mechanics, Volume 12, Nr. 7, July 1972, pp 335-340

Harvey, W.D., "Continuous Skin Construction Technique For Fabricating Models For Aerodynamic Heat Transfer Studies Involving Very Small Transient Heating Rates", ISA Preprint 17.12-7-65, 20th Annual Conference, October, 1965

Hayashi, M., Sakurai, A. and Aso, S., "An Investigation of a Multi-Layered Thin Film Heat Transfer Gauge", Memoirs of the Faculty of Engineering. Kyushu University, Volume 44, Nr. 1, March 1984, pp 113-124

Hayashi, M., Sakurai. A. and Aso, S., "A Study oF Multi-Layered Thin Film Heat Transfer Gauges and a New Method of Measuring Heat Transfer With It" Trans. of Japan Society of Aero. and Space Sciences, Volume 30, #88, pp 91-101. 1987

Hayes. J.R., "A Water Heated Platinum Thin-Film Heat Transfer Gage for Use in Cold Flow Wind Tunnels", AFWAL TM 83-158-FIMG

Hayes, J.R., "Notes on Coax Gage Data Reduction", AFWAL TR 89-xxxx (To be Published)

Hedlund, E., "Heat Transfer testing in the NSWC Hypervelocity Wind Tunnel Utilizing Co-Axial Surface Thermocouples", NSWC MP80-151, 1980

Hodge, J.K. and Woo, Y.K. and Cappelano, P.Y., "Parameter Estimation for Imbedded Thermocouples in Space Shuttle Wind Tunnel Test Articles with Nonisothermal Wall", AIAA 83-1533, 1983

Hornbaker, D.R. and Rall, D.L., "Heat Flux Measurements: A Practical Guide", Instrumentation Technology, February 1968, pp 51-56

Jenke, L.M., "Application of Digital Fourier Analysis in Processing Dynamic Aerodynamic Heating Measurements", AIAA Journal, Volume 17, Nr. 6, pp 641-642, 1979

Jenke, L.M. and Strike. W.T., "Application of Digital Fourier Analysis in Processing Heat Transfer Measurements on an Oscillating Cone in a Hypersonic Stream", AIAA 78-778

Jones, R.A. and Hunt, J.A.,, "An Improved Technique for Obtaining Quantitative Aerodynamic Heat-Transfer Data with Suitable Coating Materials", NASA TR R-230 and AIAA 65-131, 1965

Jones, R.A., and Hunt, J.L., "Use of Fusible Temperature Indicators for Obtaining Quantitative Aerodynamic Heat-Transfer Data", NASA TR R-230, 1966

Jones, T.V., "Heat Transfer, Skin Friction Total Temperature and Concentration Measurements", Chapter 4 to the book "Measurement of Unsteady Fluid Dynamic Phenomena", Edited by Dr. B.E. Richards, McGraw-Hill, 1977

Kendall, D.N., Dixon, W.P. and Schulte, E.H., "Semi-Conductor Surface Thermocouples for Determining Heat Transfer rates", IEEE Transactions on Aerospace and Electronic Systems, Volume AES-3, Number 4, July 1967

Kidd, C.T., "A Durable, Intermediate Temperature, Direct Reading Heat Flux Transducer For Measurements in Continuous Wind Tunnels", AEDC TR 81-19, 1981

Kidd, C.T., "Determination of the Uncertainty of Experimental Heat-Flux Calibrations", AEDC 83-13

Kidd, C.T., "Thin Skin Technique Heat Transfer Measurement Errors Due to Heat Conduction into Thermocouple Wires", Instrument Society of America Trans., Vol. 24, Nr. 2, pp 1-9, 1985

Kidd, C.T., "Lateral Heat Conduction Effects on Heat Transfer Measurements with the Thin Skin Technique", Instrument Society of America Trans., Vol. 26, Nr. 3, pp 7-18, 1987

Maegley, W.J. and Carroll, H.R., "MX Missile Thermal Mapping and Surface Flow Results", AIAA Jour. of Spacecraft and Rockets, Volume 19, Nr. 3, May-June 1982, pp 199-204 (see also AIAA 80-1310)

Matthews,. R.K., "Wind Tunnel Testing in Hypersonic Facilities", Notes from a Short Course on Hypersonics, University of Texas, October 1987

Mentre, V. and Consigny, H., "An Improved Data Reduction Technique for Heat Transfer Measurements Using Surface Thermocouples or Thin-Films", ICIASF '87 Record, pp 369-377

Miller, C.G., "Comparison of Thin-Film Resistance Heat Transfer Gages with Thin Skin Transient Calorimeter Gages in Conventional Hypersonic Wind Tunnels", NASA TM 83197, December 1981

Miller, C.G., "Refinement of an 'Alternate' Method for Measuring Heating Rates in Hypersonic Wind Tunnels", AIAA Journal, Volume 23, Nr.5, pp 810-812

Oldfield, M.L.G., Jones, T.V. and Schultz, D.L., "On-Line Computer for Transient Turbine Cascade Instrumentation", IEEE Transactions on Aerospace and Electronic Systems, Volume AES 14, Number 5, September 1978, pp 738-749

Schmitz, L.S., "Nonlinear Analog Network to Convert Surface Temperature to Heat Flux", CAL Report 130, 1963 (N64-18176)

Schultz, D.L. and Jones, T.V., "Heat Transfer Measurements in Short Duration Hypersonic Facilities", AGARD-AG-165, February 1965

Simonich, J.C., and Moffat, R.J., "New Technique for Mapping Heat Transfer Coefficient Contours", Rev. Sci. Instrum. May 1982, pp 678-683

Stalmach, C.J., Jr., "Developments in Convective Heat Transfer Models Featuring Seamless and Selected Detail Surfaces, Employing Electroless Plating", NASA CR 144364, (N75-29356)

Thomann, H. and Frisk, B.,"Measurement of Heat Transfer with an Infrared Camera", Intl. Jour. of Heat and Mass Transfer, Volume 11, pp 819-826

Thompson, W.P., "Heat Transfer Gages", pp 663-685 of Methods of Experimental Physics: Fluid Dynamics, Volume 18, Academic Press, 1981, ISBN 0-12-475956-4 (v.18B)

Throckmorton, D.A., "Model Wall and Recovery Temperature Effects on Experimental Heat Transfer Data Analysis", NASA TM X-71967, 1974

Wannenwetsch, G.D., Ticatch, L.A., Kidd, C.T. and Arterbury, R.L., "Measurements of Wing Leading Edge Heating Rates and Wind Tunnel Models Using the Thin Film Technique", AIAA 85-0972, 1985

MEASUREMENTS OF HYPERSONIC FLOWFIELDS

F. K. Owen

Complere Inc.

P.O. Box 1697

Palo Alto, CA 94302

USA

ABSTRACT

Although extensive progress has been made in computational fluid mechanics, reliable flight vehicle designs and modifications still cannot be made without recourse to extensive wind tunnel testing. Future progress in the computation of hypersonic flowfields is restricted by the need for a reliable turbulence modeling data base which could be used for the development of empirical models for use in numerical codes. Currently, there are few compressible flow measurements which could be used for this purpose and, since additional shear stress terms may be significant at high Mach numbers, models based on incompressible measurements may not be realistic. In this lecture, techniques for mean, transitional and turbulent flow measurements will be reviewed and the status of transition and turbulence research in support of turbulence modeling programs discussed. Procedures for hot wire and hot film measurements in hypersonic flows will be outlined and assessments made of the potential for hot wire and laser velocimeter measurements of turbulent fluctuations in hypersonic flowfields. The results of recent experiments conducted in two hypersonic wind tunnels will be presented and comparisons made with previous hot wire turbulence measurements.

1. INTRODUCTION

Current hypersonic flowfield instrumentation is insufficient to meet present and future ground test requirements. Measurements are required to establish the basic physical mechanisms and turbulence models required for reliable prediction of transitional and turbulent hypersonic flowfields. With concepts such as orbiting high altitude, high drag aerobraking vehicle configurations such as aero-assisted orbital transfer vehicles (AOTV's), high lift trans-atmospheric vehicles (TAV's) and the National Aerospace Plane (NASP), we have embarked upon a new era of hypersonic research and development which will stretch our experimental and design capabilities to the limit.

To put possible future challenges in perspective, consider, for example, the concepts discussed in Ref. 1. Such a vehicle would attain a cruise Mach number of 25 in low earth orbit. It will experience skin temperatures of up to 2,000°F and dynamic loads which will exceed current flight vehicle loading by an order of magnitude. The performance of such a vehicle will be extremely sensitive to the characteristics of the external flowfield. For example, skin friction will account for up to 50 percent of the total cruise drag and ram thrust will exceed the drag by less than 10 percent. Thus, at flight vehicle Reynolds numbers of 100 million, transition location will be critical. It will determine heating rates, overall drag and ramjet/scramjet engine inlet performance. Knowledge of transitional and turbulent hypersonic flows will be a key area in the design and development of future hypersonic flight vehicles. Unfortunately, in the post-Apollo era, a time of reduced space effort in the United States and Europe, the subject of hypersonic aerodynamics has been neglected and many hypersonic simulation facilities have either been scrapped or decommissioned. Table 1, taken from Ref. 2, lists the number of test facilities in the categories of continuous flow, intermittent flow (blowdown) using air, nitrogen or helium, arc discharge, shock tunnels and other miscellaneous types. Clearly, there has been a significant decline since the

early sixties. However, with the resurgence of planned hypersonic research, facilities and experimental methods for hypersonics are once again in strong demand.

During this period of hypersonic neglect, great strides have been made in our capabilities to compute complex fluid flows. But, reliable flight vehicle designs and modifications still cannot be made without recourse to extensive wind tunnel testing. At present, progress in computational fluid dynamics of hypersonic flows is restricted by the need for reliable experimental data and an improved understanding of both the physics and structure of turbulence in high speed flows which can be used for the development of empirical turbulence models and to validate Navier-Stokes codes. Although some hot wire data have been obtained in previous years, they are of questionable reliability due to the assumptions which must be made to determine thermodynamic fluctuation levels from the measured hot wire variables. Currently, there are few compressible flow measurements which could be used for modeling purposes, and, since additional shear stress terms may be significant at high Mach numbers, models based on incompressible measurements may not be realistic. Experiments designed to aid turbulence modeling of hypersonic flows and verify computer codes will require extensive flowfield mean flow and turbulence measurements.

In recent years, experimental methods in lower speed regimes have made significant advances due primarily to the availability of high power lasers. Their introduction has enabled the field of laser velocimetry to expand from low speed, small scale, closely controlled laboratory applications to the measurement of compressible flows in large scale wind tunnels (Ref. 3.) The advent of the laser velocimeter allows us to measure velocity fluctuations directly in a linear, non-intrusive manner. Of particular value is the capability it offers to measure some of the compressible turbulent shear stresses, since this is an impractical task with hot wires. The challenge now is to apply these new computational and experimental capabilities to the solution of current and future hypersonic flow problems.

Flowfield measurements in support of new hypersonic designs can be classified into two general categories. In one category of experiments, fundamental experiments, sometimes referred to as "benchmark" experiments, are selected to provide a reliable mean flow and turbulence modeling data base to guide computational designs. These experiments are usually selected to simulate a simplified element of a more complex flowfield. In the second category, less detailed measurements of complex flows of a more immediate practical interest are required which will provide details for initial vehicle design formulations. At present, there are two fundamental questions to be answered, namely: where do we stand now and what are the prospects of achieving these measurement goals in a timely and cost effective manner? The purpose of this paper is to address these questions and to discuss the pitfalls and prospects for flowfield measurements of hypersonic flows.

2. BACKGROUND

Since transition from laminar to turbulent flow can account for significant changes in such important parameters as skin friction, heat transfer, and flight vehicle performance, it is important that the variation of transition Reynolds number with Mach number be accurately determined. However, there is much speculation at present regarding the effects of Mach number and unit Reynolds number on transition location at hypersonic speeds. The collection of transition data shown in Fig. 1 shows that the measurements, at fixed Mach numbers, vary by factors of twenty or more and, although there is a trend of increasing transition Reynolds number with increasing Mach number, the data base is clearly insufficient for design purposes. Transition location uncertainties of these magnitudes could lead to serious heating, drag and performance consequences. Although at first glance Fig. 1 seems to suggest a lost cause, consistent and careful measurements can alleviate the situation. Apart from the complex coupling of the usually unknown freestream turbulence levels and spectra and model

boundary layer transition a major source of scatter in transition data can be attributed to inconsistent choice of transition "point" indicated by different techniques. This will be discussed in more detail later in the paper.

A large quantity of mean flow compressible turbulent boundary layer data are also available in the open literature. A significant number of these studies have been critically reviewed in Ref. 4. Boundary layer measurements are generally used in the prediction of skin friction and heat transfer. However, although mean profile data are reasonably reliable outside the sub-layer, due to probe resolution they are generally insufficient near the wall to infer surface quantities. Thus, the principal areas of difficulty in mean flow measurements remain in the determination of the wall shear stress and heat transfer. Estimates of wall values from flowfield studies should be regarded with caution. Even direct wall measurements can be subject to significant errors, especially in pressure gradient flows (see Ref. 4.)

At present, the principal research tools for turbulence measurement in low speed flows are hot wire and laser anemometers. In hypersonic flows, hot wires can be used reliably to measure freestream mass flux and total temperature fluctuations but cannot be used in flows which involve high levels of turbulence, separation or time-dependent flow reversal which are often associated with shock/boundary layer interactions (Ref. 5). On the other hand, due to resolution limitations, the laser anemometer is not suitable for low turbulence, freestream measurements. But, with its linear and directional sensitivity it probably represents the instrument of last resort for the non-intrusive measurement of large scale, unsteady turbulent flows. Thus, it is important that the practical problems associated with both hot wire and laser anemometry are addressed and that redundant hot wire and laser velocimeter experiments and comparisons be carried out to determine their reliable ranges of application. Measurements to support turbulence modeling could then be chosen so that the attributes of both techniques could be applied with care.

A hot wire anemometer senses any changes in the variables which affect the rate of heat-transfer between the wire and the fluid. Variations in heat transfer coefficient can change both wire temperature and resistance. If the wire is made part of a suitable electrical circuit, these changes can be used to generate a signal which is related to the instantaneous heat transfer. Thus, as Morkovin (Ref. 6) points out, for the correct interpretation of the electrical signal we need to know: 1) the identity of possible fluid flow variations (eg. turbulence or sound), 2) the laws of heat transfer between the wire and fluid, 3) the variation of wire resistance with temperature and the effects of conduction to the supports, and 4) the response of the associated electrical system which produces the measured current or voltage variations. Unfortunately, our knowledge in each of these categories is far from complete and could well be responsible for the current lack of reliable data. A recent review (Ref. 7) of supersonic and hypersonic hot wire data taken in zero pressure gradient, adiabatic or isothermal wall boundary layers illustrates the problem. Fig. 2, taken from Ref. 7, shows data from several sources for the fluctuating axial velocity component. The scatter is so large that it is impossible to construe that any form of similarity with Reynolds or Mach number exists. The picture is even more confusing when the distributions of the other two normal stresses are reviewed. The measured shear stress distributions (Fig. 3) once again show that no pattern of similarity can be observed. Indeed, only Klebanoff's incompressible measurements (shown for comparison) approach the anticipated limiting value of unity in the wall region. These results give some indication of the deficiencies in the measurement techniques and data reduction assumptions.

The problem is further compounded by the fact that a significant portion of the available studies were conducted in wind tunnel nozzle wall boundary layers in which unknown upstream influences could have affected the turbulent structure. Also, many measurements have been made with thin film gages which have doubtful validity for quantitative turbulence measurements, since substrate thermal feedback causes probe sensitivities to vary with frequency. It is particularly serious and complex for multiple films mounted on the same substrate

which are the type of probes used for shear stress measurement. Even with crossed-wire probes, data interpretation is involved and can be unreliable. For instance, the time-averaged expression for one component of the compressible turbulent shear stress is $\overline{(\rho v)'u'}$ whereas the hot wire, after questionable assumptions (Ref. 8), measures $\overline{(\rho u)'v'}$ which differs by a first-order term. Thus, it is clear that systematic investigations of fluctuating velocities are still needed, even in zero-pressure gradient compressible boundary layers to establish a reliable data base for turbulence modeling. Clearly, hot wire turbulence measurements in compressible shear flows still present a formidable scientific challenge. Most flows of practical interest can be extremely sensitive to probe interference. Local turbulence levels also normally exceed those for which reliable hot wire measurements can be expected. Directional intermittency can give rise to substantial hot wire errors (Ref. 9).

There are other factors which affect the reliability of hot wire measurements in flows where more than one mode fluctuation is significant. In these flows, a fundamental hot wire anemometer requirement for meaningful quantitative measurements is one of high-frequency response over a wide range of wire overheat ratios. This requirement is needed to separate mass flux and total temperature fluctuations in compressible, non-isothermal flows. But it brings out a basic flaw in the most widely used tool for current turbulence research, namely, the constant temperature anemometer (CTA). This weakness is illustrated by the following equation for the CTA frequency response

$$M_{CTA} = M_w/(1 + 2rR_wG) \qquad\qquad 2.1$$

where M_{CTA} and M_w are the time constants of the anemometer system and the wire alone, respectively, r is the wire overheat, R is the wire resistance and G is the anemometer transconductance. It can be seen that the CTA frequency response is directly proportional to the wire overheat ratio and at low overheat ratios (r–>0) the anemometer system time constant approaches the wire time constant. Since M_w can range from 1 to 5 ms (frequency response from 32 to 160 Hz), low-overheat, constant temperature anemometer measurements are clearly open to question. Unfortunately, low overheat measurements are required to determine the total temperature fluctuations and the mass flux-total temperature cross correlations. But, with the use of compensating amplifiers, adequate constant current anemometer response can be maintained even at the lowest overheat ratios. Comparisons of the two basic hot wire systems have been made in Ref. 10. These measurements clearly show that there will be a need for alternate constant current anemometer measurements in many hypersonic flow situations.

Other sources of hot wire turbulence measurement uncertainty are the assumptions involved in reducing the hot wire measurements of mass flux and total temperature fluctuations to terms which appear directly in the momentum and energy equations. For example, to obtain the axial velocity fluctuation levels, we assume that the flowfield is isentropic. Using conventional variables permits us to write the energy equation in its differential form as

$$\frac{1}{\alpha}\frac{\partial T_t}{T_t} = (\gamma - 1)M^2\frac{\partial u}{u} + \frac{\partial p}{p} - \frac{\partial \rho}{\rho} \qquad\qquad 2.2$$

$$\text{where } \alpha = 1/\{1 + (\gamma - 1)/2\ M^2)\}$$

Then we consider the equation for the mass flow per unit area and time in its differential form

$$\frac{\partial m}{m} = \frac{\partial u}{u} + \frac{\partial \rho}{\rho} \qquad\qquad 2.3$$

Substituting for $\partial\rho/\rho$ in equation 2.2 gives

$$\frac{1}{\alpha}\frac{\partial T_t}{T_t} = (\gamma - 1)M^2\frac{\partial u}{u} + \frac{\partial p}{p} - \frac{\partial m}{m} + \frac{\partial u}{u} \qquad 2.4$$

or, collecting terms, we obtain

$$\frac{\partial u}{u} = \frac{1}{\alpha\,[1 + (\gamma - 1)M^2]}\frac{\partial T_t}{T_t} - \frac{1}{[1 + (\gamma - 1)M^2]}\left[\frac{\partial p}{p} - \frac{\partial m}{m}\right] \qquad 2.5$$

which, defining $\beta = \alpha(\gamma - 1)M^2$, can be written as

$$\frac{\partial u}{u} = \left(\frac{1}{\alpha + \beta}\right)\frac{\partial T_t}{T_t} - \left(\frac{\alpha}{\alpha + \beta}\right)\left[\frac{\partial p}{p} - \frac{\partial m}{m}\right] \qquad 2.6$$

In past shear layer studies, the effect of pressure fluctuations has been negelected so that, with $p'/p \ll 1.0$, equation 2.6 may be written as

$$\frac{u'}{\overline{u}} = \left(\frac{1}{\alpha + \beta}\right)\frac{T_t'}{\overline{T_t}} + \left(\frac{\alpha}{\alpha + \beta}\right)\frac{(\rho u)'}{(\overline{\rho u})} \qquad 2.7$$

Squaring both sides of this equation leads to an expression for the streamwise turbulence intensity in the form

$$\frac{\overline{u'^2}}{\overline{u}^2} = \left(\frac{1}{\alpha + \beta}\right)^2\frac{\overline{T_t'^2}}{\overline{T_t}^2} + \frac{2\alpha}{(\alpha + \beta)^2}\frac{\overline{(\rho u)'T_t'}}{(\overline{\rho u}\,\overline{T_t})} + \left(\frac{\alpha}{\alpha + \beta}\right)^2\frac{\overline{(\rho u)'^2}}{(\overline{\rho u})^2} \qquad 2.8$$

Clearly the measurement accuracy is governed by a pressure fluctuation assumption which is probably not valid in hypersonic flows, and questionable, low-overheat determinations of the first two terms in equation 2.8. The procedures used to evaluate other terms which appear in the momentum and energy equations are reviewed in Ref. 8 These analyses show that previous hypersonic hot wire measurements could be subject to substantial errors. In more complex flows which involve separation or time-dependent flow reversals, additional problems occur due to directional ambiguity effects (Ref. 9.)

3. MEAN FLOW MEASUREMENTS

Mean flow properties are generally deduced from measured pitot profiles and measured or assumed total temperature and static pressure profiles. Using standard nomenclature, local Mach numbers within the flowfield are determined, by iteration, from the Rayleigh pitot formula

$$\frac{p}{p_{t2}} = \frac{\left(\frac{2\gamma}{\gamma + 1}M_1^2 - \frac{\gamma - 1}{\gamma + 1}\right)^{1/(\gamma - 1)}}{\left(\frac{\gamma + 1}{2}M_1^2\right)^{\gamma/(\gamma - 1)}} \qquad 3.1$$

using a measured wall static pressure and assuming a constant static pressure distribution across the flow. The Mach number may then be converted into an appropriate dimensionless speed ratio using

$$\left(\frac{u}{a^*}\right)^2 = M^{*2} \approx \frac{\gamma + 1}{(2/M^2) + (\gamma - 1)} \qquad 3.2$$

Since

$$\left(\frac{a^*}{a_t}\right)^2 = \frac{2}{\gamma + 1} \qquad 3.3$$

then

$$\left(\frac{u}{a_t}\right)^2 = \frac{2}{(2/M^2) + (\gamma - 1)} \qquad 3.4$$

If the flow is adiabatic up to the point of measurement, a_t is equal to the reservoir value a_o. It may be obtained

from a measurement of the reservoir temperature T_o, using the perfect gas relation $a_t^2 = \gamma R T_o$.

In a non-equilibrium region such as a boundary layer, it is necessary to make a local estimate of the total temperature distribution. In turbulent adiabatic flows, the model surface temperature is assumed to be equal to the adiabatic wall temperature for turbulent flow calculated using a recovery factor equal to the cube root of the Prandtl number. The temperature distribution across the boundary layer is then found by assuming the Crocco or linear total temperature-velocity relationship

$$(T_t - T_w) / (T_o - T_w) = u/u_e \qquad\qquad 3.5$$

The above equations can then be used to determine the velocity profile. The density profile can be determined from the static temperature profile and the equation of state. However, when heat transfer, adverse pressure gradient and flow curvature are present, both the total temperature and static pressure profiles must be experimentally determined. At high Mach numbers, the effective radii of curvature required to produce significant normal pressure gradients may be as large as 500δ. Thus, curvature due to displacement thickness variations even on flat model surfaces can be significant, as shown in Fig. 4 taken from Ref. 11.

The geometries and construction of typical pitot and static pressure probes used for hypersonic boundary layer studies reported in Refs. 10 and 12 are shown in Figs. 5 and 6. In this work, pitot pressure probes were calibrated in a free-jet facility, matching Mach number, velocity and density with the anticipated test conditions. These calibrations were used to assess the potential errors due to rarefaction effects (Ref. 13). The static pressure probes were geometrically similar to those used previously in Ref. 13. Independent calibrations to account for viscous interaction effects agreed with the Behren's calibration. Total temperatures in the flowfield were measured with the probes shown in Fig. 7. These probes were designed using a concept suggested by Vas (Ref. 14) and consisted of an unshielded, butt-welded chromel-alumel thermocouple 0.3 cm long by 0.007 cm thick supported by tapered chromel and alumel posts. A second chromel-alumel thermocouple was formed at the end of the alumel support. This provides a simultaneous measurement of the butt welded thermocouple junction and the probe support. Corrections for radiation, conduction and recovery factor can then be made following the method described in Ref. 14. To make these corrections, the local Mach number and Reynolds number must be known, thus requiring an iterative procedure using the pitot and static pressure data. Different designs have been used by other workers (see for eg. Refs. 15 and 16). Flowfield surveys were obtained using traverse mechanisms such as the one shown in Fig. 8. Here, a precision power screw was driven by a stepping motor, whose shaft was capable of turning in controlled increments as small as 1.8 deg. or any multiple. The vertical resolution of this mechanism was 0.0003 cm. The rotary motion of the motor shaft is coupled to the precision screw with antibacklash bevel gears and the vertical position was obtained from a three-turn precision potentiometer driven by an anti-backlash worm gear.

Surface heat transfer is usually measured by the transient thin-skin technique in which thermocouples measure the rate of change of skin temperature with thermocouples which are spot welded to the interior surface. The data are reduced by obtaining a least squares linear fit of $\ln\{(T_t - T_w)/(T_t - T_{wi})\}$ versus time.

Any variation of the wind-tunnel total temperature (T_t) with time is included. Estimates of longitudinal conduction errors can be made following procedures outlined by Ref. 17. Short duration facilities offer great advantages in the ability to measure heat transfer rate using proven transient techniques (Ref. 18.)

Skin friction measurement presents a more difficult problem. The most common methods of measurement are the floating element balance, surface pitot tube and surface hot film. In Ref. 19, the local skin friction was measured directly by means of the skin friction element shown in Fig. 9. The element consisted of a disc, 0.312 inches in diameter suspended from two flexures. The streamwise force on the disc was measured by means of a

difterential transformer. The transformer itself maintained a fixed position while the core, attached to the floating element, completed the magnetic circuit. In the neutral position, the gap between the element and the housing was 0.003 inch at the front and 0.007 inch at the back. The element had no nulling device and simply deflected under the load and had a sensitivity of 0.6 volts per gram. An electrolevel was mounted close to the balance to measure changes in plate incidence and deflection during each test and the zero reading of the balance was then adjusted accordingly.

Surface pitot probes generally consist of circular or flattened impact-pressure tubes similar to those suggested and used by Preston (Ref. 20) as indirect sensors of skin friction. The tubes are mounted so that the tube leading edge rests firmly on the surface of the model. In 1952, Cope (Ref. 21) used a surface pitot tube to make the first supersonic measurements at a Mach number of 2.5 and concluded that the device was reliable for making skin friction measurements. Hakkinen (Ref. 22) found that although his subsonic calibration agreed reasonably well with those obtained previously, at supersonic speeds the calibration had an apparent Mach number effect when based on the usual calibration factors. This phenomenon was further examined by Trilling and Hakkinen (Ref. 23) and it was concluded that there was a genuine Mach number effect on the surface pitot calibration. Later, Abarbanel et al (Ref. 24) found that, with the usual calibration factors based on the wall temperature, the calibration for a laminar boundary layer was not affected by Mach number, but that the turbulent boundary layer calibration was still Mach number dependent. In 1957, Fenter and Stalmach (Ref. 25) developed calibration factors based on the Von Karman mixing-length theory, following the compressible skin friction theory of Wilson (Ref. 26), which collapsed their supersonic Preston tube data onto a single curve between Mach numbers of 1.7 and 3.7. However, Smith et al (Ref. 27) obtained a turbulent boundary layer calibration curve, based on wall temperature, which was independent of Mach number but which was different from the subsonic turbulent calibration, there being a transitional region for Mach numbers between 0.8 and 1.5. Sigalla (Ref. 28) was the first to show that the hypothesis of a reference temperature or enthalpy can be used to obtain a calibration formula for Preston tubes that may be applied to both incompressible and compressible turbulent boundary layers.

A comparison of Preston surface pitot and Stanton tubes (a modified static pressure orifice) by Hopkins and Keener (Ref. 29) has shown that, with the flow properties based on the Sommer and Short reference temperature (see Ref. 30), the supersonic data obtained between $M = 2.4$ and 3.4 fall on the Preston incompressible calibration curve provided that the measured dynamic pressure is replaced by an equivalent incompressible pressure coefficient. But it was also found in Ref. 29 that the Stanton tube calibration was greatly affected by the streamwise location of the tube leading edge relative to the static orifice over which it was mounted. For these reasons it was concluded that a Preston tube, which is geometrically easier to duplicate than a Stanton tube, is a superior device for measuring local skin friction. The calibration proposed by Hopkins and Keener was used to estimate the local skin friction coefficient from the dynamic pressure readings. However, they found that the supersonic Preston tube calibration was not linear on a log-log plot and differed from the incompressible calibration below a value of

$$\left(\frac{\mu_\infty}{\mu^*}\right)^2 \frac{\rho^*}{\rho_\infty} \ Re_d \, c_f \cong 10^4 \qquad\qquad 3.6$$

so that only surface pitot readings above this value should be used to estimate the local skin friction.

It has been shown (ref 31) that the wall shearing stress of a laminar or turbulent boundary layer in incompressible flow can also be determined from heat transfer measurements at the surface. In this case it is possible to restrict the temperature difference ΔT, to values small enough to neglect variations of μ, ρ and k. However, in order to extend the previous equations to high speed flow, variations of fluid properties due to temperature variations in the boundary layer must be considered. In this case the quantity ΔT denotes the

temperature difference from the recovery value, except where heat transfer is present initially.

In incompressible flow, the heat transfer from a heated film of streamwise length L is related to the mass flow rate by the equation

$$Nu \equiv \frac{q_w L}{k \Delta T} \propto \left(\rho \tau_w / \mu^2 \right)^{1/3} \left(\sigma L^2 \right)^{1/3} \qquad 3.7$$

where all symbols have their usual significance and all properties are evaluated at freestream conditions. However, the thermal boundary layer produced by a heated film is confined to a region close to the wall so that in compressible flow it might by expected that the average fluid properties across the thermal boundary layer produced by the heated film would be close to the wall values as proposed by Bellhouse and Schultz in Ref. 32. So that if the specific heat C_p and the Prandtl number σ are taken to be constant, equation 3.7 may be written

$$Nu \equiv \frac{q_w L}{k \Delta T} \propto \left(\rho_w \tau_w / \mu_w \right)^{1/3} L^{2/3} \qquad 3.8$$

In a continuous running tunnel, the right hand side of equation 3.8 will depend on the wall temperature and pressure. Thus for a heated film

$$\frac{q_w L}{k \Delta T} = A \left(\tau \right)^{1/3} + B \qquad 3.9$$

where B represents the heat loss to the substrate. Calibration and test results obtained in high speed compressible boundary layers are reported in Ref. 33.

Measurements of mean velocity, Mach number and density, taken from Ref. 10, are presented in Fig. 10. For this compressible non-adiabatic boundary layer, the boundary-layer edge defined by the velocity profile $(U/U_e = 0.995)$ was located at $y/\theta = 22$ and does not include the entire "density" boundary layer. For the experiment the boundary layer edge $y = \delta$ was defined as the height in the boundary layer where the measured pitot pressure reached 99% of the local free-stream value $(y/\theta = 25.8)$. Important methods used to predict compressible turbulent boundary-layer flowfields are compressible-incompressible transformation techniques. These techniques mathematically transform the compressible layer into an equivalent incompressible form which can be predicted with greater confidence. Stretching functions are used to relate the two stream functions, the density ratio and the differential distances. Several transformation techniques have been previously evaluated for this flow (Ref. 35). It was concluded that the Van Driest (Ref. 36) transformation was superior to the other methods. The present data have been transformed to incompressible law-of-the-wall coordinates (Fig. 11a) and velocity-defect coordinates (Fig. 11b) using the Van Driest transformation with a wall friction velocity determined from direct skin-friction measurements. A comparison with the incompressible correlation curve of Coles (Ref. 37) indicates the adequacy of the transformation. Near the wall (Fig. 11a), the data are in good agreement with the incompressible law-of-the-wall correlation with the sublayer data (y+ < 15), closely approaching the linear relationship u+ = y+. In the outer or wake portion of the boundary layer (Fig. 12) the data are in good agreement with the incompressible velocity-defect correlation.

The experimentally determined temperature and Mach number profiles present an opportunity to test available semi-empirical relationships between temperature and velocity at high Mach number and with heat transfer. The two most popular being the linear and quadratic relationships. The linear relationship is strictly valid for adiabatic, zero pressure gradient boundary layers and Prandtl numbers of unity. It can be extended to turbulent flow if both the laminar and turbulent Prandtl numbers are assumed to be unity. Differences in temperature profiles between laminar and turbulent flows with the same boundary conditions are due then to differences in the velocity profiles. The quadratic form results from attempts to account for pressure gradient and to allow for variable Prandtl number. This modification which becomes more important at higher Mach

numbers is plotted in Fig. 12. Also shown are the linear (Crocco) and the experimental temperature-velocity relationship. Except in the region close to the wall, where the Prandtl number deviates from unity, the data are approximated by the linear relationship. This is in contrast to previous non-equilibrium data (e.g. Laderman & Demetriades (ref.34)), which follow the quadratic relationship through most of the boundary layer.

With the recent advances of finite-difference calculation methods for computing the compressible turbulent boundary-layer, the need for accurate models for the turbulent shear (Reynolds stress) term and the turbulent Prandtl number which appear in the "time-averaged" momentum and energy equations for the mean flow are clearly evident. However, despite the extensive experimental and analytical work which has been conducted in supersonic and hypersonic turbulent boundary-layers, very few measurements are of a quality high enough to serve as a guide for the various calculation schemes and even fewer are of the type that could give more insight into the turbulent motion itself. Consequently, very little is known about the structure of compressible turbulent boundary-layers. However, one can either compute the flow using various models for the turbulent shear stress and heat flux terms and compare these with experimental profiles, or one can calculate the turbulent shear-stress and heat-flux distributions using experimental mean-flow data and the "time-averaged" conservation equations and compare the results with the assumed models. This last method has been used by several investigators (Refs. 38-42) for both incompressible and compressible flows. For incompressible and adiabatic supersonic flows, this calculation technique has resulted in correlations which are suitable for finite difference calculations. In addition, Maise and McDonald (Ref. 43) have used experimental velocity profile correlations which provide mixing-length and eddy-viscosity correlations across the boundary-layer valid for adiabatic compressible flows up to M = 5. However, this calculation technique also has the inherent disadvantage that the major portion of the experimental studies of nonadiabatic supersonic and hypersonic turbulent boundary-layers are mostly incomplete in that limited measurements were obtained for each flow. In addition, a significant portion of the available studies are for wind tunnel nozzle wall boundary-layers where unknown upstream influences, including non-equilibrium effects, have yielded unexplained differences between flat plate and nozzle-wall flows. Bushnell and Morris (Ref. 42) have examined several such hypersonic boundary-layer flows with only limited success in obtaining a general correlation for the shear-stress model. The turbulent Prandtl number could not be evaluated for these flows due to insufficient data.

In Ref. 44, both the turbulent shear stress and heat flux have been evaluated at several streamwise locations on an axisymmetric cone-ogive-cylinder test model at M = 7 (Ref. 44). In this experiment, extra care was taken to measure all the mean properties of a fully developed compressible turbulent boundary-layer with known and documented edge conditions so that accurate and reliable mean-flow profiles were obtained. The data have been demonstrated to be representative of a "fully-developed" turbulent boundary-layer by comparisons with existing law-of-the-wall, defect law and skin friction correlations. In addition, these present axisymmetric data gave excellent agreement with previous flat plate results (Ref. 45) obtained at similar test conditions. The experiment also provided an accurate measurement of the streamwise variation of boundary-layer edge properties which were used in the calculations. The resulting eddy-viscosity, mixing-length and turbulent Prandtl number distributions across the boundary-layer were then compared with previous data and other assumed models.

A solution procedure similar to that outlined in Ref. 42 was used to compute the eddy-viscosity, mixing length and turbulent Prandtl number distrubutions. Two representative models for the turbulent flow properties were chosen to compare with the calculated results. Cebecci's model (Ref. 46) is derived from incompressible flow measurements and is typical of many distributions currently used in prediction methods. Maise and McDonald (Ref. 43) have correlated two-dimensional adiabatic supersonic flow measurements resulting in expressions for the eddy-viscosity and mixing-length distributions across the boundary-layer. These predictions, when suitably normalized, did not vary appreciably (less than 10%) for $10^3 < Re_\theta < 10^5$ and $0 < M < 5$.

Although the Maise and McDonald correlation was obtained for flow conditions far removed from the present conditions, a comparison was made since this model is at least based on compressible data whereas Cebecci's model is not. Of course, any disagreement between the present results and these models could be attributed to compressibility, heat transfer or transverse curvature effects. Comparisons are shown in Figs. 13 and 14. The static Prandtl number results (Fig. 15) appear to be invariant with distance except for $y/\delta = 0.75$ where the results are subject to uncertainty since accurate normal enthalpy derivatives could not be determined at the outer edge of the boundary layer. In general, these results are in excellent quantitative and qualitative agreement with previous incompressible and adiabatic compressible results (Refs. 38 and 39).

4. TRANSITION MEASUREMENTS

It is a well-established fact that in incompressible flows transition to turbulence is the result of not one but several instability mechanisms and there are many indications that in compressible flows the transition phenomenon is basically the same. In the absence of large disturbances in the freestream transition involves a sequence of processes occurring in the following order: the amplification of weak disturbances; the non-linear development of disturbances; the development of high-shear layer and high frequency disturbances; and the development of turbulent randomness.

Early records of the velocity fluctuations in a transition region measured using sensitive hot wire methods have shown intermittent regions of laminar and then turbulent flow. This was interpreted as transition being an abrupt process, the gradual change in measured mean flow in this region being caused by the abrupt spanwise line of transition fluctuating rapidly in the streamwise direction. Emmons (Ref. 47) introduced the idea of turbulent spots which originate in more or less random fashion and increasingly overlap as they enlarge during their transit downstream, finally covering the entire flowfield and resulting in fully turbulent motion. The passage of these spots over points on the surface results in alternations of laminar and turbulent flow. These alternations can be quantitatively described by an intermittency factor γ which represents the fraction of time any point spends in turbulent flow. More recent experiments, including those of Schubauer and Klebanoff (Ref. 48) and Elder (Ref. 49) verified Emmons' observations, and added much detailed information. It was shown that spot formation is essentially "point-like" in the sense that the size of the spot is initially of the order of the boundary layer thickness, and it was also found that there are essentially no interaction effects between spots. This latter characteristic ensures that the intermittency factor at any point can be calculated by adding the effects of individual spots. This gave justification to the good correlation of Dhawan and Narasimha's theory with experiment (Ref. 50) in which it was shown that the intermittency factor could be used to predict the velocity profile and skin friction variation through transition when the spots were assumed to originate within a small streamwise region. The Schubauer-Klebanoff studies of isolated turbulent spots growing in time, linked the temporal rate of growth with the lateral rate of propagation downstream of a fixed strong disturbance. At low subsonic speeds the angle of propagation of this transverse contamination appears to be constant, 8.5 to 11.5 degrees, despite the fact that the laminar layer is getting increasingly more unstable with distance downstream. Schubauer and Klebanoff (Ref. 48) generated their artificial turbulent spots by spark discharge in the boundary layer. The sparks were always strong enough to create turbulence locally, no matter what the Reynolds number. However, there was no lateral propagation of this turbulence to the surrounding laminar shear layer until the Reynolds number exceeded the critical minimum for amplification of the Tollmien-Schlichting waves.

The optical properties of the turbulent spots at supersonic speeds make them more readily observable than at low speeds, especially on bodies of revolution. However, the variety of observed patterns of seeding and growth reported in the literature is considerable. Many shadowgraphs showing bursts at Mach numbers from

about 3.7 to 7 are presented by James in Ref. 51. In all cases, the turbulent spots appear to travel downsream at a uniform speed, and to grow laterally at a constant rate. James also found that the shape of the turbulent spots was very similar to those observed in subsonic flow. The angle defining the zone of influence appears to be nearly independent of Mach number since it was found to be about the same in James' observations at Mach 3.7 as at subsonic speeds--about 10 degrees. However, there is some suggestion in James' data that this angle may decrease at higher Mach numbers. There is also some evidence that the frequency of spot production increases with increasing unit Reynolds number and increasing surface roughness. Spangenberg and Rowland (Ref. 52) also found that the spot production rate increased with roughness and unit Reynolds number and that the growth rate of the spots normal to the model surface was precipitous at the time of birth. The spots grew to about three laminar layer thicknesses while they travelled a distance equal to their spacing. However, the Spangenberg-Rowland view of turbulent burst breakdown far from the leading edge is somewhat contradictory to the data of James (Ref. 51) and Jedlicka et al (Ref. 53) who report a substantial proportion of cases where spots originate at or very close to the leading edge. Whereas, Evvard et al (Ref. 54) reported that only 3 per cent of their Schlieren pictures on a 5 degree half angle cone at M = 3.12 showed any bursts separated from the main body of turbulence. Jedlicka et al also reported that seemingly identical models often produced decidedly different numbers of bursts from which they inferred that the bursts were produced by surface roughness especially near the leading edge.

In spite of the extensive experimental and analytical work which has been conducted in supersonic and hypersonic transitional boundary layers, there is still much speculation regarding the detailed structure of and mechanisms influencing boundary-layer transition. Morkovin (Ref. 55) and Laufer (Ref. 56) have pointed out that, at high freestream Mach numbers, the sound field which radiates from the turbulent boundary layers on the wind tunnel walls is a major source of freestream disturbances and must be considered in all transition experiments. Pate and Schueler (Ref. 57) have shown that the effects of aerodynamic noise on boundary-layer transition may be related to a number of wind-tunnel parameters including Mach number and unit Reynolds number. But noise cannot explain the unit Reynolds number effect observed in the ballistic range experiments of Potter (Ref. 58) where, in the absence of significant freestream disturbances, the variation of transition Reynolds number with unit Reynolds number was comparable to those observed in noise-contaminated wind tunnels. It is apparent that more data are needed to determine the effect of freestream disturbances on boundary- layer transition. A better understanding of the transition mechanism could be obtained if experiments were designed to obtain a more complete picture of the structure and extent of the transition region, together with fluctuation measurements in the freestream rather than the mere determination of a single transition "point" from mean surface measurements, which has usually been the case. Indeed, many transition anomalies could well be explained by consistent and detailed measurements.

For example, one of the activities of the NASA Transition Study Group (Ref. 17) was undertaken to resolve previously reported differences between boundary-layer transition Reynolds number data measured at similar test conditions in two different wind tunnels. These data (see Fig. 16) were obtained on two similar 5 deg. half-angle cones in the Ames 3.5-Foot Hypersonic Wind Tunnel using thermocouples and in the Langley 18-in. Variable Density Wind Tunnel using thermal paint and thermocouples. To investigate these transition Reynolds number differences, new boundary-layer transition measurements were obtained in both facilities on two different 5 degree half-angle cone models. One was a thin-skin thermocouple model, instrumented with iron-constantan thermocouples. The second model was instrumented with platinum thin-film gages which were operated at constant temperature and installed flush with the model surface. The variation of the RMS thin-film voltage fluctuations of a single gage over a range of unit Reynolds numbers is shown in Fig. 17. The curves clearly show a rise from the laminar to the turbulent level, with an intermediate peak. These curves enable three

distinct points in the transition region to be accurately and consistently determined: namely, the onset of transition, defined as the point where the rms signal begins to increase from its laminar value (this onset of intermittency can be clearly seen on the oscilloscope traces); the peak rms signal, which coincides with the point of maximum turbulent burst frequency (Ref. 59) and the end of transition. Examples of the characteristics of the film voltage fluctuations through the transition region are shown on Fig. 17.

Variations in Stanton number through the transition region as measured in the Langley facility using the thermocouple technique are shown in Fig. 18. In this case, four values of transition Reynolds number could be determined: namely, the onset of transition, defined as the point where the Stanton numbers first consistently exceed the laminar value; the "beginning," obtained by fairing straight lines through the laminar and transitional data; the "end," obtained by fairing straight lines through the turbulent and transitional data; and finally the peak Stanton number. However, at the lower unit Reynolds numbers, anomalous heat-transfer data were observed only in the Langley facility and can be clearly seen in Fig. 18. That is, apart from the scatter in the laminar data, an initial unexplained deviation from the laminar value occurs before what appears to be the "true" onset of transition. This region of anomalous heating decreased with increasing Reynolds number.

The influence of unit Reynolds number on the magnitude of the transition Reynolds numbers and the extent of the transition region as measured in both facilities with the thin-film gage model is shown in Fig. 19. Contrary to the previous measurements, there is excellent agreement between the two sets of data obtained in the two facilities. However, comparison of the thermocouple transition data obtained in the two wind tunnels still shows some differences when the conventional beginning and end of transition points are used (Fig. 20). The beginning data clearly show that the thermocouple technique does not provide consistent transition point data. This is probably caused by the anomalous heating data discussed earlier since this causes the beginning of transition to be determined at different values of turbulent intermittency depending on the unit Reynolds number and test facility. Differences between transition detection methods have also been observed in Ref. 59 where it was concluded that heated thin film gages operated at constant temperature provide a ready means of detecting the onset and length of transition in subsonic and supersonic flows, thus enabling the effects of Mach number and unit Reynolds number on transition "point" data to be more accurately determined. Much of the scatter in transition data can be attributed to the inconsistent choice of transition "point" indicated by different techniques, mostly locating positions near the end of transition, which have a strong Mach number and unit Reynolds number dependence.

A more complete picture of transition dependence on the various parameters can only be obtained from experiments in which the positions of the beginning and end of transition are accurately determined. It is of interest to note that transition data reported for supersonic and hypersonic flows are not generally based on observations of turbulent spots but rather some macroscopic quantity such as skin friction, heat transfer, or surface pitot pressure, whose departure from laminar values can be detected only when the intermittency is appreciably greater than zero. Intermittency measurements in the transition region, obtained by passing the ac components of the hot film signals through a Schmidt trigger circuit, are shown in Fig. 21. There is a close similarity between the intermittency variations in subsonic and hypersonic transitional boundary layers as shown by the good agreement between the present data and the incompressible data of Dhawan and Narashima (Ref. 50). The extent of transitional flow at hypersnic speeds leads to problems in the prediction of turbulent skin friction and heat transfer. The prediction of transition sensitive data such as turbulent skin friction at supersonic speeds is not yet at an advanced state and there are large differences between available theories. Since skin friction drag forms such a large part of the total drag of proposed hypersonic transports, and since most of the methods used to estimate the heat transfer to hypersonic vehicles require a knowledge of the wall shear stress, it is essential that it is accurately determined at the design stage.

Peterson, Ref. 60, has reviewed a number of experimental and theoretical results for compressible turbulent boundary layer skin friction over a wide range of conditions up to $M = 10$. Of the seven theories reviewed, the reference temperature method of Sommer and Short (Ref. 30), gave the best agreement with experiment over the whole range. In this method, the fluid properties are evaluated at some intermediate temperature in the boundary layer. This reference temperature T^*, is a function of freestream Mach number and of the wall to freestream temperature ratio. These properties are then used with incompressible turbulent skin friction forlumae to obtain compressible skin friction. Since 1963, a new method for the prediction of compressible turbulent skin friction has been developed by Spalding and Chi (Ref. 61). Also, additional experimental data for supersonic skin friction at high Reynolds numbers (e.g., Refs. 62 and 63) have extended the range over which experimental results are available. A comparison has been made between experimental data and the predictions obtained from the Sommer and Short and Spalding and Chi methods in Ref. 64 in which it is shown that neither method gives completely satisfactory results over the entire range of Reynolds numbers. The Sommer and Short method provides the better predictions in supersonic flow, and the Spalding and Chi method is more accurate in hypersonic flow. The authors concluded that the comparison between theory and the latest experimental results for compressible turbulent skin friction had shown that more data are needed to increase confidence in the prediction of skin friction at hypersonic speeds and high Reynolds numbers.

However, in all empirical analyses of turbulent skin friction, a basic parameter is the Reynolds number based on the length of turbulent flow, where it is generally assumed that a fully developed turbulent boundary layer originates at the leading edge. But in practice, extensive laminar flow always exists near the leading edge, followed by a transition region and then by fully developed turbulent flow. Therefore, in analyses of experimental results, the conditions and rate of growth of the turbulent boundary layer at a given position are assumed to be equivalent to the conditions in a fully turbulent boundary layer originating at a point somewhere behind the leading edge. This fictitious origin of the turbulent boundary layer is known as the virtual origin and the Reynolds number based on the length from the virtual origin as the effective Reynolds number. Since at high supersonic speeds the length of the transition region is often as long as the length of laminar flow preceeding it, the choice of the virtual origin can account for large differences between theory and experiment, especially if the properties of the turbulent boundary layer close to transition are required. Far downstream the choice of the virtual origin is less critical.

The method most commonly used to determine the position of the virtual origin is by extrapolation of the boundary layer momentum thickness to zero. The virtual origin is then taken as the point where the momentum thickness would have been zero if the boundary layer had always been turbulent. Various methods of determining this origin are outlined in Ref. 60, but their application requires previous selection of a compressible boundary layer theory. Alternatively, the virtual origin can be assumed to be at approximately the same location as the point of minimum shear, or minimum heat transfer, which is assumed to be at the end of laminar flow. Although these methods do not have the theoretical basis of the methods of extrapolating momentum thickness, they are more convenient experimentally. They do, however, rely on changes in average velocity profile through the transition region which will be different from the true time mean.

At subsonic speeds, Dwahan and Narasimha (Ref. 50) showed that the intermittency factor can be used to predict the velocity profile and skin friction variations within the transition region and that the origin of the turbulent boundary layer is approximately coincident with the onset of intermittency. But, at supersonic speeds, an analysis of a large body of heat transfer data by Bertram and Neal (Ref. 65) has shown that the choice of the virtual origin at the point of peak shear or peak heating gave the most consistent results. However, this choice of the virtual origin close to the end of transition is somewhat unrealistic. The problem of choosing a consistent virtual origin is far from resolved as evidenced in the discussion on boundary layer transition at the AGARD

meeting in May 1968 (Ref. 66). Thus, it is felt that the more accurate location of onset, peak fluctuation level, and end of transition provided by heated thin film gages should help to resolve the difficulty of choosing consistent transition and virtual origin positions.

There are numerous methods for predicting compressible skin friction, but many theories have been shown to be at large variance with experimental data. Accordingly, only those theories which are generally accepted will be considered. In incompressible turbulent flow, the use of the mixing length law of either Prandtl (ky) or Von Karman ((du/dy)/(d²u/dy²)) leads to the same form for the skin friction coefficient. A large amount of experimental data have been accumulated at subsonic speeds, and by adjusting an arbitrary constant to fit the data, Von Karman obtained the following equation for incompressible turbulent skin friction, namely,

$$\frac{0.242}{\sqrt{c_F}} = \log(c_F Re) \qquad 4.1$$

which is known as the Karman-Schoenherr equation and is the most widely accepted formula for calculating incompressible skin friction.

In compressible flow however, the two mixing lengths of Von Karman and Prandtl do not give the same form for the skin friction coefficient. Results obtained by Van Driest (Ref. 67) with the Prandtl mixing length are different to those obtained by Wilson (Ref. 26) with the Von Karman mixing length. By using Prandtl's mixing length hypothesis in compressible flow, Van Driest obtained

$$\frac{0.242}{\sqrt{c_{F,w}}} \phi = \log \{c_{F,w} Re_w \sqrt{(T_\infty/T_w)}\} \qquad 4.2$$

where ϕ is a function of the wall and freestream temperatures. But the use of the Von Karman mixing length leads to the following form

$$\frac{0.242}{\sqrt{c_{F,w}}} \phi = \log(c_{F,w} Re_w) \qquad 4.3$$

which was given by Wilson for zero heat transfer, and by Van Driest (Ref. 68) for heat transfer. Among the simplifications used by Wilson and Van Driest was the assumption that the mixing length hypothesis applied all the way through the boundary layer to the wall. This assumption which neglects the "laminar sub-layer," resulted in a simplified expression for ϕ. However, Monaghan (Ref. 69) gave another form for ϕ in which the laminar sub-layer was included. Originally it was believed that taking the laminar sub-layer into account would improve the two mixing length theories. But in Ref. 60 it was shown that there was only slight improvement in the agreement between theory and experiment at zero heat transfer and reduced agreement under conditions of heat transfer.

The remaining theories are more empirical in nature. Cope (Ref. 70) assumed that the equation for the non-dimensional velocity profile was the same in compressible flow as in incompressible flow if the wall conditions of density and viscosity were used. With this assumption, the compressible skin friction formula was found to be

$$\frac{0.242}{\sqrt{c_{F,w}}} = \log \{c_{F,w} Re_w (T_\infty/T_w)\} \qquad 4.4$$

The intermediate temperature method of calculating skin friction was originally used by Rubesin and Johnson (Ref. 71) for laminar flows, and was adapted to turbulent flows by Eckert, Sommer and Short and others. The constants used by Sommer and Short (Ref. 30) have been used in this comparison as their predictions are generally regarded as being in better agreement with the experiment. The results of Sommer and Short give

$$\frac{0.242}{\sqrt{c_{F,T*}}} = \log(Re_{T*}c_{F,T*}) \qquad\qquad 4.5$$

where

$$\frac{T*}{T_w} = 1 + 0.035M_\infty^2 + 0.45\{(T_w/T_\infty) - 1\} \qquad\qquad 4.6$$

Spalding and Chi (Ref. 61) postulated that a unique relation exists between $c_f F_c$ and $Re F_R$ where F_c and F_R depend only on Mach number and wall to freestream temperature ratio. The experimental data were found to be too scanty for both F_c and F_R to be deduced empirically, so that F_c was calculated by means of the mixing length theory and F_R was found semi-empirically. Tables and charts for F_c and F_R to be used in the calculation of skin friction were presented.

Since the correct choice of the virtual origin is so important in evaluating empirical predictions which cover a large range of conditions, a number of assumptions, ranging from the leading edge to the end of transition, have been made in Fig. 22 where the experimental data at Mach 4.0 (Ref. 19) have been compared with various predictions. For this comparison, the virtual origin has been chosen at (a) the physical leading edge, (b) onset of transition, (c) peak fluctuation level, and (d) end of transition. The exact positions of (b), (c) and (d) were determined by hot film measurements. The choice of the virtual origin at the leading edge of the flat plate gives results which are much higher than predicted, but the data are improved somewhat when the virtual origin is taken to be at the onset of transition although the experimental data are still too high. However, good agreement is obtained when the Reynolds number is based on the distance from the peak fluctuation level. When the Reynolds number is based on distance from the end of transition, the data fall below the predicted skin friction. This would indicate that Reynolds numbers based on distance from peak skin friction or heat transfer, which are close to the end of transition, would also underestimate the skin friction. The data in Fig. 22 clearly show the importance of choosing a consistent virtual origin location, especially at low Reynolds numbers. Since the length of transition increases with Mach number, the choice of virtual origin becomes much more important at hypersonic speeds. As mentioned earlier, this choice though still important, is less critical at high Reynolds numbers.

The measured local skin friction data are compared in Fig. 23 with the theoretical predictions over a range of Mach numbers, at a constant Reynolds number of 10^7. In calculating the ordinate c_f/c_{fi}, the c_{fi} value was in all cases taken as the Karman-Schoenherr value. The curves and data shown are all for adiabatic wall temperatures. The choice of a Reynolds number of 10^7 was an arbitrary one and it should be noted that the relation between the data and the theories may alter slightly with Reynolds number, but any Reynolds number effect on c_f/c_{fi} for a given Mach number is small, especially above 6×10^6 (see Ref. 65). Experimental data obtained by other authors are also plotted in Fig. 23. A comparison between the two mixing length theories shows that the Von Karman mixing length gives better agreement at zero heat transfer than the Prandtl mixing length. At the lower Mach numbers, however, the Spalding and Chi and the intermediate temperature methods are in much better agreement with the data. But at Mach numbers greater that 4.5, it can be seen that the data casts doubt as to which theory will provide reasonable estimates of skin friction. This apparent scatter in the data could be accounted for by inconsistent choice of the virtual origin which becomes more important with the increasing length of transition at high Mach numbers. Additional experimental research on turbulent skin friction is, therefore, required at hypersonic speeds. Methods of assessing heat transfer distributions are more complicated since skin friction theories can be used to predict Stanton number only if a Reynolds analogy factor is known or assumed.

5. THE HOT WIRE IN COMPRESSIBLE FLOW

Hot wire fluctuation measurements require detailed knowledge of the steady-state heat loss laws. Wire response to mean flow is well defined for the incompressible case. For isothermal, incompressible flow, a hot wire responds only to velocity changes and the output can be correlated quite well over a wide range of Reynolds numbers. Fig. 24 is a summary plot of heat transfer measurements for circular cylinders in subsonic, continuum flow. However, at high speeds, wire response is more complex since wire recovery factor (η) is a function of both Mach number and Knudsen number. Fig. 25 was prepared as a guide to the experimental variation of Nusselt number as a function of Reynolds number and Mach number. The sensor output is reasonably well behaved for supersonic Mach numbers as indicated by the lower curve of Fig. 25. However, the output is Mach number dependent in the transonic range particularly at low Reynolds number. It will be seen that the slope of the Nu vs. Re relationship is of particular concern in turbulence measurements. Fig. 26 shows the measured exponents as a function of Reynolds and Mach numbers for several investigations. At high Mach numbers, the exponent is seen to vary monotonically between the free molecular and continuum values. For an insulated wire, the slope begins to deviate from the continuum value at wire Reynolds numbers below 200. In continuum flow, wire recovery temperature is a function of Mach number since there is a changing relationship between frictional and compression effects. But, as Mach number increases, these effects cancel so that the recovery temperature ratio becomes approximately constant at supersonic Mach numbers (Fig. 27). In the transitional regime, measurements indicate that at Knudsen numbers of about 0.1 the recovery temperature begins to rise above the high Reynolds number value. Thus the recovery temperature can range from below to above total temperature. Measurements have been made over the complete range range from continuum to free molecular Knudsen numbers. These results are summarized in Fig. 28. The direct effect of wire Reynolds number on wire recovery temperature in supersonic flow can be determined from Fig. 29.

The derivation of the general fluctuation sensitivities of a hot wire anemometer involves the perturbation of the steady-state heat transfer law and expressing the result in measurable electrical and fluid flow properties. Following Morkovin and Phinney (Ref. 72) the hot wire sensitivities may be derived and written as

$$\Delta\Theta_{T_t} = \frac{E'}{100}\left[n_t - m_t\left(\frac{\partial \ln Nu}{\partial \ln Re_t}\right) - \left(\frac{\partial \ln Nu}{\partial \ln \Theta}\right)\right.$$
$$\left. - \frac{1}{\tau_{wr}}\left\{1 - \frac{1}{2\alpha}\frac{M}{n}\frac{\partial n}{\partial M} - m_t\frac{Re_t}{n}\frac{\partial n}{\partial Re_t}\right\} - \frac{1}{2\alpha}\left(\frac{\partial \ln Nu}{\partial \ln M}\right)\right]$$

(5.1)

$$\Delta\Theta_\alpha = \frac{E'}{100}\left[\left(\frac{\partial \ln Nu}{\partial \ln Re_t}\right) + \frac{1}{\alpha}\left(\frac{\partial \ln Nu}{\partial \ln M}\right)\right.$$
$$\left. - \frac{1}{\tau_{wr}}\left(\frac{1}{\alpha}\left(\frac{\partial \ln n}{\partial \ln M}\right) + \left(\frac{\partial \ln n}{\partial \ln Re_t}\right)\right)\right]$$

(5.2)

$$\Delta\Theta_\rho = \frac{E'}{100}\left[\left(\frac{\partial \ln Nu}{\partial \ln Re_t}\right) - \frac{1}{\tau_{wr}}\left(\frac{\partial \ln n}{\partial \ln Re_t}\right)\right]$$

(5.3)

and

$$\Delta\Theta_v = \frac{E'}{100}\left[\frac{1}{\tau_{wr}}\left(\frac{\partial \ln n}{\partial \phi}\right) - \left(\frac{\partial \ln Nu}{\partial \phi}\right)\right]$$

(5.4)

where E' is the finite circuit parameter, $m_t = d \log \mu/d \log T_w$, $n_t = d \log k/d \log T_w$, θ is the overheat parameter T_w/T_t and τ_{wr} is the temperature loading $(T_w - T_r)/T_r$. The proportionality constants are related to the particular electrical system and are different for constant current and constant temperature applications. However, these hot wire sensitivities apply to all flows whether subsonic, supersonic, incompressible or

compressible whether continuum or free molecular.

Kovasznay (Ref. 73), suggested that the basic equation for a hot wire inclined to the flow may be written as

$$\frac{e'}{\bar{e}} = \Delta e_\rho \frac{\rho'}{\bar{\rho}} + \Delta e_u \frac{u'}{\bar{u}} + \Delta e_{T_r} \frac{T_t'}{\bar{T_t}} \pm \Delta e_\phi \frac{v'}{\bar{u}} \qquad 5.5$$

where the sign conventions must be determined separately for constant current and constant temperature operation (Ref. 8.) For supersonic Mach numbers ie. M sin $\phi > 1.2$ all derivatives with respect to Mach number are negligible so that $\Delta e_\rho = \Delta e_u$. So that, using equation 2.3, equation 5.5 may be rewritten as

$$e' = \Delta e_{T_r} \frac{T_t'}{\bar{T_t}} + \Delta e_{\rho u} \frac{(\rho u)'}{\overline{\rho u}} \pm \Delta e_\phi \frac{v'}{\bar{u}} \qquad 5.6$$

To evaluate various fluctuating terms for the case of a normal hot wire, we can rewrite equation 5.6 as

$$e' = \Delta e_{T_r} \frac{T_t'}{\bar{T_t}} + \Delta e_{\rho u} \frac{(\rho u)'}{\overline{\rho u}} \qquad 5.7$$

Squaring both sides of equation 5.7 we obtain

$$\overline{e'^2} = \Delta e_{T_r}^2 \frac{\overline{T_t'^2}}{\bar{T_t}^2} + 2(\Delta e_{T_r})(\Delta e_{\rho u}) \frac{\overline{(\rho u)' T_t'}}{(\overline{\rho u}\, \bar{T_t})} + \Delta e_{\rho u}^2 \frac{\overline{(\rho u)'^2}}{(\overline{\rho u})^2} \qquad 5.8$$

Dividing through by $(\Delta e_{T_t})^2$ the above expression becomes

$$\frac{\overline{e'^2}}{(\Delta e_{T_r})^2} = \frac{\overline{(\rho u)'^2}}{(\overline{\rho u})^2} \left(\frac{\Delta e_{\rho u}}{\Delta e_{T_r}}\right)^2 + 2 \frac{\overline{(\rho u)' T_t'}}{(\overline{\rho u}\,\bar{T_t})} \left(\frac{\Delta e_{\rho u}}{\Delta e_{T_r}}\right) + \frac{\overline{T_t'^2}}{\bar{T_t}^2} \qquad 5.9$$

If we now define

$$\frac{\overline{e'^2}}{(\Delta e_{T_r})^2} = s^2 \quad \text{and} \quad \frac{\Delta e_{\rho u}}{\Delta e_{T_r}} = r$$

then our expression can be rewritten as

$$s^2 = \frac{\overline{(\rho u)'^2}}{(\overline{\rho u})^2} r^2 + 2 \frac{\overline{(\rho u)' T_t'}}{(\overline{\rho u}\,\bar{T_t})} r + \frac{\overline{T_t'^2}}{\bar{T_t}^2} \qquad 5.10$$

Since the sensitivity ratio (r) varies with wire overheat, in principle, only three overheat settings are required to solve equation 5.10. But, in practice, at least three times that number should be made in order to provide consistency checks and reduce the scatter. The results can also be determined from the so-called Kovasznay diagram (Ref. 73) or by regression. The Kovasznay diagram can be obtained by plotting $v = e'/\Delta e_{T_0}$ against the sensitivity ratio. Typical curves showing the dependence on the relative magnitude of the three unknown quantities are presented in Fig. 30. If only mass flow fluctuations are present the diagram will be a straight line from the origin with the slope proportional to the mass flow fluctuation level. If only total temperature fluctuations are present, the diagram is a horizonal line at the total temperature fluctuation level. If both fluctuations are present, the plot varies according to the correlation coefficient between the two fluctuations. For perfectly correlated or anti-correlated fluctuations, the curve becomes a straight line, and when there is zero correlation it is a hyperbola. In these cases, the two fluctuation levels can be determined as indicated in Fig. 30.

For a yawed wire we have

$$e' = \Delta e_{\rho u} \frac{(\rho u)'}{\overline{\rho u}} + \Delta e_{T_t} \frac{T_t'}{\bar{T_t}} \pm \Delta e_\phi \frac{v'}{\bar{u}} \qquad 5.11$$

so that, when we difference the mean square of two readings taken 180 deg. apart, we obtain

$$\overline{e'^2} = \overline{e_{0^\circ}'^2} - \overline{e_{180^\circ}'^2} = 4\left[\Delta e_{\rho u}\Delta e_{\phi}\overline{(\rho u)'v'} + \Delta e_{\phi}\Delta e_{T_t}\overline{v'T_t'}\right] \qquad 5.12$$

which we may write as

$$s^* = \frac{\overline{e'^2}}{4\,\Delta e_{\phi}\Delta e_{T_t}} = 4\left[\overline{v'T_t'} + r^*\overline{(\rho u)'v'}\right] \qquad 5.13$$

where

$$r^* = \frac{\Delta e_{\rho u}\,\Delta e_{\phi}}{\Delta e_{\phi}\Delta e_{T_t}} \qquad 5.14$$

If we plot s^* against r^* we obtain $\overline{(\rho u)'v'}$ and $\overline{v'T_t'}$ from the intercept and slope respectively. In order to obtain the terms which appear directly in the turbulent momentum and energy equations, we must assume that we have an isentropic flowfield. This permits us to determine the fluctuating flow variables outlined in (Ref. 8.) Although many years of effort have been expended in hot wire anemometry research, it is still clearly an inexact science. Numerous assumptions must be made to estimate the fluctuating flow variables from the measured hot wire quantities.

One of the largest sources of uncertainty in proposed testing of hypersonic flight vehicles will be consistent documentation of the extent of transitional flow on wind tunnel test models. However, past research has stressed the dominant role that freestream fluctuations have on model boundary layer stability at supersonic speeds. Not only do the external fluctuation amplitudes influence transition, their spectra are also significant. Unfortunately, freestream turbulence intensity and scale vary with facility so that a reliable model transition data base may be difficult to establish. This problem could be alleviated if assessments were made of flow quality in facilities which are likely to be used in future hypersonic flight vehicle development. These documentations would allow judgements to be made as to the meaningful operational range of adequate flow quality in each facility relative to the proposed test program.

With these thoughts in mind, freestream hot wire measurements have been made in the AFWAL M=6 facility (Ref. 74) and have been compared with data obtained previously in the NASA Ames 3.5ft. Hypersonic Wind Tunnel and the Langley VDT (Ref. 17). The present hot wire data, plotted in mode diagram form, are shown in Fig. 31. Since these mode diagrams are linear, the two hot wire sensing variables namely the mass flux and total temperature fluctuation levels can be determined from the slope and intercept respectively. The total temperature measurements obtained from the intercept determinations have been confirmed by independent constant current anemometer measurements. Disturbance levels obtained over the entire operating range are shown in Fig. 32. It can be seen that the mass flow fluctuations increase with tunnel total pressure and range from 0.6 to 1.6 per cent. On the other hand, the total temperature fluctuations range between 0.5 and 1.0 per cent. Two sets of data obtained in the Ames 3.5 ft. facility are shown for comparison. The first set was taken in the original test configuration, the latter after the tunnel was converted to a free jet test section. The lower levels in the AFWAL M=6 facility could be due in part to the favorable influence of flow treatment screens installed in the stagnation chamber.

But, if we assume that the disturbances sensed by the hot wire are predominantly sound waves radiated from the turbulent nozzle wall boundary layers, the pressure fluctuation levels can be estimated from hot wire data. Hot wire theory shows this assumption to be consistent with linear mode diagrams which are shown in Fig. 31. The results of these calculations are shown in Fig. 33 and comparison made with the Ames HWT and Langley VDT facilities. These results clearly show the improved flow quality in the M=6 facility. But, sound is not the only disturbance mode, temperature spottiness probably due to non-uniform heating of the supply gas is not negligible (Fig. 31). Thus, the pressure level estimates from the hot wire data should be viewed as upper bounds, the actual levels should be somewhat lower. Direct pressure measurements should confirm this.

Turbulent integral length scales have also been determined from the hot wire time histories. The characteristics of two hot wire signals are shown in Fig. 34. One for a pressure of 930 psia, the other for a pressure of 1860 psia. These traces clearly show the increased high frequency (smaller length scale) contribution at the high tunnel total pressure. Low frequency (large-scale) contributions are also apparent in both hot wire traces. In general, most of the energy is concentrated at low frequencies. Auto-correlation measurements show the turbulent integral length scales to be of the order of the jet exit diameter. Assessments must be made to determine if wind tunnel turbulent length scales affect boundary layer stability.

The mass-flow and total-temperature measurements through a hypersonic boundary layer (Ref. 10) are compared in Figs. 35(a) and (b) with previous adiabatic compressible measurements of Kistler (Ref. 75) and with the only available non-adiabatic results, of Laderman & Demetriades (Ref. 34). Although Kistler found that the intensities of both fluctuation modes increased with Mach number, the mass-flow fluctuations do appear to be independent of Mach number above $M \approx 5.0$, while the total-temperature fluctuations appear to decrease with increasing Mach number in the non-adiabatic hypersonic regime. This implies that the effect of heat transfer is to reduce the total-temperature fluctuations. Assuming zero pressure fluctuations, the hot wire signals are interpreted in terms of velocity and density fluctuations in Figs. 36, 37 and 38. These results are compared with previous compressible data (also decomposed assuming zero pressure fluctuations) and with the incompressible zero-pressure-gradient results of Klebanoff (Ref. 76). The key to previous data is given in Fig. 35. The present velocity fluctuations normalized by the wall friction velocity (calculated using a direct measurement of wall shear) shown in Fig. 36, agree very well with the Mach number trend set by previous incompressible and compressible results. However, if Morkovin's coordinate stretching density factor is applied (Fig. 37), neith.. set of high Mach number data collapses onto the Klebanoff-Kistler curve. The data in Fig. 38 show another instance where hypersonic measurements do not follow the trend set by lower Mach number results, since the density fluctuations seem to be independent of Mach number above $M \approx 5.0$.

From the turbulence modeling viewpoint, information on the turbulence scales and lifeti..es are also of crucial importance. Since turbulent flows vary not only in time but also in space, their investigation must involve an examination of both the spatial and temporal statistical structure. Space-time correlations can make a contribution to this study since they give evidence of the heredity and structure of turbulence, as well as values of the convection velocities of the vorticity and entropy modes compared with the average mass transport velocities. Examples of both auto and space-time correlations in a compressible turbulent boundary layer (Ref. 35) are given in Figs. 39 and 40. These data were obtained on a cone-ogive-cylinder model in the Ames 3.5-ft. wind tunnel. Fig. 39 shows the autocorrelation of the fluctuating signals on the cylindrical portion of the model, at two positions in the boundary layer and in the far field. It can be seen that there is a marked variation of energy distribution with frequency across the boundary layer and that, as expected, the far field contains proportionately much less energy in the high wave number range than the wall region. The results of a series of filtered (4 kHz) cross-correlation measurements at several wire separations in the boundary layer are shown in Fig. 40. It can be seen that each cross-correlation curve reaches a maximum at a non-zero value of the time delay, clearly indicating the presence of convection. Due to decay, the amplitude of this maximum is a function of the wire separation distance. A convection velocity of these disturbances may be determined from the time delay at which the maximum of a particular cross-correlation occurs. The variation of the convection velocity profiles for the total and filtered turbulent fields are compared with the mean velocity profile in Fig. 41. At a distance from the wall $y/\delta \approx 0.15$, the convection velocity corresponding to the various scales is equal to the local fluid velocity, i.e. $U_c \approx 0.78 U_e$, where U_e is the velocity at the edge of the boundary layer. At greater values of y/δ the differences increase with the scale; in the outer portion of the boundary layer the large-scale disturbances are convected more slowly than the mean velocity and in the inner region more rapidly than the mean velocity. In

fact, the convection velocity of the large-scale disturbances varies little across the boundary layer.

The values of the cross-correlation coefficient were also determined for various separation distances normal to the wall as a function of the time delay. These space-time correlations may be interpreted in terms of a disturbance inclination angle to the wall. This time-averaged angle may be determined by dividing the normal wire separation distance by the product of the observed time delay for the maximum correlation coefficient and the disturbance convection velocity at the outer wire location. The results, presented in Fig. 42, show that the time-averaged inclination angle is smallest in the wall region and increases with increasing distance from the wall. Close to the wall, the measured disturbance convection velocities increased with increasing wire separation. This implies an outward dispersion of the turbulent fluctuations from the low velocity region close to the wall. It is suggested, therefore, that in hypersonic turbulent boundary layers the turbulent fluctuations originate close to the wall and propagate outwards as they are convected downstream. The time-averaged trajectory of such a disturbance is shown in Fig. 42. The propagation angle α of between 10 and 20 deg. measured close to the wall is in surprisingly good agreement with the incompressible experiments of Kline et al. (Ref. 77) in which ejected streaks were observed to leave the wall layer at an angle of about 10 to 12 deg.

Some insight into the three-dimensional structure of these turbulent disturbances may be obtained from the variation in the optimum lateral correlation across the boundary layer. These results indicate that the disturbances are very narrow close to the wall and that they grow laterally as they propagate away from the wall. These data, together with those discussed previously, suggest that turbulence production in a hypersonic turbulent boundary layer is created by highly three-dimensional disturbances originating close to the wall. The form of such a disturbance, suggested by the hot wire correlation data, is shown in Fig. 43. At first sight, the steep trajectories in the outer portion of the boundary layer suggest that the bursts may move across Mach lines. However, it must be borne in mind that the relative velocity between the disturbance and the local mean velocity is always subsonic so that the bursts are as free to propagate as they would be in an incompressible boundary layer. The qualitative space-time correlation measurements have also been used to estimate the "lifetimes" of the fluctuations as they are swept along by the mean flow. Although the idea of a "turbulent lifetime" should not be taken too literally, the measured optimum space-time correlations were assumed to decay exponentially and the appropriate time constants were then determined from these curves. Previously measured disturbance convection velocities were used to calculate the "decay constants" for the filtered turbulent field. The results for various turbulent length scales are shown in Fig. 44 where $\lambda_c/\delta \approx 0.6$ is representative of the total turbulent field. It is evident that these decay constants are strong functions of both scale and local mean-flow gradients (i.e. y/δ). Since the duration of any phenomenon is approximately three times its time constant, it is also evident that large eddies persist for extremely long distances (i.e. many boundary-layer thicknesses). The long turbulence lifetimes which can be inferred from these space-time correlation measurements illustrate a major oojection to turbulence models based on local flow conditions. It cannot be assumed that turbulence is uniquely related to local conditions, and flow history must be considered, especially when attempting to calculate non-equilibrium flows.

Flows of more practical interest often involve separation or time-dependent flow reversal. These features cause additional problems due to directional ambiguity effects which if not realized will lead to wrong or misleading results. For example, some of the flow features involved in a hypersonic shock-boundary layer interaction can be determined from Ref 5. Indications of the unsteady character of turbulent boundary-layer separation can be inferred from thin-film-gage fluctuating voltages, which are related to the flow character above the film. In the example, two typical variations of the rms thin-film voltage fluctuations through a shock-wave boundary-layer interaction region, are shown in Fig. 45. Also indicated are the measured pressure distributions for the two cases. Data are shown for attached and separated flow. For both flows, detailed

pitot-pressure surveys, floating element surface skin-friction, and surface oil-flow data were obtained. The region of measured negative wall shear, as determined from a floating element skin-friction balance, is indicated on Fig. 45. The thin-film results show a marked difference in the attached and separated flows.

Normalized power spectra of the fluctuations in the turbulent separated region and after reattachment are shown in Fig. 46. It can be seen that the energy increase in the separated region is confined to a narrow band around 14 kHz while the increased energy due to the pressure rise after reattachment is broad band. It is felt that this peak is associated with turbulent separation unsteadiness. The scale of this unsteadiness, based on measured convection velocities and frequency, is of the order of the length of the separated region. The decrease and subsequent increase in rms voltage after the first peak for the separated flow (Fig. 45) can also be explained by this unsteadiness. The minimum rms corresponds to the location where the flow remains separated most of the time and is least affected by the increased voltage fluctuations due to unsteady flow reversal in the intermittent separation onset and reattachment regions. These large scale, directional fluctuations can cause substantial and unknown hot wire and surface film measurement errors. The problem is illustrated in Fig. 47 where Gaussian probability density distributions of the instantaneous velocities corresponding to local turbulent intensities of 30% and 70% are presented. With directional ambiguity, negative velocities are assigned their equivalent positive values, leading to errors in the calculated mean value and standard deviation. The resultant errors are seen to rise sharply for local turbulence intensities above 40%. Large scale fluctuations can have a significant influence on turbulence structure and modeling. For example the instantaneous axial velocity may be written as

$$u = \bar{u} + u' + \tilde{u} \qquad\qquad 5.15$$

where $\bar{u}$ is the conventional mean, u' is the random fluctuation and $\tilde{u}$ is the unsteady contribution. Using a similar expression for the vertical velocity and assuming that the random large and small fluctuations are uncorrelated, the streamwise momentum equation may be written as

$$\bar{u}\frac{\partial \bar{u}}{\partial x} + \bar{v}\frac{\partial \bar{u}}{\partial y} = -\frac{1}{\rho}\frac{\partial \bar{p}}{\partial x} + \upsilon\frac{\partial^2 \bar{u}}{\partial y^2} - \frac{1}{\rho}\frac{\partial}{\partial y}(\overline{u'v'} + \overline{\tilde{u}\tilde{v}}) \qquad 5.16$$

Thus, the large scale fluctuations introduce an additional stress term which will not be necessarily related to the local mean gradient.

6. THE LASER VELOCIMETER

Although much more costly, laborious and tedious to operate, the laser velocimeter probably represents the instrument of last resort for the measurement of flow in compression corners, shock boundary-layer interactions and other large-scale unsteady turbulent flows. Once in operation, linear, non-intrusive unambiguous turbulent velocity and shear stresses can be obtained once seeding problems have been overcome. Flows of most practical interest and importance often involve high turbulence, flow separation and large-scale unsteadiness. It is in these flow regimes where caution must be exercised before applying our research tools. For example, even at low-speed, separated flows are extremely sensitive to local geometry and probe interference and as seen, directional intermittency can render both hot wire and surface-film gage quantitative measurements subject to large inaccuracies. Here the inherent linearity, non-perturbing, directionally sensitive properties of the laser velocimeter come to bear. Recent developments in laser velocimetry facilitate the non-intrusive, linear measurement of complex high speed turbulent flows and the direct measurement of some shear stress terms. But, before laser velocimetry can be extended to hypersonic flow, some basic questions must be addressed. The primary question is that of particle size requirement for reliable response combined with adequate Mie scattering.

The motion of a spherical particle in a fluid flow has been reviewed and summarized by Hinze (Ref. 78). The results show that, given the particle diameter, specific gravity and the local flow conditions, the particle response to sinusoidal velocity fluctuations of the surrounding fluid can be estimated from

$$(d^2\rho_p/18m_f)(dV_p/dt) = (V_f - V_p) = 0 \qquad 6.1$$

The analysis, which assumes Stoke's drag with the Cunningham correction, gives the particle response to turbulent fluctuations in the moving frame of reference of the particle. Equation 6.1 may be transformed to

$$V_p(S)/V_f(S) = 1/(T_pS + 1) \qquad 6.2$$

where S is the Laplace operator and T_p is the time constant defined as

$$T_p = d^2\rho_p/18\mu_f \qquad 6.3$$

By substituting $i\omega$ for S in equation 6.2, the particle response in the frequency domain may be written as

$$V_p/V_f = 1/(T_p^2\omega^2 + 1)^{0.5} \qquad 6.4$$

where ω is the frequency of the fluid flow fluctuations in radians/sec. However, in the low density and static temperature environments associated with hypersonics, corrections are required to the Stoke's drag coefficient which extend its range of application to flows where the Knudsen number is significant. The form used in Ref. 79 results in a modified time constant which may be written as

$$T_p = (\rho_p \, d_p^2/18\mu_f)(1 + k \, L/d_p) \qquad 6.5$$

where k is the Cunningham constant and L is the mean free path. Clearly, the effect of increasing Knudsen number is to degrade particle response. However, when the Knudsen number is large, equation 6.5 shows that relative seed particle response is proportional to the product of the diameter and specific gravity rather than the square of the diameter. In hypersonic flow, low static density and gas viscosity associated with low static temperature result in relatively large Knudsen numbers. Therefore, the use of large diameter, low specific gravity particles becomes a possibility. As an example, Fig. 48 shows some calculated particle response curves for the two operational extremes of the AFWAL 20 inch Hypersonic Wind Tunnel. The curves are for M=12 assuming particle densities of 1 gm/cc. Also shown is the response of a 0.1 gm/cc, 5 micron particle of the type used previously in combustion studies (Ref. 80). It can be seen that, when the mean free path is large, Knudsen number effects dominate the seed particle response to such an extent that the lighter 5 micron particle response can exceed that of a 1 micron water droplet. Indeed, when the Knudsen number is large, the lighter seed material can have essentially the same response as that of a 0.5 micron droplet. Since the intensity of the scattered light, and hence signal to noise ratio, is proportional to the square of the particle diameter and, since the number of photons emitted is proportional to the time of flight through the focal volume, the advantages of using large, low density particles in some hypersonic flows is clearly evident. These initial calculations indicate that final seed particle choice will be governed by the ratio of particle size to mean free path and may well be different in other test facilities. Fig. 49 shows the significance of this effect. Clearly, the flow conditions in the 20 inch facility and other hypersonic test facilities will be in the Knudsen number range where careful choice of seed material must be exercised. Mie scattering calculations (Fig. 50) which show the effects of particle size and scattering angle on light collection indicate that the use of larger particles may be mandatory in most back-scatter applications where the scattered light intensity can be reduced by several orders of magnitude.

Although, at first glance, particle response appears to be generally poor in hypersonic flows, we must remember that the seed material is convected in the Lagrangian frame so that frequency response requirements are relaxed by a factor porportional to the difference between the turbulence convection and the local mean velocities. To compare with hot wire turbulence spectra observations, we must convert the frequencies to their equivalent counterparts in a fixed (Eulerian) frame of reference. To do this, we assume that the turbulent

fluctuations relative to the moving particle approximate those observed in a frame of reference moving with the local mean velocity. Thus the turbulent frequencies in the two cases are related by a velocity ratio $U_c/U - U_c$ where U_c is the turbulence convection velocity. Previous hot wire work in the Ames 3.5 ft. Hypersonic Wind Tunnel (refs. 10 and 35) has shown that the broad-band disturbance convection velocity is close to 0.8 of the freestream value over most of the boundary layer. Thus, the particle response estimates could well be increased by a factor of five. However, close to the wall, where the turbulence levels are highest, filtered space-time cross-correlation measurements (Ref. 35) show that the high frequency, small scale turbulence is convected at velocities within 5 per cent of the local mean. This indicates that the particle response calculations could underestimate the actual response by a factor of twenty. Thus, practical particle response may well be adequate for some, if not all, hypersonic flows. Particle trajectory calculations also suggest that adequate particle response and recovery across shock waves may be possible in some flow situations. Fig. 48(b) shows the effect of a normal shock on particle response in the AFWAL 20 inch facility. In these calculations, the particles are assumed to be moving with the gas flow ahead of the shock in a nominal, 0.1 ft. thick boundary layer. It can be seen that 3db ($\Delta u_p/\Delta u_f = .707$) response could be achieved in distances comparable to or smaller than those of the model boundary layer thickness in many flow situations. This arises since the density and temperature increases which occur across shock waves dramatically improve particle trackability (see Fig. 51). Clearly, extensive particle research will be required to optimize the seed materials for hypersonic flows.

Laser velocimeter measurements have been made in two hypersonic test facilities (Refs. 74 and 82.) Measurements reported in Ref. 74 were made in the AFWAL M=6 High Reynolds Number Wind Tunnel, which is an open jet, blow down facility. It was designed to produce a maximum free stream unit Reynolds number of 3×10^7 per foot and operates over a stagnation pressure range from 700 to 2100 psia at a fixed stagnation temperature of 1100 R. The supply air is heated in a pebble bed storage heater which allows run times of up to 100 seconds at the maximum mass flow rate of 90 pounds per second. The measurements were obtained in this facility on two model configurations namely, on a zero pressure gradient smooth flat plate and in a pressure gradient flow imposed by the introduction of a 30 deg. ramp. The most recent laser velocimeter investigation (Ref. 81) was conducted in the Ames 3.5-ft. Hypersonic Wind Tunnel. In this facility, high-pressure air, which can be heated up to 3400°K in a pebble-bed heater, flows through an open jet test section to lower pressure spheres. The useful test time was approximately two minutes. The test model used for this turbulent boundary layer study was a 10° cone-ogive-cylinder 79 inches long and 8 inches in diameter. The cone-ogive section, which was 27 inches long, was designed to produce a zero pressure gradient flow over the cylindrical portion. Measurements were also made across oblique shock waves generated by the introduction of 20 and 30 deg. flares installed 55 inches from the nose.

The laser velocimeter systems, which were used for the flowfield measurements, utilized the 4880 and 5145 Angstrom lines of an argon-ion laser. The laser and most of the optical components were fixed on a table outside the tunnel where color separation, Bragg-cell frequency shifting and the establishment of the four-beam matrix were accomplished. Only the transmitting and collecting optics moved. In the AFWAL tests all components were located outside the tunnel. But as shown in Fig. 52 the Ames 3.5 ft. wind tunnel test configuration was more complex. To help alleviate potential optical and electronic problems due to the harsh test section environment, only the transmitting and receiving optics and the fiber optic probe were mounted inside the pressure vessel. The traversing system on the laser side of the test section supported the transmitting mirrors and lens. The traverse system on the opposite side of the test section from the laser held the collecting lens and fiber optic probe for forward scatter light collection. The collection optics were used to focus the scattered light onto the face of the fiber optic probe which was used to transmit the signal to photo multiplier

tubes located outside the tunnel.

Mean boundary layer flow results obtained in the Ames facility (Fig. 53) are shown along with the mean profile measurements which were obtained from previous conventional probe measurements (Ref. 35.) The good agreement between the two measurement methods confirms the seed particle response for mean velocity measurements in the zero pressure gradient boundary layer. As we have seen, important methods used to predict compressible turbulent boundary layer flowfields are compressible-incompressible transformation techniques. Their appeal is the desire to employ their simplicity and accuracy for simple zero pressure gradient flows. Fig. 54 shows the results of the law-of-the-wall transformation when the data are compared with the incompressible correlation of Coles. This transformation, made using a wall friction velocity, based on the previously measured local skin friction, confirms the validity of the laser velocimeter mean velocity measurements. In the law-of-the-wall region, the data have the correct incompressible slope and show a wake-like region near the outer edge of the boundary layer similar to the incompressible observations.

The results of a more stringent test of the particle response and the laser velocimeter measurements are shown in Fig. 55 where the zero pressure gradient axial and vertical turbulence measurements are presented. These data show similarities in levels and trends to previous incompressible test results. The streamwise turbulence component has a pronounced maximum close to the wall whereas the vertical component, which is approximately half the axial value, is relatively flat in the wall region. These similarities are not altogether surprising since previous hot wire turbulence convection velocity measurements showed that the relative velocity between the disturbances and the local mean flow was always subsonic which allows the turbulent bursts to propagate as they would in an incompressible flow. The axial component measurements are also compared with Klebanoff's incompressible results and previous hot wire hypersonic measurements in Fig. 55. There is reasonably good agreement between the hypersonic laser velocimeter and incompressible hot wire data when normalized by the wall friction velocity. This is in contrast to previous hot wire compressible flow results, reviewed in Ref. 10, which show a monotonic decrease with increasing Mach number. However, all these past hot wire results have been evaluated assuming zero pressure fluctuations which we would expect to become more important with increasing Mach number. It can be seen from equation 2.8 and by comparison with the data from Ref. 10, that this assumption can have a significant influence on the calculated hot wire velocity fluctuations at high Mach numbers. The turbulent velocity cross correlations are presented in Fig. 56, which shows the variation of the turbulent velocity correlation coefficient across the boundary layer. The maximum value of aproximately -0.4 is in close agreement with incompressible shear layer observations.

Adverse pressure gradient effects on the mean and turbulent flowfields can be seen from measurements obtained at the same streamwise station on the flat plate model with and without the ramp (Figs. 57 and 58). These measurements obtained at a station 0.3 boundary layer thicknesses ahead of the ramp clearly show retardation of the flow due to the imposed adverse pressure gradient and a significant increase in turbulence level over a wide region. Local flow angularity profiles across the boundary layer have been calculated from the two component laser measurements. These results, show that particle response is sufficient to produce local flow angles close to the flare deflection angle in the shear layer just upstream of the interaction. A comparison (Fig. 58) of the zero pressure gradient and ramp induced turbulence level profiles shows that the streamwise turbulent kinetic energy for the ramp flow is more than three times that for the flat-plate boundary layer. Turbulent mixing length scales, calculated using local rms levels and mean flow gradients, are an order of magnitude larger, an indication of the large scale, unsteady character of the flowfield ahead of the interaction. Turbulence levels based on local mean flow values exceed 30 per cent in the wall region so that significant hot-wire measurement errors and flow interference would arise. At this high intensity, large-scale turbulence results in directional intermittency of up to 15 per cent ahead of the time-averaged recirculation zone. Clearly, hot-wire

measurement errors associated with directional intermittency would be considerable.

The most stringent test of particle response was made by perturbing the flow and measuring the particle velocity variation across an oblique shock wave and shear layer generated by the introduction of 20 and 30 deg. flares. Unfortunately, these attempts to determine particle response were complicated by the proximity of the shock to the shear layer on the flare and by shock boundary/layer interaction instabilities. The results of a scan taken 2 inches above the model surface are presented in Fig. 59 which shows the measured mean streamwise velocity and flow angularity distributions through the shock and shear layer region compared with conical flow theory and shadowgraph measurements of the shock location. The location of the measured mean velocity gradient is in good agreement with the shadowgraph shock location and the velocity change across the shock is comparable to conical flow predictions until the shear layer is encountered. The flow angularity measurements are consistent with conical flow predictions and the experimental flare angle. These comparisons indicate adequate particle response since some of the velocity and flow angularity gradient discrepancies across the shock are probably caused by small scale, time dependent oscillations of the shock wave about its mean location. Indeed, attempts to measure particle response across the 30 deg. shock wave were unsuccessful as the increased tunnel blockage led to excessive flowfield instabilities and extensive shock motions.

Although these preliminary test results confirm the feasibility of obtaining flowfield data, efficient laser velocimeter measurements of more complex flows will require prior flowfield visualization to determine the regions of primary interest. With this in mind, minor modifications were made to the sending optics which enabled laser light to pass through a plane-cylindrical lens system. The lens assembly was designed so that a sheet of laser light was generated and optimized to provide vapor-screen flow visualization by illuminating liquefied vapor in the cross flow plane. The model selected was the Ames All-Body Hypersonic Aircraft which was tested at 15 deg. angle of attack. Fig. 60 shows the laser light sheet visualization of the cross flow plane 24 inches from the nose where the shock layer location and symmetric lee-side vortex structures are clearly visible. Streamwise scans of such flowfields will enable shock envelope and vortex trajectories to be determined and the characteristics of their interactions with control surfaces to be documented. Grid shot overlays will then enable an a priori determination of the extent and location of laser velocimeter flowfield documentation.

Unfortunately, measurement requirements for hypersonic flows are further compounded by the presence of fluctuations in the static thermodynamic quantities. Density and temperature fluctuations, which are generally small enough to be neglected in most low speed flows, increase to levels where they can become the most significant varying properties. At high Mach numbers, other turbulent stress and heat fluctuation terms may well be important and may not be adequately represented by the incompressible terms alone. Integration of mean flow data obtained in hypersonic shear flows (Ref. 44) shows that the turbulent compressible shear stress and heat fluctuation distributions are given by

$$\overline{(\rho v)'u'} = \overline{\rho}\ \overline{u'v'} + \overline{v}\ \overline{\rho'u'} + \overline{\rho'u'v'} \quad \text{and} \quad \overline{(\rho v)'T} = \overline{\rho}\ \overline{v'T} + \overline{v}\ \overline{\rho'T} + \overline{\rho'u'T} \qquad 6.6$$

Generally, the last two terms on the right-hand side of each equation are considered to be negligible. However, since density and temperature fluctuation levels scale with the square of the local Mach number and significant flowfield angularity can be induced in shock-boundary layer interactions, the latter two sets of terms could become important in high speed interacting compressible flows. The measurement of these additional terms will require new experimental approaches.

Means for local temperature and density fluctuation measurement have been sought for many years with only limited success. Electron beam fluorescence approaches have been reviewed by Muntz (Ref. 82). This technique is based upon excitation of fluorescence from electron impact with gas molecules in the flow and

analysis of the resulting fluorescence for its temperature and density dependent features. In general, for constant electron beam operating conditions, the emitted light intensity is related to the local gas density and temperature by the relationship

$$I = k_1\rho/(1+k_2\rho Q(T)T^D)$$ 6.7

Most uses of the electron beam fluorescence techniques have been restricted to conditions in which the second term in the denominator is negligible. In these cases the observed intensity is linearly related to the gas density. But, it is unlikely that the quenching term will be negligible at the number densities associated with hypersonic turbulent flows. Indeed, at high number densities, the intensity is solely a function of temperature. This sensitivity to more than a single gas property is analogous to the problems associated with the hot wire in compressible flow. But, if two line intensities with different values of k_2 and $Q(T)$ are measured simultaneously, density and temperature can be determined. In Ref. 83, this approach was used to obtain density and temperature fluctuations across an adiabatic wall boundary in a hypersonic helium tunnel. More recently, the electron beam fluorescence technique has been extended to flows with number densities of up to 3.7×10^{18} molecules/cc which is equivalent to an altitude of 150,000 ft. (Ref. 84.)

Rayleigh and Raman scattering have also been considered for flowfield measurements. Rayleigh scattering is the strongest of the molecular scattering processes. But, this process occurs without energy exchange with the internal states of the molecule and so the scattered light has almost the same wavelength as the incident beam. Thus, it is difficult to separate the Rayleigh scattered light from background light caused by particle or surface scattering. On the other hand, the Raman effect is an inelastic light scattering process where the frequency of the scattered light is shifted from that of the incident light by an amount which depends on the structure of the scattering gas molecules. The intensity and intensity variations in the scattered light spectrum can be directly related to the gas molecular density and temperature. In Ref. 85, the static temperature was determined by taking the ratio of the intensities of two pure rotational Raman lines of nitrogen. The relationship for the temperature T is given by

$$T = H/\ln(R/G)$$ 6.8

H and G are constants which are determined by the specified transitions used and R is the intensity ratio. The density measurements were obtained in two ways. By monitoring the intensity of the vibrational Q-branch of nitrogen and by using the intensity of the anti-Stokes transition. The density measurement based on vibrational Raman scattering is almost completely independent of temperature, and the temperature measurement technique involving the ratio of rotational to vibrational Raman scattering is entirely independent of density. Laser induced fluorescence methods have also been developed by introducing trace elements. A method developed to measure temperature and density fluctuations in turbulent, unheated compressible flows is described in Ref. 86. The technique which relies on nitric oxide fluorescence is restricted to nitrogen flows to avoid excessive collisional quenching by atmospheric oxygen.

7. CONCLUDING REMARKS

Diagnostic tools are available to attempt the measurement of transitional and turbulent hypersonic flows, an area where comprehensive studies are lacking. However, measurement techniques must be used with understanding and care in appropriate test situations. Comparisons of new laser velocimeter turbulence measurements with previous hot wire results indicates that past data reduction assumptions can result in significant measurement errors in hypersonic flows. Extensive work is needed to establish a reliable data base for turbulence modeling and to define the reliable ranges of hot wire and laser anemometer application. At

present our transition data base is inadequate for design purposes although some of the scatter could be resolved by using detection schemes which accurately and consistently resolve the extent of transitional flow on test models. Turbulent shear stress and heat transfer cannot be accurately predicted especially close to transition. Since proposed hypersonic test vehicles are expected to have extensive regions of transitional flow, further studies of transitional and turbulent boundary layers are required. Unfortunately, complete hypersonic ground based simulation and measurement will not be possible. Accordingly, selective experiments must be defined which most closely simulate specific flow features. These experiments should then be conducted in facilities which are suited for advanced flowfield diagnostics.

REFERENCES

1.   Johnston, J. J., Whitehead, A. H. Jr. and Chapman, G. T., *Fitting Aerodynamics and Propulsion into the Puzzle*, Aerospace America, pp. 32-42, Sept. 1987.

2.   Wittliff, C. E., *A Survey of Existing Hypersonic Ground Test Facilities-North America*, Paper No. 5, AGARD-CP-428, 1987.

3.   Owen, F. K., *Application of Laser Velocimetry to Unsteady Flows in Large Scale, High Speed Wind Tunnels*, ICIASF '83 Record, IEEE Publication 83CH1954-7, 1983.

4.   Fernholtz, H. H. and Finley, P. J., *A Critical Commentary on Mean Flow Data for Two-Dimensional Compressible Turbulent Boundary Layers*, AGARD-AG-253, 1980.

5.   Horstman, C. C. and Owen, F. K., *New Diagnostic Technique for the Study of Turbulent Boundary Layer Separation*. AIAA J., Vol. 12, No. 10, 1974.

6.   Morkovin, M. V., *Fluctuations and Hot Wire Anemometry in Compressible Flows*, AGARDograph 24, 1956.

7.   Fernholtz, H. H. and Finley, P. J., *A Further Compilation of Compressible Boundary Layer Data with a Survey of Turbulence Data*, AGARD-AG-263, 1981.

8.   Owen, F. K. and Fiore, A. W., *Turbulent Boundary Layer Measurement Techniques*, AFWAL-TR-86-3031, 1986.

9.   Owen, F. K. and Johnson, D. A., *Separated Skin Friction - Source of Error, an Assessment and Elimination*, AIAA-80-1409, 1980.

10.   Owen, F. K., Horstman, C. C. and Kussoy, M. I., *Mean and Fluctuating Flow Measurements of a Fully Developed, Non-adiabatic Hypersonic Boundary Layer*, J. Fluid Mech., Vol. 70, part 4, p. 393, 1975.

11.   Kemp, J. H., and Owen, F. K., *Nozzle Wall Boundary Layers at Mach Numbers 20-47*, AIAA J., Vol. 10, No. 7, July, 1972.

12.   Kussoy, M. I. and Horstman, C. C., *An Experimental Documentation of a Hypersonic Shock-Wave Turbulent Boundary Layer Interaction Flow--With and Without Separation*, NASA TMX 62412, 1975.

13.   Behrens, W., *Viscous Interaction Effects on a Static Pressure Probe at M = 6*, AIAA J., Vol. 1, No. 12, Dec. 1963.

14.   Vas, I. E., *Flow Field Measurements Using a Total Temperature Probe at Hypersonic Speeds*, AIAA J., Vol. 10, No. 3, pp. 317-323, March, 1972.

15.   East, R. A. and Perry, J. J., *A Short Response Stagnation Temperature Probe*, ARC-CP-909, 1967.

16.   Winkler, E. M., *Design and Calibration of Stagnation Temperature Probes for Use at High Supersonic Speeds and Elevated Temperatures*, J. Appl. Phys., Vol. 25, No. 2, pp. 231-232, Feb. 1954.

17. Owen, F. K., Horstman, C. C., Stainback, P. C. and Wagner, R. D., *Comparison of Transition and Freestream Disturbance Measurements Obtained in Two Wind Tunnel Facilities*, AIAA Paper No. 74-131, 1974.

18. Schultz, D. L. and Jones, T. V., *Heat Transfer in Short Duration Hypersonic Facilities*, AGARDograph 165, 1973.

19. Owen, F. K., *Application of Thin Film Heated Elements to Problems in High Speed Air Flow*, D. Phil. Thesis, Oxford University, 1969.

20. Preston, J. H., *Determination of Skin Friction by Means of Pitot Tubes*, J. R. Aero. Soc., Vol. 58, p. 109, 1954.

21. Cope, W. F., *The Measurement of Skin Friction in a Turbulent Boundary Layer at a Mach Number of 2.5, including the Effect of a Shock Wave*, Proc. Roy. Soc. A. 215, 1952.

22. Hakkinen, R. J., *Measurement of Skin Friction in Turbulent Boundary Layers at Transonic Speeds*, Ph.D. Thesis, Calif. Inst. Tech., 1954.

23. Trilling, L. and Hakkinen, R. J., *The Calibration of the Stanton Tube as a Skin Friction Meter*, 50 Jahre Grenzchichtforschung, Fried. Vieweg an Sohn, p. 201, 1955.

24. Abarbanel, S. S., Hakkinen, R. J. and Trilling, L., *Use of a Stanton Tube for Skin Friction Measurements*, NASA Memo 2-17-59W, 1959.

25. Fenter, F. W. and Stalmach, C. J., *The Measurement of Local Turbulent Skin Friction at Supersonic Speeds by Means of Surface Impact Pressure Probes*, DRL.392, CM.878, Univ. of Texas, 1957.

26. Wilson, R. E., *Turbulent Boundary Layer Characteristics at Supersonic Speeds--Theory and Experiment*, J. Aero. Sci. Vol. 17, No. 9, p. 585, 1950.

27. Smith, K. G., Gaudet, L. and Winter, K. G., *The Use of Surface Pitot Tubes as Skin Friction Meters at Supersonic Speeeds*, ARC R & M 3351, 1964.

28. Sigalla, A., *Calibration of Preston Tubes in Supersonic Flow*, AIAA J. Vol. 3, No. 8, 1965.

29. Hopkins, E. J. and Keener, E. R., *Study of Surface Pitots for Measuring Turbulent Skin Friction at Supersonic Mach Numbers--Adiabatic Wall*, NASA TN D-3478, 1966.

30. Sommer, S. C. and Short, B. J., *Free Flight Measurements of Turbulent Boundary Layer Skin Friction in the Presence of Severe aerodynamic Heating at Mach Numbers from 2.8 to 7.0*, NACA TN 3391, 1955.

31. Liepmann, H. W. and Skinner, G. T., *Shearing Stress Measurements by use of a Heated Element*, NACA TN 3268, 1954.

32. Bellhouse, B. J. and Schultz, D. L., *The Measurement of Skin Friction in Supersonic Flow by means of Heated Thin Film Gages*, ARC R & M 3490, 1968.

33. Owen, F. K., *Skin Friction Measurement at Supersonic Speeds*, AIAA J., Vol. 8, No. 7, July, 1970.

34. Laderman, A. J. and Demetriades, A., *Mean and Fluctuating Flow Measurements in the Hypersonic Boundary Layer Over a Cooled Wall*, J. Fluid Mech., Vol. 63, p. 121, 1974.

35. Owen, F. K. and Horstman, C. C., *On the Structure of Hypersonic Turbulent Boundary Layers*, J. Fluid Mech., Vol. 53, part 4, p.611, 1972.

36. Van Driest, E. R., Turbulent Boundary Layer in Compressible Fluids, J. Aero. Sci., Vol. 18, No. 3, March, 1951.

37. Coles, D., *The Problem of the Turbulent Boundary Layer*, Rep. No. 20-69, Jet Propulsion Laboratory, 1953.

38. Meier, H. U. and Rotta, J. C., *Temperature Distributions in Supersonic Boundary Layers*, AIAA J., Vol. 9, No. 11, pp. 2149-2156, 1971.

39. Simpson, R. L. Whitten, D. G. and Moffat, R. J. *An Experimental Study of the Turbulent Prandtl Number of Air with Injection and Suction*, International Journal of Heat and Mass Transfer, Vol. 13, pp. 125-142, Feb. 1970.

40. Simpson, R. L., *Characteristics of Turbulent Boundary Layers at Low Reynolds Numbers with and without Transpiration*, J. Fluid Mech., Vol. 42, pp. 769-802, July 1970.

41. Bushnell, D. M. and Morris, D. J., *Eddy Viscosity Distributions in a Mach 20 Turbulent Boundary Layer*, AIAA J., Vol. 9, No. 4, pp. 764-766, April 1971.

42. Bushnell, D. M. and Morris, D. J., *Shear-Stress, Eddy-Viscosity and Mixing Length Distributions in Hypersonic Turbulent Boundary Layers*, TM X-2310, NASA, 1971.

43. Maise, G. and McDonald, H., *Mixing Length and Kinematic Eddy Viscosity in a Compressible Boundary Layer*, AIAA J., Vol. 6, No. 1, pp. 73-80, Jan. 1968.

44. Horstman, C. C. and Owen, F. K., *Turbulent Properties of a Compressible Boundary Layer*, AIAA J., Vol. 10, No. 11, pp. 1418-1424, Nov. 1972.

45. Hopkins, E. J. , Kenner, E. R. , Polek, T. E. and Dwyer, H. A., *Hypersonic Turbulent Skin-Friction and Boundary-Layer Profiles on Nonadiabatic Flat Plates*, AIAA J., Vol. 10, No. 1, pp. 40-48, Jan. 1972.

46. Cebeci, T., *Calc lation of Compressible Turbulent Boundary Layers with Heat and Mass Transfer*, AIAA J., Vol. 9, No. 6, pp. 1091-1097, 1971.

47. Emmons, H. W., *The Laminar-Turbulent Transition in a Boundary Layer*, J. Aero Sci. Vol. 18, No. 7, p. 490, 1951.

48. Schubauer, G. B. and Klebanoff, P.S., *Contributions on the Mechanics of Boundary Layer Transition*, NACA TN 3489, 1955.

49. Elder, J., *An Experimental Investigation of Turbulent Spots and Breakdown to Turbulence*, J. Fluid Mech. Vol. 9, p. 235, 1960.

50. Dhawan, S. and Narasimha, R., *Some Properties of Boundary Layer Flow during Transition from Laminar to Turbulent Motion*, J. Fluid Mech. Vol. 3, p. 418, 1958.

51. James, C. S., *Observations of Turbulent-Burst Geometry and Growth in Supersonic Flow*, NACA TN 4235, 1958.

52. Spangenberg, W. G. and Rowland, W. R., *Optical Study of Boundary Layer Transition Processes in a Supersonic Air Stream*, Phys. Fluids, Vol. 3, No. 5, 1960.

53. Jedlika, J. R., Wilkins, M. E. and Seiff, A., *Experimental Determination of Boundary Layer Transition on a Body of Revolution at M = 3.5*, NACA TN 3342, 1954.

54. Evvard, J. C., Tucker, M. and Burgess, W. C. Jr., *Transition Point Fluctuations in Supersonic Flow*, J. Aero. Sci., Vol. 21, 1954.

55. Morkovin, M., *On Supersonic Windtunnels with Low Freestream Disturbances*, Journal of Applied Mechanics, Vol. 26, pp. 319-324, 1959.

56. Laufer, J., *Aerodynamic Noise in Supersonic Wind Tunnels*, Journal of Aerospace Sciences, Vol. 28, pp. 685-692, Sept. 1961.

57. Pate, S. and Scheuler, C., *Effects of Radiated Aerodynamic Noise on Model Boundary Layer Transition in Supersonic and Hypersonic Wind Tunnels*, AIAA J., Vol. 7, No. 3, pp. 450-457, March, 1969.

58. Potter, J. L., *Observations on the Influence of Ambient Pressure on Boundary Layer Transition*, AIAA J., Vol. 6, No. 10, p. 1907, Oct. 1968.

59. Owen, F. K., *Transition Experiments on a Flat Plate at Subsonic and Supersonic Speeds*, AIAA J., Vol. 8, No. 3, pp. 518-523, March, 1970.

60. Peterson, J. B., *A Comparison of the Experimental and Theoretical Results for the Compressible Turbulent Boundary Layer Skin Friction with Zero Pressure Gradient*, NASA TN D-1795, 1963.

61. Spalding, D. B. and Chi, S. W., *The Drag of a Compressible Turbulent Boundary Layer on a Smooth Flat Plate With and Without Heat Transfer*, J. Fluid Mech. Vol. 18, pt. 1, p. 117, 1964.

62. Monta, W. J. and Allen, J. M., *Local Turbulent Skin Friction Measurements on a Flat Plate at Mach Numbers from 2.5 to 4.5 and Reynolds Numbers up to 69 x 10^6*, NASA TN D-2896, 1965.

63. Moore, D. R. and Harkness, J., *Experimental Investigations of the Compressible Turbulent Boundary Layer at very high Reynolds Numbers*, AIAA J., Vol. 3, No. 4, p. 631, 1965.

64. Peterson, J. B. and Monta, W. J., *Considerations Regarding the Evaluation and Reduction of Supersonic Skin Friction*, NASA TN D-3588, 1966.

65. Bertram, M. H. and Neal, L., *Recent Experiments in Hypersonic Turbulent Boundary Layers*, AGARDograph 97, 1965.

66. Supplement to Conference Proceedings No. 30 AGARD Meeting on Hypersonic Boundary Layers and Flow Fields, 1968.

67. Van Driest, E. R., *Turbulent Boundary Layer in Compressible Fluids*, J. Aero. Sci., Vol. 18, No. 3, p. 145, 1951.

68. Van Driest, E. R., *The Turbulent Boundary Layer with Variable Prandtl Number*, Rep. No. AL-1914 North American Aviation, Inc., 1954.

69. Monaghan, R. J., *A Review and Assessment of Various Formulae for Turbulent Skin Friction in Compressible Flow*, RAE TN 2182, 1952.

70. Cope, W. F., *The Turbulent Boundary Layer in Compressible Flow*, ARC R & M 2840, 1943.

71. Johnson, H. A. and Rubesin, M. W., *A Critical Review of Skin Friction and Heat Transfer Solutions of the Laminar Boundary Layer on a Flat Plate*, Trans. ASME, Vol. 71, No. 4, 1949.

72. Morkovin, M. V. and Phinney, R. E., *Extended Applications of Hot-Wire Anemometry to High-Speed Turbulent Boundary Layers*, AFOSR TN—58—469, Johns Hopkins University, Department of Aeronautics, 1958.

73. Kovasznay, L. S. G., *Turbulence in Supersonic Flow*, Journal of the Aeronautical Sciences, Vol. 20, No. 10, p. 657, 1953.

74. Owen, F. K. and Calarese, W., *Turbulence Measurement in Hypersonic Flow*, Paper No. 5, AGARD-CP-428, 1987.

75. Kistler, A. L., *Fluctuation Measurements in a Supersonic Turbulent Boundary Layer*, Phys. Fluids, Vol. 2, 1959.

76. Klebanoff, P. S., *Characteristics of Turbulence in a Boundary Layer with Zero Pressure Gradient*, NACA TN 3178, 1954.

77. Kline, S. J., Reynolds, W. C., Schraub, F. A. and Runstadler, P. W., *The Structure of Turbulent Boundary Layers*, J. Fluid Mech., Vol. 50, part 4, pp. 741-773, 1967.

78. Hinze, J. D., *Turbulence, An Introduction to its Mechanism and Theory*, McGraw Hill, 1959.

79. Yanta, W. J. and Gates, D. F., *The Use of a Laser Doppler Velocimeter in Supersonic Flows*, AIAA Paper 71-287, 1971.

80. Owen, F. K., *Laser Velocimeter Measurements of a Confined Turbulent Diffusion Flame Burner*, Progress in Astronautics and Aeronautics, Vol. 53, 1976.

81. Owen, F. K., *An Assessement of Laser Velocimeter Potential in Hypersonic Flows*, 4th National Aero-Space Plane Technology Symposium, 1988.

82. Muntz, E. P., *The Electron Beam Fluorescence Technique*, AGARDograph No. 132, 1968.

83. Smith, J. A. and Driscoll, J. F., *The Electron Beam Fluorescence Technique for Measurements in Hypersonic Turbulent Flows*, J. Fluid Mech., Vol. 72, part 4, pp. 695-719, 1975.

84. Lin, Z. B. and Harvey, J. K., *The Investigation of the Structure of Hypersonic Turbulent Boundary Layers on a 5° Sharp Cone Using the Electron Beam Fluorescence Technique*, IC Aero Report 82-02, Jan. 1986.

85. Hillard, M. E. Jr., Morrisette, E. L. and Emory, M. L., *Raman Scattering Applied to Hypersonic Air Flow*, AIAA J., Vol. 12, No. 8, pp. 1160-1162, Aug. 1974.

86. Gross, K. P., McKenzie, R. L. and Logan, P., *Measurements of Temperature, Density, Pressure, and their Fluctuations in Supersonic Turbulence using Laser-Induced Fluorescence*, Experiments in Fluids, Vol. 5, pp. 372-380, 1987.

Table 1 (Ref. 2)

SUMMARY OF HYPERSONIC WIND TUNNELS - NORTH AMERICA

	1963	1971	1985	1987
Continuous	14	7	3	2
Intermittent (Air/N_2)	31	32	10	15
Intermittent (He)	6	4	3	3
Hotshot	14	6	0	0
Shock Tunnel	16	14	2	2
Other	1	12	1	2
Total	82	75	19	24
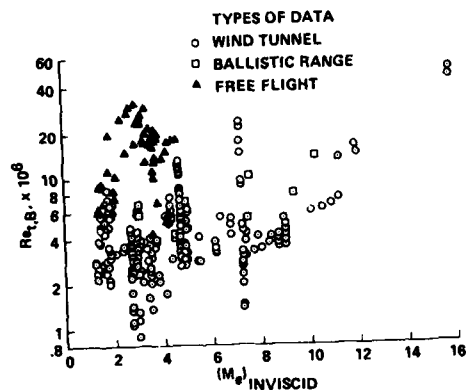
Fig. 1 The transition dilemma - beginning of transition measurements as a function of local inviscid edge Mach number.
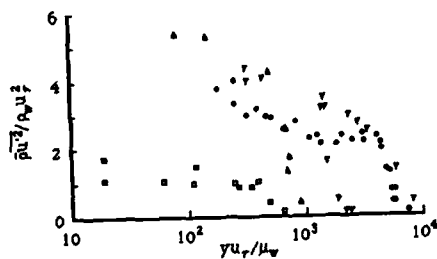
Fig. 2 Reynolds normal stress distribution in compressible turbulent boundary layers (Ref. 7).
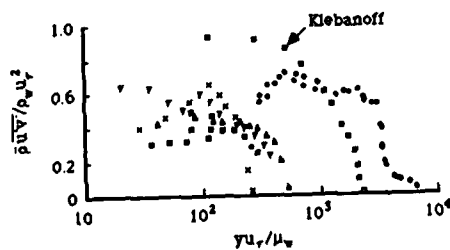
Fig. 3 Reynolds shear stress distribution in compressible turbulent boundary layers (Ref. 7).
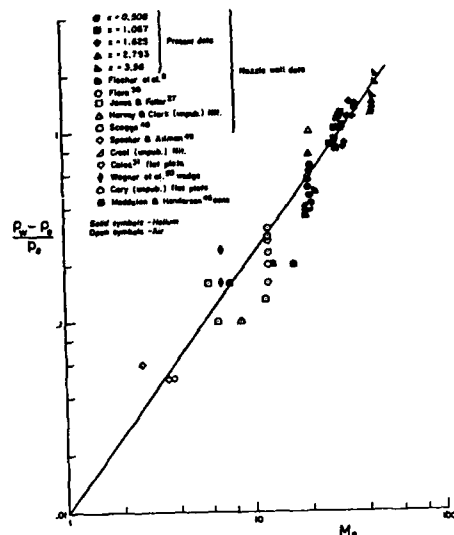
Fig. 4 Overall static pressure differences across boundary layers.
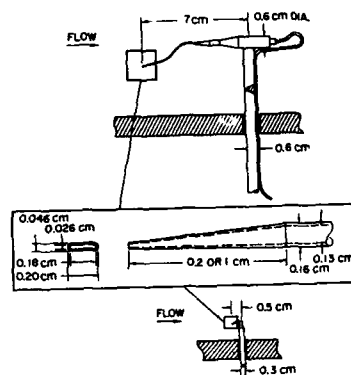
Fig. 5 Pitot pressure probes.
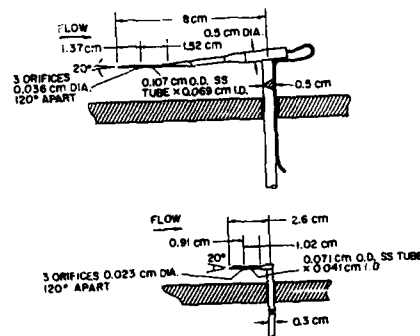
Fig. 6 Static pressure probes.
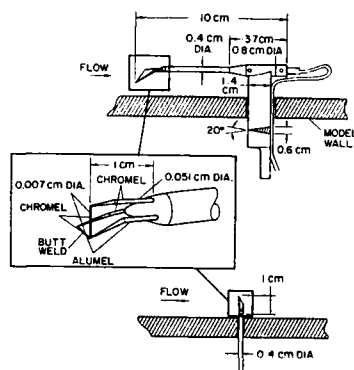
Fig. 7   Total temperature probes.
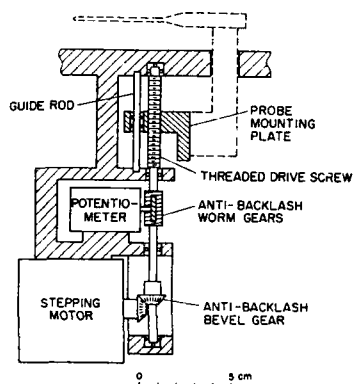
Fig. 8   Survey mechanism.
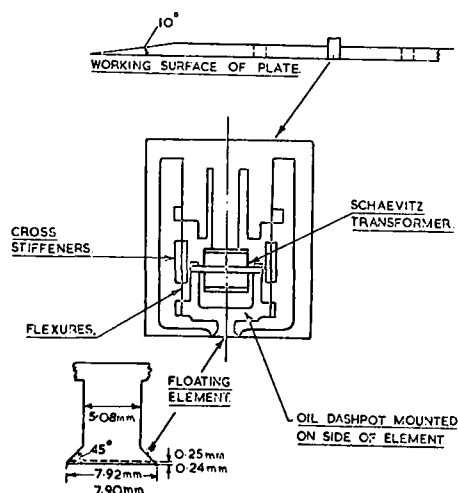
Fig. 9   Floating element balance.
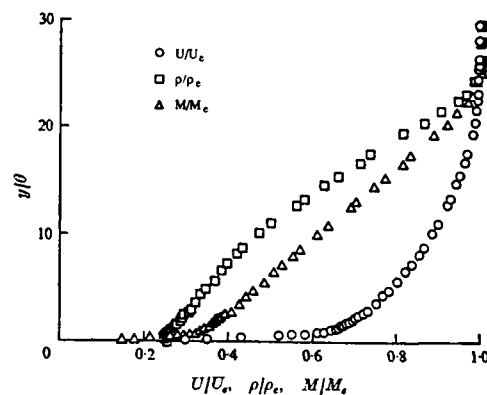
Fig. 10   Mean measurements across the boundary layer.
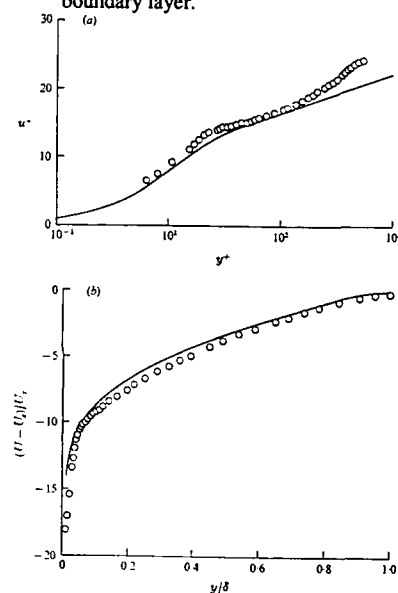
Fig. 11   (a) Law-of-the-wall correlation and (b) velocity-defect profile in incompressible coordinates using the Van Driest transformation. ——, incompressible correlation, Coles (1953).
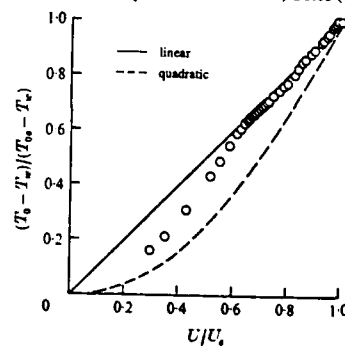
Fig. 12   Relation between velocity and total temperature distribution across the boundary layer.
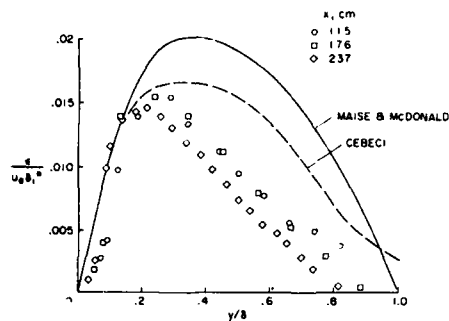
Fig. 13   Eddy-viscosity distributions.

Fig. 16   Comparison of previous transition
Reynolds number data (beginning)
from two wind tunnels, $M_\infty \approx 7.5$,
$\theta_c = 5°$, $T_w/T_0 \approx 0.4$.

Fig. 14   Mixing-length distributions.
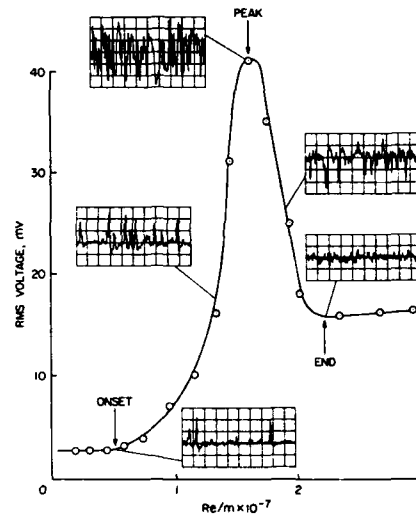
Fig. 17   Thin-film technique for determination
of transition location.

Fig. 15   Static turbulent Prandtl number
distributions.
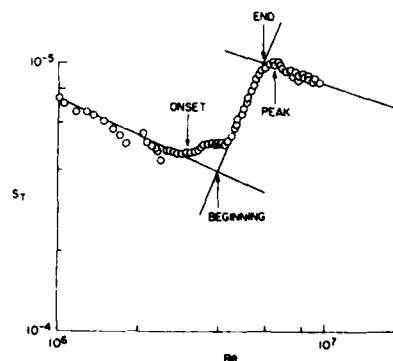
Fig. 18   Thermocouple technique for
determination of transition location.
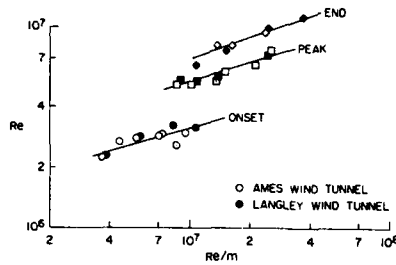
Fig. 19   Comparison of thin-film transition data in two wind tunnels, $M_\infty \approx 7.5$, $\theta_c = 5°$, $T_w/T_o \approx 0.4$

Fig. 22   Effect of virtual origin location on skin friction data.
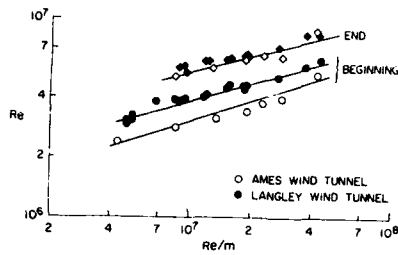
Fig. 20   Comparison of thermocouple transition data in two wind tunnels, $M_\infty \approx 7.5$, $\theta_c = 5°$, $T_w/T_o \approx 0.4$.

Fig. 23   Variation of various theoretical and experimental local skin-friction coefficients with Mach number, $Re_x = 10^7$

a) Data

b) Incompressible correlation
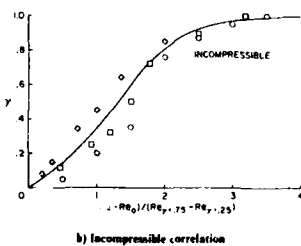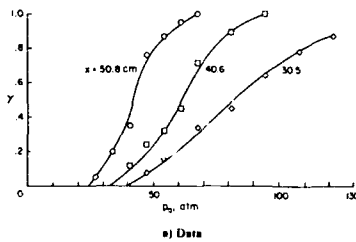
Fig. 21   Intermittency distribution through the transitional region on a sharp 5° cone.
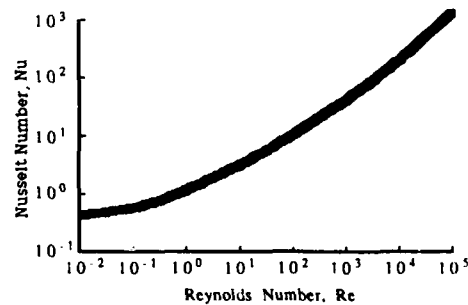
Fig. 24   Summary of heat loss from circular cylinders in cross-flow.
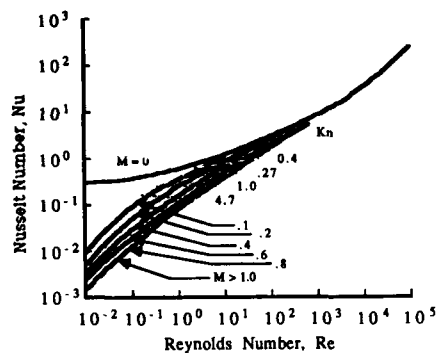
Fig. 25 Empirical correlations of hot-wire heat transfer at low Reynolds number.

Fig. 29 Variations of recovery temperature in supersonic flow (ref. 6).
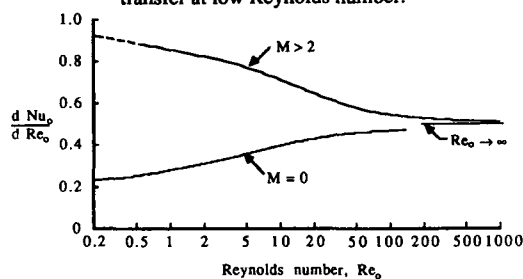
Fig. 26 Slope of Nusselt number - Reynolds number relation.
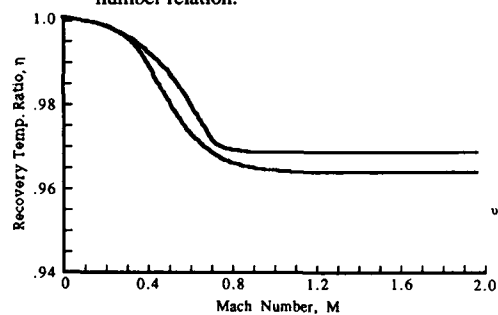
Fig. 27 Recovery temperature variations.

a) velocity fluctuation alone
b) temperature fluctuation alone

c) R = -1
d) R = +1
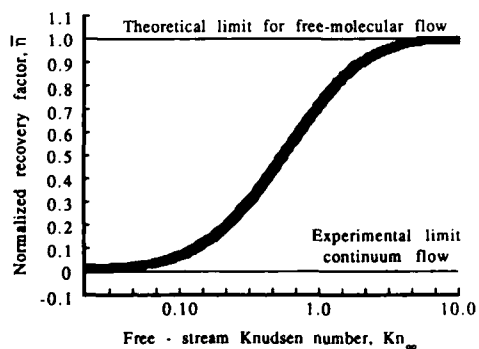
Fig. 28 Normalized variation of recovery temperature with Knudsen number.

e) R = 0
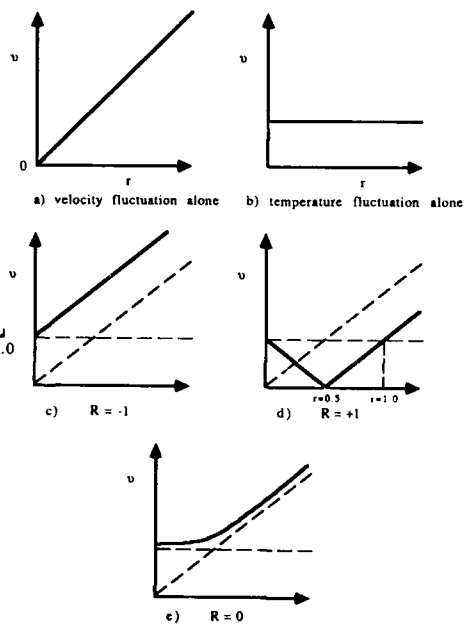
Fig. 30 Typical mode fluctuation diagrams.
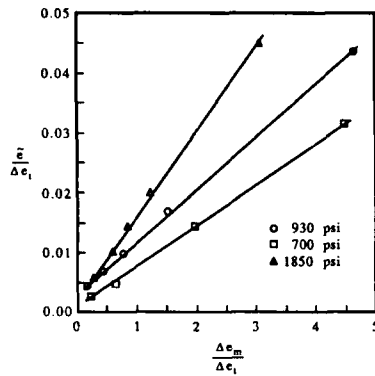
Fig. 31   Mode diagrams, AFWAL, M = 6.0.
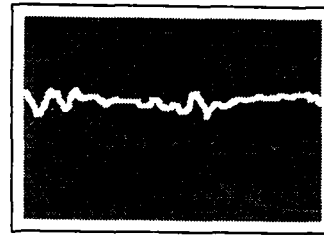
$p_o = 930$
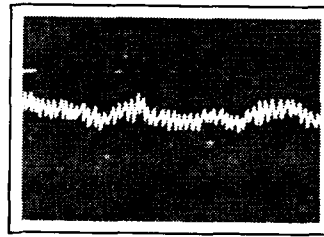
$p_o = 1860$

Fig. 34   Hot-wire traces, AFWAL, M = 6.0, time scale 1 ms/cm.

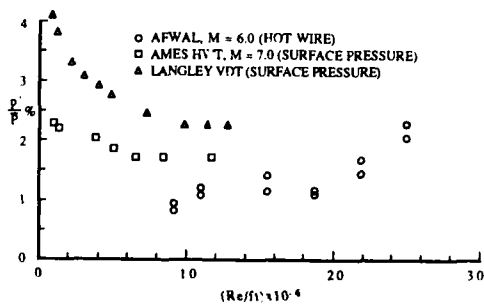

Fig. 32   Mass flow and total temperature fluctuations.

- ○ Owen et al (1975), $M_e = 6.7$, $T_w/T_o = 0.46$
- —— Kistler (1959), $M_e = 4.67$, $T_w/T_o = 1.0$
- — — Kistler (1959), $M_e = 3.56$, $T_w/T_o = 1.0$
- — — — Kistler (1959), $M_e = 1.72$, $T_w/T_o = 1.0$
- ////// Laderman & Demetriades (1974), $M_e = 9.4$, $T_w/T_o = 0.38$
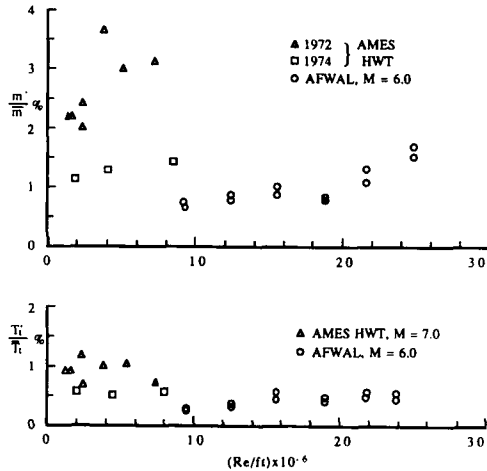
Fig. 33   Freestream pressure fluctuations.
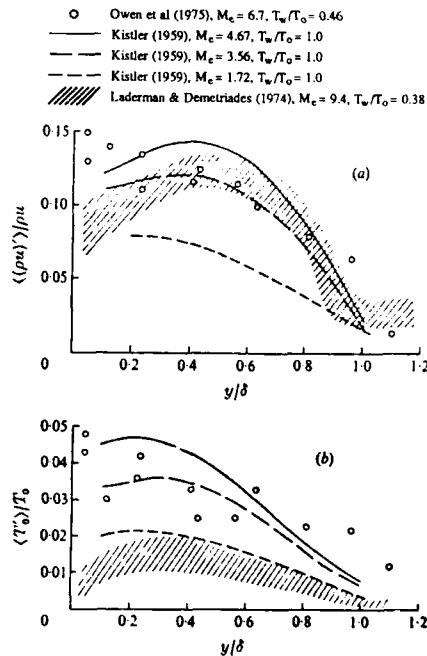
Fig. 35   Distributions of (a) mass-flow fluctuations, (b) total-temperature fluctuations.
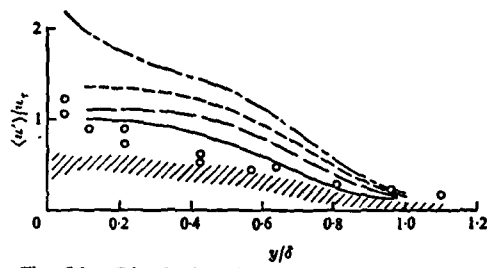
Fig. 36 Distribution of the normalized velocity fluctuations across the boundary layer. — · —, Klebanoff (1954). (Other notation as in Fig. 35.)
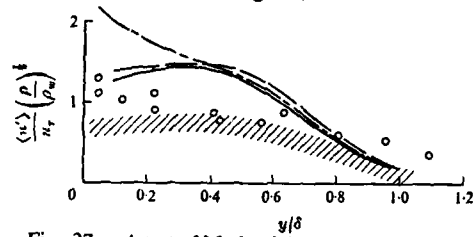

Fig. 37 A test of Morkovin's coordinate stretching density factor applied to the velocity fluctuations. (Other notation as in Fig. 35.)
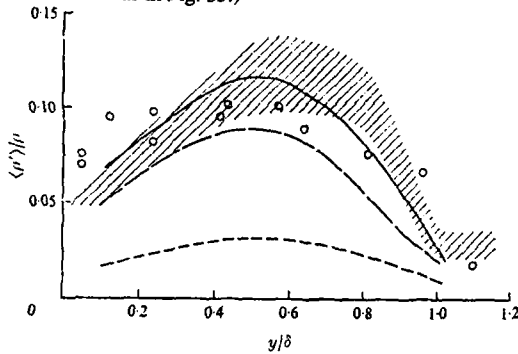

Fig. 38 Distribution of the density fluctuations across the boundary layer. (Other notation as in Fig. 35.)
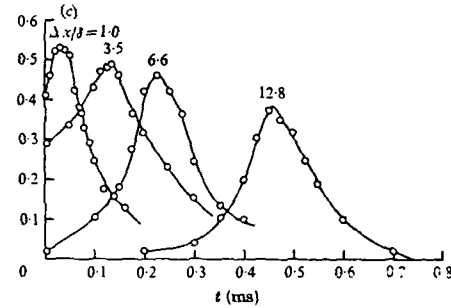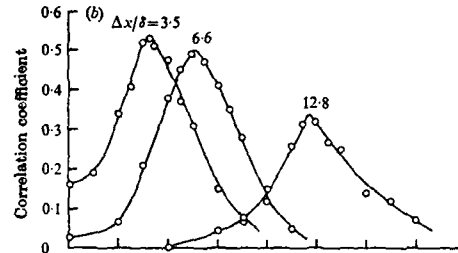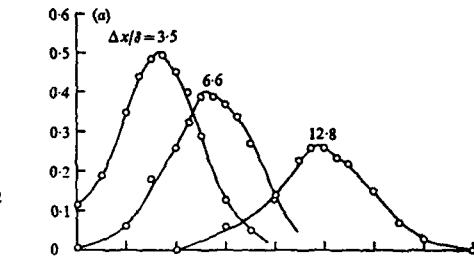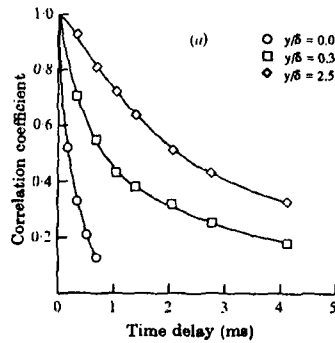

Fig. 40 Examples of the filtered space-time correlation coefficients (4 kHz) obtained for various longitudinal wire separations $\Delta x/\delta$ at three locations in the boundary layer. (a) $y/\delta = 0.08$, (b) $y/\delta = 0.16$, (c) $y/\delta = 0.33$.
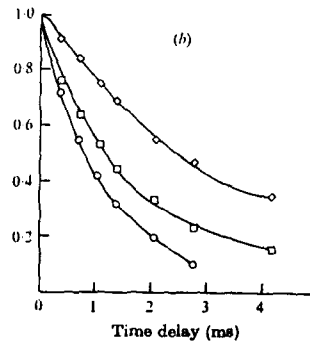

Fig. 39 Auto-correlation measurements at three positions in the flow. (a) x = 176 cm. (b) x = 237 cm.
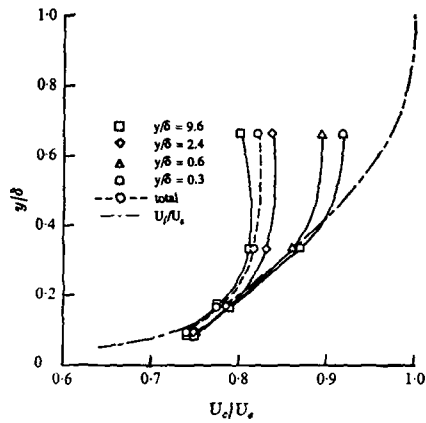
Fig. 41   The distribution of disturbance
convection velocities U_c for various
disturbance scales.
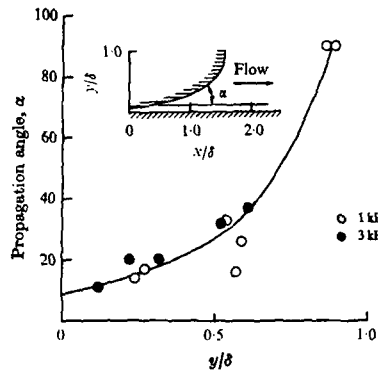
Fig. 42   Variation of the measu. ed disturbance
inclination angles across the boundary
layer.
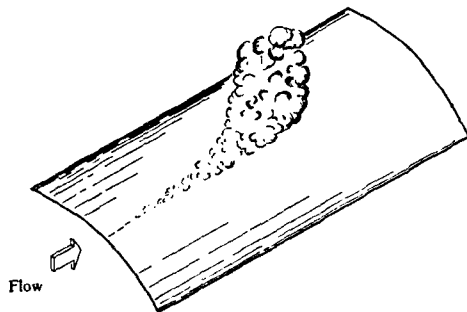
Fig. 43   Proposed model of turbulence
generation.
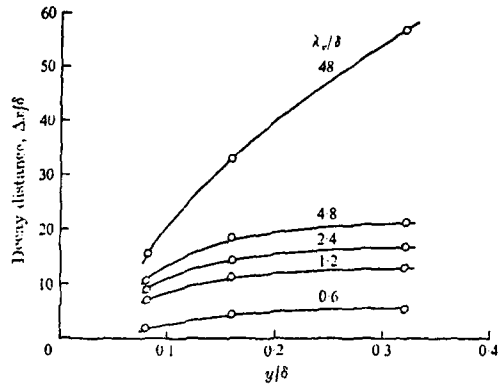
Fig. 44   Turbulence lifetime distributions for various
turbulent scales of the mass-flow fluctuations
across the boundary layer.
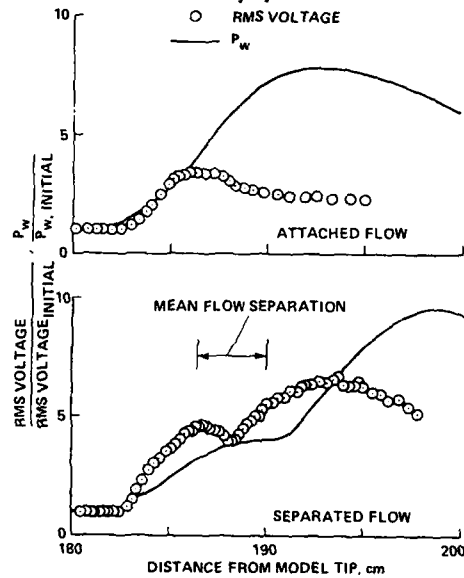
Fig. 45   Normalized rms voltage and surface
static pressure distributions for an
attached and separated flow.
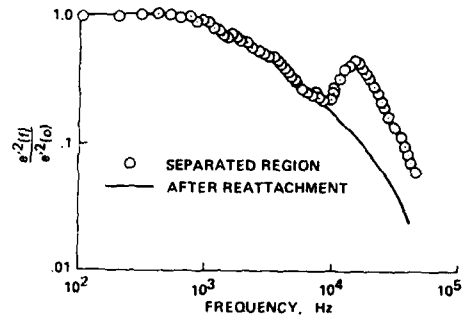
Fig. 46   Normalized energy spectra in the
separated region (187 cm) and after
rea.tachment (195 cm).
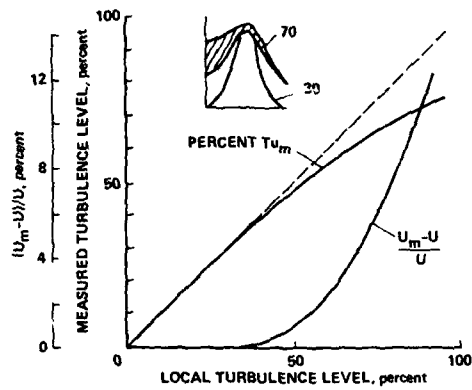
Fig. 47   Errors in measured mean and rms
quantities due to directional ambiguity.
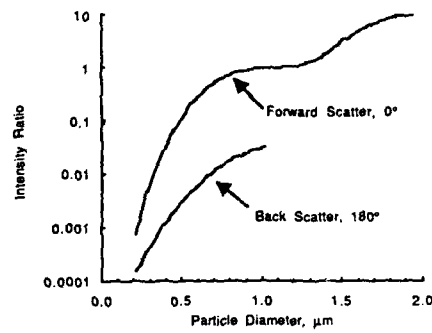
Fig. 50   Light scattered relative to forward
scatter of a 1μm particle.
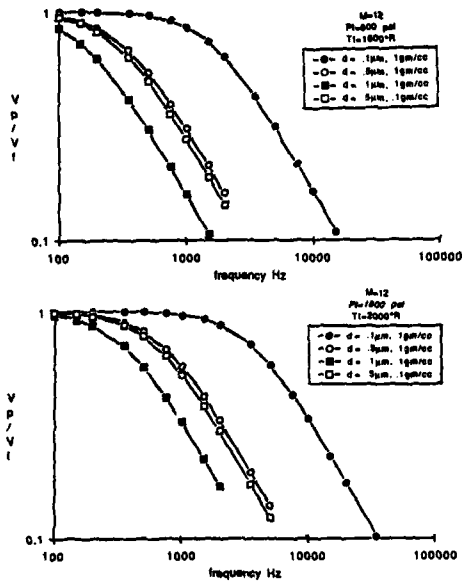
Fig. 48a   Particle trackability in the AFWAL 20
inch Hypersonic Wind Tunnel.
Frequency response
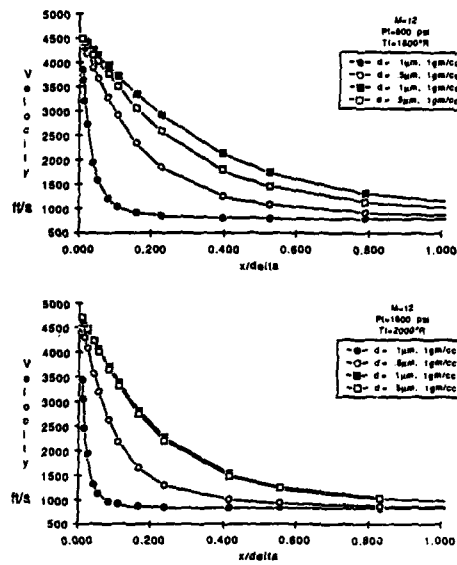
Fig. 48b   Particle trackability in the AFWAL 20
inch Hypersonic Wind Tunnel.
Particle trajectories.
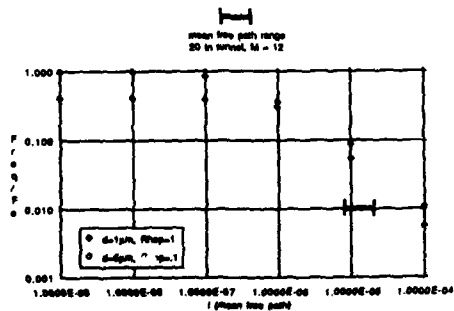
Fig. 49   The influence of mean free path on
particle response.
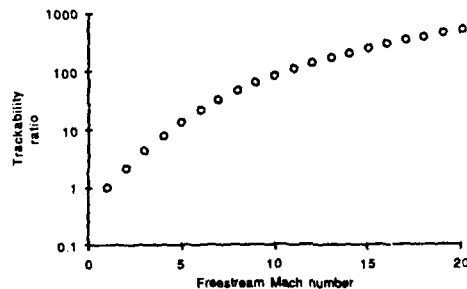
Fig. 51   Particle trackability variation.
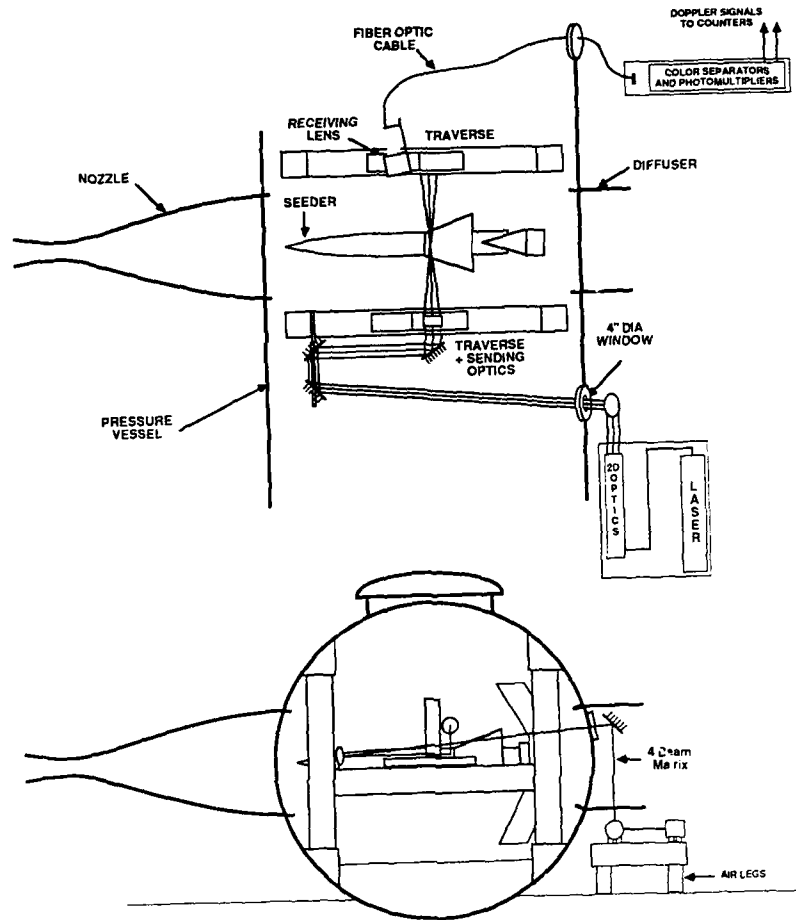
Fig. 52   Ames 3.5ft Hypersonic Wind Tunnel
LDV installation.
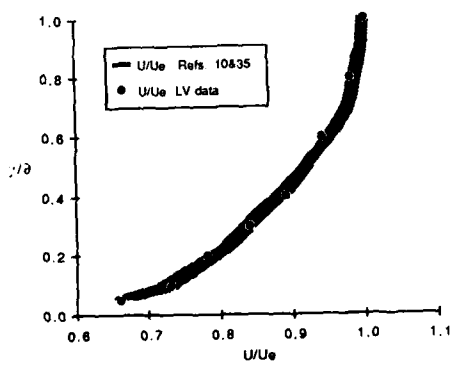
Fig. 53   Laser velocimeter and probe
measurements of mean velocity.
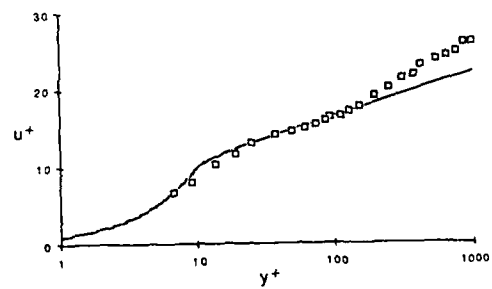
Fig. 54a   Laser velocimeter velocity
transformations.
Law-of-the-wall.
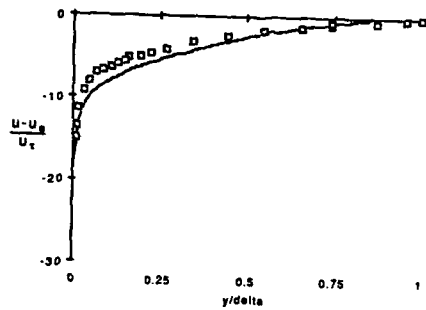
Fig. 54b Laser velocimeter velocity
transformations.
Velocity-defect.
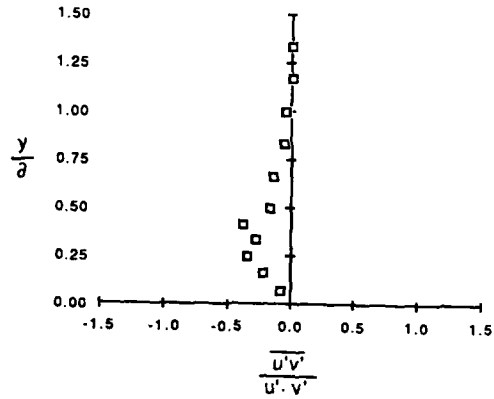
Fig. 56 Turbulent velocity cross-correlation
coefficient.

Fig. 57 Mean velocity profiles.

Fig. 55 Velocity fluctuations across the zero
pressure gradient boundary layer.
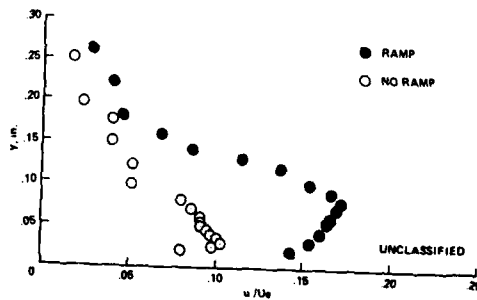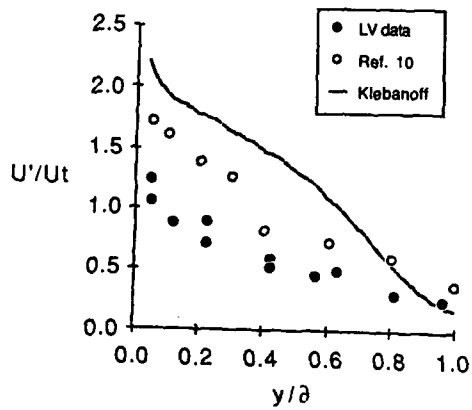
Fig. 58 Turbulent fluctuation levels.
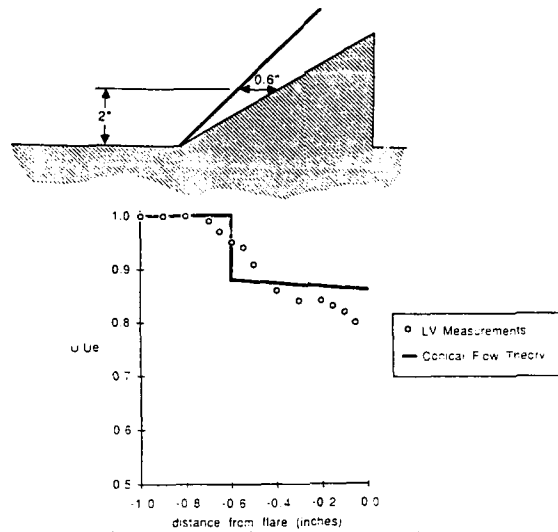
Fig. 59a Laser velocimeter measurements across an oblique shock wave. Velocity-defect.
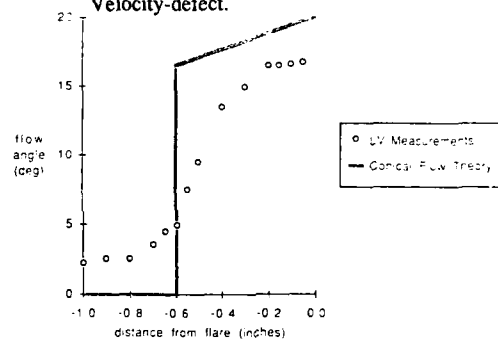
Fig. 59b Laser velocimeter measurements across an oblique shock wave. Flow angularity.

Fig. 60 Laser light sheet flow visualization.

SPECIES COMPOSITION MEASUREMENTS IN
NONEQUILIBRIUM HIGH-SPEED FLOWS

by
Donald W. Boyer
Calspan Corporation
P.O.B. 400
Buffalo, N Y 14225
USA

1. INTRODUCTION

The early development of the wind tunnel for aerodynamic research basically assumed an essential reciprocity between flight through the ambient atmosphere, and phenomena generated about a stationary test vehicle in a moving airstream. At modest velocity requirements, such test facilities could be continuous in their operation.

As research interests encompassed higher velocity regimes, requirements on the total enthalpy level of the fluid test medium also increased, rendering the continuous-flow facility less viable as its steady-state operational limits were approached.

Short-duration test facilities such as the hypersonic shock tunnel, however, have afforded a means for extending research study capabilities into the hypervelocity flight regime. The development of ground test facilities to simulate the flow about hypersonic vehicles is nevertheless very challenging because of the high total enthalpies required. The stagnation enthalpies encountered in flight at hypersonic speeds result in flowfield temperatures high enough to dissociate and even ionize the chemical species in air. The reservoir state in a short-duration test facility, which then undergoes expansion to high velocity is, of course, at comparable enthalpies to the flight case. The test gas in the reservoir is therefore also dissociated and ionized. In the subsequent expansion to hypersonic speeds, the flow can depart from thermal and chemical equilibrium.

It is in these test flow environments that "perfect-gas" reciprocity is lost since, at comparable velocities, the freestream in the high-enthalpy facility test section differs from that existing for flight in the atmosphere. The static pressures and temperatures (and hence Mach numbers) differ and the composition of the air in the nozzle contains oxygen atoms and nitric oxide, in addition to the molecular O_2 and N_2. At higher enthalpies, nitrogen is also appreciably dissociated and ionized species begin to appear in significant concentration. The ionization introduces plasma properties into the flow environment which can give rise to additional interaction phenomena associated with the presence of a free electron concentration in the flowfield. The effect of a nonequilibrium freestream composition on flowfield measurements around a test vehicle must then be understood in order to relate to the flight case. Numerical codes exist, of course, for the calculation of nonequilibrium flow expansions, and for flows about hypervelocity vehicles. The important questions are then:

- is the chemistry fully specified?
- are the reaction rates reliable?

In high enthalpy facility operations, therefore, it is necessary that consideration be given to the diagnostic methods and techniques available for independent measurement of species compositions. A description of such complementary techniques will comprise the substance of the lecture discussions. The methods to be discussed have all appeared, in various forms, in the archival literature on research studies covering a range of different flow environments and gas mixtures. The techniques involve laser, optical, and electron-beam "probes" to interrogate the flow, all of which are classed as non-intrusive diagnostics.

The methods will involve laser interrogation of the flow via such techniques as spontaneous Raman spectroscopy (SRS), coherent anti-Stokes Raman spectroscopy (CARS) and laser-induced fluorescence (LIF). These methods provide for good spatial resolution, either via the use of crossed beams (CARS) or by monitoring a small elemental length of the laser beam (SRS, LIF).

Other optical methods to be discussed involve emission or absorption phenomena which exploit the fact that critical air species in real-gas flows are optically active and permit emission or absorption spectrometric techniques to be used. These latter approaches are integrated line-of-sight measurements which are appropriate, for example, for the quasi one-dimensional flows in a nozzle expansion. As with all such measurements which are a function of species composition, they allow for critical comparison with calculated values.

Point measurements of number density may also be made by means of an electron beam. Beam electrons injected into the flow collisionally excite a selected species whose specific fluorescent emission is monitored via well-focussed collection optics, interference filters and, most usually, photomultipliers. The choice of band system monitored depends upon the density levels anticipated. For complementary calibration data obtained under static conditions, species number densities in a flow system can be directly inferred from a single radiometer measurement of the beam fluorescence.

For higher-enthalpy flow situations in which the flow may be partially ionized, reference will also be made to the use of swept-voltage electrostatic probes for the point measurement of electron temperature and number density. This is an intrusive-probe measurement, and one applicable to both the freestream and vehicle flowfields. In the uniform freestream, integrated line-of-sight diagnostic measurements of the plasma state are afforded, as well, by microwave interferometry.

The implementation of these techniques for species composition measurements in nonequilibrium flow systems will be described in subsequent sections. A brief review is first given, however, of the flight regimes wherein changes in the gas composition begin to take place as a result of dissociation processes, and of the consequences of these processes in the expansion flows simulating flight velocities in a test facility.

The note, perhaps trivial, is also made that the gas, though dissociated or ionized, may still be in thermochemical equilibrium in some regions, as in the vicinity of the stagnation point on a large nose radius vehicle, or in the reservoir region of a reflected-shock tunnel. Nonequilibrium phenomena appear when the fact that chemical adjustment

ra s are not infinitely fast becomes manifest. These appear, for example, in the rapid expansion of high-enthalpy flows such as those into the afterbody region around a blunt vehicle, or in the flow in a hypersonic nozzle.

2. FLIGHT SIMULATION AND NONEQUILIBRIUM PHENOMENA

The gasdynamic parameters and composition of equilibrium air behind a normal shock wave have appeared in tabular or graphical form in many publications. Such computations have also been performed at this laboratory for a range of velocities (2000-50000 ft/sec) and altitudes (sea level-300,000 ft) from which the data shown in Figure 1 were obtained.

Figure 1 shows the regimes corresponding to 10% a^d 90% dissociation behind a normal shock wave for both O_2 and N_2 as a function of velocity and altitude. The ti. eshold for 10% ionization is also included. It is seen that O_2 dissociation is essentially complete before N_2 dissociation begins. This is due to the weaker valence bond of O_2 compared with N_2. Profiles of normal shock temperatures of 4,000, 6,000, 8,000 and 10,000°K have also been included in the figure. The stagnation temperature would only be about 1% higher than the normal shock value for any of the velocity-altitude conditions shown. Also included, as appropriate, is the hypersonic flight trajectory of the shuttle vehicle.

In order to relate the flight regimes shown in Figure 1 to hypersonic facility test requirements, the thermodynamic state of the atmosphere at a given altitude and flight velocity condition can be used to define a reservoir condition from which expansion would produce a test flow providing the required flight condition. At high enthalpy levels, however, full duplication of a selected flight condition cannot be achieved in any test facility because of pressure limitations and nonequilibrium phenomena[1].

Full duplication is necessarily relaxed in order to duplicate the flow velocity and one of the thermodynamic state variables corresponding to conditions at the selected altitude. Usually the density corresponding to a given altitude is matched. If the test airflow is then expanded from an equilibrium reservoir to the desired velocity and density at the given altitude, the static temperature will, in general, be higher than the static temperature at that altitude. The freestream Mach number will therefore be lower than the flight Mach number. For hypersonic flows, however, the duplication of the velocity and density-altitude afford a match in the total enthalpy, or stagnation temperature, and in the dynamic pressure. For blunt bodies, therefore, real gas flowfields can be simulated to good approximation in hypersonic flow facilities[1]

As noted earlier, however, airflow expansion from a high enthalpy reservoir state undergoes a departure from chemical equilibrium. Computer codes have been written for the calculation of nonequilibrium expansions of air with coupled chemical reactions[2] and employed in numerical calculations for a wide range of high-enthalpy reservoir expansions[3]. The results of an illustrative calculation are shown in Figure 2. The calculated species distributions correspond to the expansion from an equilibrium reservoir or reflected shock condition at a temperature of 6,000°K and a pressure of 600 atmos., in one of the nozzles of the 96-inch hypersonic shock tunnel at this laboratory. The expansion in this case will produce a test flow velocity of about 14,000 ft/sec, at a density altitude of about 130 kft.

The figure illustrates the considerable departure from composition equilibrium for some species, including electrons, which occur in the nozzle freestream at these conditions, which are typical of high enthalpy shock tunnel operation. The species concentrations are shown in mass concentration units ($\mathcal{Y}_i$, moles/gm). This removes the density dependence from the distributions and highlights the freezing process, i.e., when frozen, $\mathcal{Y}_i$ = constant. It is seen that O and NO freeze out in the early portion of the nozzle expansion so that the test freestream composition is about 5% NO, which exceeds the O-atom concentration. On the other hand the dissociation energy of N_2 is essentially completely recovered in the expansion due to the efficient binary paths provided by the so-called shuffle reactions.

$$NO + O \longrightarrow N + O_2$$
$$N + NO \longrightarrow O + N_2$$
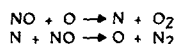
These reactions have been written in their operative direction during the expansion process. The binary path for the return of N to N_2 is evident. The dominant mechanism for the control of the electron concentration in airflows at these conditions is the dissociative recombination process $NO^+ + e^- \rightleftharpoons N + O$. This process also rapidly loses effectiveness as the density decreases in the expansion hence a free electron concentration is present in the hypervelocity freestream flow.

The departure from equilibrium in species composition also effects associated departures from equilibrium behavior in other gasdynamic properties. The static temperature in the expansion is lower than for equilibrium because of the chemical energy frozen out in nonequilibrium species concentrations. The static pressure and the local flow velocity are also slightly lower than in an equilibrium expansion, whereas the gas density is essentially unaffected by nonequilibrium effects.

It is important, however, that the effects of the nonequilibrium state of the test flow, as illustrated in Figure 2 for example, be thoroughly understood in the interpretation of experiments in a hypersonic test facility. While this can be done by computation, the reliability of numerical calculations in the description of the nonequilibrium state must be well validated. The independent measurement of species concentrations in such facility-generated flows constitutes a logical data base in the corroborative process.

3. NONINTRUSIVE DIAGNOSTICS FOR SPECIES CONCENTRATION MEASUREMENTS

Several diagnostic methods will be discussed which can be employed for the measurement of species concentrations in nonequilibrium flows. The laser optical methods, in particular, have demonstrated their applicability for the measurement of temperatures and species concentrations in such hostile environments as flames and combustors.

The methods to be described are nonintrusive techniques which employ the remote focusing of optical radiation into the region of diagnostic interest. Physical probes do, and will continue to, provide for unique and specific gasdynamic measurements in high speed flows. However, depending upon the flow situation or the measurement requirements, physical probes may perturb the flow properties they seek to measure. They may also be limited in their spatial resolution or temporal response, and may not survive at the high temperature and pressure conditions

associated with high-enthalpy flow simulations. Species concentration measurements, however, can be performed via remote, non-perturbing techniques, mainly optical, provided line of sight access to the measurement region of interest can be made available. In most cases, provision for such access can be factored into the design of the particular experiment.

The optical method may involve either the traditional incoherent radiation sources such as lamps or arcs for absorption measurements, or the highly collimated, coherent radiations provided by lasers. Prior to more detailed discussions concerning these optical methods, a few introductory comments should be made concerning the spectroscopy associated with the passage of optical radiation through gases. This will serve to introduce some of the phenomena, such as scattering, Raman spectra, fluorescence, etc., that are fundamental to the diagnostic measurement techniques to be discussed. The presentation of the theory underlying the several processes to be presented will, by intent, be quite brief so as to maintain focus on the measurement methods. The corresponding theoretical backgrounds are fully covered in the literature to be cited.

3.1 Induced Polarization Phenomena in Gases

When radiation passes through a gas, the electric field of the incident electromagnetic radiation induces a polarization in the molecules. The electric polarization may be written as a power series of the form

$$P = \chi^{(1)}E + \chi^{(2)}E^2 + \chi^{(3)}E^3... \tag{1}$$

where P is the induced polarization, χ is the dielectric susceptibility and E is the electric field strength. The linear susceptibility term, $\chi^{(1)}$, is responsible for Rayleigh and Raman scattering phenomena, whereas the nonlinear terms lead to resonant phenomena at new frequencies. In isotropic media such as gases, there are no second-order effects and the second-order nonlinear susceptibility, $\chi^{(2)}$, is zero. The lowest order nonlinear term for gases is therefore the third-order term, $\chi^{(3)}$. This latter term will be referred to subsequently as it is responsible for the CARS process.

The oscillating polarization induced via the linear susceptibility term, $\chi^{(1)}$, produces electromagnetic radiation and Rayleigh scattering[4] results from the induced polarization oscillating at the same frequency as the incident radiation. That is, the photon is elastically scattered without change of energy. In addition, the induced polarization changes slightly as a result of the vibrational and rotational motions of the molecule. This results in inelastic or Raman scattering where the frequency of the scattered light is shifted by the vibrational or rotational frequency of the molecular motions. The incident light photon may cause the molecule to undergo a quantum transition to a higher level, so that the incident photon loses energy and is scattered at a lower frequency. If the molecule is already in an energy level above its ground state, the photon may cause the molecule to return to its lowest level with the photon scattered at increased frequency. These frequency changes are the Raman shifts which are characteristic of the particular molecule[4]. If a different incident frequency is used, other Raman spectra are obtained for the same molecule. However, the Raman shifts from the exciting frequency remain the same.

The frequency shifts to lower energy (or longer wavelengths) are called Stokes lines, and those displaced to higher frequencies (shorter wavelengths) are called anti-Stokes lines. At ordinary temperatures, both Stokes and anti-Stokes lines are evident in the rotational Raman spectra of diatomic molecules, with which molecules these discussions will be primarily concerned. However, most diatomic molecules are in the lowest vibrational state at ordinary temperatures, the fraction of molecules in a higher vibrational level being extremely small. For example, at $300°K$, the ratio of nitrogen molecules in the first vibrational level to those in the ground state is 1.4×10^{-5} for a Boltzmann distribution[4]. Accordingly, only the Stokes lines are observed in the vibrational Raman spectrum of diatomic gases. The intensities of the anti-Stokes lines at shorter wavelengths are so weak that they are not observed.

In this context, the comment should be included that infrared spectra derive from a permanent dipole moment in the molecule, not present in homonuclear molecules like N_2 or O_2, whereas Raman spectra result from polarization effects which are independent of the presence of a permanent dipole moment in the molecule. Thus Raman spectra exist for homonuclear diatomic molecules like H_2, O_2 or N_2, which have no infrared spectrum.

Finally, it should also be noted that fluorescence is a phenomenon entirely separate from the Raman effect, even though the use of the terms Stokes and anti-Stokes lines have as their origin reference to fluorescent spectra. In fluorescence, the incident photon is absorbed, the molecule elevated to an excited state with re-emission of the photon after a certain lifetime, to return the molecule to a lower energy state. The fluorescence, therefore, is always emitted at a lower frequency than that of the incident radiation in accordance with Stokes law, i.e., the fluorescence corresponds to Stokes lines.*

3.2 Spontaneous Raman Spectroscopy

One of the early spectroscopic techniques employed for species concentration and temperature measurements is spontaneous Raman spectroscopy (SRS). A schematic of an experimental arrangement for SRS is shown in Figure 3. Only a single radiation source is required for this measurement technique, which can operate at any wavelength. However, since the intensity of the Raman signal is proportional to the fourth power of the incident radiation frequency, visible wavelength sources are usually employed.

Early sources employed the $4358Å$ line of mercury, which is the most intense. Current sources are usually lasers (e.g., Nd:YAG, $5320Å$, Argon ion, $4880Å$). The incident radiation is brought to a focus in the measurement volume, and the radiation scattered at right angles is collected via large-solid-angle optics and passed into an appropriate detector (monochrometer, spectrometer) for analysis. The recorded spectrum of the interrogated species may be a pure rotational Raman spectrum (low temperatures) wherein no change in vibrational energy is involved, or it can be a vibrational Raman spectrum in which both vibrational and rotational transitions are involved. The type of spectra recorded will depend upon the source frequency, as well as the identity and temperature of the targeted molecule.

---

*As noted in Ref. (4), lines which would contradict Stokes law for fluorescence were referred to as anti-Stokes lines. This terminology was carried over to the Raman effect to denote those lines which are emitted at frequencies higher than that of the incident radiation.

The Raman transitions are described in terms of the selection rules for the changes allowed in the vibrational quantum number, v, and the rotational quantum number, J. For the rotational Raman spectrum of a diatomic molecule, v = 0 and ΔJ = +2, giving the S branch lines equidistant either side of the exciting line (ΔJ = 0). For the vibrational spectrum, Δv = ± 1, i.e., transition can occur only to the adjacent vibrational state, and three branches corresponding to ΔJ = +2 (S branch), ΔJ = -2 (O branch) and ΔJ = 0 (Q branch).

In a given environment, the distribution of populations among the different energy levels will vary with the temperature. The recorded Raman spectrum will therefore be a sensitive function of the temperature of the scattering molecule. A smoothed representation of the measured Raman spectrum recorded for N_2 by Lapp et al.[5] in a lean H_2-air flame is shown by the solid line in Figure 4. The source in these experiments was an Argon-ion laser at 4880Å (20492 cm^{-1}). The Raman shift for N_2 is 2331 cm^{-1}[4] hence the fundamental (v = 0) Stokes line is centered at 20492 - 2331 = 18161 cm^{-1}, or 5506Å. The peaks labeled G, 1, and 2 correspond to, respectively, the ground state Stokes vibrational Q-branch, the Q-branch for v = 1 to v = 2, and the upper state Q-branch for v = 2 to v = 3. The G profile is the fundamental and the v = 1, v = 2 profiles correspond to the "hot" bands.

The intensity and the width of each particular band depends upon the rotational temperature and can be calculated [5-7] hence a fit to the measured profile will determine the rotational temperature. The bandwidth and successive band ratios are temperature-dependent. If the gas is in equilibrium, i.e., equilibrium populations of the vibrational and rotational energy levels, then the vibrational and rotational temperatures are equal. The illustrative flame data for N_2 in Figure 4 correspond to the equilibrium situation. The calculated Raman spectral profiles for several different temperatures are also included on the measured profile, indicating quite satisfactory correlation for an N_2 temperature of 1600°K. The calculated relative intensity profiles were performed on a computer via convolution with the measured slit function of the monochrometer. This will improve the match between the computed and measured spectra.

If nonequilibrium population conditions exist, separate fits to the shape of each band can be iteratively performed for different rotational and vibrational temperatures[8]. Vibrational temperatures can also be obtained from the band peak height ratios[9], or from the ratio of Stokes to anti-Stokes lines[9-11].

In this technique, the intensity of the scattered radiation depends upon the number of molecular scatterers in the probed volume. The species concentration is then readily obtained from the ratio of the scattered to incident radiation intensity which is a linear function of the number density. Quenching effects are not involved. In a general form, the intensity ratio can be written[9,11,12]

$$\frac{I_R}{I_0} = N \frac{\partial \sigma}{\partial \Omega} \Omega \mathcal{L} \mathcal{E} \tag{2}$$

where I_R and I_0 are the collected scattered intensity and incident radiation intensity, N is the number density of the specific molecular scatterers, $\partial \sigma / \partial \Omega$ is the Raman scattering cross section, Ω is the collection solid angle, $\mathcal{L}$ is the sampled length (Figure 3) and $\mathcal{E}$ represents the overall optical collection efficiency. Values of the Raman cross sections are available in the literature.

Many applications of spontaneous Raman spectroscopy have been reported for species concentration and temperature measurements. The references cited herein comprise such measurements on species that include N_2, O_2, OH, CO, H_2O, and CO_2. Some of the measurements were performed in nozzle expansion flows [6], although the majority have been applied to the quantitative diagnosis of flames and post-combustion processes.

The SRS method has, as its advantages, the comparative simplicity of experimental setup, the capability for fine spatial resolution, the need for only a single source, freedom from collision quenching effects (since it is a scattering process), and freedom from interference radiation due to the simultaneous scattering from other species. The latter is due to the fact that at the same incident frequency, the Raman spectra of other species will occur at different wavelengths. This also means that the determination of the concentration of a particular species in a gas mixture is independent of the other components of the gas mixture. The shortness of laser-source pulses also enables the technique to be applied for in-situ concentration measurements in high speed flows.

The prime disadvantage of the technique, however, is the low value of the Raman scattering cross sections. For example, typical spontaneous Raman cross sections for rotational and vibrational transitions are of order 10^{-30} cm^2/sr, which are about 3 orders of magnitude smaller than Rayleigh scattering and about 10 orders of magnitude smaller than those for molecular absorptions[13]. The scattered radiation is also incoherent, being distributed over 4π sr, hence the need, as noted earlier, for large solid-angle collection optics. These factors lead, overall, to a weak process, which is limited to the measurement of species in reasonably large concentration (~ 1%) and in essentially clean flows. The latter requirement is to avoid other interferences arising from background luminosity or particulates, which can mask the Raman signals.

In nonequilibrium airflows, however, using high-power pulsed lasers, the method can be appropriate. As noted in Figure 2, N_2 is essentially equilibrated in a high-enthalpy nonequilibrium air expansion, but SRS could usefully monitor N_2 for thermometry. The measurement of O_2 and NO concentrations, furthermore, is important as a means of verification of the kinetics description of the nonequilibrium state.

3.3 Coherent Anti-Stokes Raman Spectroscopy

Owing to the deficiencies in the strength of signals associated with spontaneous Raman spectroscopy, recent years have witnessed a most significant growth in the application of the technique of Coherent anti-Stokes Raman Spectroscopy (CARS). This is, however, a technique of considerable complexity in its experimental configuration, its theoretical foundation, and in data reduction. At the same time, the method is a powerful one because of the coherence of the generated signal and the orders of magnitude improvement in signal response over spontaneous Raman scattering, and hence in the ratio of signal to interference levels.

The nonlinear optical effects responsible for the CARS process were first reported by Maker and Terhune[14] in 1965. There the feasibility was shown for the creation of a new frequency component at $\omega + \Delta$ due to the presence of frequencies ω and $\omega - \Delta$, where Δ is a Raman frequency. The process was referred to as three-wave mixing[14], and depends upon the third-order nonlinear susceptibility term, $\chi^{(3)}$, in the induced polarization equation presented earlier (Eqn. (1), Sec. 3.1). Mixing of the field frequency components by the third-order susceptibility can be used,

for example, to triple a fundamental frequency or to combine two or three different frequencies which can be resonantly enhanced, leading to the generation of coherent radiation at a new frequency.

High electric fields are necessary, however, for the generation of the nonlinear optical effects in media, hence it was not until the development of high peak power laser sources that such phenomena could be observed experimentally. The method was first employed for gas-phase concentration measurements by Regnier and Taran[15] in 1973.

A diagrammatic representation of the CARS process is shown in the sketch below, from literature on the theory and application of CARS.[12,16-18]
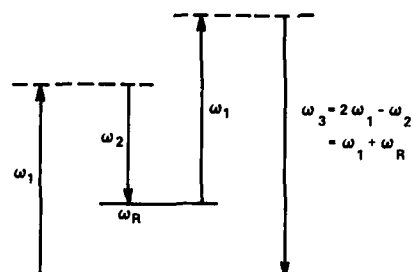
ENERGY LEVEL DIAGRAM

Incident laser beams at frequencies ω_1 and ω_2 , termed the pump and Stokes beams, respectively, interact through the third-order nonlinear susceptibility, $\chi^{(3)}$, to generate a polarization field which produces coherent radiation at a frequency $\omega_3 = 2\omega_1 - \omega_2$. When the frequency difference $(\omega_1 - \omega_2)$ is close to the frequency of a Raman-active resonance, ω_R, the CARS signal at frequency ω_3 will then be resonantly enhanced and emerge as a laser-like signal whose spectral properties are unique to the molecule being probed. It can be seen from the above sketch that the CARS signal lies on the anti-Stokes side of ω_1 , hence the name of the effect.

Only a brief overview of the theory of CARS is included here, as the process is thoroughly described in the cited literature and in the references noted therein. The third-order nonlinear susceptibility which governs the effect is complex and can be written[19-23],

$$\chi^{(3)} = \chi_R + \chi_{NR} = \chi_R' + i\chi_R'' + \chi_{NR} \tag{3}$$

where $\chi_R = \chi_R' + i\chi_R''$ is the resonant part of the susceptibility, due to the closest vibrational-rotational resonances (Raman-active transitions) in the species of interest, and χ_{NR} is a slowly varying nonresonant term which is a background contribution due to electrons and remote resonances from the other species present.

The susceptibility is a fourth-rank tensor characterized by four distinct frequencies with the full expression consisting of some 80 independent tensor elements[23]. Considerable simplification exists, however, for the case of an isotropic medium when the number of tensor elements is reduced to three. A further reduction to two elements exists for frequency-degenerate CARS wherein two of the four frequencies are equal. It is this situation, with frequencies ω_1 , ω_2 and ω_3, that is involved in current diagnostic applications of CARS. There are, nonetheless, still a large number of resonant denominator terms in the nonlinear susceptibility expression which, apart from the vibrationally resonant terms, can become large when one or more of the field frequencies ω_1 , ω_2 or the CARS frequency ω_3 become resonant with an electronic transition in the probed molecule leading to electronically-resonant CARS. However, the normal CARS process is vibrationally resonant for $\omega_R = \omega_1 - \omega_2$. For these situations, when far from electronic resonances, the susceptibility can be written in the general form:

$$\chi^{(3)} \simeq \frac{2\,c^4}{\hbar\omega_2^4}\ N \sum_{v,J} \frac{\Delta(v,J)\ \left(\frac{d\sigma}{d\Omega}\right)_{v,J}}{\omega_R - (\omega_1 - \omega_2) - i\Gamma(v,J)} \tag{4}$$

where N is the total number density of the probed molecule, $\Delta(v,J)$ is the population difference between the upper and lower vibration-rotation states, $d\sigma/d\Omega$ is the Raman-scattering cross section and $\Gamma(v,J)$ is the line width of the Raman transition. As vibrational modes of molecules are mainly symmetric, only Q-branch transitions are important. It is evident that for a given pump frequency ω_1, the selection of a particular frequency ω_2 can pick out a resonance condition for a given ω_R via the detuning denominator factor $\omega_R - (\omega_1 - \omega_2)$. All other remote resonances are lumped under the background nonresonant term, χ_{NR}.

The susceptibility is seen to be number density dependent, and because of the Boltzmann population factor $\Delta(v,J)$, the CARS spectra will also be temperature dependent. This is the basis of the diagnostic. The nonresonant part, χ_{NR}, of the susceptibility is real and independent of ω_1 and ω_2 and for gases is of order $10^{-4} - 10^{-5}$ of χ_R[15]. Also, near resonance, the real part of the resonant susceptibility $\chi_R' \rightarrow 0$. Measurements of the third-order nonlinear susceptibilities for a number of different gases have been reported by Rado[24].

The intensity of the CARS signal is given by:[15,19,25]

$$I_3 \simeq \left(\frac{4\pi^2 \omega_3}{c^2}\right)^2 I_1^2 \, I_2 \, \left|\chi^{(3)}\right|^2 L^2 \qquad (5)$$

where I is the power density at frequency ω , $\chi^{(3)}$ the third-order susceptibility, and L is the distance over which the laser beam interaction occurs. The magnitude of the CARS signal is thus dependent on the intensities of the mixing pump and Stokes laser beams. For focused beams, the power in the CARS signal is then

$$P_3 \simeq \left(\frac{\omega_1}{\pi c}\right)^2 \left(\frac{4\pi^2 \omega_3}{c^2}\right)^2 P_1^2 P_2 \left|\chi\right|^2 \qquad (6)$$

From these expressions, it is seen that the resonant part of the CARS signal is proportional to the square of the probed molecule number density, via $|\chi|^2$.

A schematic of the laser system geometry for the generation of the CARS signal is shown in the sketch below:
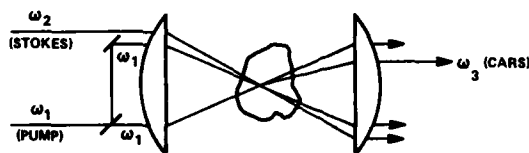
OPTICAL ARRANGEMENT FOR CARS

The two beams from the pump laser at ω_1 and the Stokes beam at ω_2 are focused into the probe volume and generate the CARS signal at ω_3 .

Phase matching is extremely important in this process. The incident laser beams must be aligned so that the three-wave mixing process is properly phased to ensure that the CARS signal generated at one location in the probed volume will be in phase with that generated at another location so that the signal builds up constructively. If proper phase matching is not realized, the CARS signals generated at different spatial locations will destructively interfere and no CARS signal will build up. Phase matching in gases occurs when the incident laser beams are collinearly mixed. Such phase matching is shown by the wave vector diagram of sketch A below. k is the wave vector at frequency ω and has the magnitude $\omega \eta / c$ where η is the refractive index at frequency ω and c is the speed of light.
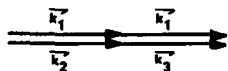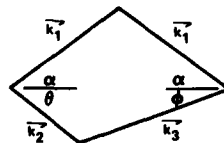
A. Collinear Phase Matching   **B. BOXCARS Phase Matching**

However, there are disadvantages to collinear mixing[26]. Collinear phase matching can result in poor spatial resolution particularly if the diagnostic situation requires the use of long focal length lenses, which can then result in long probe-volume lengths. Resolution can be degraded further if density gradients are present because, as shown previously, the CARS power is proportional to the square of the species density. With a collinear system, there is also the possibility of CARS signal generation from elements in the optical train that pass the collinear beams. A method which ensures phase matching, yet permits large angular separation of the input beams, was described by Eckbreth[26]. The wave vector diagram for this approach is shown above in sketch B. The system is referred to as BOXCARS because of the shape of the phase-matching diagram. In the BOXCARS or crossed-beam approach, the pump beam, ω_1 , is split into two components which are crossed at a half-angle α prescribed by the spatial resolution desired. The Stokes beam, ω_2, is introduced at an angle θ , to generate the phase-matched CARS signal at angle ϕ from the region of beam intersection. The angles ($\theta > \alpha > \phi$) are not independent but are related to one another through simple geometric equations[26].

The BOXCARS configuration is that shown above in the schematic of the CARS optical arrangement. It is seen that this system avoids overlap in all regions except the desired measurement location. Spatial resolution can therefore be very precise ($\lesssim 1$ mm^3). The crossed beam geometry also need not be coplanar. The plane containing the Stokes beam at angle θ can be at right angles to the plane of the pump beams at angle α, a configuration referred to as folded BOXCARS[27].

A schematic diagram of a typical CARS experimental arrangement, in the BOXCARS configuration, is shown in Figure 5.[28,29] The pump laser most commonly employed in CARS systems is a neodymium:YAG (yttrium aluminum garnet) whose 1.06 micron output is frequency doubled (2 x Nd) to provide a pump beam ω_1 at 5320Å. The ruby laser has also been employed in CARS, but it does not have the repetition rate capability (10 Hz) of the 2xNd, nor is it as well located spectrally. The Stokes beam, ω_2, is usually provided by a tunable dye laser which is pumped by a portion of the pump laser. The dye laser can be operated in either a narrowband or broadband mode, determined by the spectral resolution required. This will be discussed further below. Several of the adjustable telescope lenses have been omitted from the optical trains to simplify the figure and include only the general elements.

The Nd laser produces two beams at 5320Å, labeled primary and secondary in Figure 5. A portion of the primary beam is split off via a beam splitter (BS) to pump, slightly off axis, a flowing dye cell (DC) laser. By proper dye selection and dye concentration the laser can be made to lase at any desired center wavelength.

The secondary 5320Å beam optically pumps a second dye cell which serves to amplify the Stokes laser component at ω_2. The dye is circulated through the dye laser and amplifier in series. The transmitted primary ω_1 beam from the first beam splitter is divided at a second beam splitter into equal parts which are sent to the beam crossing lens (L) by means of a mirror (M) and a dichroic mirror (D) through which also passes the Stokes ω_2 beam from the dye laser/amplifier. The proper phase-matching angles of the three beams used for BOXCARS are obtained by the appropriate beam displacements on the crossing lens (L). All three beams incident on the crossing lens are parallel to each other and in the same plane. Adjustable telescopes in the ω_1 and ω_2 optical trains (not shown) are used to ensure that the beam waists occur at the crossing point. The rotatable optical flat (OF) in the Stokes beam permits the displacement of the ω_2 beam on the crossing lens should it be necessary to change the phase-matching angle θ.

After passing through the crossing point, the four beams $\omega_1, \omega_1, \omega_2$ and CARS at ω_3 are recollimated by a second lens, similar to the first. Two of the components, ω_1 and ω_2, are passed to a beam dump (BD) or to a reference leg, if necessary. The CARS signal is then separated from the other ω_1 component by dispersion through a prism and sent to the detector (photomultiplier, optical multichannel analyzer, etc.).

It was noted previously that the CARS signal levels may be several orders of magnitude stronger than those produced by spontaneous Raman scattering. Furthermore, because the signal is coherent and laserlike, it emerges as a narrow beam so that all of the signal can be collected. Recall that the spontaneous Raman signal is incoherent and distributed over 4π sr.

The CARS spectrum can be generated in two ways. For high spectral resolution, a tunable narrowband dye laser is scanned through the Raman resonances to generate the CARS spectrum over a period of time. However, in short duration flow diagnostics, faster time resolution is necessary. Also, in turbulent environments, frequency scanning would distort the spectral signature because of the nonlinear dependence of the CARS signal on density and temperature (Eqns. (4) and (6)). It is necessary in these situations, therefore, to generate and record the entire CARS spectrum in a single laser pulse. This is accomplished by the use of a broadband dye laser centered at the desired ω_2 and with a bandwidth large enough ($\sim$100-200 cm^{-1}) to encompass all of the vibrational or rotational resonances.

Because all of the Stokes power is now not used to drive each Raman resonance as it is in narrowband spectral scanning, spectral intensities are lower in the broadband mode. The use of a single laser pulse to record an entire Q-branch* (vibrational) CARS spectrum was first reported by Roh et al.[30]. The entire rotational CARS spectrum has also been recorded using a single pulse broadband Stokes laser in cold N_2 thermometry measurements[31]. An optical multichannel analyzer (OMA) is most appropriately used for the single pulse recording of entire CARS spectra.

The computation of synthetic spectra plays a fundamental role in the interpretation of the measured CARS spectra for the determination of the temperature and species number density. The equations presented earlier in a brief summary of the theory of the CARS effect, Equations (3)-(6), indicated that three parameters are involved in the CARS spectrum, and therefore in its computer generation, namely, the temperature T, number density N and the nonresonant susceptibility χ_{NR}. In many instances, the temperature is determined first, and then used in a subsequent determination of number density.

Temperature measurement is most reliably performed on a dominant molecular species. N_2 has most frequently been employed for thermometry in CARS as it is a dominant species not only in airflows but in air-fed combustion processes. In such major species χ_{NR} is very much smaller than χ_R and does not interfere so that both N and χ_{NR} are relatively unimportant in these instances and the temperature can be determined from the shape of the CARS spectrum, ie., by comparison of the measured spectra with the computer generated spectra, in a similar manner to spontaneous Raman spectroscopy.

Computer programs have been written by Hall[22, 23] for the computation of spectra in N_2, CO, H_2, O_2 as well as for the triatomic molecules H_2O and CO_2. Extension of such programs to the diatomic molecule NO, which is an important constituent in nonequilibrium airflows (Figure 2) should not pose any problem. The equations (3)-(6) are employed for the computation of the third-order susceptibility term $|\chi^{(3)}|^2$ which for non-monochromatic sources is convolved over the pump and Stokes laser linewidths. A final convolution must then be performed over the slit function of the detector instrument to broaden the spectra and afford a better match to the experimental spectra. In broadband CARS, the Stokes laser bandwidth is large so that the ultimate resolution of the spectrum will depend upon the pump laser linewidth or the slit function of the instrument. The resolution for CARS is far superior to that for SRS.

An example of the sequences in the computation of the N_2 spectra in a flame due to Hall[22] is shown in Figure 6. The figure shows, first, the computed $|\chi|^2$ for monochromatic CARS generation (Figure 6(a)), its subsequent convolution for the finite linewidths of the pump (1.2 cm^{-1}) and Stokes (175 cm^{-1}) lasers (Figure 6(b)) and the final convolution over a triangular slit function of resolution 1 cm^{-1} (Figure 6(c)). These calculations were performed for a constant Raman linewidth Γ of 0.1 cm^{-1}.

Figures 6 and 7 are calculated Q branch N_2 spectra. At low temperatures (Figure 7(a))[17], the low J branches are not resolved but as the temperature increases the fundamental band broadens, individual Q branches can be resolved, and the hot band (v = 1 $\rightarrow$ 2) peaks appear. It is evident from Figure 7, however, that even at low spectral resolution when detailed spectral definition is lost (as in Figure 7(b)[22] which looks like an SRS spectra) that the calculated spectra provide for excellent thermometry. The temperature of the dominant thermometric species is obtained either from the hot band, whose intensity relative to the normalized intensity of the fundamental band is a sensitive function of temperature, or from an overlaid comparison of the measured vs calculated spectra as shown in the illustrative case for N_2 CARS spectra[22] in Figure 8.

---

*The vibrational/rotational selection rules for CARS are essentially the same as for spontaneous Raman spectroscopy[23].

The thermometry discussed above is more readily performed than is the measurement of species number density N. The number density may be obtained in two ways: for a major species component, from an integration of the CARS spectrum and, for a minor species in certain concentration ranges, from the shape of the CARS spectrum.

Once the temperature has been determined, the number density for a dominant species, i.e., no nonresonant χ_{NR} background interference, may be calculated from[32,33]

$$N_T = N_{300}\sqrt{\frac{R_T\,P_{300}}{P_T}}$$

where N_T is the probed molecule number density at temperature T, N_{300} is the reference gas density at 300°K, $R_T = \int P_{300}d\nu / \int P_T d\nu$ is the ratio of the calculated integrated powers of the CARS signal at 300°K to the signal at temperature T, P_T is the experimentally measured integrated CARS power at temperature T, and P_{300} is the measured integrated CARS power at 300°K. The ratio R_T accounts for the change in the Raman linewidths and population redistribution with temperature.

The values at 300°K are obtained from a reference cell which must be incorporated into the optical trains for the primary CARS. Small fractions of the wave-mixing beams are split off and routed so as to generate a CARS spectrum in a reference cell which contains a resonant gas such as N_2 at known temperature and pressure, hence number density, and whose CARS signal magnitude is readily calculable. This is the power reference (P_{300}) for the number density measurements.

Because of the CARS signal dependence on N^2 (via $|\chi^{(3)}|^2$, Equation (4)), the signal decreases rapidly as the number density decreases. The lower limit on detectivity occurs when the CARS signal merges into the nonresonant susceptibility, χ_{NR}, signal established by the background gas concentration. This is a departure from the normal situation, such as in spontaneous Raman spectroscopy, where detection sensitivity is limited by low signal level. It is in this merging regime, however, that the number density can be obtained from the shape of the CARS spectrum. This is a unique feature of CARS, applicable over a limited range of concentrations.

The calculation of the CARS signal in this regime of minor species concentrations involves a two-parameter fit as, for a given temperature, the CARS signal depends on both N and χ_{NR}. Contrast this with Figure 8, for example, where thermometry is essentially a one-parameter fitting of measured and calculated specrtra. The process for the determination of N is illustrated by the representations of calculated CO spectra, shown in Figure 9, from Hall[22], and which correspond to the methane-air flame measurements of Eckbreth[28]. In this illustration, the temperature was known (1700°K) via independent CARS thermometry. The spectra in Figure 9 were calculated for a fixed value of χ_{NR} (~9 x 10^{-19} cm^3/erg). It is seen that as the CO concentration increases, its spectrum emerges from the nonresonant background and the hot band appears. It was noted previously that χ', the real part of the resonant susceptibility (Eqn. (3)) changes sign at resonance. The destructive interference between the resonant and background contributions at this point causes a characteristic dip in the profile, evident in Figure 9 at 20940 cm^{-1}. Comparison of the calculated CO spectrum with the measured CARS spectrum of the flame is shown in Figure 10 and shows the excellent agreement for a CO mole fraction of 0.04.

The calculations corresponding to the examples shown in Figures 9 and 10 were performed for a fixed value of χ_{NR}. Since the calculations are a two-parameter fit involving both N and χ_{NR}, the result is therefore not unique. A slightly different value for χ_{NR} would effect agreement with the measured CARS spectra for a slightly different value of N. Hence this method for the determination of number density from the shape of the CARS spectrum is one whose accuracy is dependent upon the knowledge of an appropriate value for χ_{NR}.

The range of concentrations over which a spectral shape determination of number density can be performed will vary from molecule to molecule, and with background gas composition and temperature. For molecules like O_2 and N_2, the concentration rnage is from about 0.1 - 20%. It is also possible to extend the method to lower number density measurements by essentially eliminating the background nonresonant susceptibility[17, 23]. This is accomplished by appropriately orienting the laser field and CARS polarizations. However, by removing the nonresonant contributions, a significant loss in the resonant signal intensity is also incurred. Complementary methods are available however. The measurement of minor constituent to trace species is appropriate to the implementation of laser induced fluorescence, which will be discussed in the next section.

The CARS technique, while quite complex, is a powerful one for unintrusive diagnostics in the measurement of temperature and species number density. Some of its prime advantages are the orders of magnitude increase in signal strength over other methods and the coherent nature of the output signal. This affords excellent collection efficiency. The geometry of the CARS-generating beams provides for very fine spatial resolution and, because of the capability to generate the entire CARS spectrum in a single laser pulse, diagnostic measurements can be performed in short-duration flows as well as in regions of turbulent flow. Also, because the CARS signal is at a higher frequency (anti-Stokes) than the exciting signal, other interferences such as fluorescence and background luminosity are eliminated.

3.4   Laser-Induced Fluorescence

Laser-induced fluorescence (LIF) is a considerably more sensitive method than one based on scattering phenomena, such as Raman spectroscopy, as it involves the absorption of laser photons and the creation of an electronically excited state in the absorbing species. It is therefore applicable to the measurement of species in very small concentrations, including trace species. The major application of laser-induced fluorescence to date has been in the study of combustion processes for the measurement of concentrations and temperatures of radical species, such as OH, in the characterization of flame chemistry. The objectives for nonequilibrium airflow diagnostics are, of course, similar to such laser probe applications in flames in that similar measurements are necessary to validate the descriptive kinetic models for high-enthalpy airflows.

The technique has some similarity to SRS, at least in its experimental arrangement, which basically would resemble that shown in Figure 3. Unlike SRS, however, wherein any laser frequency can be employed, it is necessary to use a tunable laser for LIF. For a selected species, the laser is tuned to afford resonance with an allowed transition in the molecule. When the beam is directed into the gas, the molecule absorbs a laser photon and undergoes

transition from the ground to an excited electronic level. The molecule then spontaneously radiates (fluoresces) to a lower level in the ground state. The emitted fluorescence is detected using either photomultipliers or optical multichannel analyzers. As with SRS, good spatial resolution is achieved by observing the fluorescence from a short elemental length of the laser beam, from a direction perpendicular to the laser beam. The depth of the probed volume is then essentially only the thickness of the laser beam.

Laser-induced fluorescence is, in principle, applicable to both atoms and molecules. The basis of the method is that the observed fluorescent intensity can be related to the ground state number density of the atom or molecule prior to laser irradiation. However, there are difficulties associated with the use of LIF whose severity is species dependent. The laser must be tuned to a resonance transition. For most molecules of interest, such as O_2, N_2, however, the resonance lines are in the ultraviolet (UV) region, where tunable laser sources are still being developed or improved. Also, the spectroscopy of the particular molecule must be understood; its spectrum as well as the transition probabilities, or Einstein coefficients, must be known.

The primary difficulties associated with LIF, however, are the deexcitation processes that will affect the fluorescent yield, and whose effects must be properly accounted for, or circumvented, in the diagnostic interpretation of the fluorescence signal. Consider the illustrative sketch below of the potential energy transfer processes that can be involved in laser-induced fluorescence.

SCHEMATIC LEVEL DIAGRAM FOR LIF SPECTROSCOPY
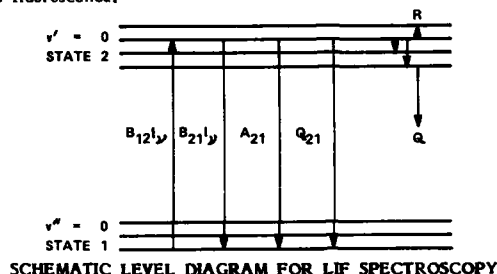
The molecule may be excited from the ground state (state 1) to a specific rotational-vibrational level in the excited electronic state (state 2), which has a finite radiative lifetime. The excited molecule may then spontaneously decay, emitting a fluorescence photon. These direct excitation, deexcitation processes are described by the appropriate values of B_{12}, B_{21} and A_{21}, the Einstein coefficients for induced absorption, stimulated emission (at laser intensity I_ν) and spontaneous emission. The molecule may also undergo a radiationless transition back to the ground state by collision denoted in the sketch by the electronic quenching term Q_{21}. In addition, the molecule may undergo a change in its rotational or vibrational level due to collisions. The rotational redistributions, R, to other rotational levels in the excited vibrational level are indicated in the sketch[34-37]. Vibrational level transitions, V, could similarly have been indicated[34,38,39]. Similar V, R transition considerations may also be appropriate for the ground state (state 1) as well, though such are usually slower than excited state redistributions. Finally, spontaneous emission, Q, may also occur to other rotation-vibration levels in the ground electronic state whose fluorescence may then be outside the spectral bandwidth of the detector, i.e., undetected fluorescence[40,41]. The fluorescence yield is defined as the ratio of the radiative rate, A_{21}, to the total deexcitation rate, $A_{21} + Q_{21} + Q + R + V$.

The complexity for LIF applications arises because the collisional rates can be very much faster than the radiative decay rates. The collisional redistributions among excited state rotational and vibrational levels, for example, will then serve to broaden the fluorescence spectrum. However, in spite of the complications due to quenching processes, LIF has been employed in diagnostic investigations involving O, N, O_2, NO and N_2, which comprise the neutral species complement of nonequilibrium airflows. Triatomics such as NO_2 have also been investigated, although the method becomes less sensitive in larger molecules because of the greater effect of collisions due to the increased number and closer spacing of the energy levels.

For applications to high speed flows, or to turbulent environments, pulsed laser sources are necessary. High laser intensities are therefore required, with their wavelengths in the ultraviolet. Nd:YAG-harmonic pumped dye lasers are frequently employed as well as excimer and nitrogen laser pumped dye lasers.

Several methods have been employed in order to circumvent the effects of quenching in LIF applications. One is to employ a very short laser pulse, τ_L, short compared to a time scale on which Q and A can become operative, i.e., $\tau_L < 1/(Q+A)$ where Q and A represent the quenching and emission rates introduced earlier. Referring to the previous energy level sketch for LIF spectroscopy, the rate equation for the excited level population can be written

$$\frac{dN_2}{dt} = N_1 B_{12} I_\nu - \left(Q_{21} + A_{21} + B_{21} I_\nu \right) N_2 \tag{7}$$

where all terms are noted on the sketch. When the laser is shut off, the exponential decay of the fluorescent intensity affords an in-situ determination of $Q+A$[42,43]. From Equation (7) for $I_\nu = 0$,

$$\frac{N_2(t)}{N_2(t=0)} = \exp\left[-(Q+A)t\right] = \frac{I(t)}{I(t=0)} \tag{8}$$

as fluorescent intensity is proportional to the excited state population N_2. Here t = 0 denotes the value at the instant of laser pulse termination. The number density N_2 at pulse shutoff is then

$$N_2 \ (t=0) = \left(\frac{Q+A}{A}\right) \frac{4\pi}{\hbar \nu L} \int_{t=0}^{\infty} I(t) \, dt \tag{9}$$

where I is the fluorescence intensity and L the length of the beam element. Thus, the integration of the fluorescent intensity measured as a function of time yields the excited state number density.

The concentration N_2 can then be related to the ground state number density prior to laser irradiation (N_1^0) by considering the steady state limit for Equation (7), for which

$$N_2 = \frac{N_1^0 \, B_{12} I_\nu}{Q_{21} + A_{21} + \left(B_{12} + B_{21}\right) I_\nu} \tag{10}$$

and with $N_1 + N_2 \approx N_1^0$. From detailed balancing ($g_1 B_{12} = g_2 B_{21}$) and for large incident laser intensity,

$$N_2 \simeq \frac{1}{1+g_1/g_2} \, N_1^0 \tag{11}$$

where g_1 and g_2 are the degeneracies of levels 1 and 2. Substitution for N_2 in Equation (9) then yields the ground state number density.

For a representative short laser pulse of 10 ns (Nd:YAG), this method would only be applicable to density levels which are low enough to satisfy the above requirement on the magnitude of ($Q_{21} + A_{21}$) relative to τ^{-1}.

Another approach is optical saturation of the excited level, in which the observed fluorescence becomes independent of quenching rates and laser power[44,45,46]. From Equation (7) in the steady state, and for large laser intensity,

$$N_2 = \frac{B_{12}}{B_{21}} \, N_1 \tag{12}$$

which is the saturation condition. This condition therefore requires $B_{21} I_\nu \gg Q_{21} + A_{21}$. Then from an observation of the laser beam at a selected station, the collected saturated fluorescent intensity is written

$$I = \hbar \nu \ \frac{A_{21}}{4\pi} \ \Omega_c V_c \left(\frac{g_1}{g_2}\right) N_1 \tag{13}$$

where Ω_c is the solid angle of the collection optics and V_c is the laser volume defined by the collection optics. The relation $N_1 + N_2 \approx N_1^0$ can again be used to relate N_1 under laser irradiation conditions to the ground state number density, N_1, in the absence of the laser. Therefore, when the transition is saturated by high intensity, focussed laser irradiation, the observed fluorescence is independent of quenching rates, lifetime, fluorescence yield and laser intensity.

The excitation model considered above is essentially a two-level system. For other than saturation conditions, however, this model is not expected to be widely applicable for diatomic molecules and must be modified to account for the rapid coupling between rotational levels. Three and four-level molecular models have been developed to account for the rotational energy redistributions[35,36]. For such near-saturation conditions, the fluorescent intensity is found to be inversely proportional to the laser intensity. A plot of the measured fluorescent intensity vs I_ν^{-1} yields a straight line with negative slope (linear fluorescence region), whose intercept yields N_1^0, and whose slope gives Q_{21}. As the laser intensity increases, such curves bend over and approach zero slope, i.e., the saturation condition with I independent of I_ν.

While saturation LIF measurements have been performed on diatomic flame species, e.g., C_2[45], CH and CN[47], from a practical point of view saturation may be difficult to obtain experimentally for some molecules because of the excitation wavelengths required. Resort has been made to two-photon excitation processes. It has been noted that LIF-suitable transitions for some species of interest, which could include O_2, N_2 and NO, may require far UV to vacuum UV frequencies. Higher laser harmonics can be used, for example, frequency-tripled Nd:YAG has been employed for the excitation of NO[48]. However, instead of frequency doubling or tripling into the UV, a two-photon excitation process can be employed using identical laser pulses in the visible, each tuned to half the transition frequency. The two-photon excitation of CO and N_2 has been reported[49]. However, although fluorescence may be excited by the two-photon process, the problems due to quenching remain the same as for the one-photon process. Another problem also associated with the implementation of high laser intensities is the potential for laser-induced chemical effects.

The LIF techniques discussed so far have accounted for the quenching either by in-situ measurement with short laser pulses, or by rendering it uninfluential by optical saturation of the excited level via high-intensity excitation. Another method is to calculate the quenching rates for the deexcitation paths. This requires an information base—measured, estimated, or calculated—on the collision rate constants with other species colliders in the system. This approach has been employed for OH[37], which is probably the most extensively studied molecule in LIF spectroscopy. The quenching cross sections for other molecules, however, are not well known.

Recent studies at this laboratory have been concerned with the detection of excited metastable species using laser induced fluorescence[50]. The species of interest were the CO ($a^3\Pi$) and N_2 ($A^3\Sigma$) states. An objective in the further development of these studies was then in the application of LIF to the measurement of NO number density and temperature in the short-duration, high-enthalpy flows in the Calspan hypersonic shock tunnels. The energy level diagrams for these three molecules are shown in Figure 11.

The lowest downward electronic transitions for CO and N_2 are forbidden triplet to singlet transitions which therefore cannot be detected in emission. The research aim was to employ the much more sensitive method of LIF for their detection and measurement. The purpose of this discussion is simply to include some illustrative LIF spectra. The procedure here was to use a CO laser to optically pump a flowing CO gas mixture to high ground state vibrational levels ($v'' \gtrsim 40$). The high v'' states can then transfer energy by collisional vibrational-electronic processes to populate other electronic states or other molecules. This technique was used to populate the CO ($a^3\pi$) and, by the addition of N_2, the N_2 ($A^3\Sigma$) excited metastable states (Figure 11). A frequency doubled N_2 laser/dye laser was used and the CO (A-X) fourth positive spectrum generated to check the LIF method. The LIF spectra of CO ($A^1\pi$-$X^1\Sigma$) and CO ($b^3\pi$-$a^3\pi$) are shown in Figure 12.[50] These spectra were recorded at a fixed UV wavelength by scanning the wavelength passed by the monochrometer detector through the wavelength range of the vibrational band emissions. The ability to record a single pulse (~ 20 ns) CO (A-X) LIF spectrum was also demonstrated in these experiments.

3.5 Emission and Absorption Spectroscopy

Emission and absorption spectroscopy are well established in the analysis of the radiation associated with transitions between excited states of an atom or molecule. Historically, of course, these diagnostic approaches considerably pre-date the coherent-beam probe methods discussed thus far.

In an absorption measurement, a radiation source of intensity I_0 is observed through the gas and the transmitted intensity, I, is carefully measured. The absorption by the gas depends on the number of absorbers available to make transitions corresponding to the particular wavelength, hence a measurement of the relative transmission or transmittance, $T = I/I^0$, of the gas as a function of wavelength can be used to determine the population of molecules in the lower of the energy levels involved.

These optical methods exploit the fact that critical air species in real-gas flows are optically active. O_2 and NO in particular are well suited to absorption studies. These molecules both strongly absorb in the ultraviolet via excitation transitions which are well known. The dominant system for NO is the NO gamma band, from about 2200-2700 Å in the UV. The NO γ system comprises transitions between the first excited electronic level and the ground state, $A^2\Sigma \leftarrow X^2\pi$. These states are indicated on the NO potential energy diagram included in Figure 11. The absorption for O_2 is in the broad Schumann-Runge system which can cover the spectral range from about 1300 - 3000 Å or so, depending upon the temperature. The potential energy diagram for the O_2 molecule is shown in Figure 13.

It is seen from this diagram that at low temperatures, when almost all of the O_2 molecules are in the lowest vibrational level ($v'' = 0$) of the ground $X^3\Sigma_g^-$ state, absorption of radiation is confined to transitions with energies in excess of about 60,000 cm^{-1}, i.e., to high vibrational levels (v') in the excited state. This results from the large difference in the equilibrium internuclear separation distance (R) between the ground and excited states (Figure 13). These transitions correspond to wavelengths from about 1300-1800 Å in the vacuum ultraviolet, VUV, as indicated in the figure. This regime is so called because of the requirement that the optical paths in spectrometers, etc., be evacuated in order to avoid complete UV absorption by the O_2 in ambient air. It is seen that the only likely transitions (by the Franck-Condon principle) in VUV absorption are those that go to the dissociated region of the excited $B^3\Sigma_u^-$ state. The absorption transitions in the $v'' = 0$ progression then effect dissociation in the molecule and the absorption spectrum is a photodissociation continuum.

At higher temperatures, the higher vibrational levels of the ground state become populated and absorption transitions to the lower v' levels of the excited state can then occur. Such transitions, like the (0,13) or (0,14) indicated in Figure 13, occur at longer wavelengths and, since they are between discrete vibrational levels, these absorptions give rise to the Schumann-Runge band spectra.

When the gas is of uniform density along the optical line of sight, the change in transmission intensity at a given wave number is given by the Brouguer-Beer law as[4]

$$\frac{I_\nu}{I_\nu^o} = \exp\left(-k_\nu \frac{N_\ell}{L_0}\ell\right) \tag{14}$$

where I_ν^o is the intensity of the incident beam (i.e., no flow), k_ν is the spectral absorption coefficient, N_ℓ is the number density of molecules in the lower state of the absorption transition, L_0 is the Loschmidt number (2.687 x 10^{19} cm^{-3}) and ℓ is the path length through the gas. If not in the lowest ground state energy level, the number of molecules N_ℓ is related to the total number density N_0 of the species molecules by the Boltzmann expression[4]

$$N_\ell = N_0 \frac{2J''+1}{Q} e^{-E_{J''v''}/kT} \tag{15}$$

where Q is the total internal partition function, k is the Boltzmann constant, T the temperature, $E_{J''v''}$ is the energy of the lower vibrational/rotational level from which the transition occurs, and v'',J'' the corresponding quantum numbers.

The spectral absorption coefficient k_ν may be a rapidly varying function of ν. However, in the case of air, k_ν values have been well documented for the O_2 Schumann-Runge continuum[51,52] and band systems[51-54], and also for NO γ[55-57]. Sometimes such data are given in terms of electronic oscillator strengths or f-values, as well as transition probabilities. All of these parameters are related, however[4]. That is, over the spectral interval of the intensity measurement,

$$\int k_\nu \, d\nu = \frac{\pi e^2}{m c^2} N_\ell f \tag{16}$$

$$= N_\ell B_{\ell u} h\nu_{u\ell}$$

where e and m are the charge and mass of the electron, f is the oscillator strength, $\gamma_{u\ell}$ is the wave number of the transition and $B_{\ell u}$ is the electronic transition probability for absorption from the lower to the upper state, introduced earlier in Section 3.4 as B_{12} (Eqn. (7)). Hence, if the temperature is known, by independent measurement, the number density of O_2 and NO can be obtained directly from a measurement of the transmittance, I/I°.

Such optical methods are integrated absorption measurements and hence require that the number density be uniform along the line of sight. They are not suitable for concentration measurements in flows with arbitrary gradients.* In application, such a UV absorption measurement could comprise an arrangement like that shown in Figure 14. The path length, ℓ , would be defined by sharp leading edge splitter plates across the nozzle exit plane freestream. Sapphire windows in the splitter plates would transmit down to 1500 Å, and the radiation source could be a deuterium or hydrogen gas discharge lamp. With such a source, both O_2 and NO could be monitored simultaneously, from the same sample of test flow, by means of an interference filter selected to transmit a narrow wavelength band of O_2 radiation to one detector (e.g., high sensitivity photomultiplier tube) and reflect the NO γ-monitored wavelength region, through a narrow bandpass filter, to another photomultiplier.

Depending upon operational configurations or environments, other factors may also be taken into account, such as slit width to spectral line width ratio considerations and collision broadening effects. These are discussed in some of the literature cited, but have not been treated here in order to focus on the basic methodology.

Absorption studies are inherently better suited for obtaining quantitative data than are emission studies, as absolute calibrations are required for the latter. The emission from a gas at high temperature must be determined in absolute rather than relative terms. The detection system must then be able to view a radiance calibration source, such as a blackbody cavity or a calibrated lamp, through the same optical path and optical elements that are used to monitor the radiant emission from the gas.

To outline such an approach, the species spectral intensity may be obtained from a spectral interval scan as

$$\mathcal{I}_\lambda(gas) = \frac{S_\lambda\ gas}{S_\lambda\ BB}\ \mathcal{I}_{BB_\lambda}(T_{BB})$$

(17)

where S_λ (gas) and S_λ (BB) are the measured inband detector signal voltages from the gas and calibration blackbody sources, respectively, and $I_{BB\ \lambda}(T_{BB})$ is the known (Planck function) blackbody spectral intensity at the blackbody temperature T_{BB}. Provided, then, the temperature, T, of the gas is known from a separate measurement, the spectral emissivity of the species radiator is obtained from

$$\mathcal{E}_\lambda = \frac{\mathcal{I}_\lambda(T)}{\mathcal{I}_{BB_\lambda}(T)}$$

(18)

the blackbody ($\mathcal{E} = 1$) radiance being evaluated at the gas temperature T. In terms of the absorption coefficient terms introduced earlier, the species emissivity is also written as

$$\mathcal{E} = 1 - exp\left(-k_\gamma\ \frac{N}{L_o}\ \ell\right)$$

(19)

over the wavelength interval of the measurement. Again, if k_γ is known as a function of temperature over the wavelength interval, the number density of the species radiators can be determined for a defined path length ℓ . Under equilibrium temperature conditions, the total species number density can be obtained from the Boltzmann distribution, Equation (15).

The above discussion, which has assumed knowledge of k_γ, is essentially a variation of a method of measurement for k_γ itself, or of the molecular oscillator strengths, for $\int k_\gamma\,d\gamma$. In such measurements, a source of species radiators at known equilibrium conditions of pressure, temperature and number density is generated, usually in a shock tube, wherein similar calibration procedures are followed to convert the measured I_λ to k_γ as a function of wavenumber γ via the known values for N, T and ℓ . Quadrature then affords the f values.

3.6 Electron Beam Fluorescence Techniques

The final measurement technique to be reviewed for the determination of neutral species concentrations is the use of electron beam fluorescence. Although the probe in this case is a beam of electrons, the diagnostic is still an optical method in that the beam-stimulated fluorescence is measured using conventional optical collection methods.

The technique, which has been thoroughly described by Muntz[60], has been employed for the measurement of both density[61-63] and temperature[62,64-65] in high speed flows. An energetic (20-50 keV) beam of electrons is directed through the gas, and the inelastic collisions of the beam electrons with the gas species effect electronic excitation and produce fluorescence which is largely confined to the beam region itself. In essence, the vibrational and the rotational fine structure details of the emitted fluorescence can be used to determine the vibrational and rotational temperature of the emitting molecule, and the fluorescence intensity can be related directly to the number density of the radiating molecule. The use of high beam energies minimizes the effect of elastic collisions in causing spreading of the beam.

Most studies have been concerned with the beam-induced fluorescence in N_2, either from the predominant N_2^+ first-negative system ($\sim$3900-4800 Å) which is shown in the sketch below (taken from Ref. 60), or from the second-positive system of neutral N_2 ($\sim$ 3300-3800 Å), the latter (which is the $C^3\Pi \to B^3\Pi$ transition shown in Figure 11) affording measurements up to somewhat higher density levels. Beam fluorescence can also be produced in other

*An exception would be flows with radial symmetry, such as line of sight traverses across an entire nozzle exit plane. Quantitative determinations of local temperature and number density can then also be extracted by standard Abel-inversion methods.[58,59].

gases, however, including O_2, NO, CO, CO_2, Ar and He[60,67]. The requirement is that the excitation process be fast and direct, and the emission an allowed spontaneous process.

SCHEMATIC ENERGY LEVEL DIAGRAM FOR N_2, N_2^+
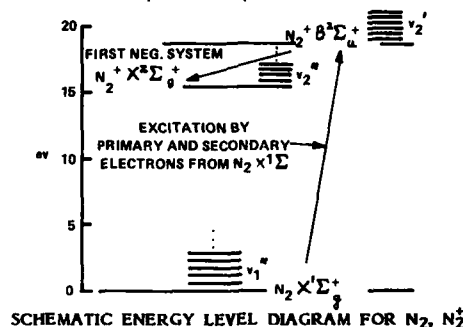
The narrow electron beam can afford good spatial resolution as, like SRS and LIF, the radiation is observed from a selected incremental length of the beam to provide a "point" measurement. For N_2, even though this molecule is essentially equilibrated in nozzle expansions (Figure 2), the N_2 number density is density dependent and its measurement can corroborate the magnitude of an effective inviscid nozzle area ratio, A/A*, at the measurement station, determined from boundary layer displacement thickness calculations. The electron beam technique has also been used, however, to measure density and density fluctuations in the turbulent boundary layer on a nozzle wall.[68]

An experimental configuration for the electron beam would take a form similar to that shown in Figure 14 for the radiometer except that the electron beam would be oriented vertically, with a Faraday cup to receive the beam, and monitor beam current, after traversal across the flow. Observation of the selected incremental length of beam fluorescence would then be performed at right angles to the beam. The beam-induced fluorescence is monitored via narrow-band filter, slit-optics radiometers using photomultiplier detectors for high-speed-flow environments. A calibration for the N_2 number density is performed, a priori, in a static chamber. The intensity measurement may be of the entire band system, or of the intensity of a single vibrational band such as the intense (0,0) band at 3914 Å, or of the intensity of a particular rotational line in a vibrational band. Ideally, the calibration affords a linear increase in fluorescence intensity with number density. Consideration must also be given to the effects of collisional quenching, which become manifest by a departure from linearity in the calibration.

In the case of high-enthalpy airflows, flow expansion calculations like that shown in Figure 2 can provide a good prediction of the freestream test flow composition. Other than O atoms, all the neutral species constituents of the nonequilibrium freestream are stable gases, i.e., a calibration gas either of the calculated freestream molar composition, or of O_2, N_2, Ar and a range of NO partial pressures, can be provided for static calibration purposes.

The electron beam fluorescence technique is restricted in its application to quite low densities. It is limited at very low density by low fluorescence yield, and at higher densities by collision quenching of the radiation by the ambient gas species. The number of radiationless transitions occurring is a function of the collision cross sections of the colliders and of their mean speed. Under these conditions the technique becomes temperature dependent. Quenching cross sections and their temperature dependence are required for a specific flow situation in order that the useful upper limit of the fluorescence measurement technique for number density measurement can be increased. Expressions for the fluorescent emission intensity from the excited state depend, in fact, on the ratio of quenching collision frequency to transition probability (A coefficients) in similar manner to the intensity relationships discussed previously with respect to LIF.

Consideration also needs to be given to the effects of secondary electron production. While most secondaries are of very low energy, some are of sufficiently high energy and, scattered in the forward beam direction, can add to the fluorescence.

It is appropriate to add here that a recent technique has been described by Muntz et al.[69] aimed at extending the fluorescence diagnostic to higher densities. The approach, which is currently under development, is to use a pulsed electron beam (to avoid gas motion effects) to excite the neutral N_2 to the ground state of the ion ($N_2^+ X^2\Sigma^+$), instead of the ion $B^2\Sigma^+$ state. Because of the slow recombination for ions, the ground ion state is effectively metastable compared with collision periods. The absorption of a laser photon is then used to elevate the ion to the $B^2\Sigma^+$ state, which then undergoes spontaneous transition back to the ion ground state. Because of the relative magnitudes of the ionization cross sections involved, this pulsed electron-photon fluorescence technique[69] can afford signals much larger than the corresponding electron beam fluorescence signal.

Because of the relatively long lifetime of the ground state ions, it is not necessary that the laser pulse be in time coincidence with the electron beam; it is, in fact, preferable that the laser pulse lag the electron beam several collision times in order that the ion rotational distribution has time to equilibrate with thermal motions.[69]

For room temperature pressures in air, the number density is given approximately by $n \approx 3 \times 10^{16} p$ cm^{-3}, where p is the gas pressure in torr. Electron beam measurements via N_2 (1-) fluorescence have been performed up to equivalent room temperature pressures of a few torr ($n \sim 10^{17}$ cm^{-3}). Some N_2 (2+) fluorescence studies have been made up to 8-10 torr ($n \sim 3 \times 10^{17}$ cm^{-3}). Muntz[69] suggests that the electron/laser beam method may permit measurements to be extended up to about 3×10^{18} cm^{-3}.

The basic electron beam fluorescence method has, nevertheless, been well utilized now for several decades in quantitative measurements of species number density and temperature in flow systems, including profile measurements through regions with gradients (boundary layers, shock regions). Method applicability considerations need to be addressed, however, which are specific to the gas composition and environment conditions.

4. IONIZED FLOW DIAGNOSTICS

The emphasis throughout these discussions has been on the measurement of neutral species concentrations. This is where almost all of the energy of the system resides. For example, expansion from the shock tunnel reservoir condition corresponding to Figure 2 will generate a freestream velocity of about 4270 m/sec (14000 ft/sec). For a blunt body immersed in this test flow, the entropy layer region behind the bow shock will be ionized, with a free electron number density of about 2×10^{13} cm^{-3}. This electron concentration is above critical for microwave frequencies up to 40 GHz, yet the energy contained in all of the ionized species at this nose region condition is about 0.25% of the total internal energy of the flow.

Hypervelocity flow generation in test facilities, however, encompasses investigations wherein the plasma properties of the flow, about a blunt test vehicle for example, are of primary research interest. It is appropriate then to conclude with a brief account of two diagnostic methods for the determination of the plasma state of the flow. The first is microwave interferometry, which, though non-intrusive, is an integrated line of sight measurement for the electron number density over a uniform path length. The second method is the use of thin-wire, swept-voltage electrostatic probes for the point measurement of ion number density and electron temperature in a flowing plasma. The latter is the equivalent of the Langmuir probe in stationary plasmas and is an intrusive technique, although one affording a point measurement of plasma properties.

4.1 Microwave Inteferometry

Omitting any circuitry considerations, the microwave interferometer consists of a pair of microwave horns, transmitter and receiver, placed either side of the plasma flow region to be interrogated. The basis of the measurement is to record the change, from the free space or no-flow value, in the amplitude and phase of the signal propagated between the two horns. The received signal is actually detected in terms of in-phase and quadrature components, which are simply related to signal amplitude and phase.

The two parameters which characterize a plasma are the electron number density, n_e, and the electron collision frequency, ν_c. It is assumed that the plasma is neutral, i.e., $n_e = \Sigma$ ions. For high-temperature air, the predominant ion is NO^+. The collision frequency is given by

$$\nu_c = \frac{4}{3} \left(\frac{8kT_e}{\pi m_e} \right)^{1/2} \sum_j n Q$$

$$= 8 \cdot 28 \times 10^5 \, (T_e)^{1/2} \sum_j n \, Q \tag{20}$$

where k is the Boltzmann constant, m_e is the electron mass and T_e is the electron temperature. The number density, n, collision cross section, Q, product is summed over all neutral species. The Q are functions of electron energy and an earlier compilation of the cross section data for the neutral air species from various determinations has been presented in graphical form[70]. The ion contribution to the collision frequency is usually negligible compared with the neutrals.

The electron number density is obtained quite directly from the interferometric measurement of phase shift if the plasma is underdense, i.e., if the microwave frequency is less than the plasma frequerncy. The plasma frequency is given by

$$\omega_p = \left(\frac{n_e e^2}{m_e \varepsilon_o} \right)^{1/2}$$

$$\text{or} \quad f_p = 8 \cdot 98 \times 10^3 \sqrt{n_e} \tag{21}$$

where e is the electronic charge and ε_o the free space permittivity. The phase shift per unit length is given by

$$\frac{\Delta \phi}{\ell} = 1 \cdot 2 \times 10^{-8} \, f \left(1 - \eta_+ \right) \, deg/cm \tag{22}$$

where, neglecting fourth order terms

$$\eta_+ = \left\{ \frac{1 + \left(\frac{f_c}{f} \right)^2 - \left(\frac{f_p}{f} \right)^2}{1 + \left(\frac{f_c}{f} \right)^2} \right\}^{1/2}$$

η_+ is the real part of the refractive index, f_c is the collision frequency ($\nu_c/2\pi$) and f is the microwave interferometer operating frequency. The collision frequency in most cases is small compared with the microwave frequency; hence, Equation (22) becomes

$$\frac{\Delta \phi}{\ell} \approx 1 \cdot 2 \times 10^{-8} f \left(1 - \sqrt{1 - \left(\frac{f_p}{f} \right)^2} \right) \tag{23}$$

where ℓ is the plasma thickness between the interferometer horns. The electron number density is then obtained from f_p and Equation (21).

An example of interferometrically measured electron number density distributions in expanding N_2 and Ar plasmas is shown in Figure 15. These measurements were performed in hypersonic nozzle flows at this laboratory[71] utilizing two microwave interferometers operating at 17 and 35 GHz.

4.2 Thin-Wire Swept-Voltage Electrostatic Probes

Voltage-swept thin-wire electrostatic probes can be used to measure the electron temperature and ion number density in hypervelocity ionized freestream flows, as well as in the inviscid shock layer and viscous boundary layer plasma flows over blunt bodies.

The probe consists of a thin tungsten wire (of nominal 0.007 cm diameter and length-to-diameter ratios of 80-100), which protrudes from a length of thin Pyrex tubing. The probes may be installed in a rake so that multiple point measurements may be recorded simultaneously at different positions in the plasma flowfield. A linear voltage ramp is applied to the probe to provide a voltage excursion from negative (ion collecting) to positve (electron collecting) probe voltages, V_p, e.g., -5 to +2 volts in air plasma, over a period of about 70-100 μs. The current collected by the probe during the applied voltage excursion comprises the probe characteristic, from which, under appropriate conditions, the electron temperature and ion number density of the locally sampled plasma may be determined. For high total enthalpy, shock-tunnel-facility generated airflows, $n_{NO^+} = n_e$.

Essentially all of the electrons are repelled when the probe is significantly negative with respect to the plasma potential and an ion sheath surrounds the probe. The sheath is a non-neutral region of charge separation around the probe corresponding to the extent of its electric field into the plasma. As the probe voltage becomes less negative, more and more electrons reach the probe, resulting in a rapidly increasing electron current. An illustration of this ion-current portion of the probe characteristic is shown in Figure 16 for the case of a high-velocity N_2 plasma. The potential at which the probe current is zero is called the floating potential, V_F, where most of the electrons are repelled by the probe in order to balance ion and electron currents. At the plasma potential, V_∞, the probe collects the random ion and electron fluxes as no electric field is present. The current is predominantly an electron current at this instant, however, because of the higher thermal speed of the electrons compared with that for the ions of heavier mass. The region of rapidly increasing electron current with decreasing negative probe potential is called the retarding field region because only those electrons of sufficient energy can overcome the retarding field to reach the probe.

In the analysis of probe data, free-molecular sheath conditions are assumed in that the attracted particle undergoes a collisionless trajectory upon entering the sheath to annihilation at the probe surface.

For a non-dimensional probe voltage, χ_p, defined by

$$\gamma_p = \frac{e}{kT_e}\left(V_p - V_\infty\right) \tag{24}$$

the collected ion and electron currents at negative values of χ_p can be written[72,73]

$$j_i = e n_e \left(\frac{kT_e}{2\pi m_e}\right)^{1/2} i_+ \tag{25}$$

$$j_e = e n_e \left(\frac{kT_e}{2\pi m_e}\right)^{1/2} e^{\chi_p} \tag{26}$$

where $i_+ = i_+ (\chi_p, r_p/\lambda_D, T_i/T_e)$ is a normalization factor representing the increase in the collected ion current over the random kinetic ion flux to the probe at $\chi_p = 0$ and is a function of the probe potential, χ_p, the ratio of probe radius to the Debye length, λ_D, and the ratio of ion to electron temperatures[73]. By differentiating Equation (26),

$$\frac{d \ln j_e}{d V_p} = \frac{e}{kT_e}$$

which is the basis for the determination of the electron temperature. The slope of a semi-log plot of the retarding-field region current vs. probe voltage is a straight line of slope e/kT_e.

The ion number density is obtained from the ion current portion of the probe characteristic at large negative values of χ_p via Equation (25) and derived values for i_+[73]. Unlike the microwave interferometer, which responds to n_e, the current collected by the electrostatic probe is ion dependent, but plasma neutrality ensures $n_i = n_e$.

Electrostatic probe measurements of the electron number density profiles in the ionized boundary layer over a flat plate in a shock tunnel N_2 plasma flow[71] are shown in Figure 17. The measured n_e is normalized by the boundary layer edge value, and the measured profiles are shown at two different stations from the plate leading edge. The solid curves are calculated profiles using Blottner's[74] nonequilibrium boundary layer program adapted to flat plate flows. It is seen that the electrostatic probe affords an excellent technique for plasma species diagnostics.

Empirical studies have also been described[75] which allow for the effect of collisions on ion current collection to be calculated. These approximate analyses represent a bridging function between the continuum and free molecular limits, thereby extending probe data interpretation into the transition regime.

5. SUMMARY

The discussions in the preceding sections comprise review descriptions of some diagnostic methods for species concentration measurements which are applicable to high-speed flows. Some of the theoretical framework has been included but only as background to support the descriptions. Referral is intended, of course, to the literature cited, and references therein, for greater detail concerning analysis and implementation.

The summaries here can help to apprise as well as guide in the selection of a method most suitable for a given flow situation. Some of the methods are not new. The more recent and yet-developing laser techniques have singular advantages by virtue of their ability to interrogate very fast flows, and to be applicable to reactive and hostile environments. As noted, however, they can be quite complex both analytically and in their optical requirements and configurations.

REFERENCES

1. Lordi, J.A., Boyer, D.W., Dunn, M.G. Smolarek, K.K. and Wittliff, C.E. AIAA Paper 88-0476, AIAA 26th Aerospace Sciences Mtg. January 1988, Reno, Nevada.

2. Eschenroeder, A.Q., Boyer, D.W. and Hall, J.G. Phys. Fluids $\underline{5}$, 615 (1962).

3. Lordi, J.A. and Mates, R.E. AIAA J. $\underline{3}$, 1972 (1965).

4. Herzberg, G. Molecular Spectra and Molecular Structure, I. Spectra of Diatomic Molecules. 2nd Edition, D. Van Nostrand Co., Inc. 1950.

5. Lapp, M., Goldman, L.M. and Penney, C.M. Science 175, 1112 (197.).

6. Williams, W.D. and Lewis, J.W. AIAA J. $\underline{13}$, 1269 (1975).

7. Coney, T.A. and Salzman, J.A. NASA TN D-7126 (1973).

8. Bechtel, J.H. Applied Optics, $\underline{18}$, 2100 (1979).

9. Lederman, S., Celentano, A. and Glaser, J. Phys. Fluids $\underline{22}$, 1065 (1979).

10. Lapp, M., Penney, C.M. and Goldman, L.M. Optics Comm. $\underline{9}$, 195 (1973).

11. Widhopf, G.F. and Lederman, S. AIAA J. $\underline{9}$, 309 (1971).

12. Eckbreth, A. Proc. 18th Symp. (Intl.) Combustion, 1471 (1981).

13. Bechtel, J.H., Dasch, C.J. and Teets, R.E. Laser Applications, Vol. 5, p. 129. (Ed. Ready and Erf) Academic Press, Inc. 1984.

14. Maker, P.D. and Terhune, R.W. Phys. Rev. $\underline{137}$ A801 (1965).

15. Regnier, P.R. and Taran, J.P. Appl. Phys. Letters $\underline{23}$, 240 (1973).

16. McIlwain, M.E. and Harris, L.E. 17th JANNAF Combustion Mtg. Vol. 2, 379, Hampton, VA (1980).

17. Hall, R.J. and Eckbreth, A.C. Optical Eng. $\underline{20}$, 494 (1981).

18. Hall, R.J. Optical Eng. $\underline{22}$, 322 (1983).

19. Regnier, P.R., Moya, F and Taran, J.P. AIAA J. $\underline{12}$, 826 (1974).

20. Moya, F., Druet, S.A. and Taran, J.P. Optics Comm. $\underline{13}$, 169 (1975).

21. Roh, W.B. and Schreiber, P.W. Appl. Optics, $\underline{17}$, 1418 (1978).

22. Hall, R.J. Combust. Flame $\underline{35}$, 47 (1979).

23. Hall, R.J. and Eckbreth, A.C. Laser Applications, Vol. 5, p. 213 (Ed. Ready and Erf), Academic Press Inc. 1984.

24. Rado, W.G. Appl. Phys. Letters $\underline{11}$, 123 (1967).

25. Pealat, M., Druet, S., Attal, B and Taran, J.P. Proc. 16th Symp. (Int'l) Combustion, 789 (1976).

26. Eckbreth, A.C. Appl. Phys. Letters, $\underline{32}$, 421 (1978).

27. Shirley, J.A., Hall, R.J. and Eckbreth, A.C. Optics Letters $\underline{5}$, 380 (1980).

28. Eckbreth, A.C. Proc. 17th Symp. (Int'l) Combustion, 975 (1978).

29. Eckbreth, A.C. and Hall, R.J. Combust. Flame $\underline{36}$, 87 (1979).

30. Roh, W.B., Schreiber, P.W. and Taran, J.P. Appl. Phys. Letters, $\underline{29}$, 174 (1976).

31. Murphy, D.V. and Chang, R.K. Optics Letters $\underline{6}$, 233 (1981).

32. Goss, L.P., Switzer, G.L., Trump, D.D. and Schreiber, P.W. AIAA Paper 82-0240, AIAA 20th Aerospace Sciences Mtg. Jan. 1982 Orlando, Florida.

33. Goss, L.P., Trump, D.D., MacDonald, B.G. and Switzer, G.L. Rev. Sci. Instrum. $\underline{54}$, 563 (1983).

34. Crosley, D.R. Optical Eng. $\underline{20}$, 511 (1981).

35. Lucht, R.P. and Laurendeau, N.M. Appl. Optics, $\underline{18}$, 856 (1979).

36. Berg, J.O. and Shackleford, W.L. Appl. Optics, $\underline{18}$, 2093 (1979).

37. Bechtel, J.H. and Teets, R.E. Appl. Optics, $\underline{18}$, 4138 (1979).

38. Bechtel, J.H. Appl. Optics $\underline{18}$, 2100 (1979).

39. Crosley, D.R. and Smith, G.P. Appl. Optics, $\underline{19}$, 517 (1980).

40. Schofield, K. and Steinberg, M. Optical Eng., $\underline{20}$, 501 (1981).

41. Muller, C.H., Schofield, K., Steinberg, M., and Broida, H.P. Proc. 17th Symp. (Intl.) Combustion, 867 (1978).

42. Daily, J.W. Appl. Optics, 15, 955 (1976).

43. Stepowski, D. and Cottereau, M.J. Appl. Optics 18, 354 (1979).

44. Daily, J.W. Appl. Optics 16, 568 (1977).

45. Baronavski, A.P. and McDonald, J.R. Appl. Optics, 16, 1897 (1977).

46. Lucht, R.P., Sweeney, D.W. and Laurendeau, N.M. Appl. Optics 19, 3295 (1980).

47. Verdieck, J.F. and Bonczyk, P.A. Proc. 18th Symp. (Intl.) Combustion, 1559 (1981).

48. Gross, K.P. and McKenzie, R.L. AIAA J. 23, 1932 (1985).

49. Filseth, S.V., Wallenstein, R. and Zacharias, H. Optics Comm. 23, 231 (1977).

50. DeLeon, R.L. Internal communication, Aug. 1987. Calspan Independent Research and Development.

51. Ditchburn, R.W. and Heddle, D.W. Proc. Roy. Soc. A220, 61 (1953); A226, 509 (1954).

52. Blake, A.J., Carver, J.H. and Haddad, G.N. J. Quant. Spect. Rad. Transfer 6, 451 (1966).

53. Treanor, C.E. and Wurster, W.H. J. Chem. Phys. 32, 758 (1960).

54. Bethke, G.W. J. Chem. Phys. 31, 669 (1959).

55. Weber, D. and Penner, S.S. J. Chem. Phys. 26, 860 (1957).

56. Bethke, G.W. J. Chem. Phys. 31, 662 (1959).

57. Daiber, J.W. and Williams, M.J. J. Quant., Spect. Rad. Transfer 1, 135 (1961).

58. Griem, H.R. Plasma Spectroscopy, McGraw Hill Inc. New York 1964.

59. Young, S.J. J. Quant. Spect. Rad. Transfer, 25, 479 (1981).

60. Muntz, E.P. AGARDograph 132, (1968).

61. Robben, F. and Talbot, L. Phys. Fluids 9, 653 (1966).

62. Marrone, P.V. Phys. Fluids 10, 521 (1967).

63. Harbour, P.J. Rarefied Gas Dynamics. 6th Symposium (ed. Trilling and Wachman) Academic Press, New York, Vol. II, 1713 (1969).

64. Muntz, E.P. Phys. Fluids 5, 80 (1962).

65. Robben, F. and Talbot, L. Phys. Fluids 9, 644 (1966).

66. Ashkenas, H. Phys. Fluids 10, 2509 (1967).

67. Muntz, E.P. and Marsden, D.J. Rarefied Gas Dynamics, 3rd Symposium (ed. Laurmann) Academic Press, New York Vol. II, 495 (1963).

68. Wallace, J.E. AIAA J. 7, 757 (1969).

69. Muntz, E.P., Kunc, J.A. and Erwin, D.A. AIAA Paper 87-1526, AIAA 22nd Thermophysics Conference, June 1987, Honolulu, Hawaii.

70. Shkarofsky, I.P., Bachynski, M.P. and Johnston, T.W. Electromagnetic Effects of Re-entry (ed. Rotman and Meltz), Pergamon Press, New York, 24 (1961).

71. Boyer, D.W. and Touryan, K.J. AIAA J. 10, 1667 (1972).

72. deLeeuw, J.H. Physico-Chemical Diagnostics of Plasmas (ed. Anderson, Springer, Warder), Northwestern University Press, Evanston, 65 (1964).

73. Sonin, A.A. AIAA Paper 66-5, AIAA 3rd Aerospace Sciences Meeting, January 1966. New York, NY.

74. Blottner, F.G. AIAA J. 8, 193 (1970).

75. Talbot, L. and Chou, Y.S. Rarefied Gas Dynamics, 6th Symposium (ed. Trilling and Wachman), Academic Press, New York, Vol. II, 1723 (1969).
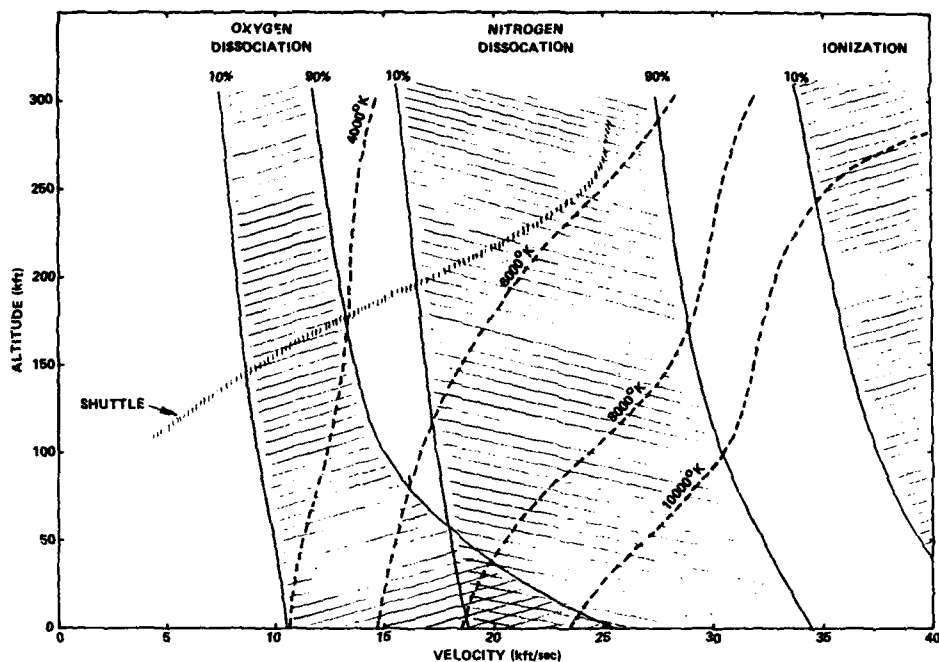
Figure 1 ILLUSTRATIVE DISSOCIATION FRACTIONS FOR EQUILIBRIUM AIR BEHIND A NORMAL SHOCK WAVE
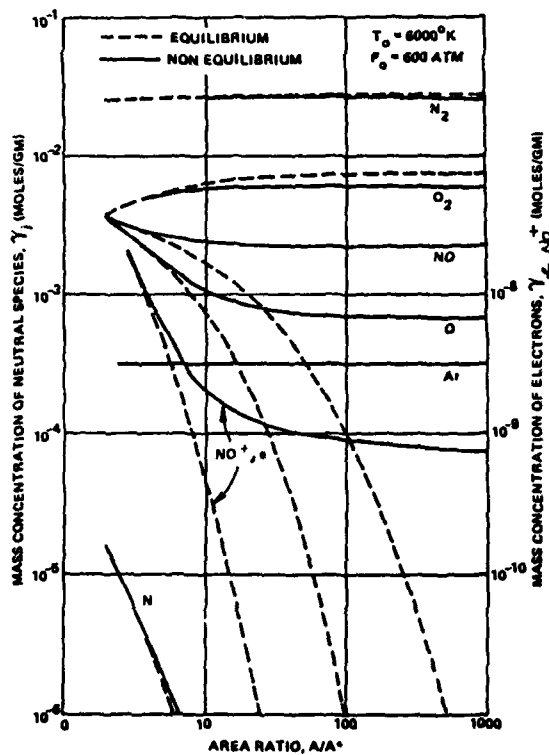
Figure 2   SPECIES DISTRIBUTIONS FOR AIRFLOW EXPANSION IN A HYPERSONIC NOZZLE
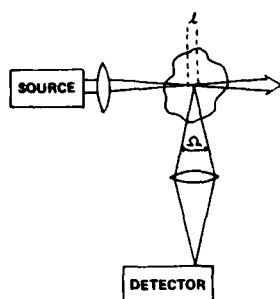
Figure 3 SCHEMATIC OF SPONTANEOUS RAMAN SPECTROSCOPIC MEASUREMENT ARRANGEMENT
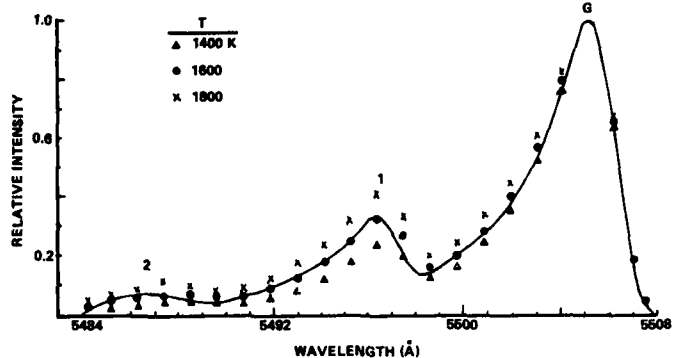
Figure 4 TRACING OF AN EXPERIMENTAL RECORD OF RAMAN SCATTERING FROM N_2 IN A FLAME (Ref. 5)

WAVELENGTH (Å)

RELATIVE INTENSITY

T	
▲	1400 K
●	1600
✕	1800
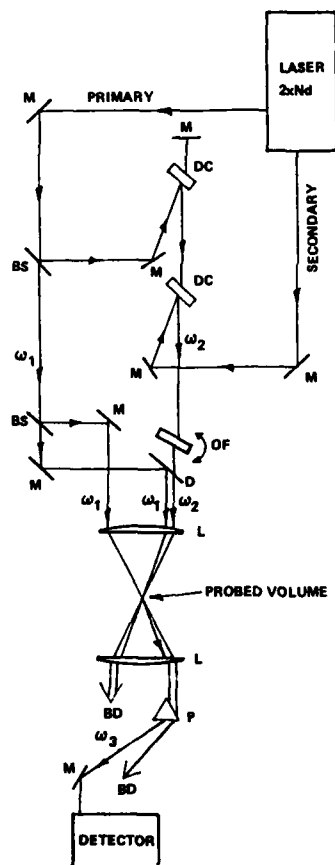
Figure 5 SCHEMATIC OF A BOXCARS EXPERIMENTAL CONFIGURATION: M = MIRROR, BS = BEAM SPLITTER, DC = DYE CELL, OF = OPTICAL FLAT, D = DICHROIC, L = LENS, P = PRISM, BD = BEAM DUMP

(a) SIGNAL FOR MONOCHROMATIC LASER POWERS

$|\chi|^2 \times 10^{-36}$

(b) CORRECTION FOR FINITE LASER LINEWIDTHS

INTENSITY (ARB. UNITS)

(c) FURTHER CONVOLUTION WITH AN INSTRUMENTAL SLIT FUNCTION

NORMALIZED INTENSITY

WAVENUMBER – CM^{-1}
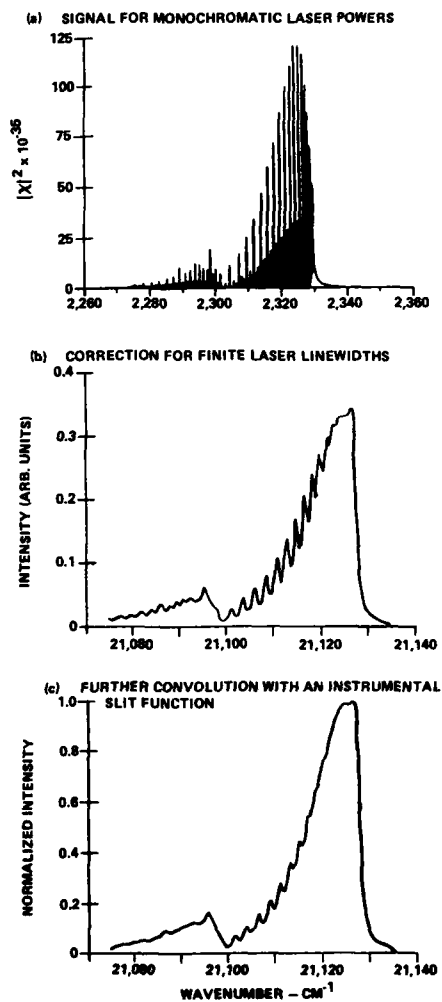
Figure 6 CALCULATED EVOLUTION OF CARS SPECTRUM FOR N_2 IN A FLAME (Ref. 22)

(a) HIGH RESOLUTION (1.0 cm⁻¹ SLIT) (Ref. 17)

300 K INCREMENTS

2400 K

300 K

NORMALIZED CARS INTENSITY

FREQUENCY – cm⁻¹

(b) LOW RESOLUTION (2.7 cm⁻¹ SLIT) (Ref. 22)

100°K INCREMENTS
2.7 CM⁻¹ SLIT

2600°K

1500°K

NORMALIZED INTENSITY

WAVENUMBER – CM⁻¹
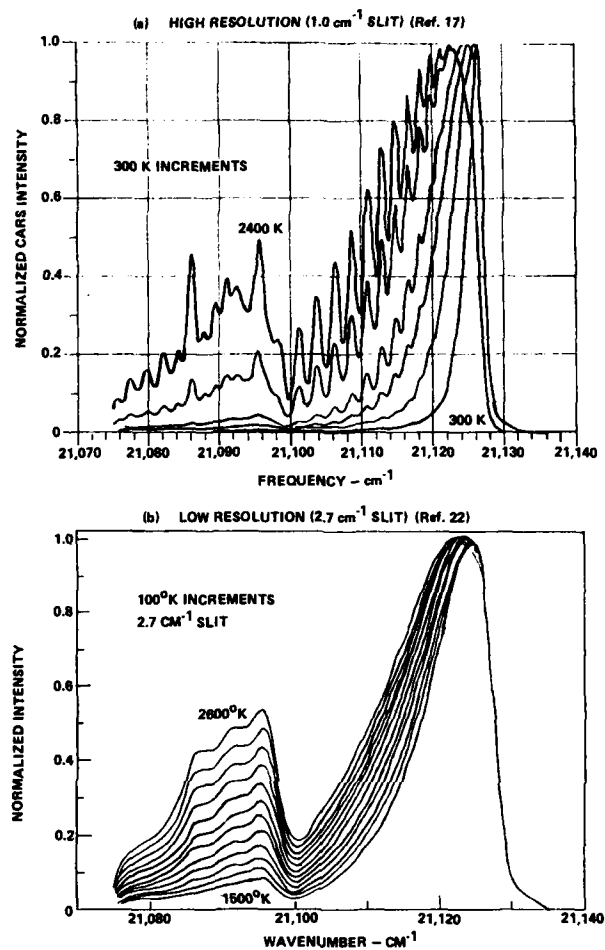
Figure 7 CALCULATED N₂ CARS SPECTRA FOR RANGE OF TEMPERATURES

——— 1 CM⁻¹ RESOLUTION,

••••••• COMPUTER FIT, T=2150°K,
0.8 CM⁻¹ SLIT

NORMALIZED INTENSITY

WAVENUMBER · CM⁻¹
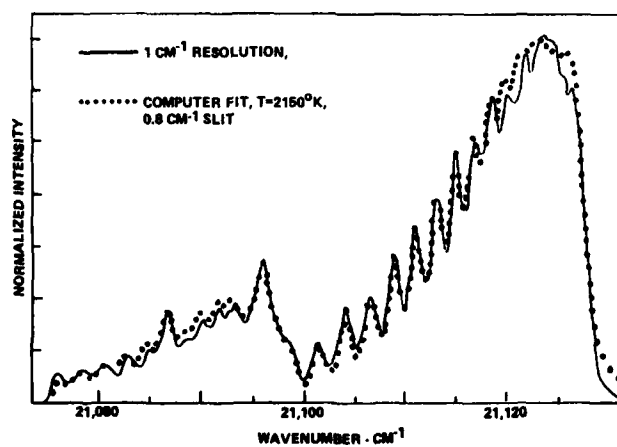
**Figure 8 COMPARISON OF EXPERIMENTAL AND CALCULATED N₂ CARS SPECTRA
FOR DETERMINATION OF TEMPERATURE (Ref. 22)**
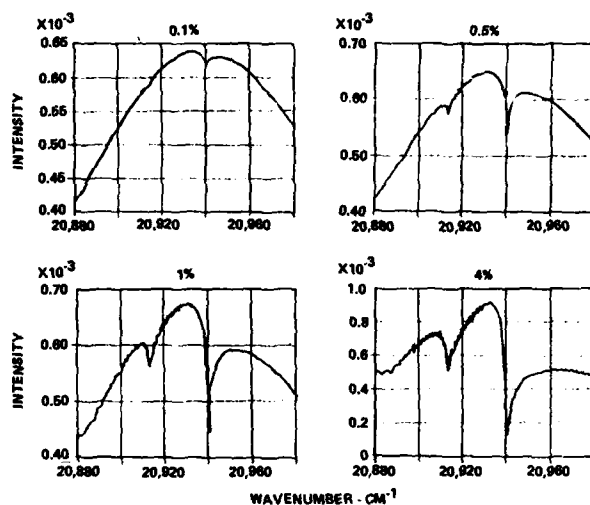
Figure 9 CALCULATED CO CARS SPECTRA FOR VARIATIONS IN CO MOLE FRACTION
$T = 1700^{\circ}K$, $X_{NR} = 9 \times 10^{-19}$ cm^3/erg (Ref. 22)
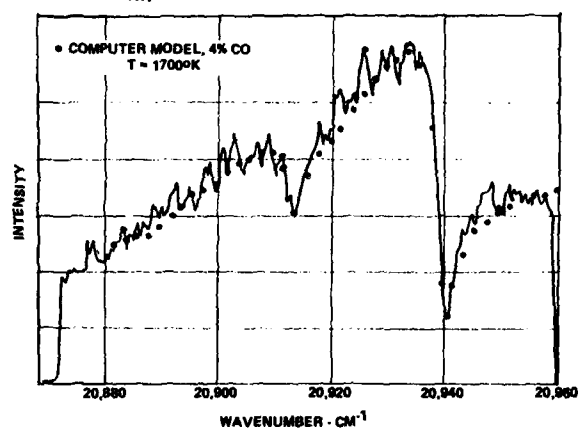
Figure 10 COMPARISON OF EXPERIMENTAL AND CALCULATED CO CARS SPECTRA
AT KNOWN TEMPERATURE FOR DETERMINATION OF CO CONCENTRATION
(Ref. 22)
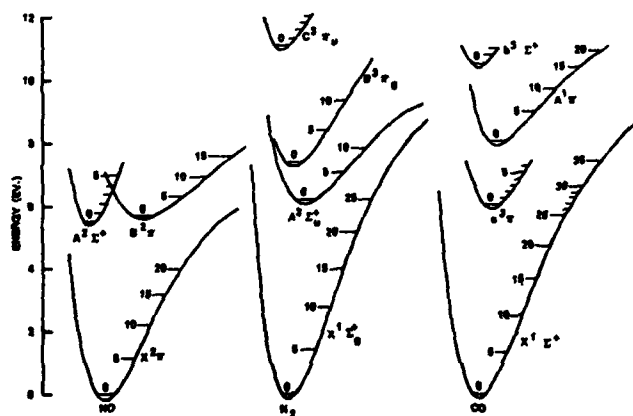
Figure 11 POTENTIAL ENERGY DIAGRAMS OF NO, N_2 AND CO

(a) CO ($A^1 \pi - X^1 \Sigma^+$)

(b) CO ($b^3 \Sigma^+ - a^3 \pi$)
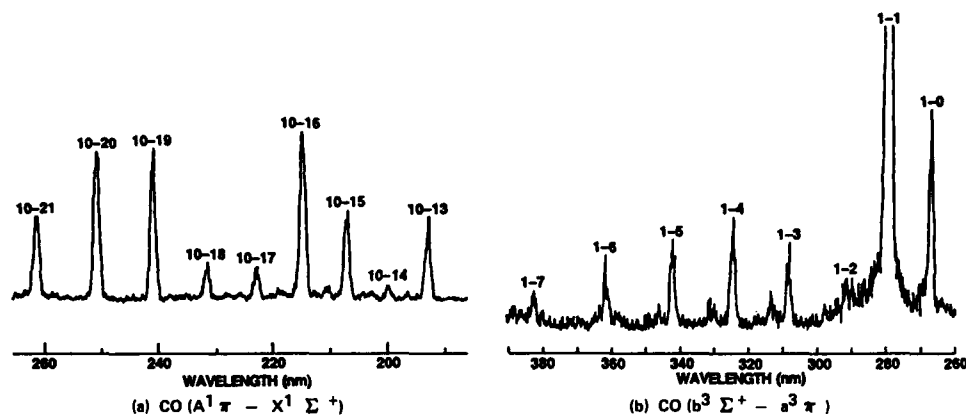
Figure 12   LASER INDUCED FLUORESCENCE SPECTRA OF CO
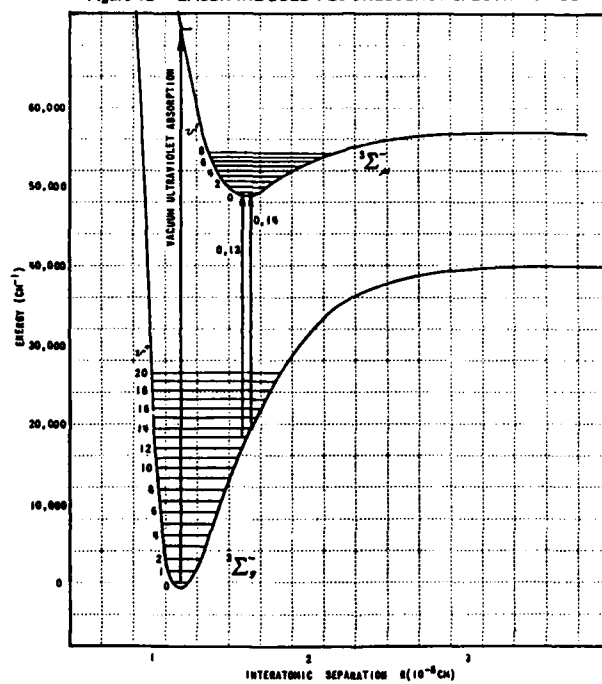
Figure 13   POTENTIAL CURVES OF THE OXYGEN MOLECULE
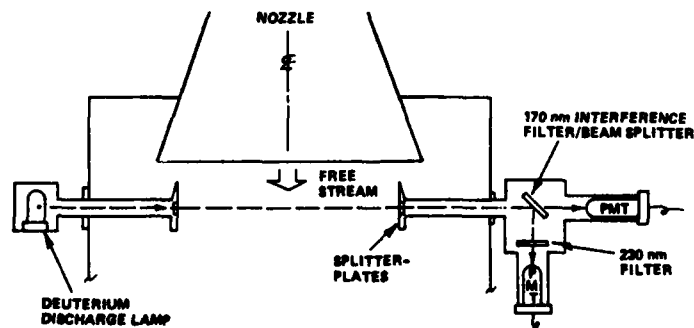
Figure 14 PRINCIPAL ELEMENTS OF A DUAL WAVELENGTH ABSORPTION RADIOMETER
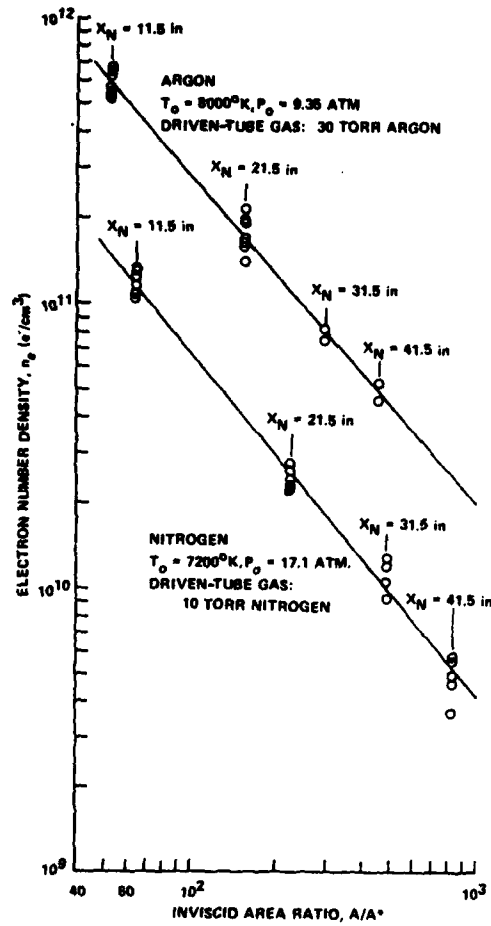
Figure 15 MICROWAVE INTERFEROMETRIC MEASUREMENTS OF ELECTRON NUMBER DENSITIES IN EXPANDING N_2 AND Ar PLASMAS
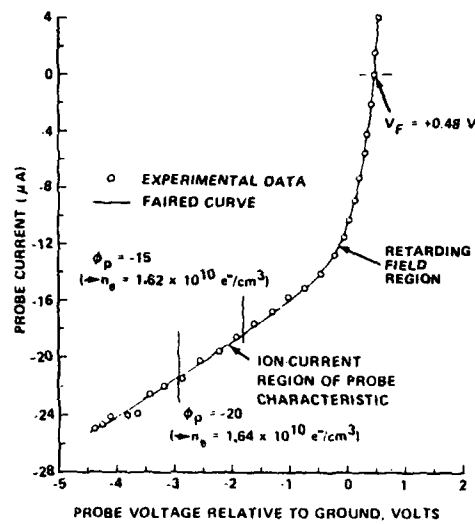
Figure 16 ION-PROBE CHARACTERISTIC RECORDED IN HIGH VELOCITY N_2 PLASMA
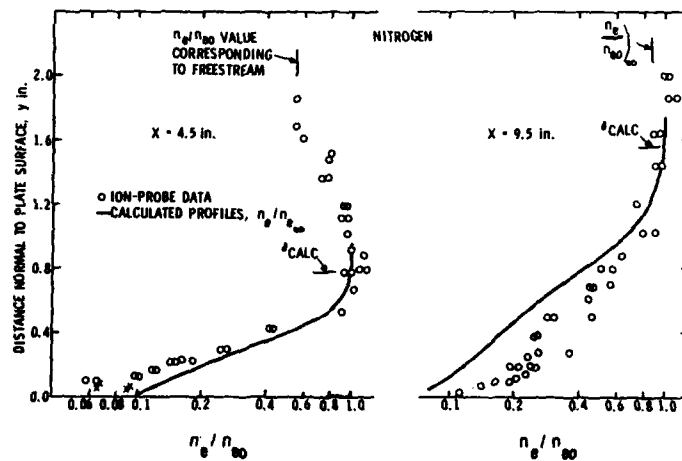
Figure 17 ELECTROSTATIC PROBE MEASUREMENTS OF ELECTRON NUMBER DENSITY PROFILES IN N_2 PLASMA OVER A FLAT PLATE

COMPUTATIONAL TECHNIQUES FOR HYPERSONIC FLOWS
- Selected recently applied techniques -

by
W. Kordulla
DFVLR-Institute for Theoretical Fluid Mechanics
Bunsenstr. 10, D-3400 Göttingen, FRG

SUMMARY

This paper provides some insight into several currently used numerical techniques to simulate hypersonic flows. After describing the particular features of hypersonic flows occuring e.g. during reentry of vehicles such as Hermes the necessary input for computational methods is discussed including the simulation of viscous flow which is emphasized in the paper. If then becomes evident that dedicated experimental work is badly needed to determine thermo-physical and chemical property data as well as to provide appropriate tests for the prediction methods needed to support the designer in his work. Finally, selected recently applied numerical methods are presented for high-speed ("cold") hypersonic flows, for flows in equilibrium and in non-equilibrium. Thereby weaknesses and strengths are being pointed out.

1. INTRODUCTION

The preflight aerodynamic predictions for the US Space Shuttle performance were based on 27 000 hours of wind tunnel occupancy and employed semi-empirical methods for correction purpose owing to the incomplete simulations in the tunnels [1]. The experiences gained in flight in comparison with the experimental and theoretical design are discussed in particular in [2], see also e.g. [3,4]. These experiences reveal, in part, large discrepancies between preflight predictions and flight results.

In contrast to the design of the Space Shuttle computational fluid dynamics (CFD) is expected to play a major role in the development and planning of new spacecrafts. This is true for HERMES [5,6], a smaller, improved version of the US Space Shuttle, but in particular in the case of the development of new technologies such as for HOTOL [7,8] or for SÄNGER [9,10] or the planning of future hypersonic airplanes [11 to 17]. In doing so the gap between preflight predictions and flight results will not be bridged unless the corresponding CFD methods are validated properly requiring new activities in experimental techniques and investigations, see also [19 to 22]. Note that the design of reusable hypersonic vehicles such as HOTOL or SÄNGER with in-flight changing propulsion systems lead to increased requirements for the computational aerothermodynamicist which are different from those present in the design of vehicles such as the Space Shuttle or Hermes [13,15]. The most important difference is that the shape of the spacecraft and the propulsion system form a unity. Also the combustion problems in the propulsion system for hypersonic flight conditions must be considered. In any case the use of CFD is expected to result in a reduction of cost and time requirements associated with the experimental design phase. This attitude spurs the development of new, more efficient and robust numerical methods, and the application of existing methods to more complicated realistic configurations. For the aerodynamic simulations with ideal gases a high standard is already achieved as can be seen from the work reported e.g. in [23 to 25]. The simulation of realistic hypersonic flows, e.g. past reentry vehicles, however, requires more than the simulation of high-speed flows [18].

In figure 1 the flow regimes which are traversed by a typical spacecraft are sketched as a function of altitude and velocity (and also of the Knudsen number, i.e. the ratio of the average mean free path and a characteristic length of the flow field). It is evident from the plot that the ideal-gas assumptions made typically in high-speed flow simulations are only of interest in a very narrow band width of the lower speed range. Reactions may occur within the flow field between shock wave and body which will be discussed briefly later. Depending on the altitude or the Knudsen number the usual assumption of continuum flow is now longer valid due to the reduced density, and a gaskinetic approach becomes necessary, see e.g. [26 to 31]. In the following, only the continuum-flow approach will be discussed based in particular on the numerical integration of the Navier-Stokes equations. It would, however, be of special interest to study the overlapping ranges of the applicability of Navier-Stokes and gas-kinetic approaches, see figure 1, but - to the author's knowledge - there are only a few investigations in that direction, and never for multi-dimensional real flow. At the author's working place both approaches exist, and a comparison is intended to be carried out for three dimensions, in future [32]. Information on flow simulations based on the integration of the boundary-layer equations, can be obtained for realistic hypersonic conditions e.g. in [33], or in another paper contained in the present Proceedings volume.

In the following, first, typical features of realistic hypersonic flows will briefly be discussed, see also [34 to 48] together with the corresponding critical issues for numerical flow simulations. Then an overview over some of the numerical approaches for high-speed flow simulations are presented, see e.g. a few examples for more recent work [49 to 66]. The remaining chapters will deal with the equilibrium or non-equilibrium approximation of reactive flows, see e.g. [67 to 132]. Therein the approximation of the necessary set of reactions and of the transport properties, including the verification of the flow simulations remains a challenge, see e.g. [42,43,133 to 143]. In fact, the numerical simulations of complex *hypersonic flows will not be of too much help unless appropriately designed experiments allow for a validation of the codes for real-flight conditions.* With the exception of tunnels in Australia [21], such
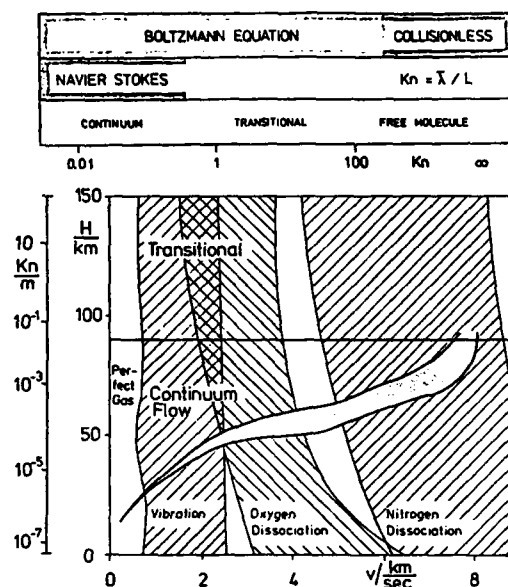
Fig. 1: Sketch of the range of flow regimes with corresponding speeds, altitudes and Knudsen number ranges, including the flight envelope of a typical spacecraft.

simulations seem not to be possible at the time [19,20], and has hence created tunnel construction activities everywhere, see e.g. [135].

2. CHARACTERISTIC FEATURES OF HYPERSONIC FLOWS

The following discussion is, in part, based on references 26 to 28, 30, 34, 38, 41 and 42. The major parameters characterizing the classical high-speed continuum flow [e.g. 144 to 146] are Mach number M and Reynolds number Re, i.e. the ratio of the local fluid speed and the local speed of sound, and the ratio of inertia forces and viscous forces, respectively:

$$M = u/c \quad ; \quad Re = \rho u L/\mu ,$$ (1)

where ρ is the density, L the characteristic length and μ the dynamic viscosity. Note that Mach and Reynolds number can be interpreted as the ratio of acoustic signal time and viscous diffusion time, respectively, to the characteristic flow time. In continuum flow theory the bow shocks in front of bodies are considered infinitely thin such that shock fitting procedures can be applied to determine their shapes. The free stream Mach number and the shape of the body determine the strength of the shock wave. The Reynolds number allows to distinguish between laminar and turbulent flow. Having in mind that the density ρ decreases roughly exponentially with altitude, with ρ at 100 km being about 10^{-7} times the value at sea level, while speed and characteristic length hardly vary, it is clear that the Reynolds number for a spacecraft reflects essentially the influence of altitude.

In figure 2, taken from [27], the variations of pressure, density, temperature and mean free path λ with respect to altitude are displayed. Of current interest for reentry vehicles are the altitudes up to roughly 120 km, see figure 1. Note that below 40 km the windward boundary-layer flow on the space shuttle can be considered turbulent near the nose, with the onset of turbulent flow near the base region being reported around 55 km. The peak heat transfer on the windward symmetry line occurs in the laminar flow regime at 70 km as is shown by the plot of data of different origins in [27]. The smaller the Reynolds number is the thicker the boundary layer becomes, and the inviscid-viscous coupling procedure which is also known as the two-layer concept [30] becomes increasingly impossible. This is because the boundary layer is covering more and more the entire space between body and bow shock wave. An alternative is then to consider the entire region as viscous [148]. In passing it is noted that for the two-layer approach one will have to consider the entropy-swallowing of the boundary layer. This essentially means that along the edge of the boundary layer the entropy varies according to the oncoming different streamlines which pass the strong bow shock at different locations, and thus carry different amounts of entropy into the boundary layer [27,149].

While the Reynolds number is in some sense corresponding to the density of the atmosphere, a parameter which characterizes best the diluteness of the air is the Knudsen number Kn, the ratio of the
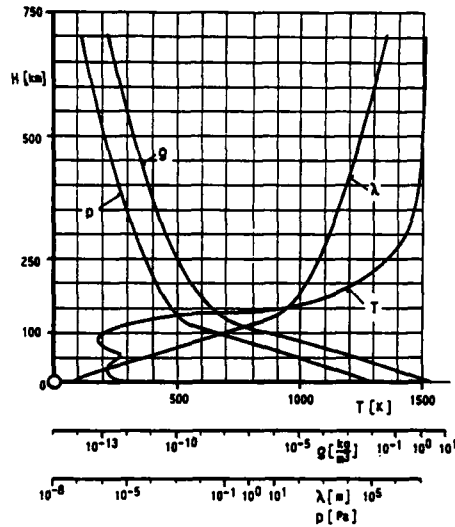
Fig. 2: Distribution of pressure p, density ρ, temperature T and mean free path λ versus the altitude [26].
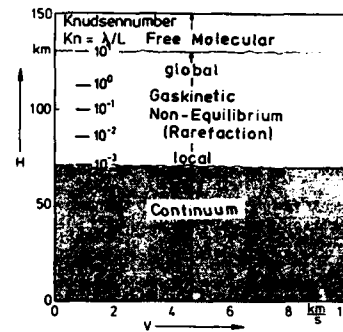
Fig. 3: Influence of the altitude on the characterization of the flow domains [27].

mean free path λ and the characteristic length L,

$$Kn = \lambda/L ,\qquad(2)$$

where e.g. free stream quantities are employed to obtain Kn_∞ for the atmosphere. This parameter can also be viewed as the ratio of acoustic signal to viscous diffusion time. Replacing the mean free path by some molecular expression [31,151] the following relation is obtained.

$$Kn_\infty \sim M_\infty/Re_{\infty L} .\qquad(3)$$

Assuming the relationship for laminar boundary layers $\delta \sim L\,(Re_L)^{-1/2}$ one obtains the result that the Knudsen number based on the "edge" of the boundary layer is proportional to the hypersonic similarity parameter divided by M_∞^2 [144] and to the viscous and rarefaction parameter [29]:

$$Kn_\delta \sim M_\infty/(Re_{\infty L})^{1/2} .\qquad(4)$$

In terms of the Knudsen number Kn_∞ the following distinctions between the atmospheric regions can be made [26]:

Kn_∞	H [km]	Characterization
⪇ 1	≤ 80	Continuum flow
~ 0.01 - ~ 0.1	~ 80 - ~ 120	Continuum flow with slip conditions, etc.
~ 0.1 - ~ 10.	≥ 120	Gas-kinetic flow
≥ 10	> 120	Free molecular flow

Note that because of equation (3) continuum flow is equivalent to $Re_\infty \gg M_\infty$ while free molecular flow corresponds to $M_\infty \gg Re_\infty$. Slip flow conditions for the velocity and the jump in temperature change the friction drag as well as the heat transfer to the wall, and influence the reactions occuring in the boundary layer and at the wall. The exact definition of the boundaries of the domains is rather difficult, in figure 3 e.g. a slightly different interpretation is given [27].

In hypersonic flows with large Mach numbers one can observe some Mach number independency properties, see figure 4 [27]. Thus for real gas flows the Mach number - more or less - ceases to be the essential parameter, and the speed of the considered vehicle, or the kinetic energy of the flow colliding with the vehicle becomes important. For sufficiently high speeds the total enthalpy is virtually identical with the kinetic energy, $h_t = h + 0.5 \cdot u^2 \approx 0.5 \cdot u^2$, and near stagnation points this energy is transformed into heat, and thus into an increase in temperature. In practice this occurs by way of the shock wave embedding the body in question. When passing some critical values real-gas effects are introduced into the air flow as is indicated in figure 5 [27], namely vibration and dissociation in the speed range of main interest here, up to ≈ 8 km/s. Once chemical effects are present the thermal and caloric equations of state must be changed accordingly, as well as the transport coefficients. Also the influence of the surface
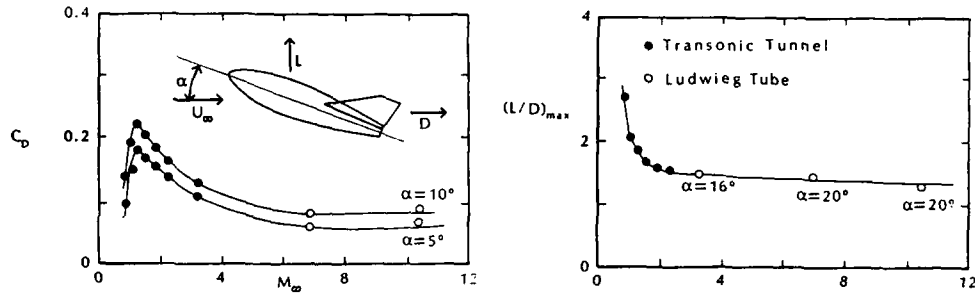
Fig. 4: Aerodynamic coefficients of the MBB-Lifting Body as a function of the Mach number [30], after [155].

on the reactions must be considered, see e.g. [40,41]. If the surface is catalytic recombination effects will lead to increased heat transfer at the surface.

In terms of flight speed real-gas and non-equilibrium effects start at about 1 km/s, see figure 1. Parameters which characterize the real-gas and non-equilibrium state are Damköhler numbers DAM1 and DAM2 [152]. These numbers can apply to internal degrees of freedom of the molecules or to chemical reactions in the fluids. DAM1 is the ratio of the characteristic time of particles passing a region of the flow t_u to the relaxation time τ in question, where the flow time is usually the ratio of the characteristic dimension L and the free stream speed u_∞

$$DAM1 \approx t_u/\tau = L/(u_\infty\tau) . \tag{5}$$

Thus DAM1 = 0 indicates frozen flow, if it varies between $\approx$ 0.01 and $\approx$ 1000 the flow exhibits non-equilibrium, and if the number tends to infinity the fluid is in equilibrium [26]. The second Damköhler number relates the enthalpy difference q for a single reaction between reaction products and reactants to the total enthalpy of the mixture before reaction h_0:

$$DAM2 \approx q/h_0 . \tag{6}$$

If DAM2 tends to vanish this corresponds to equilibrium, otherwise a non-equilibrium or frozen flow is present. If the number is small the corresponding exact simulation may be neglected.

A major role, not only for predictions but in particular for experimental simulations of flows past spacecrafts, play the reaction lengths involved. In figure 6 an example of the variation of the speed of hypersonic flow encountering a normal shock wave is sketched with the typical idealization of assuming the translational and rotational degrees of freedom of a diatomic gas to be in equilibrium instantaneously. This is assumed to occur within the few mean free paths across which the shock is spread, while the vibrational and chemical non-equilibrium (if the free-stream speed is high enough, see figure 5) requires some finite distance to relax. In [27] it is shown that the reaction lengths l_R are much larger than the mean free path assuming reactions with simple binary collisions, and therefore vary also with the altitude (density):

$$l_R \sim M\lambda/z' , \quad l_R/L \sim M Kn/z' , \tag{7}$$

where z' indicates the small fraction of the collisions contributing to the considered reaction. This becomes evident if one considers that the number of particles per unit volume decreases with altitude, and therefore also the number of collisions between particles. Hence it takes longer to achieve equilibrium. Stalker (lecture series at the DFVLR, Göttingen, 1987) shows for binary reactions that the binary scaling parameter
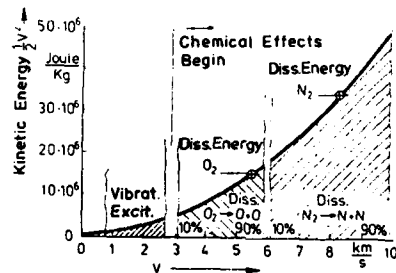

Fig. 5: Kinetic energy of the flow and real-gas effects as a function of the speed of air, including the activation energies for real gas flows [27].
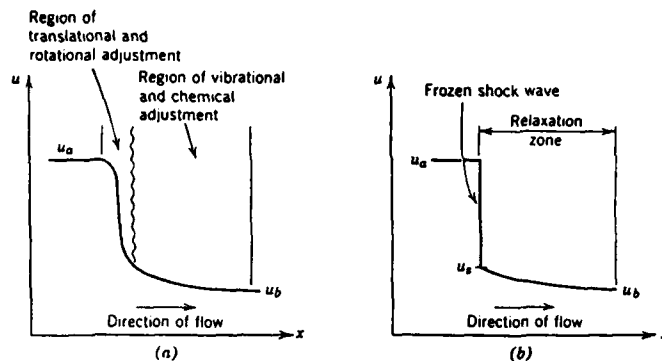
Fig. 6: Velocity distribution through a normal shock wave with the assumption of the flow with states a and b being in equilibrium. Left: true situation, right: idealized [31].

$$\zeta = \int_0^x \frac{\rho}{u}\, dx \tag{8}$$

must be the same in experiment and free flight to produce meaningful results. This leads to the requirement that the quantity $\rho_\infty L/u_\infty$ and therefore $\rho_\infty L$ must be the same.

Other important parameters in hypersonic flows are the thermal and chemical states of the surface of the vehicle in question, i.e. the wall temperature and whether the surface is catalytic or not.

For viscous flow simulations many of the above parameters vary due to the large changes of velocity as well as of temperature and of density across the boundary layer. Therefore the corresponding viscous flow simulation is rather difficult. The main inviscid effects are due to the transformation of kinetic energy across the bow shock wave. Thereby the effective temperature increases with the free-stream speed until the activation energy for vibration and dissociation is reached. Thus quite different length and time scales exist simultaneously which need to be resolved. Note that ionization or radiation are not specifically mentioned, here, these topics are of large interest for aero-assisted orbital transfer vehicles for speeds above 8 km/s, see e.g. [35,36,112 to 115].

3. SOME CLASSICAL HYPERSONIC FLOW SIMULATION APPROACHES

This paragraph mentions a few methods which have evolved over the years starting when hypersonic flow research was popular about 15-20 years ago, and some date back even much earlier. Some of these methods have become very efficient aerodynamical tools, and are discussed in more detail elsewhere in the present proceedings: boundary layer methods by Aupoix and Euler simulations by Anderson, see also [30,4].

The most simple approach to predict the pressure distributions and thus forces on hypersonic bodies is based on the Newtonian flow model, see e.g. [30,132,144 to 146]. This model assumes that the shock layer is very thin and that the bow shock wave is practically attached to the surface. The speed and direction of the gas particles are supposed to remain unchanged until they encounter the surface of the body. Then the tangential component of momentum is conserved while the normal component vanishes. As the free-stream does not collide with the leeward side of a body because it lies in the shadow of the free-stream, this portion does not contribute to the pressure coefficient distribution. The simple version of this concept leads to a pressure coefficient $c_{p_{stag}}$ of 2 at the stagnation point which is not true. In order to correct this the appropriate value of the pressure coefficient at the stagnation point (instead of 2) is used as the coefficient in the modified Newtonian flow model:

$$c_p = c_{p_{stag}} \sin^2\Theta_b \, , \tag{9}$$

where Θ_b is the angle between the free-stream direction and the surface. Some examples of applications, mainly for the Apollo capsule, are given in [30]. Note that the usefulness of the above formula is questionable if the flow field is influenced by e.g. shock-boundary layer or vortex-boundary layer interactions.

Boundary layer theory has been used extensively to predict the heat transfer to the body surface in question, see e.g. [147], in particular in similarity form in the stagnation point region, and also including chemical effects. In general, to perform boundary layer computations an inviscid-flow solution is required to prescribe the boundary conditions at the "edge" of the boundary layer, see e.g. the computations in [33,149,154].

Classical in the sense that the approach is around for about two decades are viscous shock layer methods used to predict the flow between bow shock wave and body surface based on a set of parabolic equations derived from the Navier-Stokes equation, see e.g. [148] and also other listed references. Since

the domain is not divided into inviscid and viscous regions, the viscous shock layer methods are - to a certain extent - also useful for low density and hence low Reynolds number flows where the boundary layer extends to the shock surface. The equations are obtained by introducing boundary layer coordinates and performing an order of magnitude analysis on the terms in the Navier-Stokes equations in terms of the inverse square root of the Reynolds number. The terms up to second order are then retained. The result is a set of steady state equations. The solution is started at the stagnation point and is marched downstream. If separation occurs the computation cannot proceed further. The shock position is obtained as a result of the solution procedure. It is not clear to the present author how the correct stagnation point location can be obtained in general. For more general shapes, in particular at an angle of attack the stagnation point is not given by the location of the surface tangential which is orthogonal to the free-stream direction. This is even not the case for the shock tangential because it is well-known that the stagnation streamline does not necessarily experience the largest jump in entropy owing to crossing the shock wave. A streamline next to the stagnation streamline may encounter the shock wave in an orthogonal manner, depending on the shape of the body in question and on the angle of incidence [145].

Another solution method which looks similar to the viscous shock layer approach is the concept of "parabolized Navier-Stokes" (PNS) which is, however, quite different, because the boundary layer assumptions are not introduced at all. In order to reduce the Navier-Stokes equations to a set of "easily" solvable steady-state equations the viscous terms with respect to a chosen direction are dropped, and the solution can be obtained by marching in that direction until inviscid subsonic or reversed flow is encountered, see more recent textbooks such as [159] or e.g. [30,62,68]. The advantage of PNS-methods compared with full Navier-Stokes solutions is the relatively low cost to run the codes because sequences of two-dimensional problems have to be solved. In this sense all mentioned viscous-flow methods (in fact also the corresponding inviscid methods not mentioned here e.g. [90]) offer the opportunity to check out the physical models required to simulate realistic hypersonic flows. Note that PNS methods require a starting solution near the stagnation point because of the subsonic flow there. The initial conditions for the marching solution must not contain subsonic inviscid nor reversed flow.

4. SALIENT INGREDIENTS FOR HYPERSONIC FLOW SIMULATIONS

For later discussions it is useful to have a common basis in terms of a set of equations governing the fluid flow, see e.g. [31,33,34,42,43,50,67,132,144 to 147,156]. It was mentioned earlier that the main interest here is in viscous flows, although some of the techniques used have been developed, originally, for Euler equations. The Navier-Stokes equations comprise the set of equations due to conservation of mass, momentum and energy *for viscous* flows. Most of the algorithms are based on the conservation-law form. This choice is mainly motivated by the corresponding ability to treat flow discontinuities automatically without the need to fit them. While it is fairly easy to fit bow shocks by using them as a boundary of the computational domain, this is not at all easy for embedded shock waves. Conservation-law forms for differential equations are discussed in [157,158]. The more fundamental integral formulation is naturally conservative. The difference between finite-difference methods, based on differential forms, and finite-volume formulations appear to result mainly in different formulations of the metric terms in the equations in the case of non-Cartesian grids, or in the manner the field grid is being used.

Realistic hypersonic flows experience a large increase in temperature due to the bow shock wave which excites internal modes of the molecules of the air and may cause dissociation and even ionization depending on the magnitude of the free-stream, see the figures 1 and 5. Therefore, in general, the above equations have to be complemented with a set of equations for the masses of the single species including terms describing the creation and consumption of them. The sum of all species must, of course, result in the total mass. This fact can be used to eliminate one equation or else to obtain a check for the accuracy of the solution procedure, see also [111]. If the vibrational modes are in non-equilibrium, i.e. if one distinguishes between translational and vibrational temperatures (note that the rotational temperatures are usually assumed to be equal to the translational ones because of the short relaxation times in comparison with vibration) additional equations have to be solved for the vibrational energies of the different molecules, see e.g. [36,96,97]. If ionization effects must be considered, these equations are further complicated due to the presence of electrons [36].

The conservation equations are not complete without relations for the thermal equation of state, for the caloric equation of state as well as for the vibrational energies. For a multi-component mixture such as air in non-equilibrium the assumption of a mixture of ideal gases is generally advocated and accepted, see e.g. [36,42,43]. Thus the relation between specific heats and the general gas constant holds for each species. And the problem boils down to the determination of e.g. the specific heat at constant volume for pure gases. The vibrational contribution is the result of statistical and quantum mechanics, see e.g. [31,43]:

$$\left(\frac{C_v}{R}\right)_{vib} = \left(\frac{\Theta_v/2T}{\sin h(\Theta_v/2T)}\right)^2 \tag{10}$$

which has to be added to 1.5 to obtain the value for a diatomic species (Θ_v is the activation energy for the vibrational mode of the species in question). In the case of non-negligible ionization effects another contribution must be considered.

Note that in the case of equilibrium flows the air is quite often considered as a single species where the real gas effects are introduced via tabulated Mollier-diagrams or approximations thereof, see e.g. [69 to 73,91]. This has the advantage that the code employed for ideal-gas simulations need not be changed dramatically. It would be interesting to know whether there is a difference in such flow simulations compared with those relying on the assumption of a mixture of ideal gases and a set of non linear algebraic equations to determine the composition, see e.g. [137,160] for a mixture with five components (O_2, N_2, NO, N, O). Three linearly independent reactions result e.g. from the system (11) and two components (the atoms N and O) thus yielding five equations as a function of e.g. the pressure of the mixture and the three equilibrium constants.

The composition of dissociating air is generally computed based on the five-components model of air just mentioned [31,137,160]. Here, a reduced set of the reactions is taken [137]:

$$N_2 + M \Leftrightarrow N + N + M, \quad 9.8\,eV,$$

$$O_2 + M \Leftrightarrow O + O + M, \quad 5.1\,eV,$$

$$NO + M \Leftrightarrow N + O + M, \quad 6.5\,eV, \tag{11}$$

$$O + N_2 \Leftrightarrow NO + N, \quad 3.3\,eV,$$

$$N + O_2 \Leftrightarrow NO + O, \quad 1.4\,eV,$$

where the energies involved (1 eV = 23,4 Kcal/g mol = 97.85 J/kmol) are taken from [31]. The different characteristic times of the reaction rates of the single reactions cause the system of the equations to become "stiff". This virtually precludes the use of explicit methods for the integration of the species equations with the source terms. A major cause of uncertainty is given by the forward and backward reaction rate coefficients which must be determined from experiments. The forward or backward rate coefficient which is the coefficient in the corresponding law of mass action [43,67,137], is usually approximated with the improved Arrhenius formula with a temperature dependent coefficient:

$$k = A\,T^b \exp(-E_a/RT). \tag{12}$$

A, b and the activation energy E_a are the constants to be determined experimentally for each reaction. In particular the constant A may vary by many orders of magnitude. The ratio of forward to backward reaction rate coefficient is the equilibrium constant which can be expressed in terms of the temperature [67]. The chemical reactions may be influenced considerably by vibrational excitation such that the characteristic times are changed, and the difficulty of the simulation is increased [137].

The above brief remarks show the importance of theoretical and experimental research with respect to the determination of thermo-physical and chemical property data in the context of the simulation of high temperature hypersonic air flow. This importance is further emphasized when considering the boundary conditions at solid surfaces. Molecules are adsorbed on or by surfaces and may react yielding products which leave the surface. Such heterogeneous reaction rates may be much larger than homogeneous rates [43]. With respect to the rate coefficients and the corresponding activation energies one has to rely on experimental work [43]. This is a handicap since the species conservation equations require boundary conditions at the wall, namely the surface kinetics. Therefore often the surface is simply considered either fully catalytic or non-catalytic, i.e. the limiting states.

Some other boundary conditions which are needed in flow with sufficiently low density are also dependent on experimental research: if the Knudsen number is sufficiently high slip flow is present near surfaces, and a jump in temperature occurs which can be formulated as a function of accommodation coefficients for the transfer of momentum and energy of the molecules encountering the surface.

Last not least, the formulation of transport coefficients needed to simulate reacting ideal gas mixtures are not entirely understood and need further work, in particular in view of the application to higher temperatures. The transport coefficients with respect to mass, momentum and energy transfer can be determined as a function of inter molecular force potentials based on gaskinetic theory, see e.g. [42,43,151]. In multicomponent mixtures with thermodiffusion due to the large temperature gradients within the boundary layer, approximations are quite useful involving binary diffusion coefficients in multicomponent formulae, see also the paper by Aupoix in the present proceedings.

Owing to the fact that other papers in these proceedings deal in more detail with the afore-mentioned topics they were just mentioned, and they will be discussed in the presentation of numerical approaches whenever suitable. Note also that the problem of transition and turbulence modelling has not been addressed for the same reason although those play an important role in the aerothermal load predictions.

5. SELECTED COMPUTATIONAL FLOW SIMULATION TECHNIQUES

Inviscid flow, boundary layer, viscous shock layer and PNS methods are treated elsewhere in the present proceedings. It is only noted, in passing, that 3-D inviscid flow (Euler) simulations have been carried out, including full chemistry, in the early seventies, e.g. at NASA, Ames. The main interest focusses on time-dependent Navier-Stokes solutions here, although the listed references cite a large body of work and reports covering all types of applications, carried out only recently.

Let us summarize the features of a simulation code required to ultimately simulate the hypersonic flow past a vehicle such as HERMES or HOTOL. Since the computational methods by themselves cannot produce the needed better physical modelling as was indicated earlier, it is assumed that neither that is a problem nor the generation of a suitable surface-fitted grid system. Such a code needs to be robust and accurate at the same time as is the wish for any code. From the preceding two paragraphs it it clear that the code must be able to treat or resolve the following features: extremely strong change of flow variables across the bow shock wave, excitation and relaxation of internal degrees of freedom of the molecules, dissociation of molecules and recombination of atoms, gas-surface interactions with possible heat sources due to recombination near the wall, slip at the surface and a corresponding jump in temperature, coping with the stiffness of the solution of the equations owing to the multiple time scales because of the different reactions, and finally resolving properly the flow phenomena occuring within the flow field such as e.g. shock-on-shock, shock-boundary layer, shock-vortex or vortex-boundary layer interactions. Also, steep gradients need to be resolved near curved boundaries not only with respect to velocity but also with respect to density and temperature. This is different from the requirements in the usual transonic flow regime where, already, the solution of the energy equation seemed to converge worst. The simulation of hypersonic flows past vehicles such as SÄNGER or NASP for design purpose would require, in addition, the combustion problem imbedded in the air flow.

The state-of-the-art is viewed by the author to be transitional going from purely engineering methods (see e.g. [2] and consecutive papers) to more advanced techniques. While the engineering methods need more "overall calibration" by means of wind tunnel testing, the newer methods seem to require more subtle, realistic and detailed investigations, including the development of transport and reaction models, and, of course, transition recognition criteria and turbulence modelling. As could be expected most of the available methods consider first high-speed, so-called "cold" hypersonic flows before a more realistic and more costly approach is carried out.

Note that no attempt was made to use a single notation for all discussions which follow due to the involved complications. For details of the numerical schemes the reader is referred to the literature, in particular in the case of real gases where the equations and transport processes become rather complicated.

5.1 High-Speed Hypersonic Flows

High-speed hypersonic flows are generally encountered in wind tunnel environments whenever the temperature in the stagnation chamber is sufficiently low. Thus these flows can, in principle, be employed to check out the codes for accuracy of heat transfer and skin friction prediction for non-reacting fluids. Two examples are given below, which are both based on a thin-layer formulation of the viscous terms, and on the unsteady form of the equations to arrive at a steady state if there exists one. Experience shows that the thin-layer approximation is a very reasonable approximation in view of the presently used grids. The first method is using local time stepping to accelerate the rate of convergence, while the second approach employs a constant time step in order to be able to detect unsteady behavior.

The Navier-Stokes equations for laminar, thermally and calorically perfect gas and for general surface-fitted coordinates (using the free-stream quantities ρ_∞, u_∞, μ_∞, k_∞ and L as reference quantities, where the viscosity coefficient is obtained from Sutherland's law and where the heat conduction coefficient is computed with a constant Prandtl number) can be written as follows:

$$\hat{Q}_t + \hat{E}_\xi + \hat{F}_y + \hat{G}_\zeta = Re^{-1} \hat{S}_\zeta \tag{13}$$

where solution and the flux vectors are

$$\hat{Q} = J^{-1} \begin{bmatrix} \rho \\ \rho u \\ \rho v \\ \rho w \\ e \end{bmatrix} \qquad \hat{E} = J^{-1} \begin{bmatrix} \rho U \\ \rho u U + \xi_x P \\ \rho v U + \xi_y P \\ \rho w U + \xi_z P \\ U(e + p) - \xi_t P \end{bmatrix}$$

$$\hat{F} = J^{-1} \begin{bmatrix} \rho V \\ \rho u V + \eta_x P \\ \rho v V + \eta_y P \\ \rho w V + \eta_z P \\ V(e + p) - \eta_t P \end{bmatrix} \qquad \hat{G} = J^{-1} \begin{bmatrix} \rho W \\ \rho u W + \zeta_x P \\ \rho v W + \zeta_y P \\ \rho w W + \zeta_z P \\ W(e + p) - \zeta_t P \end{bmatrix} \tag{14}$$

with the contravariant velocity components

$$U = \xi_t + \xi_x u + \xi_y v + \xi_z w$$

$$V = \eta_t + \eta_x u + \eta_y v + \eta_z w \tag{15}$$

$$W = \zeta_t + \zeta_x u + \zeta_y v + \zeta_z w$$

with the stress flux vector

$$\hat{S} = J^{-1} \begin{bmatrix} 0 \\ \mu m_1 u_\zeta + (\mu/3)m_2\zeta_x \\ \mu m_1 v_\zeta + (\mu/3)m_2\zeta_y \\ \mu m_1 w_\zeta + (\mu/3)m_2\zeta_z \\ \mu m_1 m_3 + (\mu/3)m_2(\zeta_x u + \zeta_y v + \zeta_z w) \end{bmatrix} \tag{16}$$

where the following abbreviations are used:

$$m_1 = \zeta_x^2 + \zeta_y^2 + \zeta_z^2$$

$$m_2 = \zeta_x u_\zeta + \zeta_y v_\zeta + \zeta_z w_\zeta \tag{17}$$

$$m_3 = (u^2 + v^2 + w^2)/2 + Pr^{-1}(\gamma - 1)^{-1}(a^2)_\zeta$$

The equation of state is used in the caloric equation of state to obtain the pressure:

$$p = (\gamma - 1)\left(e - \frac{1}{2}\rho(u^2 + v^2 + w^2) \right) \tag{18}$$

The metric terms are as usual and are given e.g. in [163, 166].

Implicit Up-wind High Resolution Scheme of Hänel and Schwane [161 to 163]

The numerical solution is implicit and based on an upwind formulation of the convective terms and a central differencing of the viscous terms. This is the usual approach for upwind Navier-Stokes solutions. The inversion of the implicit coefficient matrix is achieved by means of a relaxation procedure.

In order to apply upwind discretization to the hyperbolic part of equation (13) the flux vectors $\hat{E}$, $\hat{F}$ and $\hat{G}$ are split into forward- and backward flux vectors $\hat{E}^\pm$, $\hat{F}^\pm$ and $\hat{G}^\pm$. The splitting proposed by van Leer is preferred to that one of Steger/Warming because the split fluxes do not exhibit discontinuities when an eigenvalue vanishes, and because previous experiences have shown a very robust and effective behavior. For high Mach number flows, however, the non-preservation of total enthalpy of the original splitting concept leads to unphysical results for the wall temperature, see [161] and figure 7. Therefore a modified splitting concept is used [161,163] resulting in the following general flux $\hat{P}^\pm$ (for $| W/c| \nabla \omega || < 1$):

$$\hat{P}^\pm = J^{-1} \begin{bmatrix} |\nabla\omega|\hat{P}_I^\pm \\ \hat{P}_I^\pm [u|\nabla\omega| - \hat{W}\dfrac{\omega_x}{\gamma|\nabla\omega|} \pm \dfrac{2c}{\gamma}\omega_x] \\ \hat{P}_I^\pm [v|\nabla\omega| - \hat{W}\dfrac{\omega_y}{\gamma|\nabla\omega|} \pm \dfrac{2c}{\gamma}\omega_y] \\ \hat{P}_I^\pm [w|\nabla\omega| - \hat{W}\dfrac{\omega_z}{\gamma|\nabla\omega|} \pm \dfrac{2c}{\gamma}\omega_z] \\ |\nabla\omega|\hat{P}_I^\pm \cdot H \end{bmatrix} \tag{19}$$

with

$$\hat{P}_I^\pm = \pm\rho c\left[\frac{1}{2}\left(\frac{\hat{W}}{c|\nabla\omega|} \pm 1 \right) \right]^2,$$

$$\hat{W} = u\omega_x + v\omega_y + w\omega_z, \tag{20}$$

$$H = \frac{1}{\rho}(e + p).$$

Substituting $\omega = \zeta$ one recovers $\hat{E}^\pm = P^\pm$ with $\hat{U} = \hat{W}$, etc. Thus the Navier-Stokes equations read

$$\hat{Q}_t + Res\hat{Q} = 0 \tag{21}$$

with

$$Res\hat{Q} = \hat{E}_{\zeta}^{+} + \hat{E}_{\zeta}^{-} + \hat{F}_{y}^{+} + \hat{F}_{y}^{-} + \hat{G}_{\zeta}^{+} + \hat{G}_{\zeta}^{-} - Re_{\infty}^{-1}\hat{S}_{\zeta} .$$ (22)

An implicit finite difference method is used with a spatially conservative approximation with the cell boundaries Γ determined by averaging over the neighboring grid points. A first order accurate implicit backward Euler scheme is employed for the time linearization such that equation (21) becomes

$$[\delta_t + \delta_\xi (A^+ + A^-) + \delta_y(B^+ + B^-) + \delta_\zeta(C^+ + C^- - Re_{\infty}^{-1}D)]^n \Delta\hat{Q}^n = -Res\hat{Q}^n ,$$ (23)

where the superscript n denotes the time level, $\hat{A}^{\pm}$, $\hat{B}^{\pm}$, $\hat{C}^{\pm}$ and D are the Jacobians of the fluxes i.e. $A^{\pm} = \partial\hat{E}^{\pm}/\partial\hat{Q}$, δ, indicates the inverse of the time increment $t^{n+1} - t^n$, and $\Delta\hat{Q}^n$ is the usual forward difference $\Delta\hat{Q}^n = \hat{Q}^{n+1} - \hat{Q}^n$.

For the Euler fluxes the van Leer MUSCL-type differencing is used (Monotonic Upstream Centered Schemes for Conservation Laws):

$$\hat{E}_{i\pm1/2}^{\pm} = \hat{E}^{\pm}(Q_{i\pm1/2}^{\pm}, \Gamma_{i\pm1/2}),$$ (24)

where the variable at the interface Γ is determined according to

$$Q_{i+1/2}^{+} = Q_i + \delta Q_i , \qquad Q_{i+1/2}^{-} = Q_{i+1} - \delta Q_{i+1} .$$ (25)

Second-order accuracy is obtained by assuming a piecewise linear distribution of the variable Q:

$$\delta Q_i = \left[\left(\frac{\vec{S}}{\vec{S} + \tilde{S}} \right) \cdot \left(\frac{\vec{\Delta QS} + \tilde{\Delta QS}}{\vec{S} + \tilde{S}} \right) \right]_i .$$ (26)

In order to avoid over- or undershoots near points of extrema or discontinuities the term δQ_i is limited by means of a switching function φ_i which is zero near discontinuities and one in regions with smooth solutions. The arrows in equation (26) indicate forward or backward differencing and the corresponding differences between mesh points across the surface in question. The left-hand implicit side uses a first-order approximation of the fluxes ($\delta Q_i = 0, \delta Q_{i+1} = 0$ in (25)) in the case of steady state solutions to reduce the computational effort, see also [164]. The relaxation scheme is based on a collective point or collective line Gauß-Seidel relaxation scheme in alternating directions. The time step is increasing with decreasing maximum Residual $Res\hat{Q}^n$ to accelerate further convergence.

Flux-split schemes exhibit inherent numerical diffusion due to the upwinding of the discretization. Note that it seems that this numerical diffusion is not sufficient (combined with the flux limiter) to suppress oscillations near the bow shock wave beyond certain hypersonic free-stream Mach numbers if the shock is captured (private communications: D. Hänel, Aerodynamisches Institut, Aachen and M.Schmatz, MBB, München). The consequence is perhaps to apply an adaptive grid or else to fit the bow shock wave the shape of which evolves with the solution. Initially the position and shape of the shock wave must be guessed. A particular procedure had to be introduced to treat the shock wave differently: a regularly triangulized mesh on the shock surface was used to obtain a solution [162,163]. Note that Hänel and Schwane point at a weakness of the use of limiters which react to large gradients by introducing addi-
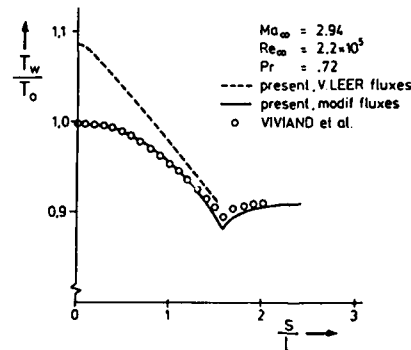

Fig. 7: Wall temperature distribution related to the inflow stagnation temperature as a function of the arc length in the mid-plane of a hemisphere-cylinder body predicted with the original and the improved van Leer splitting [161, 163].
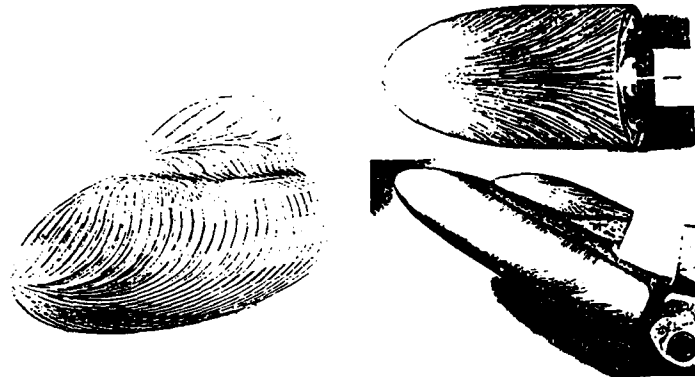
Fig. 8: Simulation of the flow past a double ellipsoid at $M = 8.15$, $Re = 2 \cdot 10^6$, $\alpha = 25°$ (cold hypersonic flow [165]), [163].

tional numerical diffusion (making the upwinding tend to first-order accuracy). This has been found by studying flat plate flows [161], and may result in errors in particular for hypersonic flows with anticipated large gradients of temperature and concentration. Thus further investigations are needed in that direction for any flux-split scheme. Figure 8 shows a sample result for the flow past a double ellipsoid at large angle of attack for cold hypersonic flow conditions.

Explicit-Implicit Central Finite-Difference Solution by Riedelbauch and Müller [32,166,167]

The used set of governing equations is practically identical with that one in the preceding paragraph. This holds also for the formulation of the transport coefficients. Shock fitting is also applied, see the sketch in figure 9. No special treatment of the shock surface is, however, employed. Instead the pressure behind the shock is calculated based on the energy equation in non-conservative form as is usually done. Then the shock velocity and the remaining flow variables behind the bow shock are evaluated from the Rankine-Hygoniot relations. With the shock velocity known the shock surface is moved along the coordinate lines intersecting that surface, and a re-meshing is performed. This procedure leads to oscillations in the shock shape if a strong shock-on-shock interaction occurs as is the case for the embedded shock in a $M = 8.15$ flow past a double-ellipsoid at zero angle of attack [165], where the interaction is strongest. There is work in progress to investigate whether an implicit treatment of the shock boundary conditions ameliorates these conditions considerably.

The numerical scheme is first-order accurate with respect to time and second-order accurate in space due to central differencing. The temporal scheme is actually hybrid because only the wall-normal differentials are discretized in an implicit fashion while the surface-tangential ones are determined explicitly:

$$\hat{Q}_t^{n+1} + \hat{G}_\zeta^{n+1} - Re_\infty^{-1}\hat{S}_\zeta^{n+1} = -(\hat{E}_\xi + \hat{F}_\eta)^n . \tag{27}$$

The advantage of reducing the computational effort in inverting the implicit terms and of reducing the storage requirements is at the expense of a CFL-dependency due to the explicit differencing in the surface-tangential directions. Note that a checker-board type relaxation scheme with alternating directions is used to efficiently solve the linearized and discretized equations (27) on vector computers. The solution is implicit in the direction of the coordinates between body and shock wave since in that direction the largest time step restriction is expected due to the fine mesh near the surface. It turns out, however, that in particular the fine surface-tangential grids near the nose of practical spacecrafts with small radius of curvature result in too small time steps such that an overall implicit treatment of equation (27) seems to become advantageous. Note that this problem does not arise usually for simple body shapes such as blunted cones.

Since central differencing is being used explicitly added numerical diffusion is required to damp high-frequency oscillations and those near captured discontinuities. While previously only fourth-order damping was employed [166] with the coefficient on the explicit side being proportional to the time step, the simulation of the flow past the double ellipsoid is much improved by introducing second-order diffusion with a flow-dependent coefficient (the normalized second difference of pressure known to be used MacCormack and Jameson) [167].

The coordinate system used is singular near the nose, see fig. 9, and the conservative variables are determined there by averaged two-point extrapolations [166]:

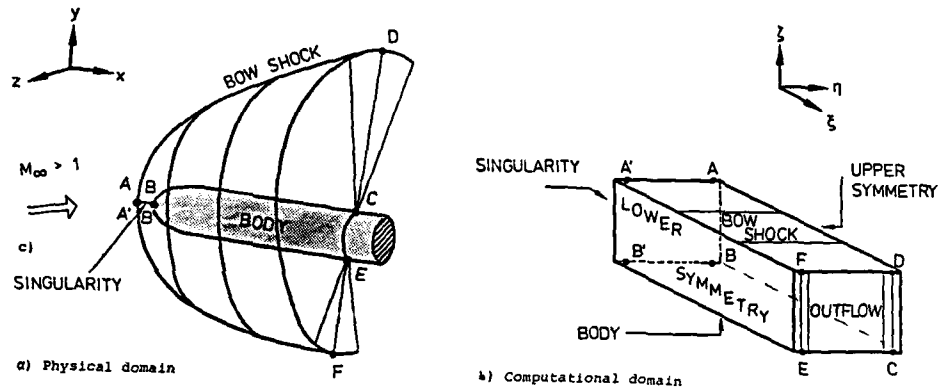$$q_{1j} = J_{max}^{-1} \sum_{j=1}^{j_{max}} (a_1 q_{2j} + a_2 q_{3j}) , \tag{28}$$

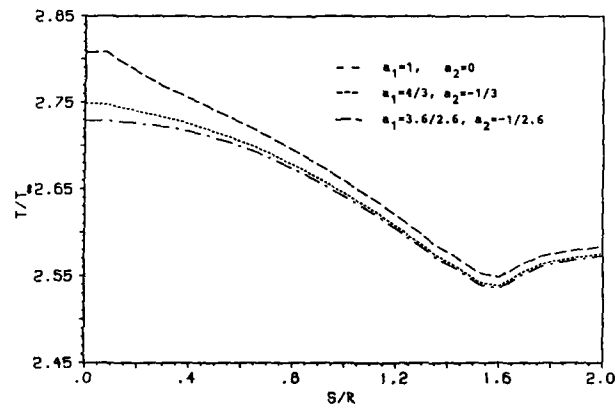Fig. 9: Sketch of the computational and physical domains.

Fig.10: Influence of the coefficients in the averaging formula for the flow variables at the singular point (nose) on the wall temperature. Hemisphere-Cylinder, adiabatic, $M \approx 2.94$, $\alpha = 0°$, $Re_{\infty,n} = 2.2 \cdot 10^6$.

where j is the azimuthal direction with j_{max} being the maximum number of points in that direction. The difference of the stagnation temperatures is surprisingly large, see figure 10, influencing also the downstream distribution somewhat, while the pressure distribution is virtually unaffected. This feature needs to be kept in mind when tackling the simulation of reacting hypersonic flows.

After the validation of the code by comparison with experimental heat transfer and pressure data for a blunted cone and sphere [166], it is applied to a more complicated flow case, namely the flow past an ellipsoid and a double ellipsoid [165]. Figure 11 shows results for the simulation of the flow past a single ellipsoid [167]. The robustness of the scheme is intended to be improved by implementing the TVD concept advocated e.g. in [52,61,66] which shows promising results also for reacting air flow, see e.g. [83]. As a first step towards the consideration of real-gas effects the air flow will be treated as one species in chemical equilibrium such that the change of the code is minimum if the approach of [69 to 72] is employed.

While computing the flow past the single or double ellipsoid the flow at the downstream exit plane, where extrapolation boundary conditions are used in the entire cross section, reversed at a certain angle of attack. This problem was overcome by simply extending the body further downstream since there are no downstream boundary conditions available (although the length of the experimentally investigated body is smaller). In test cases as such there may thus arise the need to consider the base flow as well. Note that the scheme is used with constant time step in the computational domain such that unsteady flow behavior can in fact be called unsteady.
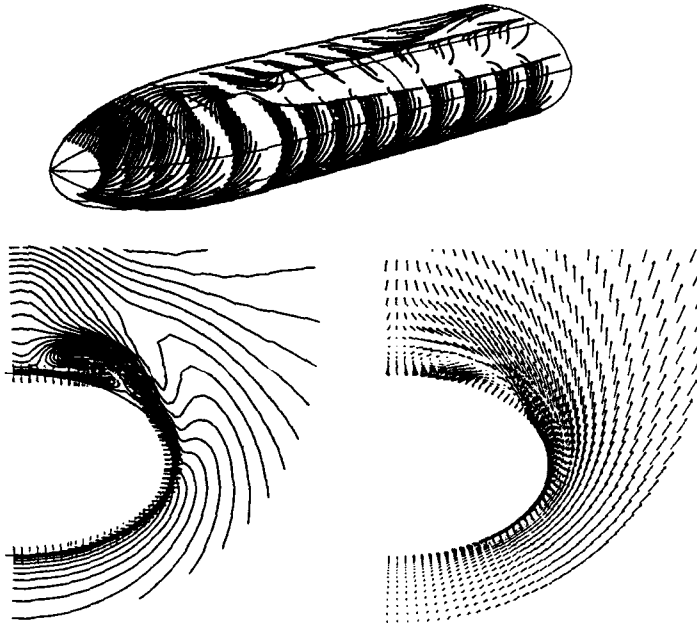
Fig.11: Skin friction lines on an ellipsoid (top), Mach number contours (left; + + + : sonic line) and velocity vectors at $x/L \approx 1.3$ (L = large half axis). $M_\infty = 8.15$, $Re_{\infty,L} = 960000$, $\alpha = 25°$, $T_w = 296K$, $T_{s\infty} = 800K$, mesh: 65×63×41.

5.2 Real-Gas Equilibrium Flow Simulations

As a first step towards the consideration of real gas effects the assumption of thermal and chemical equilibrium is usually made to consider one limiting case. In addition, to facilitate the computational effort the air is not considered a mixture of species (see e.g. [31,137]) but one species. The caloric relations and the transport coefficients are then determined by looking at tables or by using curve-fits, see e.g. [69-72]. From the titles in the list of references it is evident that there exist quite a few approaches for equilibrium air computations. Here, the attention is focussed on flux-difference or flux-split and TVD (Total Variation Diminishing) approaches which became quite popular recently because they allow for the use of relaxation schemes but have generally been used for transonic or supersonic free-stream conditions employing directly the ideal gas law for the formulation of the schemes. In [60] different numerical flux formulations for the convection terms in the ideal-gas Euler and Navier-Stokes equations are analyzed with respect to their accuracy in representing steady waves.

The most commonly used upwind formulations of the inviscid terms in the numerical solution of conservation laws are based on either flux-vector splittings of Steger-Warming or van Leer, or on the Roe approximate Riemann solver. These formulations all utilize properties of the Flux Jacobian matrix and involve the use of the law for thermally perfect gases, where the speed of sound is given as

$$c^2 = \left(\frac{\partial p}{\partial \rho}\right)_S = \gamma \frac{p}{\rho} . \tag{29}$$

For an equilibrium gas with the volume averaged enthalpy $h = (\tilde{e} + p)/\rho$, with $\tilde{e}$ being the internal energy per unit volume and $p = p(\rho, \tilde{e})$, c^2 is however given by:

$$c^2 = \left(\frac{\partial p}{\partial \rho}\right)_{\tilde{e}} + \left(\frac{\partial p}{\partial \tilde{e}}\right)_\rho h = \chi + \kappa h . \tag{30}$$

Generalizations for such flows treating air as one species are reported e.g. in [77,78], and results for 1-D shock-tube problems are compared with each other and with other formulations in [81]. The eigenvalues and eigenvectors of the Jacobian matrices $\hat{A}$, $\hat{B}$ (e.g. in 2-D) are used in approximate Riemann solvers. Given two states whose difference is ΔU, Roe obtains an average $\bar{A}$ in e.g. the ζ-direction satisfying $\Delta \hat{F} = \bar{A}\Delta U$ for a perfect gas. The generalization in [78] involves the pressure derivatives χ and κ, see equation (30). Introducing $H = h + (u^2 + v^2)/2$, the same expressions for $\bar{u}, \bar{v}$ and $\bar{H}$ as for the perfect gas are found with χ and κ satisfying

$$\bar{\chi} \Delta \rho + \bar{\kappa} \Delta \tilde{e} = \Delta p . \tag{31}$$

The values for $\bar{\chi}$ and $\bar{\kappa}$ do not seem to be always uniquely defined [81] such that a reasonable choice must be made.

The formation of Roe's Riemann solver requires the use of the derivatives of the pressure, see equation (30), while the others just need the speed of sound. Thus the quality of the curvefits of the thermodynamic data may become important [69 to 72] as is noted in [81]. This situation may become worse in viscous-flow simulations if second derivatives are needed, and the approximations exhibit kinks. The Steger-Warming flux-vector splitting, which is more diffusive than the other solvers (also shown by larger robustness in ideal gas simulations), is reported to be less sensitive to a lack of regularity in the curve fits.

Flux-vector splitting methods divide the flux $\hat{F}$ into several parts each of which has a Jacobian matrix whose eigenvalues are all of one sign. The approach of Steger and Warming made use of the relation $F = A U$ valid for thermally perfect gases. Van Leer contructed a different splitting in which the eigenvalues of the split-flux Jacobians are continuous and one of them vanishes resulting in a crisper simulation of captured shocks. In [77] the expressions of both of these splittings can be generalized to an arbitrary gas by using the variable $\gamma = \rho c^2/p$, and adding to the split energy flux a term equal to the product of the split mass flux and the quantity $\epsilon - c^2/[\delta(\gamma - 1)]^{-1}$ with $\epsilon = \tilde{\epsilon}/\rho$.

The recent activities in using TVD methods associated with H. Yee is e.g. described in the papers [52,61,66,82] regarding ideal as well as equilibrium gas simulations. The applications include 2-D steady and unsteady viscous flow simulations for which a temporally second-order implicit algorithm is reported to be slightly more stable than the temporally first-order implicit algorithm. A variety of TVD schemes for equations of the type given earlier in thin-layer approximation has been investigated [82], where the spatial accuracy depends on the form of the numerical flux functions. There exists many ways to achieve higher order spatial accuracy and at the same time have TVD-type properties, see for more details [82]. For general fluids Yee concentrates the forthcoming efforts on the so-called non-MUSCL approach in the formulation for the flux-vector, e.g. resulting in:

$$F_{j+1,k} = \frac{1}{2}\left[\left(\frac{\xi_x}{J}\right)_{j+1/2} (F_{j,k} + F_{j+1,k}) + \left(\frac{\xi_y}{J}\right)_{j+1/2} (G_{j,k} + G_{j+1,k}) + R_{j+1/2}\,\Phi_{j+1/2}\,{}^t J_{j+1/2} \right], (32)$$

where the last term is some numerical diffusion providing the TVD properties for the scheme. The MUSCL approach would replace the average of the fluxes at $j+1/2$ by the sum of the fluxes from right and left hand side information at $j+1/2$.

For hypersonic flow simulations enhancements of stability and convergence rates are necessary in comparison with transonic and supersonic flow simulations, see [82] for details. Figures 12 and 13 show
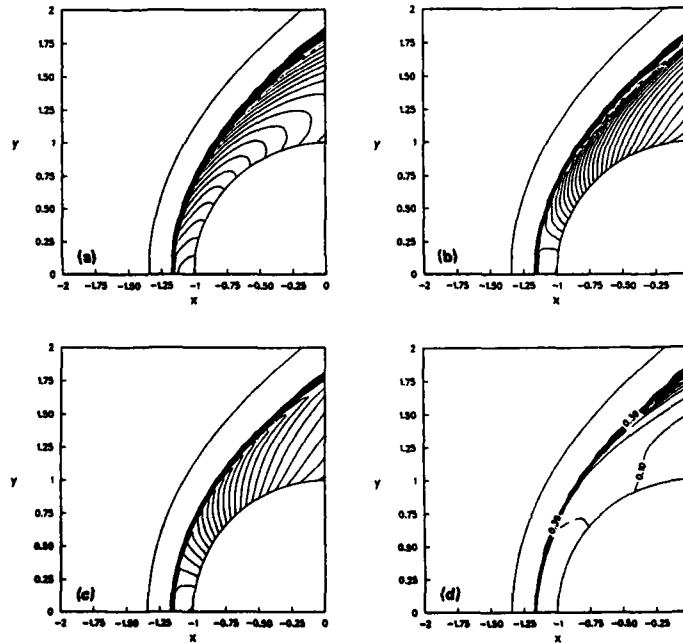

Fig.12: Mach contours (a), density contours (b), pressure contours (c) and k (d) computed with an implicit TVD scheme ($\theta = 1, \omega = 0$) for an equilibrium real gas at $M_\infty = 25$ [82]. ($p_\infty = 1220N/m^2$, $\rho_\infty = 0.0188kg/m^3$, $T_\infty = 226K$).
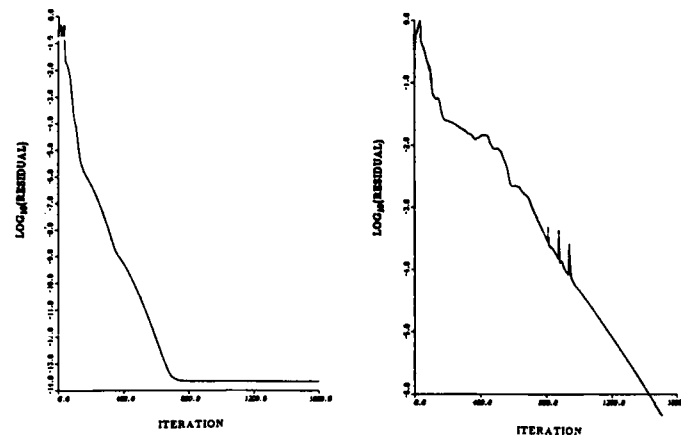
Fig.13: Convergence history corresponding to the solution of figure 12, note the different scales for the ordinates [82].

sample results for a first-order implicit solution for a M = 25 flow past a 2-D blunt body where the mesh is fixed using shock capturing. Note that the real gas simulation requires roughly 25 times as many time steps to obtain a drop in residual by six orders, see figure 13. This is interpreted in [82] to be possibly influenced by the "glitches" in the thermodynamic representations of Tannehill and coworkers. The bow shock wave is nicely captured because one family of the grid lines is nearly aligned with the shock wave.

It is noted that with this type of scheme perfect gas simulations have been carried out for steady and unsteady shock-on-shock interaction for hypersonic Mach number flow past a blunt (2-D) body based on shock capturing [52,61]. Owing to the strong shocks a mesh adaptation was necessary which aligned the coordinates with the shock structure locally. This was achieved by applying the spring concept of Nakahashi and Deiwert.

5.3 Non-Equilibrium Flow Simulations

In [150] an analysis of numerical formulations of time-dependent conservation laws for non-equilibrium flow computations is carried out. From the present list of references two computational approaches are picked for discussion which treat three-dimensional flows. One is the approach of Candler and MacCormack [65,96,97], the other one is associated with Yee [83,86,117], see also [103].
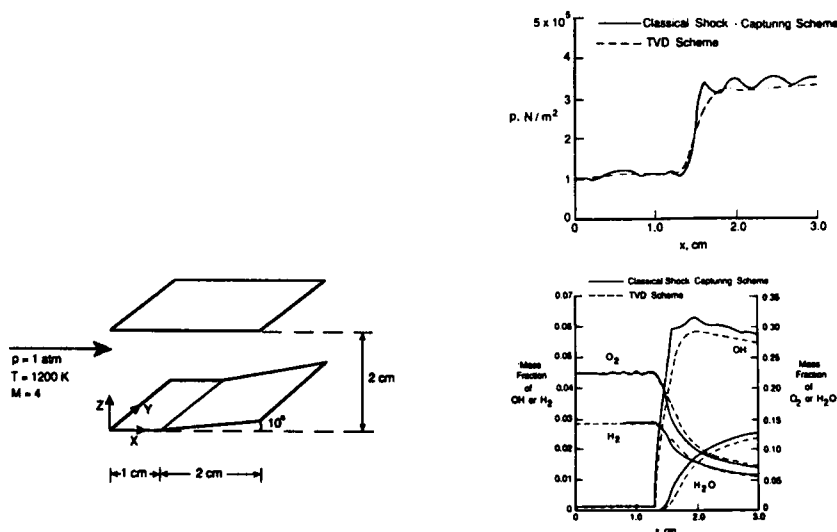
Fig.14: Comparison of pressure (top) and species mass fractions (bottom) for a scramjet type flow (left) of air oxidizing hydrogen [117]. $Z = 0.13$ cm.
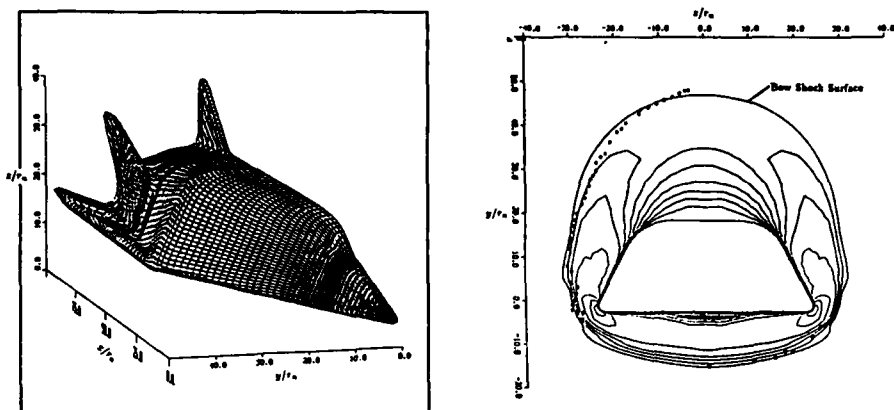
Fig.15: Results for the ideal-gas flow simulation for the X24C body [65]. Left: body surface, right: Pitot pressure survey in front of the fins. o Experiment by Carver. $M_\infty = 5.95$, $\alpha = 6°$, $Re = 16.4 \cdot 10^6/m$.
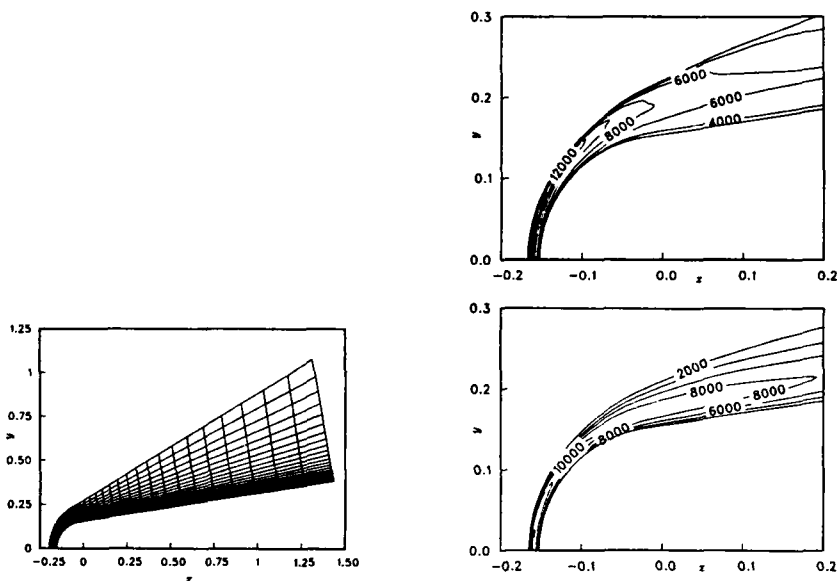
Fig.16: Results for the non-equilibrium flow past a sphere-cone [96]. Mesh (left), contours of translational temperature (top) and of vibrational temperature of N_2 (bottom). $M_\infty = 25.9$, $Re = 6280$, $H = 71km$.

Considering the solution of the combined fluid mechanical and chemical problem it is not clear whether it is more suitable to solve the set of coupled equations, or to solve the fluid dynamical equations and the remaining equations, separately. The intuition favors the coupled solution which should improve the convergence, see also [83]. The typical equations for the conservation of species including the form of the stiff source terms, and the equations for the vibrational energies can be found elsewhere in the proceedings. This holds also for the formulation of the multicomponent transport coefficients, see also [168]. It is noted that according to [42, 43] it is possible to extend the range of validity of the transport coefficients by determining the collision integrals and other statistical quantities new with more accurate methods.

In [83] and [117] a semi-implicit shock-capturing algorithm for the fully coupled governing equations in generalized coordinates is proposed which can be viewed as the explicit predictor-corrector MacCormack scheme with a more appropriate numerical dissipation for the computation of strong shock waves and an implicit source term treatment for stability. In the formulation of the problem the global mass conservation equation is replaced by all species continuty equations. The shock-capturing technique is a second-order accurate, total variation deminishing (TVD) method which considers fully and

directly the coupling of the fluid and the species equations. Note that the diffusion terms are central differenced without influence from the TVD terms, as is usual. For a detailed description see [117], where a more efficient procedure than anticipated is given as well. This method is applied to a five species oxidation of H_2 in a scramjet related test case, see figure 14. In this figure the improved shock capturing capabilities are clearly seen. It remains to be shown how the procedure works for high hypersonic speeds with stronger shocks. A word of caution is expressed in [86] where this method is said to produce incorrect numerical propagation speeds of discontinuities for a model problem. This is shown to be associated with insufficient local mesh resolution of the discontinuity for the evaluation of the TVD-producing numerical diffusion terms. One alternative is to use mesh adaptation, the other is to reformulate the diffusion terms.

Candler and MacCormack [65] have developed an implicit numerical method to integrate the three-dimensional time-dependent Navier-Stokes equations using flux-splitting and shock fitting. The flux-splitting is due to Steger-Warming, and is used in a second-order formulation in all spatial directions. Although the origin is referred to the reference [169] where a corresponding predictor-corrector version is described, this property is not obvious from reading [65]. Shock-fitting is employed to prevent oscillations near the strong bow shock and to capture the very strong gradients in the flow variables near the bow shock wave. A compatibility equation is used for the outward running characteristic to obtain a relation for the pressure behind the shock. The method is fully implicit using Gauß-Seidel line relaxation to invert the implicit coefficient matrix. Note that explicitly added numerical diffusion is not needed due to the flux-splitting. The method has been applied to the hypersonic ideal-gas flow past the X24C body [65], see figure 15.

This method has been extended in two dimensions to simulate hypersonic ionized flows in chemical and thermal non-equilibrium. The chemical and thermal source terms are treated in an implicit fashion so that the stiff chemical source terms do not degrade convergence to steady state. Note that the bow shock wave is captured with the help of the diffusive Steger-Warming flux-splitting, and not fitted. For the following application this is probably not important because the show wave is anyway aligned with the surface-fitted grid. 2-D results have been obtained for a five-species composition of air (N_2, O_2, NO, O, N) and three vibrational temperatures. Further results are obtained with NO ionized thus increasing the number of species by two and the temperatures by two as well (NO^+, e^-). The set of equations used has been taken and modelled following [36]. Figure 16 shows the obtained results in term of contours of temperatures.

An interesting approach is pursued in [100] where the flow field in chemical non-equilibrium is computed by first obtaining solutions for approximate (non-stiff) chemical source terms.

6. CONCLUDING REMARKS

This paper points out the difficulties encountered by computational fluid dynamics for the numerical simulation of hypersonic flows in comparison with the classical ideal-gas simulations e.g. for transonic free-stream. Thereby the main interest is focussed on the numerical integration of the time-dependent Navier-Stokes equations although the involved numerical techniques for the corresponding convective terms have, originally, been developed for inviscid flow simulations. Such solutions are expected to help to minimize the efforts of the designer of future spacecrafts. There seems to be still a long way to go. Several reasons are responsible for this regardless of the ever growing computer capabilities. There are, in particular, the uncertainties with regard to the thermo-physical modelling of air including the availability of appropriate transport and surface property and chemical kinetics data for the range of interest, e.g. for reentry vehicles. Also a lack of transition and turbulence modelling has to be noted in this context. The capabilities of numerical methods to simulate high-speed ideal-gas flows in three dimensions shows that there is a large potential to do realistic hypersonic flow simulations as well. However, some of the new developments, involving flux-split relaxation schemes, have profited from the gas law for (thermally) perfect gases, and need generalizations for use in non-equilibrium reacting air calculations. Therefore it is not surprising to see the old explicit 2-step MacCormack scheme survive improved by combination with a TVD procedure and implicit treatment of the species source terms. A question of major concern is whether the methods can live with strong shocks, bow shock waves as well as embedded ones. This is shown to be possible for some methods if the grid system is adapted such that grid lines are roughly aligned with the shock structure locally. It is interesting to note that a scheme which uses bow-shock-wave fitting for ideal gases gives up this if used for non-equilibrium flow. All these technical questions will undoubtedly find positive answers, sooner or later.

The author believes, however, that owing to the uncertainties in physical modelling dedicated experiments have to be designed to systematically validate CFD-methods in order to avoid again discrepancies between preflight analysis based on advanced numerical techniques and flight data. First moves are made in this direction wherever there is interest in space vehicles in spite of the instrumental difficulties to simulate real flight experimentally.

7. REFERENCES

[1] Koppenwallner, G.: "Rarefied Gas Dynamics". Notes, 1st Joint Europe-US Short Course on Hypersonics. ESA, Paris, December 7-11, 1987.

[2] Arrington, J.P.; Jones, J.J. (eds.): "Shuttle Performance: Lessons Learned". Part I and II, NASA CP 2283, 1983.

[3] Griffith, B.J.; Maus, J.R.; Majors, B.M.; Best, J.T.: "Addressing the Hypersonic Simulation Problem". J. Spacecraft, Vol. 24, No. 4, pp. 334-341, 1987.

[4] Sutton, K.; Zoby, E.V.; Hamilton, H.H.: "Overview of CFD Methods and Comparisons with Flight Aerothermal Data". AGARD CP-437, Paper 13, 1988.

[5] Langereux, P.: "Europe Aims for Space Independence". Aerospace America, Vol. 10, Special Report, February 1986.

[6] Perrier, P.; Caupenne, Ph.: "Concepts Generaux Aérodynamiques - Aérothermiques D'Hermes". AGARD CP-428, Paper 33, 1987.

[7] DeMeis, R.: "HOTOL: the other Aerospaceplane". Aerospace America, pp. 10-12, July 1986.

[8] Wake, A.J.: "Hypersonic Aerodynamics - Applications for HOTOL". AGARD CP-428, Paper 34, 1987.

[9] Vogels, H.A.: "Von der Mikrosystemtechnik zum Raumtransporter Sänger II". Luft- und Raumfahrt, Jahrgang 7, Heft 4-86, S.99-108, 1986.

[10] Högenauer, E.: "Raumtransporter". ZFW, Vol. 11, S. 309-316, 1987.

[11] Williams, R.M.: "National Aero-Space Plane - Technology for America's Future". Aerospace America, pp. 18-22 , November 1986.

[12] Jones, R.A.; Donaldson, C. du P.: "From Earth to Orbit in a Single Stage". Aerospace America, pp. 32-34, August 1987.

[13] Dwoyer, D.L.; Kumar, A.: "Computational Analysis of Hypersonic Airbreathing Aircraft Flow Fields". AIAA Paper 87-0279, 1987.

[14] Rieger, H.; Jameson, A.: "Solution of Steady Three-Dimensional Compressible Euler and Navier-Stokes Equations by an Implicit LU-Scheme". AIAA Paper 88-0619, 1988.

[15] Dwoyer, D.L.; Kutler, P.; Povinelli, L.A.: "Retooling CFD for hypersonic aircraft". Aerospace America, pp. 32-35, 41, October 1987.

[16] White, M.E.; Drummond, J.P.; Kumar, A.: "Evolution and Application of CFD Techniques for Scramjet Engine Analysis". Journal Propulsion and Power, Vol. 3, No. 5, pp. 423-439, 1987.

[17] Davis, N.W.: "Japan takes charge". Aerospace America, pp. 22-26, March 1988.

[18] Bogdonoff, S.M.: "Technical Evaluation Report on the Fluid Dynamics Panel Symposium on Aerodynamics of Hypersonic Lifting Vehicles". AGARD AR 246, 1988.

[19] Witcliff, C.E.: "A Survey of Existing Hypersonic Ground Test Facilities - North America". AGARD CP-428, Paper 1, 1987.

[20] Wendt, J.F.: "European Hypersonic Windtunnels". AGARD CP-428, Paper 2, 1987.

[21] Stalker, R.J.: "Shock Tunnels for Real Gas Hypersonics". AGARD CP-428, Paper 4, 1987.

[22] Deiwert, G.S.; Strawa, A.W.; Sharma, S.P.; Park, C.: "Experimental Program for Real Gas Flow Code Validation at NASA Ames Research Center". AGARD CP-437, Paper 21, 1988.

[23] - : "Applications of Computational Fluid Dynamics in Aeronautics". AGARD CP-412, 1986.

[24] - : "Aerodynamics of Hypersonic Lifting Vehicles". AGARD CP-428, 1987.

[25] - : Proceedings. AIAA 8th Computational Fluid Dynamics Conference. AIAA CP 874, 1987.

[26] Hirschel, E.H.: "Aerothermodynamische Probleme bei Hyperschall-Fluggeräten". Jahrestagung der DGLR, 9./10.10.1986, München. (MBB S/PUB/270).

[27] Koppenwallner, G.: "Aerothermodynamik - Ein Schlüssel zu neuen Transportgeräten der Luftund Raumfahrt". ZFW, Vol. 12, S. 6-18, 1988.

[28] Bird, G.A.: "Low Density Aerothermodynamics". AIAA Paper 85-0994, 1985.

[29] Koppenwallner, G.: "Low Reynolds Number Influence on Aerodynamic Performance of Hypersonic Vehicles". AGARD CP-428, Paper 11, 1987.

[30] Bertin, J.J.: "General Characterization of Hypersonic Flows". Notes, 1st Joint Europe-US Short Course on Hypersonics. ESA, Paris December 7-11, 1987.

[31]   Vincenti, W.G.; Kruger, C.H.: "Introduction to Physical Gasdynamics". John Wiley and Sons, New York, 1965.

[32]   Riedelbauch, S.; Wetzel, W.; Kordulla, W.; Oertel, H. Jr.: "On the Numerical Simulation of Three-Dimensional Hypersonic Flow". AGARD CP-428, Paper 19, 1987.

[33]   Cousteix, J.; Aupoix, B.: "Calculations of Hypersonic Laminar Boundary Layers". Notes, 1st Joint Europe-US Short Course on Hypersonics. ESA, Paris, December 7-11, 1987.

[34]   Sarma, G.S.R.: "Some Problems of Continuing Interest in Hypersonics". DFVLR-IB 221-88, A 08, 1988.

[35]   Nelson, H.F. (ed.): "Thermal Design of Aeroassisted Orbital Transfer Vehicles". Progress in Astronautics and Aeronautics, Vol. 96, AIAA, Inc., New York, 1985.

[36]   Lee, J.-H.: "Basic Governing Equations for the Flight Regimes of Aeroassisted Orbital Transfer Vehicles". AIAA Paper 84-1729, 1984.

[37]   Deiwert, G.S.; Green, M.J.: "Computational Aerothermodynamics". NASA TM 89450, 1987.

[38]   Bussing, T.R.A.; Eberhardt, S.: "Chemistry Associated with Hypersonic Vehicles". AIAA Paper 87-1292, 1987.

[39]   Graves, R.A.; Hunt, J.L.: "NASA's Hypersonic Fluid and Thermal Physics Program (Aerothermodynamics)". AIAA Paper 85-0922, 1985.

[40]   Scott, C.D.: "A Review of Nonequilibrium Effects and Surface Catalysis on Shuttle Heating". In [2], pp. 865-889, 1983.

[41]   Scott, C.D.: "The Effects of Thermochemistry, Nonequilibrium, and Surface Catalysis in the Design of Hypersonic Vehicles". Notes, 1st Joint Europe-US Short Cource on Hypersonics. ESA, Paris, December 7-11, 1987.

[42]   Bruno, C.: "Real Gas Effects". Notes, 1st Joint Europe-US Short Course on Hypersonics. ESA, Paris, December 7-11, 1987.

[43]   Bruno, C.: "Nonequilibrium Chemically Reacting Flows". VKI-Lecture Series on CFD, March 2-6, 1987, von Karman Inst. for Fluid Dynamics, Rhode-St-Genèse, Belgium.

[44]   Romere, P.O.; Whitnah, A.M.: "Space Shuttle Entry Longitudinal Aerodynamic Comparisons of Flights 1-4 with Preflight Predictions". In [2], pp. 283-307, 1983.

[45]   Woods, W.C.; Arrington, J.P.; Hamilton II, H.H.: "A Review of Preflight Estimates of Real-Gas Effects on Space Shuttle Aerodynamic Characteristics". In [2], pp. 309-346, 1983.

[46]   Graves, R.A. Jr.; Hunt, J.L.; Wander, S.M.: "Hypersonic Aerothermodynamics Status Report". Proceedings, 18th Annual Electronics and Aerospace Systems Conference, Washington, D.C., Oct. 28-30, 1985.

[47]   Arnold, J.O.: "Computational Chemistry". NASA CP 2454, pp. 299-311, 1987.

[48]   Bray, K.N.C.: "Chemical and Vibrational Nonequilibrium in Nozzle Flows". In: Wegener, P.P. (ed.), Nonequilibrium Flows. Part II. Marcel Dekker, Inc., New York, pp. 60-157, 1970.

[49]   Rudy, D.H.; Kumar, A.; Thomas, J.L.; Gnoffo, P.A.; Chakravarthy, S.R.: "A Comparative Study and Validation of Upwind and Central-Difference Navier-Stokes Codes for High-Speed Flows". AGARD CP-437, Paper 38, 1988.

[50]   Vinokur, M.: "An Analysis of Finite-Difference and Finite-Volume Formulations of Conservation Laws". NASA CR 177416, 1986.

[51]   Szema, K.Y.; Chakravarthy, S.R.; Pan, D.; Bihari, B.L.; Riba, W.T.; Akdag, V.M.; Dresser, H.S.: "The Application of a Unified Marching Technique for Flow Over Complex 3-Dimensional Configurations Across the Mach Number Range". AIAA Paper 88-0276, 1988.

[52]   Klopfer, G.H.; Yee, H.C.: "Viscous Hypersonic Shock-On-Shock Interaction on Blunt Cowl Lips". AIAA Paper 88-0233, 1988.

[53]   Hung, C.M.; Barth, T.J.: "Computation of Hypersonic Flow Through a Narrow Expansion Slot". AIAA Paper 88-0232, 1988.

[54]   Shirazi, S.A.; Truman, C.R.: "A Study of Algebraic and Half-Equation Turbulence Models for Hypersonic PNS Predictions". AIAA Paper 88-0222, 1988.

[55]   Stewart, J.R.; Thareja, R.R.; Wieting, A.R.; Morgan, K.: "Application of Finite Element and Remeshing Technique to Shock Interference On a Cylindrical Leading Edge". AIAA Paper 88-0368, 1988.

[56]   Newberry, C.F.; Dresser, H.S.; Byerly, J.W.; Riba, W.T.: "The Evaluation of Forebody Compression at Hypersonic Mach Numers". AIAA Paper 88-0479, 1988.

[57] Hindmann, R.G.: "On Shock Capturing Methods and Why They Work". AIAA Paper 88-0622, 1988.

[58] Walters, R.W.; Ren, T.; McGrory, W.D.; Thomas, J.L.; Richardson, P.F.: "A Longitudinally - Patched Grid Approach with Applications to High-Speed Flows". AIAA Paper 88-0715, 1988.

[59] Bush, K.H.; Vogel, P.G.; Norby, W.P.; Haeffele, B.A.: "Two Dimensional Numerical Analysis for Inlets at Subsonic Through Hypersonic Speeds". AIAA Paper 87-1751, 1987.

[60] Leer, B. van; Thomas, J.L.; Roe, P.L.; Newsome, R.W.: "A Comparison of Numerical Flux Formulas for the Euler and Navier-Stokes Equations. AIAA Paper 87-1104, 1987.

[61] Klopfer, G.H.; Yee, H.C.; Kutler, P.: "Numerical Study of Unsteady Viscous Hypersonic Blunt Body Flows with an Impinging Shock". NASA TM 100096, 1988.

[62] Chaussee, D.S.: "NASA Ames Research Center's Parabolized Navier-Stokes Code: A Critical Evaluation of Heat-Transfer Predictions". AIAA Paper 87-1474, 1987.

[63] Montagné, J.L.: "Recherches Fondamentales sur des Méthodes de Calcul pour des Ecoulements Supersoniques et Hypersoniques". ONERA RSF 23/1285 AY, 1985.

[64] Johnston, P.J.; Whitehead, A.H.; Chapman, G.T.: "Fitting Aerodynamics and Propulsion into the Puzzle". Aerospace America, pp. 32-37, 42, Sept. 1987.

[65] Candler, G.V.; MacCormack, R.W.: "Hypersonic Flow Past 3-D Configurations". AIAA Paper 87-0480, 1987.

[66] Yee, H.C.: "Upwind and Symmetric Shock-Capturing Schemes". NASA TM 89464, 1987.

[67] Penner, S.S.: "Introduction To The Study Of Chemical Reactions In Flow Systems". Pergamon Press Book, 1957.

[68] Prabhu, D.K.; Tannehill, J.C.; Marvin, J.G.: "A New PNS Code for Three-Dimensional Chemically Reacting Flows". AIAA Paper 87-1472, 1987.

[69] Scrinivasan, S.; Tannehill, J.C.; Weilmuenster, K.J.: "Simplified Curve Fits for the Thermodynamic Properties of Equilibrium Air". NASA RP 1181, August 1987.

[70] Scrinivasan, S.; Tannehill, J.C.; Weilmuenster, K.J.: "Simplified Curve Fits for the Thermodynamic Properties of Equilibrium Air. Final Report". NASA CR 180422, Sept. 1987.

[71] Tannehill, J.C.; Mugge, P.H.: "Improved Curve Fits for the Aerodynamic Properties of Equilibrium Air Suitable for Numerical Computation Using Time-Dependent or Shock-Capturing Methods". NASA CR 2470, Oct. 1974.

[72] Scrinivasan, S.; Tannehill, J.C.; Weilmuenster, K.J.: "Simplified Curve Fits for the Thermodynamic Properties of Equilibrium Air". ISU-ERI-Ames 86401, ERI Project 1626, June 1986.

[73] Prabhu, D.K.; Tannehill, J.C.: "Numerical Simulation of Space Shuttle Orbiter Flowfield Including Real-Gas Effects". Journal Spacecraft, Vol. 23, No. 3, pp. 264-272, 1986 (also AIAA Paper 84-1747, 1984).

[74] Ota, D.K.; Chakravarthy, S.R.; Darling, J.C.: "An Equilibrium Air Navier-Stokes Code for Hypersonic Flows". AIAA 88-0419, 1988.

[75] Shuen, J.S.; Yoon, S.: "Numerical Study of Chemically Reacting Flows Using an LU Scheme". AIAA Paper 88-0436, 1988.

[76] Vinokur, M.; Liu, Y.: "Equilibrium Gas Flow Computations II: "An Analysis of Numerical Formulations of Conservation Laws". AIAA Paper 88-0127, 1988.

[77] Vinokur, M.; Montagné, J.-L.: "Generalized Flux-Vector Splitting for an Equilibrium Real Gas". Preliminary draft version, to appear as NASA TM.

[78] Vinokur, M.: "Flux Jacobian Matrices and Generalized Roe Average for an Equilibrium Real Gas". Preliminary draft version, to appear as NASA CR.

[79] Tannehill, J.C.; Jevalts, J.O.; Lawrence, S.L.: "An Upwind Parabolized Navier-Stokes Code for Real Gas Flows". AIAA Paper 88-0713, 1988.

[80] Wilson, G.J.; Davis, W.H.: "Hypersonic Forebody Performance Sensitivities Based on 3-D Equilibrium Navier-Stokes Calculations". AIAA Paper 88-0370, 1988.

[81] Montagné, J.-L.; Yee, H.C.; Vinokur, M.: "Comparative Study of High-Resolution Shock-Capturing Schemes for a Real Gas". NASA TM 100004, 1987.

[82] Yee, H.C.; Klopfer, G.H.; Montagné, J.-L.: "High-Resolution Shock-Capturing Schemes for Inviscid and Viscous Hypersonic Flows". NASA TM 100097, 1988.

[83] Yee, M.C.; Shinn, J.L.: "Semi-Implicit and Fully Implicit Shock-Capturing Methods for Hyperbolic Conservation Laws With Stiff Source Terms". AIAA Paper 87-1116, 1987. (also: NASA TM 89415, 1986).

[84]   Gnoffo, P.A.: "Hypersonic Flows Over Biconics Using a Variable-Effective-Gamma, Parabolized - Navier-Stokes Code". AIAA Paper 83-1666, 1983.

[85]   Eberhardt, S.; Brown, K.: "A Shock Capturing Technique for Hypersonic, Chemically Relaxing Flows". AIAA Paper 86-0231, 1986.

[86]   LeVeque, R.J.; Yee, H.C.: "A Study of Numerical Methods for Hyperbolic Conservation Laws with Stiff Source Terms". NASA TM 100075, 1988.

[87]   Montagné, J.-L.; Yee, H.C.; Klopfer, G.H.; Vinokur, M.: "Hypersonic Blunt Body Computations Including Real Gas Effects". NASA TM 100074, 1988.

[88]   Palmer, G.: "An Implicit Flux-Split Algorithm to Calculate Hypersonic Flowfields in Chemical Equilibrium". AIAA Paper 87-1580, 1987.

[89]   Grossman, B.; Walters, R.W.: "An Analysis of Flux-Split Algorithms for Euler's Equations with Real Gases". AIAA Paper 87-1117, 1987.

[90]   Hollanders, H.; Maraffa, L.; Montagné, J.-L.; Morice, Ph.; Viviand, H.: "Computational Methods for Hypersonic Flow - Special Techniques and Real Gas Effects". Notes, 1st Joint Europe-US Short Course on Hypersonics. ESA, Paris, December 7-11, 1987.

[91]   Pfitzner, M.; Weiland, C.: "3-D Euler Solution for Hypersonic Mach Numbers". AGARD CP-428, Paper 22, 1987.

[92]   Liou, M.-S.; Leer, B. van; Shuen, J.-S.: "Splitting of Inviscid Fluxes for Real Gases". NASA TM 100856, 1988.

[93]   Lordi, J.A.; Boyer, D.W.; Dunn, M.G.: "Description of Nonequilibrium Effects on Simulation of Flows about Hypersonic Vehicles". AIAA Paper 88-0476, 1988.

[94]   Shang, J.S.; Josyula, E.: "Numerical Simulation of Non-Equilibrium Hypersonic Flow Past Blunt Bodies". AIAA Paper 88-0512, 1988.

[95]   York, B.J.; Sinha, N.; Dash, S.M.: "Computational Models for Chemically-Reacting Hypersonic Flow". AIAA 88-0509, 1988.

[96]   Candler, G.V.; MacCormack, R.W.: "The Computation of Hypersonic Ionized Flows in Chemical and Thermal Nonequilibrium". AIAA Paper 88-0511, 1988.

[97]   Candler, G.V.; MacCormack, R.W.: "The Computation of Hypersonic Flows in Chemical and Thermal Nonequilibrium". 3rd National Aero-Space Plane Technology Symposium, NASA, Ames,June 2-4, Paper 107, 1987.

[98]   Gökçen, T.; MacCormack, R.W.; Chapman, D.R.: "Computational Fluid Dynamics Near the Continuum Limit". AIAA Paper 87-1115, 1987.

[99]   Botta, N.; Pandolfi, M.; Germano, M.: "Nonequilibrium Reacting Hypersonic Flow About Blunt Bodies: Numerical Prediction". AIAA Paper 88-0514, 1988.

[100]   Krispin, J.; Anderson, J.D., Jr.: "Accelerating the Computation of Steady State Solutions for Non-Equilibrium, Chemically Reacting Flow Fields". AIAA Paper 88-0513, 1988.

[101]   Prabhu, D.K.; Tannehill, J.C.; Marvin, J.G.: "A New PNS Code for Chemical Nonequilibrium Flows". AIAA Paper 87-0284, 1987.

[102]   Shinn, J.L.; Simmonds, A.L.: "Comparison of Viscous-Shock-Layer Heating Analysis with Shuttle Flight Data in Slip Flow Regime". AIAA Paper 84-0226, 1984.

[103]   Gnoffo, P.A.; McCandless, R.S.; Yee, H.C.: "Enhancements to Program LAURA for Computation of Three-Dimensional Hypersonic Flow". AIAA Paper 87-0280, 1987.

[104]   Yu, S.-T.; McBride, B.J.; Hsieh, K.-C.; Shuen, J.-S.: "Numerical Simulation of Hypersonic Inlet Flows with Equilibrium or Finite Rate Chemistry". AIAA Paper 88-0273, 1988.

[105]   Marraffa, L.; Dulikravich, G.S.; Deiwert, G.S.: "Numerical Simulation of Two-Dimensional Viscous, Unsteady Dissociating Nitrogen Flows". AIAA Paper 87-2549, 1987.

[106]   Thompson, R.A.; Zoby, E.V.; Wurster, K.E.; Gnoffo, P.A.: "An Aerothermodynamic Study of Slender conical Vehicles". AIAA Paper 87-1475, 1987.

[107]   Peery, K.M.; Imlay, S.T.; Katsandres, J.T.: "Real-Gas Blunt-Body Flow Simulations". AIAA Paper 87-2179, 1987.

[108]   Gnoffo, P.A.: "Application of Program LAURA to Three-Dimensional AOTV Flow Fields". AIAA Paper 86-0565, 1985.

[109]   Drummond, J.P.; Hussaini, M.Y.: "Numerical Simulation of a Supersonic Reacting Mixing Layer". AIAA Paper 87-1325, 1987.

[110]   Drummond, J.P.; Rogers, R.C.; Hussaini, M.Y.: "A Numerical Model for Supersonic Reacting Mixing Layers". Comp. Meth. Appl. Mech. and Engineering, Vol. 64, pp. 39-60, 1987.

[111] Park, C.: "On Convergence of Computation of Chemically Reacting Flows". AIAA Paper 85-0247, 1985.

[112] Park, C.: "Radiation Enhancement by Nonequilibrium in Earth's Atmosphere". J. Spacecraft, Vol. 29, No. 1, pp. 27-36, 1985.

[113] Park, C.: "Calculation of Nonequilibrium Radiation in AOTV Flight Regimes". AIAA Paper 84-0306, 1984.

[114] Park, C.: "Problems of Rate Chemistry in the Flight Regimes of Aeroassisted Orbital Transfer Vehicles". AIAA Paper 84-1730, 1984.

[115] Park, C.: "Assessment of Two-Temperature Kinetic Model for Dissociating and Weakly-Ionizing Nitrogen". AIAA Paper 86-1347, 1986.

[116] Kim, M.D.; Swaminathan, S.; Lewis, C.H.: "Viscous Shock-Layer Predictions of Three-Dimensional Nonequilibrium Flows Past the Space Shuttle at High Angle of Attack". In [2], pp. 805-825.

[117] Shinn, J.L.; Yee, H.C.; Uenishi, K.: "Extension of a Semi-Implicit Shock-Capturing Algorithm for 3-D Fully Coupled, Chemically Reacting Flows in Generalized Coordinates". AIAA Paper 87-1577, 1987.

[118] Matsuzaki, R.; Hirabayashi, N.: "Prediction of Temperatures and Velocity in a Nonequilibrium Nozzle Flow of Air". AIAA Paper 87-1477, 1987.

[119] Glaz, H.M.; Colella, P.; Collins, J.P.; Ferguson, R.E.: "High Resolution Calculations of Unsteady, Two-Dimensional Nonequilibrium Gasdynamics with Experimental Comparisons". AIAA Paper 87-1293, 1987.

[120] Balakrishnan, A.: "Application to a Flux-Split Algorithm to Chemically Relaxing, Hypervelocity Blunt-Body Flows". AIAA Paper 87-1578, 1987.

[121] Gupta, R.N.: "Navier-Stokes and Viscous Shock-Layer Solutions for Radiating Hypersonic Flows". AIAA Paper 87-1576, 1987.

[122] Thompson, R.A.: "Comparison of Non-Equilibrium Viscous-Shock-Layer Solutions with Windward Surface Shuttle Heating Data". AIAA Paper 87-1473, 1987.

[123] Radhakrishnan, K.: "Integrating Combustion Kinetic Rate Equations by Selective Use of Stiff and Nonstiff Methods". AIAA Journal, Vol. 25, No. 11, pp. 1449-1455, 1987.

[124] Bell, J.B.; Colella, P.; Traugenstein, J.A.; Welcome, M.: "Adaptive Methods for High Mach Number Reacting Flow". AIAA Paper 87-1168, 1987.

[125] Kuntz, D.W.; Polansky, G.F.; Buffington, R.J.: "A Comparison of Predicted and Measured Aero-heating on a Reentry Vehicle Flap Geometry". AIAA Paper 87-0517, 1987.

[126] Swaminathan, S.; Song, D.J.; Lewis, C.H.: "High Altitude Effects on Three-Dimensional Nonequilibrium Viscous Shock-Layer Flows". AIAA Paper 84-0304, 1984.

[127] Gupta, R.N.; Moss, J.N.; Simmonds, A.L.; Shinn, J.L.; Zoby, E.V.: "Space Shuttle Heating Analysis with Variation in Angle of Attack and Surface Condition". AIAA Paper 83-0486, 1983.

[128] Eklund D.R.; Hassan, H.A.; Drummond, J.P.: "The Efficient Calculation of Chemically Reacting Flow". AIAA Paper 86-0563, 1986.

[129] Gnoffo, P.A.; McCandless, R.S.: "Three-Dimensional AOTV Flowfields in Chemical Nonequilibrium". AIAA Paper 86-0230, 1986.

[130] Li, C.P.: "Chemistry-Split Techniques for Viscous Reactive Blunt Body Flow Computations". AIAA Paper 87-0282, 1987.

[131] Dwyer, H.; Otey, G.: "A Numerical Study of the Interaction of Fast Chemistry and Diffusion". AIAA Paper 78-946, 1978.

[132] Li, C.P.: "Computation of Hypersonic Flow Fields". Notes, 1st Joint Europe-US Short Course on Hypersonics. ESA, Paris, December 7-11, 1987.

[133] Ford, D.J.; Johnson, R.E.: "Dependence of Rate Constants on Vibrational Temperatures; An Arrhenius Description". AIAA Paper 88-0461, 1988.

[134] Oertel, H. Jr.: "Oxygen Vibrational and Dissociation Relaxation Behind Regular Reflected Shocks". JFM, Vol. 74, pp. 477-495, 1976.

[135] Hornung, H.: "High Enthalpy Wind Tunnel for the Simulation of Chemical Nonequilibrium Effects, HEG". DFVLR-IB 222-86 A 43, 1986.

[136] Levin, E.; Partridge, H.; Stallcop, J.R.: "High Temperature Transport Properties of Air". AIAA Paper 87-1632, 1987.

[137] Warnatz, J.: "Air Dissociation, Thermochemistry and Problems Resulting from the Coupling of Flow and Chemistry". Notes, 1st Joint Europe-US Short Course on Hypersonics. ESA, Paris, December 7-11, 1987.

[138] Biolsi, L.; Biolsi, D.: "Transport Properties Of Ions". AIAA Paper 87-0409, 1987.

[139] Zoby, E.V.; Gupta, R.N.; Simmonds, A.L.: "Temperature Dependent Reaction-Rate Expression for Oxygen Recombination at Shuttle Entry Conditions". AIAA Paper 84-0224, 1984.

[140] Jaffe, R.L.: "The Calculation of High-Temperature Equilibrium and Nonequilibrium Specific Heat Data for N_2O_2 and NO". AIAA Paper 87-1633, 1987.

[141] Kee, R.J.; Dixon-Lewis, G.; Warnatz, J.; Coltrin, M.E.; Miller, J.A.: "A Fortran Computer Code Package for the Evaluation of Gas-Phase Multicomponent Transport Properties". Sandia Report SAND 86-8246, 1986.

[142] Kee, R.J.; Warnatz, J.; Miller, J.A.: "A Fortran Computer Code Package for the Evaluation of Gas-Phase Viscosities, Conductivities and Diffusion Coefficients". Sandia Report SAND 83-8209, 1983.

[143] Hornung, H.: "Laboratory Simulation of the Real Gas Effects of Re-entry". ESA SP-265, pp. 13-19, 1986.

[144] Zierep, J.: "Theorie der schallnahen und der Hyperschallströmungen". G. Braun Verlag, Karlsruhe, 1966.

[145] Hayes, W.D.; Probstein, R.F.: "Hypersonic Flow Theory. Vol. I, Inviscid Flows". 2nd edition, Academic Press, New York, 1966.

[146] Truitt, R.W.: "Hypersonic Aerodynamics". The Ronald Press Company, New York, 1959.

[147] Dorrance, W.H.: "Viscous Hypersonic Flow". McGraw-Hill Book Company, Inc., New York, 1962.

[148] Davis, R.T.: "Numerical Solution of the Hypersonic Viscous Shock-Layer Equations". AIAA J., Vol.8, No. 5, pp.843-851, 1970.

[149] Adams, J.C. Jr.; Martindale, W.R.; Mayne, A.W. Jr.; Marchand, E.O.: "Real-Gas Scale Effects on Shuttle Orbiter Laminar Boundary-Layer Parameters". AIAA J., Vol. 14, No. 5, pp.273-279, 1977.

[150] Liu, Y.; Vinokur, M.: "Nonequilibrium Flow Computations. I. An Analysis of Numerical Formulations of Conservation Laws". Draft version of a paper to be published in 1988.

[151] Bird, R.B.; Stewart, W.E.; Lightfoot, E.N.: "Transport Phenomena". J. Wiley & Sons, New York, 1960.

[152] Karman, Th. von: "Fundamental Equations in Aerothermochemistry". In: Selected Combustion Problems, Part 2, Butterworth Scientific Publications, pp. 167-184, 1956, or Collected Works on Theodore von Karman 1952-1963, VKI, Rhode-St-Genèse, pp. 131-150, 1975.

[153] Macrossan, M.N.; Stalker, R.J.: "Afterbody Flow of a Dissociating Gas Downstream of a Blunt Nose". AIAA Paper 87-0407, 1987.

[154] Rakich, J.V.; Lanfranco, M.J.: "Numerical Computation of Space Shuttle Laminar Heating and Surface Streamlines". J. Spacecraft and Rockets, Vol. 14, No 5, pp. 265-272, 1977.

[155] Krogmann, P.: "Aerodynamische Untersuchungen an Raumflugkörpern im Machzahlbereich Ma = 3 bis 10 bei hohen Reynoldszahlen." ZFW, Vol. 21, pp.81-88, 1973.

[156] Kordulla, W.: "Integration of the Navier-Stokes Equations in Finite-Volume Formulation". VKI LS 1987-04, Computational Fluid Dynamics, March 2-6, 1987, Rhode-St.-Genese.

[157] Viviand, H.: "Formes Conservatives des Equations de la Dynamique de Gaz". La Recherche Aérospatiale, No. 1974-1, pp. 65-66, 1974.

[158] Vinokur, M.: "Conservation equations of Gasdynamics in Curvilinear Coordinate Systems". J. Comp. Physics, Vol. 14, pp. 105-125, 1974.

[159] Anderson, D.A.; Tannehill, J.C.; Pletcher, R.H.: "Computational Fluid Mechanics and Heat Transfer". Hemisphere Publishing Corporation, McGraw-Hill Book Company, New York, 1984.

[160] Schönauer, W.; Spreuer, H.; Straub, D.; Adams, E.: "Die numerische Lösung der stationären laminaren Hyperschall-Grenzschichtgleichungen unter der Voraussetzung thermo-chemischen Gleichgewichts". DFVLR-FB 73-68, 1973.

[161] Hänel, D.; Schwane, R.; Seider, G.: "On the Accuracy of Upwind Schemes in Solutions of the Navier-Stokes Equations". AIAA Paper 87-1105, 1987.

[162] Schwane, R.; Hänel, D.: "Computaion of Viscous Supersonic Flow Around Blunt Bodies". 7th GAMM-Conference on Num. Meth. In Fluid Mechanics, Louvain-La-Neuve, 1987. To appear in Vieweg Verlag, Notes on Numerical Fluid Mechanics, 1988.

[163] Hänel, D.; Schwane, R.: "Computation of Hypersonic Viscous Flows". 1st Joint Europe - US Short Course On Hypersonics, ESA, Paris, December 7-11, 1987.

[164] Schröder, W.; Hänel, D.: "An Unfactored Implicit Scheme with Multigrid Acceleration for the Solution of the Navier-Stokes Equations". Computers and Fluids, Vol.15, pp.313-336, 1987.

[165] DaCosta, J.L.; Aimer de la Chevalerie, D.; Alziary de Roquefort, T.: "Ecoulement Tridimensionnel Hypersonique sur une Combinaison D'Ellipsoides". CEAT, Poitiers, Rapport No. 4RDMF86, 1987.

[166] Riedelbauch, S.; Müller, B.: "The Simulation of Three-Dimensional Viscous Supersonic Flow Past Blunt Bodies with a Hybrid Implicit / Explicit Finite-Difference Method". DFVLR-FB 87-32, 1987.

[167] Riedelbauch, S.; Müller, B.; Kordulla, W.: "Semi-Implicit Finite-Difference Simulation of Laminar Hypersonic Flow over Blunt Bodies". Proceedings, 11th ICNMFD, Williamsburg, Virginia, June 27 - July 1, 1988. To appear in Springer Verlag.

[168] Kordulla, W.: "Helium- und Wasserstoffwandstrahlen in atmosphärischen Grenzschichten". Dissertation, RWTH Aachen, FRG, 9.12.1974.

[169] MacCormack, R.W.: "Current Status of Numerical Solutions of the Navier-Stokes Equations". AIAA Paper 85-0032, 1985.

LAMINAR-TURBULENT TRANSITION PROBLEMS

IN SUPERSONIC AND HYPERSONIC FLOWS

by Daniel ARNAL

Office National d'Etudes et de Recherches Aérospatiales (ONERA)
Centre d'Etudes et de Recherches de Toulouse (CERT)
Departement d'Aérothermodynamique (DERAT)
?, avenue Edouard Belin
31055 TOULOUSE Cedex - FRANCE

SUMMARY

The lecture is devoted to a survey of theoretical and experimental problems related with boundary layer transition at high speeds. On the theoretical point of view, emphasis is given on the linear stability theory, which describes the first stages of the transition process. It allows to explain the effects of various factors affecting transition, such as wall cooling or bluntness. In incompressible flow, it is often associated with the e^n method for predicting transition onset. The extension of this method to compressible flows will be discussed.

As far as the experimental results are concerned, the main problem is that free-flight conditions are very difficult to simulate in conventional wind tunnels, where the transition location depends on the noise radiated by the nozzle walls. Typical experimental results are presented in order to illustrate the influence of unit Reynolds number, wall curvature, wall roughness, etc. Three-dimensional problems are also considered.

MAIN NOTATIONS

A	wave amplitude
f	frequency
hi	total enthalpy
k	roughness-element height
M	Mach number
P	pressure
p'	pressure fluctuation
R	unit Reynolds number
$Rx = \dfrac{u_e x}{\nu_e}$	
$R\delta_1 = \dfrac{u_e \delta_1}{\nu_e}$	Reynolds numbers
$R\theta = \dfrac{u_e \theta}{\nu_e}$	
$Tu = (\tilde{u}'/u)_e$	free-stream turbulence level
T	mean temperature
u, v, w	mean velocities in the x, y, z directions
u', v', w'	velocity fluctuations
x	longitudinal direction
y	direction normal to the wall
z	spanwise direction
U, W	mean velocities in the X, Z directions
X	direction normal to the leading edge
Z	attachment line direction
α, β	components of the wave number vector

two-dimensional flows

three-dimensional flows

δ boundary layer thickness

$$\delta_1 = \int_0^\delta (1 - \frac{\rho u}{\rho_e u_e})\,dy \qquad \text{displacement thickness}$$

$$\theta = \int_0^\delta \frac{\rho u}{\rho_e u_e} (1 - \frac{u}{u_e})\,dy \qquad \text{momentum thickness}$$

μ	viscosity
ν	kinematic viscosity
ρ	density
ϕ	angle of sweep
ϕ_w	wall heat flux
ψ	wave number direction
ω	circular frequency

Subscripts and superscript

aw	adiabatic wall
c	cone
cr	critical
e	boundary layer edge (equal to ∞ condition for flat plate case)
fp	flat plate
i	imaginary part
o	value at neutral stability point
r	real part
t	turbulent
T	transition onset
w	wall
∞	free-stream
$\sim$	root-mean-square value

1. INTRODUCTION

Since the classical experiments performed by OSBORNE REYNOLDS (1883), the instability of laminar flow and the transition to turbulence have maintained a constant interest in fluid mechanics problems . This interest results from the fact that transition controls important aerodynamic quantities such as drag or heat transfer. For example, the heating rates generated by a turbulent boundary layer may be several times higher than those for a laminar boundary layer, so that the prediction of transition is of great importance for hypersonic reentry spacecrafts, because the thickness of the thermal protection is strongly dependent upon the altitude where transition occurs. Drag reduction for supersonic aircrafts requires also a good knowledge of the transition mechanisms.

The present paper is devoted to a general survey of transition phenomena in supersonic and hypersonic flows. The subject is rather wide, and several review papers have described the state-of-the-art in the last years (MORKOVIN /1/ /2/, RESHOTKO /3/, MACK /4/, PATE /5/ ...). What we will try to do is to illustrate the two completely different faces of the transition problems at high speeds. On one side, we have the linear stability theory. It is based on the linearized NAVIER-STOKES equations and describes the behaviour of the normal modes which constitute the first appearance of boundary layer instability. The mathematical as well as the numerical problems involved in this theory become increasingly complex as the Mach number increases. On the other side, we have a large body of experimental results which are often difficult to analyze or to correlate; for practical purposes, these data have been used for developing fully empirical criteria, the accuracy of which is rather poor in many

circumstances.

The purpose of this article is to show how both aspects can be associated for a better understanding and a better prediction of the transition processes. For instance, the so-called "e^n method" is empirical in nature, but it includes results of the linear stability theory. From the experimental point of view, the development of measurement techniques and the improvement of the flow quality in wind tunnels make possible to confirm theoretical results. The first part of the paper summarizes the main elements of the linear stability theory ; in the following sections, typical experimental results are described in order to see if this theory is able (or unable) to explain the observed features in different situations.

2. FORMULATION OF LINEAR STABILITY THEORY

2.1. Historical background

The instability leading to transition starts with the growth of sinusoïdal disturbances, the existence of which has been first demonstrated by the experiments of SCHUBAUER and SKRAMSTAD (1948, /6/), in incompressible flow. In fact, the development of small, regular oscillations travelling in the laminar boundary layer was postulated by RAYLEIGH (1887) and PRANDTL (1921) many decades ago. Some years later, TOLLMIEN worked out a complete theory of boundary layer instability (1929) and SCHLICHTING calculated the total amplification of the most unstable frequencies (1933). For this reason, the instability waves are often referred to   the "TOLLMIEN-SCHLICHTING waves". A complete description of this pioneering work can be found in SCHLICHTING's book /7/. Nevertheless, the so-called "linear stability theory" received little acceptance, essentially because of the lack of experimental results. The experiments performed by SCHUBAUER and SKRAMSTAD completely revised this opinion by demonstrating that T.S. waves constitute the first stage of the transition process. In the last forty years, a large amount of work was devoted to a more and more complete understanding of the linear mechanisms occuring at low speeds.
In compressible flow, the problem becomes more complex. The first attempt to develop a compressible linear stability theory was made by KÜCHEMANN (1938). One of the most important theoretical investigation was carried out by LEES and LIN (1946, /8/), who used an asymptotic theory and deduced from the inviscid equations some fundamental results related with the "generalized inflexion point" (see below, paragraph 2.3.). Subsequent papers by LEES /9/, DUNN and LIN /10/, LEES and RESHOTKO /11/ were also based on asymptotic theories. However, as it was pointed out by MACK, "some major differences between the incompressible and compressible theories were not uncovered until extensive calculations had been carried out on the basis of a direct numerical solution of the differential equations". From 1960 to the present time, MACK performed a thorough numerical investigation of the linear stability characteristics of compressible laminar boundary layer /12/ to /17/ ; his most important finding is the discovery of the higher unstable modes at supersonic speeds. Compressible stability computations were recently published by MALIK /18/, /19/, GASPERAS /20/, /21/, ARNAL /22/, among others.

2.2. Stability equations

A complete account of the linear stability theory is out of the scope of this paper (see MACK's review papers /4/, /13/ for complete information). However, one needs to introduce some theoretical elements for a comprehensive study of the experimental results.

The principle is to introduce sinusoïdal small disturbances into the linearized state, continuity, momentum and energy equations, in order to compute the range of unstable frequencies. It is assumed that any fluctuation r' (velocity, pressure, density or temperature) is expressed by :

$$r' = r(y) \exp\left[i(\alpha x + \beta z - \omega t)\right] \qquad (1)$$

The amplitude function r depends on y only : it is the so-called parallel flow approximation. α, β and ω can be either real or complex quantities ; in fact, two theories are essentially used :

- in the temporal theory, α and β are real and ω is complex, so that (1) can be written :

$$r' = r(y) \exp(\omega_i t) \exp\left[i(\alpha x + \beta z - \omega_r t)\right] \qquad (2)$$

ω_i represents the temporal amplification factor. Depending on its sign, the disturbances are amplified ($\omega_i > 0$), neutral ($\omega_i = 0$) or damped ($\omega_i < 0$). ω_r is a circular frequency. α and β are the components of the wavenumber vector in the x and z directions, respectively. It will be shown that the wavenumber direction $\psi = \tan^{-1}(\beta/\alpha)$ is a very important parameter.

- in the spatial theory, ω is real, α and β are complex. It follows from (1) that

$$r' = r(y) \exp\left[-(\alpha_i x + \beta_i z)\right] \exp\left[i(\alpha_r x + \beta_r z - \omega t)\right] \qquad (3)$$

We may define a real wavenumber $\vec{k}$ with an amplitude $|k|$ and a direction ψ :

$$|k| = (\alpha_r^2 + \beta_r^2)^{1/2} \quad \text{and} \quad \psi = \tan^{-1}(\beta_r/\alpha_r) \qquad (4)$$

The spatial amplification rate is a vector with magnitude $\sigma = (\alpha_i^2 + \beta_i^2)^{1/2}$ and direction $\bar{\psi} = \tan^{-1}(\beta_i/\alpha_i)$. If β_i is set equal to zero, the waves can be amplified $(\alpha_i < 0)$, neutral $(\alpha_i = 0)$ or damped $(\alpha_i > 0)$.

As a general rule, GASTER's relation makes possible to convert a temporal to a spatial amplification rate by using the group velocity concept /23/.

Introducing (1) into the linearized equations leads to a system of 6 ordinary differential equations in y for the amplitude functions r(y). Due to the homogeneous boundary conditions (all fluctuations must vanish at the wall and in the free-stream except the pressure fluctuations which have a non-zero amplitude at the wall), the problem is an eigenvalue one : when the mean flow is specified, a non-zero solution exists only for peculiar combinations of the four parameters α, β, ω and Re, where Re is the Reynolds number. In fact, there are five real parameters in temporal theory $(\alpha$, β, ω_r, ω_i, Re) and six in spatial theory $(\alpha_r,\alpha_i$, β_r, β_i, ω, Re or k, ψ, σ, $\bar{\psi}$, ω, Re).

From a numerical point of view, the data are the boundary layer mean velocity and temperature profiles, the free-stream Mach number, the wall temperature, the characteristics of the fluid and all but two parameters. The computation gives the two remaining parameters (eigenvalues) as well as the disturbances amplitude profiles (eigenfunctions).

2.3. Inviscid theory

In this theory, it is assumed that the viscosity acts only on the mean profiles ; furthermore, the terms of the order 1/Re are neglected in the stability equations. The mathematical study of the inviscid theory shows up the importance of two parameters :

a - The first one is the so-called "generalized inflexion point", which corresponds to the altitude y_s where :

$$\frac{d}{dy}\left[\rho\frac{du}{dy}\right]_{y_S} = 0 \qquad (5)$$

where ρ and u are the mean density and the mean velocity. It was demonstrated by LEES and LIN /8/ that the presence of such a point is a sufficient condition for the appearance of unstable disturbances ; it is also a necessary and sufficient condition for the existence of a neutral subsonic wave (the definition of a subsonic disturbance will be given below) ; the phase velocity of this wave is the mean velocity at y_S. However, these results are valid only if :

$$\frac{u}{u_e}(y_S) > 1 - \frac{1}{M_e} \qquad (6)$$

Let us consider the flat plate case. When the Mach number increases, the generalized inflexion point goes from the wall towards the outer edge of the boundary layer, and the numerical results indicate that the range of unstable frequencies is enlarged at high Reynolds numbers. It is clear that this "inflexional instability" plays a crucial role for instability and transition in hypersonics.

b - The second parameter is the "relative Mach number", $\hat{M}$, which is defined as :

$$\hat{M} = M - c/a \qquad \text{(see figure 1)} \qquad (7)$$

M is the local Mach number ; for classical boundary layer profiles, it increases from 0 to Me between the wall and the free-stream. c is the phase velocity of the waves ; it does not depend on y : for two-dimensional waves $(\beta = 0)$, $c = \omega_r/\alpha$ in temporal theory, and $c = \omega/\alpha_r$ in spatial theory. a represents the local speed of sound, which depends on the mean temperature distribution ; obviously, it takes a non-zero value at the wall. The disturbances are subsonic if $\hat{M}^2 < 1$, sonic if $\hat{M}^2 = 1$, supersonic if $\hat{M}^2 > 1$.
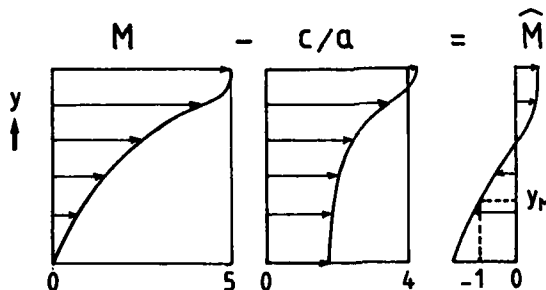

Figure 1 - Typical evolution of the relative Mach number $\hat{M}$

If a wave is locally supersonic, say between $y = 0$ and $y = y_M$ (figure 1), the mathematical nature of the stability equations changes, and any eigenvalue problem admits an infinite sequence of neutral solutions ; for instance, in the temporal theory and for two-dimensional disturbances, there is an infinity of neutral waves ($\omega_i = 0$) having the same phase velocity ω_r/α but different wavenumbers α. These multiple solutions (the higher modes) were first discovered by MACK for boundary layer flows /12/ ; in the case of adiabatic wall conditions, they appear when the free-stream Mach number exceeds 2.2.

3. STABILITY COMPUTATIONS FOR ZERO PRESSURE GRADIENT FLOW ON ADIABATIC WALLS

3.1. Basic flow and assumptions

The stability diagrams which will be presented below were obtained by using a computer code developed at ONERA/CERT /22/. The results are in good agreement with those published by other authors (at least for the neutral curves). In these calculations, the basic profiles are two-dimensional mean velocity profiles and the corresponding mean temperature profiles computed for the flat plate case by solving the classical compressible similarity equations :

$$\frac{d}{d\eta} \left(\frac{\rho\mu}{\rho_w \mu_w} f'' \right) + ff'' = 0$$

$$\frac{d}{d\eta} \left(\frac{\rho\mu}{\rho_w \mu_w} \frac{1}{P_r} S' \right) + fS' + \frac{U_e^2}{hi_e} \frac{d}{d\eta} \left(\frac{P_r-1}{P_r} \frac{\rho\mu}{\rho_w \mu_w} f'f'' \right) = 0 \qquad (8)$$

with $\quad f' = \dfrac{u}{u_e} \quad , \quad S = \dfrac{hi}{hi_e} - 1$

$$\eta = \frac{u_e}{\sqrt{2\xi}} \int_0^Y \rho \, dt \quad , \quad \xi = \int_0^Y \rho_w \mu_w u_e \, dt \qquad \text{(LEVY-LEES transformation)}$$

The real gas effects are not taken into account, and the Prandtl number P_r is constant ($P_r = 0.725$). The ' denotes derivatives with respect to η.

In the stability computations, the spatial theory is used, and it is assumed that the amplification vector is aligned with the mean flow direction x, i.e. $\beta_i = 0$ or $\overline{\psi} = 0$. Justifications of this assumption are given by MACK /17/.

3.2. Stability diagrams for two-dimensional waves

Figure 2 shows examples of stability diagrams computed for two-dimensional waves ($\psi = 0°$) and for Mach numbers ranging from 0 to 10. For the sake of clearity, only some iso-amplification curves ($-\alpha_i > 0$) are plotted in the (Reynolds number, wavenumber) plane. The Reynolds number is computed from the displacement thickness δ_1, the free-stream velocity u_e and the kinematic viscosity ν_e of the outer flow. α_r and α_i are made dimensionless with this displacement thickness. For each Mach number, there is a critical Reynolds number ($R\delta_{1cr}$) below which all disturbances are damped.

The first observation is that the stability diagrams do not change very much when the Mach number increases from 0 to 1.3. (Figure 2a-b). This can be explained by the fact that the generalized inflexion point remains very close to the wall in this Mach number range, and the boundary layer is unstable essentially through the action of viscosity : this phenomenon, whereby the maximum amplification rate increases with decreasing Reynolds number at a fixed value of ω or α_r, is called viscous instability ; stability diagrams where viscous instability is present exhibit a local maximum of $-\alpha_i$ at finite Reynolds numbers, and the curves of equal amplification rate are closed around this peak. Another important observation is that the amplification factors of the unstable waves are clearly smaller in the transonic range than in incompressible flow, even if the critical Reynolds number remains of the same order.

At higher Mach numbers, the altitude of the generalized inflexion point increases, and the inflexional instability plays a more and more important role : the inviscid theory shows that there is a range of unstable α_r or ω at infinite Reynolds number and this range is enlarged with increasing Mach numbers ; as a consequence, at large but finite Reynolds numbers, the curves of equal amplification rates tend to be parallel with the $R\delta_1$- axis. For Me = 2.2 (figure 2c), the stability diagram clearly shows the viscous instability (below $R\delta_1 \approx 7000$) and the inflexional instability (beyond $R\delta_1 \approx 7000$). The later becomes predominant for Me = 3 (figure 2d).

It has been noticed previously that higher modes could be computed as soon as the free-stream Mach number becomes larger than 2.2, but they are at first associated with very large wavenumbers. For this reason, only the first unstable mode is plotted in Figures 2c and 2d for Me = 2.2 and 3. However, when the Mach number is increased, the second unstable mode appears at lower and lower wavenumbers. This is illustrated in Figure 2e (Me = 4.5), where the first and the second modes are close together. Let us observe that
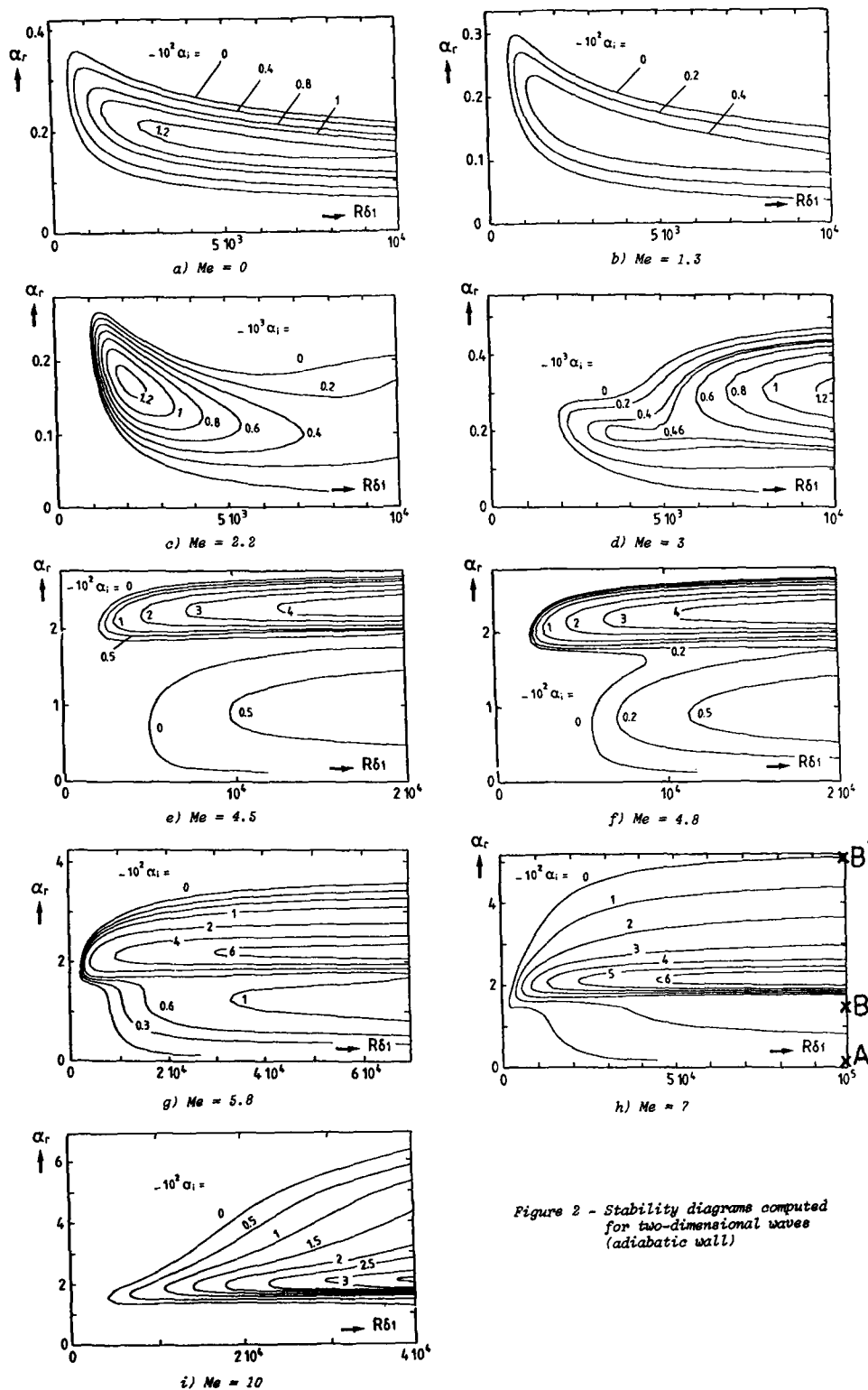
Figure 2 - Stability diagrams computed for two-dimensional waves (adiabatic wall)

the second mode is more unstable than the first one : the ratio of the maximum amplification rates is of the order of four or five. At Me = 4.8 (Figure 2f), the two unstable regions join each other and there is only one neutral curve in hypersonic conditions (Figure 2g to 2i). However, when the phase velocity $c = \omega/\alpha_r$ is plotted as a function of α_i, two well defined regions can be observed ; as an example, the curve $c(\alpha_i)$ is shown in Figure 3 for Me = 7 and $R\delta_1 = 10^5$. The bump between points A and B corresponds
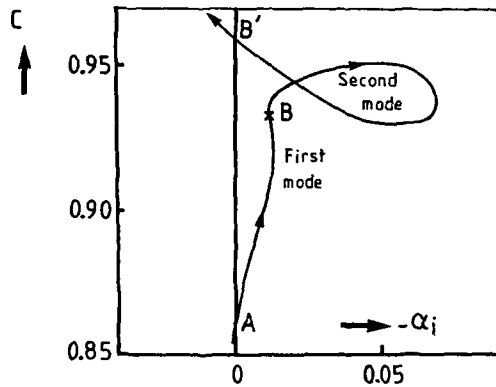

Figure 3 - Phase velocity as a function of the amplification rate. The points A, B and B' are reported in figure 2h. The arrows indicate increasing frequencies

to the first mode, and the loop between B and B' corresponds to the second mode. At larger Reynolds number, the growth rate at point B will tend to zero ; at infinite Reynolds number, the phase velocity at points B and B' will be equal to the mean velocity at the generalized inflexion point. Let us recall that the concept of higher modes deals essentially with the phase velocity of some particular neutral disturbances, whatever the number of separated neutral curves is.

3.3. Stability diagrams for oblique waves

The previous results were obtained for two-dimensional waves. However, an important aspect of instability in compressible boundary layer is the effect of the wave direction ψ on the amplification rates. In incompressible flow, only the two-dimensional waves need to be considered, because it can be demonstrated that they are the most unstable ones (SQUIRE's theorem). This is no longer the case in compressible flow, even at moderate Mach numbers. Figure 4 shows the evolution of the maximum amplification rate at a given
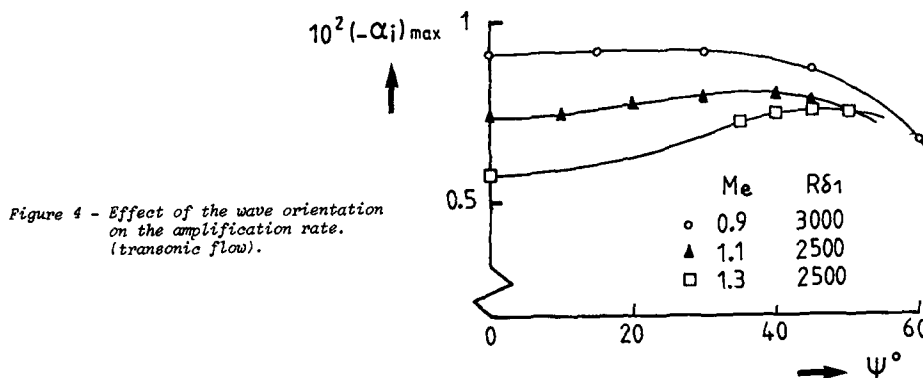

Figure 4 - Effect of the wave orientation on the amplification rate. (transonic flow).

Reynolds number, as a function of the wave direction. Three Mach numbers in the transonic range are considered. Up to Me = 0.9, the maximum value of $-\alpha_i$ corresponds to $\psi = 0°$. But at higher Mach numbers, it is clear that the largest amplification rate is obtained for a non zero value of the ψ angle.

In supersonic and hypersonic conditions, the evolution becomes more and more complex, as it can be seen in Figure 5, where two stability diagrams are represented for $M_e = 4.5$ and two values of ψ : 0° and 60°. Changing the wave orientation stabilizes the second mode, but increases the instability of the first one, so that it becomes difficult to define the "most unstable direction".
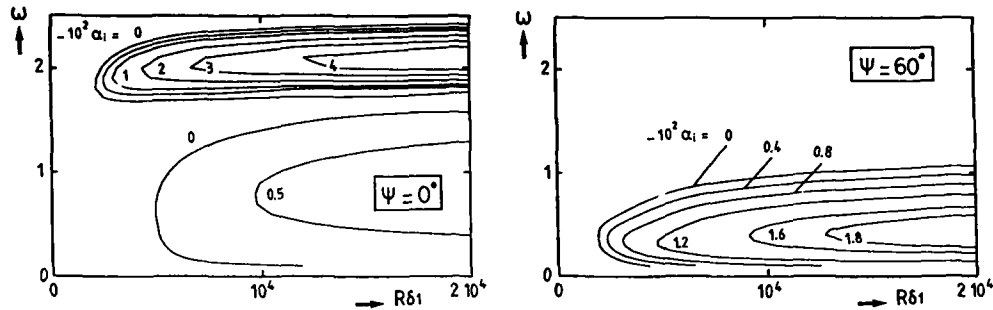
Figure 5 - Effect of the wave orientation on the amplification rate (Me = 4.5)

3.4. Examples of eigenfunctions

Figure 6 shows the amplitude profiles $\tilde{u}'$, $\tilde{v}'$, $\tilde{T}'$ computed at point B' in Figure 3. The velocity fluctuations and the temperature fluctuations are made dimensionless with the free-stream velocity u_e and the static temperature T_e, respectively. As the stability equations are linear, the amplitude profiles are known with an arbitrary multiplicative factor. In the present computations, this arbitrary constant was chosen in such a way that $\max(\tilde{u}') = 1$. The crosses indicate the location of the generalized inflexion point y_S, and the disturbances are locally supersonic between the wall and the altitude y_M indicated by the square symbol. The main observation is that the amplitude of the temperature fluctuations is two orders of magnitude larger than that of the velocity fluctuations. In addition, the narrow peak of $\tilde{T}'$ is located around the altitude of the generalized inflexion point, near the outer edge of the boundary layer. This remark is also valid at lower Mach numbers : when M_e increases, the generalized inflexion point moves outwards, the peak of the temperature fluctuations follows its movement and becomes sharper and sharper.
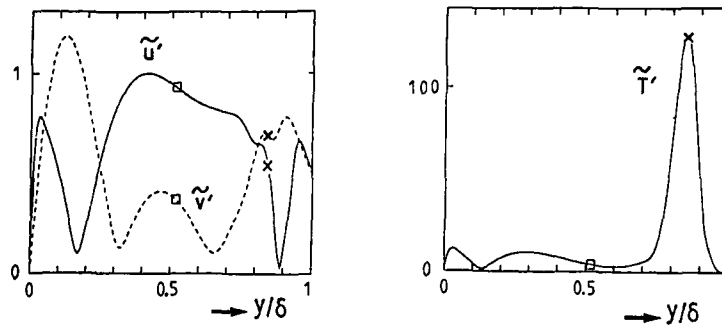

Figure 6 - Amplitude profiles of the velocity and temperature fluctuations
(Me = 7, point B' in figure 3)

Amplitude profiles of the pressure fluctuations are plotted in Figure 7, as well as the corresponding phase distributions. The calculations were performed at points B and B' of figure 3 and illustrate the differences between eigenfunctions of the first and second modes. At point B (first mode region), the sign of p' does not change between the wall and the free-stream. At point B' (second mode region), a sudden phase shift of 180° is observed at $y/\delta \approx 0.15$: at each instant, the pressure fluctuations are of opposite sign below and beyond this altitude. A complete discussion of this behaviour was given by MACK /4/ /13/ in the light of the inviscid theory.
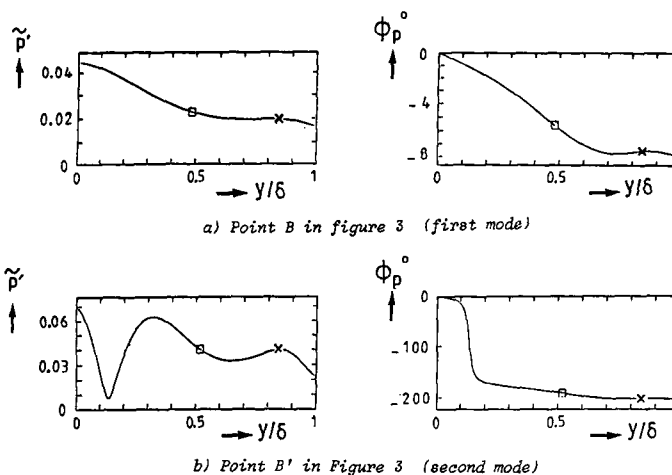
a) Point B in figure 3   (first mode)

b) Point B' in Figure 3   (second mode)

Figure 7 - Amplitude and phase profiles of the pressure fluctuations (Me = 7)

4. ORIGIN AND THREE-DIMENSIONAL EVOLUTION OF THE T-S WAVES

4.1. Receptivity

Some properties of the laminar boundary layer as a linear oscillator have been reviewed. But how are the TOLLMIEN-SCHLICHTING waves excited by the available distur-bance environment ? This question is a part of the problem which is usually addressed under the word of "receptivity", introduced by MORKOVIN /1/ (see also RESHOTKO /3/). The receptivity describes the means by which forced disturbances (free-stream turbulence, sound field, surface roughness, etc.) enter the laminar boundary layer ; it describes also their signature in the disturbed flow. At this point, two different cases need to be considered :

a - If the forced disturbances are small, they will tend to excite the TOLLMIEN-SCHLICHTING waves, which constitute free responses of the laminar boundary layer to the disturbance environment. The problem is to find the link between the characteristics of the forced disturbances and the initial properties of the instability waves as they start to grow. In fact, each class of disturbances imposes its particular signature and there is no general receptivity theory. The question will be discussed below for some factors affecting transition : free-stream turbulence (section 5.1.), wind tunnel noise (section 9.1), unit Reynolds number (section 11), sweep angle (section 16.2).

b - If the forced disturbances are large, transition occurs very rapidly, without resorting to linear mechanisms : it is a "bypass" (MORKOVIN , /24/). The transition Reynolds number can be lower than the critical Reynolds number computed from the linear stability theory. A typical example of "bypass" is the leading edge contamination, which is described in section 16.

4.2. Non linear evolution and breakdown

Let us assume now that there is no bypass and that TOLLMIEN-SCHLICHTING waves were generated through the action of a certain receptivity process. These waves grow according to the linear theory ; when they reach a finite amplitude, the quadratic terms neglected in the theory become appreciable and three-dimensional effects appear. The problem is fairly well documented at low speeds, both theoretically and experimentally
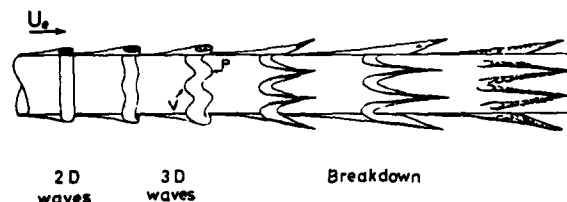

Figure 8 - Smoke visualisation of the different stages leading to transition on a cylinder (Knapp et al.)

(see review paper by HERBERT /25/) ; Figure 8 shows an example of smoke visualization made by KNAPP et al. /26/ on an ogive nose cylinder. The waves are initially two-dimensional and look like smoke rings around the cylinder ; they are then distorted into a series of "peaks" and "valleys". As the flow proceeds downstream, this pattern becomes more and more pronounced. A high concentration of vorticity appears at the peak positions and forms a high shear layer, which finally breaks down into small vortices. These vortices in their turn produce smaller vortices ; then, a turbulent spot is formed.

Unfortunately, very little is known about the non-linear mechanisms in supersonic and hypersonic flows. "The non-linear effects responsible for transition at high speeds are still very much a mystery /27/". It can be guessed that the non-linearities are created by the temperature or density fluctuations, the amplitude of which is several times larger than the velocity or pressure fluctuations. Experiments on cones revealed the existence of unstable frequencies which are not predicted by the linear theory ; they are probably the result of a non linear behaviour (see section 9.2).

To our knowledge, the only direct numerical simulation related to this problem was carried out by ERLEBACHER and HUSSAINI /27/. They studied the non linear interactions between a two-dimensional wave and two oblique waves at Mach 4.5. These interactions trigger a secondary instability, with the appearance of a peak-valley system, but, by contrast with the incompressible case, the high shear layer develops in both the peak and valley planes, which lose their characteristic distinctions. The spatial evolution of the secondary instability is very slow, and the question arises of the length of the non linear zone at high speeds. In incompressible flows, the distance between the end of the linear region and the breakdown to turbulence is rather short ; this explains that calculation methods based on linear theory (such as e^n method) provides us with good results for predicting the transition location. Due to the lack of information, it is assumed that similar techniques can be used in compressible flows, as it will be discussed in the following section.

5. INSTABILITY AND TRANSITION

5.1. e^n method

The problem is now to establish a link between the instability properties and the transition onset. So far, the most commonly used method is based on the computation of the total amplification rate of unstable waves.

For a given mean flow, it is possible to compute a stability diagram (Figure 9) showing the range of unstable frequencies f as a function of the streamwise distance x. Let us consider now a wave which propagates downstream with a fixed frequency f. This wave passes at first through the stable region ; it is damped up to x_0 , then amplified up to x_1, and at last it is damped again downstream of x_1 . At a given station x, the total amplification rate can be defined as :

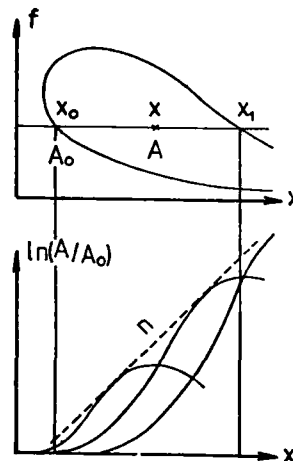$$\ln(A/A_o) = \int_{x_o}^{x} - \alpha_i \, dx \qquad (9)$$

Figure 9 - Typical stability diagram in physical coordinates. Definition of the total amplification rate and of the envelope curve.

A   is the wave amplitude, and the index o refers to the streamwise position where
the wave becomes unstable. In equation (9), x and α_i are dimensional quantities. For
self-similar boundary layer profiles on a flat plate, it can be demonstrated that :

$$K = R\delta_1/\sqrt{R_x} = \text{constant} \tag{10}$$

and relation (9) is also expressed by :

$$\ln(A/A_o) = \frac{2}{K^2} \int_{R\delta_{10}}^{R\delta_1} - \alpha_i dR\delta_1 \tag{11}$$

where α_i is made dimensionless with δ_1, as in the previous paragraph.

The total amplification rates are then calculated for various frequencies. The
envelope of these curves is :

$$n = \underset{f}{\text{Max}} \left(\ln A/A_o \right) \tag{12}$$

At the present time, to predict transition, one must place reliance on empirical
procedures. The e^n method, proposed by SMITH and GAMBERONI /28/ and VAN INGEN /29/, was
the first one to correlate amplification and transition in incompressible flow. By
comparing theoretical envelope curves with measured transition locations, the breakdown
was found to occur for n = 7 to 9. This means that turbulent spots appear when the most
unstable frequency is amplified by a factor e^7 to e^9. In fact, the value of n at transi-
tion onset depends on the disturbance environment, and MACK /15/ suggested the following
empirical relationship :

$$n = -8.43 - 2.4 \ln Tu \quad \text{at transition,} \tag{13}$$

where Tu is the free-stream turbulence level. For instance, for Tu = 10^{-3}
("clean" wind tunnels), n = 8.15 and for Tu = 10^{-2}, n = 2.62. Let us observe that this
equation can be related with the receptivity concept ; if it is assumed that transition
occurs for a fixed value of A, then the initial amplitude of the disturbances is propor-
tional to $Tu^{2.4}$.

Let us recall that the e^n method was developed for low speed flows. The problem is
to know if it remains valid for compressible boundary layers.

5.2. Applications to the flat plate case

Envelope curves are plotted in Figure 10 for 4 supersonic Mach numbers ; we consi-
dered two-dimensional waves ($\beta_r = 0$), as well as oblique waves ($\beta_r \neq 0$) associated with
the most unstable ψ angle (strictly speaking, this angle depends on the Reynolds number
for each Mach number, but its variation is rather weak). Up to $M_e \approx 5$, the oblique waves
are the most unstable ones ; however for hypersonic flows, the two-dimensional waves
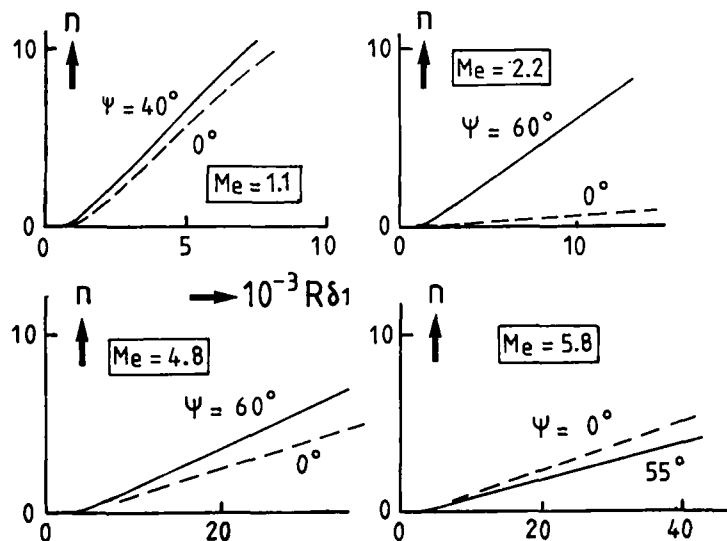become the most amplified again.

Figure 10 - Examples of envelope curves

Figure 11 shows an application of the e^n method for adiabatic flat plates. The stability diagrams were used for computing the theoretical streamwise Reynolds numbers which correspond to different values of the n factor, as a function of the free-stream Mach number. If it is assumed that transition occurs for a fixed value of the n factor, each curve represents the evolution of the transition Reynolds number when M_e increases. It can be observed that compressibility has a strong stabilizing effect in transonic flow ; it becomes destabilizing for Mach numbers between 2 and 3.5, and stabilizing again in hypersonic conditions.

Figure 11 - Application of the e^n method (flat plate, adiabatic wall).

- - - - : Mack /14/

● : experiments /30/
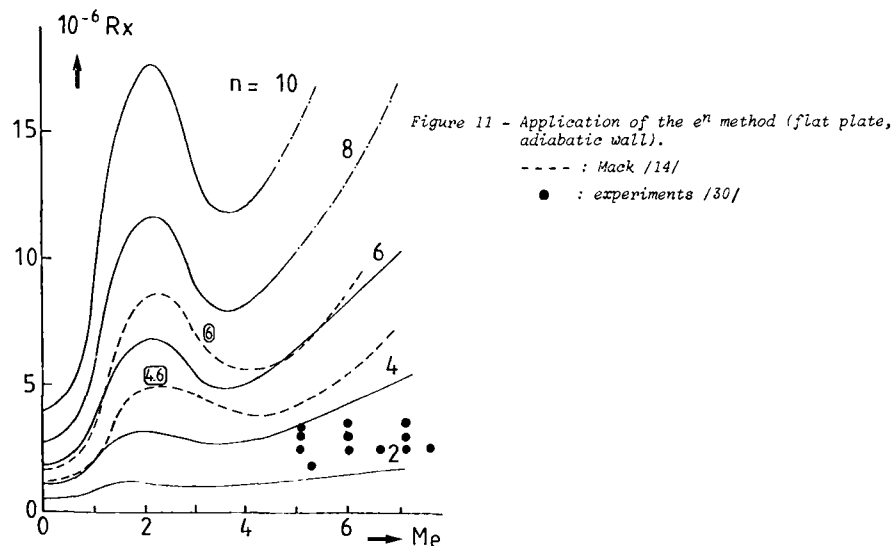
Curves computed by MACK /14/ for n = 4.6 and 6 are also plotted in Figure 11. Although there are some differences between these results and our calculations, the general trends are the same.

It has been noticed previously that the value of n at transition onset is usually between 7 and 10 in "clean" subsonic wind tunnels. The problem is obviously to know if similar values of n are observed at high speeds. The solid symbols in Figure 11 represent experimental data obtained at ONERA some years ago /30/ : they correspond to low values of the n factor, between 2 and 4. Numerous examples could be given for illustrating the fact that in conventional hypersonic wind tunnels, the measured transition Reynolds numbers are rather low, say between 2 and 3 millions. Possible origins of this behaviour are discussed below.

6. THE PROBLEM OF WIND TUNNEL SIMULATIONS

It is well known that transition on a smooth surface can be triggered by the disturbances which are present in the free-stream : velocity fluctuations u' (free-stream turbulence), pressure fluctuations p' (acoustic disturbances), temperature fluctuations T'. The problem is very complex, because the effect of these various disturbances depends on the Mach number range (PATE, /5/).

At low speed, the transition Reynolds number is very sensitive to the free-stream turbulence level Tu, as it is indicated by the relation (13) ; however, if Tu becomes very low, pressure fluctuations (fan noise for instance) can be of major importance for inducing transition.

In transonic flow, acoustical phenomena linked with slotted or perforated walls give rise to strong pressure disturbances, which cause early transitions. Better results are obtained in transonic wind tunnels with solid walls.

In supersonic and hypersonic flows, the main factor affecting transition is also the noise, the origin of which lies in the pressure disturbances radiated by the turbulent boundary layers developing along the wind tunnel walls. The effects of u' and T' have not been firmly established for M_e > 3.5.

The rms value of the pressure fluctuation intensity, $\hat{p}'$, was measured in many supersonic and hypersonic wind tunnels. Figure 12 shows a correlation proposed by HARVEY /31/, who collected a large amount of measurements for Mach numbers up to 50. The free-stream disturbance intensity $\hat{p}'_\infty$ is plotted versus M_∞ in two dimensionless forms, $\hat{p}'_\infty/P_\infty$ and $\hat{p}'_\infty/q_\infty$. P_∞ is the free-stream mean static pressure and q_∞ is the mean dynamic
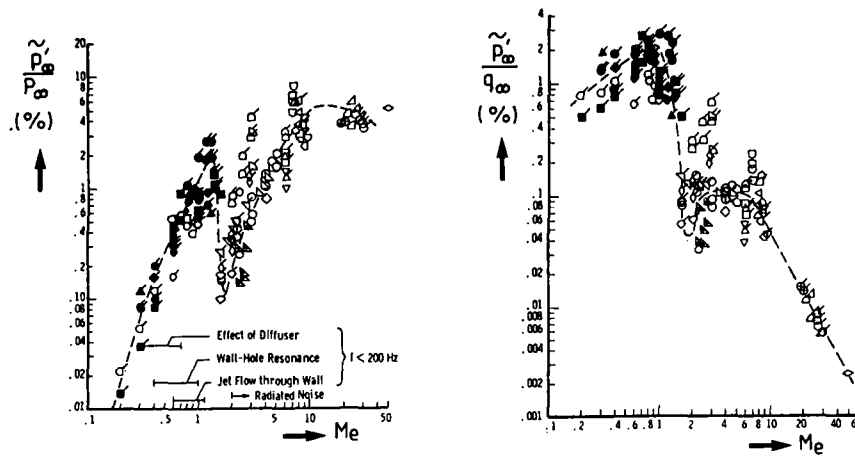
Figure 12 - Free-stream pressure disturbances in wind tunnels (Harvey).

pressure. The strong effect of the wind tunnel noise on the transition Reynolds number is illustrated in Figure 13 (HARVEY, /31/), where values of Rx_T measured on cones and flat plates are given as a function of $\tilde{p}'_\infty/q_\infty$, for $4 < M_\infty < 23$. There are two separate mean curves for cones and flat plates, but the effect of the Mach number disappears completely in this representation.
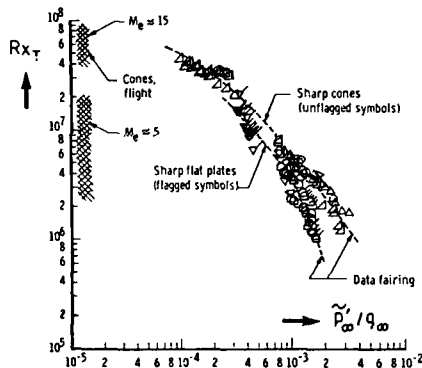

Figure 13 - Effect of wind tunnel noise on

the transition Reynolds number (Harvey).

PATE analyzed also available wind tunnel data and developed an empirical criterion for "natural" transitions measured in supersonic and hypersonic facilities. This criterion is a correlation between the transition Reynolds number Rx_T on the model and the parameters acting on the noise intensity : the tunnel test section circumference P and two characteristic parameters of the turbulent boundary layer on the nozzle walls (mean skin friction coefficient C_F and displacement thickness δ_1). As for HARVEY's criterion (Figure 13), data for cones and flat plates can be represented by two different curves, the general expression of which is /5/ :

$$Rx_T = a_1 C_F^{a_2} a_3(P) / (\delta_1/P)^{1/2} \quad , \quad \text{with}$$

	a_1	a_2	$a_3(P)$, P in meters
Flat plates	0.0126	− 2.55	1 if P < 1.22 m
			0.56 + 0.536 / P if P > 1.22 m
Cones	48.5	− 1.40	1 if P < 1.22 m
			0.8 + 0.244 / P if P > 1.22 m

(14)

This correlation is shown in Figure 14.

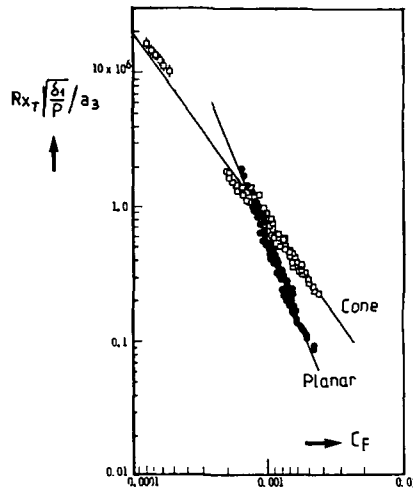$$Rx_T \sqrt{\frac{\delta_1}{P}} / a_3 \uparrow$$

Figure 14 - Correlation proposed
by Pate

If the free-stream Mach number and the wall temperature ratio T_w / T_{aw} are constant,
the flat plate relations lead to the following expression :

$$Rx_T \sim (u_e/\nu_e)^{0.5} \quad g(P) \tag{15}$$

g increases as the test section circumference increases. This shows that the
transition Reynolds number increases with increasing unit Reynolds number u_e/ν_e and
increasing wind tunnel size. The effect of the latter parameter was first demonstrated
by PATE and SCHUELER (1969, /32/), who conducted an extensive research program to
study the correlation of Rx_T with radiated noise in supersonic flow.
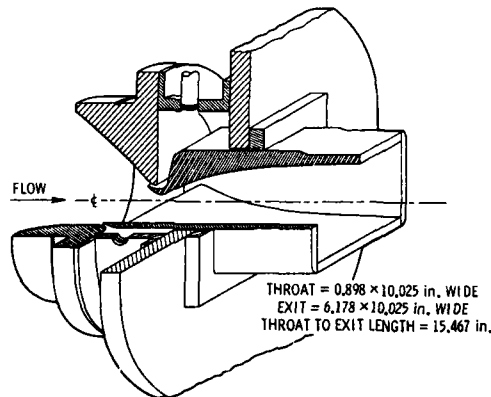
Another correlation, which was used during wind tunnel tests of a smooth model
of Columbia space shuttle, is expressed by the simple relationship :

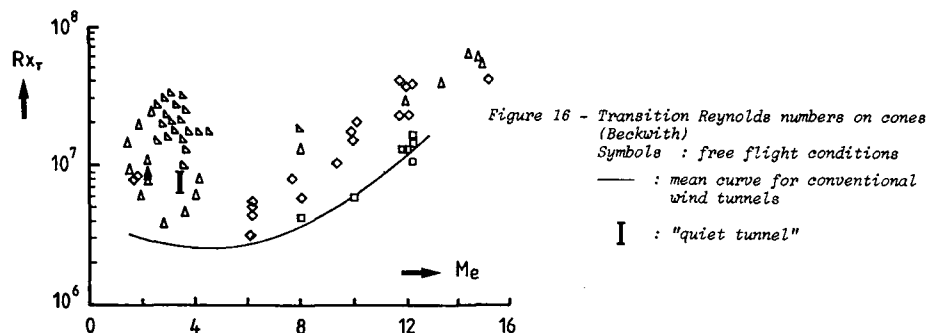$$(R\theta/M_e)_T = \text{constant, of the order of 200.} \tag{16}$$

$R\theta$ is the momentum thickness Reynolds number of the laminar boundary layer
which develops on the model. The values of $R\theta_T$ deduced from (16) are too low when
compared with free flight data on smooth models.

Since the radiated noise is inherent in the presence of walls around the model,
there is little doubt that wind tunnel conditions cannot simulate properly flight
conditions. In order to reduce the noise level, it is necessary to delay transition on
the nozzle walls, because a laminar boundary layer is less noisy than a turbulent one.
This was done in the "quiet tunnel" built in NASA LANGLEY with a free-stream Mach
number $M_\infty = 3.5$. A cutaway isometric sketch of the nozzle is presented in Figure 15, and
a detailed description of the wind tunnel was given by BECKWITH et al /33/. The nozzle

Figure 15 - Sketch of the nozzle
of the "quiet tunnel"
(Beckwith et al.).

FLOW

THROAT = 0.898 × 10.025 in. WIDE
EXIT = 6.178 × 10.025 in. WIDE
THROAT TO EXIT LENGTH = 15.467 in.

is two-dimensional and differs in design substantially from more conventional ones. Three notable features are the use of a rapid expansion contour, a wide separation of the two planar side-walls and the provision of boundary layer bleed slots shortly upstream of the nozzle throat. For unit Reynolds numbers between 2.5 10^5 and 15 10^5 per inch, the observed values of $\hat{p}'_\infty/P_\infty$ were found to vary from 0.03 10^{-2} up to about 0.8 10^{-2} , depending upon the unit Reynolds number, the axial location and the bleed slot flow (bleed valve open or closed). The minimum value is one or two orders of magnitude below that which is measured in conventional wind tunnels, see figure 12 ; it corresponds to laminar boundary layers on the nozzle walls. The higher no_se levels are caused by radiations from transitional or turbulent wall boundary layers ; they are comparable with the levels reported for other tunnels at the same Mach number. With the lower value of $\hat{p}'_\infty/P_\infty$, the transition Reynolds number measured on a 5° half-angle sharp cone are two or three times larger than those obtained in conventional wind tunnels.

Figure 16 - Transition Reynolds numbers on cones (Beckwith)
Symbols : free flight conditions
——— : mean curve for conventional wind tunnels
I : "quiet tunnel"

The situation is summarized in Figure 16 ; it shows flight transition data which were collected for sharp cones by BECKWITH /34/. The transition Reynolds numbers are plotted as a function of the Mach number. The figure also contains a correlation for wind tunnel transition data, which lies much below the flight experiments. The range of results obtained in the "quiet tunnel" are reported for comparison.

The general trend of the flight data seems to be in qualitative agreement with stability computations (Figure 24): Rx_T exhibits a maximum for $M_e \approx 3$ and a minimum for $M_e \approx 5-6$. A quantitive comparison, however, cannot be made, because the flight data have been obtained for varying conditions of wall temperatures, the distribution of which is not known in many cases. It will be shown in the next section that the ratio T_w/T_{aw} is a very important parameter in the experimental results as well as in stability computations.

7. WALL TEMPERATURE EFFECTS

7.1. Experimental results

The first effect of wall cooling is to modify the evolution of the mean properties of the laminar boundary layer. For instance, when the wall is cooled, the shape factor H decreases, as well as the ratio $R\delta_1/\sqrt{Rx}$.

As far as the influence of T_w/T_{aw} on transition onset is concerned, Figure 17 shows experimental results collected by POTTER /35/ : the ratio Rx_T/Rx_{TO} is plotted as a function of T_w/T_{aw} for Mach numbers between 1.4 and 11. Rx_{TO} is the transition Reynolds

Figure 17 - Effect of wall cooling on the transition Reynolds number (experiments collected by Potter).
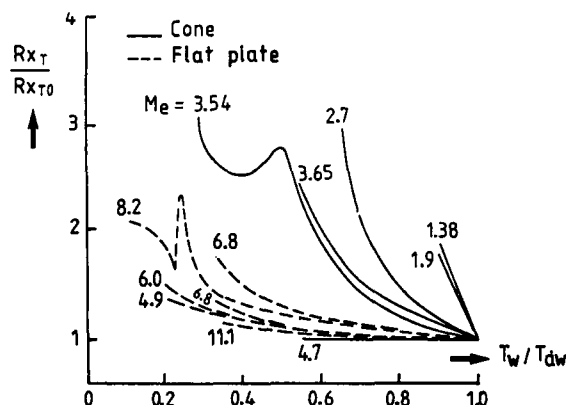
number measured under adiabatic conditions. At a given M_e, only data for a constant unit
Reynolds number $R = u_e/v_e$ were used, but different values of R had to be accepted at
different Mach numbers. In fact, the influence of wall cooling varies somewhat with unit
Reynolds number : this is illustrated by the two curves for M_e = 6.8 in Figure 17, where
the upper curve corresponds to a smaller value of R.

Although there is some scatter in the data, it appears that cooling the wall
delays transition onset. This effect is rather strong in the transonic range, but it is
greatly reduced when the Mach number increases. Some experiments in hypersonic flow did not
reveal any wall cooling influence ; for instance, SANATOR et al. /36/ covered the range
$0.08 \leq T_W/T_{aw} \leq 0.4$ at M_e = 8.8 and found no significant change in Rx_T on a sharp cone.
These results were not reported in Figure 17, because the value of Rx_{TO} is not known.
Recently, NAGAMATSU et al. /37/ stated that over a Mach number range of 8 to 10, wall
cooling effects "do not seem to influence the stability of the hypersonic laminar
boundary layer".

Another interesting feature which can be observed in Figure 17 is the appearance
of "transition reversals" and "transition re-reversals" : in some cases (M_e = 3.54 and 8.2),
when the wall temperature decreases, the transition Reynolds number is at first increasing,
then decreasing (transition reversal) and increasing again (transition re-reversal). This
phenomenon was observed in conventional wind tunnels, but also in completely different
facilities : BOISON /38/ conducted a series of experiments in a shock tube and measured
several transition reversal loops ; SHEETZ /39/ and REDA /40/ both studied cones in an
aeroballistics range and reported also multiple reversals.

The origin of this behaviour has not been clearly established . When T_W/T_{aw}
decreases, the boundary layer thickness is reduced and surface roughness becomes a more
and more critical parameter. Roughness elements can be caused by undetected frost formation
at low surface temperatures (the tripping effect of ice cristals was convincingly demons-
trated by LYSENKO and MASLOV /41/). Another explanation could lie in the complex evolution
of the stability characteristics when the wall is cooled.

7.2. Stability analysis

The stability of laminar boundary layers on cooled walls was studied by BOEHMAN and
MARISCALCO /42/ in transonic flow, by MACK /13/, WAZZAN et al. /42/, MALIK /18/ in
supersonic flow. Systematic computations are currently performed at ONERA/CERT by
F. VIGNAU /44/ ; most of the results which are presented below come from this latter
work.

At first, it is interesting to look at the evolution of the generalized inflexion
point when the free-stream Mach number and the wall temperature are changed. As an
an example, Figure 18 shows the variations of $\rho \frac{du}{dy}$ through the boundary layer thickness,
for M_e = 7 and four values of the ratio T_W/T_{aw}. We recall that the generalized inflexion
point, which plays a crucial role for stability analysis in compressible flow, corresponds
to the altitude where $\frac{d}{dy}\left(\rho \frac{du}{dy}\right) = 0$. For adiabatic conditions, the generalized inflexion
point is associated with the maximum value of $\rho\, du/dy$ and is located near the boundary
layer outer edge. As cooling is applied, a second generalized inflexion point appears
close to the wall ; at this point, $\rho\, du/dy$ is minimum. With increasing cooling, the
second generalized inflexion point moves outwards, whereas the altitude of the first one
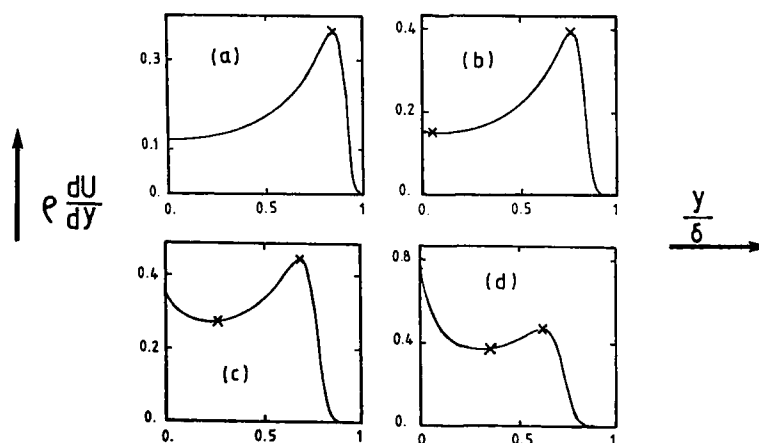decreases slightly.

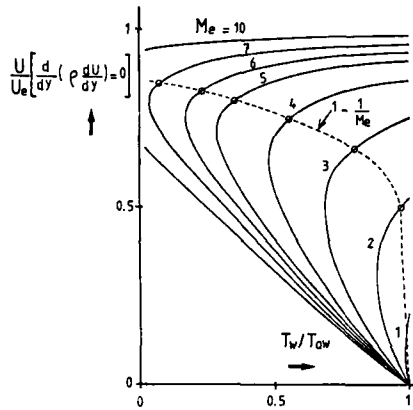Figure 18 - Evolution of $\rho \frac{du}{dy}$ for M_e = 7, T_W/T_{aw} = 1(a), 0.9(b), 0.5(c), 0.3(d)

Figure 19 - *Location of the generalized inflexion points as a function of Me and Tw/Taw*

These observations can help to understand the set of curves which are plotted in figure 19 : the mean velocity taken at the position of the generalized inflexion points is given as a function of M_e and T_w/T_{aw}. At a given Mach number, the two generalized inflexion points draw nearer as T_w/T_{aw} decreases, join each other (except for $M_e = 10$) and finally both of them disappear . The curve defined by $\frac{u}{u_e} = 1 - \frac{1}{M_e}$ is also plotted in this figure. As it has been previously noticed, LEES and LIN deduced from the inviscid theory that the sufficient condition for the existence of amplified disturbances is the presence of a generalized inflexion point at some altitude y_s such that $\frac{u}{u_e} (y_s) > 1 - \frac{1}{M_e}$. It is clear from this restriction that only the upper generalized inflexion point has to be considered for applying LEES and LIN results. This is confirmed by the fact that a sharp peak in the temperature fluctuations appears at this point, whereas no particular behaviour is observed at the lower generalized inflexion point.

Figure 20 shows stability diagrams computed for $M_e = 3$, $\psi = 70°$ and four values of T_w/T_{aw}. For $T_w/T_{aw} = 1$, the diagram is mostly governed by the inflexional instability: when $R\delta_1$ increases, the curves of equal amplification rate tend to be parallel with the Reynolds numbers axis. With increasing wall cooling ($T_w/T_{aw} = 0.8$ and 0.7), the viscous
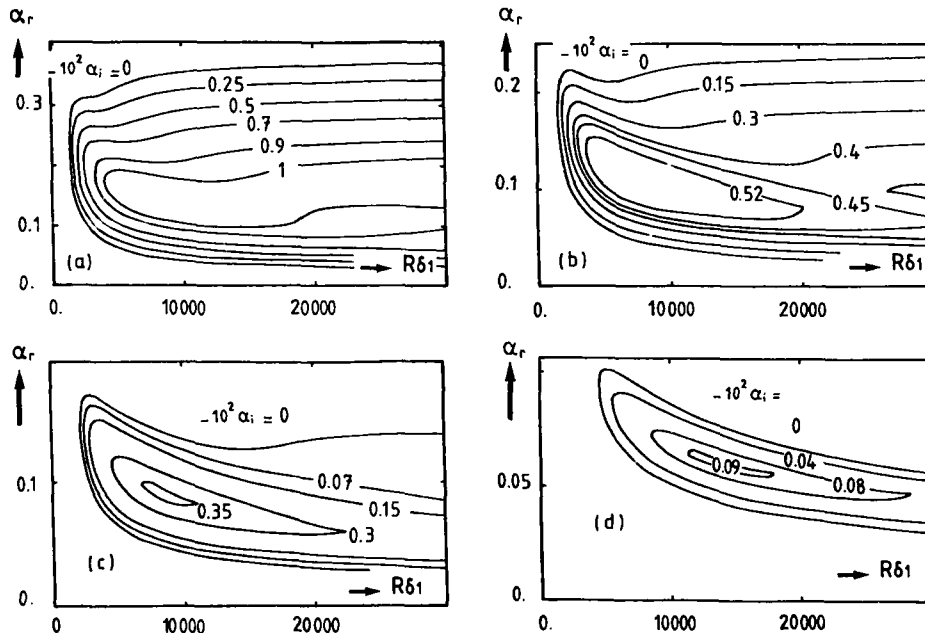

Figure 20 - *Stability diagrams for Me = 3, ψ = 70°, Tw/Taw = 1(a), 0.8(b), 0.7(c) and 0.6(d)   (Vignau, /44/).*

instability (meaning that the maximum amplification rate increases as $R\delta_1$ is decreased) becomes more and more apparent. For $T_w/T_{aw} = 0.6$, the generalized inflexion point disappears, and the stability diagram is entirely of the viscous type : the shape of the neutral curve looks like that of the BLASIUS flow.

Two other examples of stability diagrams are given in Figure 21 for $M_e = 7$, $\psi = 0°$, $T_w/T_{aw} = 1$ and 0.3. A noticeable feature is that increasing wall cooling tends to separate the second mode from the first one : for $T_w/T_{aw} = 0.3$, two distinct neutral curves are observed, as it was the case on adiabatic walls at lower Mach numbers.
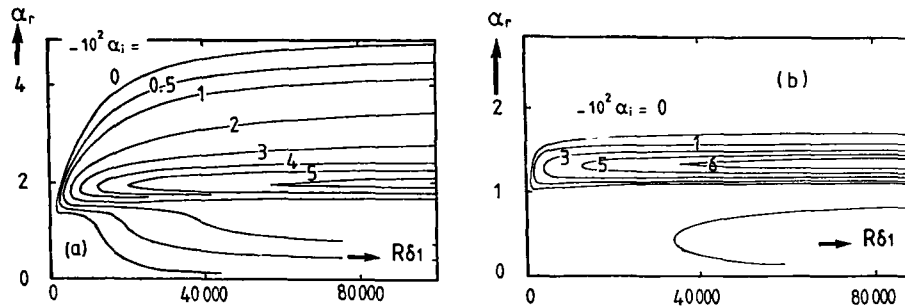

Figure 21 - Stability diagrams for Me = 7, ψ = 0°, Tw/Taw = 1(a) and 0.3(b) (Vignau, /44/).

As T_w/T_{aw} decreases, the instability of the first mode decreases and vanishes for sufficiently low values of the cooling rate. This is in agreement with "the most cele-brated result of the early stability theory", which was obtained by LEES (1947, /9/). LEES found that the critical Reynolds number could become infinite if a sufficient cooling was applied. This result is correct for the first mode, but LEES did not take into account the existence of higher unstable modes, which were discovered later on by MACK.

Figure 22a shows the effect of wall cooling on the maximum amplification rates of the second mode for Me = 7 , $R\delta_1 = 17\,500$, $26\,000$ and $30\,000$. As the wall is cooled, the second mode remains practically unaffected. However, care must be taken before to draw defini-tive conclusions. In these calculations, the reference length is the displacement thickness δ_1 . Other authors (MACK, MALIK) work with $L = (\nu_e x/u_e)^{1/2}$, so that the Reynolds number $u_e L/\nu_e$ is in fact the square root of Rx. Figure 22b shows the same results as in Figure 22a, except that L is used instead of δ_1. It can be easily demonstrated that the ratio δ_1/L is equal to $R\delta_1/\sqrt{Rx}$, which decreases when the wall temperature decreases. As a consequence, when α_i is made dimensionless with L, the maximum amplification rate increases for cooled walls, and it can be said that cooling has a destabilizing effect on the second mode.
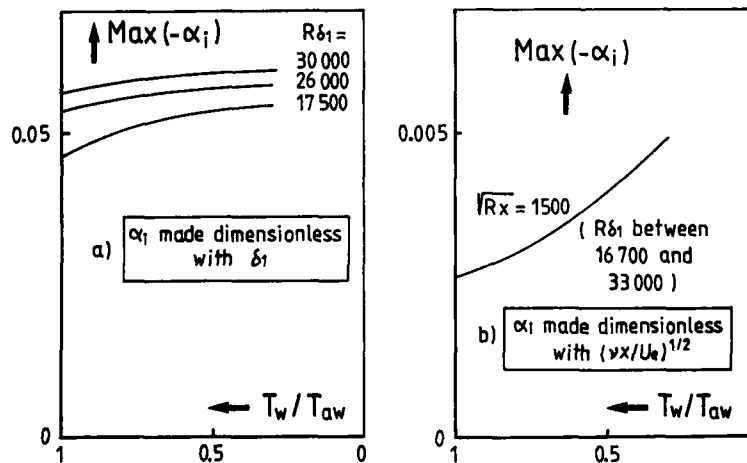

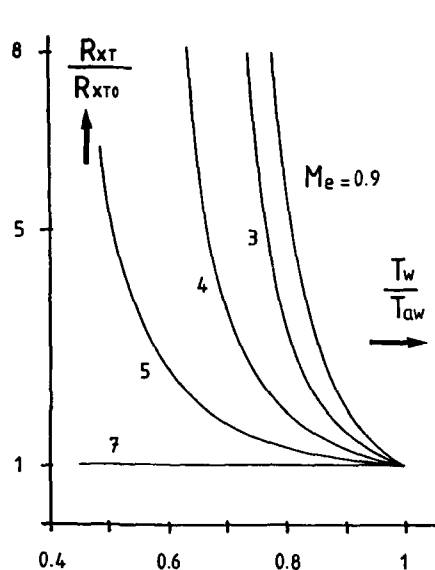Figure 22 - Maximum value of - αi as a function of Tw/Taw for Me = 7, ψ = 0°

Figure 23 - Theoretical effect of wall cooling
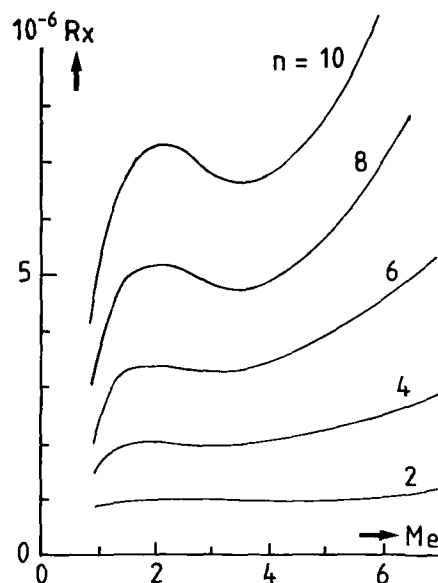on the transition Reynolds number,
for n = 9 (Vignau, /44/)

Figure 24 - Application of the e^n method
(sharp cone, adiabatic wall)

Obviously, when the total amplification rates are computed, the results do not depend on the reference length which was used in the stability calculations. Figure 23 shows the variation of the Reynolds number Rx corresponding to n = 9 as a function of T_w/T_{aw}, for some values of the free-stream Mach number. The computations are in fairly good agreement with the experimental trends. In particular, there is no effect of T_w/T_{aw} on Rx_T for M_e = 7.

8. CONE AND FLAT PLATE FLOW

The flow on a supersonic sharp cone at zero angle of attack is of particular interest, because the free-stream Mach number is constant in the streamwise direction ; the mean properties of the laminar boundary layer can be obtained by the Mangler transformation from flat plate boundary layer computations, if the boundary layer thickness is negligible with respect to the cone radius. The result is that, for the same value of the Reynolds number Rx, the boundary layer thicknesses (δ, δ_1, θ...) on a cone are $\sqrt{3}$ times smaller than those obtained in the flat plate case. This can be expressed by :

$$(R\delta_1)_{fp} = K\sqrt{Rx} \quad \text{and} \quad (R\delta_1)_c = K\sqrt{Rx}/\sqrt{3}, \text{ for identical } M_e, T_e, T_w \qquad (17)$$

On the other side, it is often assumed that the stability equations are the same on cones and on flat plates. (This assumption was discussed by GASPERAS /21/ and MACK /45/). It follows that :

$$(R\delta_{1cr})_{fp} = {}^{'}R^{\delta}{}_{cr}{}^{'}{}_c \quad \text{but} \quad (Rx_{cr})_c = 3(Rx_{cr})_{fp} \qquad (18)$$

As pointed out by MACK /45/, this result "led originally to the unwarranted conclusion that the transition Reynolds number on a cone should be three times that on a flat plate". In fact, relation (11) shows that :

$$(\ln A/Ao)_c = 3(\ln A/Ao)_{fp} \quad \text{at the same } R\delta_1 \qquad (19)$$

On a cone, the disturbances begin to grow at a further downstream abscissa than on a flat plate, but they grow faster, so that the ratio between transition Reynolds numbers on cones and flat plates depends upon the value of n which is imposed at transition onset :

. for "large" values of n, $(Rx_T)_c < (Rx_T)_{fp}$, the faster growth on cones prevails ;

. for "small" values of n, $(Rx_T)_c > (Rx_T)_{fp}$, the critical Reynolds number effect prevails ; for the limiting case n = 0, $x_T = x_{cr}$ and relation (18) holds for x_T.

Figure 24 shows the theoretical transition Reynolds numbers on cones as a function of n and M_e, under adiabatic conditions. Comparison with Figure 11 indicates that the ratio $(Rx_T)_c / (Rx_T)_{fp}$ is of the order of 0.5 for n = 10.

PATE /46/ collected experimental data on cones and flat plates and deduced the evolution of $(Rx_T)_c/(Rx_T)_{fp}$ as a function of the free-stream Mach number. This correlation is given in Figure 25, where "flat plate" data include also measurements performed on hollow cylinders. The ratio is about 2.5 at $M_\infty = 3$ and decreases steadily to unity at hypersonic Mach numbers. If the previous theoretical elements are correct, this means that the values of n at transition are low, i.e. the noise radiated by the wind tunnel walls strongly reduces the transition Reynolds numbers. Recently, experiments on cones and flat plates were performed in the "quiet tunnel" : the ratio $(Rx_T)_c/(Rx_T)_{fp}$ was found to be less than unity, in agreement with stability results for $n \approx 10$ (MALIK, /18/).
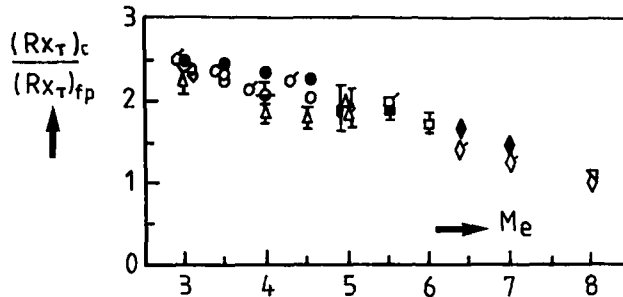

Figure 25 - Transition Reynolds numbers on cones and flat plates : experimental data collected by Pate.

9. STABILITY EXPERIMENTS ON SMOOTH WALLS WITH ZERO PRESSURE GRADIENT

Experimental results were already presented in Sections 5 to 8, but in these experiments, nothing was measured except a transition Reynolds number Rx_T. Although such measurements can be useful for checking the e^n method, they are difficult to relate directly to stability theory. For this reason, fundamental stability experiments, where disturbance growth is measured in the laminar boundary layer, have been performed for relating more closely theory to experiment. The main results of these studies are summarized in this section.

9.1. Flat plate experiments

Experimental investigations into the nature of unstable waves propagating in compressible flow began with the work of LAUFER and VREBALOVICH (1960, /47/). These authors discovered and studied the natural oscillations in the laminar boundary layer at free-stream Mach numbers between 1.6 and 2.2. They measured also the development of artificial disturbances generated by a vibrating ribbon, as it was done by SCHUBAUER and SKRAMSTAD (1948, /6/) for low speed flows.

DEMETRIADES (1960, /48/) performed experiments at a Mach number of 5.8, and found that the range of stable and unstable frequencies varied in a manner which was qualitatively similar to that observed in incompressible flow. However, the spatial amplification rates were found to be much lower.

KENDALL measured the amplification and the damping of artificially excited oscillations at Mach 4.5 (1966, /49/) and later studied the growth of "natural" fluctuations at Mach 2.2. (1975, /50/). The agreement with the linear stability theory was good in the first case, and less favourable in the second series of experiments.

More recently, LYSENKO and MASLOV (1984, /51/) studied the effects of wall cooling for Mach numbers between 2 and 4. As it is predicted by the stability theory, they found that cooling stabilized the first mode disturbances, whereas the second mode disturbances where destabilized.

Beside problem associated with linear stability theory, KENDALL /50/ studied some aspects of the receptivity mechanism. He found that free-stream radiated noise disturbances are amplified by the laminar boundary layer and that all frequencies grow from the leading edge (well ahead of the critical point) up to transition onset. In other words, growing disturbances exist in a laminar boundary layer in a region which is stable according to the linear theory. Figure 26 shows the ratio A/A_∞ as a function of $\sqrt{Rx}$ for three dimensionless frequencies $F = 2\pi f \nu/u_e^2$. A is the rms amplitude measured by a hot wire in the boundary layer at the altitude where it is maximum ; A_∞ is the free-stream rms amplitude for the same frequency. The vertical arrows denote the theoretical neutral points, that is to say the points where each frequency begins to be unstable according to the linear stability theory.
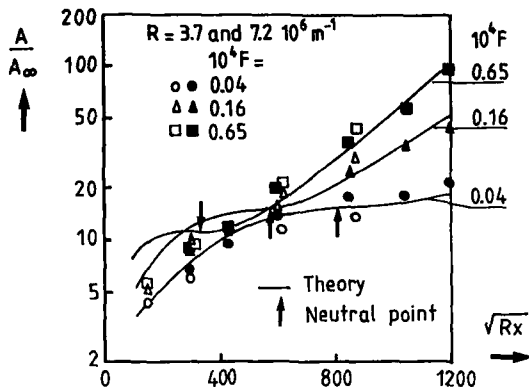
Figure 26 - Streamwise evolution
of the amplitude of various
frequencies at Me = 4.5.
Comparison between experiments
(Kendall) and theory (Mack).

MACK attempted to account for these observations by developing a theory which gives an answer to this particular aspect of the receptivity problem /14/. The calculations were divided in two parts :

. from the leading edge to the neutral point, MACK computed the **forced** response of the boundary layer to incoming sound waves (forcing theory). This requires solutions of homogeneous equations, with non homogeneous boundary conditions ;

. downstream of the neutral point, the linear stability theory (homogeneous equations with homogeneous boundary conditions) was then used to compute the development of **free** disturbances having the same frequencies.

Although the mechanism by which the forced wave turns into a free wave is ignored in this theory, the agreement with KENDALL's experiments is remarkable (Figure 26).

9.2. Sharp cone experiments

The flow on supersonic sharp cone constitutes a second case where the free-stream Mach number is constant in the streamwise direction. However, it has been shown that the link between the instability properties on a cone and on a flat plate is not straight-forward. Stability experiments on sharp cones have been lacking until relatively recently ; at the present time, three series of measurements that provided us with detailed data have been carried out by KENDALL (1975, /50/), DEMETRIADES (1977, /52/), STETSON et al. (1983) /53/). The following table gives the main characteristics of these experiments ($\hat{a}$ is the half-angle of the cone, M_∞ the free-stream Mach number, Me the edge Mach number) :

Author	$\hat{a}°$	M_∞	Me	
KENDALL	4.5	8.5	7.7	Cooled wall, $T_w/T_{aw} = 0.6$
DEMETRIADES	4	8	7	Cooled and uncooled wall
STETSON et al.	7	8	6.8	Uncooled

Figure 27 shows evolutions of the spatial amplification rate $-\alpha_i$ as a function of the frequency ω (in this figure, the reference length is $L = (\nu_e x/u_e)^{1/2}$). The experimental curves were obtained in the three experiments at (nearly) the same value of the

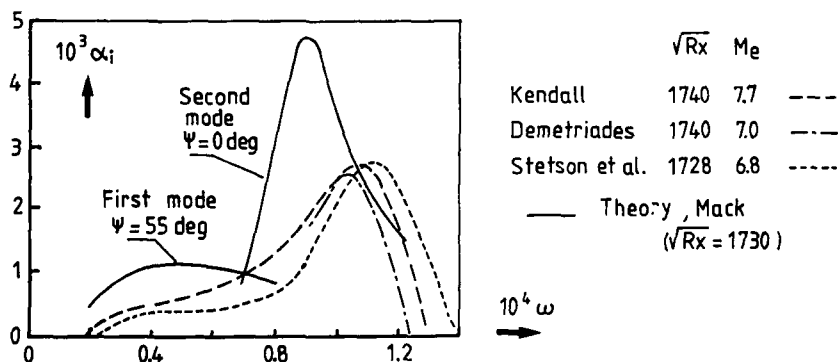|	$\sqrt{Rx}$	M_e	
Kendall	1740	7.7	---
Demetriades	1740	7.0	--.---
Stetson et al.	1728	6.8	-----

Theory , Mack
($\sqrt{Rx} = 1730$)

Figure 27 - Calculated amplification rate compared with experimental
data on sharp cones.

streamwise Reynolds number Rx. "There is some disagreement in detail among the experiments, but general agreement that there is a band of unstable frequencies, with the lower frequencies being only weakly amplified and the higher frequencies more strongly amplified with a marked peak in amplification rate" (MACK, /45/). Theoretical curves computed by MACK are also plotted in this figure. Although the agreement is not perfect, the calculation seems to indicate that first and second mode instabilities are simultaneously present with different ψ angles.
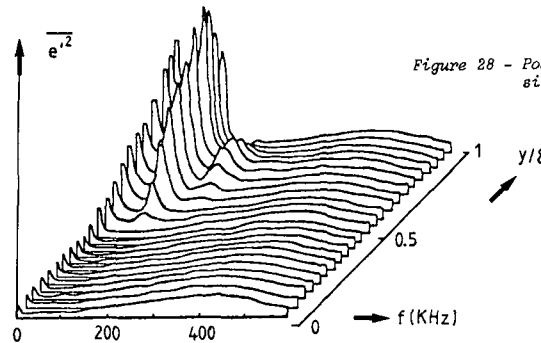

Figure 28 - Power spectra of hot-wire signals. Sharp cone experiments.

Another example of result by STETSON et al. is presented in Figure 28. It shows power spectra of the hot-wire signals obtained at a given station for various distances above the wall. As it is predicted by the theory, the largest disturbances amplitudes are observed near the outer edge of the boundary layer. However, it must be noticed that the hot wire signals contain all types of fluctuations (pressure, temperature, velocity) and, as it has been pointed out by MORKOVIN, (see /54/), extraction of u', T' and p' information cannot be made in this case by using KOVASZNAY's modal decomposition.

An interesting feature is that all three experiments gave another band of unstable frequencies starting at a frequency above the upper-branch neutral frequency of the second mode. This band does not exist in linear stability theory. As the temperature and density fluctuations are large, a possible explanation is that the additional unstable region "is probably the result of non-linearity. The frequency band where it occurs suggests a first harmonic of the second mode" (MACK, /45/).

10. BLUNTNESS EFFECTS

POTTER and WHITFIELD /55/ performed measurements and collected available experimental data in order to study the effect of slight nose bluntness on transition location. For the flat plate case, the nose bluntness can be characterized by two parameters (Figure 29) :

. the bevel angle θ

. the leading edge thickness b, which is used for calculating the bluntness Reynolds number $R_b = u_e b / \nu_e$.
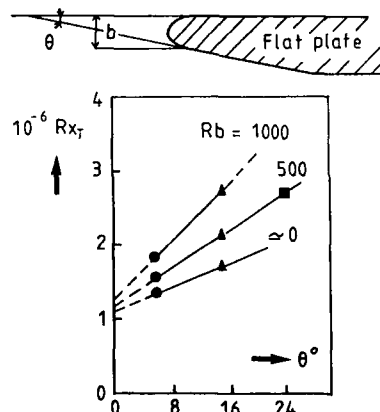

Figure 29 - Effect of bluntness : flat plates
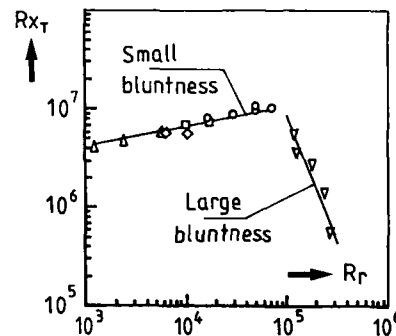(Potter and Whitfield)

Figure 30 - Effect of bluntness : cones
(Softley et al.).

Figure 29 shows the evolution of the transition Reynolds number as a function of θ and R_b, for fixed values of the free-stream Mach number and of the unit Reynolds number ($M_e = 3$, $u_e/v_e \approx 13.4 \ 10^6 \text{m}^{-1}$). It is clear that increasing the bluntness parameters delays transition onset, even if these small degrees of nose bluntness have a negligeable effect on measured pressure distributions. POTTER and WHITFIELD correlated these results with the following relationship :

$$Rx_T = Rx_{TO} + 160 \ R_b + 36 \ 500 \ \theta + 55 \ R_b\theta \qquad (20)$$

where θ is in degrees and Rx_{TO} corresponds to $\theta = R_b = 0$.

It must be kept in mind that relation (20) holds for small bluntness only ; this was verified by STETSON et al. /54/, who studied the transition mechanisms on a blunt-cone. The model and the experimental conditions were identical to those already described in the previous section ($\hat{\alpha} = 7°$, $M_\infty = 8$), except that the cone could be equipped with interchangeable spherically blunted noses of various radii r. For small values of r, the entropy swallowing region has a stabilizing effect, since disturbances which were observed on the sharp cone were no longer detected ; STETSON et al. estimated that the transition Reynolds number might be multiplied by a factor 2 for an "optimum" nose bluntness, in qualitative agreement with the observations of POTTER and WHITFIELD on flat plates. But the trend is reversed as soon as the nose bluntness exceeds a certain limit : Rx_T decreases with increasing nose radii. For large values of r, STETSON et al. measured large amplitude disturbances <u>outside</u> the laminar boundary layer. This seems to indicate the existence of an inviscid instability, which can be related with the appearance of a generalized inflexion point in the entropy layer, somewhere between the boundary layer edge and the shock. These disturbances grow in the streamwise direction, enter the boundary layer and lead to premature transition, as it is the case for boundary layers subjected to a strong external disturbance environment.

To summarize these results, experimental data by SOFTLEY et al. /56/ are reported in Figure 30. Transition Reynolds numbers measured on blunted cones are plotted vs $R_r = u_er/v_e$. ERICSSON noted that the delay of transition caused by "small" bluntness is attenuated by the wind tunnel noise, but in free flight an order of magnitude increase in Rx_T can be obtained for the "optimum" nose bluntness /57/. It is also important to recall that the effects of bluntness can be explained within the scope of the linear theory as it was demonstrated, for instance, by RESHOTKO and KHAN /58/ (presence of a generalized inflexion point inside and/or outside the boundary layer) ; however, stability computations require accurate calculations of the mean flow, and this requirement is not always easy to meet.

11. UNIT REYNOLDS NUMBER EFFECTS

An experimental observation is that, for a given model and a given free-stream Mach number, an increase of the unit Reynolds number $R = u_e/v_e$ leads to an increase of the transition Reynolds number Rx_T. It is the mythical "Unit Reynolds number effect", which is often represented by the simple power relation :

$$Rx_T \sim R^l \qquad (21)$$

l is an empirical constant. For "noisy" hypersonic wind tunnels, it lies roughly between 0.1 to 0.6. Figure 31 presents typical experimental results obtained by STAINBACK et al. /59/ on sharp cones : there is no well defined Mach number effect, and the data are well correlated by relation (21) with l = 0.45 . In fact, the problem is much more complex : in the same wind tunnel, there are some operating conditions where the R dependence disappears, although it is present at others (see SOFTLEY et al. /56/ for instance).
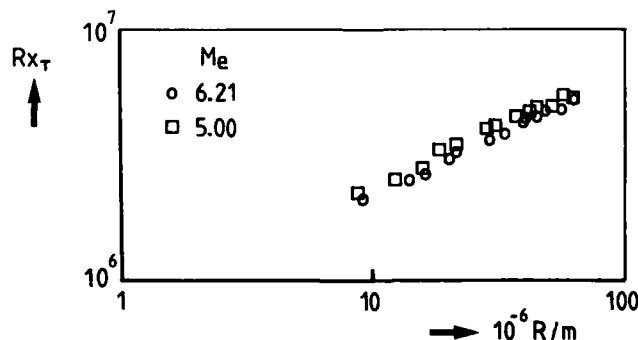

Figure 31 - Effect of unit Reynolds number (Stainback et al.)

It is clear that the unit Reynolds number effect represents a combined response to many factors, three of which are listed below :

a - Radiated noise - When R varies, the characteristics of the wall turbulent boundary layer are modified, so that the radiated noise is also modified. This factor is accounted for by PATE's relation (15), which implies that Rx_T increases as the square root of R. Consequently, if the acoustic irradiations are removed (flight tests), the R dependence would disappear.

b - Nose bluntness - Even with very small nose radii r or very small leading edge thickness b, Rx_T is very sensitive to R_r or R_b (see previous section). As $R_r = Rr$ and $R_b = Rb$, increasing R for fixed r or b can modify the transition Reynolds number.

c - Receptivity and stability theory - As it has been demonstrated in Section 4.1, the amplitude A of a given eigenoscillation of frequency f can be expressed by :

$$A(x,f) = A_o(f) \int_{x_o}^{x} - \alpha_i \, dx \qquad (22)$$

where A_o is the amplitude taken at the position x_o where the wave begins to be amplified. The receptivity problem consists in establishing the link between $A_o(f)$ and the amplitude $E(f)$ of the free-stream disturbances having the same frequency. Intuitively, one can think that $E(f) = 0$ implies $A_o(f) = 0$; it follows that $A(f) = 0$ at all downstream locations, whatever the amplification rate is.

Let us consider now the simplest example of a flat plate with a constant free-stream Mach number. Changing the unit Reynods number R has the following consequences :

. the free-stream disturbances spectrum is changed. Its upper frequency limit f_1 is a (generally increasing) function of R ;

. in the boundary layer, the range of potentially unstable frequencies is also changed ; the stability diagram remains the same when expressed in dimensionless variables, but this is no longer true when physical variables are used.
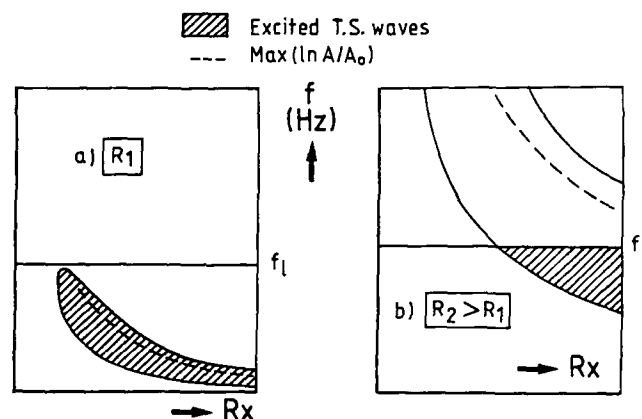
Figure 32 - Effect of unit Reynolds number on stability characteristics

As it is illustrated in Figure 32, the relative motion of the environmental distur- bances spectrum and of the linearly unstable frequency range can give rise to a strong unit Reynolds number effect. For instance, if f_1 exceeds the upper limit of the unstable waves fre- quencies, then all instability waves will be excited and the transition Reynolds number will be low (Figure 32a). On the contrary, if f_1 is close to the lower branch of the stability diagram (Figure 32b), a certain band of eigenoscillations will be excited at high Reynolds number : for $f > f_1$, $E(f) = 0$, so that $A_o(f) = 0$ and $A(f) = 0$, even if these frequencies are un- stable according to the linear stability theory. In this case, large values of Rx_T can be measured. On the other side, as the dimensionless frequency appearing in stability computa- tions is $2\pi f\nu/u_e^2$, the characteristic frequency u_e^2/ν is also an important parameter.

These problems were carefully investigated by STETSON et al. /60/, who concluded that "knowledge of the stability characteristics of a boundary layer is only part of the problem. The external disturbances must be prescribed in order to make a boundary layer transition prediction based upon stability considerations". By the way, it becomes clear that the e^n method has a limited physical meaning, because it assumes impliciteiy that all unstable waves have the same initial amplitude.

12. STREAMWISE CURVATURE EFFECTS

For flows developing over a convex surface, centrifugal forces exert a stabilizing effect, in the sense that a displaced fluid element tends to be restored to its equilibrium position. The magnitude of this effect is small : in incompressible flow, it was found that on convex surfaces up to $\delta_1/\mathcal{R} = 0.0026$ ($\mathcal{R}$ is the radius of curvature), the same TOLLMIEN-SCHLICHTING instability occurs as for the flat plate and the transition Reynolds number remains unchanged.
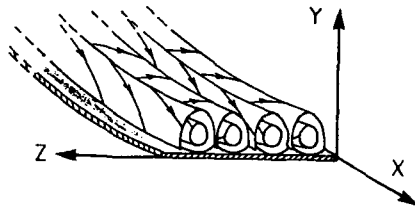

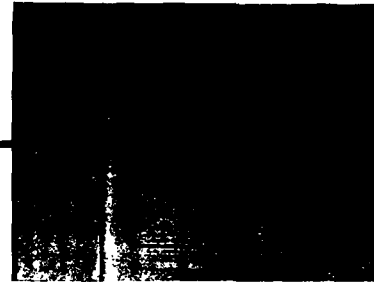Figure 33 - Görtler vortices in a flow along a concave wall.

Figure 34 - Görtler vortices behind a backward facing step at Mach 3 (Ginoux)

On the other hand, the destabilizing effect of centrifugal forces on concave walls leads to the formation of pairs of counter-rotating vortices, the axes of which are parallel to the principal flow direction (Figure 33). This instability, which was first treated by GÖRTLER /61/, acts in two ways on the boundary layer development. At first, the GÖRTLER vortices affect indirectly the transition process by modifying the development of unstable waves and the breakdown to turbulence occurs earlier than on a flat plate. The second aspect is essentially important in compressible flows : the vortices induce spanwise variations of the wall heat flux, which result in strong nonhomogeneities of the wall temperature in the laminar regime.

In fact, the appearance of GÖRTLER instability is not necessarily linked with the presence of a concave surface ; arrays of longitudinal vortices can be observed on flat plates as soon as the model geometry imposes a concave curvature in the streamlines. For example, GINOUX /62/ showed evidence of streamwise vortices at a Mach number of 3, behind a backward facing step. The sublimation picture reported in Figure 34 shows a typical example of striation pattern observed in the reattachment region. In this case, the boundary layer streamlines, in separating from the corner and reattaching on the plate, exhibit a strong concave curvature which induces streamwise vortices. GINOUX measured the local heat transfer rates and noted that the effect of these vortices was to produce locally very large peaks in the heat rate, much larger than the usually measured turbulent values immediatly after transition.

Streamwise vortices were also observed by many authors behind a wire roughness or downstream the reattachment line in a compression corner (DELERY-COET /63/). TOBAK /64/ demonstrated that concave curvature in the streamlines may be connected with the origin of "cross-hatching" on the surface of re-entry vehicles. In all cases, the vortices are responsible for large spanwise variations of the wall heat flux.

On the theoretical side, the problem of GÖRTLER vortices can be treated by using a linearized stability theory. Several papers were devoted to stability analyses in incompressible flow (see /65/ for example), but calculations including compressibility effects are not numerous. EL-HADY and VERMA /66/ investigated the growth of streamwise vortices in two-dimensional boundary layers along curved surfaces over a range of Mach numbers from 0 to 5 ; similar computations are currently performed at ONERA/CERT by S. JALLADE /67/. These calculations use a curvilinear system of coordinates representing streamlines and potential lines of the inviscid flow. It can be demonstrated that the mean flow is described at the first order by the conventional compressible boundary layer equations. A steady three-dimensional small disturbance is then superposed on this two-dimensional basic flow ; the disturbances under consideration are assumed in the form :

$$r' = \hat{r}(y)\cos(\alpha z)\exp(\sigma x), \quad \text{with} \quad r' = u', \, v', \, p' \text{ or } T'$$
$$\text{and} \quad w' = \hat{w}(y)\sin(\alpha z)\exp(\sigma x), \tag{23}$$

where α is the wavenumber in the spanwise direction and σ the spatial growth rate in the x-direction along the curved wall. α and σ are usually made dimensionless with the characteristic length $L = (\nu_\infty x/u_\infty)^{1/2}$.

As for the TOLLMIEN-SCHLICHTING waves problem, relation (23) are substituted into the linearized NAVIER-STOKES equations. Keeping the leading term leads to an eighth order system of homogeneous, linear, ordinary differential equations with homogeneous boundary

conditions. This forms an eigenvalue problem for the three real parameters α, σ and G. G is the GÖRTLER number, defined as :

$$G = \frac{u_\infty L}{\nu_\infty} \left(\frac{L}{\mathcal{R}}\right)^{1/2} \tag{24}$$

where $\mathcal{R}$ is the radius of curvature of the wall.

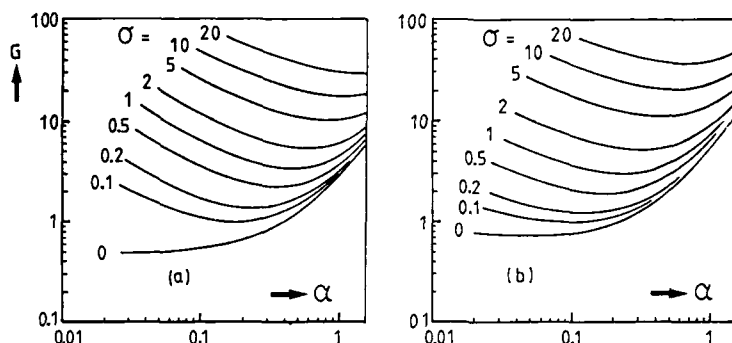*Figure 35 - Stability diagrams for M = 0 (a) and 3 (b) (Jallade, /67/)*

Two stability diagrams are presented in Figure 35 for an adiabatic wall and two Mach numbers (M_∞ = 0 and 3). Curves of constant amplification rate are plotted in the GÖRTLER number-wavenumber plane. The shape of these curves does not change very much when the Mach number increases ; as for the TOLLMIEN-SCHLICHTING waves, there is a critical GÖRTLER number, G_{cr} , below which the flow is stable for any disturbance wavenumber. It can be observed that compressibility has a stabilizing effect : as M_∞ increases , the maximum growth rate at a given GÖRTLER number decreases ; however, the influence of compressibility on reducing σ becomes very small at high values of G. Computations by EL-HADY and VERMA /68/ showed also that GÖRTLER instability is more difficult to influence and control by suction or cooling than TOLLMIEN-SCHLICHTING instability.

It is then possible to calculate the total amplification rate $\ln A/A_0$ by integrating the local growth rate in the streamwise direction. For the TOLLMIEN-SCHLICHTING waves, this integration is carried out for each frequency ; for the GÖRTLER vortices, it is performed for each spanwise wavelength. This was done by EL-HADY and VERMA, who concluded that compressibility reduces the maximum amplitude ratio by 20 % as Mach number increases from 0 to 5. BECKWITH et al. /69/ used the e^n method in order to predict transition location along the nozzle walls of the "quiet tunnel" ; they found that TOLLMIEN-SCHLICHTING instability is weak, and that transition results in the growth of GÖRTLER vortices along the concave walls. Nevertheless, calibration of the e^n method for the GÖRTLER instability remains an open question.

13. EFFECTS OF 3D ROUGHNESSES IN 2D MEAN FLOW

It has been emphasized that conventional wind-tunnel facilities cannot properly simulate flight transition conditions. This is essentially true for "natural" transitions occuring on smooth surfaces. Nevertheless, when large roughness elements are introduced into the laminar boundary layer, on can expect that their effects would overwhelm those of wind tunnel noise, so that the experimental results become representative of flight conditions. This section is devoted to a survey of available information related to the effects of three-dimensional roughness elements (spheres or cylinders normal to the wall) in a two-dimensional laminar boundary layer.

13.1. Flow field around and downstream of a roughness element

Figure 36 shows a proposed flow model for a spherical roughness element ; this model is based on oil patterns obtained by MORRISETTE et al. /70/. The free-stream Mach number is equal to 5.5, and the sphere diameter is about twice the boundary layer thickness. The visualization indicates that the flow separates well ahead of the element. The shock from the separation wedge is assumed to interact with a bow shock produced ahead of the protuberance. A group of vortices initiate ahead of the sphere and pass around the element. The downstream development of the vortices is illustrated in Figure 37, which presents a wall visualization obtained at ONERA /71/ by using a thermosensitive paint (Me = 5.25 , k/δ = 1.5 , where k is the roughness height). The "legs" of the vortices remain parallel with the wind tunnel axis up to a certain distance L from the roughness ; a close examination of the photographs indicate that one to three vortices are at first visible around the sphere (depending on its diameter), but, in all cases, a single vortex remains visible at the distance L. At this point, one can observe the onset of a "turbulent" wedge which spreads slowly downstream. The exact mechanism of this breakdown is not very well known at this time.
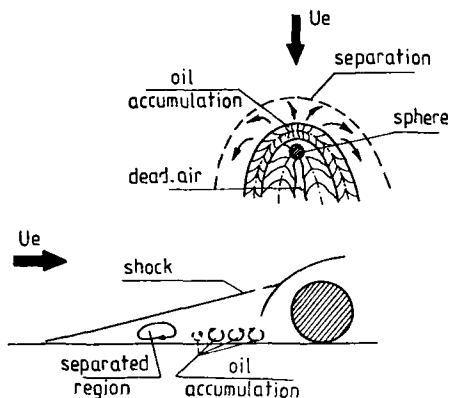
Figure 36 - Flow field around a spherical
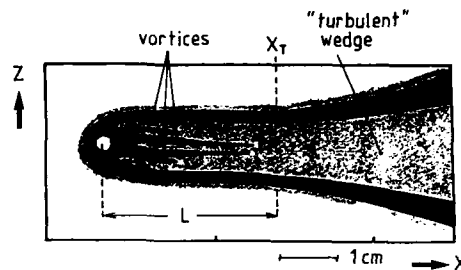roughness element (Morisette)

Figure 37 - Example of visualization using
thermosensitive paint.

13.2. The effective roughness height

Some notations are given in Figure 38a, in order to introduce quantitative results. x_{TO} represents the "natural" transition location (without roughness), and x_T is the transition location when a roughness element is present ; x_T is defined as the point where the turbulent wedge begins to develop, i.e. $x_T = x_k + L$, where x_k corresponds to the roughness location. x_{TO} , x_T , x_k and k are used for obtaining the Reynolds numbers Rx_{TO} , Rx_T , Rx_k and R_k ; these are computed with the velocity and the kinematic viscosity taken in the free-stream.
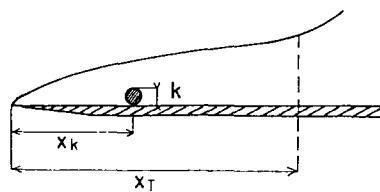
a) Notations
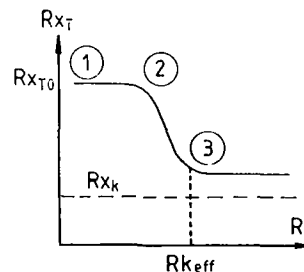
b) Transition location

Figure 38 - Effect of a three-dimensional roughness element on transition

Figure 38b shows schematically the influence of the roughness size on transition location. Between (1) and (2) , the roughness has very little effect , indicating that the streamwise vortices wrapped around the protuberance do not dominate the boundary layer development before they decay. The region between (2) and (3) is characterized by a relatively small change in roughness size, causing a large change in transition position ; however, as Mach number increases, this movement becomes more and more gradual. The curve beyond point (3) shows only a small change in transition location with trip size. Point (3) in the bend of the transition curve is defined as the "effective trip" size, and the value of R_k at this point is denoted Rk_{eff} ; for a constant unit Reynolds number and for increasing roughness heights such that $R_k > Rk_{eff}$, the distance L between the trip and the turbulent wedge apex remains pratically constant. In fact, the Reynolds number $R_L = u_e L / \nu_e$ depends on the Mach number and on the model geometry. This can be seen in Figure 39, published by MORISETTE et al. /70/, which presents the evolution of R_L as a function of Me for flat plates and cones.. ; some additional data obtained at ONERA /71/ are also plotted on this figure. For incompressible flow, the turbulent wedge begins to spread immediatly downstream of the roughness, but R_L increases for increasing Mach numbers. On the other side, there are large differences between the curves obtained for cones and for flat plates.

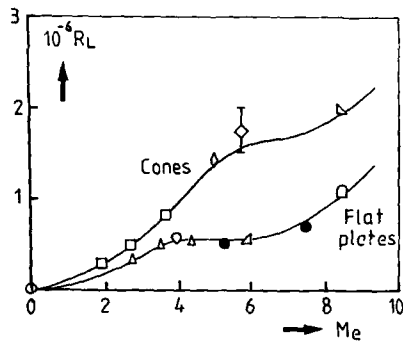Figure 39 - Variation of Reynolds number based on distance from trip to transition with Mach number : open symbols : experimental data collected by Morrisette

● : O.N.E.R.A. experiments.

13.3. Transition criteria

From a practical point of view, the value of Rk_{eff} is of great importance . VAN DRIEST and BLUMER performed a series of experiments in order to deduce empirical correlations between Rk_{eff} , Rx_k and the flow parameters. The measurements were made on cones, for free-stream Mach numbers within the range of 1.9 to 3.67. The results were obtained on adiabatic walls /72/ /73/ and later on cooled walls /74/. Spheres were used as tripping devices and the transition position was measured with a schlieren system.

VAN DRIEST and BLUMER correlated their experimental results with the following relationship, which includes variations in Mach number and heat transfer :

$$Rk_{eff} = 33.4 \left[1 + \frac{\gamma - 1}{2} M_e^2 - 0.81 \frac{T_{aw} - T_w}{T_e} \right] Rx_k^{1/4} \tag{25}$$

Let us recall that this relation was deduced from cone experiments. VAN DRIEST and BLUMER assumed that it was also applicable to flat plate flows by using MANGLER's transformation, which simply consists in replacing the coefficient 33.4 by 33.4 $(3)^{1/4}$ = 44. On adiabatic walls, relation (25) reduces to :

$$(Rk_{eff})_{aw} = K \left[1 + \frac{\gamma - 1}{2} M_e^2 \right] Rx_k^{1/4} \tag{26}$$

with K = 33.4 and 44 for cones and flat plates, respectively. It can also be demonstrated that :

$$\frac{Rk_{eff}}{(Rk_{eff})_{aw}} = 1 - 0.81 \left(\frac{T_{aw} - T_w}{T_{ie}} \right) \tag{27}$$

where T_{ie} is the stagnation temperature in the free-stream.

Figure 40 shows the application of VAN DRIEST - BLUMER relation to some experimental results on cones. Values of $(Rk_{eff})_{aw}$ computed from measured values of Rk_{eff} by using relation (27) are plotted as a function of Rx_k for Mach numbers between 1.9 and 8.5. The dotted lines represent theoretical values of $(Rk_{eff})_{aw}$ given by (26). The agreement is good for Me = 1.9 , 2.7 and 3.67 ; this is not suprising because these experimental data were obtained by VAN DRIEST and BLUMER who used them for obtaining relation (25). For Me = 8.5 (Mc CAULEY et al. experiments /75/),the criterion underestimates $(Rk_{eff})_{aw}$ by a factor two.
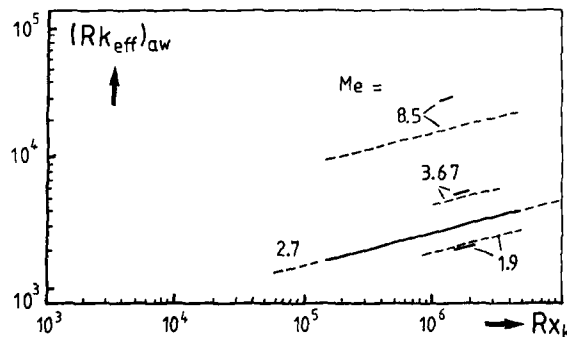

Figure 40 - Variation of effective roughness Reynolds number with Rx_k and Me for cones. —— experiments - - - - van Driest - Blumer correlation.
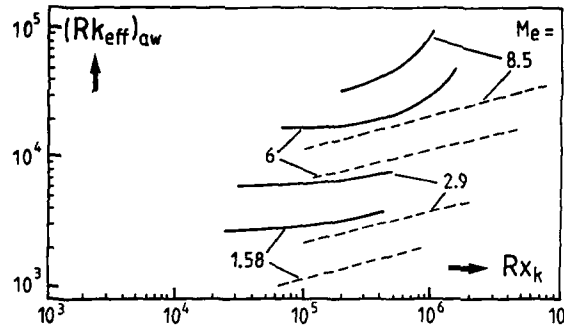
Figure 41 - Variation of effective roughness Reynolds number with Rx_k and Me for flat plates. For legend, see previous figure.

The same kind of comparisons is presented in Figure 41 for flat plate experiments. In this case, there are large discrepancies between the correlation (26) and the measurements, even for the lowest Mach numbers. For fixed values of Me and Rx_k, the ratio between $(Rk_{eff})_{aw}$ values on flat plates and cones is only $44/33.4 = 1.32$ by applying relation (26). The experiments give a much larger ratio (between 2 and 3) ; this can be seen by comparing the experimental results at Me = 8.5 and $Rx_k \approx 10^6$ in Figures 40 and 41. The conclusion is that MANGLER's transformation is generally correct for the mean flow properties, but cannot be used for stability and transition problems.

Relations (25) to (27) give only the value of the effective roughness size. POTTER and WHITFIELD /55/ deduced a correlation describing the variation of transition position with change in roughness Reynolds number R_k. In fact, R_k is modified by a temperature function which gives a new Reynolds number R'_k defined as :

$$R'_k = R_k \left(T_k/T_w \right)^{\omega + 0.5} \tag{28}$$

T_k is the static temperature at the top of the roughness and ω represents the exponent in viscosity-temperature relation $(\mu \sim T^\omega)$.

R'_k is then divided by a parameter ε , which is a given function of the free-stream Mach number, and the ratio R'_k/ε is then correlated on a curve such that :

$$\frac{R'_k}{\varepsilon} = f \left[\sqrt{\frac{x_T}{x_{TO}}} - \sqrt{\frac{x_k}{x_{TO}}} \left(\frac{R'_k}{\varepsilon} \right) \right] \tag{29}$$
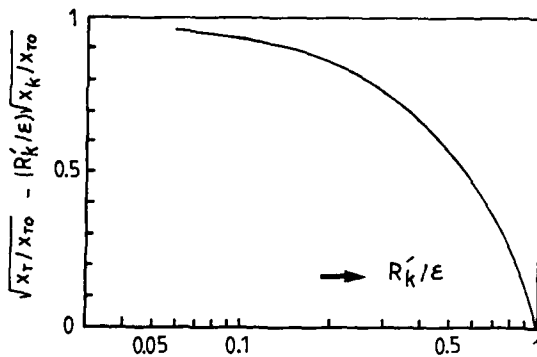
Figure 42 - Correlation proposed by Potter and Whitfield.
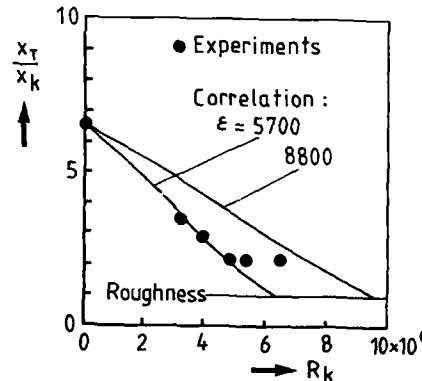
Figure 43 - Correlation used to predict transition position (Me = 8.5). Effect of the parameter ε

This curve is plotted in Figure 42. MORISETTE et al. /70/ applied this correlation to their experiments ; an example of comparison is shown in Figure 43. It appears that the transition movement is fairly well predicted, except close to the roughness : for $R'_k = \varepsilon$, the curve in Figure 42 implies that $x_T = x_k$. This means that transition can be moved back up to the roughness location, in contradiction with the concept of "effective" roughness height. It follows that the correlation of POTTER and WHITFIELD can be used only between points ① and ③ of figure 38, provided the smooth wall transition location is known.

13.4. Effect on wall heat flux

Up to now, attention was focused on the transition position. Another important aspect of the problem is the variation of the wall heat flux in the presence of roughness elements. Some experimental results are described below in order to illustrate the complexity of this problem ; they were obtained at ONERA for the following conditions : Me = 5.25 , Tw/Taw = 0.33 , R = 11 10^6 m^{-1} /71/. The roughness elements are small cylinders, the height of which is equal to the diameter. They are placed on a flat plate, 7 cm downstream of the leading edge. The length of the plate is c = 25 cm.
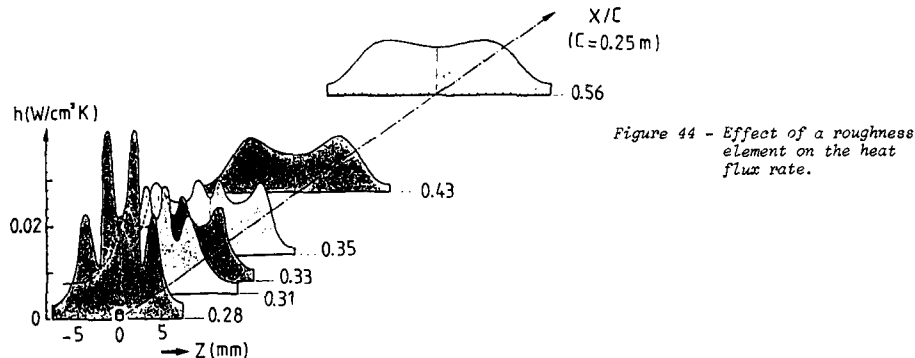
Figure 44 - Effect of a roughness element on the heat flux rate.

Figure 44 shows the evolution of the heat flux coefficient   h = $\emptyset_w$ / (T_w - T_{aw}) in the streamwise and spanwise directions, downstream of a cylinder of height k = 1.2 mm ≈ 1.5 δ . In these conditions, two vortices are clearly visible around and downstream of the roughness, and the turbulent wedge starts to develop at x/c ≈ 0.40. Upstream of this position, the "legs" of the vortices induce values of the heat flux which can be two times greater than those which are measured in the turbulent region. Let us observe also that a local maximum of the heat flux is detected on each side of the turbulent wedge.
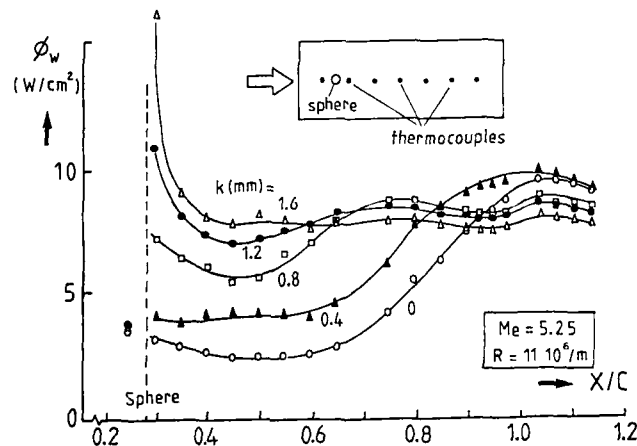
Figure 45 - Heat flux rate behind roughness element of increasing size (spheres)

Streamwise evolutions of the wall heat flux are plotted in Figure 45 for various roughness sizes. The measurements are made with a row of thermocouples located along the symmetry plane of the roughness . Immediatly downstream of the protuberance, the wall heat flux increases with increasing values of k ; and it becomes difficult to define a "transition point". For k ≥ 1.2 mm, the heat transfer rate is practically constant downstream of the roughness element (except close to the element where it reaches values larger than the turbulent ones). To summarize, the problem of minimizing the heat transfer rates in hypersonic boundary layers requires not only to delay transition, but also to avoid streamwise vortices in the laminar boundary layer (GÖRTLER vortices or roughness-induced vortices.

14. TRANSITION REGION (TWO-DIMENSIONAL FLAT PLATE FLOWS)

14.1. Definition of the transition region

Transition starts when the first turbulent structures (spots) appear in the laminar boundary layer. In natural conditions, the spots originate in a more or less random fashion. Once created, they are swept along with the mean flow, growing laterally and axially, and finally covering the entire surface. The transition region is defined as the region where the spots grow, overlap and form a turbulent boundary layer. When a hot wire is placed in the boundary layer (or when a film gage is mounted flush with the model surface), the fluctuations which are recorded in the transition region show the successive appearance of turbulent spots and of laminar regions : it is the intermittency phenomenon. The intermittency factor γ represents the fraction of the total time that the flow is turbulent. Experimentally, it is not always easy to define the beginning ($\gamma = 0$) and the end ($\gamma = 1$) of transition.

The beginning of transition is often taken at the point of initial measurable deviation of a characteristic parameter from its laminar evolution. This can be, for instance, the beginning of a faster growth of the boundary layer thickness, the point of minimum surface temperature (or surface Pitot pressure, or wall heat flux), the location where the increase in the rms voltage from a hot wire becomes steeper... As it has been pointed out by OWEN and HORSTMAN /76/, most of the transition data reported for high speed flows are not based on direct observations of turbulent spots, but rather on the evolution of some macroscopic parameter (skin friction, heat transfer...) ; their departure from laminar values can be detected only when the intermittency is appreciably greater than zero.

In the transition region, it is well known that quantities such as rms voltage, skin friction, wall heat flux... reach a maximum at nearly the same location /77/ and then decrease more or less slowly. The peak value of these quantities is often used to define the end of transition, because its position is easy to measure accurately. However, these points are located upstream of the end of transition. For instance, it is established (OWEN, /77/) "that the peak rms signal coincides with the point where the turbulent burst frequency is maximum" and not with the point where the boundary layer is fully turbulent.

These observations can explain to a great extent the large scatter which is observed in transition data. Inconsistent choices of criteria for the beginning and the end of transition make difficult to compare experimental results obtained through different techniques. However, in spite of these problems, some general trends have been put forward, as it will be shown below.

14.2 Extent of the transition region

Let us assume now that the locations of transition onset, x_T , and of transition end, x_E , are measured in a consistent way. $\Delta x = x_E - x_T$ represents the transition extent, and the Reynolds numbers Rx_T , Rx_E, $R\Delta x$ are based on x_T, x_E and Δx, respectively. The evolution of $R\Delta x$ as a function of Rx_E is given in Figure 46 for free-stream Mach numbers between 0 and 8 ; these data were obtained or collected by POTTER and WHITFIELD /55/, who defined x_T and x_E by examining the boundary layer growth from schlieren photographs. At a given value of Rx_E it is clear that a significant increase in $R\Delta x$ is associated with increasing Mach number. CHEN and THYSON /78/ suggested the following relationship :

$$R\Delta x = (60 + 4.86 \ Me^{1.92}) Rx_T^{2/3} \qquad (30)$$

which reflects the experimental trend. Parameters such as wall temperature, unit Reynolds number.. are not taken into account in this correlation. It was noted by MORKOVIN /79/

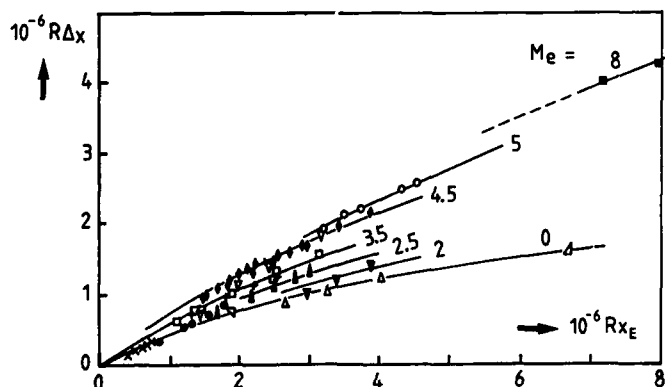
Figure 46 - Extent of the transition region (Potter and Whitfield)

that "the lateral or transverse growth of a turbulent spot decreases from about 11°
semiangle at low speeds to about half the angle at hypersonic speeds". The same observa-
tion can be made for the spreading of a turbulent wedge behind an isolated roughness
element. Both phenomena involve the same physical mechanism which is called "transverse
contamination".

14.3. Transition region modelling

From a practical point of view, the modelling of the transition region becomes a
more and more important problem when the Mach number increases : this is due to the fact
that, for supersonic and hypersonic flows, the evolution from the laminar to the turbulent
state occurs along a streamwise distance which can be much more important than the laminar
region extent which precedes it.

A practical calculation method was developed at ONERA/CERT for the two-dimensional,
incompressible flows /80/ and then extended to high speed conditions : it is assumed that
the turbulent shear stress is expressed by :

$$- \rho \overline{u'v'} = \widehat{\epsilon} \mu_t \partial u / \partial y \tag{31}$$

μ_t is an eddy viscosity coefficient, which is computed by using a classical
turbulence model. At first sight, the coefficient $\widehat{\epsilon}$ represents the intermittency factor γ,
in this sense that it increases from 0 in laminar flow to 1 in turbulent flow. From
experimental data at **low speeds**, it was found that the momentum thickness θ_E at the
completion of transition was about twice the momentum thickness θ_T at the transition
onset. This led to the idea that $\widehat{\epsilon}$ could be represented as a function of θ/θ_T. This
function was determined to fit available experimental results in zero and positive
pressure gradients. It is shown in Figure 47 ; one of the problems was to model the over-
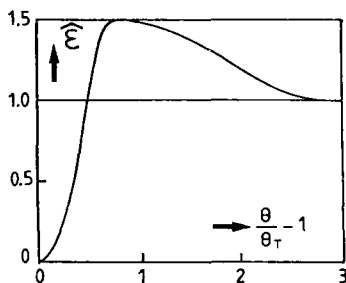
Figure 47 - "Intermittency" function
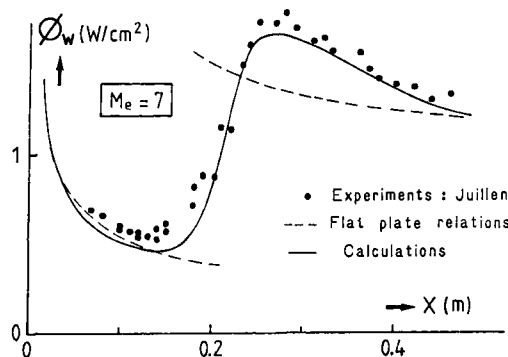
Figure 48 - Comparison with experimental
results obtained by Juillen

shoot in the skin friction coefficient, which exists in the middle of the transition
region due to the intermittency phenomenon. This was done by imposing an overshoot to
the function $\widehat{\epsilon}$, which does not represent the physical intermittency factor, but rather an
empirical weighting coefficient for the Reynolds shear stress.

This method was extended to **supersonic and hypersonic flows** by taking into account
the lengthening of the transition region at high speeds. For this, the analytical expres-
sion of the function $\widehat{\epsilon}$ remains the same, the parameter $\theta/\theta_T - 1$ being simply replaced
by $(\theta/\theta_T - 1) / (1 + 0.02 \ M_e^2)$.

A first example of application is given in Figure 48. The calculated wall heat
flux is compared with measurements performed by JUILLEN /30/ on a flat plate for Me = 7.
The location of transition onset is imposed ($x_T = 0.1$ m). Laminar and turbulent curves
deduced from analytical flat plate relations are also shown. The "intermittency" method
gives good results ; in particular, the maximum of the heat flux is well predicted.
This maximum represents an overshoot above the fully turbulent value, as it can be
seen by comparison with the turbulent curve ; it has been noticed previously that this
point is associated with the maximum spots frequency, and not with the completion of
transition. In fact,the fully turbulent properties are only achieved towards the end of the
plate.

Figure 49 shows another example of comparison between experiments and calculations.
The measurements were carried out by COLEMAN et al. /81/ at a free-stream Mach number
equal to 9 and for three values of the unit Reynolds number. As for the previous case,
the position of transition onset is given in the computations. The increase in the wall
heat flux and the location of its maximum are well predicted, but large discrepancies
are observed further downstream. The calculations indicate that the transition region
extends up to x ≈ 0.6 m.

$10^{-5} R_e$/cm

o	5.5
△	2.76
□	1.46

Experiments : Coleman , Elfstrom and Stollery

—— Calculations

ϕ_w
(W/cm^2)

Me = 9   Ti = 1070 K
Tw = 295 K
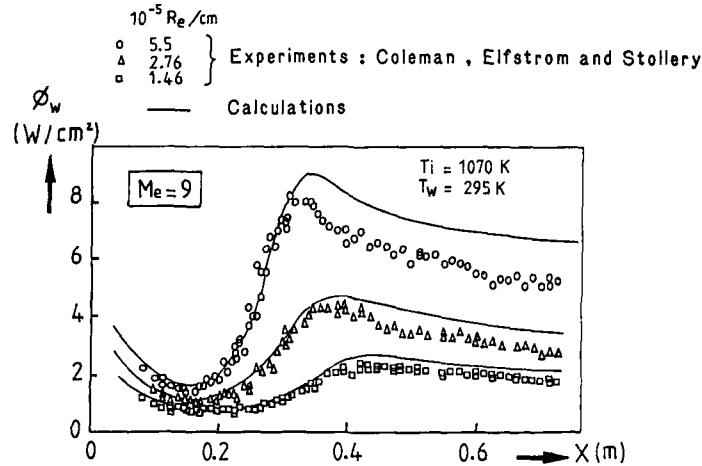
Figure 49 - Comparison with experimental results obtained by Coleman et al.

15. THREE-DIMENSIONAL FLOWS : CROSS-FLOW INSTABILITY

When a boundary layer develops on a three-dimensional geometry, such as a swept wing, a swept cylinder or a body at incidence, the mean velocity profile becomes twisted. It is usually decomposed into a streamwise profile u (in the direction of the external streamline) and a cross-flow profile w (in the direction normal to this streamline), as illustrated in Figure 50.
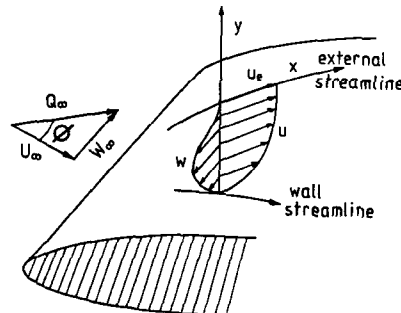
Figure 50 - Streamwise and cross-flow mean velocity profiles

In incompressible flow, the mechanisms of three-dimensional transition are relatively well understood, see review papers by POLL /82/, ARNAL /83/, SARIC and REED /84/. As a first approximation, it can be assumed that transition is induced either by streamwise instability or by cross-flow instability. The streamwise mean velocity profiles look like classical two-dimensional profiles ; they are essentially unstable in positive pressure gradients, where they induce transition through the action of an inflexional instability. On the other side, an inflexion point is always present in the cross-flow mean velocity profiles. As these profiles develop rapidly in regions of strong negative pressure gradients, transitions of the cross-flow type are expected to occur in accelerated flows, for instance in the vicinity of the leading edge of a swept wing. In addition, a linear stability analysis shows that cross-flow instability can amplify zero frequency disturbances ; this leads to the formation of stationary, corotating vortices aligned in the local streamwise direction. In the experiments, cross-flow vortices are observed as regularly spaced streaks.

Experimental and numerical results on cross-flow instability are not numerous for supersonic and hypersonic flows. Transition on a cone at angle of attack was investigated by MARCILLAT at M_∞ = 5 /85/ and by STETSON et al. at M_∞ = 8 /86/. In a recent paper, CREEL et al. /87/ reported oil flow studies on circular cylinders at sweep angles of 45 and 60 deg. The data were obtained in the Mach 3.5 "quiet tunnel" at NASA LANGLEY. The visualizations revealed the presence of cross-flow vortices as a series of widely spaced streaks. The ratio of the wavelength of the vortices to the attachment line boundary layer thickness was $\lambda/\delta \simeq$ 5 to 7. Values of λ computed by MALIK for the most amplified stationary disturbances using compressible linear stability theory are in excellent agreement with the measured values.

To our knowlege, no attempt has been made to apply the e^n method for predicting the transition onset in three-dimensional, supersonic flows. Even at low speeds, the calculation of the total amplification rates for the cross-flow unstable waves is not straightforward. A much simpler method is to use empirical correlations, such as the OWEN and RANDALL criterion /88/, which is based on a crossflow Reynolds number $\chi = w_{max} \delta / \nu_e$. From experiments on subsonic swept wings, OWEN and RANDALL observed that cross-flow transitions occur when χ reaches a value of 150 to 175. PATE /5/ noted that this criterion appears to hold also in supersonic flow regime. However subsequent investigations in

incompressible flow indicated that the value of χ at transition could vary up to 300. There are at least two explanations to these discrepancies : the first one is that the experimental data used by OWEN and RANDALL were biased by leading edge contamination problems (see below) ; the second one is that the value of χ at the transition onset is not necessarily unique. ARNAL et al. /89/ proposed an incompressible cross-flow criterion in which a cross-flow Reynolds number taken at transition onset was a function of the streamwise shape factor. Further investigations are needed to check this correlation at high speeds.

16. THREE-DIMENSIONAL FLOWS : LEADING EDGE CONTAMINATION AND ASSOCIATED PROBLEMS

The attachment line is a particular streamline, which divides the flow into one branch following the upper surface of the body and another branch following the lower surface, see Figure 51.
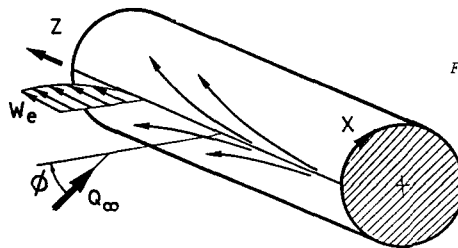
Figure 51 - Flow field along the attachment line of a swept cylinder.

Let us consider the simplest case of a swept cylinder of constant radius r. If the cylinder is in contact with a solid wall (fuselage, wind tunnel wall...), it has been observed that large turbulent structures coming from the wall at which the model is fixed may develop along the attachment line : it is the so-called leading edge contamination, which occurs for particular combinations of the flow parameters (sweep angle, leading edge radius, unit Reynolds number), without resorting to linear processes. In this Section, the main results obtained in incompressible flow will be summarized, as well as their extension for supersonic and hypersonic flows.

16.1. Results in incompressible flow

In the coordinate system (X,Z,y) linked to the cylinder, Z coincides with the attachment line, X is normal to Z on the cylinder surface, and the y-axis is normal to the wall. U and W are the projections of the mean velocity along X and Z (Figure 51). In the neighbourhood of the attachment line, the flow at the edge of the boundary layer is given by :

$$Ue = \hat{k}X \qquad \text{and} \qquad We = Q_\infty \sin\phi = \text{constant} \qquad (32)$$

If the derivatives along the spanwise direction Z are set equal to zero, the boundary layer equations have a similarity solution :

$$U/Ue = f'(\bar{\eta}) \qquad \text{and} \qquad W/We = g(\bar{\eta}) \text{ with } \bar{\eta} = y(\hat{k}/\nu) \qquad (33)$$

Tabulations of $f'(\bar{\eta})$ and $g(\bar{\eta})$ may be found in standard books , e.g. ROSENHEAD /90/. Along the attachment line, $U = 0$, because $Ue = 0$. An important parameter is the Reynolds number $\bar{R}$ defined as :

$$\bar{R} = \frac{We\,\eta}{\nu} \qquad (34)$$

$\eta = (\nu/\hat{k})^{1/2}$ is a characteristic length scale.

A number of experiments have shown that, if $\bar{R}$ is lower than 250, the bursts of turbulence convected along the wall are damped and vanish as they travel along the attachment line. However, for $\bar{R} > 250$, these burst are self-sustaining ; they grow, overlap, and the leading edge region becomes turbulent. This simple criterion was used by PFENNINGER /91/ in 1965 ; it was successfully checked in many further investigations (GASTER /92/, CUMPSTY-HEAD /93, POLL /94/, ARNAL-JUILLEN /95/ for instance).
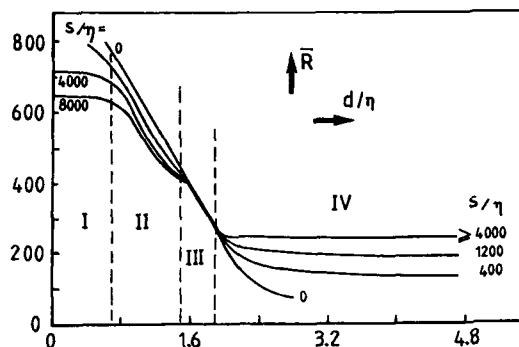
Figure 52 - Location S where the first
turbulent bursts are observed.
S is measured from the wire along
the attachment line (Poll).
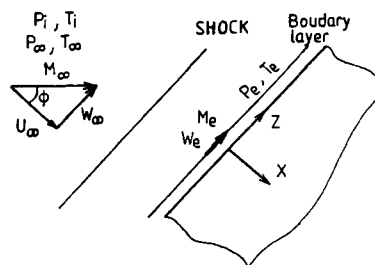
Figure 53 - Notations for compressible flows

A detailed experimental study was carried out by POLL /94/, who investigated the response of the attachment line boundary layer to the presence of wires, the axis of which was normal to the le»ding edge direction. If the wire diameter, d, is made dimensionless with the length scal« η , four d/η ranges have to be distinguished, as it is illustrated in Figure 52 :

. Region I : for $0 < d/\eta < 0.7$, the wire has no effect, and transition is triggered by linear mechanisms ; the main parameter is the free-stream disturbances level.

. Region II : for $0 < d/\eta < 1.5$, the wire begins to control transition ; the location of the first turbulent spots moves closer to the wire when $\bar{R}$ is increased.

. Region III : for $1.5 < d/\eta < 1.9$, the flow is either fully laminar or fully turbulent behind the wire. At a fixed value of d/η, this change in the boundary layer structure occurs for a very small variation of $\bar{R}$. GASTER /92/ and CUMPSTY-HEAD /93/ observed this phenomenon in 1967, and POLL called it "flashing".

. Region IV : for $d/\eta > 1.9$, turbulent bursts always appear immediatly behind the wire. But, if $\bar{R}$ is lower than 245, they decay more or less rapidly as they are convected along the attachment line. If $\bar{R}$ is greater than 245, the size of the bursts increases, and leading edge contamination occurs. It is clear that there is a strong similarity with the leading edge contamination induced by a wing-wall junction.

What is important to keep in mind is that there exists a minimum Reynolds number $(\bar{R} = 245)$ beyond which every turbulent structure generated by a gross disturbance source

becomes self-sustaining, develops and makes the leading edge turbulent. It is an example of transition mechanism in which the linear stages are "bypassed".

16.2. Extension to compressible flows

If the Mach number $Mn = M_\infty \cos\phi$ is supersonic, a bow shock is formed some distance upstream of the attachment line (Figure 53). If the shock is parallel to the cylinder axis, the mean velocity We at the edge of the attachment line boundary layer remains equal to $W_\infty = Q_\infty \sin\phi$. The Reynolds number $\bar{R}$ and the length scale η are now defined as previously, with the kinematic viscosity νe computed at the boundary layer edge. $\bar{R}$ can be written :

$$\bar{R} = \sqrt{\frac{\nu_\infty}{\nu e}} \ (\sin\phi \ \mathrm{tg}\phi \ R_{\infty,D})^{1/2} / \left(\frac{\hat{k}D}{U_\infty} \right)^{1/2}_{X = 0} \tag{35}$$

where $R_{\infty,D} = \frac{U_\infty D}{\nu_\infty}$ and $D = 2r$ is the cylinder diameter. For $M_\infty \sin\phi > 1.5$, the dimensionless pressure gradient parameter $(\hat{k}D/U_\infty)_{X = 0}$ is deduced from the newtonian theory /94/ :

$$\left(\frac{\hat{k}D}{U_\infty} \right)_{X = 0} = \frac{2}{M_\infty \cos\phi} \left[\frac{2}{\gamma} \frac{Te}{T_\infty} \left(1 - \frac{P_\infty}{P_e} \right) \right]^{1/2} \tag{36}$$

Several sets of experiments were devoted to the study of leading edge contamination at high speeds. In most of the cases, end plates were used as sources of gross disturbances (BUSHNELL /96/, BRUN et al /97/, YEOH /98/, ALZIARY et al./99/). Figure 54 illustrates the complexity of the shock pattern at the cylinder_end plate junction. In order to correlate the experimental data, POLL /100/ introduced a transformed Reynolds number $\bar{R}^*$, which has the same definition as $\bar{R}$, except that νe is replaced by ν* , so that :
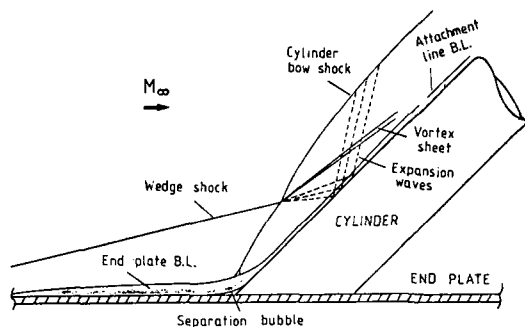
Figure 54 - Schock pattern at cylinder/end plate junction.

$$\overline{R}^* = \overline{R} \ \frac{\nu^*}{\nu e} \ ^{1/2} \tag{37}$$

ν^* is the kinematic viscosity computed at a reference temperature T^* which may be estimated by using the following empirical relationship (POLL, /100/) :

$$T^* = Te + 0.10 (Tw - Te) + 0.60 (Taw - Te) \tag{38}$$

POLL analyzed available experimental data for $0 < Me < 6$ (let us recall that Me is the spanwise Mach number at the boundary layer edge ; it is obviously lower than M_∞) and showed that leading edge contamination occurs for $\overline{R}^* = 245 \pm 35$, as illustrated in Figure 55. There are no effects of the Mach number, of the unit Reynolds number and of the wall temperature. This means that region IV in Figure 52 exists from subsonic to hypersonic flows, provided $\overline{R}$ is replaced by $\overline{R}^*$. The question arises if the other three regions have a counterpart at high speeds in the $*$ variables.
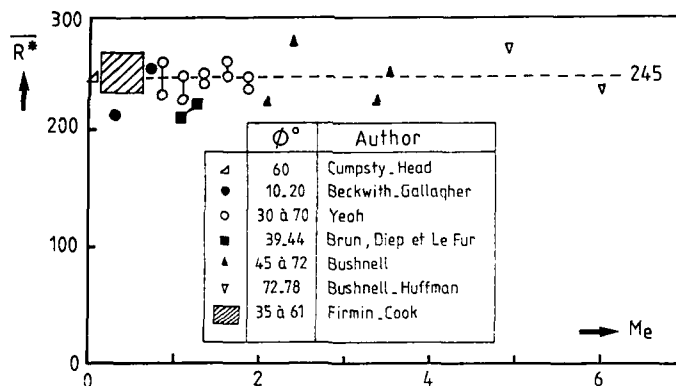
Figure 55 - Leading edge contamination criterion at high speeds (Poll)

Region I was studied by CREEL et al. /87/ in the quiet tunnel of NASA LANGLEY. Transition was detected along the attachment line of swept cylinders, without disturbance sources and with small roughness elements. By opening or closing the "bleed" valve, free-tream noise levels were varied from extremely low values to much higher values approaching those in conventional wind tunnels. The main results are reported in Figure 56, which shows the evolution of $\overline{R}^*$ at transition as a function of k/η^*. k is the roughness height and $\eta^* = (\nu^*/k)^{1/2}$ is a modified length scale. The following effects are observed :

a - On smooth cylinders (k = 0), "natural" transition occurs for $\overline{R}^* = 650$ to 700, in agreement with the values of $\overline{R}$ found by POLL at low speeds (see figure 52). Twenty years ago, BUSHNELL and HUFFMAN /101/ had shown from correlations of data for Mach numbers up to 10 that the flow on an undisturbed leading edge was always laminar up to $R_\infty, D = 8 \ 10^6$; CREEL et al. observed that their results are also in reasonable agreement with this crite-rion. Another interesting feature is that the wind tunnel noise has no effect on "natural" transition Reynolds number. This surprising behaviour could be explained by a recent theory on the receptivity of supersonic laminar boundary layer to acoustic disturbances ; calcu-lations by GAPONOV (referenced by CREEL et al.) demonstrated that external noise cannot generate instability waves when the boundary layer thickness is constant, as it is the case along an attachment line. On the other side, boundary layers on cones or flat plates are growing, so that the wind-tunnel noise has large effects on transition.
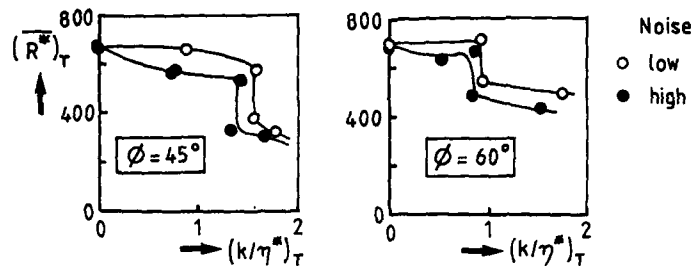
Figure 56 - Transition Reynolds number along the attachment line
with small roughness elements (Creel et al.).

b - Small trips have no well defined influence on transition Reynolds number until a "critical" value of k/η^* is reached. This value is around 0.9 for $\phi = 60°$ and around 1.5 for $\phi = 45°$. As soon as the critical roughness height is exceeded, $\overline{R^*}$ at transition decreases rapidly. A detailed comparison with POLL's diagram (Figure 52) is not easy to perform, but the trends are roughly similar. For given values of ϕ and k/η^*, an increase in the wind tunnel noise reduces $(\overline{R^*})_T$; CREEL et al. interpretation is that the external noise generates instability at the location where the boundary layer is disturbed locally by the roughness element.

17. TRANSITION ON THE WINDWARD FACE OF SPACE SHUTTLE

17.1. Flight conditions and instrumentation

Extensive wall temperature measurements were performed on the windward face of the "Columbia" orbiter during five flights (STS-1 through STS-5). The thermal protection system on the lower surface of the shuttle was composed of insulating tiles with nominal surface dimensions of 15 cm by 15 cm, and nominal gaps of about 1 mm. Approximately 90 thermocouples were mounted within the tiles, and the temperature-time histories make possible to reconstruct the transition movement during re-entry. Figure 57 shows an example of surface temperature evolution recorded by a thermocouple located close to the symmetry axis. The beginning and the end of transition are defined as the limits of the abrupt increase in temperature, which occurs between $t \approx 1260$ sec and $t \approx 1280$ sec. ($t = 0$ sec at altitude 400 000 ft).
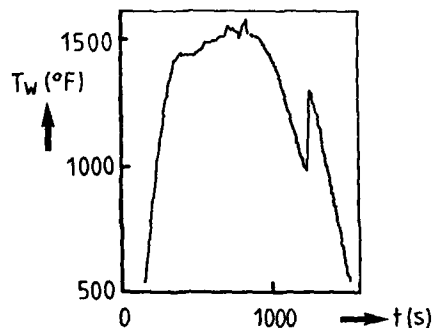
Figure 57 - Example of temperature-time
history during re-entry
(x/L = 0.3)
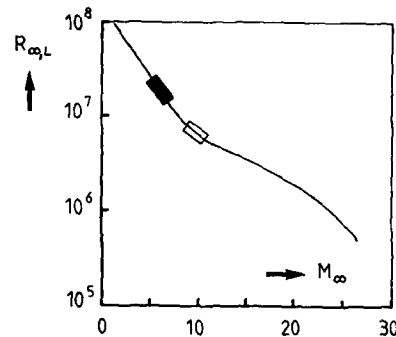
Figure 58 - Entry conditions :
—— mean curve
▢ transition at x/L = 0.99
■ transition at x/L = 0.10

The mean entry conditions for the five flights are depicted in Figure 58 by the dimensionless parameters $R_{\infty,L}$ and M_∞ . $R_{\infty,L}$ is the Reynolds number based on free-stream flow properties and the orbiter length L. The conditions at which transition occurs at x/L = 0.10 and 0.99 on the center line are also reported. It can be seen that transition is first detected at the trailing edge for $M_\infty \approx 10$, and that 90 per cent of the shuttle length is turbulent for $M_\infty \approx 7$. The local Mach numbers at the boundary layer edge are obviously much lower (of the order of 2), for angles of attack between 25 and 40 deg.

17.2. Analysis of transition mechanisms

The first problem was to avoid premature transitions caused by the gaps between adjacent tiles. Wind tunnel experiments have shown "that grooves parallel to the surface streamlines produced strong boundary layer tripping disturbances, whereas grooves perpendicular to streamlines produced much weaker disturbances" (HARTHUN et al, /102/). The tile orientation was consequently chosen for eliminating the gap tripping effects.

For the first flight, surface temperature data were only available after t = 1050 sec. As this time, the flow on the aft fuselage and on the right wing was turbulent. Post-flight inspection revealed that transition was induced by a gouge in a tile on the right nose landing gear door. This anomaly resulted in a higher drag on the right side. The asymmetry disappeared at 1252 sec when the left-hand side became turbulent.

During the other flights, transition onset was characterized by the sudden appearance of turbulent wedges, the apex of which moved very rapidly from the trailing edge of the orbiter to the nose of the fuselage and to the leading edge of the wings. This sudden forward movement is an indication of roughness-caused transition. It is now recognized that the surface irregularities resulted from the corners of misaligned tiles, which can be considered as three-dimensional, randomly spaced, roughness elements.

Most of the analysis of these flight transition data are restricted to the center line of the shuttle. HARTHUN et al. /102/ estimated that the assumption of conical flow was a good approximation for $x/L < 0.5$ and used VAN DRIEST-BLUMER criterion, equation (25), to calculate the effective roughness size. At $x/L = 0.1$, the calculations indicated $k_{eff} = 3.4$ mm for flight 4 and $k_{eff} = 2.9$ mm for the other flights. BERTIN et al. /103/ /104/ used the $R\theta/Me$ criterion to correlate wind tunnel data and flight data.

$$\alpha = 0° \qquad \alpha = 15° \qquad \alpha = 30° \qquad \alpha = 60°$$
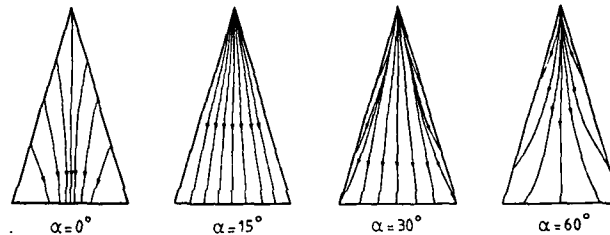
Figure 59 - Flow patterns on the windward face of a delta wing (Bertram et al.).

However, there is no proof that the transition process on the windward face of the orbiter was entirely determined by conditions on the plane of symmetry. To illustrate this point, Figure 59 shows the evolution of the flow patterns on the windward face of a delta wing when the angle of attack increases (BERTRAM et al. /105/, referenced by POLL /106/). At zero incidence, the attachment lines lie along the leading edges ; as incidence is increased, they move towards the centerline ($\alpha = 30°$) and ultimately meet to form a single line ($\alpha = 60°$) . POLL /106/ introduced the hypothesis that transition occurs at first on the attachment line , because a roughness element on this line "can produce turbulent flow at a much lower Reynolds number than an identical element which is off the attachment line". This means that the first turbulent wedge can appear at any spanwise position, depending on the location of the attachment lines. MORISETTE performed wind tunnel experiments which supported this view /107/ ; a delta wing orbiter model was set at 20° incidence in a flow with a free-stream Mach number of 6, and several three-dimensional roughness elements were distributed across the span at the same chordwise position. When the unit Reynolds number was increased, transition was observed at first behind the trip located on the attachment line (which did not coincide with the centerline).

These elements led POLL to analyze the space shuttle data under consideration of leading edge contamination /106/. He assumed that the results presented in Figure 52 for incompressible flows were also valid at high speeds when $\bar{R}$ and η were replaced by $\bar{R}^*$ and η^*. It has been shown in Section 16 that this assumption was correct for $d = 0$ ($\bar{R}^* = 650 - 700$ at transition onset) as well as for large tripping elements ($\bar{R}^* = 250$ when leading edge contamination occurs). Although information is lacking for the intermediate regimes, POLL deduced from boundary layer computations that the sudden forward movement of the turbulent wedges could be explained by a "flashing" mechanism (regime III in Figure 52). It is obvious that this attractive theory is by now rather speculative.

18. CONCLUSIONS

This paper demonstrated that the problems associated with boundary layer transition in supersonic and hypersonic flows are numerous and that many of them are far from being solved.

On the theoretical point of view, the linear stability theory constitutes a very efficient tool to understand the fundamental mechanisms leading to transition, and sophisticated experimental studies gradually confirm these theoretical elements. The linear theory can also explain, at least qualitatively, the influence of more or less controlled parameters (unit Reynolds number, wall cooling for instance). But the key problem lies in the understanding of the receptivity mechanisms and the exact relation between instability and transition is not very well known. Despite these facts, the extension of the e^n method in supersonic and hypersonic flow could provide a reliable prediction of transition ; for a low disturbance environment, the n factor has roughly the same value as in incompressible flow.

Beside the strong mathematical and numerical difficulties inherent in the linear stability theory, there is a lot of experimental problems which remain unsolved. Obviously, the measurements are much more difficult to perform in supersonic and hypersonic flows than at low speeds, and the results are often not easy to explain. These problems are discussed during these Lecture Series by F.K. OWEN. From a physical point of view, it must be kept in mind that wind tunnel experiments cannot duplicate free-flight environmental conditions, so that in many cases, transition Reynolds numbers measured in conventional facilities are much lower than those occuring on hypersonic vehicles. However, even if the results are not quantitavely correct, one may expect that varying flow parameters (wall cooling, pressure gradient...) would give the correct trends. It is also important to remind that wind tunnel tests make possible to obtain fundamental information which is difficult to reach in flight conditions (linear and non linear stability results, effect of streamwise vortices imbedded in laminar boundary layer for instance).

ACKNOWLEDGEMENTS

R E F E R E N C E S

/1/ MOLKOVIN M.V.　　Critical evaluation of transition from laminar to turbulent shear layers with emphasis on hypersonically travelling bodies. Report AFFDL-TR-68-149, Wright-Patterson Air Force Base, Ohio (1968).

/2/ MORKOVIN M.V.　　Transition at hypersonic speeds. ICASE NASA Contractor Report 178 315 (1987).

/3/ RESHOTKO E.　　Boundary Layer stability and transition. Annual Review in Fluid Mechanics, Volume 8 (1976).

/4/ MACK L.M.　　Boundary-Layer linear stability theory. AGARD Report N° 709 (1984).

/5/ PATE S.R.　　Effects of wind tunnel disturbances on boundary-layer transition with emphasis on radiated noise : a review. AIAA Paper 80-0431, Colorado Springs, Colo. (1980).

/6/ SCHUBAUER G.B.
　　SKRAMSTAD H.K.　　Laminar boundary layer oscillations and transition on a flat plate. Report 909 NACA (1948).

/7/ SCHLICHTING H.   Boundary layer theory.
                            6th ed. Mc Graw-Hill, New-York (1968)

/8/ LEES L.   Investigation of the stability of the laminar boundary layer in
     LIN C.C.   a compressible fluid.
                            NACA TN N° 1115 (1946).

/9/ LEES L.   The stability of the laminar boundary layer in a compressible
                            fluid.
                            NACA TN N° 876 (1947).

/10/ DUNN D.W.   On the stability of the laminar boundary layer in a compressible
     LIN C.C   fluid.
                            J. Aero. Sci., Vol. 22, pp. 455-477 (1955).

/11/ LEES L.   Stability of the compressible laminar boundary layer.
     RESHOTKO E.   J. FLuid Mech., Vol. 12, Part 4, pp. 555-590 (1962).

/12/ MACK L.M.   Stability of the compressible laminar boundary layer according
                            to a direct numerical solution.
                            AGARDograph 97, Part 1, pp. 329-362 (1965).

/13/ MACK L.M.   Boundary layer stability theory. (2 volumes).
                            Jet Propulsion Laboratory, CALIFORNIA Institute of Technology,
                            Pasadena, California (november 1969).

/14/ MACK L.M.   Linear stability and the problem of supersonic boundary layer
                            transition.
                            AIAA J., Vol. 13, N° 3, pp. 278-289 (1975).

/15/ MACK L.M.   Transition prediction and linear stability theory.
                            AGARD Conference Proceedings N° 224, NATO, Paris (1977).

/16/ MACK L.M.   Compressible boundary layer stability calculations for sweptback
                            wings with suction.
                            AIAA J., Vol. 20, pp. 363-369 (1981)

/17/ MACK L.M.   Remarks on disputed numerical results in compressible boundary
                            layer stability theory.
                            Phys. Fluids 27(2) (February 1984).

/18/ MALIK M.R.   Prediction and control of transition in hypersonic boundary layers.
                            AIAA Paper N° 87-1414 (June 1987).

/19/ MALIK M.R.   Instability and transition in supersonic boundary layers.
                            In Laminar-Turbulent Boundary Layers (E.M. URAM and H.E. WEBER,
                            Ed.) - Proc. of Energy Resources Technology Conference,
                            New Orleans, Louisiana (February 1984).

/20/ GASPERAS G.   Instability of compressible laminar boundary layers.
                            AIAA Paper N° 85-1699 (1985).

/21/ GASPERAS G.   The stability of the compressible boundary layer on a sharp cone
                            at zero angle of attack.
                            AIAA Paper N° 87-0494 (1987)

/22/ ARNAL D.   Stabilité et transition des couches limites laminaires bidimen-
                            sionnelles en écoulement compressible, sur paroi athermane.
                            To be published in "La Recherche Aérospatiale".

/23/ GASTER M.   A note on the relation between temporally increasing and spatially
                            increasing disturbances in hydrodynamic stability.
                            J. FLuid Mech., Vol. 14, pp. 222-224 (1962)

/24/ MORKOVIN M.W.   Bypass transition to turbulence and research desiderata.
                            Symposium "Transition in Turbines", Cleveland, Ohio (1984).

/25/ HERBERT T.   Nonlinear effects in hydrodynamic stability. Secondary instability
                        of shear flows.
                        AGARD Report N° 709 (1984).

/26/ KNAPP C.F.   A combined visual and hot-wire anemometer investigation of
     ROACHE P.J.   boundary layer transition.
     MUELLER T.J.   UNDAS-TR-866 CK (1966)

/27/ ERLEBACHER G.   Stability and transition in supersonic boundary layers.
     HUSSAINI M.Y.   AIAA Paper 87-1416 (1987).

/28/ SMITH A.M.O.   Transition, pressure gradient and stability theory.
     GAMBERONI N.   Douglas Aircraft Co. Rept. ES 26 388, El Segundo, California (1956)

/29/ VAN INGEN J.L.   A suggested semi-empirical method for the calculation of the
                        boundary layer transition region.
                        Univ. of Technology, Dept. of Aero. Eng., Rept. UTH-74 DELFT (1956).

/30/ JUILLEN J.C.   Détermination expérimentale de la région de transition sur une
                        plaque plane à M = 5, 6 et 7.
                        ONERA Technical Report N° 10/2334 AN (1969).

/31/ HARVEY W.D.   Influence of free-stream disturbances on boundary layer transition
                        NASA Technical Memorandum 7863ᶠ (1978).

/32/ PATE S.R.   Radiated aerodynamic noise effects on boundary layer transition
                        in supersonic and hypersonic wind tunnels.
                        AIAA Journal, Vol. 7, N° 3 (1969).

/33/ BECKWITH I.E.   Free-stream noise and transition measurements on a cone in a Mach
     CREEL Jr, T.R.   3.5 pilot low-disturbance tunnel.
     CHEN F-J   NASA Technical Paper 2180 (1983)
     KENDALL J.M.

/34/ BECKWITH I.E.   Development of a high Reynolds number quiet tunnel for transition
                        research.
                        AIAA Journal, Vol. 13, N° 3 (1975).

/35/ POTTER J.L.   Review of the influence of cooled walls on boundary layer
                        transition.
                        AIAA Journal, Vol. 18, N° 8 (1980).

/36/ SANATOR R.J.   Hypersonic boundary layer transition data for a cold-wall slender
     DE CARLO J.P.   cone.
     TORRILLO D.T.   AIAA Journal, Vol. 3, pp. 758-760 (1965).

/37/ NAGAMATSU H.T.   Wall cooling effects on hypersonic boundary layer transition,
     SHERR R.E. M_l = 7.5 - 15.
     WISLER D.C.   AIAA Paper 86-1088 (1986).

/38/ BOISON J.C.   Investigation of test facility environmental factors affecting
                        boundary layer transition.
                        USAF Flight Dynamics Lab., TR-73-106 (1973).

/39/ SHEETZ Jr. N.W.   Ballistic range boundary layer transition measurements on cones
                        at hypersonic speeds.
                        Symposimum on Viscous Drag Reduction, Dallas, Texas (1968),
                        Plenum press, New York (1969).

/40/ REDA D.C.   Boundary layer transition experiments on sharp, slender cones
                        in supersonic free flight.
                        AIAA Paper 78-1129 R or AIAA Journal, Vol. 17 N°8 (1979).

/41/ LYSENLO V.I.   The eſ ₋ct of cooling on the supersonic boundary layer stability
     MASLOV A.A.   and transition.
                        IUTAM Symposium on Laminar-Turbulent Transition.
                        Novosibirsk (1984) - Springer Verlag, Ed. V.V. KOZLOV.

8-42

/42/ BOEHMAN L.I.   The stability of highly cooled compressible laminar boundary
     MARISCALCO M.G.   layer.
                        AFFDL-TR-76-148 (1976).

/43/ WAZZAN A.R.   The effect of theat transfer on three-dimensional spatial stabi-
     TAGHAVI H.   lity and transition on flat plate boundary layer at Mach 3.
                        Int. J. Heat Mass Transfer, Vol. 25, N° 9, pp. 1321-1331 (1982).

/44/ VIGNAU F   Thesis, in preparation.

/45/ MACK L.M.   Stability of axisymmetric boundary layers on sharp cones at
                        hypersonic Mach numbers.
                        AIAA Paper N° 87-1413 (1987).

/46/ PATE S.R.   Measurements and correlations of transition Reynolds numbers on
                        sharp slender cones at high speeds.
                        AIAA Journal Vol. 9, N° 6, pp. 1082-1090 (1971).

/47/ LAUFER J.   Stability and transition on a supersonic laminar boundary layer
     VREBALOVICH T.   on an insulated flat plate.
                        J. FLuid Mech., Vol. 9, Part 2, pp. 257-294 (1960).

/48/ DEMETRIADES A.   An experiment on the stability of hypersonic laminar boundary
                        layers.
                        J. Fluid Mech. Vol. 7, pp. 385-396 (1960).

/49/ KENDALL J.M.   Boundary layer stability experiments.
                        JPL SPace programs Summary 37-39, 4, 147-149 (1966).

/50/ KENDALL J.M.   Wind tunnel experiments relating to supersonic and hypersonic
                        boundary layer transition.
                        AIAA Journal, Vol. 13, N° ", pp. 290-299 (1975)

/51/ LYSENKO V.I.   The effect of cooling on supersonic boundary layer stability.
     MASLOV A.A.   J. FLuid Mech., Vol. 147, pp. 39-52 (1984).

/52/ DEMETRIADES A.   Laminar boundary layer stability measurements at Mach 7
                        including wall temperature effects.
                        AFOSR-TR-77-1311 (1977).

/53/ STETSON K.F.   Laminar boundary layer stability experiments on a cone at Mach 8.
     THOMPSON E.R.   Part 1 : sharp cone.
     DONALDSON J.C.   AIAA Paper n° 83-1761 (1983).
     SILER L.G.

/54/ STETSON K.F.   Laminar boundary layer stability experiments on a cone at Mach 8.
     THOMPSON E.R.   Part 2 : blunt cone.
     DONALDSON J.C.   AIAA Paper n° 84-0006 (1984).
     SILER L.G.

/55/ POTTER J.L.   Effects of slight nose bluntness and roughness on boundary layer
     WHITFIELD J.D.   transition in supersonic flows.
                        J. Fluid Mech., Vol. 12, Part 4, pp. 501-535 (1962).

/56/ SOFTLEY E.J.   Experimental observation of transition of the hypersonic boundary
     GRABER B.C.   layer.
     ZEMPEL R.C.   AIAA Journal, Vol. 7, N° 2, pp. 257-263 (1969).

/57/ ERICSSON L.E.   Effect of nose bluntness and cone angle on slender vehicle
                        transition.
                        AIAA Paper 87-`415 (1987).

/58/ RESHOTKO E.   Stability of the laminar boundary layer on a blunted plate in
     KHAN M.M.S.   supersonic flow.
                        First IUTAM Symposium on Laminar-Turbulent Transition.
                        Stuttgart (1979) - Springer Verlag.

/59/ STAINBACK P.C.   Experimental studies of hypersonic boundary-layer transition and
     WAGNER R.D.   effects of wind tunnel disturbances.
     OWEN F.K.   NASA TN D-7453   (1974).
     HORSTMAN C.C.

/60/ STETSON K.F.   Laminar boundary layer stability experiments on a cone at Mach 8 -
     THOMPSON E.R.   Part 4 : on unit Reynolds number and environmental effects.
     DONALDSON J.C.   AIAA Paper N° 86-1087   (1986).
     SILER L.G.

/61/ GÖRTLER H.   On the three-dimensional instability of laminar boundary layers
                       on concave walls.
                       NACA Tehc. Memo 1375   (1954).

/62/ GINOUX J.J.   Streamwise vortices in laminar flow.
                       Recent Developments in Boundary Layer Research, AGARDograph 97,
                       Part I, pp. 395-422   (1965).

/63/ COET M.C.   Private communication.

/64/ TOBAK M.   Hypothesis for the origin of cross-hatching.
                       AIAA Journal, Vol. 8, N° 2, PP. 330-334   (1970).

/65/ FLORYAN J.M.   Stability of GÖRTLER vortices in boundary layers.
     SARIC W.S   AIAA Journal, Vol. 20, N° 3   (1982).

/66/ EL-HADY N.M.   Growth of GÖRTLER vortices in compressible boundary layers along
     VERMA A.K.   curved surfaces.
                       J. of Engineering and Applied Sciences, Vol. 2, pp. 213-238
                       (1983).

/67/ JALLADE S.   Thesis, in preparation.

/68/ EL-HADY N.M.   Instability of compressible boundary layers along curved walls
     VERMA A.K.   with suction or cooling.
                       AIAA Journal, Vol. 22, N° 2   (1984).

/69/ BECKWITH J.E.   Effects of nozzle design parameters on the extent of quiet test
     MALIK M.R.   flow at Mach 3.5.
     CHEN F.J.   IUTAM Symposium on Laminar-Turbulent Transition.
     BUSHNELL D.M.   Novosibirsk (Juillet 1984) - Springer Verlag, Ed. V.V. KOZLOV.

/70/ MORRISETTE E.L.   Boundary layer tripping with emphasis on hypersonic flows.
     STONE D.R.   Viscous Drag Reduction, Ed. C.S. WELLS   (1969).
     WHITEHEAD Jr, A.H.

/71/ ARNAL D.   ONERA Internal Report   (1988).

/72/ VAN DRIEST E.R.   Boundary layer transition at supersonic speeds. Three-dimensional
     BLUMER C.B.   roughness effects (spheres).
                       Journal of the Aerospace Sciences, Vol. 29, N° 8   (1962).

/73/ VAN DRIEST E.R.   The effect of controlled three-dimensional roughness on boundary-
     Mc CAULEY W.D.   layer transition at supersonic speeds.
                       Journal of the Aerospace Sciences, Vol. 27, N°4   (1960).

/74/ VAN DRIEST E.R.   Boundary layer transition at supersonic speeds : roughness effects
     BLUMER C.B.   with heat transfer.
                       AIAA Journal, Vol. 6, N° 4, pp. 603-607   (1968).

/75/ Mc CAULEY W.D.   The effect of controlled three-dimensional roughness on hypersonic
     SAYDAH A.   laminar boundary layer transition.
     BUECHE J.   AIAA Paper N° 66-26   (1966).

8-44

/76/ OWEN F.K.   Hypersonic transitional boundary layers.
      HORSTMAN C.C.   AIAA Journal, Vol. 10, N° 6, pp. 769-775 (1972).

/77/ OWEN F.K.   Transition experiments on a flat plate at subsonic and supersonic
                      speeds.
                      AIAA Journal, Vol. 8, N° 3, pp 518-523 (1970).

/78/ CHEN K.K.   Extension of EMMONS' spot theory to flows on blunt bodies.
      THYSON N.A.   AIAA Journal, Vol. 9 N° 5, pp 821-825 (1971).

/79/ MORKOVIN M.V.   Transition to turbulence at high speeds.
                      AFOSR Scientific Report, AFOSR-TR-70-1731 (1970).

/80/ ARNAL D.   Etude expérimentale et théorique de la transition sur une aile en
      COUSTOLS E.   flèche infinie.
      JUILLEN J.C.   La Recherche Aérospatiale, 1984-4 (1984).

/81/ COLEMAN G.T.   Turbulent boundary layers at supersonic and hypersonic speeds.
      ELFSTROM G.M.   AGARD Conference Proceedings N° 93 (1971).
      STOLLERY J.L.

/82/ POLL D.I.A.   Transition description and prediction in three-dimensional flows.
                      AGARD Report N° 709 (1984).

/83/ ARNAL D.   Three-dimensional boundary layers : laminar-turbulent transition.
                      AGARD Report N° 741 (1986).

/84/ SARIC W.S.   Three-dimensional stability of boundary layers.
      REED H.L.   Perspective in Turbulence Studies, Springer-Verlag (1987).

/85/ MARCILLAT J.   Etude du développement de la couche limite tridimensionnelle en
                      régime de transition.
                      Technical Report N° 19/2334 (1976).

/86/ STETSON K.F.   Laminar boundary layer stability experiments on a cone at Mach 8 -
      THOMPSON E.R.   Part 3 : sharp cone at angle of attack.
      DONALDSON J.C.   AIAA Paper N° 85-0492 (1985).
      SILER L.G.

/87/ CREEL Jr. T.R.   Transition on swept leading edges at Mach 3.5.
      BECKWITH I.E.   J. Aircraft, Vol. 24, N° 10 (1987).
      CHEN F.J.

/88/ OWEN P.R.   Boundary layer transition on a sweptback wing.
      RANDALL D.G.   R.A.E. TM 277 (1952).
                      Boundary layer transition on a sweptback wing : a further inves-
                      tigation.
                      R.A.E. TM 330 (1953).

/89/ ARNAL D.   Théorie de l'instabilité laminaire et critères de transition
      HABIBALLAH M.   en écoulement bi et tridimensionnel.
      COUSTOLS E.   La Recherche Aérospatiale N° 1984-2 (1985).

/90/ ROSENHEAD L.   Laminar boundary layers.
                      Oxford University Press (1963).

/91/ PFENNINGER W.   Flow phenomena at the leading edge of swept wings.
                      Recent Developments in Boundary Layer Research, Part IV.
                      AGARDograph 97 (1965).

/92/ GASTER M.   On the flow along swept leading edges.
                      The Aeronautical Quarterly, Vol. XVIII, Part 2 (1967).

/93/ CUMPSTY N.A.   The calculation of three-dimensional turbulent boundary layers.
      HEAD M.R.   Part II : attachment line flow on an infinite swept wing.
                      The Aeronautical Quarterly, Vol. XVIII, Part 2 (1967).

/94/ POLL D.I.A.   Some aspects of the flow near a swept attachement line with
                          particular reference to boundary layer transition.
                          Cranfield Institute of TEchnology, CoA Report N° 7805   (1978).

/95/ ARNAL D.   Three-dimensional transition studies at ONERA/CERT.
     JUILLEN J.C.   AIAA Paper n° 87-1335   (1987)

/96/ BUSHNELL D.M.   Interference heating on a swept cylinder in region of intersection
                          with a wedge at Mach number 8.
                          NASA TN D-3094   (1965).

/97/ BRUN E.A.   Transport de chaleur et de masse sur des cylindres circulaires
     DIEP G.B.   en flèche dans un écoulement supersonique.
     LE FUR B.   Recent Developments in Boundary Layer Research, Part 2.
                          AGARDograph 97   (1965).

/98/ YEOH K.B.   Transition along the attachment line of a swept circular cylinder
                          in supersonic flow.
                          M. Sc. Thesis, Cranfield Institute of Technology   (1980).

/99/ DA COSTA J.L.   Transition de bord d'attaque en écoulement hyper-
     AYMER de la CHEVALIERE D.   sonique.
     ALZIARY de ROQUEFORT T.   24ème Colloque d'Aérothermodynamique Appliquée.
                                        Poitiers (1987)

/100/ POLL D.I.A.   The development of intermittent turbulence on swept attachment
                          line including the effects of compressibility.
                          The Aeronautical Quatarly, Vol. XXXIV   (1983).

/101/ BUSHNELL D.M.   Investigation of heat transfer to a leading edge of a 76° swept
      HUFFMAN J.K.   fin with and without chordwise slots and correlations on swept-
                          leading-edge transition data for Mach 2 to 8.
                          NASA TMX-1475   (1967).

/102/ HARTHUN M.H.   Orbiter windward surface entry heating : post orbital flight
      BLUMER C.B.   test program update.
      MILLER B.A.   NASA CP 2283 (March 1983).

/103/ BERTIN J.J.   Shuttle boundary-layer transition due to distributed roughness
      HAYDEN T.E.   and surface cooling.
      GOODRICH W.D.   J. Spacecraft, Vol. 19, N° 5   (1982).

/104/ GOODRICH W.D.   Shuttle orbiter boundary layer transition at flight and wind
      DERRY S.M.   tunnel conditions.
      BERTIN J.J.   VASA CP 2283 (March 1983).

/105/ BERTRAM M.H.   Flowfields, pressure distributions and heat transfer for delta
      FELLER W.V.   wings at hypersonic speeds.
      DUNAVANT J.C.   NASA TM X-316 (1960).

/106/ POLL D.I.A.   Boundary layer transition on the windward face of space shuttle
                          during re-entry.
                          AIAA Paper N° 85-0899 (1985).

/107/ MORRISETTE E.L.   Roughness induced transition criteria for space shuttle-type
                          vehicles.
                          Journal of Spacecraft and Rockets, Vol. 13, N° 2 (February 1976).

SHOCK/SHOCK AND SHOCK-WAVE/BOUNDARY-LAYER INTERACTIONS

IN HYPERSONIC FLOWS

by

J. DELERY

ONERA - 92320 CHATILLON - France

SUMMARY

Shock interference phenomena and shock-wave/boundary-layer interactions are of special importance in hypersonic flows since they can be at the origin of extremely high local heat-transfer rates and loss of control effectiveness. The physical aspects of these ph· nena are first considered by examining the characteristic features and the scaling laws of typical 2-D interacting flows. 'ation laws allowing the prediction of separation pressures, peak heat-transfer rates and incipient shock-induced separation are presented. Various methods have been developed to obtain a more complete prediction of shock-wave/boundary-layer interactions. These methods can be classified into four categories, namely: global methods, inviscid-viscous interactive methods, analytical methods and solution of the Navier-Stokes equations. Here, emphasis is placed on the solution of the problem by integration of the full time averaged Navier-Stokes equations. A review of the turbulence models most currently used to compute strongly interacting turbulent flows is presented. Examples of applications concerning both 2-D and 3-D flows are discussed.

TABLE OF CONTENTS

1 - INTRODUCTION

The flow past a vehicle flying at hypersonic velocity is the seat of strong shock-waves forming ahead of the vehicle nose, the rounded leading edge of wings and tails, at an air intakes compression ramp, etc... These shock-waves are at the origin of interference phenomena resulting firstly from intersection of two shock-waves, secondly from interactions with the boundary-layer developing on the fuselage or the wing. Due to their great practical importance, these phenomena have been extensively studied in the past and are still the subject of very active investigations (see, for example Korgegl, 1971 and Holden 1986).

Shock interferences are more likely to occur at hypersonic Mach numbers because of the small inclination of the shock-waves with respect to the vehicle. On the other hand, at hypersonic speeds, phenomena resulting from such interferences lead to particularly severe problems because of the intensity of the shocks and the extremely high stagnation enthalpy level of the upstream flow. Also, a typical feature of hypersonic flights is the existence of fully laminar boundary-layers over the major part of the vehicle during an important portion of the :eentry trajectory. Thus, laminar interactions which were rarely met in classical aeronautical applications are now of great practical importance.

Practical examples of shock interference situations are given in Fig. 1.1. In the first case (see Fig. 1.1a), the fuselage bow shock meets a fin bow shock; the second example (see Fig. 1.1b) is relative to an interference between a launcher bow shock and a booster bow shock. A similar situation is encountered when the vehicle bow shock meets the shock forming ahead of the canopy. Such shock intersections result in more or less complex shock patterns including shear-layers or jets which can impinge on the vehicle causing high local heating rates, well in excess of those occurring at a nose stagnation point.
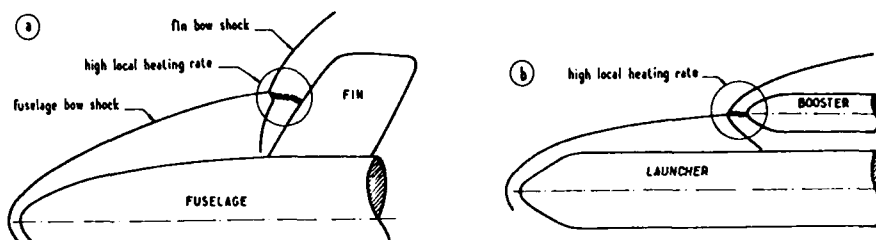

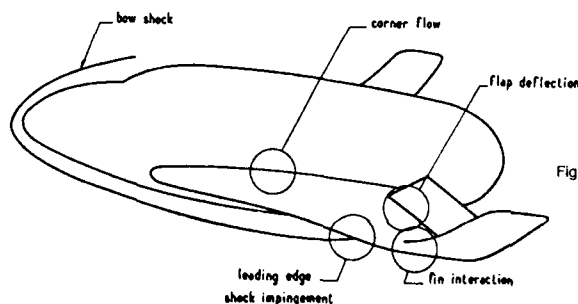Fig. 1.1   Examples of Shock Interference Heating

Fig. 1.2   Regions of Shock-Wave/Boundary-Layer Interactions

As shown in Fig. 1.2, shock-wave/boundary-layer interactions occur at impingement of a bow shock or a refracted shock resulting from shock interference, at a deflected flap, along axial corners in wing-body and fin-wing junctions, etc... Shock-wave/boundary-layer interactions also occur in air-intakes of airbreathing propulsive systems. Such interactions can induce separation of the boundary-layer which causes loss in control effectiveness or flow degradation in an engine inlet. Also, the subsequent reattachment of the separated shear-layer gives rise to heat-transfer rates that can far exceed those of an attached boundary-layer.

The present Lecture is divided into three main Sections.

Section 2 deals with interference phenomena resulting from intersection of two shock-waves

Section 3 gives a physical description of the phenomena involved in two-dimensional interactions. Emphasis is placed on the elucidation of the flow physics rather than on presentation of empirical correlation laws which can be found in the cited references. The distinctive features of laminar ant turbulent interactions are displayed as also the specific properties of hypersonic interactions. Information on 3-D interactions, which are of great practical importance but which are more difficult to analyse, can be found elsewhere (see for example Peake and Tobak, 1980 and Délery and Marvin, 1986).

Section 4 is devoted to theoretical methods available to predict shock-wave/boundary-layer interactions. The various flow models developed to treat this kind of flows include:

- Global or semi empirical methods which, in addition to their historical interest, can still be useful for a rapid estimation of some essential flow properties.

- Inviscid-Viscous interactive (or coupling) methods. These methods, which have known a considerable development since the pionnering work of Crocco and Lees (1952), can give accurate predictions in 2-D flows.

- Analytical or Multi-Deck theories which have greatly contributed to our basic understanding c' strong interaction phenomena.

However due to the lack of space, we will here focus our attention on the methods calling upon the numerical solution of the Navier-Stokes equations. This way of tackling the problem has received a considerable development during the past fifteen years as a consequence of the progress in computers performance and numerical methods efficiency. Since the turbulent case is of special interest, this subsection comprises a rather thorough review of the turbulence models which are presently employed along with the time averaged Navier-Stokes equations (for a review of the above cited methods, see Délery and Marvin, 1986).

2 - SHOCK INTERFERENCE PHENOMENA IN HYPERSONIC FLOWS

2.1 - General Remarks

The high local heating rates caused by shock interaction at hypersonic speeds have been the subject of numerous experimental and theoretical studies which will not be reviewed in detail here (for references on the subject, see: Keyes and Hains, 1973; Birch and Rudy, 1975; Holden, 1986; Wieting and Holden, 1987). In evaluating the effects of shock interference, it is necessary to first determine the type of flow that exists when two shocks intersect, specially when these two shocks are of different strength.

Thus, the basic shock interference problem appears as a perfect fluid problem consisting in finding the inviscid flow which establishes itself downstream of the region where the two shocks meet. The severe local heating and high pressure are caused by the impingement on the vehicle of disturbances emanating from the shock interaction. These disturbances can be shear-layers, supersonic jets or shocks and the overall flowfield can be dominated by resulting viscous and/or inviscid effects depending on the nature of the interaction and on its geometry.

The intersection of two shock-waves leads to different shock patterns which are encountered when considering, for example, an oblique impinging shock (C_1) which intersects the bow shock (C_2) forming ahead of the rounded nose of a hypersonic vehicle.

Let us imagine that (C_1) comes from below, as sketched in Fig. 2.1. When (C_1) meets (C_2) below the obstacle far from the nose, the situation corresponds to the intersection of two oblique weak shocks of opposite families. This means that (C_1) and (C_2) are inclined at a small angle relatively to the freestream velocity vector and that they impart to this velocity deflections of opposite sign.

As the intersection point I moves towards the nose region, (C_2) becomes more and more intense so that - the strength of (C_1) being unchanged - the intersection involves two shocks which are still of the same family but which are of largely different strengths.

When I is above the nose region, shocks (C_1) and (C_2) belong to the same family and the nature of the solution to the intersection problem will change accordingly.

By analyzing very carefully made experiments, including flowfield visualizations by optical techniques, Edney (1968) identified six basic types of shock interactions. The terminology Edney introduced to classify these interactions has been universally adopted and it will be used in the presentation that follows.
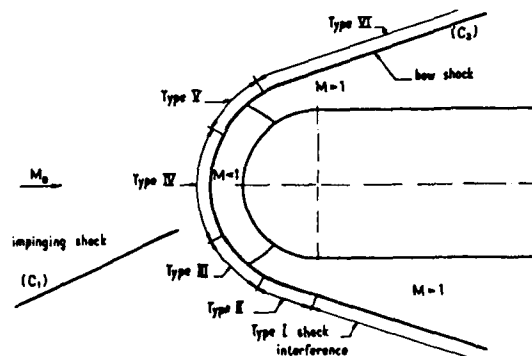

Fig. 2.1   Location of the Types of Interference on a Hemisphere

2.2 - The Basic Shock Interference Patterns

The present discussion will be greatly helped by utilizing the shock polar representation of the solution of the oblique shock equations. Let us recall that this polar is the locus of the states which are connected to an initial state through an attached oblique shock transition. The polar is most often represented in the plane of the two variables: pressure p (or pressure jump p_1/p_0 through the shock) - flow direction φ. An interesting feature of the shock polar representation is that two contiguous flows, separated by a slip-line, have the same image point in the shock polar plane since compatibility conditions require that these flows have same pressure and be parallel. Shock polars are closed curves with two branches corresponding respectively to the weak solution and the strong solution of the oblique shock equations. An isentropic simple wave evolution can be similarly represented by a polar curve in the [pressure-direction] plane.

In the following discussion, the analyzed situations will correspond to a uniform incoming stream for sake of simplicity. However, the local properties of the solution at an intersection point I are not changed if the flow is non uniform or axisymmetric.

Type I interference. A Type I interference pattern exists when two weak shocks of opposite families intersect at point I, as shown in Fig. 2.2. The impinging shock (C_1) provokes a pressure rise from p_0 to p_1 and an upward deflection $\Delta \varphi = \varphi_1$ (we adopt $\varphi_0 = 0$ for the upstream uniform flow). The bow shock (C_2) induces a pressure rise from p_0 to p_2 and a downward deflection φ_2.

The two shocks (C_1) and (C_2) intersect - or are refracted - at point I from which emanates shocks (C_3) and (C_4) leading to pressure levels p_3 and p_4 and flow directions φ_3 and φ_4 respectively. In regions 3 and 4, the static pressures must be the same and the flow directions parallel. Thus, unless the strengths of the two shocks (C_1) and (C_2) are equal, a slip line (Σ) will be produced at point I, the entropy rise (or stagnation pressure loss) being not the same through $(C_1) + (C_3)$ and $(C_2) + (C_4)$.

For a perfectly inviscid flow, density, temperature and velocity are discontinuous across (Σ). In fact, due to the viscosity of the fluid, a shear-layer develops along (Σ) ensuring a continuous variation of flow properties between states 3 and 4. This shear-layer can be either laminar or turbulent depending on the local Reynolds number.
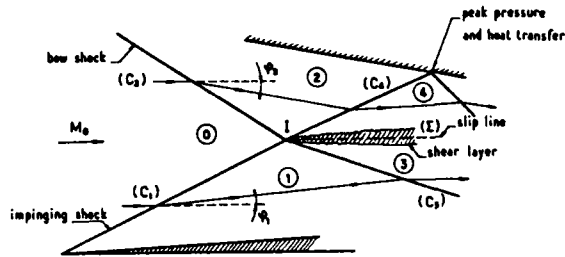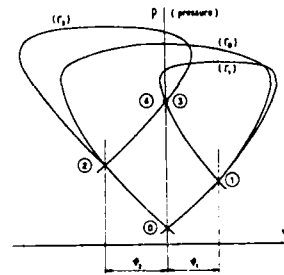
Fig. 2.2   Type I Shock Interference Pattern

Fig. 2.3   Shock Polar Representation of Type I Interference

The situation at I in the shock polar diagram is sketched in Fig. 2.3. Flows 1 and 2, downstream of (C_1) and (C_2) are represented by points 1 and 2 on the shock polar (Γ_o) attached to the uniform upstream flow 0. The shock polars (Γ_1) and (Γ_2) attached to states 1 and 2 intersect at a point which is the common image of flows 3 and 4 co-existing on each side of the slip line (Σ).

For the present interference, the actual rise in pressure and heating at the surface is caused by the interaction of the transmitted impinging shock (C_4) and the wall boundary-layer. The flow associated with Type I is supersonic throughout and we are faced with a "classsical" shock-wave/boundary-layer interaction phenomenon which is discussed in detail in Sections 3 and 4.

Type II Interference. Now, let us imagine that the strength of shock (C_2) is increased, which corresponds to a displacement of the interference zone towards the vehicle nose, as shown in Fig. 2.1. In these conditions, the image point 2 on the shock polar (Γ_o) moves to the left of the diagram in Fig. 2.3. Hence, a situation can be reached where shock polars (Γ_1) and (Γ_2) do not intersect each other.

The preceding solution is no longer possible and the flow pattern sketched in Fig. 2.4 occurs. The corresponding situation in the shock polar plane is represented in Fig. 2.5. Now, shock polars (Γ_1) and (Γ_2) intersect the strong shock solution branch of shock polar (Γ_o). Consequently, an intermediate nearly normal shock (C_5) forms which joins the two triple points I_1 and I_2, the flow behind (C_5) being subsonic. Situations at I_1 and I_2 are represented by points 3-5 and 4-6 in Fig. 2.5, 5 and 6 being the images of the flows just behind (C_5) at I_1 and I_2 respectively.

A detailed analysis of the complete flowfield is difficult because the extent of the subsonic region is unknown and depends on the size and shape of the body. Such a pattern with triple points and a nearly normal shock (in fact a strong oblique shock) is called a Mach reflection or Mach phenomenon. It can also occur at the surface of the vehicle if the regular reflection of shock (C_4) is no longer possible for similar reasons (see sketch in Fig. 2.4).
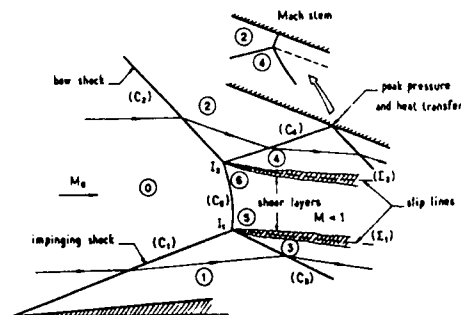
Fig. 2.4   Type II Shock Interference Pattern
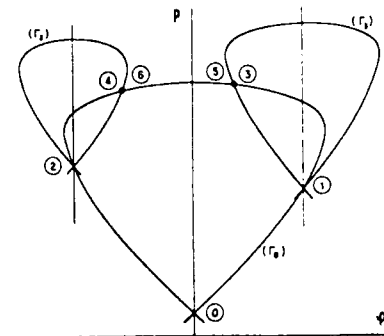
Fig. 2.5   Shock Polar Representation of Type II Interference

In certain situations, shock polars (Γ_1) and (Γ_2) may intersect at a pressure level above the strong shock part of (Γ_o). Then, there exists the possibility of either Type I or Type II interference. The shock polar diagram does not indicate which shock configuration is the most stable nor the circumstances where one type of interference pattern would occur in preference of the other. This problem has been examined in detail by Crawford (1979) who proposed an interesting shock polar construction to solve shock interaction problem.

As in the preceding case, for Type II interference, the heating problem results from the reflection of the oblique shock (C_4) at the wall.

Type III Interference. A Type III interference pattern occurs when a weak impinging oblique shock intersects a strong detached bow shock as shown in Fig. 2.6. The situation in the shock polar diagram is represented in Fig. 2.7. In this case, the shock polar (Γ_1) intersects the strong shock branch of the shock polar (Γ_o). A solution similar to Type I is here impossible because of downstream boundary conditions imposing the strong solution for the bow shock.
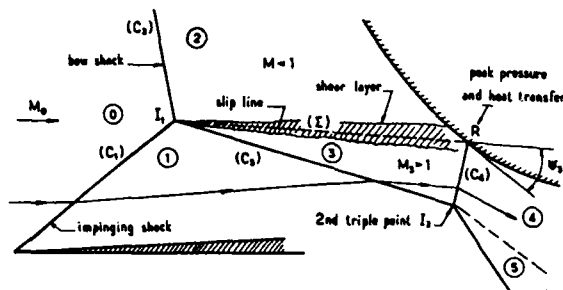
Fig. 2.6   Type III Shock Interference Pattern

Fig. 2.7   Shock Polar Representation of Type III Interference

Downstream of the two weak oblique shocks (C_1) and (C_2), the flow 3 is still supersonic, whereas the flow 2 is subsonic. Thus, a large velocity difference exists across the slip line (Σ) along which a shear-layer develops. This shear- layer attaches to the surface with subsonic flow above the layer turning upward and supersonic flow below the layer passing through an oblique shock (C_4) in order to turn parallel with the surface. Whether the shear-layer attaches 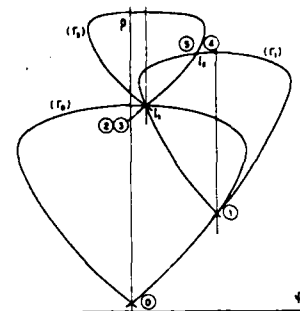to the surface depends on the Mach number M_3 in region 3 and the angle ψ_3 between the shear-layer and the surface. If M_3 is sufficiently high and ψ_3 does not exceed the maximum turning angle for M_3, then the layer will be attached. If the maximum turning angle is exceeded, the shear-layer will detach and a Type IV interference pattern will be formed (see below). If the shear layer attaches at point R and an oblique shock (C_4) does exist, then another triple point shock system will occur, as shown in Fig. 2.6.

Peak heating caused by attaching of the free shear-layer is analogous to that due to the reattachment of a supersonic separated flow. This problem, essential for base flow prediction, has been the subject of a large number of publications which cannot be cited here (for a recent review of the question, see Délery and Lacau, 1987). Supersonic reattachment theory shows that the reattachment angle ψ_3 is a well defined function of the Mach number M_3 at the shear-layer supersonic outer edge. So that, inclination of slip-line (Σ) with respect to the reattachment wall is not arbitrary and the overall flowfield results from a coupling between the angular reattachment law and the perfect fluid compatibility conditions to be satisfied at the triple point I.

Figure 2.8 shows an example of peak pressure and peak heating resulting from Type III interference. These distributions have been measured on a hemisphere at a Mach number of 6. One sees that the maximum heat transfer is 14 times the heat transfer at the stagnation point. Similar results were found by Ginoux and Matthews (1974).

It must be realized that the compression undergone by the shear-layer flow is much more efficient than the compression through the intense bow shock. This fact enables very high static pressures, well in excess of the freestream pitot pressure recovered behind the bow shock-wave, to be achieved in the shear-layer attachment region at R. This also causes the local heat-transfer rate to increase sharply.
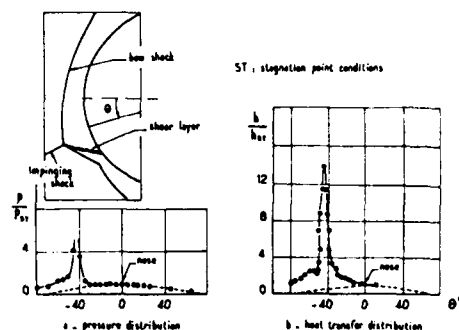
Fig. 2.8   Type III Interference on a Hemisphere at $M_0 = 6$ (Keyes and Hains, 1973)
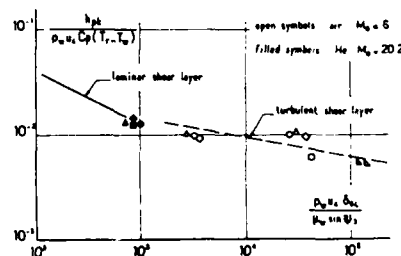
Fig. 2.9   Peak Heat Transfer Correlations for Type III Interference (Keyes and Hains, 1973)

There exist correlation laws to predict heat-transfer rate in the reattachment region of a free shear-layer. For instance, Keyes and Morris (1972) have proposed the correlation shown in Fig. 2.9 for laminar and turbulent shear-layer attachments. This correlation is derived from a correlation initially established by Bushnell and Weinstein (1968) for the peak heat-transfer at the reattachment of a separated boundary-layer (see Section 3.2.7 below).

Type IV interference. When the weak impinging shock intersects the nearly normal part of the bow shock, a situation is reached where it is no longer possible for the shear-layer to satisfy the reattachment law at R. Then, Type IV interference occurs. This interference results in a complex flow pattern with a supersonic jet embedded in the subsonic flow domain between the bow shock and the obstacle (see Fig. 2.1).

Up to region 3, the flow model is the same as Type III, therefore Type IV interference can be considered as a special case of Type III interference with a detached shear-layer. From Fig. 2.10 it can be seen that the flow in region 4 impinges on the wall nearly normally after having crossed the oblique shock (C_4) behind which the flow is still *supersonic*. Thus, a supersonic jet develops surrounded by subsonic flows in which the pressure in nearly constant. Hence, to maintain pressure continuity at the impact of shock (C_4) with the jet boundary (J_1), a centered expansion must form to cancel out the pressure jump through the shock (C_4) (a similar situation is analyzed in Section 3.2.2 below). This expansion is reflected by boundary (J_2) as a compression which in turn is reflected by (J_1) into an expansion wave, and so on. Thus the jet is constituted of triangular regions, the actual number of regions being dependent upon the standoff distance of the entire configuration.

Upon impingement on the wall, a jet bow shock is produced that creates a small stagnation region with high pressure and heating. As shown by Edney, the peak heating is dependent upon the peak pressure, the jet width, the jet angle of incidence with the surface and the state - laminar or turbulent - of the shear-layers developing along boundaries (J_1) and (J_2). Correlations have been proposed to predict peak heating in the jet impact region . They will not be given here (see Edney, 1968; Keyes and Hains, 1973). Peak pressure and heat-transfer caused by Type IV interference are shown in Fig. 2.11. These results are relative to a hemisphere placed in a flow of Mach number equal to 6.

In some situations, the jet can be turned to graze or move parallel to the surface without impinging. In this case (denoted Type IVa interference), even though impingement does not occur, regions of high heating are nevertheless produced because of the interaction of the jet flow with the boundary-layer.
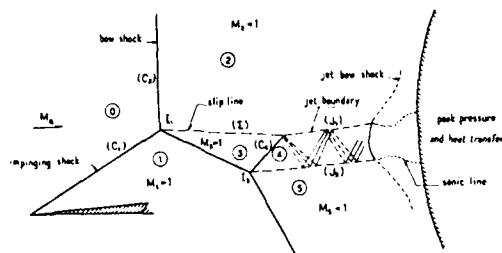
Fig. 2.10   Type IV Shock Interference Pattern
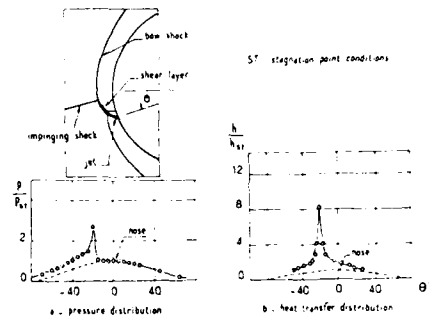
Fig. 2.11   Type IV Interference on a Hemisphere at $M_0 = 6$ (Keyes and Hains, 1973)

Type V Interference. Type V interference occurs when the impinging shock (C_1) meets the bow shock (C_2) above the nose of the obstacle, in a region where (C_2) is still a strong shock (see Fig. 2.1). Then, near the nose, the flow in front of (C_2) is the flow 1 behind (C_1).

This type of interference involves the intersection of two oblique shocks of the same family. The resulting flowfield is represented in Fig. 2.12. It consists of a rather complex shock pattern comprising a triple point I and an intersection point H where four shocks meet. The thin supersonic jet from I and the shear-layer emanating from point H converge as the subsonic flow behind shock (C_5) accelerates to sonic velocity. Both the jet and the shear-layer generally intermix and may graze the surface, thus causing some increase in heating. Impingement of shock (C_4) on the surface leads to a classical shock-wave boundary-layer interaction problem which is analyzed in detail in the coming Sections.

The flow structure in the shock polar diagram is sketched in Fig. 2.13. We will not comment this diagram which can be readily understood by referring to the shock pattern in the physical plane (see Fig. 2.12).
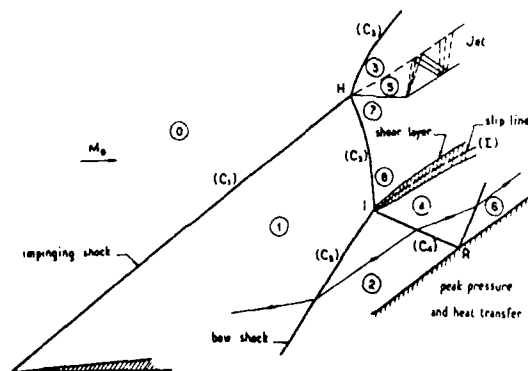
Fig. 2.12   Type V Shock Interference Pattern
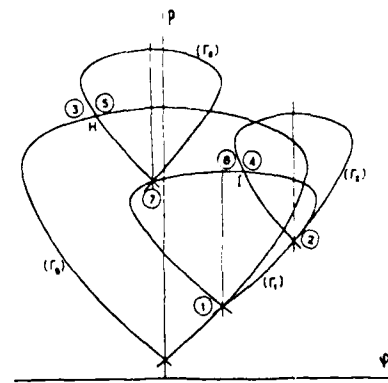
Fig. 2.13   Shock Polar Representation of Type V Interference

Type VI Interference. This type of interference takes place when (C₁) and (C₂) intersect far from the nose in a region where both (C₁) and (C₂) are weak oblique shocks (see Fig. 2.1). The corresponding shock pattern is represented in Fig. 2.14. In this situation, an expansion fan emanates from the triple point I. Impingement of this expansion on the surface leads to a decrease in the pressure distribution. This type of shock pattern, which is also associated to ramp induced flow, is commented in detail in Section 3.2.2 below.

Fig. 2.14   Type VI Shock Interference Pattern

2.3 - Calculation Methods for Shock Interference Heating

Several empirical methods have been proposed to predict peak heating due to shock interference in hypersonic flows (see for example, Hains and Keyes, 1972; Keyes and Morris, 1972; Keyes and Hains, 1973; Bramlette, 1974). These methods, which will not be given here, are based upon a simplified des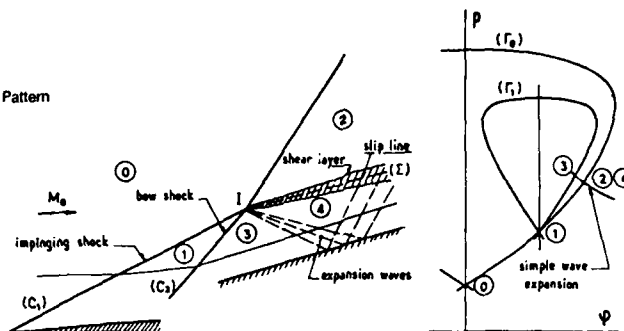cription of the inviscid flowfield resulting from the shock interference. Then, semi-empirical models are superimposed on the inviscid structure to represent the dissipative effects responsible of the transfer phenomena. In the preceding Section, we have presented correlations for predicting heat-transfer at the attachment of a shear-layer resulting from Type III interference. Similar treatments can be applied to other types of interference: jet impingement for Type IV, shock-wave/boundary-layer interaction for types I, II and V.

It is only recently that an accurate treatment of the shock interference problem by solution of the Navier-Stokes equations has become possible. Indeed, numerical simulation of shock interference flows including viscous effects with classical numerical schemes was difficult because of the intense shock-waves and shear-layers. Thus the classical shock-capturing method based on the MacCormack predictor-corrector scheme which was employed by some investigators gave poor shock-wave resolution (Tannehill et al., 1976).

However, due to progress in numerical methods (for example use of second order implicit total variation diminishing - TVD-algorithms) and adequate grid resolution normal to the wall, very promising results have been obtained recently by Klopfer and Yee (1988). Figure 2.15 shows an example of surface pressure and heat-transfer distributions obtained for a Type III interference at a Mach number of 8.03. The results compare favorably with the data of Wieting and Holden (1987), although the peak heating level is underpredicted. In this case, part of the discrepancy is attributed to uncertainty in the impinging shock location. Figure 2.16 shows Mach number contours of Navier-Stokes solutions for Types I, II, III and IV interference shock patterns at Mach 15.
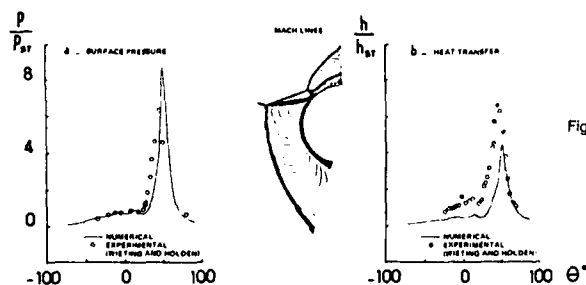

Fig. 2.15   Navier-Stokes Calculation of Type III Interference at M_0 = 8.03 (Klopfer and Yee, 1988)
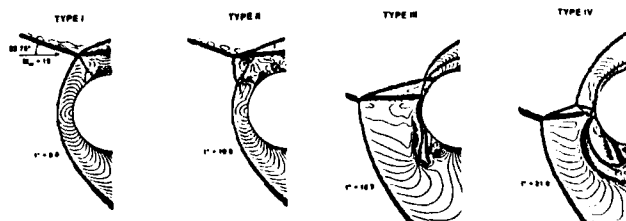

Fig. 2.16   Navier-Stokes Calculation of Several Types of Shock Interference at M_0 = 15 (Klopfer and Yee, 1988)

3 - A PHYSICAL DESCRIPTION OF SHOCK-WAVE/BOUNDARY-LAYER INTERACTION IN SUPERSONIC AND HYPERSONIC FLOWS

3.1 - General Remarks

In what follows we will consider phenomena associated to shock-wave/boundary-layer interaction from a geneal point of view: i.e. without making a well defined distinction between supersonic and hypersonic flows. This, for at least three reasons:

i - Firstly, because the essence of phenomena is basically the same, independently of the incoming flow Mach number, so that the main flow features are similar whatever the Mach number is. This conclusion would be different for transonic interactions in which the hyperbolic-elliptic nature of the outer inviscid field leads to specific characteristics. The case of transonic interactions will not be considered in the present Lecture although transonic situations are not impossible on a hypersonic vehicle (for information on this kind of interactions, see Délery and Marvin, 1986).

ii - Secondly, because supersonic interactions actually occur on a vehicle flying at a hypersonic Mach number since there is a considerable reduction in the flow Mach number behind the bow shock-wave.

iii - Lastly, a good reason to examine interactions at moderate - but frankly supersonic - Mach numbers is that phenomena are more evident at supersonic velocity than at hypersonic velocity where the interaction is confined within a thin layer close to the wall. As will be seen below, this is specially true for turbulent interactions.

Nevertheless, typical features of hypersonic interactions will be clearly established and emphasis will be placed on the specific problems met for hypersonic flow conditions. For instance, effect of wall temperature will be discussed when information on the influence of this parameter is available. As a matter of fact, one of the most typical features of hypersonic flows is the large difference that exists between the wall temperature T_w and the outer flow stagnation temperature T_{10}. This thermal situation is frequently characterized by the ratio T_r/T_r where T_r is the recovery temperature, i. e. the adiabatic wall temperature. This ratio can be well in exces of 10 for reentry conditions. The high value of the outer flow stagnation temperature leads also to extremely large heat-transfer rates at the wall, especially in shock-wave/boundary-layer interaction regions. This important problem will also receive a special attention.

3.2 - Interactions in Two-Dimensional Flows

3.2.1 - The Four Basic Interactions

What can be considered as the four basic configurations involving interaction between a shock-wave and a boundary-layer in supersonic - or hypersonic - flow are schematically represented in Fig. 3.1. In what follows, the incoming outer flow will be assumed an uniform flow streaming along a flat plate for the sake of simplicity.

i - The first and most conceptually simple situation is the wedge (or ramp) flow. Here a discontinuity α in the wall direcion is the origin of a shock-wave (C_1) through which the supersonic incoming flow undergoes a deflection $\Delta\varphi$ equal to the corner angle α.

ii - The second type of flow is associated with the impingement on the wall of an incident oblique shock (C_1). The incoming flow undergoes a deflection $\Delta\varphi_1$ through (C_1) and the necessity for the downstream flow to be again parallel to the wall entails the formation of a reflected shock (C_2) issuing from the impingement point I of (C_1). The deflection $\Delta\varphi_2$ produced by (C_2) must be such that $\Delta\varphi_2 = \Delta\varphi_1$. The pressure jumps p_1/p_0 and p_2/p_0 through each shock are not equal, though not very different.

iii - The third flow is induced by a step of height h facing the incoming flow. Such an obstacle provokes the separation of the flow at a point S. The very rapid pressure rise accompanying separation, especially in turbulent flows, gives rise to a shock-wave (C_1) emanating from a place very close to the separation point S. Downstream of S, a separated zone develops. It is characterized by the existence of a bubble of recirculating flow in contact with the step. In fact, there is some similarity between wedge flow and flow produced by a forward facing step. In the latter case, the separated region is "felt" by the outer inviscid stream as a corner whose angle is determined by the displacement effect of the dissipative region.

iv - The fourth situation corresponds to the reattachment downstream of a rearward facing step. The incoming flow separates at the base shoulder S undergoing an expansion with a (negative) downward deflection. Further downstream, the flow reattaches on the wall. The resulting positive deviation generates compression waves which coalesce into the so-called "reattachment shock". In contact with the wall, a recirculating bubble is trapped, inside which the flow is reversed.

Now we will examine in more detail the general structure of the flowfields resulting from these interactions by focusing our attention to interactions i) and ii). In fact, some properties of flow iii) are met in interactions of type i) or ii) when these interactions lead to the formation of a large separated zone, as for example the existence of a pressure plateau succeeding to the pressure rise at separation. Flow iv) concerns more specially base-flow problems that will not be considered in the present Lecture.
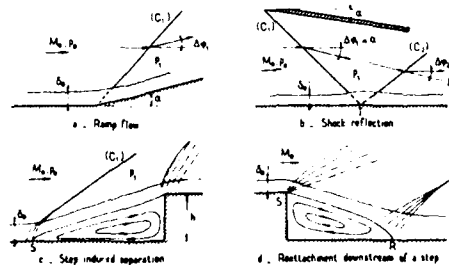

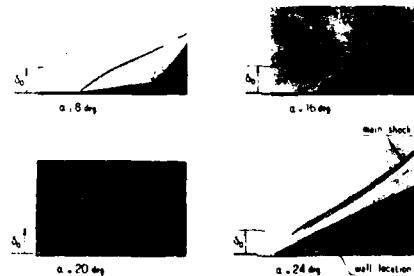Fig. 3.1   Basic Shock-Wave/Boundary-Layer Interactions in Supersonic Flow

Fig. 3.2   Ramp Flow. Flowfield Shadowgraphs. M_0 = 2.85 (Settles et al., 1979)

In what follows, we will consider in a global manner both laminar and turbulent flows since there is no basic differences between the interactions associated with these two boundary-layer régimes. However, the main - and important - differences which affect the scale (extent of the interaction domain) and intensity (pressure rises associated to the interaction) of phenomena will be emphasized.

3.2.2 - The General Flow Structure

The Compression Ramp Flow. Let us first consider the flow structure associated with a compression ramp. Figure 3.2 shows a sequence of microsecond spark shadowgraphs visualizing this type of flow for an upstream Mach number M_0 equal to 2.85 and a Reynolds number R_{δ_0} (based on the thickness δ_0 of the incoming boundary-layer) equal to 1.7 x 10^6 (Settles et al., 1978). In these conditions, the incoming boundary-layer is fully turbulent. The four pictures correspond to different values of the corner angle ranging from 8° to 24° (the appearance of a second ramp in some of the photos is due to optical interference and is not affecting flow development).

In the 8° case, a distinct shock-wave is seen to arise from the corner location. This shock-wave forms well within the boundary-layer and, in fact, most of the boundary-layer behaves like an inviscid - but rotational - fluid, viscous forces being negligible compared to pressure and inertia forces throughout the major part of the boundary-layer. Furthermore, at the high Reynolds number value of the present experiments, the velocity profile of the incoming boundary-layer is very "filled" so that the Mach number slowly decreases over the major part of the boundary-layer thickness. Transition to zero-velocity at the wall takes place over a very short normal distance and accordingly the subsonic layer is extremely thin. These features explain why the shock originates from a region very close to the wall.

Starting from the wall, the shock is first seen to be curved, the curvature being due to its propagation through a rotational layer in which the entropy (and accordingly the Mach number) changes from one streamline to the other. Outside the boundary-layer, the shock is rectilinear since the incoming flow is uniform.

The weak influence of viscosity in this kind of flow - when the ramp angle is moderate - is demonstrated by the theoretical result shown in Fig. 3.3 (Roshko and Thomke, 1969). This calculation was performed by considering the boundary-layer as a rotational inviscid flow and by applying the rotational Method of Characteristics to determine the shock shape and the flow over the ramp. To make such a calculation possible, the inner part of the incoming boundary-layer must be ignored, the "cut" being chosen in such a way that the Mach number behind the shock remain supersonic. One sees in Fig. 3.3 that there is a very good agreement between the wall pressure distribution thus computed and experiment. In the present case, this is because the low velocity portion of the boundary-layer has a nearly negligible influence on the flow field. In the present case, this is because the low velocity portion of the boundary-layer has a nearly negligible influence on the flow field, the inner subsonic layer being excessively thin. A similar calculation has been performed by Cérésuela and Coulomb (1970) and also by Don Gray and Rhudy (1973) for the flow over a compression ramp at a Mach number of 10 (see also in Section 3.2.8 below application of this approach made by Elfstrom to predict incipient shock induced separation).

For α = 8°, the upstream influence is very small, since the shock emanates practically from the corner angle. On the other hand, for α = 16° and 20°, the shadowgraph reveals a substantial increase of the upstream influence length due to an intensifying of the perturbating agency, namely the shock strength. This phenomenon will be studied in more detail below. Also, the spreading of the shock near the wall becomes clearly visible. The shock is seen to result from the coalescence of compression waves induced by the thickening of the low velocity portion of the boundary-layer.

For α = 24°, the pressure rise is high enough to provoke significant separation. The shadowgraph shows the following typical features (part of this shadowgraph is obscured by the aerodynamic fences which were necessary to insure flow field two-dimensionality):

i - The corner upstream influence has considerably increased.

ii - A first shock forms well upstream of the corner.

iii - An additional compression fan at reattachment merges with the separation shock and reinforces it.

For flow conditions different from those of the present example, the compression waves at reattachment may coalesce into a shock before reaching the separation shock (see sketch in Fig. 3.4). In this situation the two shocks meet at a bifurcation point I (also called a triple point) and the inviscid flow structure is similar to a double wedge configuration with a first wedge corresponding to the initial turn at separation and a second wedge to the final turn at reattachment (see Fig. 3.4a). This inviscid flow structure can also be conceived as a double shock system produced by a "dead-air" region at a constant pressure superior to that of the incoming flow. The free boundary of this dead-air region starts from the "separation" point S_T and hits the ramp at the "reattachment" point R_T. S_T and R_T not being coincidental with the physical separation and reattachment points, since the real flow field is more complex that the above perfect fluid model which is sketched in Fig. 3.4a. The model of the second kind (including a dead-air region) has been utilized in multi-component methods developed to compute large separated flows in hypersonic air-intakes (Délery and Masure, 1969).
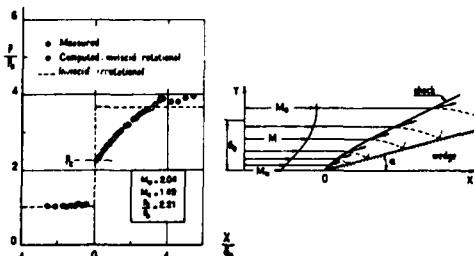

Fig. 3.3   Ramp Flow. The Rotational Inviscid Flow
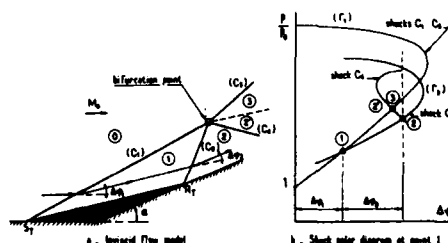Model (Roshko and Thomke, 1969)

Fig. 3.4   Ramp Flow with Separation. Inviscid Flow
Model. First Case

The shock polar construction in Fig. 3.4b shows the local flow situation at point I. In order that the two flows downstream of ,
be compatible (i.e., have same pressure and same direction) an intermediate state 2' must be introduced between the final states 2
and 3. According to the relative position of the shock polars (Γ_t) and (Γ_t), the wave connecting 2 and 2' is either a shock (most
often very weak) - as sketched in Figs. 3.4a and b - or a centered expansion wave - as sketched in Figs. 3.5a and b. This shock
pattern has been investigated by Bird (1963) and Sullivan (1963) who found that at high Mach number the wave between 2 and 2' is
an expansion wave whose amplitude increases with the Mach number. In hypersonic interactions, the existence of this wave is felt at
the wall by a sharp decrease of the pressure downstream of the reattachment region (see Section 3.2.3 below).
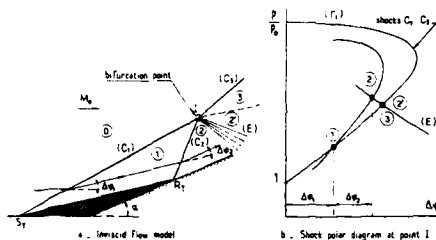

Fig. 3.5   Ramp Flow with Separation. Inviscid Flow
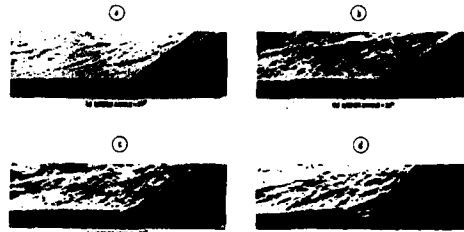Model. Second Case

Fig. 3.6   Turbulent Hypersonic Ramp Flow. Flowfield
Shadowgraphs. M_0 = 8.6 (Holden, 1972)

The features specific to a turbulent shock-wave/boundary-layer interaction in hypersonic flows are illustrated by the photographs
in Fig. 3.6 which show ramp flows for an incoming Mach number of 8.6, the Reynolds number R_{f_0} being equal to 1.4 x 10^6 (Holden,
1972 and 1977). Thus, for hypersonic flow the following features are apparent:

i   - When there is no separation, as in photo a, the main shock (C_1) is very close to the ramp and emanates practically from the
corner hinge.

ii   - The boundary-layer thickness over the ramp is much thinner than the incoming boundary-layer. This important reduction in
thickness is due to the large increase in the unit flow rate ρu (ρ : density, u : velocity) resulting from the compression through
the shock.

iii - When separation occurs, the shock pattern described above is embedded within the boundary-layer. The situation is more clearly
visible in the sketch of Fig. 3.7. One sees that the triple point I can be very close to the wall so that the expansion wave
emanating from I reaches the wall at a small distance behind reattachment leading to an important pressure decrease.
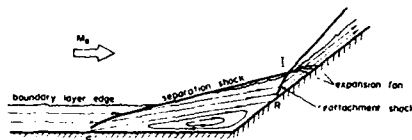
Fig. 3.7   Hypersonic Ramp Flow. Sketch of Flowfield
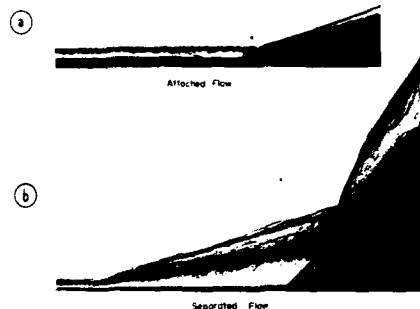
Fig. 3.8   Turbulent Hypersonic Ramp Flow. Flowfield
Shadowgraphs. M_0 = 9.22 (Elfstrom, 1971)

The shadowgraph pictures of Figs. 3.8a and b give another beautiful example of a turbulent hypersonic flow at a wedge-
compression corner (Elfstrom, 1971). In the separated case (see Fig. 3.8b), one clearly sees the separation shock and the shear-layer
which develops between the external inviscid flow, below the separation shock, and the so-called "dead-air" region in contact with
the wall. Also, one notes the strong reattachment shock that is intersected by the separation shock very close to the surface.

Thus, one of the distinctive features or hypersonic interacting flows, is the existence of a pattern of extremely strong shocks
associated to the separated flow.

On the other hand, the schlieren photographs of Fig. 3.9 emphasize the differences between a laminar and a turbulent
interaction. It is seen that for a same ramp angle (α = 15°) and at a Mach number of 5, a large separation occurs in the laminar
case whereas the flow remains attached in the turbulent case. The immediate conclusion is that the interaction length - i.e. the
streamwise extent of the interaction domain - is far more important in the laminar flow régime than in the turbulent régime. Also,
one notes that a laminar boundary-layer will separate for a much weaker shock than a turbulent one.

Figure 3.10 shows a comparison between a laminar and a turbulent interaction in terms of wall pressure distributions for nearly
the same upstream Mach number (Chapman et al., 1957). These wall pressure distributions clearly exhibit a greater spreading of the
discontinuity in the case of the laminar boundary-layer. This greater X-wise extension is far beyond the scaling by the incoming
boundary-layer thickness. Also, the various characteristic pressure rises, in particular the pressure at separation, are far less
important in laminar flows than in turbulent flows.

The above differences in the flow behaviors have at least two immediate consequences:
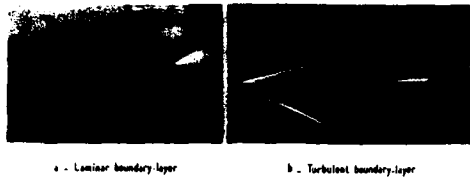
Fig. 3.9   Hypersonic Ramp Flow. $M_0 = 5$ - $\alpha = 15°$

a - Laminar flow (M_0 = 2.4)   b - Turbulent flow (M_0 = 2.9)
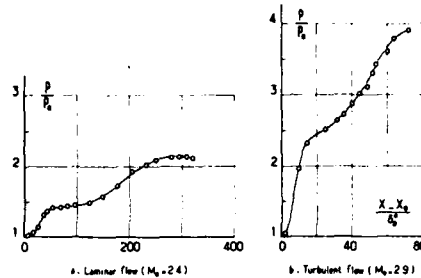
Fig. 3.10   Shock Reflection in Fully Laminar and Fully Turbulent Régimes (Chapman et al., 1957)

i   - The pressure rise required to separate a laminar boundary-layer is much lower than the pressure rise inducing separation of a turbulent boundary-layer. A direct quantitative comparison of the respective sensitivity of the two flows to shock-induced separation is difficult since such a comparison should be made by varying the pressure rise while keeping the same Reynolds number for the two flows. However, some information can be inferred from the Free Interaction Theory presented in Section 3.2.4 below. This theory establishes the fact that the normalized pressure rise at separation - which can be identified with the pressure ratio necessary for incipient Separation -is nearly five times smaller in laminar flow than in turbulent flow.

ii - Due to the wider streamwise spreading of the phenomena and the simultaneous reduction in the amplitude of the pressure rises, the X-wise gradients of the flow properties are far less intense in laminar flows. Consequently, the transverse pressure variations are also small, as is shown in the experimental data of Sfeir (1969) plotted in Fig. 3.11. These results are relative to a ramp flow at an upstream Mach number $M_0 = 2.64$. The figure gives a comparison between the pressure measured at the wall and the pressure at the boundary-layer edge deduced from local measurements. The coincidence of the two distributions must be compared to the large transverse pressure gradients existing in a turbulent interaction where, as we have seen, the shocks penetrate deeply inside the boundary-layer.
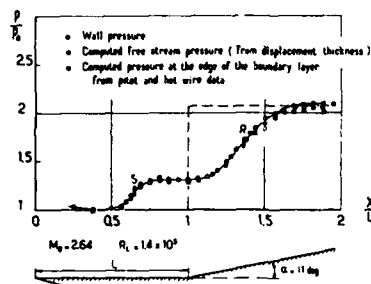
Fig. 3.11   Ramp Flow in Laminar Régime. Wall Pressure Distribution (Sfeir, 1969)
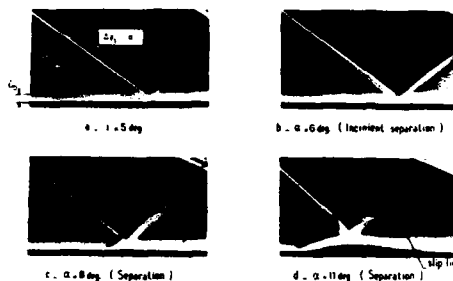
Fig. 3.12   Incident Reflecting Shock in Turbulent Flow. Flowfield Shadowgraphs. $M_0 = 1.93$ (Délery, 1970)

The absence of a significant y-wise pressure gradient in a laminar interaction is of great concern for theoretical methods since it justifies the modelling of this kind of flow by resorting to a classical boundary-layer approach as the one most often used in Inviscid-Viscous Interactive (IVI) methods.

The Impinging-Reflecting Oblique Shock. In the present simplified configuration, a shock-wave is generated by a "shock-generator" made up of a flat plate with sharp leading edge, inclined at an angle α_g relative to the uniform incoming flow. The planar oblique shock originating from the plate leading edge impinges on a straight wall facing the shock generator.

The sequence of schlieren photographs shown in Fig. 3.12 visualizes the shock reflection phenomenon for increasing values of the primary deflection $\Delta\varphi_f$ through the incident shock-wave. In the present example, the incoming flow Mach number is equal to 1.93 and the Reynolds number Rf_s to 0.75×10^4 (Délery, 1970). The apparent thickness of the shock on the photographs is the manifestation of side effects on the test-section windows. The following schlieren photographs interpretation closely resembles the schematic flow representation given by Bogdonoff and Kepler (1954).

When the incident shock is weak (as in the firt photograph in Fig. 3.12a), the general flow structure does not differ much from the perfect fluid model. However, a closer look at the picture reveals that complex phenomena take place inside the boundary-layer. A schematic sketch of the observed wave-field is represented in Fig. 3.13.

The incident shock (C_1) progressively curves as it penetrates the boundary-layer because of the decrease in local Mach number. Correlatively, its intensity weakens and becomes vanishingly small when the shock reaches the sonic line. On the other hand, the pressure rise through (C_1) tends to propagate upstream in the subsonic region $\varepsilon \delta_s$ of the boundary-layer, causing this part to thicken.

The thickening of the boundary-layer subsonic channel generates outgoing compression waves (I_1) that rapidly coalesce to form the reflected shock (C_2). The refraction of these waves - like that of the incident shock - as they propagate through the rotational quasi-inviscid layer $(1.\varepsilon)\delta_s$ induces the secondary wave system (I_2). These last waves are reflected by the sonic line as expansion waves (I_3) which are clearly visible, just behind shock (C_2) on the schlieren picture.
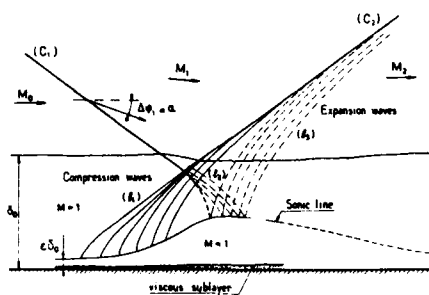
Fig. 3.13   Shock Reflection Without Boundary-Layer Separation. Schematic Representation of the Flowfield
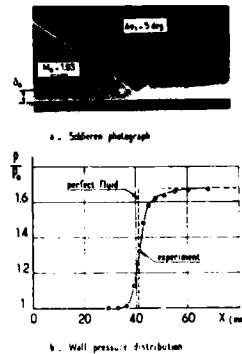
Fig. 3.14   Shock Reflection Without Separation. An Example of Weak Viscous Interaction. M_0 = 1.93

For very weak incident shocks, the upstream interaction distance is extremely short, so that the above flow pattern is embedded well within the boundary-layer. Thus, at the outer flow scale, the only reflected wave is a shock (C_2) with a deflection $\Delta\varphi_i$ equal - but with opposite sign - to that of the incident shock (C_1). In this case, the reflection of the shock is said to be a weak interaction process in the sense that the (real) viscous flow closely resembles the inviscid flow solution. This resemblance is also evident when considering the wall pressure distribution plotted in Fig. 3.14.

Let us now consider the case of an incident shock strong enough to separate the boundary-layer. The resulting typical wave pattern is visualized by the two last photographs in Fig. 3.12. A very schematic representation of the observed flow field is sketched in Fig. 3.15.

The boundary-layer separates at a point S located well upstream of the point where the shock would meet the surface if the fluid were inviscid. The rapid pressure rise at separation results in compression waves propagating at first in the supersonic part of the boundary-layer, then in the outer inviscid stream. These waves coalesce to constitute what can be interpreted as the leading reflected shock (C_2) through which the outer inviscid stream is turned upward from the wall. Shock (C_2) intersects the incident shock (C_1) at point H from which emanate the two refracted shocks (C_3) and (C_4). As the entropy rise through (C_1) plus (C_4) is generally different from the entropy rise through (C_2) plus (C_3), H is the origin of a slip line well visible on the last photograph.
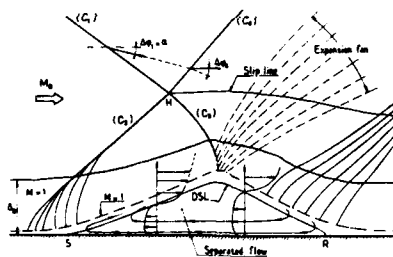
Fig. 3.15   Shock Reflection With Boundary-Layer Separation. Schematic Representation of the Flowfield
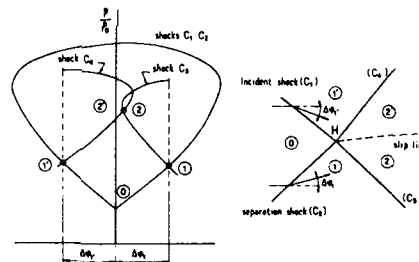
Fig. 3.16   Shock Polar Representation of Situation at Point H (See Fig. 3.15)

A shock-polar representation of the situation at point H is schematically represented in Fig. 3.16. If one increases the intensity of the incident shock, a situation can be reached where the two shock-polars representing the refracted shock-waves (C_3) and (C_4) do not intersect anymore. Then a Mach stem phenomenon appears with the formation of a quasi normal shock inside the flowfield.

After intersection with (C_1), shock (C_3) is bent because of the entropy gradient downstream of (C_2) and the compression waves generated by the thickening of the boundary-layer. Afterwards, (C_3) enters into the separated dissipative layer from which it is reflected into an expansion wave. Thus the impingement of (C_1) on the boundary-layer is seen to be similar to a shock reflection at a constant pressure free boundary, as in the case of the external boundary of a large separated region.

The viscous flow, which has separated at S, reattaches on the surface at point R. Between S and R a recirculation bubble forms where the streamwise velocity profiles contains a zone where the flow streams in a direction opposite to that of the main stream. Occurrence of this reversed flow region is typical of separated boundary-layer. The streamline emanating from the separation point S and stagnating at the reattachment point R is frequently called the Discriminating Streamline (or DSL). It delimits the flow which is "trapped" into the recirculation bubble from the flow which streams from upstream infinity to downstream infinity. The above picture is true only if the flow is two-dimensional and steady.

The incident shock and reflected expansion turn the flow towards the wall at an angle twice as large as the deflection through the incident shock alone. As this total downward turning is greater than the upward turning through the separation shock, downstream of the expansion fan, the outer stream flows towards the surface. At the same time the thickness of the dissipative layer decreases. Afterwards, the external stream is progressively turned to become parallel to the wall. Simultaneously, the boundary-layer reattaches at point R. The deviation accompanying the reattachment process is far more progressive than the deflection at separation. The resulting compression waves are barely visible on the schlieren photographs of Fig. 3.12.

In the same nature as the double-wedge (or free boundary) inviscid flow model for a separated wedge flow, one can also imagine a similar model schematizing the reflected-shock separated flow (see Fig. 3.17). It consists in a dead-air region at constant pressure whose free boundary starts from the "separation" point S_T. The incident shock (C_1) hits the free boundary at point I which is the origin of an expansion fan cancelling the shock pressure jump to insure continuity of pressure. There results an abrupt deviation of the free boundary which runs towards the wall downstream of I and meets it at the "reattachment" point R_T.

When shock reflection induces separation, there is a large difference between the perfect fluid solution and the real (viscous) flow. This difference is obvious from the schlieren photographs. It is also evident if one compares the inviscid and wall pressure distributions plotted in Fig. 3.18. Such a flow will be termed a **strong interaction process**, in the sense that the purely inviscid solution is now far from portraying the true flow field.

Shadowgraphs of turbulent interaction due to shock reflection in hypersonic flow are shown in Fig. 3.19. The incoming flow Mach number is equal to 8.6 (Holden, 1972). Conclusions similar to those pertaining to the wedge flow can be drawn. In particular, one notes the small angle relative to the surface of the reflected shock. The shock pattern associated to flow separation is practically entirely contained within the boundary-layer flow.
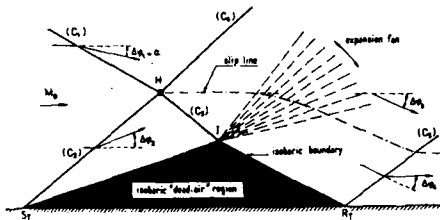
Fig. 3.17   Shock Reflection With Separation. Inviscid Flow Model
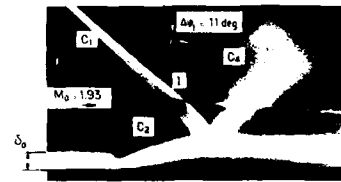
Fig. 3.18   Shock Reflection With Separation. An Example of Strong Viscous Interaction. M_0 = 1.93

a - Schlieren photograph
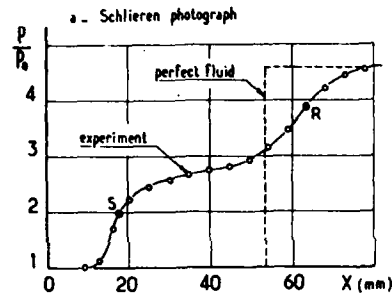
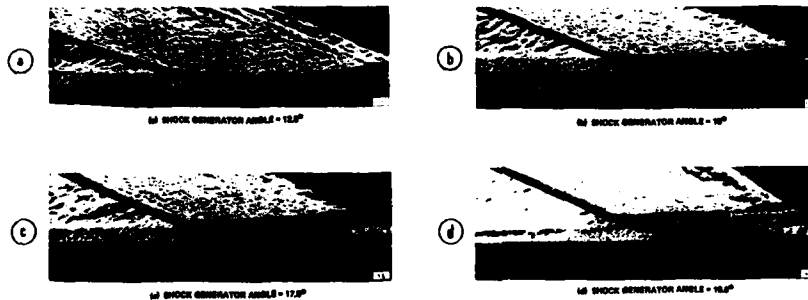b - Wall pressure distribution

Fig. 3.19   Turbulent Shock Reflection in Hypersonic Flow. Flowfield Shadowgraphs. M_0 = 8.6 (Holden, 1972)
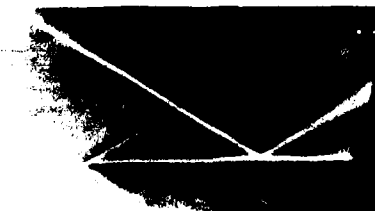
Fig. 3.20   Laminar Supersonic Shock Reflection. Schlieren Photograph. M_0 = 2.15 (Degrez et al., 1987)
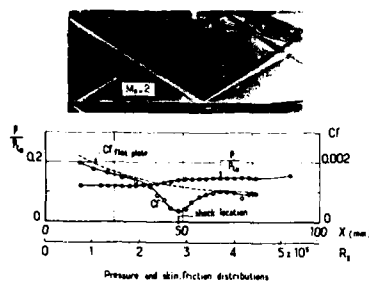
Fig. 3.21 Supersonic Shock Reflection. Fully Laminar Interaction. M_0 = 2 (Hakkinen et al, 1959)
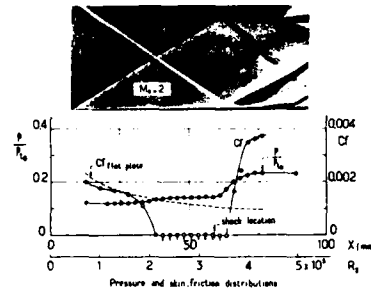
Fig. 3.22 Supersonic Shock Reflection. Transitional Interaction. M_0 = 2 (Hakkinen et al., 1959)

An example of typical oblique shock-wave/laminar boundary-layer interaction is presented in Fig. 3.20. In this case, the incoming flow Mach number is equal to 2.2, but the general flow structure would be the same at higher Mach number (Degrez et al., 1987). The general features observed here are basically the same as those corresponding to a turbulent interaction. However, for the laminar régime the streamwise extent of the interaction domain - scaled to the initial boundary-layer thickness - is far more important. Also, in laminar coalescence of the compression waves induced by boundary-layer separation most often occurs well above the surface, so that the intersecting shock pattern of Fig. 3.15 is generally not observed, except at hypersonic Mach number.

At hypersonic Mach number, if the Reynolds number is not very low, the interaction can be transitional. This means that transition from laminar to turbulent occurs in the course of the interaction process itself. In this case, the shock is a perturbation which triggers a premature transition of the boundary-layer which otherwise would take place farther downstream of the shock origin (wedge flow) or impingement point.

Transitional interactions have been recognized and analyzed by several investigators, among them Hakkinen et al., (1959), Gadd et al. (1954), Chapman et al. (1957) and also Don Gray (1967). The occurrence of a transitional régime is illustrated by comparing the shock reflection represented in Figs. 3.21 and 3.22. These experiments were carried out in a two dimensional wind-tunnel with an upstream Mach number equal to 2 (Hakkinen et al., 1959). The first situation (see Fig. 3.21) is fully laminar, transition taking place well downstream of the zone of interest. As shown in Fig. 3.22, an increase in the Reynolds number and in the shock strength provokes the transition to move into the interaction domain, more precisely into the vicinity of reattachment. The phenomenon is clearly visible on the shadowgraph picture of Fig. 3.22 as also on the corresponding wall pressure distribution. One observes a strong dissymmetry between the pressure rises respectively associated with separation and reattachment. This interaction leads to a far more ample pressure rise in the reattachment region than in the separation zone.

The consequence of the transition displacement is twofold:

i - The X-wise scale of the reattachment domain has considerably shrunk.

ii - The associated pressure rise, along with the accompanying pressure gradient, have been greatly amplified.

The various situations encountered when transition moves in the interaction domain have been thoroughly discussed by Gadd et al. (1954). Also, the effect of shock impingement on boundary-layer transition was investigated by Le Balleur and Délery (1973).

In fact, very few information is available on this phenomenon which is of great importance for hypersonic applications. Its frequent occurrence in shock-wave/boundary-layer interactions may lead to great difficulties in the prediction of the extremely large heat-tranfer rates which are associated with reattachment (see Section 3.2.7 below).

3.2.3 - Properties of the Wall Pressure Distribution

The main properties of the wall pressure distribution measured in a supersonic or hypersonic shock-wave/turbulent boundary-layer interaction will now be examined by considering typical experimental results.

i - The first example is a wedge flow at an upstream Mach number M_0 = 2.95 and a Reynolds number R_{δ_0} = 0.78 x 10^6 which was investigated in considerable details by Settles (1975). The data plotted in Fig. 3.23 show that the pressure at the wall starts to rise upstream of the corner by virtue of the upstream propagation mechanism already discussed. The correlation properties of the so-called Upstream Influence Length - or Upstream Interaction Length as defined from the wall pressure distribution will be examined in Section 3.2.5.
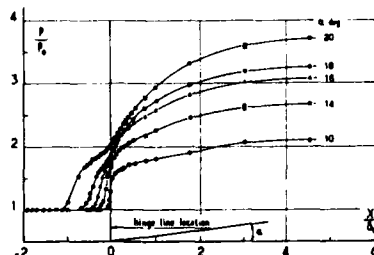
Fig. 3.23 Supersonic Ramp Flow. Wall Pressure Distributions. M_0 = 2.95 (Settles, 1975)
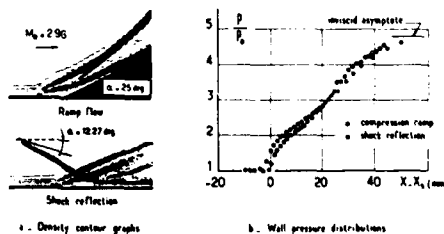
Fig. 3.24 Comparison of Ramp Flow and Shock Reflection Flow. M_0 = 2.95 (Shang et al., 1976)

ii - For the highest values of α, the pressure curves clearly exhibit three inflection points. This shape is typical of an interaction involving a noticeable separation of the boundary-layer. The three inflection points are respectively associated with separation, the onset of reattachment and the reattachment compression. Now, as we already know, the fully inviscid solution differs considerably from the real flow and such a situation is called a strong interaction.

iii - The data plotted in Fig. 3.24 were published by Shang et al. (1976). They are relative to a compression ramp and to an impinging shock giving the same overall pressure rise as the ramp. The initial conditions are identical in the two cases, namely: M_0 = 2.96 and $R_{f_0} \sim 10^5$. The left part of the figure shows lines of constant density determined from interferometric measurements. Although the structures of the two flows are very different, one sees that the two families of wall pressure distributions plotted on the same figure are nearly coincident.

iv - Figure 3.25 shows plotting of wall pressure distributions for the same incoming flow separating in front of steps of different heights. Such an obstacle provokes, even in turbulent flow, a large separation. We will see in Section 3.2.4 that the pressure rise associated with step induced separation is in fact the same as that resulting from shock induced separation - for identical incoming flow conditions. For the highest step, the pressure curve exhibits the plateau typical of an extended separated zone. If these distributions are re-plotted in such a way that the origins of the interactions coincide - as is done in Fig. 3.26 - one observes a close correlation of the curves on the whole.
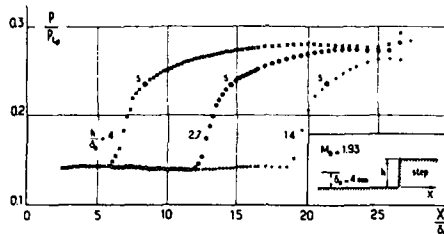
Fig. 3.25   Separation in Front of a Step. Influence of the Step Height on the Wall Pressure Distribution. M_0 = 1.93 (Délery, 1970)
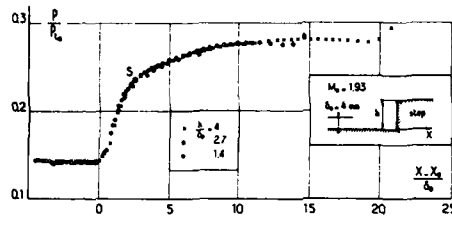
Fig. 3.26   Separation in Front of a Step. Correlation of Wall Pressure Distributions (Délery, 1970)
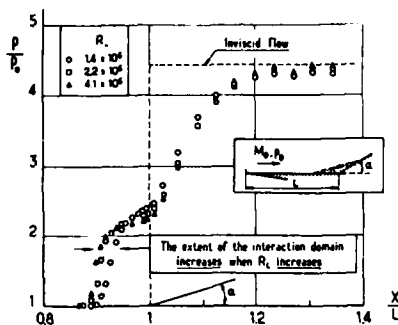
Fig. 3.27   Turbulent Ramp Flow. Reynolds Number Effect at Low to Moderate Reynolds Number. M_0 = 2.7 (Chapman et al.1957)
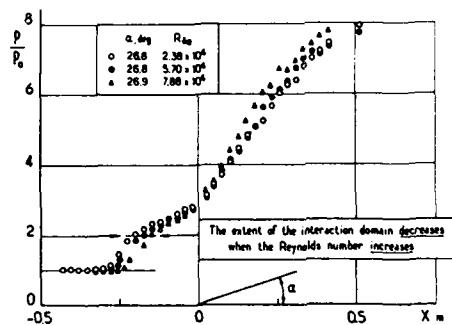
Fig. 3.28   Turbulent Ramp Flow. Reynolds Number Effect at High Reynolds Number. M_0 = 3.93 (Roshko and Thomke, 1969)

v - The pressure distributions plotted in Fig. 3.27 were measured in a compression corner at M_0 = 2.7 and for relatively low Reynolds numbers R_L varying in the range 1.4×10^6 to 4×10^6 (Chapman et al., 1957). According to these results, there is a clearly visible increase in the streamwise extent of the interaction domain when the Reynolds number increases. On the other hand, as shown in Fig. 3.28, in experiments performed at high Reynolds number (R_L of the order of 10^9, Roshko and Thomke, 1969) there is an obvious decrease in the interaction extent with increasing Reynolds number. This reversal in trend, which has been at the origin of a big controversy, will be further commented in the forthcoming Sections.

vi - This last typical feature of a turbulent shock-wave/boundary-layer interaction is observed in hypersonic interactions. As shown by the curves in Fig. 3.29, which correspond to wedge induced separation at M_0 = 9.22 (Elfstrom, 1971, 1972), a hypersonic interaction is characterized by an extremely large rise in pressure due to the high values of the pressure ratio through an oblique shock at high Mach numbers. The pressure distributions exhibit the following features:

- For moderate flow ramp angle ($\alpha < 26°$) the shape of the pressure curves does not markedly differ from that observed at smaller Mach numbers.

- Once separation has occurred, there is a large dissymmetry between the pressure rises at separation and reattachment, the latter being much more important.

- In accordance to the Free Interaction concept, already mentionned, the pressure rise associated to separation keeps a similar shape when the separation point is moving upstream as a consequence of the increase of the ramp angle .

- The extent of the pressure plateau region increases rapidly with the wedge angle, i.e. with the overall pressure jump. As previously, the pressure rise to separation does not depend on downstream conditions and is, thus, entirely determined by the flow situation at the interaction onset. Consequently, an increase in the overall pressure rise necessarily entails a higher pressure rise at reattachment. This can only be achieved by an increase in the maximum velocity reached on the Discriminating Streamline (DSL) of the separated bubble, i.e. the streamline issuing from the separation point and stagnating at the reattachment point (see sketch Fig. 3.15).

Indeed, as can be intuitively understood, the pressure rise that the separated shear-layer can negociate during the reattachment process is a function of its level of kinetic energy. This level tends to increase when the length of the DSL increases since then the mixing process which operates the transfer of energy from the outer flow to the shear layer takes place over a longer distance. Hence, the length of the separated shear-layer must be longer in order to permit a greater acceleration on the DSL before reattachment begins.

- When α is greater than 30°, the pressure distribution exhibits a decrease following the rise corresponding to reattachment and then tends to the constant level of the inviscid solution with the tendency that the greater the wedge angle, the higher the pressure overshoot. A plausible explanation of this phenomenon has been given above. Let us recall that it is observed when the flow is separated and is associated with the triple shock pattern which then forms. Some investigators has used occurrence of the overshoot as a means to detect incipient separation (Elfstrom, 1971).

The properties of the wall pressure distribution have been discussed here by considering turbulent results. The same trends are in fact observed in laminar shock-wave/boundary-layer interactions, so that we will not repeat a description of these features. In particular, the Free Interaction concept is verified in laminar flows where one observes always an increase in the spreading of the interaction domain when the Reynolds number is increased.

Further information concerning shock-wave/boundary-layer interaction can be found in the literature. Thus, Don Gray and Rhudy (1973) have studied effects of leading edge blunting and wall cooling on separation of a laminar boundary-layer in the Mach number range 3-6. They have shown that there is a well defined effect of the leading edge radius of the plate on which the boundary-layer develops.
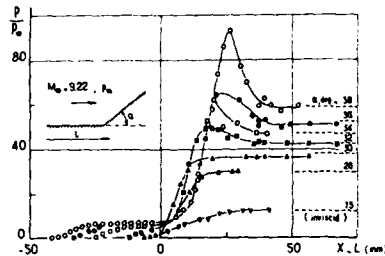
Fig. 3.29   Wall   Pressure   Distribution.   Downstream Overshoot at High Mach Number. M_0 = 9.22 (Elfstrom, 1971)
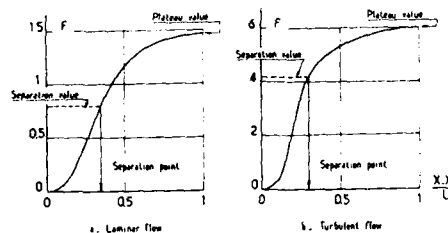
Fig. 3.30   The   Free   Interaction   Theory.   Wall Pressure Correlation Functions (Erdos and Pallone, 1962)

3.2.4 - The Free Interaction Concept

As seen in the preceding Sections, experimental data show that the major part of a supersonic interacting flow evolving towards separation does not (appreciably) depends on the agency at the origin of separation, this agency being either a solid obstacle or an incident shock-wave. That part of the flow independent of the downstream situation comprises the compression at separation as well as the development of the pressure plateau for largely separated flows. Thus, everything happens as if the flow were entirely determined by its properties at the onset of separation.

These flows that are (to a first approximation) free from direct influence of downstream geometry were termed by Chapman **Free Interactions**. Later on, a more rational definition of this concept was given within the framework of Asymptotic Theories (see section 4.1).

The Free Interaction concept permits the derivation of correlation laws explicitely displaying the dependence of the phenomenon on such basic parameters as the Mach number and the Reynolds number. Although the character of generality of these laws is now questioned, especially for high Reynolds number turbulent flows, the Free Interaction Theory is still of important historical interest since it is at the origin of ideas having led to decisive progress in the modelling of interacting flows.

By considering the boundary-layer momentum equation written at the wall:

$$d_p/dx = (\partial \tau / \partial y)_w$$

and the linearized coupling relation expressed on the boundary-layer displacement thickness:

$$0.5 \; (M_0^2 - 1)^{\frac{1}{2}} \; (p - p_0) / q_0 \; = \; d\delta^* / \partial x$$

is possible to derive the following correlation law for the pressure rise during the Free Interaction process:

$(1) \qquad (p - p_0)/q_0 \; = \; F \left[(x - x_0)/L \right] (2 \; C f_0)^{\frac{1}{2}} \; (M_0^2 - 1)^{-\frac{1}{4}}$

In Eq. 3.1, q_0 is the dynamic pressure, Cf_0 is the skin-friction coefficient at origin x_0 of interaction and F is a universal action of the scaled streamwise distance $(x - x_0)/L$.

Figure 3.30 shows the functions F_l and F_t respectively obtained for laminar and turbulent flows. In the representation of Fig. 3.30, the X-wise length scale L is the distance from the origin x_0 to the station at which F reaches the value corresponding to the pressure plateau of an extended separated flow. The particular values of F are found:

i - At the **separation point**:

$$F \quad \begin{matrix} = 0.81 \text{ for laminar flow} \\ \\ = 4.22 \text{ for turbulent flow} \end{matrix}$$

ii - For the **pressure plateau**:

$$F \quad \begin{matrix} = 1.47 \text{ for laminar flow} \\ \\ = 6.00 \text{ for turbulent flow} \end{matrix}$$

The above values reflect the fact that pressure rises in turbulent separation are far more important than in laminar separation.

A correlation law for the streamwise scale of interaction L is similarly obtained in the following form:

$$L / \delta_0^* = K C_{f_0}^{-\frac{1}{2}} (M_0^2 - 1)^{-\frac{1}{4}}$$

where the constant k must be determined experimentally.

The above analysis has been generalized by Carrière et al. (1968) in order to take into account non-uniformities in the incoming outer flow as well as wall curvature effect in the interaction region.

In the turbulent régime and at low to moderate Reynolds number (say $R_{\delta_0} \simeq 10^5$), Eq. 3.1 most often correlates very well experimental wall pressure distributions measured for greatly different situations. Thus, Fig. 3.31 gives an example of such a correlation obtained in the case of step-induced separation and shock-induced separation. One notes an excellent correlation of the results corresponding to very different flow situations. In the present example, the X-wise length scale is the distance between the interaction origin and the separation point.

Some authors have used a modified form of Chapman's scaling law which is valid for hypersonic Mach numbers (Lewis et al., 1967). By assuming $M_0 \gg 1$ and since for a laminar boundary-layer $C_f \propto R_{X_0}^{-\frac{1}{2}}$ one can derive the following equivalent form of Chapman's laws:

$$P \propto \left(\frac{\cancel{P} - P_0}{q_0} \right) \frac{1}{\sqrt{\overline{\chi}_0}} \quad ; \quad \overline{X} \propto \frac{X - X_0}{X_0} G^{-1}$$

where $\overline{\chi}_0 = M_0^3 / \sqrt{R_{\delta_0}}$ is the hypersonic strong viscous interaction parameter and:

$$G = \frac{\delta_0^*}{X_0} \frac{\sqrt{R_{X_0}}}{M_0^2 \sqrt{C_0}}$$

C_0 being the Chapman-Rubesin constant of the viscosity law.
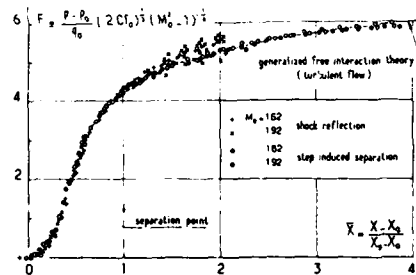
Fig. 3.31   The Free Interaction Theory. Correlation of Wall Pressure Measurements.
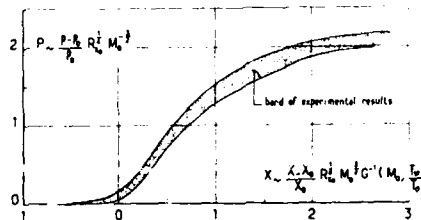
Fig. 3.32   Laminar   Separation.   Chapman's Correlation for Adiabatic Wall Conditions (Lewis et al., 1967)

Figure 3.32 shows a correlation for a laminar interaction using these new variables (Lewis et al., 1967).

The effect of wall temperature on Chapman's scaling has been assumed to enter solely through its effect on the reference quantities of the scaling (δ_0^*, etc...). The pressure distribution obtained by Lewis et al. (1967) on a plate upstream of a 10° ramp at $M_0 = 6.06$ with $T_w/T_{t0} = 0.2$ is correlated in the same manner and presented in Fig. 3.33 together with the band of adiabatic data. Although data taken at all Reynolds number for this fixed wall temperature collapse into a single curve, the curve is quite distinct from that obtained in the adiabatic case. The major difference appears to be in the X scaling which may reflect an "error" in the choice of as an appropriate scaling factor when T_w/T_{t0} is not fixed.

Using an approximate integral of the energy equation and a Pohlhausen analysis, Curle (1961) has suggested a modification of Chapman's correlation. According to Curle, P is identical to that of Chapman's scaling but now:

$$\overline{X} \propto \frac{X - X_0}{X_0} \frac{1}{\sqrt{\overline{\chi}_0}} M_0^2 \left(\frac{T_w}{T_0} \right)^{-1}$$

Adoption of this new scaling law allows to remove this additional dependence on T_w/T_0 as shown in Fig. 3.33.

The Free Interaction Theory has frequently been used for establishing correlation laws concerning the plateau pressure, the pressure rise to the separation point, the extent of the separated region, etc... (see, for example, Putnam, 1965; Needham, 1965; Popinsky and Ehrlich, 1966; Watson et al., 1969).
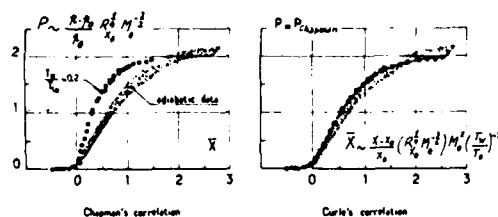
Fig. 3.33 Laminar Separation. Wall Temperature Effect on Surface Pressure Correlation (Lewis et al., 1967)
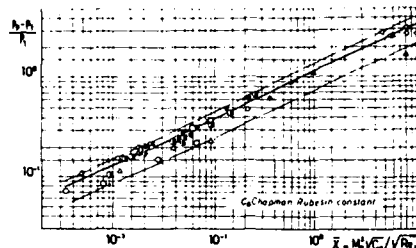
Fig. 3.34 Free Interaction Type Correlation for the Laminar Plateau Pressure (Stanewsky, 1973)
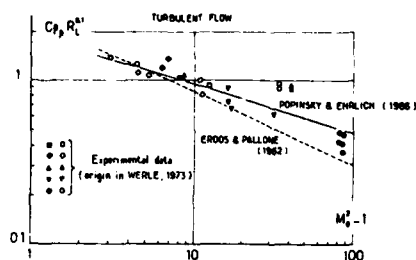
Fig. 3.35 Free Interaction Type Correlation for the Turbulent Plateau Pressure Coefficient (Werle, 1973)
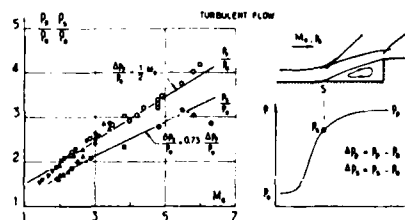
Fig. 3.36 Separation in Front of a Step. Correlations for Plateau and Separation Pressures at High Reynolds Number (Zukoski, 1967)

Thus, Fig. 3.34 presents the plateau pressure for a laminar separation as function of the hypersonic viscous interaction parameter χ_{ρ}. A similar result relative to turbulent flow is presented in Fig. 3.35. In this last correlation, the plateau pressure coefficient:

$$C_{p_{\rho}} = \frac{p_{\rho} - p_{o}}{q_{o}}$$

as given by Popinsky and Ehrlich (1966) is expressed in the form:

$$(C_{p_{\rho}}) \, R_{\chi_{o}}^{4/o} = 1.91 \, (M_{o}^{2} - 1)^{-0.303}$$

For a flat plate turbulent boundary-layer, the above equation is in fact nearly the same as the one of Erdos and Pallone (see above).

Ay high Reynolds number ($R_{\chi_{o}} > 10^{5}$), several investigators have found that the pressure rise to separation and/or to the plateau tend to become independent of the Reynolds number and even to decrease slightly with it. This change in the Reynolds number dependence was clearly established by the experiments of Zukoski (1967), of Roshko and Thomke (1974) and those of Settles (1975). To illustrate this point, Fig. 3.36 shows experimental data and correlations for the pressure plateau which depend on the upstream Mach number M_{0} only (Zukoski, 1967).

Other correlation properties concerning the essential features of shock-wave/boundary-layer interactions may be found in preceding Lectures on the subject (Stanewsky, 1973; Leblanc, 1976).

3.2.5 - Scaling Properties of the Interaction Extent in Turbulent Flow

Introductory Remarks. The "intensity" of a shock-wave/boundary-layer interaction can also be characterized by its upstream influence i.e., the distance at which the interaction - or the shock presence - is first felt. This distance is most often measured from the wedge corner or from the point where an incident shock would impinge on the wall in the absence of a boundary-layer.

A second point of interest is the separation length which is conveniently defined as the distance of the separation point from a suitably chosen origin, for example, the start of the interaction.

The basic question that arises is thus: what are the appropriate scaling laws for these characteristic lengths? The answer to this question is important, not only for practical purposes, but also for the physical understanding of the phenomenon. In particular, clear and accurate information on this subject is of great interest to help modelling of the phenomenon, especially in turbulent flows where one has to rely heavily on experiment.

As seen in the preceding Section, the Free Interaction Theory gives an answer to this question in laminar flows and in turbulent flows for which the Reynolds number is low or moderate (the régime being nevertheless turbulent). However, the question of scaling laws has to be reconsidered in high Reynolds number turbulent flows where the Free Interaction Theory does not work anymore.

The Upstream Interaction Length. Essentially we will consider scaling properties for the upstream interaction length. In the case of wedge flows. However it should be emphasized that general tendencies observed in wedge-flows are also similar to shock reflection, since in the inviscid sense there is no essential difference between these two kinds of flow as was seen above.

The upstream interaction length is most often defined from inspection of the wall pressure distribution. Theoretically, the origin of the interaction is at the point where the wall pressure distribution starts to rise. Some investigators have adopted this definition (Spaid and Frishett, 1972). Unfortunately, the experimental localization of the true interaction origin is difficult and hence inaccurate. For this reason, most investigators have chosen a conventional origin by extrapolating to the wall the quasi-linear pressure rise at separation, as is shown in Fig. 3.37 (Settles and Bogdonoff, 1973; Roshko and Thomke, 1974; Settles, 1975; Hayakawa and Squire, 198?).
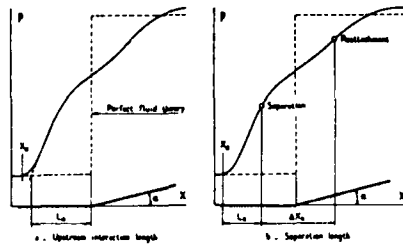
Fig. 3.37 Characteristic Length Scales of a Supersonic Interaction
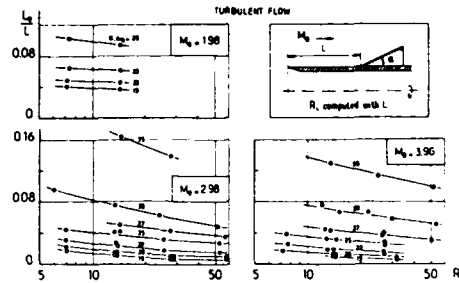
Fig. 3.38 Upstream Interaction Length. Influence of Mach Number, Reynolds Number and Ramp Angle (Roshko ant Thomke, 1974)

According to Green (1969), the main parameters likely to influence the extent of a shock-wave/boundary-layer interaction are:

i - the upstream Mach number M_0;

ii - the Reynolds number R_{f_e} :

iii - the wedge angle α (or incident shock intensity);

iv - the thickness l_e of the incoming boundary-layer.

If one considers any typical streamwise extent L_0 scaled to the incoming boundary-layer physical thickness δ_e , or displacement thickness δ_e^* , there remain the three following influence parameters: M_0, R_{f_e} and α (or shock strength). If we now focus our attention on the dimensionless length L_0/δ_e it is generally agreed that, for a fixed value of R_{f_e} :

i - L/δ_e increases with α_e for a fixed Mach number M_0;

ii - L/δ_e decreases when M_0 increases for a fixed angle α_e .

However, there is some controversy about the influence of the Reynolds number.

On the one hand, there are experiments made by several investigators (Kuehn, 1959; Elfstrom, 1971; Spaid and Frishett, 1972) at low to moderate Reynolds number ($R_{f_e} < 10^5$), both with tripped and untripped boundary-layer. These experiments indubitably show that L_0/l_e increases with the Reynolds number R_{f_e} . Such a tendency is in agreement with the Free Interaction Theory.

On the other hand, experiments performed at high Reynolds number manifestly show a reversal of this trend, L_0/l_e decreasing with increasing Reynolds number (Roshko and Thomke, 1974; Settles, 1975; Settles et al., 1975).

In what follows, we will consider results on the upstream influence length at high Reynolds number, the case of low Reynolds number being satisfactorily represented by the Free Interaction Theory.

A systematic survey of the influence of M_0, R_{f_e} and α on the interaction length L_0 was made by Roshko and Thomke (1974) for wedge flows in the Reynolds number range $10^5 < R_{f_e} < 10^6$. Some of the results that they obtained are plotted in Fig. 3.38 where L_0 is arbitrarily scaled to the distance of the corner from the leading edge of the plate on which the incoming boundary-layer develops. A rapid examination of these results leads to the following remarks:

i - For fixed Reynolds number R_L (R_L is computed for freestream conditions and with the distance of the wedge corner to the plate leading edge) and Mach number M_0, the upstream interaction length increases with α ; i.e., with the intensity of the perturbation. It is now clear that the increase in L_0 with the shock intensity has to do with the fact that a higher back pressure must feed farther upstream through the subsonic part of the boundary-layer.

ii - For fixed R_L and α , L_0 decreases when M_0 increases. This trend can certainly be explained by the reduction of the subsonic layer thickness when M_0 is higher.

iii - For fixed M_0 and α_e , L_0 decreases when the Reynolds number increases. This tendency can also result from a thinning of the subsonic layer.

It should be noticed that the above tendencies are still observed when L_0 is scaled to the physical thickness of the boundary-layer l_e (or its displacement thickness l_e^*). This fact proves that l_e (or l_e^*) alone cannot be the scale of the interaction.

Conclusions similar to those of Roshko and Thomke were arrived at by Settles (1975) (see also Settles et al., 1975) who performed experiments on corner flows at high Reynolds number ($0.5 \times 10^5 \sim 7.6 \times 10^6$).

Roshko and Thomke as well as Settles have proposed purely empirical laws to represent the evolution of the scaled upstream influence length in terms of the main parameters of influence. These laws will not be given here (see authors' publications or Délery and Marvin, 1986).

The Separation Length. Another length which is of interest for characterizing the streamwise extent of the interaction is the separation length - or separation distance - L_S. For wedge flows, L_S is defined as the distance between the corner hinge and the separation point S (see Fig. 3.37). The experimental determination of L_S is more delicate than that of the upstream interaction length, because it necessitates the accurate location of the separation point.

As for the upstream interaction length, experiments performed at low to moderate Reynolds number tend to prove that L_S increases with the Reynolds number. This tendency is illustrated by the results of Spaid and Frishett (1972) shown in Fig. 3.39. In these experiments, R_{f_o} varies in the range 3×10^4 - 6×10^4. A similar trend was also observed by Batham (1972). Such an increase of L_S with the Reynolds number is of course in agreement with the Free Interaction Theory.

On the other hand, at high Reynolds number, as observed by many investigators (Settles and Bogdonoff, 1973; Law, 1974; Roshko and Thomke, 1974) there is a clear decrease in the separation length L_S with increasing Reynolds number, in a way similar to what is observed for the upstream interaction length. This fact was clearly demonstrated by the wall pressure distributions plotted in Fig. 3.28.

The influence of the Reynolds number as well as of the ramp angle on the separation length was thoroughly studied by Settles for an upstream Mach number close to 3. His results confirm the decrease in L_S as the Reynolds number is increased.

Thus, to conclude about the effect of the Reynolds number on the separation length, it can be said that the overall tendencies observed for the upstream interaction length are still valid for the separation distance.
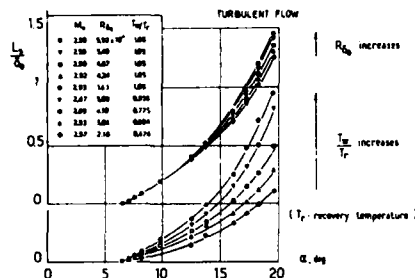
Fig. 3.39 Separation Length. Influence of Reynolds Number and Wall Temperature at Low to Moderate Reynolds Numbers (Spaid and Frishett, 1972)
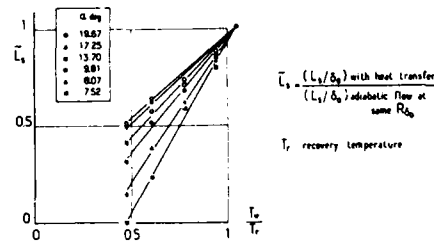
Fig. 3.40 Influence of Wall Temperature on Normalized Separation Length (Spaid and Frishett, 1972)

3.2.6 - Influence of the Wall Temperature on Interaction

Now, let us examine the influence of a particularly important parameter in the case of hypersonic flows, namely the wall temperature.

In carefully made experiments, Spaid and Frishott (1972) found that cooling the wall reduces the separation distance. The cooling effect is shown in Figs. 3.39 and 3.40. In the second figure L_S represents the value of L_S measured when heat-transfer is present, normalized by the value of L_S in adiabatic flow and evaluated at the same Reynolds number. The decrease in L_S with wall temperature can be interpreted:
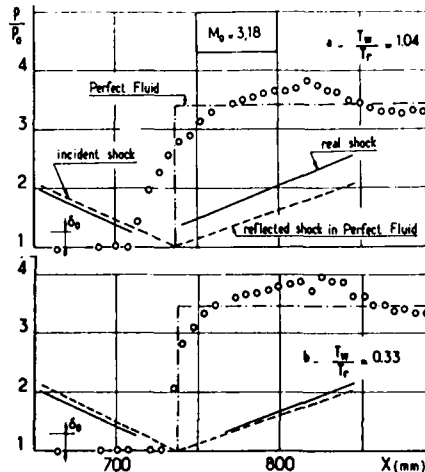
Fig. 3.41 Effect of Wall Cooling on Incident Shock Reflection. Wall Pressure Distributions (Kilburg and Kotansky, 1969)
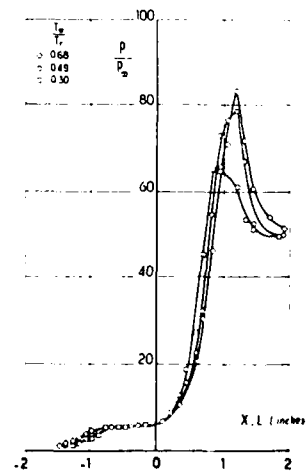
Fig. 3.42 Wall Temperature Effect on Surface Pressure Distribution in Hypersonic Flow. M_0 = 9.22 (Elfstrom, 1971)

ii - Either within the framework of the Free Interaction Theory, since a decrease of the ratio T_w/T_r (T_r being the wall recovery temperature) provokes an increase of the skin-friction coefficient.

ii - Or by an overall contraction of the interaction domain resulting from a thinning of the subsonic layer due to a lower temperature level near the wall.

The effect of wall temperature on the separation length was also investigated by Kilburg and Kotansky (1969), Elfstrom (1971), Don Gray and Rhudy (1973), Holden (1972) and by Back and Cuffel (1976). All these investigators also reached the conclusion that wall cooling reduces the streamwise extent of the interaction region. This effect is particularly well illustrated by the wall pressure distributions plotted in Fig. 3.41. These distributions were measured in a shock reflection at M_0 = 3.18. In Fig. 3.41a, the wall is adiabatic and one notes an important extension of the interaction length, the real flow field being well distinct from the perfect fluid model. In this case, the upstream interaction length is particularly important. On the other hand, as shown by Fig. 3.41b, cooling the wall shrinks considerably the interaction domain so that the real flow becomes close to the inviscid flow model.

Conversely, surface heating increases the size of the separated region.

In hypersonic flows, Elfstrom (1971) also noted that increasing the wall temperature in separated flow tends to increase both the extent of the separated region and the magnitude of the pressure overshoot, as is shown by the wall pressure distributions plotted in Fig. 3.42. Further, as noted by Elfstrom, when the wall temperature is increased, the attached flow pressure distribution develops a pressure overshoot characteristic of separated flow. Thus, the Incipient Separation angle must decrease as the wall temperature is raised. Of course, the reverse is true when the wall is cooled, i.e. Incipient Separation occurs for a higher value of the ramp angle (see Section 3.2.8 below for more ample information on this question).

3.2.7 - Heat-Transfer in Shock-Wave/Boundary-Layer Interactions

Perhaps the most salient feature of hypersonic shock-wave/boundary-layer interaction is the existence of extremely high heat-transfer rates in the interaction region, especially when separation occurs. This problem is crucial for the correct sizing of thermal protection in parts of the vehicle where such interactions are likely to occur. The problem has received considerable attention and has been studied by many investigators in laminar, as well as in turbulent flows (see, in particular, Chung and Vlegas, 1961; Sterrett and Holloway, 1964; Miller et al., 1964; Needham, 1965; Holden, 1966, 1972, 1974, 1977, 1978, 1986; Bushnell and Weinstein, 1968; Keyes et al., 1968; Nestler, 1973; Hung, 1973; Hung and Barnett, 1973; Stollery and Bates, 1974; Johnson and Kaufman II, 1974; Christophel, 1975; Johnson and Kaufman II, 1975; Stollery, 1975).

As will be seen, heat-transfer rates are extremely high in the vicinity of point R where the separated flow reattaches. This rise in heat-transfer is associated with the stagnation at R of the shear-layer developing from the separation point S (this layer is particularly visible in Fig. 3.8b). Thus, the situation at R is similar to the situation at a nose stagnation point with the difference that the flow stagnation pressure in the vicinity of a control surface can be much higher that the stagnation pressure behind the bow shock-wave in front of the nose. Thus heat transfer rates on a separated control surface can be considerably higher that those existing in the nose region, as in the case of a Type III Shock Interference (see Section 2.2 above).

Typical heat-transfer distributions in wedge induced interactions are represented in Fig. 3.43 along with the corresponding wall pressure and skin-friction distributions (Holden, 1986). These results are relative to an upstream Mach number M_0 = 14.1 and a Reynolds number, computed with upstream flow conditions and the distance L from the plate leading edge to the ramp corner, equal to 8.0 x 10^6. In this case, the boundary-layer remains laminar throughout the interaction region. Heat-transfer to the wall is here represented by the coefficient defined as:

$$C_H = h / \rho_e u_e C_h (T_r - T_w)$$

where h is the heat flux and ρ_e, u_e are relative to flow conditions at the boundary-layer edge, T_r is the recovery temperature (i.e., the wall temperature for adiabatic conditions) and T_w the actual wall temperature.

The three sets of plotted curves correspond to different wedge angles :

- for α = 15° the flow remains attached,

- for α = 18° the flow is in the condition of incipient separation at the corner,

- for α = 24° the flow is well separated.
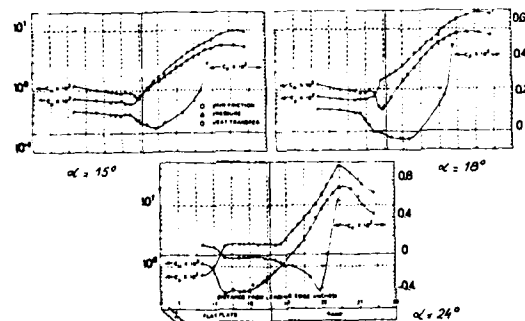
Fig. 3.43 Skin-Friction, Wall Pressure and Heat-Transfer Distributions in Hypersonic Laminar Ramp Flow. M_0 = 14.1 (Holden, 1986)
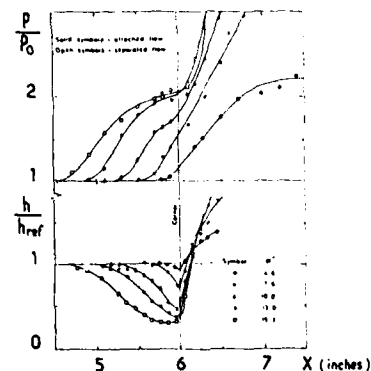
Fig. 3.44 Laminar Heat-Transfer in the Corner Vicinity. M_0 = 9.7 (Needham, 1965)

In non separated cases, the C_H distribution exhibits a progressive decrease upstream of the ramp followed by a steep increase on the ramp itself. Once separation has occurred, heat- transfer starts to decrease rapidly at a certain distance upstream of the separation point; i.e. the point where the skin-friction coefficient changes sign. Then C_H passes through a well marked minimum before starting to increase rapidly in conjunction with the reattachment process.

A more detailed view of the heat-transfer evolution in the vicinity of the corner is provided by the distribution of the h/h_{ref} ratio plotted in Fig. 3.44 (h_{ref} designates the heat-transfer at the same streamwise location for flat-plate conditions; i.e. without the ramp). These results have been obtained at a Mach number $M_0 = 9.7$ for a unit Reynolds number $R_u = 5.83 \times 10^6/m$ (Needham, 1965).

The decrease in heat-transfer ahead of the corner, always present even for very small wedge angles, coincides with the initial rise in pressure resulting from the upstream influence of the wedge. Downstream of the corner, the heat-transfer rate rapidly rises in the region of high pressure gradient, reaching a maximum value just downstream of the peak pressure. As the wedge angle is increased, a small region of flow separation is formed in the corner. The pressure distribution then exhibits a knee just upstream of the corner and the heat-transfer is seen to develop a smooth minimum with a continuously changing gradient instead of the cusp typical of the attached flow.

As the wedge angle is increased further, the size of the separated region grows as the separation point moves upstream. The heat-transfer minimum retains the smooth curvature and broadens out as the separation point moves away.

The next results, presented in Figs. 3.45a to d are relative to a turbulent flow. They have been obtained in a ramp flow for the following conditions: $M_0 = 8.2$ and $R_u = 10.6 \times 10^7/m$ (Holden, 1977). The plotted quantities are the wall pressure and heat-transfer distributions. The four sets of curves correspond to different values of the wedge angle, namely: 27°, 30°, 33° and 36°. For the greatest values of α (33° and 36°), the wall pressure distribution exhibits a plateau (well marked for $\alpha = 36°$) typical of an interaction with large separation. One sees that, in contrast to the laminar case, the present results reveal an increase in heat-transfer through separation. The heat-transfer rate is nearly constant in the separated region. This plateau extends to the beginning of the reattachment compression. Thereafter, as in the laminar case, heat-transfer rises rapidly and reaches a maximum at a location nearly coincident with that of the wall pressure distribution.
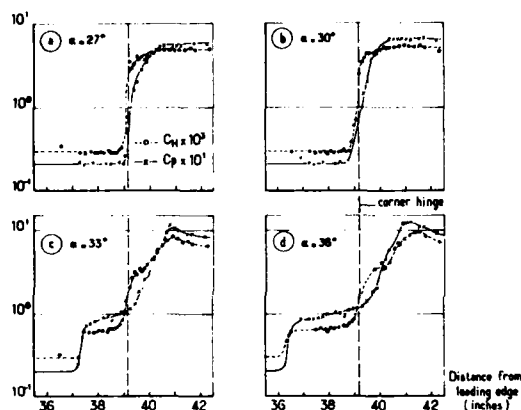
Fig. 3.45   Wall Pressure and Heat-Transfer Distributions in Hypersonic Turbulent Ramp Flow. $M_0 = 8.2$ (Holden, 1977)
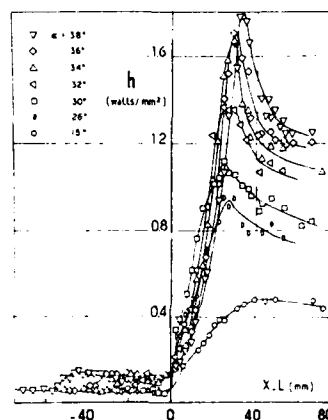
Fig. 3.46   Heat-Transfer Distributions in Hypersonic Turbulent Ramp Flow. $M_0 = 9.22$ (Elfstrom, 1971)

Other typical results concerning heat-transfer in a hypersonic flow are shown in Fig. 3.46. They have been obtained on a wedge compression corner for a Mach number equal to 9.22 and a unit Reynolds number $R_u = 4.73 \times 10^7/m$ (Elfstrom, 1971). The plotted curves, that correspond to increasing values of the wedge angle α, confirm the fact that, in complete contrast to laminar results, the heat-transfer rate rises in the separated region when the incoming boundary-layer is fully turbulent. This effect may be due to the large increase in turbulence intensity occurring in the vicinity of the separation point. The large eddies which then form can promote energy exchanges between the wall region and the outer high enthalpy flow, thus leading to an increase in heat-transfer to the surface.

A close examination of the distributions shows that, near the separation point, the heat-transfer rate rises to about three times the flat-plate value before falling again towards the corner. Just ahead of the hinge line, the heat-transfer again starts to rise due to the upstream influence at the corner. Thus, for the present situation, the total heat-transfer in the separated region ahead of the hinge line can be between two and three times the corresponding flat-plate value.

Further experimental evidence of this increase in heat-transfer rate within a turbulent separated region has been found by Gadd et al. (1960) and Holloway et al. (1965).

On the ramp itself, the heat-transfer rate increases very rapidly, reaching values largely superior to the flat-plate levels, the peak value increasing as the separated zone extends. This rise has to be correlated with the rise in the maximum pressure level observed when the sep· ·ation point moves upstream (see Section 3.2.3 and Fig. 3.29).

Due to the extreme importance of thermal problems in hypersonic flows as also of the difficulty to perform reliable predictions, particularly in turbulent flows, empirical correlations have been looked for to evaluate peak values of heat-transfer in strong shock-induced interactions.

Here, we will follow the analysis of this problem proposed by Hung and Barnett (1973). These authors have derived interference heating correlations from simple geometry models, both for laminar and turbulent flows. It should be noticed that the terms laminar and turbulent flows refer to the boundary-layer state of the undisturbed flow upstream of the interference region.
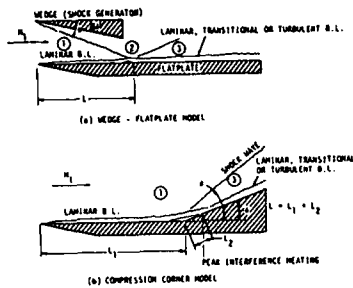
Fig. 3.47 Definition of Shock-Wave/Boundary-Layer Interference Heating Parameters (Hung and Barnett, 1973)
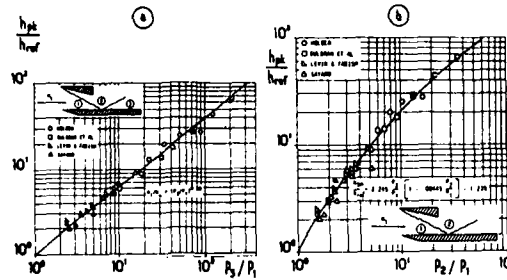
Fig. 3.48 Peak Heat-Transfer Correlation in Turbulent Flow (Hung and Barnett, 1973)

The correlations apply to the two classical situations sketched in fig. 3.47:

- The oblique shock reflection on a flat plate. In this case, pressure rises first from p_1 to p_2 through the incident shock (C_1), then from p_2 to p_3 through the reflected shock (C_2).

- The compression corner flow inducing a shock (C_1) through which the pressure rises from p_1 to p_3.

The correlation laws are generally looked for in terms of the total pressure ratio p_3/p_1.

In the case of a turbulent flow, the peak heat-transfer h_{PK} may be related to the heat-transfer h_{ref} that would exist without shock reflection by the relation:

$$\frac{h_{PK}}{h_{ref}} = \left(\frac{h_3}{h_1}\right)^{0.8}$$

This result is plotted in Fig. 3.48a. A slightly different correlation law has been adopted by Holden (1972) in the form:

$$\frac{h_{PK}}{h_{ref}} = \left(\frac{h_{PK}}{h_0}\right)^{0.85}$$

where p_{PK} is the maximum pressure which may differ from p_3 due to the overshoot phenomenon described in Section 3.2.3. This correlation, represented in Fig. 3.49, applies for maximum heating rate in wedge as well as in externally generated shock-induced turbulent separated flows.

In performing design calculations, it is often preferable to use the pressure following the incoming shock rather than the reflected shock. For this case, Hung and Barnett propose the following correlation:

$$\frac{h_{PK}}{h_{ref}} = 2.245 \left(\frac{h_2}{h_1}\right) \left[1 - 0.0045 \left(\frac{h_2}{h_1}\right)\right] - 1.235$$

This relation is compared to the data in Fig. 3.48b.

The search for the same kind of correlations in the case of a laminar flow leads to the result presented in Fig. 3.50a. One sees that the data points lie along several lines of common slope resulting in the correlation:

$$\frac{h_{PK}}{h_{ref}} = f \left(R_e, M_e, P_r, T_w/T_0\right) \left(\frac{h_3}{h_1}\right)^{1.13}$$

where f is a function of the listed parameters (Pr is the Prandtl number).

In fact, the results are seen to be strongly affected by the Reynolds number R_L. One explanation of this influence of R_L is that the boundary-layer transition may be promoted by the shock-wave (see Section 3.2.2 above).

At low Reynolds numbers, the boundary-layer is stable enough so that the shock-wave does not trigger transition. Above some critical value, the flow is unstable and the disturbance promotes transition (see Fig. 3.50b).
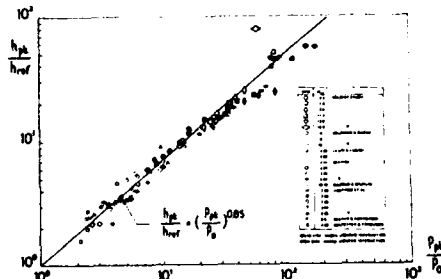
Fig. 3.49 Peak Heat-Transfer Correlation in Turbulent Flow (Holden, 1972)
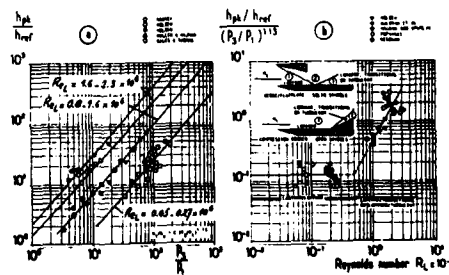
Fig. 3.50 Peak Heat Transfer Correlation in Laminar Flow (Hung and Barnett, 1973)

From these considerations, Hung and Barnett have suggested that for $R_L < 5 \times 10^5$ the flow is essentially laminar throughout the interaction region and the heat-transfer rate may be calculated from:

$$\frac{h_{PK}}{h_{ref}} = 0.13 \left(\frac{h_3}{h_1}\right)^{1.13}$$

This relation shows that in laminar flow the peak heat-transfer is nearly 10 times less intense than in turbulent flow.

Above this value, the downstream flow is either transitional or turbulent and obeys the relation:

$$\frac{h_{PK}}{h_{ref}} = 0.468 \left[Re_L \cdot 10^{-6} \right]^{1.85} \left(\frac{h_3}{h_1}\right)^{1.13}$$

These relations are compared to the data in Fig. 3.51.

Three-Dimensional Effects at Reattachment. Surface flow visualizations by oil flow techniques as well as determination of heat-transfer distribution by thermo-sensitive paintings reveal the existence in the reattachment region of striation patterns which are particularly evident in laminar or transitional separated flows. An example of such a phenomenon is given in Fig. 3.52 which shows a surface flow pattern observed in a two-dimensional ramp flow at $M_0 = 10$, the régime being laminar. Figure 3.53 shows the corresponding heat-transfer distribution on the ramp deduced from thermo-sensitive paintings. There is a clear repetitive pattern in heat-transfer distributed along the ramp spanwise dimension. The difference between the greatest and the smallest heat-transfer levels in the striations region can be in excess of 50%.
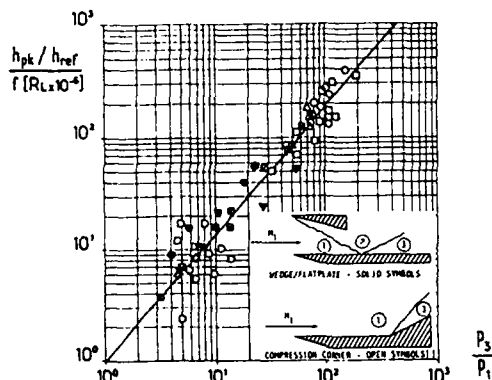
Fig. 3.51   Peak Heat Transfer Correlation in Laminar Flow (Hung and Barnett, 1973)

Fig. 3.52   Surface Flow Striation Pattern in Hypersonic Ramp Flow. $M_0 = 10$ (Coët, 1988)
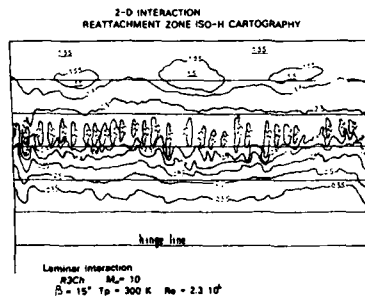
Fig. 3.53   Striation Pattern on Surface Heat Transfer in a Hypersonic Ramp Flow. $M_0 = 10$ (Coët, 1988)
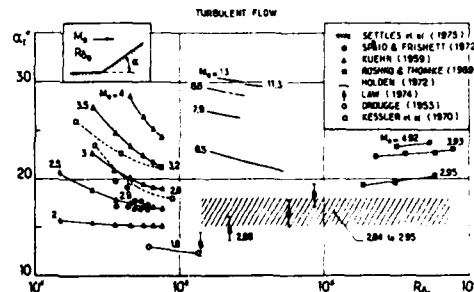
Fig. 3.54   Experimental Shock-Induced Incipient Separation Limit in Supersonic and Hypersonic Flows

This phenomenon, observed also by Miller et al (1964), has been investigated in some detail by Ginoux (1969) who performed total pressure surveys in the reattachment region to define spacings and areas affected by these regularly spaced longitudinal perturbation. The characteristics that he observed in the reattachment region are similar to subsonic Taylor-Goertler vortices on concave walls and it was hypothesized that flow curvature was sufficient to support such a system.

3.2.8 - Incipient Separation in Turbulent Flows

Introductory Remarks. The knowledge of Incipient Separation conditions is of great practical interest in supersonic and/or hypersonic flows. It is recalled that Incipient Separation is traditionally defined as the condition in which the shear-stress becomes vanishingly small at some point on the wall, while remaining positive elsewhere. However, this definition can be inadequate for practical purposes in circumstances where a tiny separated zone seems to be always present, even for very weak shock. In fact, Kuehn (1961) was the first to suggest this for a compression ramp geometry case: at the scale of the subsonic inner part of the boundary-layer, the wedge shape of the wall should inevitably provoke a local separation. Consequently, we are faced with the necessity of distinguishing between "true" Incipient Separation and "effective" (or significant) Incipient Separation, the last situation alone being of real interest for practical applications since it corresponds to the onset of most dramatic change in the flow field.

The Experimental Incipient Separation Limit. In what follows, the limit for Incipient Separation will be given in the classical form α_I for varying upstream Mach number M_0, the flow being a planar two-dimensional flow. The effect of heat-transfer at the wall will be considered below.

This presentation implies that the phenomenon depends essentially on only three parameters, namely: the upstream Mach number, the shock strength and the Reynolds number. The reality is probably more subtle. For example, the incompressible shape parameter H_{i0} of the incoming boundary-layer is also an important factor of influence whose effect is not always taken into account by the Reynolds number only. Unfortunately, the paucity of data on the specific influence of H_{i0} makes a proper correlation of the dependence of Incipient Separation on H_{i0} very difficult. It is for this reason that we will adopt the traditional form, it being understood that the results are restricted to a flat plate incoming boundary-layer.

In the case of separation induced by a shock reflection, α_I will represent the equivalent ramp angle producing the same overall pressure rise as the two successive compressions through the incident and reflected shock-waves. Experiments made by Holden (1972) and by Law (1976) have clearly shown that by considering this effective ramp angle, there is no essential difference between ramp-induced and incident shock-induced separation. As a matter of fact, the pressure rise to Incipient Separation is almost the same in both situations.

Because of its great practical importance and also because most available results are relative to this limit, in what follows we will mainly consider "effective" Incipient Separation and the term "effective" will be henceforth dropped.

Most of the published data have been plotted in Fig. 3.54. In spite of an important scatter, the following trends can be discerned:

i - The angle α_I (or the equivalent pressure jump) increases when the upstream Mach number M_0 increases.

ii - At low Reynolds number, α_I decreases as M_0 increases. Such a trend is in agreement with the Free Interaction Theory.

iii - At high Reynolds number, most investigators have noticed a reversal in the Reynolds number influence; i.e., the angle α_I increases with M_0, the variation being rather slow.

iv - According to other investigators (Settles and Bogdonoff, 1973; Settles et al.; 1981), the separation angle would in fact be independent of the Reynolds number.

It is difficult to be absolutely conclusive about the above tendencies since there is frequently a large uncertainty in the experimental determination of the angle α_I .

Experiments performed by Spaid and Frishett (1972) and by Elfstrom (1971) clearly show that cooling the wall increases the resistance to separation. Also, according to the hypersonic experiments of Elfstrom, the Incipient Separation angle must decrease as the wall temperature is raised.

However in this field, experimental results are too scarce to provide really usable correlation curves. The greater resistance to separation when the wall is cooled can be interpreted in the same terms as the increase in separation length occurring when the wall temperature is lowered; i.e., cooling the wall reduces the thickness of the boundary-layer subsonic part.

Separation Criteria in Supersonic and Hypersonic Flows. There exist several correlation laws (or criteria) to predict Incipient Separation in supersonic and/or Hypersonic flows. Some of them are derived from simplified boundary-layer type analyses applied to the interaction (Reshotko and Tucker, 1955); others from the Free Interaction Theory (Needham and Stollery, 1966; Holden, 1972). Also, Elfstrom (1971) has proposed a very attractive rotational inviscid flow model allowing an accurate prediction of Incipient Separation and giving a faithful representation of the effect of wall temperature. There is no place here to present these various criteria in detail (for further information and other references, see Délery and Marvin, 1986). We will only give the separation criterion proposed by Needham and Stollery (1966) for laminar and turbulent hypersonic flows (see. Fig. 3.55) and the very popular Zukoski's criterion applicable to turbulent flows at high Reynolds number (see Fig. 3.56).
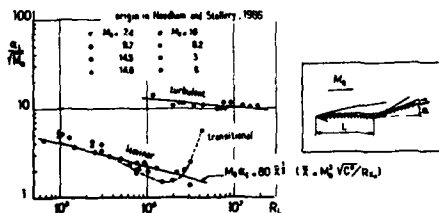
Fig. 3.55 Correlation Law for Incipient Separation in Laminar and Turbulent Flows at Low to Moderate Reynolds Number (Needham and Stollery, 1966)
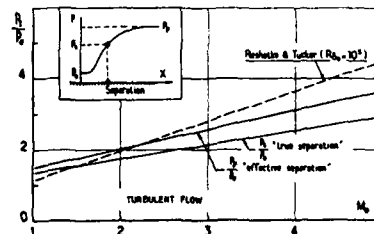
Fig. 3.56 High Reynolds Number Turbulent Flow. Incipient Separation Criterion Deduced from Zukoski's Correlation (see Fig. 3.36)

4 - PREDICTIVE METHODS FOR SHOCK-WAVE/BOUNDARY-LAYER INTERACTION

4.1 - General Comments on the Different Methods

Four different types of methods can be distinguished to compute the interaction between a shock-wave and a boundary-layer.

The first category comprises what can be calle global methods which consist in simplified analyses of the interaction domain aiming at the prediction of the most useful boundary-layer properties; namely its characteristic thicknesses (displacement and momentum) and incompressible shape parameter. In this kind of approach, global balance equations for mass and momentum are written' between two stations respectively located upstream and downstream of the interaction region. A similar technique consists in writing simplified boundary-layer equations in which the viscous terms are neglected. There exist a large number of methods belonging to this category (see, Délery and Marvin, 1986), the most popular and still largely used being that developed by Reshotko and Tucker (1955).

The second class of methods are Inviscid-Viscous Interactive (IVI) methods. According to this approach, the flow field is divided into an outer non viscous part, represented by the Euler equations, and an inner viscous part, including boundary-layers, wakes, mixing zones, which is most often computed by using the classical first order boundary-layer equations. This two flow regions are computed separately and made compatible by satisfying compatibility, or coupling, conditions along a conveniently chosen boundary (for more ample information, see Le Balleur,1987). This approach is very successful in computing complex flows including shock-waves and separated regions, but is questionable in hypersonic interactions where shock-waves penetrate deeply into the boundary-layer.

The third category includes Analytical or Multi-Deck theories which are derived from the analysis of Lighthill (1953) and the theoretical work of Stewartson and Williams (1969). These authors demonstrated that a flow region submitted to a strong interaction process has a multi layer structure consisting in:

- an Upper-Deck including the outer inviscid and irrotational flow.

- a Middle-Deck or Main-Deck covering most of the boundary-layer where the viscous forces can be neglected. Thus this part of the flow is considered as an inviscid rotational stream.

- a Lower-Deck, in contact with the wall, where viscous forces have to be considered.

This theory contributed largely to the physical understanding of strong interaction phenomena in supersonic or transonic flows and has led to the development of several predictive methods (for a more thorough review, see Délery and Marvin, 1986).

The fourth approach consists in the solution of the time averaged Navier-Stokes equations. This approach which is certainly the most promising to compute shock-wave/boundary-layer interactions in hypersonic flows will be now considered in some detail.

4.2 - Solution of the Time Averaged Navier-Stokes Equations

4.2.1 - Introductory Remarks

Solution of the full time dependent Navier-Stokes equations constitutes certainly the most satisfactory way to compute flows as complex as shock-wave/boundary-layer interactions that contain sharp pressure variations and more or less extended separated regions.

Solution of the Navier-Stokes equations for a laminar steady flow does not lead to special fundamental problems, since then the spatial variations of the flow properties take place over distances which are large enough to be accurately represented by a discretized form of the equations compatible with the present day computer capabilities. Difficulties can nevertheless be encountered if real gas effects, including non-equilibrium chemistry, have to be taken into account in some hypersonic applications. In this case, chemistry obeys system of equations which are "stiff", thus necessitating special numerical treatments. This important question will not be considered here since, to our knowledge, shock-wave/boundary-layer calculations with real gas effects have not yet been executed...the fluid dynamics problem being already sufficiently complicated. Thus, in laminar flows, the unique difficulties are essentially of numerical nature in the sense that an accurate and efficient algorithm must be devised to properly solve the equations.

The problem of solving the Navier-Stokes equations becomes much more involved, from a fundamental point of view, when the flow is turbulent. As everyone knows, the flow is then the seat of fluctuations whose frequencies cover a very large bandwidth. The highest frequencies can be well in excess of 100 kHz in the case of a supersonic flow. Furthermore, the structure of a turbulent flow is basically three-dimensional even for a nominally two-dimensional configuration.

In the case of a turbulent shock-wave/boundary-layer interaction the fine structure of the flow is so complex and so rapidly variable than a direct simulation by solution of the time dependent Navier-Stokes equations is still impossible even for the largest and fastest computers. Even large eddy simulation, in which only the largest features of the flow are directly computed while the smallest ones are averaged and modeled, remains impossible for the computation of strongly interacting flows at high Mach numbers.

The only feasible approach of the shock-wave/turbulent boundary-layer interaction problem by solution of the Navier-Stokes equations remains the classical statistical approach in which the time dependent Navier-Stokes equations are submitted to an averaging procedure prior to their integration.

This averaging procedure, introduced nearly one century ago by Reynolds, eliminates all the time dependent terms attributable to turbulence. However, due to the non linear character of the Navier-Stokes equations, the time averaged equations still contain terms of turbulent origin in the form of mean products of fluctuating quantities.

Thus, in order that the problem be properly "closed"; i.e., integration of the system of equations be possible, the turbulent terms must be expressed as known functions of other computable quantities.

The finding of such an expression constitutes the problem of turbulence modeling which will be considered in some details in the coming Section.

The numerical aspects of the solution of the Navier-Stokes equations will not be considered in this Lecture, the problem being of sufficient importance to constitute by itself the subject of a complete Lecture. Ample information on numerical methods can be found in the literature (see, for example Peyret and Viviand, 1975).

4.2.2 - The Navier-Stokes Equations for a Compressible Turbulent Flow

By using classical cartesian notations with the usual convention of repeated indices to indicate summation over the entire range of indices, the time dependent Navier-Stokes equations are (see Marvin, 1977, 1982):

Continuity:

$$(4.1) \qquad \frac{\partial \rho}{\partial t} + \frac{\partial}{\partial x_j} \left(\rho u_j \right) = 0$$

Momentum:

$$(4.2) \qquad \frac{\partial}{\partial t} \left(\rho u_i \right) + \frac{\partial}{\partial x_j} \left(\rho u_i u_j \right) = - \frac{\partial p}{\partial x_i} + \frac{\partial}{\partial x_j} \left(\tau_{ij} \right)$$

Energy:

$$(4.3) \qquad \frac{\partial}{\partial t} \left(\rho h \right) + \frac{\partial}{\partial x_j} \left(\rho u_j h \right) = \frac{\partial p}{\partial t} + u_j \frac{\partial p}{\partial x_j} + \tau_{ij} \frac{\partial u_i}{\partial x_j} - \frac{\partial \dot{q}_j}{\partial x_j}$$

where u_i designates the velocity component along direction x_i, ρ the density, p the pressure, h the specific enthalpy, τ_{ij} the molecular shear-stress and $\dot{q}_j$ the molecular heat-flux.

The shear-stress and the heat-flux are given by the following relations:

$$\tau_{ij} = \mu \left(\frac{\partial u_i}{\partial x_j} + \frac{\partial u_j}{\partial x_i} \right) + \lambda \frac{\partial u_k}{\partial x_k} \delta_{ij} \qquad \qquad \dot{q}_j = - \sigma \frac{\partial T}{\partial x_j}$$

where μ and λ are the viscosity coefficients of the fluid and σ its thermal conductivity.

The above system is completed by an equation of state for the gas (in most present applications the gas is assumed to be calorically perfect).

As already stated, when dealing with flows that are turbulent, the solution of system (4.1-3) necessitates some kind of averaging procedure due to the present incapacity of resolving the wavelengths contained in a turbulent flow.

Following the methodology introduced by Reynolds, the classical time averaged Navier-Stokes equations are obtained by decomposing any variable f into a mean value $\bar{f}$ and a fluctuating component f' such that:

$$f = \bar{f} + f'' \quad \text{with} \quad \bar{f''} = 0$$

The averaging process must be performed over a time that is long compared to the predominant frequencies of the turbulence.

However, in the case of a compressible flow, the Reynolds averaging technique leads to the introduction of a great number of terms involving the density fluctuation ρ' . There results a considerable complication coming from the necessity to model these terms in addition to the usual Reynolds stresses appearing in incompressible flows.

In order to avoid this complication, Favre (1965) has introduced the concept of **mass weighted** averaging which is presently used by most investigators performing calculations of compressible turbulent flows. The derivation of the turbulent mean-flow, Reynolds-stress and heat-flux equations in mass averaged dependend variables can be found in Rubesin and Rose (1973).

According to Favre's concept, the instantaneous velocity component u_i is expressed in the form:

$$u_i = \tilde{u}_i + u_i'$$

where $\tilde{u}_i$ is the mass weighted averaging defined by:

$$\tilde{u}_i = \frac{\overline{\rho u_i}}{\bar{\rho}}$$

the bar denoting the classical time averaged value.

From the above definition, it results that:

$$\overline{\rho u_i'} = 0$$

hence, the following relation giving u_i' in terms of the classical fluctuating components:

$$\overline{u_i'} = - \overline{\rho' u_i'} / \bar{\rho} \neq 0$$

Substituting mass averaged variables into Eqs. 4.1 to 4.3 yields:

Continuity:

$$(4.4) \qquad \frac{\partial \bar{\rho}}{\partial t} + \frac{\partial}{\partial x_j} \left(\bar{\rho} \tilde{u}_j \right) = 0$$

Momentum:

$$(4.5) \qquad \frac{\partial}{\partial t} \left(\bar{\rho} \tilde{u}_i \right) + \frac{\partial}{\partial x_j} \left(\bar{\rho} \tilde{u}_i \tilde{u}_j \right) = - \frac{\partial \bar{p}}{\partial x_i} + \frac{\partial}{\partial x_j} \left(\tau_{ij}^T \right)$$

Energy:

$$(4.6) \qquad \frac{\partial}{\partial t} \left(\bar{\rho} \tilde{h} \right) + \frac{\partial}{\partial x_j} \left(\bar{\rho} \tilde{h} \tilde{u}_j \right) = \frac{\partial \bar{p}}{\partial t} + \tilde{u}_j \frac{\partial \bar{p}}{\partial x_j} + \tau_{ij}^T \frac{\partial u_i}{\partial x_j} - \frac{\partial}{\partial x_j} \left(\dot{q}_j^T \right)$$

Here τ_{ij}^T and $\dot{q}_j^T$ denote the mass-weighted average total shear-stress and heat-flux that include the contributions of both the molecular (l) and turbulent (t) transports.

These quantities are defined as:

$$\tau_{ij}^T = \tau_{ij}^\ell + \tau_{ij}^t$$

where:

$$\dot{q}_j^T = \dot{q}_j^\ell + \dot{q}_j^t$$

$$\tau_{ij}^\ell = 2\mu \left(S_{ij} - \frac{1}{3} \frac{\partial \tilde{u}_k}{\partial x_k} \delta_{ij} \right)$$

$$\dot{q}_j^\ell = -\frac{\mu}{P_{r_\ell}} \frac{\partial \tilde{h}}{\partial x_j}$$

The mean rate of strain tensor S_{ij} is given by:

$$S_{ij} = \frac{1}{2} \left(\frac{\partial \tilde{u}_i}{\partial x_j} + \frac{\partial \tilde{u}_j}{\partial x_i} \right)$$

μ is the molecular viscosity (the second viscosity coefficient has been expressed via Stokes Hypothesis) and P_{r_l} the laminar Prandtl number defined by:

$$P_{r_\ell} = \frac{\mu C_p}{\sigma}$$

Finally, τ_{ij}^t and $\dot{q}_j^t$ are the mass-weighted averaged Reynolds stress tensor and heat-flux vector defined by:

$$\tau_{ij}^t = - \overline{\rho\, u_i' u_j'}$$

$$\dot{q}_j^t = \overline{\rho\, u_j' h'}$$

Thus Eqs. 4.4 to 4.6 now have the same form as the incompressible time-averaged equations, except that the Reynolds stresses $\overline{\rho u_i' u_j'}$ include fluctuations in density which, in principle, must be accounted for in some manner. On the other hand, the measured quantities, which are generally classical time averaged values, differ from the mass-weighted variables used to write the averaged Navier-Stokes equations.

Thus one has:

$$\bar{u}_i = \tilde{u}_i + \frac{\overline{\rho'' u_i''}}{\bar{\rho}}$$

and:

$$-\bar{\rho}\, \overline{u_i'' u_j''} = - \overline{\rho u_i' u_j'} + \overline{\rho' u_i' u_j'} - \frac{\overline{\rho' u_i'} \cdot \overline{\rho' u_j'}}{\bar{\rho}}$$

At low to moderately supersonic Mach numbers, the differences between the two kinds of variables is small and, in fact, it could be legitimate to neglect fluctuations of density. In this case, if conventional Reynolds averaging is used, the compressible turbulent Navier-Stokes equations are similar to the incompressible equations. Compressibility effects are then taken into account by considering a variable mean density. In this case, it can be readily shown that Reynolds and Favre averagings are equivalent. However, at hypersonic Mach numbers differences between time-averaged and mass-averaged variables can be significant and one should be aware of this fact when comparing computed and measured quantities (see Horstman, 1987).

The system of equations 4.4 to 4.6 is not "closed" since the number of unknowns exceeds the number of equations. One is thus confronted to the problem of expressing the turbulent quantities $-\overline{\rho u_i' u_j'}$ and $\overline{\rho u_j' h'}$ in terms of known quantities. The task of reducing the number of unknowns to the number of equations constitutes the "closure" problem. As will be seen below, solution to this problem may lead to the introduction of other equations of the transport type which must be integrated in tandem with the Navier-Stokes equations.

The closure problem in turbulent flow computations is a huge question which is at the origin of a large number of investigations still very active. It is not here the place to review, even briefly, the literature published on the subject (for more information see Marvin, 1982). In the present Lecture we will concentrate on modeling efforts specifically aimed at the prediction of shock-wave/boundary-layer interactions. Most of the models presented here have been devised to compute supersonic and transonic interactions. However, these models will be examined in some detail since there is not a well defined limit for the application of "classical" turbulence models in terms of Mach number. In reality, the great majority of hypersonic calculations have been executed by employing models which are simple extensions of incompressible models, mainly because of the lack of information on turbulence behavior in hypersonic interactions. The results thus obtained being frequently encouraging, there is no reason to be unduly pessimistic about the capability of the following "simple" turbulence models to give an acceptable prediction of hypersonic shock-wave/boundary-layer interactions.

4.2.3 - Turbulence Models for Interaction Calculations

4.2.3.1 - General remarks

The great majority of the turbulence models adopted to compute strong shock-wave/boundary-layer interactions invoke the Boussinesq effective eddy-viscosity concept. According to this concept, the turbulent shear-stresses in the mean momentum equations are replaced by the product of an effective viscosity μ_t and a mean rate of strain. Thus, one writes by analogy with the molecular stresses:

$$-\overline{\rho u_i' u_j'} = \tau_{ij}^t = 2\mu_t \left(S_{ij} - \frac{1}{3} \frac{\partial \tilde{u}_k}{\partial x_k} \delta_{ij} \right) - \frac{2}{3} \bar{\rho} \tilde{k} \delta_{ij}$$

where $\bar{k}$ is the specific turbulent kinetic energy defined as:

$$\bar{k} = \frac{1}{2} \; \frac{\overline{\rho \, u_i' \, u_i'}}{\bar{\rho}}$$

Sometimes, more complex constitutive relationships are used to model Reynolds stresses that do not necessarily align with the mean rates of strain. These relatively complex expressions will not be given here (see Wilcox and Rubesin, 1980).

Similarly, the energy equation contains the turbulent term $\overline{\rho \, u_j' \, k'}$ which is interpreted as a turbulent heat transfer term and accordingly represented by the relation:

$$\overline{\rho \, u_j' \, k'} = \dot{q}_j^t = - \frac{\sigma_t}{C_p} \; \frac{\partial \tilde{h}_j}{\partial x_j}$$

in which σ_t is an effective turbulent thermal conductivity. Thus, introducing the turbulent Prandtl number:

$$Pr_t = \frac{\mu_t \, C_p}{\sigma_t}$$

one has:

$$\dot{q}_j^T = - \left(\frac{\mu}{Pr_\ell} + \frac{\mu_t}{Pr_t} \right) \frac{\partial \tilde{h}_j}{\partial x_j}$$

Usually, the Prandtl numbers Pr_η and Pr_t are taken as constant (most often: $Pr_\eta \approx 0.75$ and $Pr_t = 0.9$ for air flow).

With the above assumption for the effective turbulent heat transfer term, the only problem which remains is to express the eddy viscosity μ_t.

More or less elaborate expressions are used to express μ_t. It is sometimes difficult to propose a clear and rational classification of these expressions, since most of them have been motivated by purely heuristic arguments.

The models are frequently classified according to the number of equations they use to represent the streamwise evolution of some key turbulent properties on which μ_t is assumed to depend. Thus, according to this classification, the purely algebraic models, in which no transport equation is used, are termed 0-equation models. In fact, it seems physically sounder to make the distinction between equilibrium models and non-equilibrium models.

In equilibrium models, the Reynolds stresses are entirely determined in terms of the local mean flow properties. This kind of modeling assumes an instantaneous adjustment between the turbulent field and the mean motion. In reality, such a behavior only exists in weakly interacting flows where turbulence has enough time to adjust itself to changes in the overall flow structure.

On the other hand, when rapid changes occur - i.e., changes taking place over a streamwise distance whose length is comparable to a characteristic scale of the turbulent structures - an instantaneous adjustment is no more possible. Then, at the scale of the interaction region, turbulence responds progressively to the perturbating agency. A shock-wave/boundary-layer interaction is a typical example of such a phenomenon where the turbulence field develops important non equilibrium - or history - effects.

In what follows, we will first present models in which there is no history effects and which are nevertheless employed by some investigators, their essential merit being their mathematical simplicity.

Then, models incorporating an history effect will be considered. As will be seen, some of these models are simple adaptations of equilibrium models, thus it is worthwhile to begin with an examination of this last category of models.

Models which do not use the eddy-viscosity concept will be considered in Section 4.2.3.4.

4.2.3.2 - Equilibrium Eddy-Viscosity Models

All equilibrium models are of the algebraic type, which means that the eddy viscosity is given by an algebraic expression involving quantities relative to the mean velocity field.

- The Mixing Length Model of Michel-Quémard and Durant

In the algebraic model proposed by Michel et al. (1969) to compute boundary-layer flows, the eddy viscosity μ_t is given by the formula:

(4.7) $$\mu_t = \bar{\rho} \; \ell^2 \, D^2 \; \frac{\partial \tilde{u}}{\partial y}$$

in which y designates the distance normal to the wall. The mixing length l is defined by the following expression valid throughout the boundary-layer:

$$\ell = 0.085 \; \delta \; \tanh \left[\left(\frac{K}{0.085} \right) \frac{y}{\delta} \right] \qquad (K = 0.41 \text{ is the Von Kàrmàn constant})$$

In the near wall region, l has the classical behavior: $l \sim K \, y$ whereas in the outer part of the boundary-layer, l becomes directly proportional to the boundary-layer thickness. Then: $l \sim 0.085 \delta$.

Function D is a modified form of the Van Driest damping factor which is given here by:

(4.8) $$D = 1 - \exp \left[- \frac{\ell}{A^+ K \mu} \; \sqrt{\tau_T \, \bar{\rho}} \; \right] \qquad (A^+ = 26)$$

where $\tau_T = \tau_\ell + \tau_t$ is the total shear-stress, sum of the laminar and turbulent contributions. The original Van Driest function has the form:

(4.9) $$D = 1 - \exp \left[- \frac{y}{A^+ \mu_w} \; \sqrt{\tau_w \, \rho_w} \; \right]$$

where subscript w d. _nates conditions at the wall. This form may lead to severe problems in the calculation of flows containing a separated region. This question will be discussed below. Expression for D is frequently written in the form:

$$D = 1 - exp \left[- \frac{y}{16 \, \nu_w} \sqrt{\frac{\tau_w}{\rho_w}} \right]$$

where ν_w is the kinematic viscosity and $\sqrt{\frac{\tau_w}{\rho_w}} = u_\tau$ is the so-called friction velocity.

In Navier-Stokes applications, the model of Michel et al. has been mainly used to compute transonic shock-wave/boundary-layer interactions (Escande and Cambier, 1985). For use in Navier-Stokes codes, μ_t is given by the following slightly modified expression:

$$\mu_t = \bar{\rho} \, \ell^2 \, D^2 \, |\omega|$$

where $|\omega|$ is the modulus of the vorticity vector.

- The Two-Layer Model of Cebeci and Smith (1974)

The very popular Cebeci-Smith model is a two-layer model in which μ_t is computed by two different expressions:

i - in the inner region, i.e. close to the surface, the expression for μ_t is based on Prandtl's mixing length hypothesis which gives:

(4.10)
$$\mu_{t_i} = \bar{\rho} \, (0.4 \, y)^2 \, D^2 \, \frac{\partial \tilde{u}_t}{\partial y}$$

where $\tilde{u}_t$ is the tangential velocity component parallel to the wall. In this model, the mixing length is adapted from Van Driest's sublayer model.

ii - in the outer region, μ_t is given by a Clauser-type expression:

$$\mu_{t_0} = 0.0168 \, \bar{\rho} \, \tilde{u}_{t_e} \, \delta_i^* \, \gamma$$

where $\tilde{u}_{t_e}$ is the tangential velocity component at the boundary-layer edge and:

$$\delta_i^* = \int_{y_0}^{\delta} \left(1 - \frac{\tilde{u}_t}{\tilde{u}_{e_t}} \right) dy$$

is the "incompressible" displacement thickness; γ designates the Klebanoff intermittency function which is computed by the approximate formula:

$$\gamma = \left[1 + 5.5 \left(\frac{y}{\delta} \right)^6 \right]^{-1}$$

The inner eddy-viscosity model μ_{t_i} is used from the wall to the match point where the eddy viscosity given by the inner model is equal to that of the outer model. Above the match point, the outer expression is used.

In fact, the two above models are not suited to compute separated flows for which they lead to unrealistic behaviors of the Reynolds stresses in the recirculation bubble. In effect, the velocity profile then exhibits a local minimum where $\partial \tilde{u}/\partial y$ near the wall. According to (4.7) or (4.10), the result is that the turbulent shear-stress vanishes in this point, leading to a nearly laminar state in a region where the flow is actually highly turbulent.

To overcome this defficiency, the following adaptations of the Cebeci-Smith basic model have been proposed.

- The Two-Layer Model of Alber (1971)

In this model, upstream of the separation point μ_{t_i} is computed by means of a two-layer model nearly identical to the Cebeci-Smith model. The only change is in the expression of the damping function which is now given by:

(4.11)
$$D = 1 - exp \left[- \frac{y}{A^+ \mu_w} \sqrt{\tau \rho_w} \right]$$

In this formula, the wall shear-stress τ had been replaced by the value of the local shear-stress at altitude y which is computed by the approximate expression:

$$\tau = \tau_w + y \, \frac{d\rho}{dx}$$

coming from the boundary-layer momentum equation written at the wall:

$$\frac{\partial \tau}{\partial y} = \frac{d\rho}{dx}$$

The same modification of the Van Driest damping function has been introduced by Cebeci et al. (1970) to represent streamwise pressure gradient effect on eddy-viscosity.

The use of Eq. 4.11, which is similar in spirit to the one proposed by Michel et al., avoids a difficulty at the separation point with the original Van Driest's formulation. Indeed, since at separation τ_w vanishes, the use of Eq. 4.9 entails, at this point, the cancellation of the turbulent contribution to shear-stress throughout the entire boundary-layer.

Other modifications of the Van Driest damping function have been proposed to avoid an unrealistic behavior at a separation point.

Baldwin and Lomax (1978) have replaced the usual expression for the friction velocity (see above) by:

$$u_\tau = \frac{1}{2} \left[\sqrt{\frac{|\tau_w|}{\rho_w}} + 0.4 \, |y \, \frac{\partial \tilde{u}}{\partial y}|_{y^+ = y_i^+} \right] \qquad with : \; y_i^+ = 60$$

This new expression is deduced from the fact that for flows with small pressure gradient $\mathcal{C}$ does not appreciably vary within the range of y at which D differs significantly from unity (i.e., the viscous sublayer). Further, the velocity varies logarithmically with y outside the viscous sublayer. Thus, for such flows, μ_c is closely approximated by the value of $[0.4 \ y \ \partial u/ \ \partial y]$ outside the viscous sublayer. This new definition of μ_c closely approximates the conventional definition for flows with small pressure gradient and remains nonzero in all regions of separated flows.

Visbal and Knight (1984) consider, in the damping function, the total shear-stress (defined in terms of the velocity component parallel to the wall) in place of τ_w. This adaptation is identical to the one introduced by Michel et al. well before them.

In calculations performed by Peters et al. (1986), the τ_w value at the last station prior to separation is used throughout the separated region, thereby eliminating the difficulty with τ_w being zero.

Once separation has occurred, μ_{t_i} and μ_{t_e} are given by the following expressions:

$$\mu_{t_i} = 0.018 \ \bar{\rho} \ y \ D^2 \ \tilde{u}_e$$

$$\mu_{t_e} = 0.0168 \ \bar{\rho} \ \tilde{u}_e \ \tilde{\delta}_c^{*} \ \gamma$$

In the equation giving μ_{t_e} , $\tilde{\delta}_c^{*}$ represents in this case the displacement thickness above the line u = 0 of the separation bubble (distinct from the wall). This lower limit of the integral can be replaced by the ordinate of the Discriminating Streamline (DSL) of the bubble; i.e., the streamline joining the separation point to the reattachment point (Benay et al., 1987). Substituting $\tilde{\delta}_c^{*}$ for $\tilde{\delta}_c^{*}$ makes it possible to avoid an abnormally high increase in the turbulent quantities for a large separation in which the boundary-layer thickens considerably.

In all the above models the length scale used to express the eddy viscosity in the outer part - or wake region - of the boundary-layer, is either the physical thickness δ of the boundary-layer or an integral thickness, such as δ_c^{*} depending directly on δ. Thus, the calculation of μ_t necessitates the localization of the edge of the dissipative regions. This localization is frequently delicate in complex flows where there is not a well defined frontier between the dissipative region and the outer inviscid flow. This is particularly true for shock-wave/boundary-layer interactions in hypersonic flows where the flow outside the boundary-layer can be highly rotational.

Thus, in contrast to the flat plate situation, the velocity presents a continuously varying profile on which it is difficult to fix a precise boundary between the dissipative and non dissipative parts of the flow.

Several methods have been used to cope with this difficulty in the execution of Navier-Stokes calculations. For example, in the case of hypersonic flows where a large total enthalpy gradient exists within the boundary-layer region (e.g., cold walls), the boundary-layer edge can be conveniently defined upon the total enthalpy profile, since the total enthalpy is constant within the inviscid part of the shock-layer region (Shirazi and Truman, 1987). In the case of adiabatic - or nearly adiabatic - flows, other techniques must be used to determine δ . Some of them are based upon the velocity distribution: then δ is located at the altitude where the relative velocity change between two mesh point is inferior to a given value (Hung and MacCormack, 1977) or is a given fraction of the maximum velocity within the shock-layer region (Shirazi and Truman, 1987). Other methods of determining boundary-layer edge use the distribution of vorticity: for example δ is defined to be the location where the vorticity is small compared to its value at the wall (Baldwin et al., 1975; Escande and Cambier, 1985).

Whatever the method used, location of δ remains a delicate task which very often leads to severe difficulties in the execution of Navier-Stokes calculations.

To overcome this difficulty, Baldwin and Lomax have proposed the following algebraic model.

- The Baldwin-Lomax Model (1978)

In the eddy-viscosity model devised by Baldwin and Lomax, the turbulence length scale is no more based upon the dissipative region thickness but is defined from the vorticity distribution. For this reason, the Baldwin-Lomax model has become extremely popular among people performing Navier-Stokes calculations.

This model is also a two layer model in which the inner and outer eddy-viscosities are given by the following equations:

(4.12)
$$\mu_{t_i} = \bar{\rho} \ (\ 0.41 \ y \ D)^2 \ | \ \frac{\partial \tilde{u}}{\partial y} \ |$$

$$\mu_{t_e} = 0.0469 \ \bar{\rho} \ F_w \ \tilde{\gamma}$$

$\tilde{\gamma}$ is the Klebanoff intermittency function which is expressed as:

$$\tilde{\gamma} = [\ 1 + 5.5 \ (\frac{0.3 y}{y_H})^6 \ ]^{-1}$$

where y_M is defined below.

Factor F_w, a function only of x, is given by whichever of the two equations below has the smallest value at abscissa considered:

$$F_w = y_H \ F_H \qquad\qquad F_w = 0.25 \ y_H \ \frac{(\Delta \tilde{u})_H^2}{F_H}$$

The quantity F_M is the maximum of function:

$$F = y \ (\frac{\partial \tilde{u}}{\partial y}) \ D$$

and y_M is the ordinate at which this maximum is reached; $\Delta \tilde{u}$ is the maximum velocity difference through the dissipative layer at a given station x. The external formulation (4.12) can be used for wakes as well as for boundary-layers; in the later case $\Delta \tilde{u}$ is equal to $\tilde{u}_e$.

Although the turbulence length scale is now defined from the vorticity distribution, difficulties can also arise with the Baldwin-Lomax model, the function F having in some circumstances more than one maximum in the region of interest.

For example, for separated supersonic flow over a compression ramp, F can display two peaks in the vicinity of separation (Visbal and Knight, 1984). It was found that the values of y_M associated with each one of these extrema may differ by one order of magnitude. Thus the selection of the peak closer to the wall can result in an abrupt and unphysical reduction in the computed outer eddy-viscosity. To avoid this unrealistic behavior, Visbal and Knight are led to adopt the value of y_M and F_M obtained from the extremum farthest from the wall.

4.2.3.3 - Non-Equilibrium Eddy-Viscosity Models

General Remarks. The non equilibrium models can in turn be divided into two broad categories, namely:

i - those which are essentially of algebraic nature, in the sense that eddy-viscosity is still given by an analytic formula (eventually of the two-layer type) valid throughout the thickness of the boundary-layer. In this case, non equilibrium effects are frequently introduced through adaptations of what is called the baseline equilibrium model;

ii - those in which eddy-viscosity is expressed in terms of one or two local turbulent quantities which are computed by means of transport type equation(s) solved in tandem with the equation of motion.

Algebraic Non Equilibrium Models. Several authors have included a history effect in the turbulence model by introducing a space-lag in the evaluation of the eddy-viscosity coefficient. This kind of modeling account for the fact that, as shown by experimental evidences, turbulent eddy motions do not rapidly adjust to local environmental changes. As we know, this is specially true in the case of a shock-wave/boundary-layer interaction.

- The Shang and Hankey Relaxation Model and Similar Models

To represent non equilibrium effects, Shang and Hankey (1975) have suggested a global relaxation model in which the eddy-viscosity μ_t is determined along lines parallel to the solid surface from:

$$(4.13) \qquad \mu_t (x) = \mu_{t_0} (x) + \left[\mu_{t_{eq}} (x) - \mu_{t_0} (x) \right] \left[1 - exp \left(- \frac{x - x_0}{\lambda} \right) \right]$$

where:

- μ_{t_0} is the eddy-viscosity evaluated just ahead of the interaction region; i.e. at $x = x_0$;

- $\mu_{t_{eq}}$ is the local equilibrium value at station x given by the baseline model (Cebeci-Smith's model in the case of the calculation performed by Shang and Hankey).

In Eq. 4.13, λ represents a relaxation length most often determined in a purely heuristic fashion as the length leading to the best agreement between calculations and a well chosen experiments. Thus Shang and Hankey have adopted $\lambda = 10 \delta_0$ where δ_0 is the boundary-layer thickness at the interaction origin.

A similar relaxation formula has been more recently used by Visbal and Knight (1984) along with the Baldwin-Lomax turbulence model. However, in their applications best agreement with experiment was obtained with $\lambda = \delta_0$; i.e., a value one tenth of that suggested by Shang and Hankey.

In a slight variant of the above approach, Mateer et al. (1976) have applied the relaxation formula only to the outer eddy-viscosity of a two layer baseline model. This way of implementing a history effect can be justified by the fact that, due to the very small thickness of the inner layer, turbulence in this part of the flow can adjust its properties nearly instantaneously to rapid changes in flow conditions. On the other hand, the large eddy motions which determine the turbulence structure in the outer part of the boundary-layer need a certain time to accommodate themselves to the new situation.

A relaxation formula identical to Eq. 4.13 has been applied by Horstman (1976) to the mixing length of his baseline model. A local relaxation model has also been used by Mateer et al. (1976) to compute a normal shock-wave/boundary-layer interaction at transonic speeds. In this model - closely inspired from that proposed by Deiwert (1975) - the eddy-viscosity is given by:

$$\mu_t (x) = \mu_t (x - \delta x) + \left[\mu_{t_{eq}} (x) - \mu_t (x - \delta x) \right] \left[1 - exp \left(- \frac{\delta x}{\lambda} \right) \right]$$

where:

- $\mu_{t_{eq}}$ is the local equilibrium value of the eddy viscosity;

- $\mu_t (x - \delta x)$ is the value of μ_t at the preceding mesh point and δx is the distance between mesh points.

The same local relaxation formula has also been applied to the mixing length by Horstman (1976).

- Models with Variable Turbulence Constants

On can envisage to introduce some history effect by acting on the basic constants involved in the turbulence model, namely: the constant A^+ of the Van Driest damping function and the Von Kàrmàn constant K of the mixing length near wall expression.

Formulae giving the evolution of A^+ and K as function of a local pressure gradient parameter have been proposed by Kays (1971) - for A^+ - and Glowacki and Chi (1974) - for K. A similar approach has been adopted by Gupta (1983). However, since the parameter adopted characterizes the local value of the streamwise pressure gradient to which the boundary-layer is submitted, formulae of this kind do not represent a true history effect.

In order to improve the situation, Horstman (1976) has suggested a new way to introduce non-equilibrium effects at the level of the basic model constants. In Horstman's model A^+ and K are represented by the following equations:

$$A^+(x) = 26 / \left[1 + 30.18 \, \overline{p^+(x)} \right] \quad , \quad K = 0.4 + 0.102 \left\{ 1 - exp \left[- 0.321 \, \overline{\beta(x)} \right] \right\}$$

In these equations, $\overline{p^+}(x)$ and $\overline{\beta}(x)$ are weigthed averages of the dimensionless pressure gradient parameters:

$$p^+ = \rho_w \, \mu_w \, (\, d\rho_w / dx\,) \, / (\rho_w \, \tau_w)^{3/2}$$

and

$$\beta = \delta_i^* \, (\, d\rho_w / dx\,) \, / \, \tau_w$$

A Gaussian weighting function, centered about a point several boundary-layer thickness $\lambda\delta$ upstream of each axial grid location was chosen to obtain the weighted averages. Thus one has for $\overline{p^+}(x)$:

$$\overline{p^+(x)} = \int_{x-\lambda\delta}^{x} \, \omega\,(\xi)\, p^+(\xi)\, d\xi$$

with:

$$\omega\,(\xi) = \frac{1}{\sqrt{2\pi}\sigma} \, exp\left\{ - \left[\xi - (x - \lambda\delta)^2 \right] / 2\,\sigma^2 \right\} \qquad \sigma = \lambda\delta/3$$

where λ is a lag length parameter. For application of the model to shock-wave/boundary-layer interactions, a lag length parameter equal to the local boundary-layer thickness ($\lambda = 1$) seems to give the best results (Horstman et al., 1977).

A similar expression is used for calculating $\beta(x)$.

In all the above models, non-equilibrium effects are introduced in a more or less empirical manner by means of relatively simple modifications of the baseline equilibrium model. History effect is represented by a space lag in the streamwise evolution of the eddy-viscosity coefficient or the "constants" of the model. This space lag involves a lag length parameter which, as shown by applications, do not obey a universal simple law. In fact, this parameter must be adjusted for each computed configuration so that the predictive capability of these models is generally poor.

- The Johnson-King Algebraic Model. A more convincing algebraic non-equilibrium turbulence model has been more recently proposed by Johnson and King (1984; see also Johnson, 1985). This model, essentially applied to transonic interacting flows, introduces a sounder transport mechanism for representing history effect on turbulence while keeping the mathematical simplicity of the classical algebraic models.

In the Johnson-King model, the kinematic eddy-viscosity ν_t is given for the complete thickness of the boundary-layer by the equation:

where

$$\nu_t = \nu_{t_e} \, \left[\, 1 - exp\,(\,-\,\nu_{t_i} / \nu_{t_e}\,)\, \right]$$

(4.14)

$$\nu_{t_i} = 0.4\, y \, D^2 \, (\, -\overline{u'v'_H}\,)^{1/2}$$

and

$$\nu_{t_e} = \alpha \, y$$

$(-\overline{u'v'})_H$ designates the maximum shear-stress level at the abscissa x considered. Constant α is determined such that:

$$\nu_t \, \frac{\partial \tilde{u}}{\partial y}\Big|_H = -\overline{u'v'_H}$$

where ν_t is given by (4.14). The shear-stress $-\overline{u'v'_H}$ satisfies a simplified transport equation with the form:

$$\frac{L_H \, \tilde{u}_H}{a_1 (-\overline{u'v'_H})} \, \frac{d(-\overline{u'v'_H})}{dx} + (\, -\overline{u'v'_H}\,)^{1/2} + \frac{L_H \, \mathcal{D}_H}{(-\overline{u'v'_H})} = L_H \, \frac{\partial \tilde{u}}{\partial y}\Big|_H$$

This ordinary differential equation is inferred from the transport equation for the turbulence kinetic energy k (see Eq. 4.16 below) with introduction of the hypothesis:

$$\frac{-\overline{u'v'_H}}{k_H} = a_1 = 0.25$$

The dissipation length $L_H = \frac{-\overline{u'v'_H}}{\epsilon}$ and the turbulent diffusion rate $\mathcal{D}_H$ are given by algebraic expressions (see Johnson, 1985).

Eddy-Viscosity Transport Equation Models.

General Remarks. A further step in the sophistication of turbulence models consists in calculating the eddy-viscosity in terms of local turbulent properties which satisfy transport equations representing history effect.

This way of tackling the problem of turbulence modeling is largely based on the concepts presented in pioneering papers by Kolmogorov (1942) and Rotta (1951). The research effort along this line has been at the origin of a vast amount of publications which cannot be considered, even briefly, within the framework of this Lecture. Here, we will concentrate on models of practical interest which are currently used in shock-wave/boundary-layer interaction calculations.

As we know, the kinematic eddy-viscosity μ_t has the dimension of a velocity times a length. Thus the problem is to find transport equations for representative scales from which μ_t will be expressed.

A universally adopted velocity scale is the square root of the turbulent kinematic energy. Let us recall that with mass weighted variables, this quantity is:

$$\overline{k} = \frac{1}{2} \, \frac{\overline{\rho u'_i u'_i}}{\overline{\rho}}$$

9-34

Hence, we will write:

$$\mu_t = \bar{\rho}\ C\ \sqrt{\bar{k}}\ L$$

where C is a constant and L the still undetermined length scale.

A transport equation for $\bar{k}$ can be deduced from the following general Reynolds stresses transport equation, written here with mass weighted variables (see Rubesin and Rose, 1973):

(4.15)
$$\frac{\partial}{\partial t}\left(\overline{\rho\, u_i'\, u_j'}\right) + \frac{\partial}{\partial x_j}\left(\tilde{u}_j\ \overline{\rho u_i'\, u_k'}\right) = \left(\overline{\rho u_i'\, u_j'}\right)\frac{\partial \tilde{u}_k}{\partial x_j} - \left(\overline{\rho u_k'\, u_j'}\right)\frac{\partial \tilde{u}_i}{\partial x_j}$$

$$- \frac{\partial}{\partial x_j}\left(\overline{\rho u_i'\, u_k'\, u_j'}\right) - \frac{\partial}{\partial x_k}\left(\overline{u_i'\,p}\right) - \frac{\partial}{\partial x_i}\left(\overline{u_k'\,p}\right) + p\left(\overline{\frac{\partial u_k'}{\partial x_i} + \frac{\partial u_i'}{\partial x_k}}\right)$$

$$+ \frac{\partial}{\partial x_j}\left(\overline{u_k'\,\tau_{ij}}\right) + \frac{\partial}{\partial x_j}\left(\overline{u_i'\,\tau_{kj}}\right) - \overline{\tau_{ij}\frac{\partial u_k}{\partial x_j}} - \overline{\tau_{ki}\frac{\partial u_i'}{\partial x_j}}$$

As $\bar{k}$ is half the trace of the Reynolds stress tensor, we obtain immediately for $\bar{k}$:

(4.16)
$$\frac{\partial}{\partial t}\left(\bar{\rho}\ \bar{k}\right) + \frac{\partial}{\partial x_j}\left(\bar{\rho}\ \tilde{u}_j\ \bar{k}\right) = -\overline{\rho u_j'\, u_k'}\ \frac{\partial \tilde{u}_j}{\partial x_k} - \frac{\partial}{\partial x_k}\left(\overline{\rho u_k'\, \bar{k}}\right) - \frac{\partial}{\partial x_i}\left(\overline{u_i'\,p}\right) + p\ \overline{\frac{\partial u_i'}{\partial x_i}}$$

$$+ \frac{\partial}{\partial x_k}\left(\overline{u_i'\,\tau_{ik}'}\right) - \overline{\tau_{ik}'\frac{\partial u_i'}{\partial x_k}}$$

In the above equation k = 0.5 $\overline{u_i'u_i'}$ and τ_{ik}' is the molecular stress tensor.

In contrast to the Navier-Stokes equations, the equations for the Reynolds stress tensor and $\bar{k}$ contain extra terms resulting from the compressibility effect, even if mass weighted variables are used. These extra terms involve pressure/velocity and molecular shear-stress/velocity correlations.

The reason for the presence of these terms is that both ρ' and its derivatives are non-zero in a compressible flow. In fact, at low to moderately supersonic Mach numbers, the extra terms are small and are most often neglected. However, if compressibility effects are important, as in hypersonic flows, attention should be paid to the consideration of these extra terms and a modeling should be looked for to represent them (Rubesin, 1976; see also information in Horstman, 1987).

The terms in the rigth hand side in Eq. 4.16 are, sequentially, the turbulence production, the turbulent diffusion, the pressure diffusion, pressure work, molecular diffusion and dissipation of the turbulent kinetic energy.

Except the production term, all other terms contain new fluctuating quantities whose determination should require the writing of new equations, which in turn, would introduce other correlation terms, and so on... Thus, in order to "close" the problem, the terms of Eq. 4.16 (and also of Eq. 4.15, if second order closure modeling is used), other than the production term, have to be modeled. We will now consider some of the modeling procedures used to compute eddy-viscosity for supersonic, or hypersonic, applications.

One Equation Model. The one equation model, or kinetic energy model, was developed for incompressible flat plate boundary-layer flows by Glushko (1965). It was studied by Beckwith and Bushnell (1968) in more complicated boundary-layer flows and was generalized by Rubesin (1976) to compressible flows using mass averaged variables. We present here the simplified version of the complete Rubesin model which was used by Viegas and Horstman (1978) in a thorough examination of turbulence modeling in shock-separated boudary-layer interaction flows.

Glushko has demonstrated that the turbulent effective viscosity μ_t is expressible in terms of a local turbulence Reynolds number defined as:

$$R_t = \frac{\bar{\rho}\ \sqrt{\bar{k}}\ L}{\mu}$$

In the present model, $\bar{k}$ is computed by a transport equation but the length scale L is still provided by an algebraic relationship which will be given hereafter.

As modeled by Glushko and Rubesin, the turbulent kinetic energy equation takes the form:

$$\frac{\partial}{\partial t}\left(\bar{\rho}\ \bar{k}\right) + \frac{\partial}{\partial x_j}\left(\bar{\rho}\ \tilde{u}_j\ \bar{k}\right) =$$

$$\bar{\rho}\ P_k - \frac{\bar{\rho}\ \bar{k}\ \mathcal{F}\ C_v\ M^2\ div\ \vec{V}}{c_p} - \frac{\mu_t\ C\ \bar{k}}{L^2} + \frac{\partial}{\partial x_j}\left(\mu_t\ \frac{\partial \bar{k}}{\partial x_j}\right) .$$

where:

- The production term P_k is $P_k = \frac{1}{\bar{\rho}}\ \tau_{ij}'\ \frac{\partial \tilde{u}_i}{\partial x_j}$ (see Section 4.2.2 above for the expression of τ_{ij}' in terms of the eddy-viscosity and the mean rate of strain rate).

- M is the local Mach number.

- C_p and C_v are constant volume and constant pressure specific heats.

- $\mathcal{F}$ and C are modeling constants.

The eddy-viscosity μ_t is given in terms of R_t by the following expressions:

$$\mu_t = \alpha \mu R_t \times \begin{cases} \bar{R}_t & \text{if} & \bar{R}_t < 0.75 \\ \bar{R}_t - (\bar{R}_t - 0.75)^2 & \text{if} & 0.75 \leq \bar{R}_t < 1.25 \\ 1 & \text{if} & \bar{R}_t > 1.25 \end{cases}$$

where $\bar{R}_t = R_t / R_0$ and R_0 and α are model constants. The variable multiplicative factor of $\bar{R}_t$ is introduced to insure a proper variation of μ_t in the near wall region.

The length scale L, as defined by Glushko, is:

$$L = \delta \times \begin{cases} \bar{y} & \text{if} & \bar{y} < 0.23 \\ (\bar{y} + 0.37)/2.61 & \text{if} & 0.23 \leq \bar{y} < 0.17 \\ (1.48 - \bar{y})/2.52 & \text{if} & 0.17 \leq \bar{y} < 1.47 \end{cases}$$

where: $\bar{y} = y / \delta$.

The expressions for the total thermal conductivity σ_T and the total turbulent kinetic energy diffusion μ_k are:

$$\sigma_T = C_\mu \left[\frac{\mu}{P_{r_t}} + \mu_t (\Gamma R_t) \right]$$

$$\mu_k = \mu + \mu_t (\lambda R_t)$$

where Γ and λ are model constants.

The values of the constants in the study of Viegas and Horstman were:

$$\alpha = 0.22 \qquad C = 4.69 \qquad R_0 = 120$$

$$\delta = 0.73 \qquad \Gamma = 1.1 \qquad \lambda = 0.4$$

Two Equation Models. The next step in the modeling improvement consists in adopting a transport equation to determine the variable f which is used in conjunction with $\bar{k}$ to define the turbulent length scale.

In the Jones-Launder model, f is the turbulent kinetic energy dissipation rate, usually designated by ε ; in the Wilcox-Rubesin model, f is the rate of dissipation of turbulent kinetic energy per unit of kinetic energy.

- **The Model of Jones and Launder (1971)**

The modeled equation for the turbulent kinetic energy has the form:

(4.17) $\qquad \dfrac{\partial (\bar{\rho} \bar{k})}{\partial t} + \dfrac{\partial}{\partial x_j} (\bar{\rho} \tilde{u}_j \bar{k}) = \bar{\rho} P_k - \bar{\rho} \varepsilon - \boxed{2\mu \left(\dfrac{\partial \sqrt{\bar{k}}}{\partial y} \right)^2} + \dfrac{\partial}{\partial x_j} \left(\mu_k \dfrac{\partial \bar{k}}{\partial x_j} \right)$

while the equation for the turbulent dissipation rate ε is :

(4.18) $\qquad \dfrac{\partial (\bar{\rho} \varepsilon)}{\partial t} + \dfrac{\partial}{\partial x_j} (\bar{\rho} \tilde{u}_j \varepsilon) = C_{\varepsilon_1} \dfrac{\varepsilon}{\bar{k}} \bar{\rho} P_k - \dfrac{C_{\varepsilon_2} f_2 \bar{\rho} \varepsilon^2}{\bar{k}} + \boxed{\dfrac{2\mu \mu_t}{\bar{\rho}} \left(\dfrac{\partial^2 \tilde{u}_t}{\partial y^2} \right)^2} + \dfrac{\partial}{\partial x_j} \left(\mu_\varepsilon \dfrac{\partial \varepsilon}{\partial x_j} \right)$

The above equations can also be written in the following forms after introduction of the eddy-viscosity concept:

(4.17a) $\qquad \dfrac{D \bar{\rho} \bar{k}}{Dt} = \mu_t \left[S_{ij} S_{ij} - \dfrac{2}{3} (\text{div } \vec{V})^2 \right] - \dfrac{2}{3} \bar{\rho} \bar{k} \text{ div } \vec{V} - \rho \varepsilon$

$\qquad\qquad + \text{ diffusion} + \text{LRT}$

(4.18a) $\qquad \dfrac{D \bar{\rho} \varepsilon}{Dt} = \dfrac{\varepsilon}{\bar{k}} \left\{ C_{\varepsilon_1} \mu_t \left[S_{ij} S_{ij} - \dfrac{2}{3} (\text{div } \vec{V})^2 \right] - C_{\varepsilon_1} \dfrac{2}{3} \bar{\rho} \bar{k} \text{ div } \vec{V} \right\}$

$\qquad\qquad - C_{\varepsilon_2} f_2 \bar{\rho} \dfrac{\varepsilon^2}{\bar{k}} \quad + \text{ diffusion} + \text{LRT}$

LRT refers to the so-called Low Reynolds number Terms which must be introduced near a solid surface, as will be seen below. The LRT terms are surrounded in Eqs. 4.17 and 4.18.

C_{ε_1} and C_{ε_2} are model constants, f_2 is a function of the turbulence Reynolds number R_t:

$$f_2 = 1 - 0.3 \exp (- R_t^2)$$

In this case, eddy-viscosity is given by:

(4.19) $\qquad \mu_t = \mu C_\mu f_\mu R_t$

where C_μ is a constant and f a function of R_t defined as:

$$f_\mu = \exp \left[-2.5 / (1 + R_t / 50) \right]$$

As the turbulence length scale is:

$$L = \bar{k}^{\frac{3}{2}} / \varepsilon$$

the turbulence Reynolds number can be expressed as:

$$R_t = \frac{\bar{\rho}\sqrt{\bar{k}}\,L}{\mu} = \frac{\bar{\rho}\,\bar{k}^2}{\mu\varepsilon}$$

and μ_t can be written in the more familiar form:

$$\mu_t = \bar{\rho}\,C_\mu\,f_\mu\,\frac{\bar{k}^2}{\varepsilon}$$

The expressions for the diffusivity coefficients for this model are given by:

$$\mu_T = \mu + \mu_t \qquad\qquad \mu_k = \mu + \frac{\mu_t}{\sigma_k}$$

$$\sigma_T = C_p \left(\frac{\mu}{P_r} + \frac{\mu_t}{P_{r_t}} \right) \qquad\qquad \mu_\varepsilon = \mu + \frac{\mu_\varepsilon}{\sigma_\varepsilon}$$

where σ_k and σ_ε are constants.

The following values of the constants are generally adopted:

$$C_{\varepsilon_1} = 1.55 \qquad C_{\varepsilon_2} = 2. \qquad C_\mu = 0.09 \qquad \sigma_k = 1. \qquad \sigma_\varepsilon = 1.3$$

The surrounded terms in Eqs. 4.17 and 4.18 are added to insure proper behavior of k and ε when the distance to the surface y is tending to zero. These terms extend the validity of the transport equations to regions of the flow where the turbulent Reynolds number is not large. In fact, the origin of these extra terms is purely empirical and their presence may lead to severe numerical difficulties since they tend to make Eqs. 4.17 and 4.18 stiff close to the wall. For the same reason, the presence of f_μ in the eddy-viscosity expression permits a proper behavior of μ_t when y tends towards zero.

On the other hand, the results given by the original Jones-Launder model are in poor agreement with experiment in the case of strongly interacting flows. For example, the size of the separated regions is most often largely underpredicted.

To avoid the numerical difficulties and to improve its accuracy in the prediction of shock-wave/boundary-layer interactions, the Jones-Launder model has been modified in the following manner.

The *dissipative layer* is divided into two regions:

i - An outer layer where the turbulent contribution to the shear-stress is largely superior to the laminar contribution. In this layer, the eddy-viscosity is computed by using formula 4.19, with $f_\mu \approx 1$. and the turbulent quantities $\bar{k}$ and ε are determined by solving the transport equations 4.17 and 4.18 without the wall correction terms (surrounded terms).

ii - An inner layer where the molecular viscosity tends to become predominant. There, a special treatment is substituted to the solution of Eqs. 4.17 and 4.18.

Several models have been proposed to represent the flow in the near wall region. The purposes of these special treatments is to provide a correct expression for the eddy-viscosity and to specify appropriate values of kinetic energy and dissipation in the fully turbulent region away from the wall. These values will be used as boundary-conditions for Eqs. 4.17 and 4.18 without the wall correction terms.

Thus Chieng and Launder (1980) start integration of the ($\bar{k}$, ε) transport equations at a point P located above the viscous sublayer, in the logarithmic region of the boundary-layer. There, by making suitable assumptions concerning the behavior of $\bar{k}$ and ε in the near wall region and considering the log-law for the velocity distribution, it is possible to write relations linking conditions at P to wall values.

A similar treatment has been adopted by Chen (1986) but with a new wall function approch based on a wall law suitable for boundary-layers under strong adverse pressure gradients. Wall functions have also been used by Gorski (1986) to derive boundary conditions for $\bar{k}$ and ε at a certain distance from the wall. Gorski's treatment is more general in the sense that it allows the inner boundary from which Eqs. 4.17 and 4.18 are solved to lie in the viscous sublayer. This situation can happen in a strongly interacting flow where an important dilatation of the dissipative layer inner part occurs (see also Gorski et al., 1987).

Another way to treat the near wall region is to adopt, close to the wall, the mixing length expression for computing the eddy-viscosity (in particular, see Benay et al., 1987). Thus, below a certain ordinate y_R, μ_t is given by Eq. 4.7. Then, by making use of Bradshaw hypothesis:

$$\frac{-\rho\,\overline{u_i'\,u_j'}}{\bar{\rho}\,\bar{k}} = 0.3$$

and assuming that in this part of the flow turbulence is in equilibrium, i.e., production of $\bar{k}$ = dissipation of $\bar{k}$, the values of k_R and ε_R at y_R are readily computed.

Above y_R, Eqs. 4.17 and 4.18 are solved with $\bar{k}_R$ and $\bar{\varepsilon}_R$ specified as boundary-conditions on y_R. Now μ_t is given by Eq. 4.19, with $f_\mu \approx 1$. The boundary y_R between the two domains is located at an altitude where the turbulence Reynolds number is high enough: $R_t = 200$ is an appropriate value.

- The Model of Wilcox and Rubesin (1980)

In this model, the eddy-viscosity is given by:

(4.20) $\qquad \mu_t = \bar{\rho}\, \gamma^* \dfrac{\tilde{k}}{\omega}$

with: $\qquad \gamma^* = \left[\, 1 - (1-\lambda^2)\, \exp\,(-R_t/R_o\,)\,\right]$

R_t is the Reynolds number of turbulence and R_0, λ model constants.

In Eq. 4.20, ω designates the rate of dissipation of kinetic energy per unit of kinetic energy which, according to authors, may be a more significant quantity than the rate of turbulence dissipation itself.

The transport equations for k and ω take the form:

(4.21) $\qquad \dfrac{\partial}{\partial t}\,(\bar{\rho}\,\tilde{k}\,) + \dfrac{\partial}{\partial x_j}\,(\bar{\rho}\,\tilde{u}_j\,\tilde{k}\,) = \tau^t_{ij}\,\dfrac{\partial \tilde{u}_i}{\partial x_j} - \beta^*\bar{\rho}\,\omega\,\tilde{k} + \dfrac{\partial}{\partial x_j}\left[\,(\mu + \dfrac{\mu_t}{\sigma_k})\dfrac{\partial \tilde{k}}{\partial x_j}\,\right]$

and

(4.22) $\qquad \dfrac{\partial}{\partial t}\,(\bar{\rho}\,\omega^2\,) + \dfrac{\partial}{\partial x_j}\,(\bar{\rho}\,\tilde{u}_j\,\omega^2\,) = \gamma\,\dfrac{\omega^2}{\tilde{k}}\;\tau^t_{ij}\,\dfrac{\partial \tilde{u}_i}{\partial x_j} - \left[\beta + \dfrac{2}{\sigma_{\omega^2}}\left(\dfrac{\partial L}{\partial x_k}\right)^2\right]\bar{\rho}\,\omega^3 + \dfrac{\partial}{\partial x_j}\left[(\mu + \dfrac{\mu_t}{\sigma_{\omega^2}})\dfrac{\partial \omega^2}{\partial x_j}\right]$

where the length scale L is represented by: $\qquad L = \dfrac{\sqrt{\tilde{k}}}{\omega}$

and

$\qquad \gamma = \gamma_o\,\left[\,1 - (1-\lambda^2)\,\exp\,(-R_t/R\omega^2)\,\right]\,/\,\gamma^*$

The constants used with this model have the following values:

$\qquad \lambda = 1/11 \qquad R_0 = 1 \qquad \beta^* = 0.09 \qquad \beta = 0.15$

$\qquad \gamma_o = 0.9 \qquad \sigma_k = \sigma_{\omega^2} = 2$

The boundary conditions at the wall for Eqs. 4.29 and 4.30 are:

$\qquad \tilde{k} = 0$

$\qquad \omega \longrightarrow 20\mu\,/\,\beta\,\bar{\rho}\,y^2$

The condition for ω was derived by Wilcox and Tracy (1976). To avoid the singularity on ω when $y \to 0$, the dissipation rate equation is solved numerically for $y^+ > 4$ and then patched smoothly to:

$\qquad \omega = 20\mu\,/\,\beta\,\bar{\rho}\,y^2$

for smaller values of y (see Viegas and Horstman, 1978).

The Wilcox-Rubesin model differs basically from the preceding models in that the form of the constitutive relation between Reynolds stress tensor and mean flow properties has been modified to represent anisotropic Reynolds stress phenomena. This more general relation will not be given here (see Wilcox and Rubesin, 1980).

4.2.3.4 - Second Order Closure Models

The General Model. A further step in turbulence modeling - within the framework of classical statistical turbulence - is to give up the eddy-viscosity concept and to consider transport equations for the Reynolds stress tensor itself. This approach is called the "Reynolds Stress Equation" (RSE) formulation or second order closure modeling.

The essential advantages for using the Reynolds stress model over the usual eddy-viscosity model lie in the removing of the postulate that the principal axis of the Reynolds stress tensor align with that of the mean strain rate tensor and that sudden changes in the mean stress tensor are reflected immediately in the Reynolds stresses.

The Reynolds stress equation has been given above in terms of mass weighted variables (see Eq. 4.23). Modeling of the general RSE has been proposed by Hanjalic and Launder (1972) as by Launder et al. (1975) and also by Wilcox and Rubesin (1980).

These last authors have proposed the following modeled Reynolds Stress Equation, in which τ^t_{ij} designates the Reynolds tensor:

$$\dfrac{\partial}{\partial t}\,(\bar{\rho}\,\tau^t_{ij}) + \dfrac{\partial}{\partial x_k}\,(\bar{\rho}\,\tilde{u}_k\,\tau^t_{ij}) = -\bar{\rho}\,\tau^t_{im}\,\dfrac{\partial \tilde{u}_j}{\partial x_m} - \bar{\rho}\,\tau^t_{jm}\,\dfrac{\partial \tilde{u}_i}{\partial x_m} + \dfrac{2}{3}\,\beta^*\bar{\rho}\,\omega\,\tilde{k}\,\delta_{ij}$$

$$-\,C_1\,\beta^*\bar{\rho}\,\omega\left(\tau^t_{ij} + \dfrac{2}{3}\,\tilde{k}\,\delta_{ij}\right) + \bar{\rho}\left(\tau^t_{jm}\,S_{mi} + \tau^t_{im}\,S_{mj} - \dfrac{2}{3}\,\tau_{mn}\,S_{nm}\,\delta_{ij}\right)$$

$$+\,\dfrac{4}{3}\,\bar{\rho}\,\tilde{k}\left(S_{ij} - \dfrac{1}{3}\,\dfrac{\partial \tilde{u}_k}{\partial x_k}\,\delta_{ij}\right) + \dfrac{\partial}{\partial x_k}\left[(\mu + \sigma^*\bar{\rho}\,\epsilon)\,\dfrac{\partial \tau^t_{ij}}{\partial x_k}\right]$$

The values of the constants figuring in this equation will not be given here.

The RSE must be supplemented by the transport equation for ω' (or ε if the more classical dissipation rate is used).

The RSE approach necesssitates the solution of a system of 12 strongly coupled partial differential equations in the case of a three-dimensional flow, namely: the 5 Navier-Stokes equations (continuity + momentum + energy), 6 equations for the Reynolds stresses, 1 equation for the turbulent dissipation rate. Due to this complication, applications of RSE closure in the case of shock-wave/bboundary-layer interactions are still extremely scarce. To our knowledge, the only convincing calculation has been performed by Vandromme and Ha-Minh(1985). It concerns a transonic flow. For this reason we will not give further details on the RSE approach (for more ample imformation, see Ha-Minh and Vandromme, 1985).

The Algebraic Stress Model. A relatively simple solution to the problem of directly determining the Reynolds tensor components, without having to solve a complicated system of partial differential equations, has been proposed by Launder (1971) and by Rodi (1972).

This modeling procedure is known as the Algebraic Stress Model or ASM. Initially developed for incompressible flows, it has been applied with success to moderately supersonic flows (see for example Benay et al., 1987). The ASM allows the calculation of the Reynolds stresses via the solution of an algebraic system of equations.

This system is derived from the general Reynolds stress transport equation by making the assumption that the ratio:

$$\frac{\overline{u_i'\, u_j'}}{k}$$

varies slowly along a streamline. We can then write:

(4.23) $$\frac{D\,(\overline{u_i'\, u_j'})}{Dt} - Diff\,(\overline{u_i'\, u_j'}) = \frac{\overline{u_i'\, u_j'}}{k}\left(\frac{D\bar{k}}{Dt} - Diff\,\bar{k}\right)$$

D/Dt is the particular derivative of the quantity and Diff represents the terms which are modeled as diffusion terms in the transport equations. By considering the difference between the convective term D/Dt and the diffusion term Diff in the modeled transport equations for k and $\overline{u_i'u_j'}$, one notes that this difference does not contain partial derivatives of the turbulent quantities.

Hence, Eq. 4.23 leads to an algebraic non-linear system for $\overline{u_i'\, u_j'}$ which can be written in the following form for an incompressible flow:

(4.24) $$\frac{\overline{u_i'\, u_j'} - \tfrac{2}{3}\bar{k}\,\delta_{ij}}{\bar{k}} = \frac{1-C_2}{C_1-1+P_k/\varepsilon}\;\frac{P_{ij}-\tfrac{2}{3}P_k\,\delta_{ij}}{\varepsilon}$$

where:

$$P_k = -\overline{u_i'\, u_j'}\;\frac{\partial\tilde{u}_i}{\partial x_j}$$

and

$$P_{ij} = -\overline{u_i'\, u_k'}\;\frac{\partial\tilde{u}_j}{\partial x_k} - \overline{u_j'\, u_k'}\;\frac{\partial\tilde{u}_i}{\partial x_k}$$

C_2 and C_1 are model constants (Launder has proposed $C_1 = 2.2$ and $C_2 = 0.55$).

Thus the $\overline{u_i'\, u_j'}$'s can be calculated as function of $\bar{k}$, ε and spatial derivatives of the mean velocity field by solving an algebraic system.

In the compressible extensions made to this day, compressibility effect is simply taken into account l, considering in the equations a variable mean density. Thus expressions similar to Eqs. 4.24 are used.

To our knowledge, the ASM has not yet been applied to the computation of shock-wave/boundary-layer interactions occurring at high Mach numbers. However, due to the very encouraging results obtained in transonic flows, the ASM could constitute an interesting model for hypersonic applications.

4.2.3.5 - Algebraic Models in Three-Dimensional Flows.

In three-dimensional calculations, some adaptation of the classical algebraic models is needed to account for the three dimensional character of the field. The following models have been proposed to compute corner flow (see Section 4.4.5 below) where one has to represent the influence of the two walls.

For the mixing length formulation used close to the surface, one may adopt the following expression suggested by Prandtl:

$$\mu_t = \bar{\rho}\,(\kappa L)^2\,|Def\,\vec{V}|\quad(\kappa = 0.41)$$

where:

$$|Def\,\vec{V}| = \left[2\left(\frac{\partial u}{\partial x}\right)^2 + 2\left(\frac{\partial v}{\partial y}\right)^2 + 2\left(\frac{\partial w}{\partial z}\right)^2\right.$$
$$\left. + \left(\frac{\partial v}{\partial x}+\frac{\partial u}{\partial y}\right)^2 + \left(\frac{\partial w}{\partial x}+\frac{\partial u}{\partial z}\right)^2 + \left(\frac{\partial w}{\partial y}+\frac{\partial v}{\partial z}\right)^2\right]^{\frac{1}{2}}$$

Shang et al. (1979) have substituted to the above mean rate of deformation, the following simpler quantity:

$$\left|\frac{\partial q}{\partial n}\right| = |\vec{n}\cdot\nabla\vec{V}|$$

where $\vec{n}$ is the outward normal with respect to the wedge surface. Thus, the inner eddy-viscosity is given by the relation:

$$\mu_{t_i} = \bar{\rho}\,(\kappa L)^2\left[1-exp\left(-\frac{\bar{\rho}\,|\partial q/\partial n/L^2|}{26\mu}\right)\right]^2\left|\frac{\partial q}{\partial n}\right|$$

where the Van Driest damping function has been introduced.

The length scale L figuring in the above formula is the asymptotic form of the relation given by Gessner (1973) for a rectangular duct. In its most basic form, L can be expressed from the integral:

$$\frac{1}{L} = \frac{1}{2}\int_0^{2\pi} \frac{d\phi}{s}$$

where ϕ is the peripheral angle of a sweep ray originating from any point (x,y,z,) inside the duct and s the distance between the point and the intersection of the ray with the corner surface (see sketch).

For the corner problem, the general relation given by Gessner takes the following asymptotic form:

$$L = 2yz \bigg/ \left[y + z + \sqrt{y^2 + z^2} \right]$$

where y and z are Cartesian co-ordinates along the corner sides.

In the outer part of the boundary-layer, the eddy-viscosity is computed by:

$$\mu_{t_0} = \bar{\rho} C q_{max} \int_0^{\eta_{max}} (1 - q/q_{max})\, d\eta \qquad (\text{with } C = 0.0168)$$

where q is the velocity magnitude and η_{max} the maximum dimension along the transformed η co-ordinate (the computational co-ordinate system adopted by Shang et al. is shown in Fig. 4.5).

A similar model was used by Hung and MacCormack (1976) for sharp fin calculations. In this model the turbulent eddy-viscosity is given by:

$$\mu_t = \bar{\rho}\,(D L)^2\,\omega$$

with:

$$D = 1 - exp\left(-\frac{d}{26\mu_w}\sqrt{|\mathcal{T}_w|\rho_w}\right)$$

ω is the absolute magnitude of vorticity, i.e.:

$$\omega = |\nabla \times \vec{V}| = \left[\left(\frac{\partial w}{\partial y} - \frac{\partial v}{\partial z}\right)^2 + \left(\frac{\partial u}{\partial z} - \frac{\partial w}{\partial x}\right)^2 + \left(\frac{\partial v}{\partial x} - \frac{\partial u}{\partial y}\right)^2\right]^{\frac{1}{2}}$$

The mixing length l is computed by the following expression valid throughout the boundary-layer:

$$\ell = 0.08\,\delta\,\tan h\,(0.41 d / 0.08\,\delta)$$

where the "modified distance" d is identified with the length scale L of the previous model. The above expression for the mixing-length is identical to that proposed by Michel et al. (see above).

4.2.4 - Navier-Stokes Calculations of Interacting Flows

4.2.4.1 - Introductory Remarks

The present Section is devoted to the presentation of applications of the Navier-Stokes approach to shock-wave/boundary-layer interaction problems. Interactions in laminar flow will be first considered, then the turbulent régime will be envisaged. Both two-dimensional and three-dimensional applications will be presented. We do not pretend to be exhaustive in the compilation of published Navier-Stokes calculations applied to strongly interacting flows. Our primary aim is to illustrate the present status of the approach and to discuss its limitations, especially in the turbulent case where, in addition to specific numerical difficulties due to the existence of regions of very high gradients, one is confronted with the delicate problem of turbulence modeling.

In the presentation that follows, both supersonic and truly hypersonic applications have been retained since there is not a well defined conceptual difference between these two situations. Real gas effects and chemical reactions, which are typical features of hypersonic flows, are still ignored in the calculation of shock-wave/boundary-layer interactions by solution of the Navier-Stokes equations. Furthermore, on a vehicle flying at hypersonic velocities, there exist flow regions where the local Mach number is in fact supersonic.

4.2.4.2 - Navier-Stokes Applications in Laminar Flows

Two-Dimensional Flows. One of the first numerical solutions of the interaction between an incident oblique shock-wave and a laminar boundary-layer was obtained by MacCormack (1971). The integration technique was the well known MacCormack predictor-corrector time marching explicit method which was later on used by many other investigators. The application concerned the shock reflection at a Mach number of 2 experimentally studied by Hakkinen et al. (1959).

The case of a supersonic flow past a two-dimensional compression corner was treated by Carter (1972) who used the two-step explicit scheme of Brailovskaya (1965). Good agreement was obtained with the experimental results of Lewis et al. (1968). Figure 4.1 shows a comparison of the computed wall pressure distribution with that measured in a 10° corner at $M_0 = 4$. The experimental data is both for a flat-plate model (without side plates) and for an axisymmetric model consisting in a cylinder-flare configuration.

Agreement with experiment is not so satisfactory in the case of the interaction occurring at $M_0 = 6.0$ over a 10.25° compression corner, as can be seen in Fig. 4.2. This figure also shows a calculation performed with the Inviscid-Viscous Interactive method of Klineberg and Lees (1969). There is a significant discrepancy between computation and experiment in the separation part of the interaction; downstream of the corner, agreement is better.

Brailovskaya's method was also applied by Hanin et al. (1974) for the computation of an incident-reflecting shock at a Mach number of 2. On the whole, the results were realistic and agreed reasonably well with experiment. Supersonic laminar flows on blunt cones with separation induced by flares were computed by Li (1974) by using the MacCormack method.
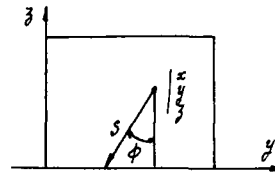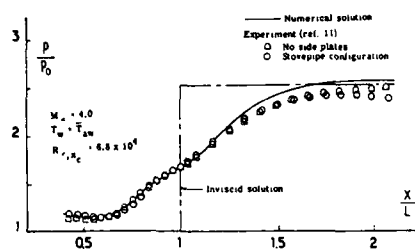
Fig. 4.1   Navier-Stokes Calculation of 2-D Laminar Ramp Flow. Wall Pressure Distribution. First Application (Carter, 1972)
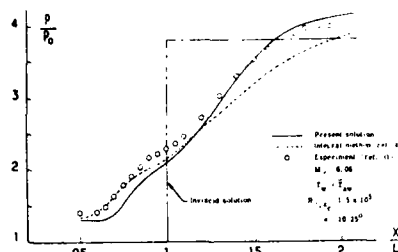
Fig. 4.2   Navier-Stokes Calculation of 2-D Laminar Ramp Flow. Surface Pressure Distribution. Second Application (Carter, 1972)
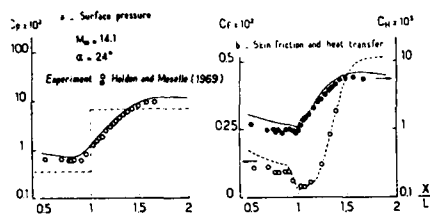
Fig. 4.3   Navier-Stokes Calculation of 2-D Hypersonic Laminar Ramp Flow Without Separation (Hung and MacCormack, 1976)
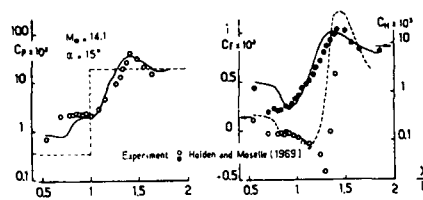
Fig. 4.4   Navier-Stokes Calculation of 2-D Hypersonic Laminar Ramp Flow With Separation (Hung and MacCormack, 1976)

Hung and MacCormack (1976) applied the explicit predictor-corrector method to the calculation of supersonic and hypersonic laminar compression corner flows. Results found at M_0 = 14.1 are presented in Figs. 4.3 and 4.4 where they are compared to Holden's data. When there is no separation at the corner (see Fig. 4.3), agreement between experiment and computation is extremely good as regards both wall pressure, heat transfer and skin-friction distributions. However, for the α = 24° case - for which separation occurs - the general features of the computed results have the correct trend but the extent of separation is underpredicted (see Fig. 4.4). Nevertheless, the plateau pressure and the magnitude and location of the peaks of surface pressure and heat-transfer are correctly predicted.

Oblique shock reflections at relatively low Mach numbers (close to 2) were computed by Li (1977) by using a mixed explicit-implicit numerical method. A shock reflection occurring at M_0 = 7.94 was computed by Hodge (1977) by means of the MacCormack explicit scheme.

Solutions of the Parabolized Navier-Stokes (PNS) equations for a compression corner flow at M_0 = 14.1 were obtained by Lawrence et al. (1986). Their calculations are relative to unseparated flows since a single pass forward marching procedure is used. Agreement with the Holden and Moselle (1969) experiments is extremely good.

Navier-Stokes calculations applied to shock reflection at M_0 = 7.4 have also been performed by Issa and Lockwood (1977) who solved the steady form of these equations by an iterative technique.

Applications of the Lax-Wendroff explicit method to the shock-wave/boundary-layer interaction problem have been carried out by Hussaini et al. (1979) and by Cambier et al. (1988).

Three-Dimensional Flows. The laminar Navier-Stokes equations for the flow developing in a corner have been solved by Shang and Hankey (1977) by employing the MacCormack explicit method. The computed flow field is a three-dimensional oblique shock-wave/boundary-layer interaction produced by a wedge attached normal to a flat surface. This configuration is also called the sharp fin problem.

Fig. 4.5   Coordinate System for 3-D Corner Flow Calculation (Shang and Hankey, 1977)

Fig. 4.6   Navier-Stokes Calculation of 3-D Laminar Corner Flow. Density Contour Map (Shang and Hankey, 1977)

Here the wedge angle is equal to 15°, the freestream Mach number was 12.5 and the Reynolds number, based upon the axial length, was 1.21×10^6. Experimental investigation of this flow shows that the inviscid dominant portion of the flow field is nearly invariant with respect to a generating radius vector from the apex of the corner, regardless of the different scaling of the growth of the viscous region. This feature of the flow field has led to the adoption of the conical co-ordinate system sketched in Fig. 4.5 (a similar system will be adopted for turbulent applications presented in next Section).

Results of Shang and Hankey's calculation are presented in Fig. 4.6 in the form of density contour maps of the three-dimensional flow field. The main features revealed by these maps are the wedge shock-wave, the shock induced by the boundary-layer growth on the flat-plate, the triple point at the intersection of the two shocks and the outer edge of the boundary-layer. Figure 4.7 shows the field resulting from the projection of the conical crossflow velocity component in a vertical plane (Y,Z). In the unperturbated flow region (upper and right portion of the graph) the conical crossflow velocities sensibly converge to the origin of the co-ordinate system. The crossflow velocity component executes a sharp turn towards the corner at the shock-wave generated by the corner. A strong vortex center is clearly visible at a location immediately below the triple point. Agreement of computation with experiment was very good.

The same configuration has been computed by Degrez (1985) for a supersonic Mach number of 2.25 and a Reynolds number of 1.08×10^5. The three-dimensional Navier-Stokes equations were solved by the implicit approximate factorization scheme of Beam and Warming.
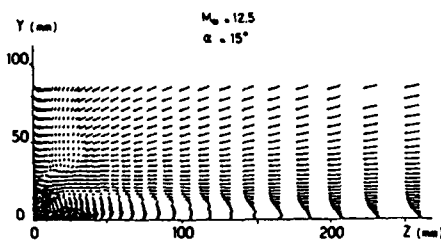
Fig. 4.7   Navier-Stokes Calculation of 3-D Laminar Corner Flow. Crossflow Vector Velocity Plot (Shang and Hankey, 1977)
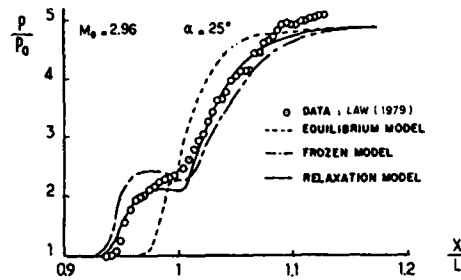
Fig. 4.8   Navier-Stokes Calculation of 2-D Turbulent Ramp Flow. Wall Pressure Distribution (Shang and Hankey, 1975)

4.2.4.3 - Navier-Stokes Applications in Turbulent Flows

Two-Dimensional Flows. The reflection of an oblique shock-wave at a Mach number of 2.96 has been treated by Wilcox (1973) by using a numerical method based upon a generalized form of the explicit time marching finite difference scheme originated by Von Neumann and Richtmeyer. This calculation probably constitutes the first documented solution of turbulent shock-wave/boundary-layer interaction. The turbulent shear-stress was computed by the Saffman transport equation model which has been at the origin of the Wilcox-Rubesin turbulence model presented in Section 4.2.3 above. Agreement with experiment was fair.

The same numerical code and the same turbulence model were then applied to the corner flow problem (Wilcox, 1974). In this case, agreement with experiment deteriorated rapidly when the size of the separated region increased as a consequence of a larger corner angle. According to Wilcox, a possible explanation of the discrepancy could be the assumption of Reynolds stress tensor to be aligned with the mean rate of strain tensor. This assumption becomes particularly questionable if the mean flow streamlines have large curvature as in a supersonic compression corner.

The interaction resulting from an oblique shock reflection has been treated by Baldwin and MacCormack (1974) with the explicit predictor-corrector method. Since, for a hypersonic flow, in the region of reattachment the viscous sublayer becomes an order of magnitude thinner than in the boundary-layer upstream of the interaction, a special treatment was adopted to avoid prohibitive computation times required by a mesh fine enough to resolve the viscous sub-layer. This treatment is based on an iterative solution of the steady state boundary-layer approximation near the wall. Two turbulence models were tested: the Cebeci-Smith algebraic model and the Saffman-Wilcox (1974) transport equation model. Agreement with experiment was only fair.

Incident shock-reflection was treated by Horstman et al. (1975) by using the MacCormack explicit scheme along with the Cebeci-Smith turbulence model incorporating modifications to account for non equilibrium effects (see Section 4.2.3).

Ramp flow calculations were performed by Shang and Hankey (1975) by using the MacCormack explicit scheme along with the Cebeci-Smith turbulence model. Due to the incapacity of this baseline equilibrium model to represent correctly strongly out of equilibrium processes, the authors introduced an history effect by means of the relaxation formula given in Section 4.2.3. As shown in Fig. 4.8, application of the relaxation concept led to a considerable improvement of the prediction in the case of an interaction at a corner at $M_0 = 2.96$. The relaxation distance λ was in fact chosen such that calculation agree with experiment. Thus the main interest of what can be considered as a numerical experiment was to establish clearly the necessity to introduce history effects in the calculation of shock-wave/boundary-layer interactions. Further applications were made to compute shock reflection in supersonic flow (Shang et al., 1976).

The same relaxation turbulence model was applied by Hung and MacCormack (1977) to compute supersonic and hypersonic interacting flows. In these calculations, the Cebeci-Smith turbulence model was used with the relaxation equation of Shang and Hankey. A comparison with experiment is given in Fig. 4.9 which shows the streamwise evolution of the wall pressure and heat-transfer coefficients. The computed case is a compression corner flow at $M_0 = 8.66$ which was experimentally studied by Holden (1972).

The two turbulence models (the baseline equilibrium model and the relaxation model) give reasonably good agreement in surface and heat transfer in the interaction region, although the peak heat transfer at reattachment is underpredicted. Also the computation leads to a sharp decrease in heat-transfer in the separation region (see Fig. 4.9b) whereas the measured heat-transfer rises continuously from the interaction onset and reaches a plateau value in the separated region. As we know, such a rise in heat-transfer
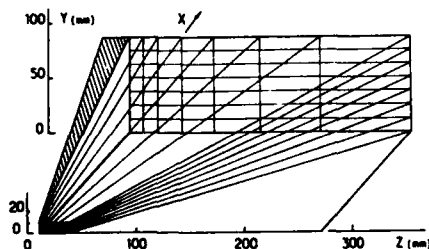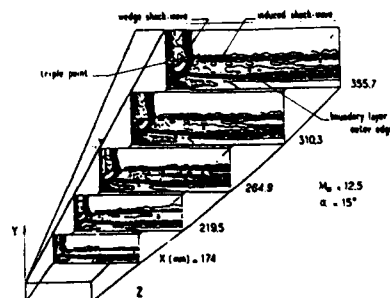
Fig. 4.9 Navier-Stokes Calculation of 2-D Hypersonic Turbulent Ramp flow (Hung and MacCormack, 1977)

at separation is typical of turbulent hypersonic shock-wave/boundary-layer interactions (see Section 3.2.7 above). It is clear that the present turbulence models lead to an unphysical decrease in the eddy-viscosity le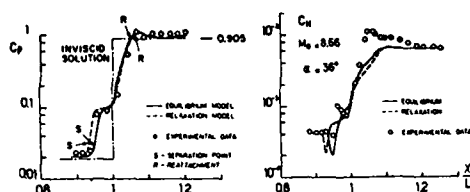vel in the vicinity of the separation point. This behavior is certainly attributable to the inadequacy of the Van Driest damping factor in a region where the wall shear-stress vanishes.

Baldwin and MacCormack (1976) performed the calculation of a shock reflection at hypersonic Mach number (M_0 = 8.47) by using an algebraic turbulence model incorporating a modification of the Van Driest damping function avoiding anomalous behavior at a separation point. Agreement with experiment was fair.

The behavior of several turbulence models in a transonic interaction (M_0 = 1.39) and a hypersonic interaction (M_0 = 6.86) was examined by Viegas and Coakley (1977). The calculations were made with the explicit MacCormack method and the following turbulence models were considered: the baseline Cebeci-Smith model, the Shang-Hankey relaxation model and the Glushko-Rubesin one-transport equation model. It was found that none of these models worked satisfactorily in the hypersonic interaction.

Horstman et al. (1977) performed a critical study of four turbulence models applied to the calculation of a compression corner flow at M_0 = 2.85. These models were the baseline Cebeci-Smith model and variants of this model including history effect plus the Glushko-Rubesin one-transport equation model. The Navier-Stokes equations were solved by using the MacCormack hybrid scheme.

A rather thorough examination of turbulence models in shock-separated boundary-layer interaction flow was carried out by Viegas and Horstman (1978). The four following turbulence models were considered:

i - The Cebeci-Smith equilibrium algebraic model.

ii - The Glushko-Rubesin one-equation model.

iii - The Jones-Launder two-equation model.

iv - The Wilcox-Rubesin two equation model.

Fig. 4.10 Navier-Stokes Calculation of 2-D Turbulent Ramp Flow. Small Separation. Comparison of Different Turbulence Models (Viegas and Horstman, 1978)

Fig. 4.11 Navier-Stokes Calculation of 2-D Turbulent Ramp Flow. Large Separation. Comparison of Different Turbulence Models (Viegas and Horstman, 1978)

The results given by these models were compared to transonic and supersonic shock-wave/boundary-layer interactions. Here we will only consider the supersonic corner flow applications in which the upstream Mach number was equal to 2.8 and the Reynolds number R_{f_0} close to 1.5 x10^5. The surface pressure and skin-friction distributions for α = 20° and α = 24° are represented in Figs. 4.10 and 4.11. Examination of these results leads to the following conclusions:

i - The computations employing the algebraic model predict the qualitative features of the two flowfields reasonably well. The overall pressure rise is predicted well but the locations of the initial pressure rise are not. Also, the computations do not predict a pressure plateau. Considering the skin-friction results, computations predict the separation point well but do not predict the reattachment locations and largely underpredict the skin-friction downstream of reattachment.

ii - The computations employing the one-equation model show no improvement in predicting the pressure distributions. However, the predicted locations of reattachment and downstream skin-friction levels are in better agreement with experiment than they are with the algebraic model.

iii - The computations employing two-equation models give almost identical results except for the magnitude of the skin-friction in the separated region. These computations show the best overall agreement with the experimental pressure distributions. Pressure plateau is predicted for both cases, although the level of the computed plateau is substantially higher than the experimental one, especially in the case of the most separated flow. The predicted skin-friction results show that the forward extent of separation is overpredicted for both flows and the downstream skin-friction levels are overpredicted for the α = 20° case.

The computations performed by Viegas and Horstman demonstrate that the two-equation models are superior for predicting surface pressure distributions and that no model predicts the correct skin-friction distributions although the one- and two-equation models are slightly better than the algebraic model.

Figures 4.12 and 4.13 show a comparison of computed and measured velocity profiles for the same experimental conditions. The algebraic model predictions show general disagreement with experiment and the one-equation model leads to substantial improvement downstream of reattachment. The two-equation models predict too large a retarded flow in the separated region and similar shaped profiles persist far downstream in general disagreement with experiment. This indicates that both two-equation models have too large a memory effect downstream a strong interaction region. Benay et al. (1987) arrived at similar conclusions in transonic shock-wave/boundary-layer interactions.
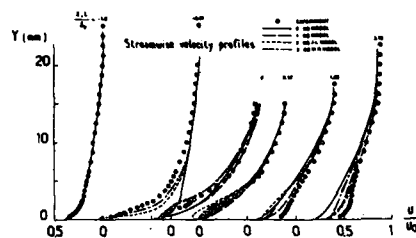
Fig. 4.12 Navier-Stokes Calculation of 2-D Turbulent Ramp Flow. Small Separation. Comparison of Different Turbulence Models (Viegas and Horstman, 1978)
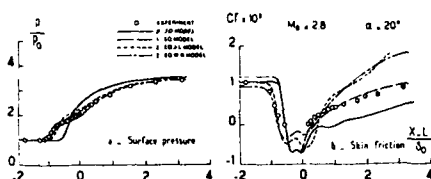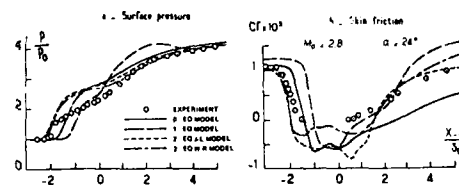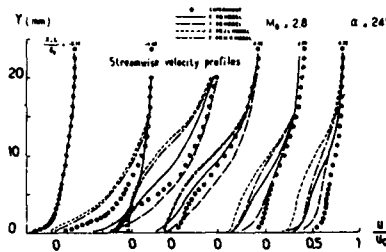

Fig. 4.13 Navier-Stokes Calculation of 2-D Turbulent Ramp Flow. Large Separation. Comparison of Different Turbulence Models (Viegas and Horstman, 1978)
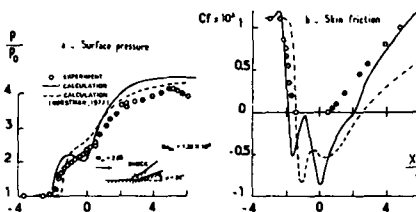
Fig. 4.14 Navier-Stokes Calculation of 2-D Turbulent Ramp Flow. Baldwin and Lomax Turbulence Model (Baldwin and Lomax, 1978)
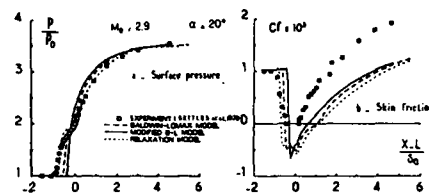
Fig. 4.15 Navier-Stokes Calculation of 2-D Turbulent Ramp Flow. Comparison of Algebraic Turbulence Models (Visbal and Knight, 1984)

Incident shock reflections and compression corner flows were computed by Baldwin and Lomax (1978) by solving the thin-layer approximation of the Navier-Stokes equations. In this paper, the authors introduced the now very popular algebraic model which has been presented in Section 4.2.3.2 above. Figure 4.14 shows a comparison between calculation and experiment in the case of a compression corner flow at $M_0 = 2.85$. One notes that with the Baldwin-Lomax model the calculated region of reversed flow is too large and that the computed wall pressure distribution shows an unrealistic decrease after the pressure rise at separation. The result obtained by Horstman et al. (1977) with their baseline algebraic model is also plotted in Fig. 4.14.

Visbal and Knight (1984) performed Navier-Stokes calculations by considering three variants of the Baldwin-Lomax turbulence model. These models are evaluated by means of detailed comparisons with experimental results for compression ramp flows at $M_0 = 2.9$ and different ramp angles. The governing equations are solved by the implicit Beam-Warming algorithm. Results relative to the ramp angle $\alpha = 20°$ are shown in Fig. 4.15 (the relaxation model is that of Shang and Hankey applied to the Baldwin-Lomax model). As a general rule, all the turbulence models tested fail to predict the rapid recovery of the boundary-layer downstream of reattachment. This is due to the incapacity of these models to simulate the amplification of the turbulence fluctuations across a shock-wave/boundary-layer interaction. In fact this conclusion holds for all the existing turbulence models, even those employing transport equations.

Compression corner flows at $M_0 = 2.85$ were computed by Deese and Agarwal (1985) by using the Baldwin-Lomax turbulence model and the modifications to this model proposed by Visbal and Knight (1984). The governing equations were solved by a Runge-Kutta time stepping scheme.

Ong and Knight (1986) made a comparative study of the hybrid MacCormack and implicit Beam-Warming algorithms for a supersonic compression corner flow. In this numerical study, turbulence was computed by the Baldwin-Lomax model along with the Shang-Hankey relaxation formula.

Numerical simulation of several shock-separated boundary-layer interaction, including compression corner flows and incident-reflecting shocks, have been performed by Peters et al. (1986). The thin-layer approximation of the Navier-Stokes equations was used. The Baldwin-Lomax algebraic model and the Jones-Launder two-equation model have been considered. The governing equations were solved by a numerical procedure based on a finite volume, time-stepping scheme.

To conclude with two-dimensional calculations, we shall now present recent calculations performed by Horstman (1987) for hypersonic interactions occurring at a hollow cylinder-flare junction, compression corners and in the impingement region of an incident shock (see Fig. 4.16). The Navier-Stokes plus turbulence transport equations were solved with the MacCormack explicit-implicit, second order predictor-corrector, finite volume method (MacCormack, 1982). The following turbulence models were considered:

i - The Cebeci-Smith algebraic model.

ii - The Baldwin-Lomax algebraic model.

iii - The compressible version of the original Jones-Launder (k, ε) model.

iv - Three modifications to the Jones-Launder model aimed at representing compressibility effects on turbulence. These modifications are briefly presented here, their justification can be found in Horstman's paper.

- Modification A (MOD A): the term $-\frac{2}{3} C_{\varepsilon_1} \bar{\rho} \, \bar{k} \, div \, \vec{V}$ in the ε-transport equation (Eq. 4.18a) is replaced by:

$$[1 - \frac{2}{3} C_1'] \bar{\rho} \, \bar{k} \, div \, \vec{V} \qquad \text{where } C_1' = 4.5$$

- Modification B (MOD B): this second modification models the additional terms which appear in the turbulent kinetic energy equation after mass averaging. These new terms are:

$$\text{NEW TERMS} = -\overline{u_i'} \, \frac{\overline{\partial \bar{p}}}{\partial x_i} + \overline{u_i'} \, \frac{\partial (\mu S_{ij})}{\partial x_j} + \overline{p' \, \frac{\partial u_i'}{\partial x_i}}$$

After suitable assumptions, the following modelizations are adopted to represent the new terms:

$$\overline{u_i'} = C_{k_1} \, \tilde{u}_k \, \frac{1-1}{n-1} \, \frac{\bar{k}}{\tilde{u}_\ell \, \tilde{u}_\ell} \, M^2$$

$$\overline{p' \, \frac{\partial u_i'}{\partial x_i}} = C_{k_2} \, \frac{n}{\gamma} \, \left(\frac{1-1}{n-1} \right)^t \bar{\rho} \, \bar{k} \, M^2 \, div \, \vec{V}$$

The following values were used for the new constants:

$$n = 1.2 \qquad C_{k1} = 0. \qquad C_{k2} = 0.12$$

Computations were systematically made varying C_{k1} and C_{k2} from 0 to 0.5. The values chosen gave the best agreement with the experimental results.

The new terms multiplied by $C_\varepsilon \left(\frac{\varepsilon}{k} \right)$ are also added to the ε-transport equation (with C = 0.3).

- The third modification C (MOD C) is an attempt to apply a correction for density fluctuations to the mass-averaged turbulent stress terms in the Navier-Stokes equations. The turbulent stresses are given by:

$$\mathcal{T}_{mass. averaged} = -\overline{\rho u_i' u_j'} = -\bar{\rho} \, \overline{u_i' u_j'} - \overline{\rho' u_i' u_j'} + \frac{\overline{\rho u_i'} \cdot \overline{\rho u_j'}}{\bar{\rho}}$$

The assumption is made that the Reynolds stress $-\bar{\rho} \, \overline{u_i' u_j'}$ is the Reynolds stress predicted by the model equations. By making suitable assumptions and neglecting third order correlations an expression for the mass-averaged stress as function of the Reynolds stress can be derived:

$$\mathcal{T}_{mass. averaged} = \frac{\mathcal{T}_{model}}{1 - C \left(\frac{1-1}{n-1} \right)^2 \frac{\bar{k}}{\bar{\gamma}^2} M^2} \qquad \text{with } C = 1.$$

It is to be noticed that the new terms to be added to the (k, ε) equations as well as the correction factor for $\mathcal{T}_{mass. averaged}$ are proportional to Mach number squared.
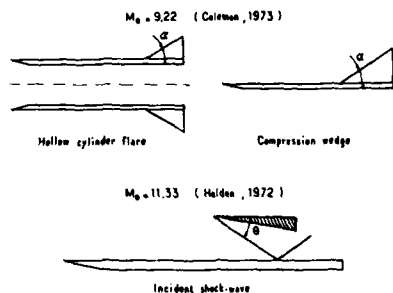
Fig. 4.16 Experimental Hypersonic Test Flows Considered by Horstman (1987)

a . Surface pressure   b . Heat transfer
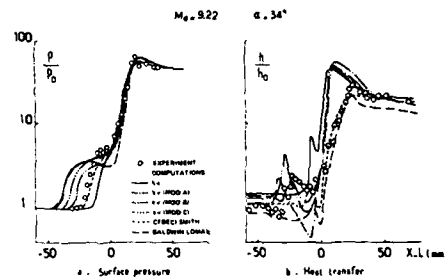
Fig. 4.17 Navier-Stokes Calculation of 2-D Hypersonic Turbulent Ramp Flow. Comparison of Turbulence Models (Horstman, 1987)

Results obtained with these models for a compression corner of angle $\alpha = 34°$ at $M_0 = 9.22$ are presented in Figs. 4.17a and b. Considering the pressure distributions (Fig. 4.17a), the results show that the Cebeci-Smith model gives the best agreement with experiment. The $[k-\varepsilon]$ model predicts too small separation and the other models too large separation. All the modifications to the $[k-\varepsilon]$ model increase the size of the separated zone. No model predicts correctly the heat-transfer distribution (see Fig. 4.17b). In particular, the two-equation models all overpredict the maximum heat-transfer near reattachment while the algebraic models underpredict the maximum heat-transfer.

The results relative to an incident shock giving a primary deflection of 15° at $M_0 = 11.33$ are shown in Figs. 4.18a and b. The surface pressure comparisons with experiment show that each model gives a different separation length. However, in this case modifications B and C of the (k, ε) model lead to a better agreement with experiment than the other models and the Cebeci-Smith results are now one of the worst. The heat-transfer comparisons lead to conclusions similar to those relative to wedge results.

Fig. 4.18 Navier-Stokes Calculation of 2-D Hypersonic Turbulent Shock Reflection. Comparison of Turbulence Models (Horstman, 1987)

Fig. 4.19 Navier-Stokes Calculation of 2-D Hypersonic Turbulent Ramp Flow. Prediction of Peak Heat-Transfer. Comparison of Turbulence Models (Horstman, 1987)

As we know, one of the most important features of hypersonic shock-wave/boundary-layer interaction is the peak heat-transfer near reattachment. This quantity is represented in Figs. 4.19a and b for the compression wedge flow and the hollow cylinder-flare flow. In general, the (k, ε) model and its modifications all predict a variation with α of the peak heat-transfer too low for attached flow (small α) and too large for separated flow (high α). The algebraic models do a better job in predicting the trends with increasing α.

Three-Dimensional Flows. There exists a relatively large number of applications of the Navier-Stokes approach to predict turbulent shock-wave/boundary-layer interaction in three-dimensional flows.

The flow produced by a sharp fin has been computed by Hung and MacCormack (1978) who used the hybrid MacCormack scheme to solve the governing equations. Eddy-viscosity was computed by the three-dimensional extension of the Escudier model. Calculations were executed for $M_0 = 5.9$ and two values of the wedge angle: $\alpha = 6°$ and $\alpha = 12°$. No example of results will be presented here, the overall computed flowfield being similar to that obtained in laminar flow.

The same problem was treated by Horstman and Hung (1979) with the same turbulence model. Comparisons were made with experiments performed at $M_0 = 3$ by Oskam et al. (1976).

The sharp fin configuration has also been considered by Knight (1985) who used the Baldwin-Lomax eddy-viscosity model. A special hybrid explicit-implicit numerical algorithm incorporating the explicit method of MacCormack and the implicit box-scheme of Keller is employed to solve the governing equations. Calculations were executed for an upstream Mach number close to 3. Fair agreement with experiment was observed.

The same numerical method was used by Gaitonde and Knight (1988) to compute a sharp fin configuration at $M_0 = 3$ and fin angle $\alpha = 20°$. The Baldwin-Lomax model was used but with a modified form of the Van Driest damping factor allowing the representation of bleed effect.

In this application also, fair agreement with experiment was observed.

Fig. 4.20 Navier-Stokes Calculation of Blunt Fin Turbulent Flow. Surface Pressure Distributions (Hung and Kordulla, 1983)

Fig. 4.21 Navier-Stokes Calculation of Blunt Fin Turbulent Flow. Particle Path in the Plane of Symmetry (Hung and Kordulla, 1983)

The case of a blunt fin was treated by Hung and Kordulla (1983). The governing equations were solved by using a finite volume version of the implicit-explicit method of MacCormack. Shear-stress was computed by the Baldwin-Lomaw model modified to account for the presence of the generator wall (see the model of Hung and MacCormack presented in Section 4.2.3.5). Comparisons of the results with the experimental data of Dolling and Bogdonoff (1982) are shown in Fig. 4.20 and 4.21. Surface pressures along the flat plate and along the fin surface are shown. It can be inferred from these comparisons that the scale of the interaction including its upstream influence on the incoming flow and its height relative to the incoming boundary-layer thickness are probably predicted quite well, although no flowfield data are available to verify such a conclusion. The predicted particle paths which represent streamlines in the plane of symmetry are shown in Fig. 4.21 to illustrate the resolution of the flow detail within the horseshoe vortex. A secondary flow forms at the junction between the blunt fin and the plate. The separation region formed by the horseshoe vortex is open and the vortex streams around the blunt fin.

Similar results concerning the same blunt fin at same flow conditions are reported by Hung and Buning (1985).

The case of a sweptback blunt fin (see sketch in Fig. 4.22) was treated by McMaster and Shang (1988). The Baldwin-Lomax turbulence model is used and the governing equations are solved by the explicit MacCormack method. Calculations were performed at M_0 = 2.98 for several values of the sweptback angle Λ. The skin-friction line patterns computed for Λ = 30°, 45°, 60° and 68° are shown in Figs. 4.23a to d. For values of Λ smaller than 68° a distinctive separation line is visible ahead of the fin. The distance of this line to the obstacle decreases when Λ increases, the separation line becoming inexistent for Λ = 68°. These results show that sweptback of the fin reduces the upstream influence of the flowfield and simultaneously weakens the horseshoe vortex which forms ahead of the fin when separation occurs. The calculation reproduces faithfully the real flow features. There is also a good quantitative agreement between computed and measured pressure distributions on the plate supporting the fin.

Calculations of configurations in which a three-dimensional shock-wave separates a two-dimensional turbulent boundary-layer were performed by Kussoy et al. (1980). The hybrid MacCormack scheme was employed along with a turbulence model similar to the Cebeci-Smith algebraic model.
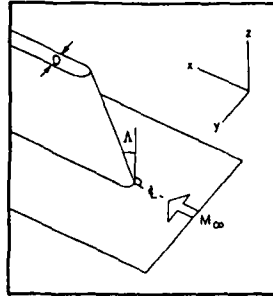
Fig. 4.22   The Swept Back Blunt Fin Case Treated by McMaster and Shang (1988)
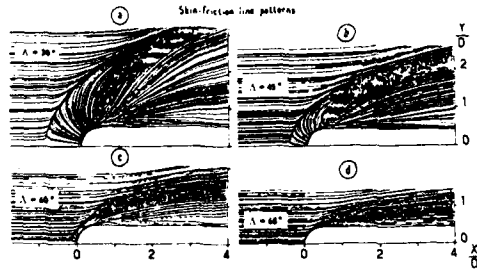
Fig. 4.23   Navier-Stokes Calculation of Swept Back Blunt Fin Turbulent Flow. Skin-Friction Line Patterns (McMaster and Shang, 1988)
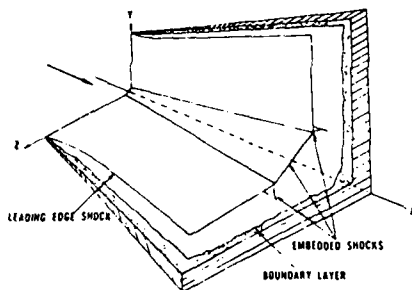
Fig. 4.24   Two Wedge Intersection. Schematic Representation of Flowfield.
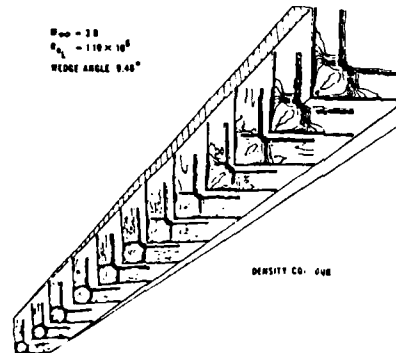
Fig. 4.25   Navier-Stokes Calculation of Two Wedge Intersection. Density Contour for the Entire Field (Shang et al., 1979)
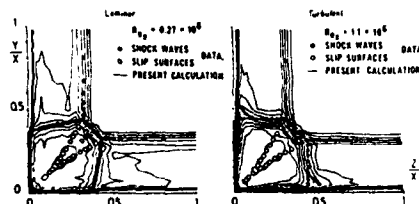
Fig. 4.26   Navier-Stokes Calculation of Two Wedge Intersection. Shock-Wave System for Laminar and Turbulent Flow. Density Contour (Shang et al., 1979)

Shang et al. (1979) have computed the flow developing at the corner formed by the intersection of two wedges for M_0 = 3. The main features of this kind of flow are schematically represented in Fig. 4.24 which shows the two shocks generated by the wedges, the triple points and embedded shocks resulting from interference of the two wedge shocks. The calculation is started in laminar, at the corner origin, and transition is introduced via an empirical model. In the turbulent part of the flow, a three dimensional adaptation of the Cebeci-Smith turbulence model is used. The basic numerical method is the explicit MacCormack scheme.

The shock-wave structure of the entire flowfield represented by density contours is shown in Fig. 4.25. One notes the intersecting wedge shock-waves and the set of triple points formed by further intersection of the embedded shock waves. Secondary features, such as the slip surfaces are also observable in some of these density contours. As the flow progresses downstream, undergoing transition from laminar to turbulent, the shock-wave system readjusts itself to accommodate the distinctive change in length scale. Two shock-wave structure and the associated slip surfaces are represented in Fig. 4.26 for laminar and turbulent conditions. Good agreement is observed between the computed and experimental values in the location of shock-waves, triple points and slip surfaces. The calculation shows the reduction in the size of the embedded lambda shock systems as the interaction length scale decreases from laminar to turbulent flow.

To conclude this Section, we will mention the calculations of Shang and MacCormack (1983) of the flow over a biconic configuration with an afterbody compression ramp. The Baldwin-Lomax model was used to compute shear-stress. This work was in fact a comparative study of the MacCormack explicit and implicit numerical schemes.

5 - CONCLUSION

Shock intersections and shock-wave/boundary-layer interactions play an important role in hypersonic flows where they can be at the origin of large local heat transfer and loss of control effectiveness resulting from separation at control surfaces.

Shock intersections lead to various wave patterns according to the relative directions and strengths of the two meeting shocks. Six types of shock interference pattern are thus recognized. Among these six types, types III and IV may result in the most damaging consequences for the vehicle. These two types of interference patterns occur when a weak oblique shock intersect a strong nearly normal shock. Then, intense shear-layers or jets are created which, when striking the vehicle, give rise to very high heat-transfer rates, well in excess of those existing at a nose stagnation point or alo[n] a leading edge.

The scaling laws as well as the flowfield physics of two-dimensional shock-wave/boundary-layer interactions are now well established due to the abundance of experimental results relative to this case. Thus, the existing correlation laws can be sufficient for estimating peak heat transfer at reattachment or for predicting incipient shock-induced separation. Nevertheless, detailed and reliable information on the mean-velocity field and turbulence properties in hypersonic interactions is extremely scarce. Such an information is urgently needed to help in turbulence modeling and to validate theoretical models.

As concerns three-dimensional interactions, the situation is still far from being so satisfactory. The structure of these flows can be extremely complex and is difficult to understand. In particular, if the surface flow properties are generally well established from surface pressure measurements and oil flow patterns, the outer field organization is most often purely conjectural because of the complete lack of field measurements at high Mach numbers.

Due to spectacular progress in computational fluid dynamics, shock interference and shock-wave/boundary-layer interaction can now be computed by solving the Navier-Stokes equations. Very encouraging results are obtained both for 2-D and 3-D flows. However, in the turbulent case, the problem of modeling the turbulent terms in the time averaged Navier-Stokes equations is far from being satisfactorily solved. Most of the present hypersonic applications use models which are simple extension to compressible flows of models developed for incompressible or weakly compressible flows. In fact, compressibility effects introduce in the averaged equations new correlation terms involving density fluctuations which can no longer be ignored in hypersonic applications. Modeling of these terms, when it is done, it still very crude due to the nearly complete lack of experimental data. In this field too, there is place for future investigations.

6 - REFERENCES

ALBER, I.E. (1971) "Similar Solutions for a Family of Separated Turbulent Boundary-Layers". AIAA Paper N° 71-203

BACK, L.H. and CUFFEL, R.F. (1976) "Shock-Wave/Turbulent Boundary-Layer Interactions With and Without Surface Cooling". AIAA Journal, Vol. 14, N° 4, pp. 526-532 (April 1976)

BALDWIN, B.S. and MacCORMACK, R.W. (1974) "Numerical Solution of the Interaction of a Strong Shock-Wave with a Hypersonic Turbulent Boundary-Layer ". AIAA Paper N° 74-558 (June 1974)

BALDWIN, B.S.; MacCORMACK, R.W. and DEIWERT, G.S. (1975) "Numerical Techniques for Compressible Navier-Stokes Equations and Implementation of Turbulence Models". AGARD LS N° 73

BALDWIN, B.S. and MacCORMACK, R.W. (1976) "Modifications of the Law of the Wall and Algebraic Turbulence Modeling for Separated Boundary-Layers". AIAA Paper n° 76-350 (July 1976)

BALDWIN, B.S. and LOMAX, H. (1978) "Thin Layer Approximation and Algebraic Model for Separated Turbulent Flows". AIAA Paper N° 78-0257 (Jan 1978)

BATHAM, J.P. (1972) "An Experimental Study of Turbulent Separating and Reattaching Flows at a High Mach Number". J. Fluid Mech., Vol. 52, Part 3, pp. 425-435

BENAY, R.; COET, M.C. and DELERY, J. (1987) "Validation of Turbulence Models Applied to Transonic Shock-Wave/Boundary-Layer Interaction". La Recherche Aérospatiale, N° 1987-3, pp. 1-16

BECKWITH, I.E. and BUSHNELL, D.M. (1968) "Detailed Description an Results of a Method for Computing Mean and Fluctuating Quantities in Turbulent Boundary-Layers". NASA TN D-4815

BIRCH, S.F. and RUDY, D.H. (1975) "Mean Flowfield and Surface Heating Produced by Unequal Shock Interactions at Hyperson[ic] Speeds". NASA TN D-8092 (Dec. 1975)

BIRD, G.A. (1963) "Effect of Wave Interactions on Pressure Distributions in Supersonic and Hypersonic Flow". AIAA Journal, Vol. 1, N°XX, pp. 634-639

BOGDONOFF, S.M. and KEPLER, E.C. (1954) "Separation of a Supersonic Turbulent Boundary-Layer". Princeton University, Dept. of Aero. Eng., Report 249 (Jan 1954)

BRAILOVSKAYA, I. Yu. (1965) "A Difference Scheme for Numerical Solution of the Top-Dimensional, Nonstationary Navier-Stokes Equations for a Compressible Gas". Sov. Phys., Doklady, Vol. 10, N° 2, pp. 107-110 (Aug. 1965)

BRAMLETTE, T.T. (1974) "Simple Technique for Predicting Type III and IV Shock Interference". AIAA Journal, Vol. 12, N° 8, pp. 1151-1152 (Aug. 1974)

BUSHNELL, D.M. and WEINSTEIN, L.M. (1968) "Correlation of Peak Heating for Reattachment of Separated Flows". J. Spacecraft and Rockets, Vol.5, N° 9, pp. 1111-1112 (Sept. 1968)

CAMBIER, L.; COUAILLIER, V. and VEUILLOT, J.-P. (1988) "Résolution numérique des équations de Navier-Stokes à l'aide d'une méthode multigrille". La Recherche Aérospatiale, N° 1988-2

CARRIERE, P.; SIRIEIX, M. and SOLIGNAC, J.-L. (1968) "Propriétés de similitude des phénomènes de décollement laminaires ou turbulents en écoulement supersonique non uniforme". 12th Int. Cong. of Applied Mech., Stanford University (Aug. 1968) and ONERA TP N° 659F

CARTER, J.E. (1972) "Numerical Solutions of the Navier-Stokes Equations for the Supersonic Laminar Flow over a Two-dimensional Compression Corner". NASA TR R-385; see also: Lecture Notes in Physics, Vol. 19, pp. 69-78 (1973)

CEBECI, T.; SMITH, A.M.O. and MOSINSKIS, G. (1970) "Calculation of Compressible Adiabatic Turbulent Boundary-Layers". AIAA Journal, Vol. 8, N° 11, pp. 1974-1982

CEBECI, T. and SMITH, A.M.O. (1974) Analysis of Turbulent Boundary-Layers, Academic Press, New-York

CERESUELA, R. and COULOMB, J. (1969) "Etudes théoriques et expérimentales de l'efficacité de gouvernes en hypersonique". 6ème Colloque d'Aérodynamique Appliquée de l'AFITAE, Toulouse, France

CHAPMAN, D.R.; KUEHN, D.M; and LARSON, H.K. (1957) "Investigation of Separated Flow in Supersonic and Subsonic Streams with Emphasis on the Effect of Transition". NACA TN-3869

CHEN, Y.S. (1986) "Application of a New Wall Function to Turbulent Flow Computations". AIAA Paper N° 86-0438 (Jan. 1986)

CHIENG, C.C. and LAUNDER, B.E. (1980) "On the Calculation of Turbulent Heat Transport Downstream from an Abrupt Pipe Expansion". Numerical Heat Transfer, Vol. 3, pp. 189-207

CHRISTOFEL, R.G. (1974) "Two-Dimensional Shock-Wave/Boundary-Layer Interactions". AFFDL-TR-74-152

CHUNG, P.M. and VIEGAS, J.R. (1961) "Heat Transfer at the Reattachment Zone of Separated Laminar Boundary-Layers". NASA TN D-1072

COET, M.-C. (1988) Private Communication

CRAWFORD, D.H. (1979) "Some Recent Developments in the Prediction of Shock Interaction Phenomena at Hypersonic Speeds". NASA TM 80115 (Oct. 1979)

CROCCO, L. and LEES, L. (1952) "A Mixing Theory for the Interaction Between Dissipative Flows and Nearly Isentropic Stream". JAS, Vol. 19, N° 10, pp. 649-676 (Oct. 1952)

CURLE, N. (1961) "The Effect of Heat-Transfer on Laminar Boundary-Layer Separation in Supersonic Flow". Aero. Quart., Vol. 12 (Nov. 1961)

DEESE, J.E. and AGARWAL, R.K. (1985) "Shock/Turbulent Boundary-Layer Interaction in a Compression Corner". AIAA Paper N° 85-1567 (July 1985)

DEGREZ, G. (1985) "Computation of Three-Dimensional Skewed Shock-Wave/Laminar Boundary-Layer Interaction". AIAA Paper N° 85-1565 (July 1985)

DEGREZ, G.; BOCCADORO, C.H. and WENDT, J.F. (1987) "The Interaction of an Oblique Shock-Wave with a Laminar Boundary-Layer Revisited. An Experimental and Numerical Study". J. Fluid Mech., Vol. 177, pp. 247-263 (April 1987)

DEIWERT, G.S. (1975) "Computation of Separated Transonic Turbulent Flows". AIAA Paper N°75-829 (1975)

DELERY,J. and MASURE, B. (1969) "Action d'une variation brusque de pression sur une couche limite turbulente et application aux prises d'air hypersoniques". La Recherche Aérospatiale, N° 129, pp. 3-12

DELERY, J. (1970) "Examen des phénomènes d'interaction choc-couche limite dans un canal interaubes". ONERA NT-2-7078AY (Feb. 1970)

DELERY, J. and MARVIN, J.G. (1986) Shock-Wave/Boundary-Layer Interactions AGARDograph N° 280 (Feb. 1986)

DELERY, J. and LACAU, R.G. (1987) "Prediction of Base-Flows". AGARD-FDP-VKI Special Course on Missile Aerodynamics

DOLLING, D.S. and BOGDONOFF, S.M. (1981) "An experimental Investigation of the Unsteady Behavior of Blunt Fin Induced Shock-Wave Boundary-Layer Interactions". AIAA Paper N° 81-1287 (June 1981)

DON GRAY, J. (1967) "Investigation of the Effect of Flare and Ramp Angle on the Upstream Influence of Laminar and Transitional Reattaching Flows from Mach 3 to 7". AEDC-TR-66-190 (Jan. 1967)

DON GRAY, J. and RHUDY, R.W. (1973) "Effects of Blunting and Cooling on Separation of Laminar Supersonic Flow". AIAA Journal, Vol. 11, N° 9, pp. 1296-1301 (Sept. 1973)

EDNEY, B. (1968) "Anomalous Heat-Transfer and Pressure Distributions on Blunt Bodies at Hypersonic Speeds in the Presence of an Impinging Shock". FFA Report N° 115

ELFSTROM, G.M. (1971) "Turbulent Separation in Hypersonic Flow". Imperial College Aero Report 71-16 (Sept. 1971)

ELFSTROM, G.M. (1972) "Turbulent Hypersonic Flow at a Wedge Compression Corner". J. Fluid Mech., Vol. 53, Part 1, pp. 113-129 (May 1972)

ESCANDE, B. and CAMBIER, L. (1985) "Turbulence Modeling in Transonic Interactions". IUTAM Symposium on Turbulent Shear-Layer/Shock-Wave Interactions, Ed. J. Délery, Springer-Verlag

FAVRE, A. (1965) "Equations des gaz turbulents compressibles". Journal de Mécanique, Vol. 4, N° 3, pp. 361-421 (Sept. 1965)

GADD, G.E.; HOLDER, D.W. and REGAN, J.D. (1954) "An Experimental Investigation of the Interaction Between Shock-Waves and Boundary-Layers". Proc. Roy. Soc., Ser. A, Vol. 226, pp.227-253

GADD, G.E.; COPE, W.F. and ATTRIDGE, J.L. (1960) "Heat-Transfer and Skin-Friction Measurements at a Mach Number of 2.44 for a Turbulent Boundary-Layer on a Flat Surface and in Regions of Separated Flow". ARC TR 3148

GAITONDE, D. and KNIGHT, D. (1988) "Numerical Experiments on the 3-D Shock-Wave/Boundary-Layer Interaction Generated by a Sharp Fin". AIAA Paper N° 88-0309 (Jan. 1988)

GESSNER, F.B. (1973) "The Origin of Secondary Flow in Turbulent Flow along a Corner". J. of Fluid Mech., Vol. 58, pp. 1-25

GINOUX, J.J. (1969) "On Some Properties of Reattaching Laminar and Transitional High Speed Flows". VKI TN N° 53 (Sept. 1969)

GINOUX, J.J. and MATTHEWS, R.D. (1974) "Effect of Shock Impingement on Heat-Transfer. Part II". VKI TN N° 96 (Feb. 1974)

GLOWACKI, W.J. and CHI, S.W. (1974) "A Study of the Effect of Pressure Gradient on the Eddy Viscosity and Mixing Length for Incompressible Equilibrium Turbulent Boundary-Layer". NOLTR 74-105 (May 1974)

GLUSHKO, G.S. (1965) "Turbulent Boundary-Layer on a Flat Plate in an Incompressible Fluid". Bull. Acad. Sci. USSR, Mech. Ser., N°4, pp.13-23

GORSKI, J.J. (1986) "A New Near Wall Formulation for the k- Equations of Turbulence". AIAA Paper N°86-0556 (Jan. 1986)

GORSKI, J.J.; OTA, D.K. and CHAKRAVARTHY, S.R. (1987) "Calculation of Three-Dimensional Cavity Flow Fields". AIAA Paper N° 87-0117 (Jan 1987)

GREEN, J.E. (1969) "Interactions Between Shock Waves and Turbulent Boundary Layers". RAE TR-69098 (May 1969); see also: Progress in Aerospace Sciences, Pergamon Press, Vol. 11, pp. 235-340 (1970)

GUPTA, R.N. (1983) "Turbulence Modeling of Flowfields with Massive Surface Ablation". Journal of Spacecraft, Vol. 20, N° 6, pp. 531-538 (Nov.-Dec. 1983)

HAINS, F.D. and KEYES, J.W (1972) "Shock Interference Heating in Hypersonic Flows". AIAA Journal, Vol. 10, N° 11, pp. 1441-1447 (Nov. 1972)

HAKKINEN, R.J.; GREBER, I., TRILLING, L. and ABARBANEL, S.S. (1959) "The Interaction of an Oblique Shock-Wave with a Laminar Boundary-Layer". NASA Memo 2-18-59W (March 1959)

HA-MINH, H. and VANDROMME, D. (1985) "Modelling of Compressible Turbulent Flows: Present Possibilities and Perspectives". IUTAM Symposium on Turbulent Shear-Layer/Shock-Wave Interactions, Ed. J. Délery, Springer-Verlag

HANIN, M.; WOLFSHTEIN, M. and LANDAU, U.E. (1974) "Numerical Solution of Navier-Stokes Equations for Interaction of Shock-Wave with Laminar Boundary-Layer". ICAS Paper N° 74-17 (Aug. 1974)

HANJALIC, K. and LAUNDER, B.E. (1972) "A Reynolds Stress Model of Turbulence and Its Application to Thin Shear Flows". J. Fluid Mech., Vol. 52, Part 4, pp. 609-638

HAYAKAWA, K. and SQUIRE, L.C. (1982) "The Effect of the Upstream Boundary-Layer State on the Shock Interaction at a Compression Corner" J. Fluid Mech., Vol. 122, pp. 369-394

HODGE, B.K. (1977) "Prediction of Hypersonic Laminar Boundary-layer/Shock-Wave Interactions". AIAA Journal, Vol. 15, N° 7, pp. 903-904 (July 1977)

HOLDEN, M.S. (1966) "Experimental Studies of Separated Flows at Hypersonic Speed. II : Two-Dimensional Wedge Separated Flow Studies". AIAA Journal, Vol. 4, N° 5, pp. 790-799 (May 1966)

HOLDEN, M.S. (1969) "Theoretical and Experimental Studies of the Shock-Wave/Boundary-Layer Interaction on Curved Compression Surfaces". Proc. of the Symp. on Viscous Interaction Phenomena in Supersonic and Hypersonic Flows, Univ. of Dayton Press

HOLDEN, M.S. and MOSELLE, J.R. (1969) "Theoretical and Experimental Studies of the Shock-Wave/Boundary-Layer Interaction on Compression Surfaces in Hypersonic Flows". CALSPAN Report AF-2410-A-1 (Oct. 1969)

HOLDEN, M. S. (1972) "Shock-Wave/Turbulent Boundary-Layer Interactions in Hypersonic Flow". AIAA Paper N° 72-74 (Jan. 1972)

HOLDEN, M.S. (1974) "Experimental Studies of Shock-Wave/Boundary-Layer Interactions". VKI LS 62 on Laminar and Turbulent Separation Includ:ng Three-Dimensional Effects

HOLDEN, M.S. (1977) "Shock-Wave/Turbulent Boundary-Layer Interaction in Hypersonic Flow". AIAA Paper N° 77-45 (Jan 1977)

HOLDEN, M.S. (1978) "A Study of Flow Separating in Regions of Shock-Wave/Boundary-Layer Interaction in Hypersonic Flow". AIAA Paper N° 78-1169 (July 1978)

HOLDEN, M.S. (1984) "Experimental Studies of Quasi-Two-Dimensional and Three-Dimensional Viscous Interaction Regions Induced by Skewed-Shock and Swept-Shock Boundary-Layer Interaction". AIAA Paper n° 84-1677

HOLDEN, M.S. (1986) "A Review of Aerothermal Problems Associated with Hypersonic Flight". AIAA Paper N° 86-0267 (Jan. 1986)

HOLLOWAY, P.F.; STERRETT, J.R. and CREEKMORE, H.S. (1965) "An Investigation of Heat-Transfer Within Regions of Separated Flow at a Mach Number of 6.0". NASA TN D-3074

HORSTMAN, C.C.; KUSSOY, M.I., COAKLEY, T.J., RUBESIN, M.W. and MARVIN, J.G. (1975) "Shock-Wave-Induced Turbulent Boundary-Layer Separation at Hypersonic Speeds". AIAA Paper N° 75-4 (Jan. 1975)

HORSTMAN, C.C. (1976) "A Turbulence Model for Nonequilibrium Adverse Pressure Gradient Flows". AIAA Paper N° 76-412 (July 1976); see also: AIAA Journal, Vol. 15, N° 2, pp. 131-132 (Feb. 1977)

HORSTMAN, C.C.; SETTLES, G.S.; VAS, I.E.; BOGDONOFF, S.M. and HUNG, C.M. (1977) "Reynolds Number Effect on Shock-Wave/Turbulent Boundary-Layer Interactions". AIAA Journal, Vol. 15, N° 8, pp. 1152-1158 (Aug. 1977)

HORSTMAN, C.C. and HUNG, C.M. (1979) "Computation of Three-Dimensional Turbulent Separated Flows at Supersonic Speeds". AIAA Journal, Vol. 17, N° 11, pp. 1155-1156 (Nov. 1979)

HORSTMAN, C.C. (1987) "Prediction of Hypersonic Shock-Wave/Turbulent Boundary-Layer Interaction Flow". AIAA Paper N° 87-1367 (June 1987)

HUNG, F.T. (1973) "Interference Heating due to Shock-Wave Impingement on Laminar Boundary Layers". AIAA Paper, N° 73-678 (July 1973)

HUNG, F.T. and BARNETT, D.O. (1973) " Shock Wave - Boundary-Layer Interference Heating Analysis". AIAA Paper N° 72-237 (Jan 1973)

HUNG, C.M. and MacCORMACK, R.W. (1976) "Numerical Solutions of Supersonic and Hypersonic Laminar Compression Corner Flows". AIAA Journal, Vol. 14, N° 4, pp. 475-481 (April 1976)

HUNG, C.M. and MacCORMACK, R.W. (1977) "Numerical Simulation of Supersonic and Hypersonic Turbulent Compression Corner Flows". AIAA Journal, Vol. 15, N° 3, pp. 410-416 (March 1977)

HUNG, C.M. and MacCORMACK (1978) "Numerical Solution of Three-Dimensional Shock Wave and Turbulent Boundary-layer Interaction". AIAA Journal, Vol. 16, N° 10, pp. 1090-1096 (Oct. 1978)

HUNG, C.M. and KORDULLA, W. (1983) "A Time Split Finite Volume Algorithm for Three-Dimensional Flow Simulations". AIAA Paper N° 83-1957

HUNG, C.M. and BUNING, P.G. (1985) "Simulation of Blunt-Fin-Induced Shock-Wave and Turbulent Boundary-Layer Interaction". J. Fluid Mech., Vol. 154, pp. 163-185 (May 1985)

HUSSAINI, M.Y.; SANKARA RAO, K. and PUROHIT, S.C. (1976) "Numerical Study of Two-Dimensional Laminar Boundary-Layer/Shock-Wave Interaction". Journal of Aero. Soc. of India, Vol. 28, N° 3, pp. 297-307 (Aug. 1976)

ISSA, R.I. and LOCKWOOD, F.C. (1977) "On the Prediction of Two-Dimensional Supersonic Viscous Interactions Near Walls". AIAA Journal, Vol. 15, N° 2, pp. 182-188 (Feb. 1977)

JOHNSON, C.B. and KAUFMAN, L.G. II (1974) "Interference Heating from Interactions of Shock-Waves with Turbulent Boundary-layers at Mach 6". NASA TN D-7649 (1974)

JOHNSON, C.B. and KAUFMAN, L.G. II (1975) "Incident Shock Interactions with Boundary-Layers". J. Spacecraft and Rockets, Vol. 12, N°6, pp. 327-328 (June 1975)

JOHNSON, D.A. and KING, L.S. (1984) "A New Turbulence Closure Model for Boundary-Layer Flows with Strong Adverse Pressure Gradients ans Separation". AIAA Paper N° 84-0175 (Jan. 1984)

JOHNSON, D.A. (1985) "Predictions of Transonic Separated Flow with an Eddy-Viscosity/Reynolds-Shear Stress Closure Model". AIAA Paper N° 85-1683 (July 1985); see also: AIAA Journal, Vol. 25, N° 2, pp. 252-259 (Feb. 1987)

JONES, W.P. and LAUNDER, B.E. (1971) "The Prediction of Laminarization with a Two-Equation Model of Turbulence". Int. Journal of Heat and Mass Transfer, Vol. 15, pp. 301-314 (1971)

KEYES, J.W., GOLDBERG, T.J. and EMERY, J.C. (1968) "Turbulent Heat-Transfer Associated with Control Surfaces at Mach 6". AIAA Journal, Vol. 6, N° 8, pp. 1612-1613 (Aug. 1968)

KEYES, J.W. and MORRIS, D.J. (1972) "Correlation of Peak Heating in Shock Interference Regions at Hypersonic Speeds". J. of Spacecraft and Rockets, Vol. 9, N°8, pp. 621-623

KEYES, J.W. and HAINS, F.D. (1973) "Analytical and Experimental Studies of Shock-Interference Heating in Hypersonic Flows". NASA TN D-7139 (May 1973)

KILBURG, R.F. and KOTANSKY, D.R. (1969) "Experimental Investigation of the Interaction of a Plane Oblique Incident-Reflecting Shock-Wave with a Turbulent Boundary-Layer on a Cooled Surface". NASA CR-66-841

KLINEBERG, J.M. and LEES, L. (1969) "Theory of Laminar Viscous-Inviscid Interactions in Supersonic Flow". AIAA Journal, Vol. 7, N° 12, pp. 2211-2221 (Dec. 1969)

KLOPFER, G.H. and YEE, H.C. (1988) "Viscous Hypersonic Shock-on-Shock Interactions on Blunt Cowl Lips". AIAA Paper N° 88-0233 (Jan. 1988)

KNIGHT, D.D. (1985) "Calculation of Three-Dimensional Shock/Turbulent Boundary-Layer Interaction Generated by Sharp Fin". AIAA Journal, Vol. 23, N° 12, pp. 1885-1891 (Dec. 1985)

KOLMOGOROV, A.N. (1942) "Equations of a Turbulent Motion of an Incompressible Fluid". Izv. Akad. Nauk. USSR, Ser. flz VI, n° 1-2, pp. 56-58

KORGEGI, R.H. (1971) "Survey of Viscous Interactions Associated with High Mach Number Flight". AIAA Journal, Vol. 9, N° 5, pp. 771-784 (May 1971)

KUEHN, D.M. (1959) "Experimental Investigation of the Pressure Rise Required for the Incipient Separation of Turbulent Boundary-Layers in Two-Dimensional Supersonic Flow". NASA Memo 1-21-59 A (Feb. 1959)

KUEHN, D.M. (1961) "Turbulent Boundary-Layer Separation Induced by Flares on Cylinder at Zero Angle of Attack". NASA TR-R117

KUSSOY, M.I.; VIEGAS, J.R. and HORSTMAN (1980) "Investigation of a Three-Dmensional Shock Wave Separated Turbulent Boundary-Layer". AIAA Journal, Vol. 18, N° 12, pp. 1477-1484 (Dec. 1980); see also: AIAA Paper N° 80-0002 (Jan. 1980)

LAUNDER, B.E. (1971) "An Improved Algebraic Stress Model". Imperial College, Mech. Eng. Dept., Report TM/TN/A8

LAUNDER, B.E.; REECE, G.J. and RODI, W. (1975) "Progress in the Development of a Reynolds Stress Turbulence Closure". J. of Fluid Mech., Vol. 68, Part 3, pp. 537-566

LAW, C.H. (1974) "Supersonic, Turbulent Boundary-Layer Separation". AIAA Journal, Vol. 12, N° 6, pp. 794-797 (June 1974)

LAW, C.H. (1976) "Supersonic Shock-Wave/Turbulent Boundary-Layer Interactions". AIAA Journal, Vol. 14, N° 6, pp. 730-734 (June 1976)

LAWRENCE, S.L.; TANNEHILL, J.C. and CHAUSSEE, D.S. (1986) "An Upwind Algorithm for the Parabolized Navier-Stokes Equations". AIAA Paper N° 86-1117 (May 1986)

LE BALLEUR, J.-C. and DELERY, J. (1973) "Etude expérimentale de l'effet de la réflexion d'une onde de choc sur la transition de la couche limite". Congrès Français de Mécanique, Poitiers (France), 17-20 Sept. 1973; see also: La Recherche Aérospatiale N° 1974-3, pp. 164-173 (May 1974)

LE BALLEUR, J.-C. (1987) "Viscous Inviscid Interaction Solvers and Computation of Highly Separated Flows". Studies of Vortex Dominated Flows, Chapter 3, pp. 158-192, Springer-Verlag

LEBLANC, R. (1976) "Recent Progress in Shock-Wave/Boundary-Layer Interaction". VKI, LS-84 on Transonic Blade to Blade Flow in Axial Turbomachinery (Feb. 1976)

LEWIS, J.E.; KUBOTA, T. and LEES, L. (1967) "Experimental Investigation of Supersonic Laminar Two-Dimensional Boundary-Layer Separation in a Compression Corner With and Without Cooling". AIAA Paper N° 67-191 (Jan. 1967; see also: AIAA Journal, Vol. 6, N°1, pp. 7-14 (Jan. 1968)

LI, C.P. (1974) "A Numerical Study of Laminar Flow Separation on Blunt Flared Cones at Angle of Attack". AIAA Paper N° 74-585 (June 1974)

LI, C.P. (1977) "A Numerical Study of Separated Flows Induced by Shock-Wave/Boundary-Layer Interaction". AIAA Paper N° 77-168 (Jan. 1977)

LIGHTHILL, M.J. (1953) "On Boundary-Layers Upstream Influence. II: Supersonic Flows Without Separation".Proc. Roy. Soc., A 217, pp. 478-507

McMASTER, D.L. and SHANG, J.S. (1988) "A Numerical Study of Three-Dimensional Separated Flows Around a Sweptback Blunt Fin". AIAA Paper N° 88-0125 (Jan. 1988)

MacCORMACK, R.W. (1971) "Numerical Solutions of the Interaction of a Shock-Wave with a Laminar Boundary-Layer". Lecture Notes in Physics, Vol. 8, pp. 151-163, Springer-Verlag

MacCORMACK, R.W. (1982) "A Numerical Method for Solving the Equations of Compressible Viscous Flow". AIAA Journal, Vol. 20, N°9, pp. 1275-1281 (Sept. 1982)

MARVIN, J.G. (1977) "Turbulence Modeling for Compressible Flows". NASA TM X-73,188 (Jan. 1977)

MARVIN, J.G. (1982) "Turbulence Modeling for Computational Aerodynamics". AIAA Paper N° 82-0164 (Jan. 1982); see also: AIAA Journal, Vol. 21, N°7, pp. 941-955 (July 1983)

MATEER, P.G.; BROSH, A. and VIEGAS, J.R. (1976) "A Normal Shock-Wave Turbulent Boundary-Layer Interaction at Transonic Speeds". AIAA Paper N° 76-161 (Jan 1976)

MICHEL, R.; QUEMARD, C. and DURANT, R. (1969) "Application d'un schéma de longueur de mélange à l'étude des couches limites d'équilibre". ONERA Note Technique N° 154

MILLER, D.S.; HIJMAN, R. and CHILDS, M.E. (1964) "Mach 8 to 22 Studies of Flow Separations Due to Deflected Control Surfaces". AIAA Journal, Vol. 2, N° 2, pp. 312-321 (Feb. 1964)

NEEDHAM, D.A. (1965) "A Heat-Transfer Criterion for the Detection of Incipient Separation in Hypersonic Flow". AIAA Journal, Vol. 3, N° 4, pp. 781-783 (April 1965)

NEEDHAM, D.A. and STOLLERY, J.L. (1966) "Boundary-Layer Separation in Hypersonic Flow". AIAA Paper N° 66-455 (June 1966)

NEEDHAM, D.A. (1967) "A Note on Hypersonic Incipient Separation". AIAA Journal, Vol. 5, N° 12, pp. 2284-2285 (Dec. 1967)

NESTLER, D.E. (1973) "Engineering Analysis of Re-Attaching Shear-Layer Heat-Transfer". AIAA Journal, Vol. 11, N° 3, pp.390-392 (March 1973)

ONG, C. and KNIGHT, D. (1986) "A Comparative Study of the Hybrid MacCormack and Implicit Beam-Warming Algorithms for a Two-Dimensional Supersonic Compression Corner". AIAA Paper N° 86-0204 (Jan. 1986)

OSKAM, B.; VAS, I.E. and BOGDONOFF, S.M. (1976) "Mach 3 Oblique Shock-wave/Turbulent Boundary-Layer Interactions in Three Dimensions". AIAA Paper N° 76-336 (July 1976)

PEAKE, D.J. and TOBAK, M. (1980) "Three-Dimensional Interactions and Vortical Flows with Emphasis on High Speeds". AGARDograph N° 252 (July 1980)

PETERS, G.R.; AGARWALL, R.K. and DEESE, J.E. (1986) "Numerical Simulation of Several Shock-Separated Boundary-Layer Interaction Flows Using Zero- and Two-Equation Turbulence Models". AIAA Paper N° 86-0248 (Jan. 1986)

PEYRET, R. and VIVIAND, H. (1975) "Computation of Viscous Compressible Flows Based on the Navier- Stokes Equations"AGARDograph N° 212

POPINSKI, Z. and EHRLICH, C.F. (1966) "Development Design Methods for Predicting Hypersonic Aerodynamic Control Characteristics". AFFDL-TR-66-85 (Sept. 1966)

PUTNAM, L.E. (1965) "Investigation of Effects of Ramp Span and Deflection Angle on Laminar Boundary-Layer Separation at M = 10.03". NASA TN D-2833

RESHOTKO, E. and TUCKER, M. (1955) "Effect of a Discontinuity on Turbulent Boundary-Layer Thickness Parameters with Application to Shock Induced Separation". NACA TN-3454

RODI, W. (1972) "The Prediction of Free Boundary-Layers by Use of a Two Equation Model of Turbulence". Ph. D. Thesis, University of London

ROSHKO, A. and THOMKE, G.J. (1969) "Supersonic Turbulent Boundary-Layer Interaction with a Compression Corner at Very High Reynolds Number". Mc Donnell Douglas, Paper 10163 (May 1969)

ROSHKO, A. and THOMKE, G.J. (1974) "Flare Induced Interaction Lengths in Supersonic, Turbulent Boundary-Layers". McDonnell Douglas, MDAC Paper WD 2416 (Dec. 1974); see also: AIAA Journal, Vol. 14, N°7, pp. 873-879 (July 1976)

ROTTA, J. (1951) "Statistische Theorie nicht-homogener Turbulenz, 1". Titteilung, Zeitschrift fuer Physik, Vol. 129, pp. 547-572

RUBESIN, M.W. (1976) "A One Equation Model of Turbulence for Use with the Compressible Navier-Stokes Equations". NASA TM X-73-128 (April 1976)

RUBESIN, M.W. and ROSE, W.C. (1973) "The Turbulent Mean-Flow, Reynolds-Stress and Heat-Flux Equations in Mass-Averaged Dependent Variables". NASA TM X- 62-248 (March 1973)

SAFFMAN, P.G. and WILCOX, D.C. (1974) "Turbulence Model Predictions for Turbulent Boundary-Layers". AIAA Journal, Vol. 12, N° 4, pp. (April 1974)

SETTLES, G.S. and BOGDONOFF, S.M. (1973) "Separation of a Supersonic Turbulent Boundary-Layer at Moderate to High Reynolds Numbers". AIAA Paper N° 73-666 (July 1973)

SETTLES, G.S (1975) "An Experimental Study of Compressible Turbulent Boundary-Layer Separation at High Reynolds Number". Ph. D. Thesis, Princeton University (Sept. 1975)

SETTLES, G.S.; FITZPATRICK, T.J. and BOGDONOFF, S.M. (1978) "A Detailed Study of Attached and Separated Compression Corner Flowfields in High Reynolds Number Supersonic Flow". AIAA Paper N° 78-1167 (July 1978); see also: AIAA Journal, Vol. 17, N° 6, pp. 579-585 (June 1979)

SFEIR, A.A. (1969) "Supersonic Laminar Boundary-Layer Separation Near a Compression Corner". University of California at Berkeley, Aeronautical Sciences Division, Report N° AS-69-6 (March 1969)

SHANG, J.S. and HANKEY, W.L. Jr (1975) "A Numerical Method for Solving the Navier-Stokes Equations with Application to Shock Boundary-Layer Interactions". AIAA Paper N° 75-1 (Jan. 1975)

SHANG, J.S. and HANKEY, W.L. Jr (1975) "Numerical Solution for Supersonic Turbulent Flow over a Compression Ramp". AIAA Journal, Vol. 13, N° 10, pp. 1368-1374 (Oct. 1975)

SHANG, J.S.; HANKEY, W.L. Jr. and LAW C.H. (1976) "Numerical Simulation of Shock-Wave/Turbulent Boundary-Layer Interaction". AIAA Journal, Vol. 14, N° 10, pp. 1451-1457 (Oct. 1976)

SHANG, J.S. and HANKEY, W.L. (1977) "Numerical Solution of the Navier-Stokes Equations for a Three-Dimensional Corner". AIAA Journal, Vol. 15, N° 11, pp. 1575-1582 (Nov. 1977)

SHANG, J.S.; HANKEY, W.L. and PETTY, J.S. (1979) "Three-Dimensional Supersonic Interacting Turbulent Flow Along a Corner". AIAA Journal, Vol. 17, N° 7, pp. 706-713 (July 1979)

SHANG, J.S. and MacCORMACK, R.W. (1983) "Flow Over a Biconic Configuration with an Afterbody Compression Flap - A Comparative Numerical Study". AIAA Paper N° 83-1668 (July 1983)

SHIRAZI, S.A. and TRUMAN, C.R. (1987) "Comparison of Algebraic Turbulence Models for PNS Predictions of Supersonic Flow Past a Sphere-Cone". AIAA Paper N° 87-0544 (Jan. 1987)

SPAID, F.W. and FRISHETT, J.C. (1972) "Incipient Separation of a Supersonic, Turbulent Boundary-Layer, Including Effects of Heat-Transfer". AIAA Journal, Vol. 10, N° 7, pp. 915-922 (July 1972)

STANEWSKI, E. (1973) "Shock-Boundary-Layer Interaction in Transonic and Supersonic Flows". VKI, LS-59 on Transonic Flow in Turbomachinery (May 1973)

STERRETT, J.R. and HOLLOWAY, P.F. (1964) "On the Effects of Transition on Parameters within a Separated Region at Hypersonic Speeds, with Emphasis on Heat-transfer". Symposium on Fully Separated Flows, ASME, New-York

STEWARTSON, K. and WILLIAMS, P.G. (1969) "Self-Induced Separation". Proc. Roy. Soc., A 312, pp. 181-206

STOLLERY, J.L. and BATES, L. (1974) "Turbulent Hypersonic Viscous Interaction". J. Fluid Mech., Vol. 63, Part 3, pp. 145-156

STOLLERY, J.L. (1975) "Laminar and Turbulent Boundary-Layer Separation at Supersonic and Hypersonic Speeds". AGARD-CP-169

SULLIVAN, P.A. (1963) "Hypersonic Flow Over Slender Double Wedge". AIAA Journal, Vol. 1, N° 8, pp. 1927-1928 (Aug. 1963)

TANNEHILL, J.C.; HOLST, T.L. and RAKICH, J.V. (1976) "Numerical Computation of Two-Dimensional Viscous Blunt Body Flows with an Impinging Shock". AIAA Journal, Vol. 14, N°2, pp. (Feb. 1976)

VANDROMME, D. and HA MINH, H. (1985) "Physical Analysis of Turbulent Boundary-Layer/Shock-Wave Interactions Using Second Order Closure Predictions". IUTAM Symposium on Turbulent Shear-Layer/Shock-Wave Interactions, Ed. J. Délery, Springer-Verlag

VIEGAS, J.R. and COAKLEY, T.J. (1977) "Numerical Investigation of Turbulence Models for Shock Separated Boundary-Layer Flows". AIAA Paper N° 77-44 (Jan. 1977)

VIEGAS, J.R. and HORSTMAN, C.C. (1978) "Comparison of Multiequation Turbulence Models for Several Shock-Separated Boundary-Layer Interaction Flows". AIAA Paper N° 78-1165 (July 1978); see also: AIAA Journal, Vol. 17, N° 8, pp. 811-820 (Aug. 1979)

VISBAL, M. and KNIGHT, D. (1984) "The Baldwin-Lomax Turbulence Model for Two-Dimensional Shock-Wave/Boundary-Layer Interactions". AIAA Journal, Vol. 22, NO 7, pp. 921-928 (July 1984)

WATSON, E.C.; MURPHY, J.D. and ROSE, W.C. (1969) "Investigations of Laminar and Turbulent Boundary-Layer Interacting with Externally Generated Shock-Waves". NASA TN D-5512

WIETING, A.R. and HOLDEN, M.S. (1978) "Experimental Study of Shock-Wave Interference Heating on a Cylindrical Leading Edge at Mach 6 and 8". AIAA Paper N° 87-1511 (June 1987)

WILCOX, D.C. (1973) "Calculation of Turbulent Boundary-Layer Shock-Wave Interaction". AIAA Journal, Vol. 11, N° 11, pp. 1592-1594 (Nov. 1973)

WILCOX, D.C. (1974) "Numerical Study of Separated Turbulent Flows". AIAA Paper N° 74-584 (June 1974)

WILCOX, D.C. and TRACI, R.M. (1976) "A Complete Model of Turbulence". AIAA Paper N° 76-351

WILCOX, D.C. and RUBESIN, M.W. (1980) "Progress in Turbulence Modeling for Complex Flow Fields Including the Effect of Compressibility". NASA TP-1517

ZUKOSKI, E.E. (1967) "Turbulent Boundary-Layer Separation in Front of a Forward Facing Step". AIAA Journal, Vol. 5, N° 10, pp. 1746-1753 (Oct. 1967)

q-5-2

REPORT DOCUMENTATION PAGE

1. Recipient's Reference	2. Originator's Reference	3. Further Reference	4. Security Classification of Document
	AGARD-R-761	ISBN 92-835-0515-8	UNCLASSIFIED

5. Originator	Advisory Group for Aerospace Research and Development North Atlantic Treaty Organization 7 rue Ancelle, 92200 Neuilly sur Seine, France

6. Title	AEROTHERMODYNAMICS OF HYPERSONIC VEHICLES

7. Presented at	the von Kármán Institute, Rhode-Saint-Genèse, Belgium on 30 May—3 June 1988

8. Author(s)/Editor(s)	9. Date
Various	June 1989

10. Author's/Editor's Address	11. Pages
Various	336

12. Distribution Statement	This document is distributed in accordance with AGARD policies and regulations, which are outlined on the Outside Back Covers of all AGARD publications.

13. Keywords/Descriptors

Hypersonic flow	Chemical reactions
Computation	Aerothermodynamics
Shock waves	Measurement

14. Abstract

This AGARD Fluid Dynamics Panel/von Kármán Institute Special Course was inspired by new ventures in the hypersonic domain moving forward on both sides of the Atlantic-HERMES in Europe and the NASP (X-30) in the United States.

Following the review of basic principles including real gas effects, a series of lectures were presented on experimental and computational methods specific to hypersonic flows. Stress was placed on measurement techniques developed primarily for flows with heat transfer, chemical reactions, strong shocks, compressible boundary layers, etc. Both surface measurements and flow field measurements including species concentration techniques, were discussed. The same spirit governed the lecture on computational methods: stress was placed on the new problems in CFD posed by high speeds and chemical reactions. The course finished with state-of-the-art reviews on three critical flow problems: transition to turbulence, interactions between shocks and boundary layers, and shock/shock impingement. This Special Course was co-sponsored by the AGARD Fluid Dynamics Panel and the von Kármán Institute for Fluid Dynamics. It was conducted at the von Kármán Institute from May 30—June 3 1988.

AGARD Report No.761	AGARD-R-761
Advisory Group for Aerospace Research and Development, NATO	Hypersonic flow
AEROTHERMODYNAMICS OF HYPERSONIC VEHICLES	Computation
Published June 1989	Shock waves
336 pages	Chemical reactions
	Aerothermodynamics
	Measurement

This AGARD Fluid Dynamics Panel/von Kármán Institute Special Course was inspired by new ventures in the hypersonic domain moving forward on both sides of the Atlantic — HERMES in Europe and the NASP (X-30) in the United States.

Following a review of basic principles including real gas effects, a series of lectures were presented on experimental and computational methods specific to hypersonic flows.

P.T.O

AGARD Report No.761	AGARD-R-761
Advisory Group for Aerospace Research and Development, NATO	Hypersonic flow
AEROTHERMODYNAMICS OF HYPERSONIC VEHICLES	Computation
Published June 1989	Shock waves
336 pages	Chemical reactions
	Aerothermodynamics
	Measurement

This AGARD Fluid Dynamics Panel/von Kármán Institute Special Course was inspired by new ventures in the hypersonic domain moving forward on both sides of the Atlantic — HERMES in Europe and the NASP (X-30) in the United States.

Following a review of basic principles including real gas effects, a series of lectures were presented on experimental and computational methods specific to hypersonic flows.

P.T.O

AGARD Report No.761	AGARD-R-761
Advisory Group for Aerospace Research and Development, NATO	Hypersonic flow
AEROTHERMODYNAMICS OF HYPERSONIC VEHICLES	Computation
Published June 1989	Shock waves
336 pages	Chemical reactions
	Aerothermodynamics
	Measurement

This AGARD Fluid Dynamics Panel/von Kármán Institute Special Course was inspired by new ventures in the hypersonic domain moving forward on both sides of the Atlantic — HERMES in Europe and the NASP (X-30) in the United States.

Following a review of basic principles including real gas effects, a series of lectures were presented on experimental and computational methods specific to hypersonic flows.

P.T.O

AGARD Report No.761	AGARD-R-761
Advisory Group for Aerospace Research and Development, NATO	Hypersonic flow
AEROTHERMODYNAMICS OF HYPERSONIC VEHICLES	Computation
Published June 1989	Shock waves
336 pages	Chemical reactions
	Aerothermodynamics
	Measurement

This AGARD Fluid Dynamics Panel/von Kármán Institute Special Course was inspired by new ventures in the hypersonic domain moving forward on both sides of the Atlantic — HERMES in Europe and the NASP (X-30) in the United States.

Following a review of basic principles including real gas effects, a series of lectures were presented on experimental and computational methods specific to hypersonic flows.

P.T.O

Stress was placed on measurement techniques developed primarily for flows with heat transfer, chemical reactions, strong shocks, compressible boundary layers, etc. Both surface measurements and flow field measurements, including species concentration techniques, were discussed. The same spirit governed the lecture on computational methods: stress was placed on the new problems in CFD posed by high speeds and chemical reactions. The course finished with state-of-the-art reviews on three critical flow problems: transition to turbulence, interactions between shocks and boundary layers, and shock/shock impingement. This Special Course was co-sponsored by the AGARD Fluid Dynamics Panel and the von Kármán Institute for Fluid Dynamics. It was conducted at the von Kármán Institute from May 30—June 3 1988.

ISBN 92-835-0515-8

Stress was placed on measurement techniques developed primarily for flows with heat transfer, chemical reactions, strong shocks, compressible boundary layers, etc. Both surface measurements and flow field measurements, including species concentration techniques, were discussed. The same spirit governed the lecture on computational methods: stress was placed on the new problems in CFD posed by high speeds and chemical reactions. The course finished with state-of-the-art reviews on three critical flow problems: transition to turbulence, interactions between shocks and boundary layers, and shock/shock impingement. This Special Course was co-sponsored by the AGARD Fluid Dynamics Panel and the von Kármán Institute for Fluid Dynamics. It was conducted at the von Kármán Institute from May 30—June 3 1988.

ISBN 92-835-0515-8

Stress was placed on measurement techniques developed primarily for flows with heat transfer, chemical reactions, strong shocks, compressible boundary layers, etc. Both surface measurements and flow field measurements, including species concentration techniques, were discussed. The same spirit governed the lecture on computational methods: stress was placed on the new problems in CFD posed by high speeds and chemical reactions. The course finished with state-of-the-art reviews on three critical flow problems: transition to turbulence, interactions between shocks and boundary layers, and shock/shock impingement. This Special Course was co-sponsored by the AGARD Fluid Dynamics Panel and the von Kármán Institute for Fluid Dynamics. It was conducted at the von Kármán Institute from May 30—June 3 1988.

ISBN 92-835-0515-8

Stress was placed on measurement techniques developed primarily for flows with heat transfer, chemical reactions, strong shocks, compressible boundary layers, etc. Both surface measurements and flow field measurements, including species concentration techniques, were discussed. The same spirit governed the lecture on computational methods: stress was placed on the new problems in CFD posed by high speeds and chemical reactions. The course finished with state-of-the-art reviews on three critical flow problems: transition to turbulence, interactions between shocks and boundary layers, and shock/shock impingement. This Special Course was co-sponsored by the AGARD Fluid Dynamics Panel and the von Kármán Institute for Fluid Dynamics. It was conducted at the von Kármán Institute from May 30—June 3 1988.

ISBN 92-835-0515-8